NATO Science for Peace and Security Series - B:
Physics and Biophysics

Nanoscience and Nanotechnology in Security and Protection against CBRN Threats

Edited by
Plamen Petkov
Mohammed Essaid Achour
Cyril Popov

Springer

NATO OTAN

This publication is supported by:

The NATO Science for Peace and Security Programme

Nanoscience and Nanotechnology in Security and Protection against CBRN Threats

NATO Science for Peace and Security Series

This Series presents the results of scientific activities supported through the framework of the NATO Science for Peace and Security (SPS) Programme.

The NATO SPS Programme enhances security-related civil science and technology to address emerging security challenges and their impacts on international security. It connects scientists, experts and officials from Alliance and Partner nations to work together to address common challenges. The SPS Programme provides funding and expert advice for security-relevant activities in the form of Multi-Year Projects (MYP), Advanced Research Workshops (ARW), Advanced Training Courses (ATC), and Advanced Study Institutes (ASI). The NATO SPS Series collects the results of practical activities and meetings, including:

Multi-Year Projects (MYP): Grants to collaborate on multi-year R&D and capacity building projects that result in new civil science advancements with practical application in the security and defence fields.

Advanced Research Workshops: Advanced-level workshops that provide a platform for experts and scientists to share their experience and knowledge of security-related topics in order to promote follow-on activities like Multi-Year Projects.

Advanced Training Courses: Designed to enable specialists in NATO countries to share their security-related expertise in one of the SPS Key Priority areas. An ATC is not intended to be lecture-driven, but to be intensive and interactive in nature.

Advanced Study Institutes: High-level tutorial courses that communicate the latest developments in subjects relevant to NATO to an advanced-level audience.

The observations and recommendations made at the meetings, as well as the contents of the volumes in the Series reflect the views of participants and contributors only, and do not necessarily reflect NATO views or policy.

The series is published by IOS Press, Amsterdam, and Springer, Dordrecht, in partnership with the NATO SPS Programme.

Sub-Series

A.	Chemistry and Biology	Springer
B.	Physics and Biophysics	Springer
C.	Environmental Security	Springer
D.	Information and Communication Security	IOS Press
E.	Human and Societal Dynamics	IOS Press

- http://www.nato.int/science
- http://www.springeronline.com
- http://www.iospress.nl

Series B: Physics and Biophysics

Nanoscience and Nanotechnology in Security and Protection against CBRN Threats

edited by

Plamen Petkov
Department of Physics
University of Chemical Technology &
Metallurgy
Sofia, Bulgaria

Mohammed Essaid Achour
Université Ibn-Tofail
Kénitra, Morocco

and

Cyril Popov
Institute of Nanostructure Technologies and Analytics
University of Kassel
Kassel, Germany

Published in Cooperation with NATO Emerging Security Challenges Division

Proceedings of the NATO Advanced Research workshop on Functional Nanostructures and Sensors for CBRN Defence and Environmental Safety and Security Chisinau, Moldova
4–17 May 2018

ISBN 978-94-024-2017-3 (PB)
ISBN 978-94-024-2044-9 (HB)
ISBN 978-94-024-2018-0 (eBook)
https://doi.org/10.1007/978-94-024-2018-0

Published by Springer,
P.O. Box 17, 3300 AA Dordrecht, The Netherlands.

www.springer.com

Printed on acid-free paper

Preface

The ever-increasing challenges regarding the security and protection of the modern society, for example, for *early detection and defence against chemical, biological, radiological and nuclear (CBRN) agents*, in *information technology and cyber defence*, in *biotechnology,* in *energy storage and conversion*,, need solutions employing the up-to-date achievements of *Nanoscience and Nanotechnology*. Novel functional materials, techniques, devices and systems allowing control of the matter on atomic and molecular levels, i.e. at the level of the matter building blocks, have to face the new security requirements. The nanostructured materials possess unique mechanical, electrical, optical, magnetic and biological properties, which are entirely different from those of the conventional micro- or millimetre sized materials, due to their distinctive sizes and shapes, and predominant surface and quantum effects determining their behaviour. In such a sense, the *Nanoscience* and *Nanotechnology* have a strong potential to be the main driving forces in the development of *novel concepts for security and safety*. It concerns not only the preparation and investigation of smart nanosized materials for different applications, such as quantum dots, nanotubes, graphene, nanowires, nanoparticles and nanocomposites, but also the combination of their performance with ICs, micro- and nano-optics, MEMS and NEMS, leading to higher level of integration and effective processing and transmission. Only the common efforts of scientists from different fields of research – chemistry, physics, biology, materials science and engineering – and from different countries can bring the complimentary expertise in the development of reliable conceptions in the security and protection against CBRN threats taking the advantages of the *Nanoscience and Nanotechnology*.

The first objective of the *NATO ASI on Nanoscience and Nanotechnology in Security and Protection against CBRN Threats* was to present to the participants the up-to-date achievements for applications of nanomaterials and nanotechnologies in different fields related to security and protection against CBRN agents and the future

perspectives and trends. The second objective was the teaching and training of the participants in the scientific and technological background of nanostructured materials used in fields, such as new generation of advanced sensors and systems for early detection of CBRN threats, efficient defence against these agents, etc. The third objective addressed the initiation of trans-border and interdisciplinary collaborations between young scientists towards the implementation of the recent nanotechnological achievements to meet the emerging security challenges. The overall objective of the ASI was the transfer of competence in the nanomaterials and nanotechnological advances in different fields of security and the networking between young scientists from NATO and Partner countries in order to meet one of the key priorities of the *NATO Science for Peace and Security Programme*.

The ASI covered topics connected with the recent achievements in different fields of security taking the advantages of Nanoscience and Nanotechnology – from synthesis and characterization of nanostructures from various material systems (carbon-based, glasses, ceramics, polymers, etc.) via their application in sensors with different detection principles to real-time CBRN monitoring and analysis. The *lectures* were given by outstanding scientists from universities and research institutes who are experts in nanoscience-related security fields. Sixteen *thematic seminars* on specific topics, not covered by the lectures, were also included in the programme. Three *poster sessions* were held in the afternoons, during which the participants presented their results, established closer contacts and discussed in less formal atmosphere.

Seventy eight participants from 14 NATO Countries (Bulgaria, Canada, Czech Republic, Germany, Italy, Latvia, Poland, Portugal, Romania, Slovak Republic, Spain, Turkey, UK, USA) and 6 Partner countries (Egypt, Jordan, Moldova, Morocco, North Macedonia, Ukraine) insured that the overall objective of transfer of competence and technology in the field of nanostructured materials and nanotechnologies was reached on a high level. Such events contribute to the scientific collaborations in these advanced fields of research between NATO and Partner countries as well as to the promotion of Nanoscience and Nanotechnology in the Partner countries. The latter objective was successfully reached by the participation of 26 scientists from Partner countries. More than half of the 78 attendees were female reflecting the increased role of the women in these fields of research.

The ASI demonstrated once again the commitment of NATO to the peace and the security by facilitating the scientific dialogue and cooperation, which was the major outcome of the meeting. It revealed that the top-leading fields of civil science are currently playing and will play also in the future a strategic role to address all emerging security challenges. Furthermore, the ASI exhibited the strength and effectiveness of modern science as a tool for international dialogue and supported the exchange of information and ideas on the recent development of Nanoscience and Nanotechnology directed to different security challenges.

We, the members of the Organizing Committee, would like to thank the NATO Science Committee for the financial support for the organisation of the ASI. The local organisation of the ASI was actively supported by the City Council of Sozopol, which we gratefully acknowledge. Finally, we cordially acknowledge the technical support of Dr. Blagovesta Popova, Universität Göttingen, Germany, for the preparation of this book.

In Memoriam Wilhelm Kulisch

During the preparation of this Advanced Study Institute, Dr. Wilhelm Kulisch passed away in the age of 61. Wilhelm was a good friend, an excellent physicist and a brilliant editor and writer. With him, we came to the idea in 2003 to organize an Advanced Study Institute. Since then he took an active part in the preparation and organization of five ASIs. His experience and erudition were inestimable for the composition of the programmes, for structuring the books of abstracts and, especially, for the edition of the ASI books. To a great extent we owe him the success of these books, being among the most downloaded in the ASI series. Therefore, we would like to devote this volume to Wilhelm.

Sofia, Bulgaria — Plamen Petkov
Kenitra, Morocco — Mohammed Essaid Achour
Kassel, Germany — Cyril Popov
February 2020

Plamen Petkov
Mohammed Essaid Achour
Cyril Popov

Sofia – Kenitra - Kassel, February 2020

Group photo of NATO Advanced Study Institute on Nanoscience and Nanotechnology in Security and Protection against CBRN Threats

Contents

Part VI Nanowires and Nanoparticles

Part VII Nanocomposites

Part VIII Polymer-Based Materials

Part I
General Topics

Chapter 1
Cyber-Physical Systems to Counter CBRN Threats – Sensing Payload Capabilities in Aerial Platforms for Real-Time Monitoring and Analysis

Ashok Vaseashta, Surik Kudaverdyan, Stepan Tsaturyan, and Nimet Bölgen

Abstract In the new and transformative era, our surrounding environments are increasingly connected through exponential growth of cyber-physical systems (CPS) and interactive intelligent technologies. One such example includes technological innovations in Unmanned Aerial Surveillance Platforms, also known as drones, for applications such as surveillance, real-time monitoring, emergency augmentation for actionable response, security and enabler of connected communities to bring about new levels of opportunity and growth, safety and security, health and wellness, thus improving the overall quality of life. Based on our previous experiences, we present a modality of smart and connected sensors platforms that have a great potential to provide enhanced situational awareness for safety and security. The objective of this investigation is to develop a mobile Unmanned Aerial Surveillance Platform (UASP) capable of monitoring in real-time, capturing, synthesizing and analyzing the information and allowing communication with ground-based systems for actionable response. Several commercial off the shelf (COTS) instruments such as hyperspectral imagers, Light Detection and Ranging (LIDAR), Laser-induced Breakdown Spectroscopy (LIBS) and Biometrics Facial Recognitions systems are discussed along with some innovative platforms that are still in experimental stages

A. Vaseashta (✉)
ICWI, Manassas, VA and NJCU – A State University of New Jersey, Jersey City, NJ, USA

Engineering Faculty, Chemical Engineering Department, Mersin University, Mersin, Turkey
e-mail: prof.vaseashta@ieee.org

S. Kudaverdyan
Optical Communication Systems Lab. Armenian National Polytechnic University, Yerevan, Armenia

S. Tsaturyan
CEO, ApolloBytes, Yerevan, Armenia

N. Bölgen
Engineering Faculty, Chemical Engineering Department, Mersin University, Mersin, Turkey

P. Petkov et al. (eds.), *Nanoscience and Nanotechnology in Security and Protection against CBRN Threats*, NATO Science for Peace and Security Series B: Physics and Biophysics, https://doi.org/10.1007/978-94-024-2018-0_1

and can potentially serve as payload to the unmanned aerial vehicle (UAV) sensor platforms. The new system under development has an airborne component to capture relevant information from a Domain of Interest (DoI). This paper summarizes the capabilities of UASP along with several potential applications and potential risk scenarios of such smart and connected by internet of everything (IOET) systems.

Keywords CBRN · Cyber-physical systems · Decision support tools · Stand-off detection · UAVs · Connected systems · Safety · Security · Monitoring · Critical infrastructure · Situational awareness · Internet of everything

1.1 Introduction

The present geo-political landscape is far more complex than ever before. International security remains as one of the top 10 primary global challenges [1]. Hybrid and kinetic threat vectors, such as those arising from chemical, biological, radiological and nuclear materials pose a wide spectrum of challenges. A paradigmatic shift in strategy is quintessential to counter such kinetic and hybrid threat vectors. In the new era of transformative progress using exponential growth of cyber-physical systems and interactive-intelligent technologies, our surrounding environments are increasingly complex and connected. Based on our previous experience, we present a modality of smart and connected sensors-based platforms that demonstrate potential of providing enhanced situational awareness for safety and security. Our earlier systems are capable of (a) monitoring environmental pollution using a GIS/GPS based interconnected sensors systems, and (b) capable of spatially sensing and/or detection of waterborne contaminants in real-time using a Contamination Identification and Level Monitoring Electronic Display Systems (CILM-EDS) prototype. With recent advances in cyber-physical systems, several sensing and detection capabilities have become available in commercial off the shelf (COTS) configurations and are conjoined to provide sampled and stand-off detection capability. Furthermore, CPSs in conjunction with decision support tools provide a comprehensive analysis and strategies to address, mitigate, perform contamination mapping, minimize false-positives and conduct consequence management. Such platforms can provide a rapid response to counter hybrid and kinetic CBRN challenges. The economic and societal potential of such systems is vastly greater than what has been realized so far, as major investments are being made worldwide to develop the technology. Hence, CPS field will further expand the boundaries of smart and connected systems and communities.

The objective of this investigation is to demonstrate feasibility of a mobile UASP that can monitor in real-time, capture, synthesize and analyze observed information and communicate with ground-based systems for a coordinated actionable response. Several commercial off the shelf (COTS) instruments such as hyperspectral imagers, Light Detection and Ranging (LIDAR), Laser-induced Breakdown Spectroscopy (LIBS) and Biometrics systems are discussed along with some innovative nano-sensors based platforms that are still in experimental stages and have the potential to

serve as payloads for sample collection and on-contact detection. We also discuss the scalability and transferability of the proposed pilot project for additional solutions and introduce framework for promoting discovery, innovation, and entrepreneurship in smart and connected communities' initiatives to address infrastructure requirements. Notwithstanding the fact that our highly interconnected world offers great promise for improved well-being and prosperity, the technology offers certain societal challenges at the intersection of technology and society. Hence one of the objectives is to discuss socio-technical issues supporting understanding of emerging technologies, the use of data analytics to enhance individuals' Quality of Life, improve health and safety, economic prosperity, data-driven decisions, and policy decisions inclusive of privacy and transparency.

1.2 Background Information

1.2.1 Cyber-Physical Systems

Cyber-physical systems conjoin the dynamics of the physical processes with those of the software and networking, provide abstractions, modeling, design and analytical techniques. The key technical challenge is to conjoin constructs for modeling physical processes with abstractions in computer science that significantly vary over timescale. The Cyber-Physical domain consists of integrated and networked system-of-systems where physical processes are monitored or controlled by algorithms. Embedded computers and networks monitor and control the physical processes, with feedback loops where physical processes affect computations and vice versa. The physical and software components interact with each other in ways that change with context within a DoI. Due to its growing significance, Cyber-Physical systems are now a multi-disciplinary technology focused engineering discipline, with a strong foundation in mathematical abstractions. Advances in CPS have significant applications in terms of capability, scalability, resiliency, safety, security, flexibility and conformity to systems within a DoI, as demonstrated below in the context of connected communities and shown in Fig. 1.1. The economic and societal potential of such systems is vastly greater than what has been realized, and major investments are being made worldwide to develop the technology and hence, CPSs will further expand the boundaries of smart and connected communities. Therefore, CPS in conjunction with decision support tools provide a comprehensive analysis and strategy to address, mitigate, perform contamination mapping, minimize false-positives and consequence management.

Unmanned aerial vehicles (UAVs) provide a unique platform [2] for remote data acquisition rapidly and at a lower cost that with fixed or rotary wings piloted aircrafts. The technology is rapidly growing, especially with respect to capabilities due to enhanced communication and onboard sensor platforms. Albeit, UAS as a disruptive technology is not the focus of this investigation, the research program is being developed to recognize the need for and impact of technology especially as it

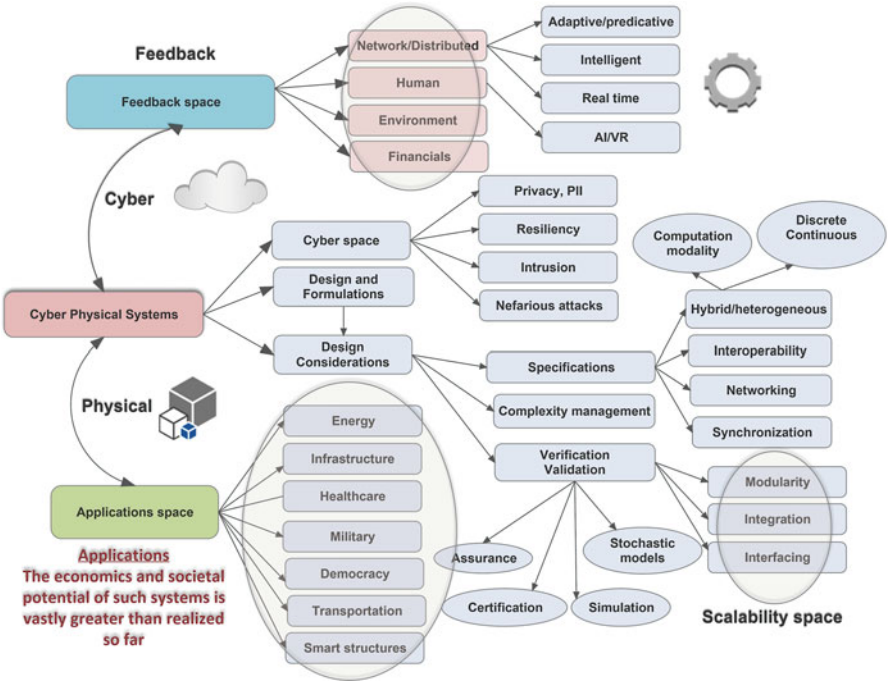

Fig. 1.1 Cyber Physical systems – Application Space, Scalability and Feedback from interactive intelligent systems

is uniquely applied within a multi-sensor UASP with a Mobile Operations Command and Communication Center (UASP-MO3C) construct. More specifically, applications of UASP-MO3C are directed for the global need for enhanced situational awareness. With the integration of vehicle-to-vehicle (V2V) and machine-to-machine (M2M) communication, integration of IoET with 5G offers possible applications in safety and security, as well as a connected world to provide enhanced situational awareness, safety and security of critical infrastructure, unmanned traffic management (UTM), Emergency Rescue Augmentation in congested traffic corridors, and Command and Control (C2) Systems for Beyond Visual Line of Sight, just to name a few applications. Indirectly, UASP helps to reduce the global carbon footprint. We further recognize the broader social and political context within which UAS technology is deployed. This is briefly recognized within the context of UAS Integration from a policy standpoint. Also, the discussion of UASP is within the domain of civil mission space.

Several detection and sensing capabilities have been reported and are now available in commercial off the shelf (COTS) configurations. Such COTS configurations along with several experimental platforms provide stand-off and sampled detection capability. We present an overview of several COTS capabilities, which in conjunction with several new nanomaterials-based platforms, CPS and decision

support tools provide a rapid-response to counter hybrid and kinetic CBRN challenges. The economic and societal potential of such systems is vastly greater than what has been realized, and major investments are being made worldwide to develop the technology and hence, CPS will further expand the boundaries of smart and connected communities.

While the rapid development of UASPs brings many opportunities for individuals and commercial entities, it also brings numerous complex challenges and concerns. It is important to assess the complex security challenges of UASPs. Rushing to develop applications of drone technology without understanding the complex security risks [3] can result in many complex challenges for which society may not be prepared for. It is indispensable to understand the associated risks and develop appropriate strategies. We demonstrate modality of an Unmanned Aerial Surveillance Platform (UASP) for applications in surveillance, real-time monitoring, emergency augmentation for actionable response, security and enabler of connected communities to bring about new levels of opportunity and growth, safety and security, and health and wellness. The new system under development has an airborne component to capture relevant information from a Domain of Interest.

1.2.2 Connected Systems

Exponential growth in intelligent technologies has created new opportunities to synergistically integrate the entire community services socially, digitally and physically. Rapid innovations in CPS around the world are in a new era of transformational change, in which people, surrounding structures and natural environments are increasingly connected by smart technologies, leading to new opportunities for innovation, improved services, and enhanced quality of life. Connected systems have enhanced mobility, access and services to include performance based on predictive planning, traffic modeling, parking solutions, geospatial services, environmental services, emergency augmentation, scenario planning and augmented reality, just to name a few. The connected communities' technologies support integrative research at the intersection of intelligent technologies and social sciences to pilot solution pathways that support productivity, sustainability, knowledge-based economy, data-driven decisions including scalability and transferability of the projected solutions. In an earlier project, the concept of cyber-physical and connected systems was demonstrated to monitor contaminants in the body of ground and surface water in real-time. The applications described here are in the context of smart and connected systems for real-time monitoring using an unmanned aerial surveillance platform.

1.2.3 Previous and Existing Capabilities

Our earlier systems were capable of (a) monitoring environmental pollution using a GIS/GPS based interconnected sensors systems, and (b) capable of spatially sensing and/or detection of waterborne contaminants in real-time using a Contamination Identification and Level Monitoring Electronic Display Systems (CILM-EDS) prototype.

For over 20 years, we have conducted several investigations to monitor, sense, detect and identify several air-borne [4] and water-borne [5–7] contaminants using several different platforms. We conducted monitoring of Aral Sea in early 1990s. Simultaneously, we conducted a study of pollution monitoring in Bangkok, Thailand, Los Angeles, CA, and Charleston, WV [8]. We monitored many pollutants, such as $PM_{2.5}$, PM_{10}, VOCs, CO, SO_2 and O_3 through a sensor network superimposed on satellite data. This investigation provided an overview of some of the desired capabilities as a Segway into the current approach, viz. smart and connected monitoring platforms. The data from the gas sensors monitoring air pollutants was uploaded in real-time via Personal Digital Assistant (PDA) to the air quality monitoring server as concentration values. Users can simply browse and view the air quality data in graphical format in real-time. The data is then compared with the satellite data and air dispersion modeling for air pollution over the area under investigation and can assist national policymakers in establishing pollution awareness policies and priorities.

Moderate Resolution Imaging Spectroradiometer (MODIS) was used to monitor forest fire and biomass burning occurrence in the Northern part of Thailand. The active fire occurrence has been monitored using the MODIS Fire Information System, generated daily by MODIS Fire product (MOD14) from local Geoinformatics Center. In order to understand the air quality conditions, the MODIS aerosol product (MOD04) was used to identify the air quality status, monitoring the ambient Aerosol Optical Thickness (AOT) over the oceans globally and over a portion of the continents. Daily Level 2 data was produced at the spatial resolution of a 10×10 km^2 (at nadir) pixel array. The product was generated in and distributed by the Level 1 and Atmosphere Archive and Distribution System (LAADS). The aerosol product employed in this investigation contained many scientific data sets. One of them was the AOT at 0.55 μm for both Ocean and Land. Moreover, the key target of SCanning Imaging Absorption SpectroMeter for Atmospheric ChartographY (SCIMACHY) was used to determine the global troposphere NO_2 column. Broad spectral and fine spatial resolution allows the estimation of NO_2 emissions. SCIMACHY was launched on Environmental Satellite (ENVISAT) observing nadir and limb viewing with spatial resolution 60×30 km^2. The data obtained from these satellites sensors and measurements conducted on ground using the gas sensors was used for numerical modeling and to identify the correlation of the air quality levels, as shown in Fig. 1.2.

Another activity, as part of a North Atlantic Treaty Organization (NATO) Science for Peace and Security project, was to monitor pollutants in water. The proposed

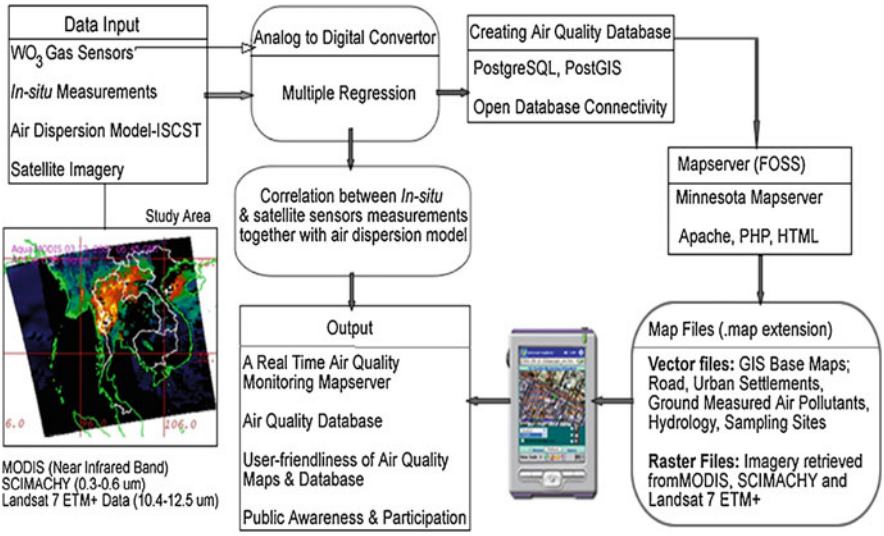

Fig. 1.2 Industrial Source Complex Short Term (ISCST) model integrated with GIS and remote sensing techniques employed to determine the affected areas

activity sought to use advanced (Nano) technology based platforms to detect and mitigate inadvertent and intentional chemical, biological, radiological, nuclear (CBRN) contamination in water supplies, develop a stand-alone prototype to supply clean water, and develop a Global Positioning System (GPS)/Geographical Information System (GIS) based Contamination Identification and Level Monitoring Electronic Display Systems (CILM-EDS) prototype to spatially monitor contaminants and water levels, in event of natural catastrophe. The research under this program focused on six distinct, yet unifying areas of the project, viz. sensing and detection of:

- Metals (As, Hg, Cr, Pb, etc.);
- Pathogenic agents (bacteria, virus, proteins, cryptosporidium etc.);
- Organic compounds (TCE, acetone, household degreasers, halogenated organics, etc.);
- Pharmaceuticals (antibiotics, steroids-fluxoymesterone, methyl-testosterone, nandrolone, oxandrolone, oxymetholone, testosterone, stanozolol, acetaminophen and ibuprofen, etc.);
- Pesticide run-off;
- Compounds with large shelf-life in water.

These sensors/detectors are intended to be capable of detecting/sensing multiple agents simultaneously in quantities comparable to minimum allowable contamination levels in drinking water [9], using a GIS/GPS based Contamination Identification and Level Monitoring Electronic Display Systems (CILM-EDS) prototype, as shown in Fig. 1.3, to spatially monitor contaminants and water levels. The unit

Fig. 1.3 (**a**) Distributed sensor system using remote, wireless data transmission and data gathering, (**b**) Artist's rendition of CILM-EDS unit

required a careful selection of GIS/GPS protocol to provide precise geographical location of sensors, user-friendly software, and accurate sensors so that they provide accurate representation of their environment and are reliable, highly sensitive and have high specificity.

In yet another project, the focus was centered on screening water quality in aquafers to monitor the groundwater quality and quantity analysis in Republic of Moldova to implement the EU Water Framework Directive (WFD) requirements.

The results [6] of groundwater monitoring can be used for:

- Assessment of quantitative and chemical status of all groundwater bodies or groups of bodies;

Table 1.1 EU-wide standards for groundwater

Name of pollutant	Quality standard
Nitrate	50 mg/l
Active ingredients in pesticides including their relevant metabolites, degradation and reaction products	0.5 μg/l[a] (total)

[a]"Total" here means the sum of all individual pesticides, including their relevant metabolites, degradation and reaction products

- Estimating groundwater flow direction and flow rate in transboundary bodies;
- Assessment of long-term trends in pollutant concentrations caused by both natural and anthropogenic factors;
- Determining the chemical status of groundwater bodies that are at risk of failing to meet WFD environmental objectives;
- Detecting upward trends in pollutant concentrations due to either natural or human impacted causes or defining starting points for trend reversal. Reducing trends in pollutant concentrations may be caused by the applied measures, increasing trends may also indicate on potential new threats to groundwater status from other human induced pressures;
- Assisting design and evaluating the effectiveness of measure program;
- Demonstrating compliance with drinking water protection areas (DWPA) and other protected area objectives, e.g. Natura2000, Habitats and Birds directives, etc.

Under this project, several chemical parameters of water were determined by study of groundwater in Nistru and Prut rivers basin, which were used for the groundwater classification. Groundwater directive lists substances for which EU-wide standards for groundwater already exist (Table 1.1).

Evaluation of groundwater quality was made [6] based on comparison of the parameters' measured values with respective national standards for potable water (sanitary norms) and for water used for irrigation.

In yet another project, we aimed at studying a viable model of a portable photo-sensor for identification and quantitative analysis of hazardous mixtures in the environment. The spatial selection of optical signatures is carried out by means of a new physical principle [10]. A prototype based on the physical principle is currently being fabricated which supports the modality, as proposed.

1.3 Multi-sensor UAV Platform Configuration and Payloads

Multi-sensors as payload on a UAV surveillance platform is a disruptive technology. The construct of a platform in conjunction with a ground based mobile operations center presents tremendous opportunity and impact of technology for safety,

security, emergency response, traffic management etc. notwithstanding having broader social and political context. This context is recognized as UAS Integration and associated policy within a social framework. The UASP policy is beyond the scope of this publication but is discussed elsewhere. The UASP research for this investigation spans a set of specific objectives, viz. Multi-UAS Mobile Operations Center and Integration for enhancement of situational awareness. The platforms described below are studied as diagnostic tools.

1.3.1 Hyperspectral Imaging

Hyperspectral imaging (HSI) is a spectral imaging acquisition methodology employed to acquire a set of images within certain spectral bands where each pixel of the image contains certain spectral information, which is added as a third dimension of values to the two-dimensional spatial image, thus generating a three-dimensional data cube, typically referred to as hypercube data [11]. Hyperspectral data cubes can contain absorption, reflectance, or fluorescence spectrum data for each image pixel. Over a short period of time, hyperspectral imaging spectroscopy has developed from a large, complex, remote-sensing satellite- or aircraft-based system into a rugged, compact, reasonably priced tool for a range of process control, monitoring, diagnostic and inspection with applications ranging from colorimetry and color matching, spectral radiometry, industrial process control and quality assurance, pharmaceuticals preparation and packaging, forensic analysis [12], bio-agents detection [12], camouflage detection, live-cell microscopy [12], genomics/proteomics research, forestry [13] and precancerous cell detection. The multiplexing of wavelengths is achieved either by switching sources to obtain different wavelengths or switching band-pass filters to gate the photons in case of broadband illumination. Historically, low-altitude data collection using hyperspectral sensors has been very difficult to achieve due to operational complexities. Recent advances in sensors and sensor system platforms when coupled with the latest models of Near Infrared (NIR) to Very Near Infrared (VNIR) hyperspectral imagers, provide UAVs with a capability of scanning with 154 discrete spectral bands covering a spectral range of 400–1000 nm. Hence, the objective of this investigation is to study feasibility of integrating a hyperspectral imager as a viable payload for UAVs to be used for intended application. Several companies that manufacture OTC hyperspectral imagers are BaySpec [12], LOT Quantum Design GmbH [14], HySpex [15], SENOP [16] and XIMEA [17], among a few others.

1.3.2 Light Detection and Ranging (LIDAR)

Light detection and ranging (LIDAR) is a broadly used technique for determining the distance to an object by transmitting a laser beam at the object and measuring the

time of flight back to the transmitter. In conjunction with GPS and Inertial Measurement Units (IMUs), the data from LIDAR provides topographical maps. With increased miniaturization and high accuracy, UAV based LIDAR sector is growing rapidly. Recently, several manufacturers of the best LIDAR sensor systems for aviation payload have engineered such sensors for UAVs. Currently, there are over 12 manufacturers of LIDAR systems with several different capabilities. Most of the latest LIDAR for UAV systems can rotate around their own axis and offer 360-degree line of sight with very high data rates, such as over one million distance points per second. A state-of-the-art integrated Real-Time Kinematic (RTK) GPS and Inertial Navigation System (INS) provides accurate position, velocity, acceleration and orientation under the most demanding conditions. The dual-antenna moving baseline RTK Global Navigation Satellite System (GNSS) solution ensures that the LIDAR can achieve the highest accuracy possible for the lowest weight. The GPS\INS sensor combines temperature calibrated accelerometers, gyroscopes, magnetometers and a pressure sensor with a multi-channel RTK GNSS receiver. These are coupled in a sophisticated fusion algorithm to deliver accurate and reliable navigation and orientation. The resulting applications of LIDARs mounted as payload UAVs range from agriculture & forestry [17], archaeology and cultural heritage documentation, corridor mapping: power line, railway track, and pipeline inspection [18], topography in open-cast mining, construction site monitoring, building and structural inspections, surveying of urban environments [19], resource management, collision avoidance, shoreline and storm surge modeling, hydrodynamic modeling to Digital Elevation Models (DEMs), among others. LIDAR in conjunction with multi/hyperspectral and photogrammetry imagery are deployed in some sectors and situations to give a comprehensive assessment of the terrain, vegetation or structure. Several manufacturers such as Ledder Tech [20], Velodyne [21], Riegl [22], Routescene [23], Yellowscan [24], Leica [25], Geodetics [26], etc. produce LIDAR for UAV applications.

1.3.3 Laser-Induced Breakdown Spectroscopy (LIBS) Scan

Laser-induced breakdown spectroscopy (LIBS) is atomic emission spectroscopy which uses a highly energetic laser pulse as source for excitation and ablation of target material. The formation of the plasma by the focused laser pulse achieves a certain threshold for optical breakdown, which generally depends on the environment and the target material. LIBS makes use of optical emission spectrometry and to this extent is very similar to arc/spark emission spectroscopy, and hence can analyze any matter regardless of its physical state, be it solid, liquid or gas. These analyses are inherently real-time, require no sample preparation, with true stand-off detection capability (distance ~ 100 m, residue explosive ~ 50 m and Chem/Bio residue ~ 25 m) and offer high sensitivity (nanograms) and specificity (typically >95% True positives, <5% False positives). LIBS provides elemental fingerprinting for the constituents of a material to be analyzed and hence may be used to evaluate

the relative abundance of each constituent element, or to monitor the presence of impurities. In practice, detection limits are a function of (a) the plasma excitation temperature, (b) the light collection window, and (c) the line strength of the viewed transition. LIBS provides all-in-one, universal hazardous materials detection, viz. Chemical, Biological, Radiological, Nuclear and Explosives (CBRNE), home-made explosives (HME), non-traditional agents (NTAs), toxic industrial chemicals (TICs), and toxic industrial materials (TIMs). The COTS LIBS are miniaturized into a hand-held size (HH LIBS) capable of analyzing elements for a wide range of materials, depending on the spectrometer and range. Unlike X-ray fluorescence (XRF), LIBS uses low-energy lasers for elemental fingerprinting without radiation concerns. Several vendors such as Applied Photonics Ltd. [27], Applied Spectra, Inc. [28], Bertin Technologies [29], Energy Research Co. [30]. IVEA [31], LTB Lasertechnik Berlin [32], Marwan [33], Ocean Optics Inc. [34], Photon Machines [35], StellarNet [36], Bruker [37], and others, produce LIBS devices. The focus for this investigation is on UAVs as payload, however benchtop models of LIBS have extensive applications for biomedical applications [38], forensics [39], and fingerprinting of conflict materials [40].

1.3.4 Biometric Based Facial Recognition

Due to enhanced security concerns, recently there is an accretion in demand for facial recognition software solutions designed to recognize people from distance, including UAVs. Face-Six's [41] FFA6Drone software allows drones to identify people from any range, if faces are unaltered and have a size allowing sufficient software data. In battlefield Intelligence, Surveillance, and Reconnaissance (ISR) capability is quintessential for technological superiority. Due to privacy concerns for civil application, the applications of software in the US are still being investigated. With the biometrics arms race competition in progress with the developing countries on fingerprint/biometric payment cards, and blockchain for financial transactions, the predictions for biometric technologies-based security for civil and personal use is very promising.

Automated license plate readers (ALPRs) are high-speed, computer-controlled camera systems that are typically mounted on street poles, streetlights, highway overpasses, mobile trailers, or attached to police squad cars and now on UAVs. ALPRs automatically capture all license plate numbers that come into its view, along with the location, date, and time. The data, which includes photographs of the vehicle and sometimes its driver and passengers, is then uploaded to a central server to develop a portrait of the driver – depending upon need. Since the data already exists in central database (Big Data), one can generate a profile to target drivers who visit sensitive places such as health centers, immigration clinics, gun shops, union halls, protests, bridges/dams, or centers of religious worship. UAVs based ALPR and biometric platforms provide a quick snapshot of the required information for traffic management in crowded corridors.

1.3.5 *Other Innovative and Disruptive Platforms*

Applications of UAV based sensor platforms include precision agriculture, construction, mining, pest detection, forestry, mammal species tracking, search and rescue, target tracking, monitoring of the atmosphere, chemical, biological, and natural disaster phenomena, fire prevention, flood prevention, reef monitoring, volcanic monitoring, Earth science research pollution monitoring, micro-climates, land use precision agriculture, ecology [18], atmospheric research, bio-security [38], forestry [11], fire monitoring, quick response measurements for emergency disaster, pollution monitoring, volcanic gas sampling, monitoring of gas pipelines [18], biological/chemo-sensing tasks [42], and humanitarian observations [43], involving and in addition to applications described above and shown in Table 1.2. In addition to commercial-off the shelf (COTS) sensors, several test flights with laboratory-based sensors are also investigated to determine additional range of capabilities.

A summary of the specifications of these capabilities is presented in Table 1.2. Most VASP can take a payload of 3–5 kg (approx. 10 lbs.), availability of quad-copter based drones (shown in Fig. 1.4) and helicopter configuration UAS are also deployed for payload capacity of up to 15 kg (~33 lbs.), thus allowing multiple capabilities with high throughput for field ready applications.

The core concept focuses on innovative technology solutions to bridge the existing gaps in mission-ready deployability. The platform as discussed above, offers the following mission-ready capabilities:

- Rapid Decision Making;
- Collaboration and Communication;
- Rapid and Adaptable Deployment;
- Technology Self Sufficiency;

Table 1.2 Specifications for selected sensing/detection/monitoring platforms

Platform	Weight	Scan rate	Power source	Field of View (FOV)	Range (for a typical system)
Lidar	Total < 4 lbs.	~ 700 K 3D pts./sec	Small (nominal)	360	100 m (<20 nm range)
Hyperspectral	Total ~ 6 lbs.	~ 500 fps	Nominal	Depends on mode	VNIR (380–1000 nm), NIR (900–1700 nm) SWIR (950–2500 nm)
LIBS	Total ~ 3 lbs.	< 3 s	Last 8–10 h	Stand-off detection	Depends upon target (1 ppm detection)
Biometrics	~ 1.5 lbs.	4 MP CMOS 60 fps	330 mA@12 V	Y/P/R 300, 180, 170	f = 4.5~135 mm, aperture diameter Φ16

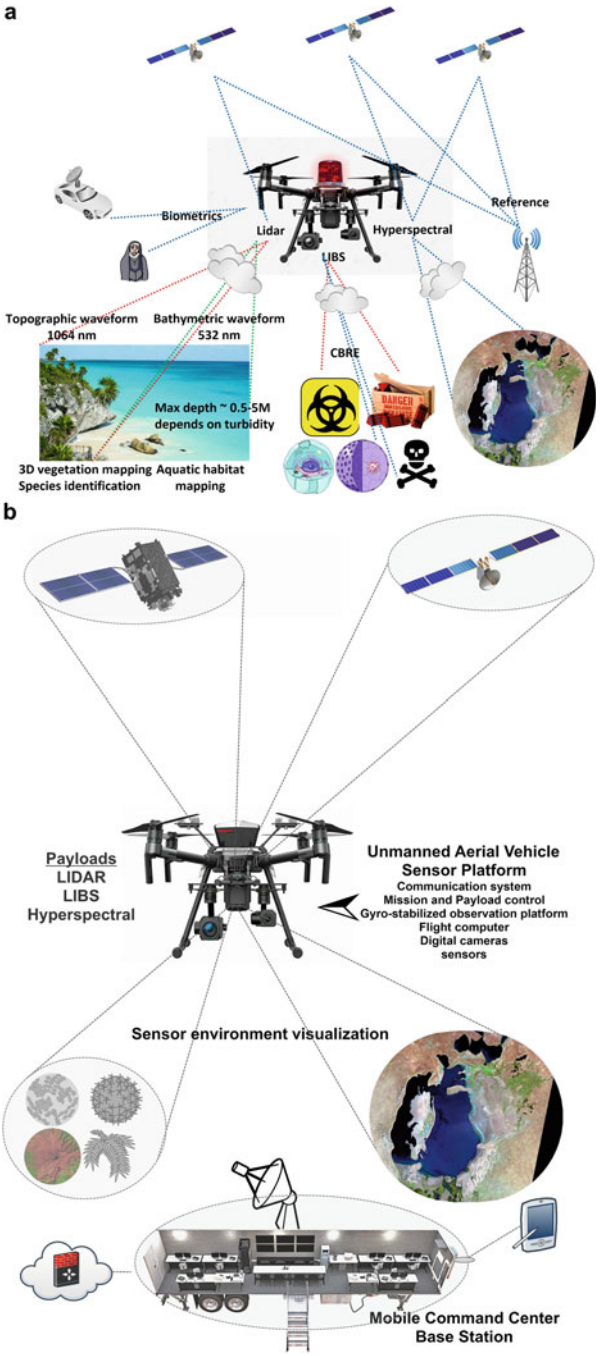

Fig. 1.4 (**a**) An integrated UAVSP – T1 for heavier payload and (**b**) T2

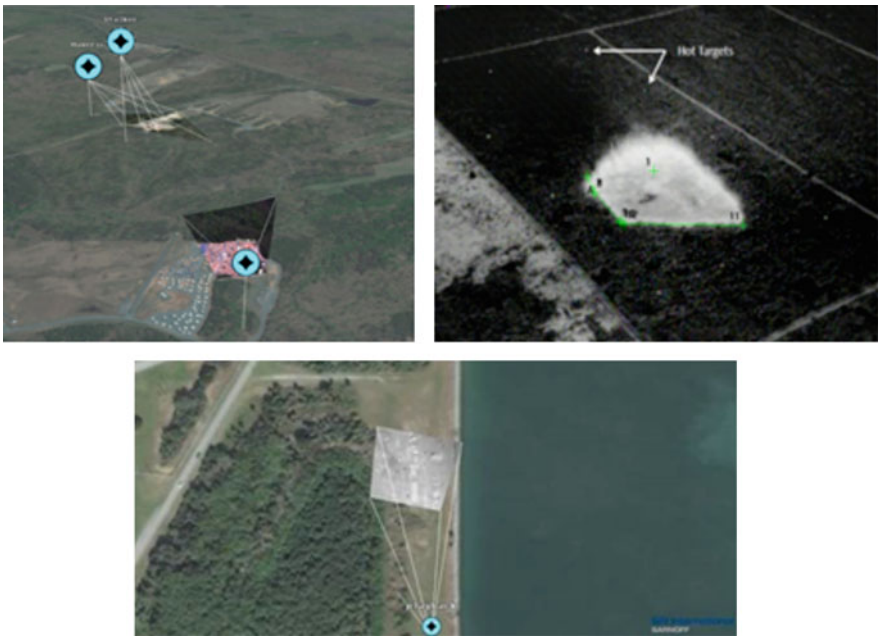

Fig. 1.5 Aerial observations from a UASP -real-time IR video draped and geo-registered overlay on reference imagery map of a coastline

- Enhanced Situational awareness;
- Emergency communication infrastructure;
- Accessibility of otherwise inaccessible proximities.

A single UASP can be equipped with sensors to capture and transmit real-time video, image and other data for a specified coverage area, its overall performance is limited by:

- Sensor range/camera Field of View (FOV);
- Size/weight and cost of payload supported by UASP;
- Power requirements/flight time (more power-hungry payloads compete with flight duration);
- Operation by remote pilot in control (RPIC) (a requirement today – FAA manual for UAVs).

Based on the considerations above, an integrated platform is being built and tested in parts, as shown in Fig. 1.4 for two different configurations as test 1 (T1) and test 2 (T2). The T2 platform shows a mobile operation command and control center (MO3C) to analyze data in real-time. Both test platforms are capable of real-time communications with ground-based systems.

Figure 1.5 shows aerial observation from UASP using a real-time video draped and geo-registered overlay on reference imagery. (Representative figure above displays capability).

1.4 Conclusion and Recommendations

Given the state-of-the-art, it is demonstrated that an integrated low cost UASP, network above ground can be assembled for an operation that supports several integrated and complementary capabilities for monitoring and capturing data which are analyzed at a ground based Mobile Operations Command and Communication Center (MO3C), which is capable of analyzing data using image and signal processing software. Depending upon required capability, the MO3C needs to be linked with several agencies for cross-confirmation of the captured data. One of the networking design goals is to deploy multiple UASPs that form reliable flying mobile ad-hoc WiFi-based networks, which may contain a number of diverse UAS operating at specified altitude and carrying a pre-determined sensor suited for CBRN capability complemented by video and telemetry sensors. Another key capability is to relay data (e.g. video) through the Multi-UAS network to the mobile ground stations and to first responders, where applicable. One of the applications of the proposed platform is to detect water contaminants and levels for areas that are prone to flash-flood, as a DOI for assistance with emergency scenarios.

The overarching capability needs fulfilled by a UAS can be succinctly stated as:

- Facilitate the conduct of emergency operations in complex or dynamic environments.
- Reduce decision making cycle times during a response to aid recovery from natural disasters and emergencies, including CBRN threats.
- Achieve mission situational understanding and development of a common operating picture – automated data processing system that can rapidly transform raw FMV data into an accurate and correct geospatial image product to minimize delays in analysis.
- Obtain clarity, context, and precision in video from UAS platforms. MU-MOCs must generate real-time, integrated actionable intelligence, e.g., real-time assessment overlays and display, with precise locations of items of interest (IoIs).
- FMV ingest, processing and exploitation from UAS platforms, providing timely mission command and intelligence through real-time situational awareness.
- Stabilizes, mosaics, geo-registers, and drapes UAS FMV over a 3D map. Data is displayed in a single Common Operating Picture (COP) for accurate EO/IR sensor viewing in context and reporting of IOIs.

While the rapid democratization of UAVs or drones brings many opportunities for individuals and entities, it also brings numerous complex challenges and concerns. The question is whether individuals or entities are prepared for the rise of drones in their operational ecosystem? Due to versatile nature of the platforms described above, there are many considerations that need to be looked into and some of them are briefly described here, as a detailed discussion is beyond the scope of this publication and will be presented in a different format. These considerations include: Detect & Avoid requirements for beyond visual line of site operations; Human Factors design standards, certification and training; Human Factors

Consideration of UAS procedures and controls; and Performance Analysis of UAS Detection Technologies Operating in airfield environments. These initiatives will enhance the co-existence of USAP with FAA. Rushing to develop applications of drone technology without understanding the complex security risks can result in many complex challenges for which the general society is not prepared for. It is important that we understand the risks and privacy issues associated with the drones or unmanned aerial vehicle (UAV) .

Acknowledgments The project related to water contamination monitoring and electronic display was funded in part by a grant by NATO – Science for Peace and Security.

References[1]

1. Vaseashta A (2015) Life cycle analysis of nanoparticles: reducing risk and liability. Destech Publications Inc, Lancaster
2. Brzozowski B et al (2018) A remote-controlled platform for UAS testing. IEEE Aerosp Electron Syst Mag 33(8):48–56
3. Sarah Ludwig (2018) Drones: a security tool, threat and challenge, security, March 2018
4. Robert OP, Vaseashta A Kiyoshi H (2016) Geoscience meets nanotechnology: a pathway of environmental monitoring, Geospatial World. https://www.geospatialworld.net/article/geoscience-meets-nanotechnology-a-pathway-of-environmental-monitoring/
5. Vaseashta A (2013) Emerging sensor technologies for monitoring water quality. In: Future science book series – applications of nanomaterials for water quality, pp 66–84. https://doi.org/10.4155/ebo.13.208
6. Nastasiuc L, Bogdevici O, Aureliu O, Culighin E, Sidorenko A, Vaseashta A (2016) Monitoring water contaminants: case study for the Republic of Moldova. Pol J Environ Stud 25 (1):221–230. https://doi.org/10.15244/pjoes/58888
7. Gevorgyan GA, Mamyan AS, Hambaryan LR, Khudaverdyan SK, Vaseashta A (2016) Environmental risk assessment of heavy metal pollution in Armenian river ecosystems: case study of Lake Sevan and Debed River catchment basins. Pol J Environ Stud 25(6):2387–2399. https://doi.org/10.15244/pjoes/63734
8. Vaseashta A, Vaclavikova M, Vaseashta S, Gallios G, Roy P, Pummakarnchana O (2007) Nanostructures in environmental pollution detection, monitoring, and remediation. Sci Technol Adv Mater 8(1):47–59
9. Vaseashta A, Braman E, Susmann P, Dekhtyar Y, Perovicha K (2012) Sensors for water safety and security. Surf Eng Appl Electrochem 48(5):478–486
10. Khudaverdyan S, Meliqyan V, Hovhannisyan T, Khudaverdyan D, Vaseashta A (2017) Identification and analysis of hazardous materials using optical spectroscopy. Optics and Photonics Journal 7(1):6–17
11. Landgrebe D (2002) Hyperspectral image data analysis. IEEE Signal Process Mag 19(1):17–28
12. BaySpec – https://www.bayspec.com
13. Adão T et al (2017) Hyperspectral imaging: a review on UAV-based sensors, data processing and applications for agriculture and forestry. Remote Sens:9, 1110. https://doi.org/10.3390/rs9111110

[1]The URLs for several products are provided as reference only and do not constitute any endorsement of these products.

14. LOT-Quantum Design GmbH https://lot-qd.de/en/products/spectroscopy/hyperspectral-cameras/
15. HySpex – https://www.hyspex.no/hyperspectral_imaging/
16. SENOP – http://senop.fi/optronics-hyperspectral
17. XIMEA – https://www.ximea.com/en/products/xilab-application-specific-oem-custom/hyperspectral-cameras-based-on-usb3-xispec
18. Höfle B (2014) Radiometric correction of terrestrial LiDAR point cloud data for individual maize plant detection. IEEE Geosci Remote Sens Lett 11(1):94–98
19. Ogai H, Bhattacharya B (2018) Pipe inspection robots for structural health and condition monitoring, Intell Syst Control Autom Sci Eng, vol 89. Springer, New Delhi. https://doi.org/10.1007/978-81-322-3751-8_2
20. Xharde R, Long B, Forbes D (2007) Accuracy and limitations of airborne LiDAR surveys in coastal environments. IEEE Int Symp Geosci Remote Sens. https://doi.org/10.1109/IGARSS.2006.625
21. Ledder Tech – https://leddartech.com/
22. Velodyne – https://velodynelidar.com/
23. Riegl – http://www.riegl.com/products/unmanned-scanning/
24. Routescene – https://www.routescene.com/the-3d-mapping-solution/uav-lidar-system/
25. Yellowscan – https://www.yellowscan-lidar.com/products
26. Leica – https://leica-geosystems.com/en-US/products/airborne-systems/topographic-lidar-sensors
27. Geodetics – https://geodetics.com/products/
28. Applied Photonics Ltd. – http://www.appliedphotonics.co.uk/
29. Applied Spectra, Inc. – http://www.appliedspectra.com/
30. Bertin Tech. – http://www.bertin.fr/en/industrial-control-systems.aspx
31. Energy Research Co. – http://www.er-co.com/
32. IVEA – http://www.ivea-solution.com/libs/
33. LTB Lasertechnik Berlin – http://www.ltb-berlin.de/
34. Marwan – http://www.marwan-technology.com/
35. Ocean Optics Inc. – http://www.oceanoptics.com/products/libs.asp
36. Photon Machines – http://www.photon-machines.com/
37. StellarNet – http://www.stellarnet-inc.com/
38. Bruker https://www.bruker.com/products/x-ray-diffraction-and-elemental-analysis/libs.html
39. Singh VK, Rai AK (2011) Prospects for laser-induced breakdown spectroscopy for biomedical applications: a review. Laser Med Sci 26:673–687
40. Dalby O, Butley D, Birkett JW (2010) Analysis of gunshot residue and associated materials – a review. J Forensics Sci 55(4). https://doi.org/10.1111/j.1556-4029.2010.01370.x
41. Harka RR et al (2012) Geographical analysis of "conflict minerals" utilizing laser-induced breakdown spectroscopy. Spectrochimica Acta Part B: Atomic Spectroscopy Vol 74–75:131–136
42. Face-Six – https://www.face-six.com
43. Bittencourt Bravo RZ, Leiras A (2015) Literature review of the applications of UAVs in humanitarian relief, XXXV ENCONTRO NACIONAL DE ENGENHARIA DE PRODUCAO Perspectivas Globais para a Engenharia de Produção, Fortaleza, CE, Brasil, 13–16 de outubro de

Part II
Material Preparation and Processing

Chapter 2
Application of Ionizing Irradiation for Structure Modification of Nanomaterials

Perica Paunović, Anita Grozdanov, Petre Makreski, Gennaro Gentile, and Aleksandar T. Dimitrov

Abstract Ionizing irradiation passing through materials interacts with their building units inducing changes in the structure. This causes modification of their properties and alteration of their performance. Generally, the ionizing irradiation used for material modification can be part of the electromagnetic spectrum (X-ray or γ-ray irradiation) or can have corpuscular nature (such as irradiation of α-particles, β-particles, electrons, and neutrons). α and β irradiations belong to low-energy irradiations, whereas X-ray, γ-ray and neutrons are high-energy irradiations. The subject of this chapter was the observation of the changes in structure and consequently in properties of nano-dimensional materials, namely TiO_2 and carbon nanostructures (graphene and multiwalled carbon nanotubes, MWCNTs), after treatment with X-ray irradiation.

Keywords Ionizing irradiation · X-ray · TiO_2 · Graphene · MWCNTs

2.1 Introduction

In the last decades, there is a strong increment in the interest in irradiation technologies, not only in the field of energy management but also in the fields of material research and human health. This implies more irradiation research facilities for materials and more radiation facilities for medicine (radiation oncology and radiation

P. Paunović (✉) · A. Grozdanov · A. T. Dimitrov
Faculty of Technology and Metallurgy, University "SS Cyril and Methodius", Skopje, Republic of North Macedonia
e-mail: pericap@tmf.ukim.edu.mk

P. Makreski
Institute of Chemistry, Faculty of Natural Sciences and Mathematics, University "SS Cyril and Methodius", Skopje, Republic of North Macedonia

G. Gentile
Institute for Polymers, Composites and Biomaterials, National Research Council, Naples, Italy

P. Petkov et al. (eds.), *Nanoscience and Nanotechnology in Security and Protection against CBRN Threats*, NATO Science for Peace and Security Series B: Physics and Biophysics, https://doi.org/10.1007/978-94-024-2018-0_2

diagnostics). Significant scientific research has been done in the fields of nanomaterials and engineering to improve the functionalities of the materials. New findings lead to further developments regarding sensors, electrode materials, environment and health protection.

Irradiation technologies, which are already established in material processing, offer possibilities that are uniquely suited for the creation and characterization of new functional materials on the nanoscale. Namely, the ability to fabricate structures with nanometric precision is of fundamental importance to any exploitation of nanotechnology. Irradiation based technology using X-rays, e-beams and ion beams is the key to a variety of different approaches for micropatterning, e.g. by lithography. Irradiation effect on resists occurs through bond breaking (positive resist) or cross-linking between polymer chains (negative resist) [1]. Polymer is becoming better or less soluble in developer. This technique has already been commercialized. Due to the small wavelength of the 30–100 keV electrons, the resolution of electron beam nanolithography is much higher than that of optical lithography. To improve the resolution, electron direct writing systems applying electrons with energy as low as 2 keV are proposed to reduce the electron scattering effects. Ion beam have also found various applications in nanotechnology. New method to grow carbon nanotubes was reported in 1996 by Yamamoto et al. [2], where they grew carbon nanotubes by argon ion-beam irradiation on amorphous carbon target under high vacuum condition ($5{\cdot}10^{-8}$ bar). The incident angle of the ion beam was normal to the target surface and the acceleration ion energy was 3 keV. Nanotubes were produced outside the sputtering region on the target surface after ion irradiation. The tubes have multilayered walls, the distance between the carbon layers is 0.34 nm, and the wall thickness of tubes ranges from 10 to 15 sheets. γ-ray irradiation was used to improve the thermal contact conductance of CNTs in thermal interface materials (TIMs), especially for space applications where the materials are exposed to high dose of gamma irradiation [3]. CNTs properties such as their low intrinsic resistance and large compliance that enables them to conform to rough surfaces combined with their low density and ability to withstand vacuum environments and extreme temperatures, make CNTs-based TIMs very suitable for space applications. Hodson et al. exposured CNTs-TIMs to γ-ray irradiation with dosages of 50 and 100 Mrad [3]. The quality of the CNTs, based on the ID/IG band ratio, was monitored by Raman spectroscopy and showed a moderate increase in the graphitic order of the CNT walls. Additionally, the thermal interface resistance was measured before and after the gamma-ray irradiation using a transient photoacoustic method. Although the exposure to such radiation has the potential to affect significantly CNT TIMs, no degradation in the thermal performance was observed.

The most used ionizing irradiation techniques for material modification are electron-beam and γ-ray [4–6]. Recently, X-ray irradiation has attracted much attention [7, 8]. This chapter deals with the effects of electron-beam and X-ray irradiation on the structure and properties of nano-dimensional TiO_2 and carbon nanostructures such as graphene (G) and multiwalled carbon nanotubes (MWCNTs). First, basic introduction to the studied materials, some fundamental aspects of ionizing irradiation and its interaction with solid matter will be given.

2.2 Structure and Photocatalytic Activity of TiO_2 Nanoparticles

Titania (TiO_2) is known as inexpensive, non-hazardous and chemically stable material possessing a variety of structures and consequently variety of properties. Considering this, TiO_2 nanoparticles found extensive range of technical and technological applications in: (i) paints as a white pigment or to make substances opaque; (ii) sun blocking materials; (iii) sensor devices; (iv) chemical and photocatalysis; (v) as reinforcement component in polymer-based nanocomposites or synergetic additive in nano-scaled metal (Pt, Ru, Co, Ni, etc) electrocatalytic materials in hydrogen economy; (vi) as additive to cement or ceramic tiles; (vii) as self-cleaning glass, etc. [9–12].

Three natural polymorphs of TiO_2 are generally known: anatase, rutile, and brookite. Brookite is more difficult to be synthesized, so rarely studied [13]. Anatase and rutile have tetragonal unit cells (Fig. 2.1, left) with different cell parameters ($a = 3.782$ Å, $b = 9.502$ Å for anatase and $a = 4.587$ Å, $b = 2.953$ Å for rutile) and different spatial orientation [10]. Elementary building unit in both crystal systems is an octahedron with different distortion, where one Ti atom is surrounded by 6 oxygen atoms. Each TiO_6^{2-} octahedron in anatase is connected with 8 neighbouring octahedra, four connected by vertices and four by corners (Fig. 2.1, right). In rutile, each octahedron is connected with10 neighbouring octahedra, two connected by edges and eight by vertices [13].

Rutile is thermodynamically more stable at higher temperatures having particles larger than 35 nm, while anatase is more stable at lower temperatures having particles of 10–20 nm [9]. The most important property of TiO_2 is semiconductivity, related to its photocatalytic activity. The photocatalytic activity is mostly used to

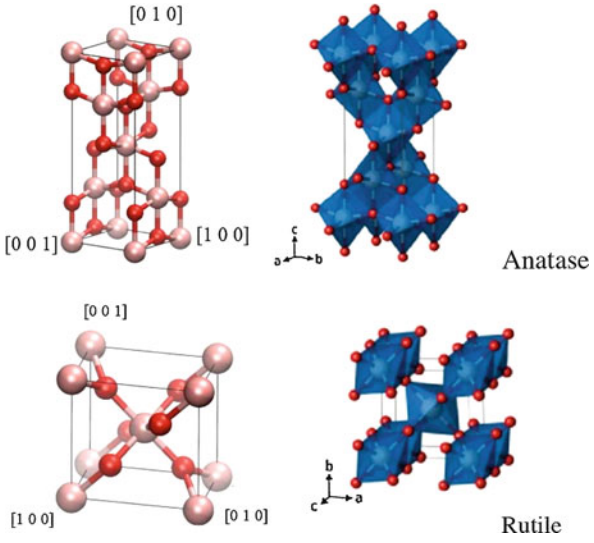

Fig. 2.1 Unit cells of TiO_2 (anatase and rutile) and connection between their basic building units

decompose toxic and heavily biodegradable organics into CO_2, H_2O and inorganics or for photocatalytic production of hydrogen. TiO_2 is n-type semiconductor due to oxygen vacancies within its crystalline lattice, with relatively large energy of the band gap (3.2 eV for anatase and 3.0 eV for rutile). But despite the larger band gap, anatase has been proven as a more efficient photocatalyst due to the following reasons [14]: (1) as a result of the higher Fermi level compared to rutile, anatase shows higher adsorption affinity to hydroxyl groups and lower affinity to oxygen adsorption; (2) due to lower temperatures of production, anatase has smaller particles than those of rutile and consequently higher specific surface area and surface adsorption capacity and (3) anatase has indirect band gap in contrast to rutile, which has direct band gap. In the case of indirect band gap, the excited electron can be stabilized at the lower level in the conduction band, which leads to its longer life and higher mobility.

Due to these values of the energy of the band gap, the light absorption is limited mainly to UV light (less than 5% of visible light). For this reason, modifications of the electronic structure of TiO_2 are needed to shift the response from the UV to the visible light. There are two approaches to decrease the bang gap energy of TiO_2 and thus to extend the light absorption of TiO_2 in the visible range [14]: (1) to incorporate alien elements (doping) into the framework of the TiO_2 crystals and (2) to enhance the surface defects, namely Ti^{3+} and oxygen vacancies. These effects can be achieved using ionizing irradiation such as e-beam, X-ray or γ-ray, as a result of their interaction with TiO_2 at atomic and crystalline level (see the section below).

Synthesis of TiO_2 nanoparticles is based mainly on bottom-up approach, involving the formation of nanostructures atom-by-atom, molecule-by-molecule or ion-by-ion [15]. Many bottom-up methods were developed for the synthesis of TiO_2 [9]: (1) sol-gel method, (2) hydrothermal/solvothermal synthesis, (3) microemulsion and micelle methods, (4) pulsed laser deposition, (5) chemical/physical vapor deposition, (6) plasma vapor deposition, (7) direct oxidation, (8) electrochemical (anodic) deposition, (9) microwave radiation, etc. Within this chapter a research on the influence of X-ray irradiation on the structural changes of TiO_2 synthesized by sol-gel method, and consequently on the visible light absorption will be presented.

2.3 Carbon Nanostructures (CNSs)

As a naturally occurring material, carbon could exist in two types of crystalline lattice: (1) sp^3 hybridized lattice of diamond, where each C atom is bonded with 4 others (single bonds) and (2) sp^2 hybridized lattice of graphite with flat layers in which carbon atoms are bonded in hexagons with single and double bonds. Subject of interest in this chapter are nanostructures based on graphitic sp^2 hybridized structure.

In Fig. 2.2 different sp^2 graphitic based structures are shown. The basic building unit of all of them is graphene – a single atomic plane of graphite that is separated enough from the other ones to be considered as independent, i.e. two-dimensional

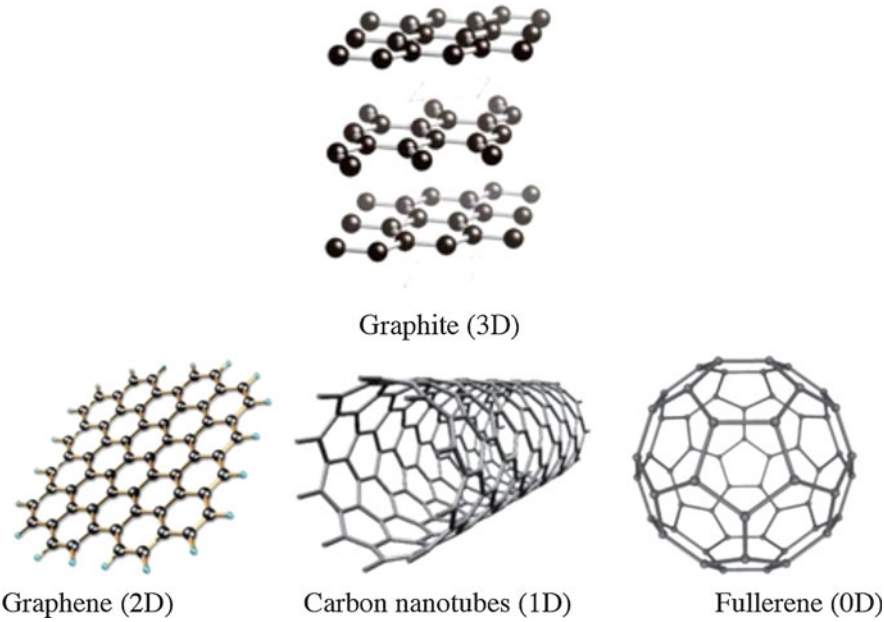

Fig. 2.2 Different types of graphite based sp^2 bonded carbon nanostructures

(2D) sheet of sp^2 hybridized carbon atoms arranged in a hexagonal (honeycomb) atomic configuration. A multitude of such layers (at least 100) arranged one above the other form the 3D thin film of graphite [16]. The distance between two neighbouring graphene layers is 3.35 Å, while the distance between neighbouring C atoms within the hexagonal network is 1.42 Å. By wrapping one graphene layer in cylindrical shape, a carbon nanotube (CNT, 1D nanostructure) is obtained, while the wrapping to spherical shape leads to formation of fullerene (OD nanostructure). The appearance of the mentioned carbon nanostructures goes in the opposite order. Fullerenes (OD) were first discovered in 1985, then carbon nanotubes (1D) in 1991 and finally the basic building unit to all of them – graphene (2D) in 2004.

Because the 2D atomic crystalline structure of graphene is stable under ambient conditions, CNSs exhibit superior physical properties, primarily electrical and mechanical [17, 18]. In the band structure of graphene, σ-states form occupied and empty states separated with a wide energy gap, whereas the π-states form a single band with conical self-crossing points – Dirac points [19]. The Fermi-level corresponds to the Dirac points, where both, the valence and the empty conduction band meet with zero band gap, revealing that the graphene is a semiconductor with zero band gap. This arrangement of the Dirac points contributes to extremely high mobility of the charge carriers (electrons) of 20,000 $cm^2 \cdot V^{-1}$ for single layered graphene.

After its discovery, graphene was recognized as the strongest material after the confirmation of its breaking strength of 42 N m^{-1} and Young's modulus of 1.0 TPa

Table 2.1 Physical properties of carbon nanostructures (CNSs)

	Graphene	SWCNTs	MWCNTs
Specific electrical resistance, μΩ·cm	1	5–50	5–50
Thermal conductivity, $W \cdot m^{-1} \cdot K^{-1}$	~5000	400–6000	600–3000
Tensile strength, GPa	130	50–500	10–60
Young modulus, TPa	1	1	0.3–1
Specific weight, $g \cdot cm^{-3}$	0.25	0.8	1.8
Surface area, $m^2 \cdot g^{-1}$	2600	400–900	200–400

[20]. Before that, diamond was considered as the strongest material. This higher strength of graphene vs. diamond can be explained by the energies needed for breaking the bonds within their structures. Diamond contains only single bonds between the C atoms. The energy needed for their breaking is 345 $kJ \cdot mol^{-1}$. In the graphene structure, one carbon atom is bonded with three neighboring C atoms by two single bonds and one double bond. The energy needed for breaking of the double bond is 611 $kJ \cdot mol^{-1}$. Therefore, the presence of double bonds increases the total energy needed for breaking of bonds between the C atoms, and consequently the mechanical strength increases.

Graphene sheets can consist of only one graphene layer (single layered graphene), two layers (bilayered graphene) or more layers (multilayered graphene). As the number of layers of graphene material increases, its properties decrease. When one graphene layer is wrapped in cylindrical shape, single wall carbon nanotube (SWCNTs) is obtained, while the nanotubes formed by wrapping of multilayered graphene with diameter of 0.75–3 nm, are called multiwalled carbon nanotubes (MWCNTs) with diameter in range of 2–30 nm [21]. Depending on the orientation of the chiral vector (m, n) which corresponds to a section of the nanotube perpendicular to the nanotube axis, and the spiral angle θ between the chiral and lattice vector, carbon nanotubes can be distinguished in three main groups [21, 22]: (1) armchair ($m = n$; $\theta = 30°$), (2) zig-zag ($m = 0$; $\theta = 0$), and (3) chiral ($m \neq n$; $0 < \theta < 30°$). The armchair CNTs have metallic electroconductivity, whereas the zigzag and chiral are semiconductors of p-type.

Due to their superior properties [22–24] (Table 2.1), such as high strength, light weight, metal or semiconductor electron conductivity, high thermal conductivity, large surface area, etc., CNSs found a wide range of applications in modern technology and almost in all segments of human live. The most important fields of their application are: (1) nanoelectronics, (2) plastic electronics, (3) nanorobotics, (4) catalysis, (5) energy storage, (6) functional nanocomposites, (7) nanosensors and many others.

There are different techniques for synthesis of CNSs. Graphene can be produced using the following methods [25, 26]: (1) arc discharge (used in their discovery by Iijima [28]), (2) laser ablation, (3) chemical vapor deposition, (4) hydrothermal synthesis, (5) molten salt electrolysis etc. Within this chapter a research of the influence of X-ray irradiation on the structural changes of graphene and MWCNTs synthesized by molten salt electrolysis will be given.

2.4 Types of Ionizing Irradiations

Ionizing irradiation initiates when a unstable atom releases its excess of energy or mass (or both), in order to achieve a stable state of minimum energy. It includes several forms such as alpha (α), beta (β) and neutron (n) particles and X-ray and gamma-ray (γ-ray) irradiations. It is evident that the ionizing irradiation can have a corpuscular or wave nature [29].

α-irradiation arises when the various atom releases particles composed of two protons and two neutrons (Fig. 2.3). α-particles are a highly ionizing form of particle radiation but have low penetration depth. They are used mainly for synthesis or treatment of polymer-based composites. When the originating atom releases electron (e^-) or positron (e^+, particle with weight and size in the range of electron, but positively charged), β-irradiation takes place. β-particles are mostly electrons, so it is known also as electron-beam or e-beam irradiation. The third type of corpuscular ionizing irradiation is neutron particles, which are released by the originating atom. The neutron irradiation is the only type that can make other materials radioactive. X-ray and γ-ray have wave nature and they are part of the electromagnetic wave spectrum. X-rays originate from an electronic cloud, while γ-rays are emitted as photon energy from an unstable nucleus. Also, their difference is in their wavelength, frequency and energy. Compared with γ-ray, X-ray possesses longer wavelength ($\lambda_{X\text{-ray}} = 10^{-9} \div 10^{-12}$ m vs. $\lambda_{\gamma\text{-ray}} = < 10^{-12}$ m), lower frequency ($f_{X\text{-ray}} = 10^{17} \div 10^{20}$ Hz vs. $f_{\gamma\text{-ray}} = 10^{20} \div 10^{24}$ Hz) and lower energy ($E_{X\text{-ray}} = 1.24 \div 124$ keV vs. $E_{\gamma\text{-ray}} = 124$ keV $\div$ 1.24 MeV). There are many well-established processes using γ-ray irradiation for fabrication of some nanomaterials, mainly metals and their polymer composites [30, 31]. X-rays are very common in medicine and in materials characterization. They are not so frequently used for production or improvement of the properties of the materials as the γ -rays or e-beam. Neutron irradiation is consisted of free neutrons, usually emitted by spontaneous or induced nuclear fission. This is the only type of irradiation that is able to make other materials radioactive, so they are not used for materials synthesis or processing.

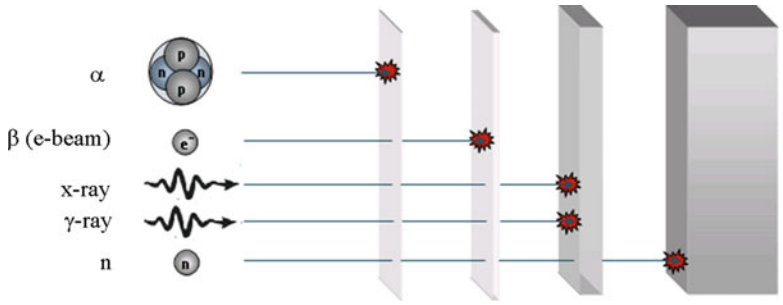

Fig. 2.3 Illustration of the interaction between ionizing irradiations and material structure

From the energetic point of view, the ionizing irradiations can be classified as low-energy low penetration depth, including α-particles and e-beam irradiations. γ-ray, X-ray and neutron particles are high-energy irradiations with greater penetration depth. Depending on the way it how ionizes the matter, the ionizing irradiation could be direct ionizing and indirect ionizing [32]. Direct ionizing radiation corresponds to the charged particles which have Coulomb interaction with an orbital electron of a target atom. Indirect ionizing radiation occurs in two stages. In the first stage, as a result of neutron kinetic energy or photon energy deposition, fast charged particles, e.g. electrons or positrons, are released. In the second stage, these electrons or positrons deposit their energy directly in the material through Coulomb interactions with the orbital electrons of an atom.

2.5 Interaction Between Ionizing irradiation and Materials

When the ionizing irradiation passes through a solid matter, an interaction takes place at atomic and crystal levels, causing different defects and disorders within the material structure.

At the atomic level, there are several effects as result of this interaction such as [33–35]: (1) excitation of electrons, ionizing of individual atoms and formation of ion pairs or electron + positron pairs; (2) Compton effect, i.e. the photon collides with the atom, being turned from its route releasing part of its energy enough to absorb an electron from the atom; (3) collective excitation of electrons (plasmons); (4) creation of phonons, causing the heating of the solid matter; (5) displacement of atoms in the bulk or sputtering of atoms from the surface of the solid matter; (6) emission of photons or secondary (Auger) electrons and (7) breaking of the bonds or cross-linking. These interactions are illustratively shown in Fig. 2.4.

At the crystal level, these interactions can cause [36]: (1) displacement of the atoms from their normal position, generating different types of crystal defects such as lattice vacancies, embed in interstitial positions or interchange of dissimilar atoms within the lattice structure and (2) production of impurities, that is, alteration of nuclei into other ones, caused by neutrons by fission and activation.

Depending of the material nature, different types of the effects noted above are possible [33]. In insulators, the ionization can play the dominant role. In metals (conductors), irradiation effects are attenuated due to the presence of conduction electrons. The damage in metal structure is limited to knock-on atom displacements. The excitation effects are less important, so the metals are relatively stable under irradiation, in particular at low energies. In molecules all types of destruction are possible, in particular bond breaking.

According to the literature [37, 38], under the irradiation alteration in the TiO_2 structure could be an increase of Ti^{3+}/Ti^{4+} ratio or generation of oxygen vacancies.

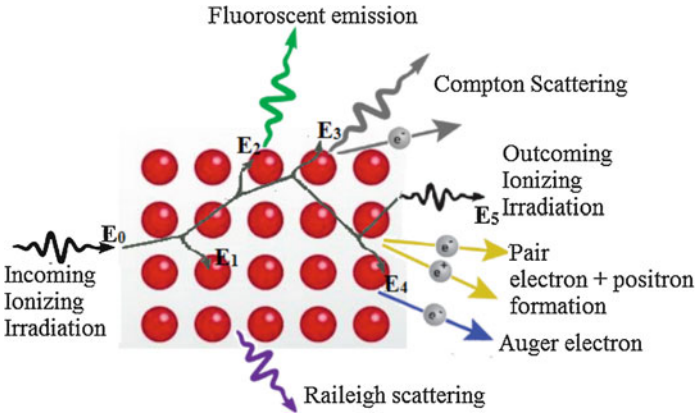

Fig. 2.4 Illustration of the interaction between ionizing irradiation and material

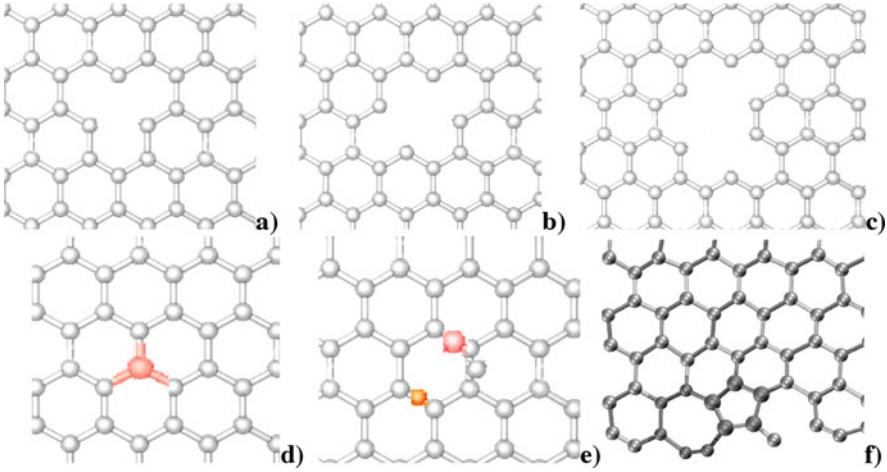

Fig. 2.5 Schematic illustration of the ionizing irradiation-induced defects in graphene structure: (**a**) single vacancy, (**b**) double vacancies, (**c**) multiple vacancies, (**d**) substitution of C atom, (**e**) interstition of C or other types of atoms and (**f**) in-plane disorder

These structural changes can promote the decrease of band gap energy and consequently, increase of the photocatalytic activity.

In the CNSs, the ionizing irradiation can cause different types of defects in their structure [39–41] as shown in Fig. 2.5. As a result of the breaking of bonds between the C atoms and sputtering of atoms from the surface, vacancies could be formed, from single (1 C atom missed, Fig. 2.5a), double (2 C atoms missed, Fig. 2.5b) to multiple (more C atoms missed, Fig. 2.5c). In Fig. 2.5d, substitution of a C atom with another one is shown. Also, interstitial adatom could be formed (C or another,

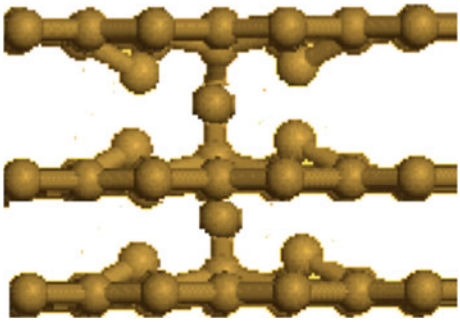

Fig. 2.6 Schematic illustration of the ionizing irradiation-induced graphitization

Fig. 2.5e). Along the vacancies and interstitials, CNSs develop an extended reconstruction of the atomic network forming a pentagon or heptagon (Fig. 2.5f) [41]. These types of defects are known as in-plane disorders or Stone–Wales (SW) defects, associated with a rotation of a bond in the CNSs atomic network.

When the ionizing irradiation passes through CNS, its energy could induce the removal of some functional groups and an addition of other C atom on their place, creating additional C–C or C=C bonds [42, 43]. The addition of these carbon atoms could be done on the same graphene plane or above it (Fig. 2.6). Because of the newly formed carbon bonds, this phenomenon could be called graphitization. The structural changes as a result of the graphitization lead to increased crystallinity, and better thermal stability and electrical conductivity.

2.6 Effect of Irradiation on the Structure of TiO_2 Nanoparticles

TiO_2 nanoparticles were prepared by sol-gel method at ambient pressure. Titanium tetraisopropoxide (TTIP) (Aldrich, 97%) was used as a precursor. The setup for sol-gel synthesis is shown in Fig. 2.7a.

TTIP was dissolved in anhydrous ethanol (Merck, p.a.) in the ratio ethanol: TTIP = 8:1. To enhance hydrolysis of Ti-tetraisopropoxide to $Ti(OH)_4$, small amount of 1 M HNO_3 was added in ratio TTIP:HNO3 = 10:1. The hydrolysis of TTIP was performed according to the following chemical reaction:

$$\mathrm{Ti}\left(\mathrm{OCH}(\mathrm{CH_3})_2\right)_4 + 4\mathrm{H_2O} \rightarrow \mathrm{Ti(OH)_4} + 4(\mathrm{CH_3})_2\mathrm{CH(OH)}$$

The mixture was evaporated at 60 °C with stirring of 900 rpm, until fine nanostructured yellow-white powder was obtained. According to our previous research [44], it was found that removal of OH^-, i.e. formation of TiO_2 begins at 220 °C. This cryptocrystalline TiO_2 is completely transformed to anatase at near 360 °C. At 520 °C transformation of anatase to rutile crystalline phase begins. In order to

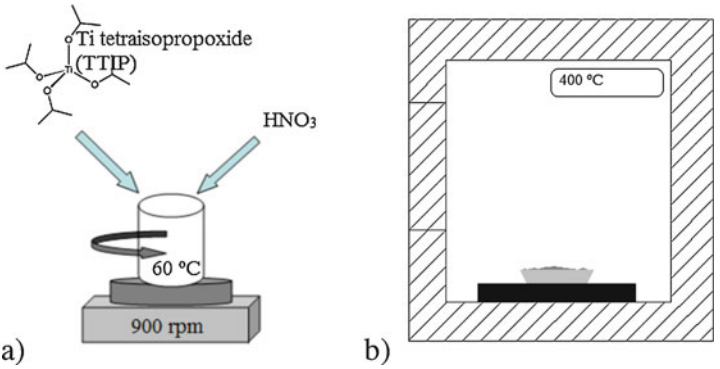

Fig. 2.7 Sol-gel synthesis of $Ti(OH)_4$ using TTIP as a precursor (a) and thermal treating of $Ti(OH)_4$ (b)

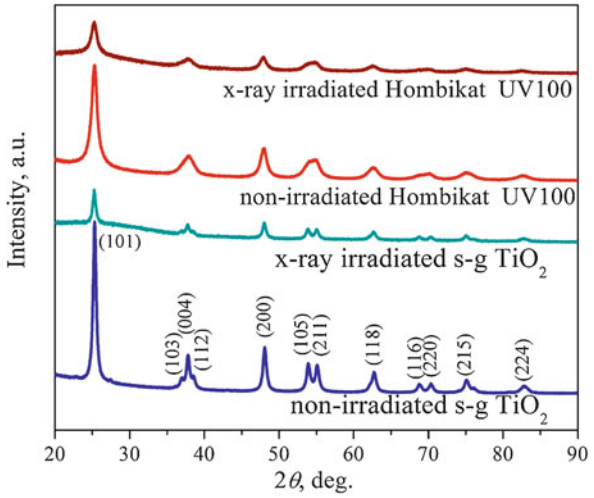

Fig. 2.8 XRD spectra of the studied TiO_2 nanoparticles

produce anatase nanoparticles, the thermal treatment of $Ti(OH)_4$ was performed at 400 °C (Fig. 2.7b). After it, a light-grey powder of TiO_2 was obtained.

The produced TiO_2 nanoparticles were exposed to X-ray irradiation with dose of 7 mGy. For comparison, commercial TiO_2 nanoparticles Hombikat UV 100 (Sachtleben Chemie GmbH, Duisburg, Germany) were irradiated under the same conditions. The structural changes caused by the X-ray irradiation were studied by X-ray diffraction (XRD) and Raman spectroscopy. The characteristic peaks of the XRD spectra of the studied samples denoted with corresponding Muller's indices, point out only the presence of anatase crystalline structure (Fig. 2.8).

The sol-gel produced TiO_2 shows better crystallinity than the commercial Hombikat UV, which consisted of anatase with smaller particle size [45]. Comparing the non-irradiated and X-ray irradiated samples, one can see that the interaction between irradiation energy and TiO_2 crystals causes lower crystallinity expressed

with less intensive and broader peaks. The changes of some structure parameters such as interplanar distance, cell parameters and particle size, calculated by corresponding equations [46], are summarized in Table 2.2. As a result of the electronic or collective electron excitation caused by the X-ray irradiation, the interplanar distance and the cell parameters increase, while the particle size decreases with ~2 nm.

The Raman spectra show the same effects as those detected by XRD analysis with Raman modes corresponding to anatase crystalline structure. The spectra of the irradiated samples are less intensive and broader, whereas the Raman modes are shifted to higher wave numbers (Fig. 2.9, Table 2.2). This shift can be a result of both, the decreasing of the particle size and the presence of the oxygen vacancies [47]. So, the ionizing irradiation (X-ray) causes a similar effect (oxygen vacancies) as the doping with some other elements [48].

These evident changes in the structure affect the properties of the TiO_2 nanoparticles. Thermal gravimetric (TG) spectra of the studied samples are shown in Fig. 2.10.

For both sol-gel prepared TiO_2 samples (non-irradiated and irradiated), at temperature near 100 °C evaporation of the physically adsorbed moisture occurs, while at about 150 °C decomposition of the chemically adsorbed moisture takes place, i.e. removing OH^- groups from $Ti(OH)_4$. From this temperature to near 500 °C unusual increase of the temperature can be observed for both samples. This is due to oxidation of the residual organic functional groups with OH^- groups released from $Ti(OH)_4$ [49]. This effect is more pronounced for the X-ray irradiated sample, which points out that its structure is already smashed and reaction between the functional groups occurs easily. The crossing at higher temperatures (near 550 °C and from 730 to 760 °C) points out the beginning and the end of the rutile transformation. The end of this transformation in the irradiated samples takes place at lower temperature. The trend of the TG curves for commercial Hombikat UV 100 is typically decreasing. Due to breaking of the bonds in the structure as a result of X-ray irradiation, the irradiated sample shows lower thermal stability with weight loss of 45%. The corresponding weight loss of the non-irradiated sample is only 10%.

The UV-Vis spectra of the sol-gel prepared TiO_2 before and after X-ray irradiation are presented in Fig. 2.11. With determination of the cut off wavelength λ_0 from the spectra and using the Eq. (2.1) the energy of the band gap E_g can be calculated [50]:

$$E_g = \frac{1240.82}{\lambda_0} \tag{2.1}$$

For non-irradiated TiO_2, λ_0 was determined to be 427.58 nm and the energy of the band gap 2.90 eV. The corresponding values for X-ray irradiated TiO_2 were 482.81 nm and 2.57 eV respectively. According to this analysis, one can conclude that the changes in the structure of TiO_2 as a result of X-ray irradiation cause a decrease of the band gap energy (from 2.9 to 2.57 eV), as well as increase and shift of its photocatalytic activity to the region of visible light.

Table 2.2 Calculated values of interplanar distance, cell parameters, particle size from XRD spectra and Eg Raman mode for (1) sol-gel as prepared TiO_2, (2) X-ray irradiated sol-gel prepared TiO_2, (3) commercial Hombikat UV 100 and (4) X-ray irradiated Hombikat UV 100

Samples	2θ	{h,k,l}	FWHM	d-space	a, Å	c, Å	D, nm	D, nm	E_g Raman mode
1	25.30933	{101}	0.4943244	3.5175	3.7832	9.5546	17.22	16.87	141.9909
	48.08112	{200}	0.5507473	1.8916			16.52		
2	25.258	{101}	0.60282	3.5245	3.7874	9.6278	14.12	14.52	144.4467
	48.0251	{200}	0.6122	1.8937			14.85		
3	25.27818	{101}	0.9209733	3.5218	3.7932	9.4811	9.24	9.30	147.3682
	47.94761	{200}	0.9717569	1.8966			9.36		
4	25.2293	{101}	1.17663	3.5285	3.7984	9.5308	7.24	7.82	150.0778
	47.8763	{200}	1.08201	1.8992			8.4		

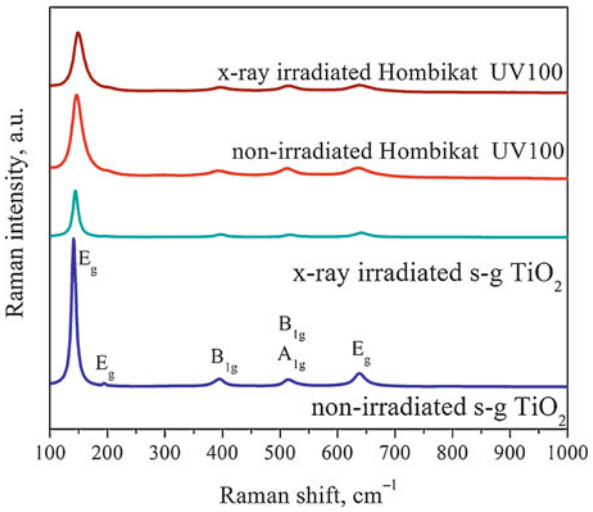

Fig. 2.9 Raman spectra of the studied TiO_2 nanoparticles

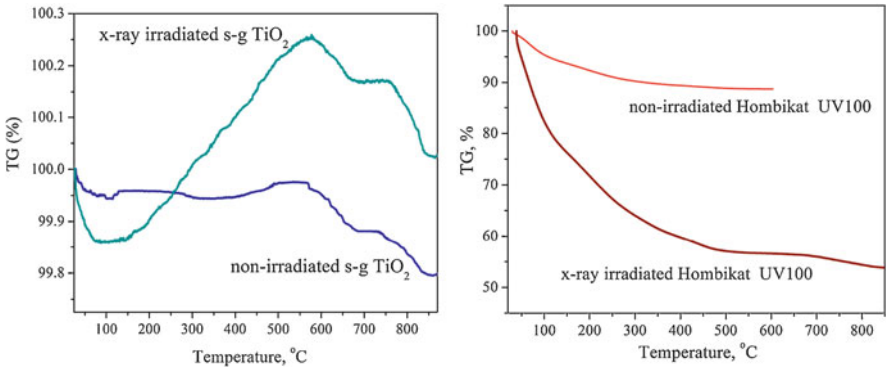

Fig. 2.10 TG spectra of the studied TiO_2 nanoparticles

2.7 Irradiation of Carbon Nanostructures

In this paragraph the results from the research of the irradiation effects on the CNSs structures will be given. The studied CNSs, such as graphene (G) and multiwalled carbon nanotubes (MWCNTs), were produced by electrolysis of molten alkaline metal salts at graphite electrodes. The setup for fabrication of CNSs is shown in Fig. 2.12. Varying the electrolysis parameters (temperature, time, current density or cell potential) [51], different kind of sp^2 hybridized carbon nanostructures could be obtained.

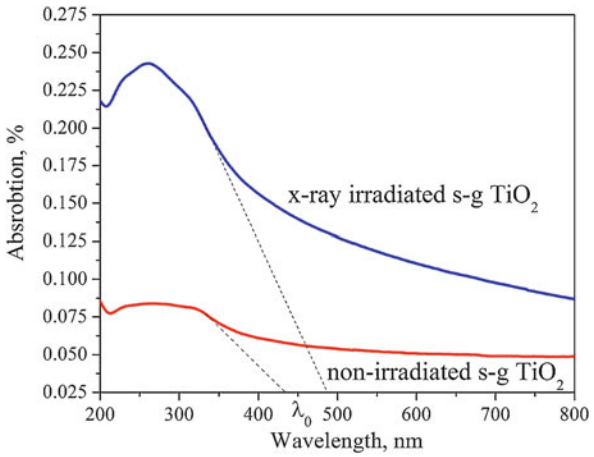

Fig. 2.11 Absorption spectra of the studied TiO_2 nanoparticles

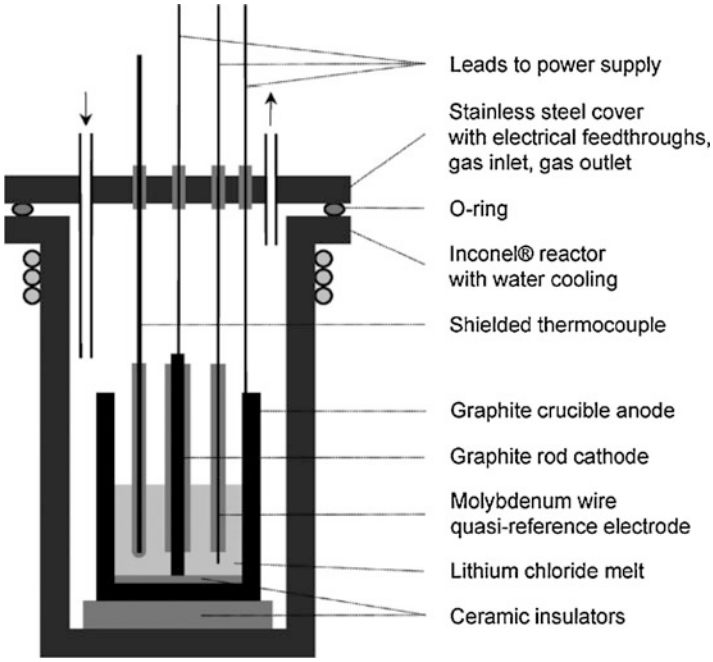

Fig. 2.12 Schematic view of the setup for fabrication of the studied CNSs

The produced CNSs were exposed to X-ray irradiation under the same conditions as TiO_2 (dose of 7 mGy).

Scanning electron microscopy (SEM) was performed on the as-produced and irradiated CNSs with JEOL JSM-7800F. Typical SEM images are presented in Fig. 2.13. It is evident that as-produced graphene exhibits well-exfoliated nano-

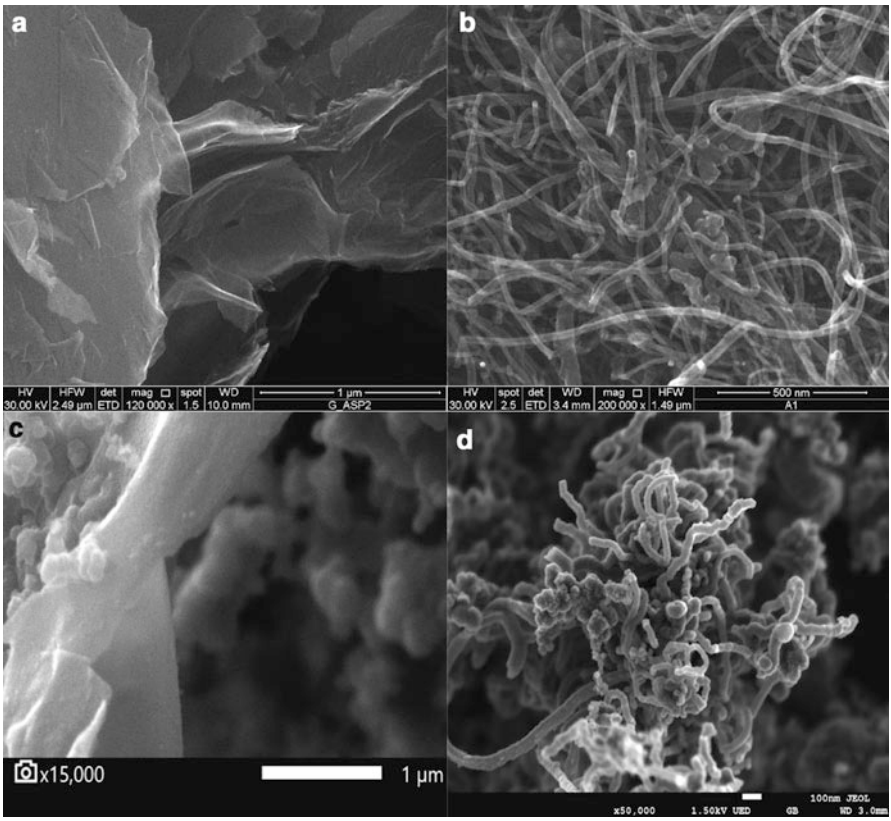

Fig. 2.13 SEM images of CNSs: (**a**) as-prepared graphene, (**b**) as-prepared MWCNTs, (**c**) X-ray irradiated graphene and (**d**) X-ray irradiated MWCNTs

sheets. The as-produced MWCNTs are entwined with diameter of 20–60 nm and length of 1–10 μm. After irradiation, graphene shows crumpled layered structure, restraining the aggregation of graphene nano-sheets, while MWCNTs are chopped, shortened and wrinkled, which enlarges their specific surface area.

Very useful tool to evaluate and study the CNSs structures and to identify order/disorder in the sp^2-bonded carbon sheets is the Raman spectroscopy. Raman spectra of the studied CNSs are shown in Fig. 2.14.

The most important Raman modes for identifying order/disorder of the CNSs are located in the region of 1200–1800 cm^{-1}. The first one, D mode, with a maximum of near 1350 cm^{-1} indicates disordered carbon atoms, defects such as pentagons and heptagons in graphite, edges of the graphite crystal, and amorphous carbon [52, 53]. The second one, G mode with a maximum near 1580 cm^{-1} is related to the highly oriented graphite (ordered structure) [54, 55]. The ratio of the intensities

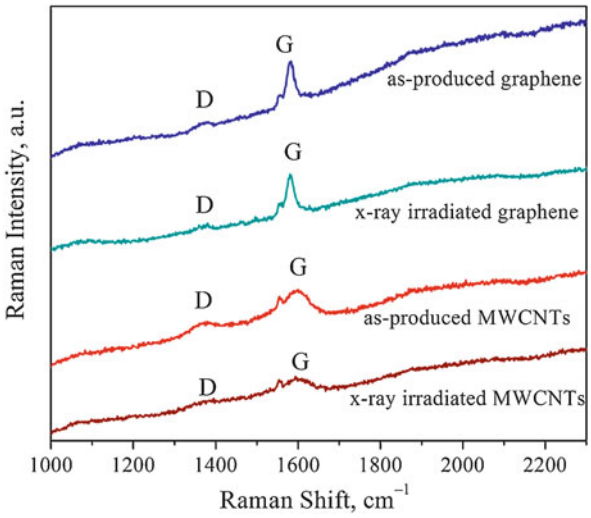

Fig. 2.14 Raman spectra of the studied CNSs

Table 2.3 I_D/I_G ratios for the studied CNSs

Carbon nanostructure	I_D/I_G
As-prepared graphene	0.21
X-ray irradiated graphene	0.18
As-prepared MWCNTs	0.30
X-ray irradiated MWCNTs	0.28

of the characteristic peaks (I_D/I_G) indicates the extent of defects and impurities, i.e. it is a measure of order/disorder of the CNSs. The calculated I_D/I_G ratios (intensity height ratio) for the studied CNSs are listed in Table 2.3.

It can be observed that the I_D/I_G ratio slightly decreases after the irradiation treatment. According to the literature data, this ratio usually increased with the total irradiation dose as a result of structural disorders (formation of defects such as vacancies or in-plane disorder) and decreased after annealing [56]. This slight decrease of I_D/I_G ratio suggests that the graphitization is the predominant mechanism of the interaction of CNSs with the applied energy irradiation [5]. This means that X-ray irradiation energy removes the functional groups and on their place addition of another C atom takes place, forming additional C–C bonds. The structural changes as result of the graphitization lead to increased crystallinity, and better thermal stability and electrical conductivity.

The additional graphitization can be detected also in the Fourier transform infrared (FTIR) spectra of the studied carbon nanostructures, shown in Fig. 2.15. Namely, during the X-ray irradiation of the carbon chains in the CNSs, additional C–C bonds are formed. The positions of all the prominent peaks remain unchanged after the irradiation, except for the peak corresponding to C=C. For non-irradiated CNSs, its position is at 1576 cm^{-1}, while after irradiation it is shifted to 1603 cm^{-1}.

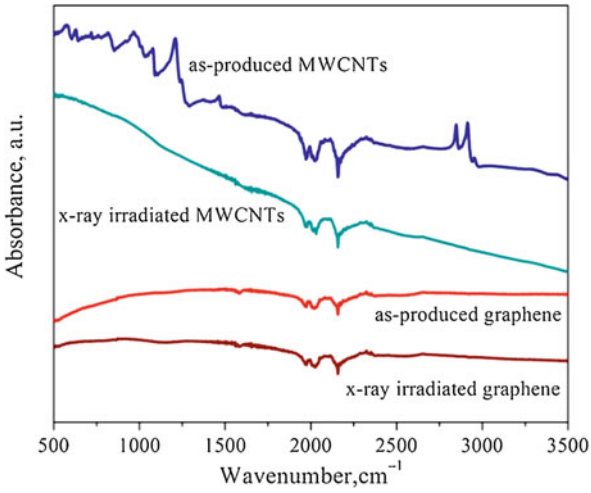

Fig. 2.15 FTIR spectra of the studied CNSs

Table 2.4 Zeta potentials of the studied CNSs

Carbon nanostructure	Zeta potential
As-prepared graphene	−32.5
X-ray irradiated graphene	−16.8
As-prepared MWCNTs	−32.4
X-ray irradiated MWCNTs	−20.4

The measured values of the zeta potential at pH ~ 7 are presented in Table 2.4. The negative values of the studied CNSs point out that their surface is negatively charged. This is very appropriate for their application as catalyst support or as reinforcement phase in nanocomposites, because the catalytic phase or the polymer matrix have positive charge. The zeta potential after X-ray irradiation decreases almost twice. This is due to electrical charge exchange during the graphitization, i.e. during the formation of additional C–C bonds.

2.8 Conclusion

According to the results presented above, we can draw the following conclusions:

1. X-ray irradiation causes changes in the TiO_2 structure expressed with the increase of the interplanar distance, change of the lattice parameters and reduction of the nanoparticle size. These changes lead to a shift of the light absorption to the region of visible light and a decrease of the band gap energy, which indicates increased photocatalytic activity.
2. X-ray irradiation causes structural changes of the carbon nanostructures (graphene and MWCNTs). The predominant mechanism of interaction of the irradiation with CNSs is graphitization, i.e. creation of additional C–C bonds.

This leads to increased crystallinity and better thermal stability. Also, the morphology of CNSs was changed. After irradiation, graphene shows crumpled layered structure, while MWCNTs are shortened and wrinkled, enlarging their specific surface area.

Acknowledgments This work has been supported by the International Atomic Energy Agency (IAEA) within the Project Application of Ionizing Irradiations in Nanotechnology for Environmental, Energy and Health purposes (NANO IRRA NET, 2018–2019). The authors would like to thank Volodymyr Yukhymchuk from the Department of Optics and Spectroscopy, National Academy of Science of Ukraine, for the collaboration on Raman spectroscopy.

References

1. Chmielewski AG, Haji-Saeid M (2005) In: Gazsó LG, Ponta CC (eds) Radiation inactivation of bioterrorism agents, NATO science series I: life and Behavioural sciences – Vol. 365. IOS Press, Amsterdam, p 1
2. Yamamoto K, Koga Y, Fujiwara S, Kubota M (1996) New method of carbon nanotube growth by ion beam irradiation, Appl Phys Lett 69:4174
3. Hodson SL, Sayer RA, Koehler TP, Serrano JR, Dalton SM, Fisher TS (2013) Proceedings of the ASME 2013 summer heat transfer conference, pp. HT2013–3047C
4. Krasheninnikov AV, Banhart F (2007) Engineering of nanostructured carbon materials with electron or ion beams, Nat Mater 6:723
5. Bzdon S, Góralski J, Maniukiewicz W, Perkowski J, Rogowski J, Szadkowska-Nicze M (2012) Radiation-induced synthesis of Fe-doped TiO_2: Characterization and catalytic propertiesRadiat Phys Chem 81:322
6. Diab KR, Doheim MM, Mahmoud SA, Shama SA, El-Boohy HA (2017) Gamma-Irradiation Improves the Photocatalytic Activity of Fe/TiO_2 for Photocatalytic Degradation of 2-Chlorophenol, Chem Mater Res 9:49
7. Liu CJ, Yang TY, Wang CH, Chien CC, Chen ST, Wang CL, Leng WH, Hwu Y, Lin HM, Lee YC, Cheng CL, Je JH, Margaritondo G (2009) Enhanced photocatalysis, colloidal stability and cytotoxicity of synchrotron X-ray synthesized Au/TiO_2 nanoparticles, Mater Chem Phys 117:74
8. Yang CC, Sun YJ, Chung PH, Chen WY, Swieszkowski W, Tianf W, Lin FH (2017) Development of Ce-doped TiO_2 activated by X-ray irradiation for alternative cancer treatment, Ceram Int 43:12675
9. Yan X, Chen X (2015) Encyclopedia of inorganic and bioinorganic chemistry. Wiley, Hoboken. https://doi.org/10.1002/9781119951438.eibc2335
10. Diebold U (2003) The surface science of titanium dioxide, Surf Sci Rep 48:53
11. Mezey EJ (1966) In: Powell CF, Oxley JH, Blocher JM (eds) Vapor deposition. New York, Wiley
12. Paunović P, Popovski O, Dimitrov AT (2011) In: Reithmaier JP et al (eds) Nanotechnological basis for advanced sensors, NATO Science for Peace and Security Series B: Physics and Biophysics. Springer
13. Noman MT, Ashraf MA, Azam Ali A (2019) Synthesis and applications of nano-TiO_2: a review, Environ Sci Pollut Res 26:3262
14. Luttrell T, Halpegamage S, Tao J, Kramer A, Sutter E, Batzill M (2014) Why is Anatase a Better Photocatalyst Than Rutile? - Model Studies on Epitaxial TiO_2 Films, Sci Rep 4:4043
15. Paunović P, Petrovski A, Načevski G, Grozdano V A, Marinkovski M, Andonović B, Makreski P, Popovski O, Dimitrov AT (2015) In: Reithmaier JP et al (eds) Nanoscience

advances in CBRN agents detection, information and energy security, NATO Science for Peace and Security Series A: Chemistry and Biology, Springer, p 239
16. Geim AK, Novoselov KS (2007) The rise of graphene, Nat Mater 6:183
17. Novoselov KS, Jiang D, Schedin F, Booth TJ, Khotkevich VV, Morozov SV, Geim AK (2005) Two-dimensional atomic crystals, Proc Natl Acad Sci U S A 102:10451
18. Katsnelson MI (2007) Graphene: carbon in two dimensions, Mater Today 10:20
19. Kavitha MK, Jaiswal M (2016) Graphene: A review of optical properties and photonic applications, Asian J Phys 25:809
20. Rocha CG, Rümmeli MH, Ibrahim I, Sevincli H, Börrnert F, Kunstmann J, Bachmatiuk A, Pötschke M, Li W, Makharza SAM, Roche S, Büchner B, Cuniberti G (2012) In: Choi W, Lee JW (eds) Graphene: synthesis and application. CRC Press/Taylor & Francis Group, Boca Raton, p 27
21. Obite F, Ijeomah G, Bassi JS (2018) Carbon nanotube field effect transistors: toward future nanoscale electronics, Int J Comput Appl 41:149 https://doi.org/10.1080/1206212X.2017.1415111
22. Saito R, Dresselhaus G, Dresselhaus MS (1998) Physical properties of carbon nanotubes. London, Imperial College Press
23. Serp P, Corrias M, Kalck P (2003) Carbon nanotubes and nanofibers in catalysis, Appl Catal A 253:337
24. Ghosh S, Balandin AA (2012) In: Choi W, Lee JW (eds) Graphene: synthesis and application. CRC Press/Taylor & Francis Group, Boca Raton, p 313
25. Das S, Choi W (2012) In: Choi W, Lee JW (eds) Graphene: synthesis and application. CRC Press/Taylor & Francis Group, Boca Raton, p 27
26. Mikhailov S (ed) (2011) Physics and applications of graphene – experiments. InTech, Rijeka
27. Journet C, Bernier P (1998) Production of carbon nanotubes, Appl Phys A Mater Sci Process 67:1
28. Iijima S (1991) Helical microtubules of graphitic carbon, Nature 354:56
29. Mirion Technologies, Learning center (2015) https://www.mirion.com/learning-center/radiation-safety-basics/types-of-ionizing-radiation
30. Ni Y, Ge X, Liu H, Zhang Z, Ye Q, Wang F (2001) Fabrication of Nano-rod Copper-polymer Composites by γ-Irradiation Route in a Heterogeneous System, Chem Lett 30:458
31. Kabir MS, Hossain MS, Mia M, Islam MN, Mahmudur Rahman MM, Hoque MB, Chowhury MS (2018) Mechanical Properties of Gamma-Irradiated Natural Fiber Reinforced Composites, Nano Hybrid Compos 23:24
32. Adlienė D (2017) In: Sun Y, Chmielewski AG (eds) Applications of ionizing radiation in materials processing, volume 1, Institute of Nuclear Chemistry and Technology, Warsaw, p 7
33. Banhart F (1999) Irradiation effects in carbon nanostructures, Rep Prog Phys 62:1181
34. Vasile C, Butnaru E (2017) In: Sun Y, Chmielewski AG (eds) Applications of ionizing radiation in materials processing, volume 1, Institute of Nuclear Chemistry and Technology, Warsaw, p 117
35. Kwatra D, Venugopal A, Anant S (2013) Nanoparticles in radiation therapy: A summary of various approaches to enhance radiosensitization in cancer, Transl Cancer Res 2:330
36. Holbert KE (2008) Radiation effects and damage, lecture notes from EEE 598, School of Electrical, Computer and Energy Engineering, Arizona State University
37. Wronski P, Surmacki J, Abramczyk H, Adamus A, Nowosielska M, Maniukiewicz W, Kozanecki M, Szadkowska-Nicze M (2015) Surface, optical and photocatalytic properties of silica-supported TiO_2 treated with electron beam, Radiat Phys Chem 109:40
38. Latthe SS, An S, Jin S, Yoon SS (2013) High energy electron beam irradiated TiO_2 photoanodes for improved water splitting, J Mater Chem A 1:13567
39. Krasheninnikov AV, Banhart F (2007) Engineering of nanostructured carbon materials with electron or ion beams, Nat Mater 6:723
40. Tian W, Li W, Yu W, Liu X (2017) A Review on Lattice Defects in Graphene: Types, Generation, Effects and Regulation, Micromachines 8:163

41. Li Z, Chen F (2017) Ion beam modification of two-dimensional materials: Characterization, properties, and applications, Appl Phys Rev 4:011103
42. Ilyin AM (2011) In: Gon GJR (ed) Graphene simulation, InTech, Rijeka, p 39
43. Krasheninnikov AV, Nordlund K (2010) Ion and electron irradiation-induced effects in nanostructured materials, J Appl Phys 107:071301
44. Paunović P, Grozdanov A, Češnovar A, Ranguelov B, Makreski P, Gentile G, Fidančevska E (2015) Characterization of Nanoscaled TiO_2 Produced by SimplifiedSol–Gel Method Using Organometallic Precursor, J Eng Mater Technol 137:021003
45. Hombikat UV 100, Technical information, Sachtleben Chemie GmbH, http://kuroppe.tagen.tohoku.ac.jp/~dsc/0075e072.pdf
46. Sands DE (1975) Introduction to crystallography. Dover Publications, New York
47. Šćepanović MJ, Grujić-Brojčin M, Dohčević-Mitrović ZD, Popović ZV (2009) Characterization of anatase TiO_2 nanopowder by variable-temperature Raman spectroscopy, Sci Sinter 41:67
48. Khan MM, Ansari SA, Pradhan D, Ansari MO, Han DH, Lee J, Cho MH (2014) Band gap engineered TiO_2 nanoparticles for visible light induced photoelectrochemical and photocatalytic studies, J Mater Chem A 2:637
49. Čenovar A, Paunović P, Grozdanov A, Makreski P, Fidančevska E (2012) Preparation of nanocrystalline TiO_2 by Sol-gel method using titanium tetraisopropoxide (TTIP), Adv Nat Sci Theory Appl 1:133
50. Paschotta R (2008) Article on 'band gap' in the encyclopedia of laser physics and technology, 1. Edition, Wiley-VCH
51. Kamali AR, Fray D (2016) Electrochemical interaction between graphite and molten salts to produce nanotubes, nanoparticles, graphene and nanodiamonds, J Mater Sci 51:569
52. Hiura H, Ebbesen TW, Tanigaki K, Takahashi H (1993) Raman studies of carbon nanotubes, Phys Chem Lett 202:509
53. Li W, Zhang H, Wang C, Xu L, Zhu K, Xie S (1997) Raman characterization of aligned carbon nanotubes produced by thermal decomposition of hydrocarbon vapor, Appl Phys Lett 70:2684
54. Tunistra F, Koenig JL (1970) Raman Spectrum of Graphite, J Chem Phys 53:1126
55. Ferrari AC, Meyer JC, Scardaci V, Casiraghi C, Lazzeri M, Mauri F, Piscanec S, Jiang D, Novoselov KS, Roth S, Geim AK (2006) Raman Spectrum of Graphene and Graphene Layers, Phys Rev Lett 97:187401
56. Zhang EX, Wang B, Newaz A (2011) Low-Energy X-ray and Ozone-Exposure Induced Defect Formation in Graphene Materials and Devices, IEEE Trans Nucl Sci 58:2961

Chapter 3
The Corona Triode Charging/Polarization System

Pedro Rafael dos Santos Prezas, Manuel Jorge de Araújo Pereira Soares, Mauro Miguel Costa, and Manuel Pedro Fernandes Graça

Abstract The development and understanding of the corona triode charging technique, in the seventies and in the eighties is intimately related to Brazilian researchers and academic institutes. Contrarily to older two-electrode systems, the corona triode system comprises three electrodes: the discharge point electrode, the metallic grid and the plane electrode, where the charging current can be measured and controlled. It has been widely applied in the electrical charging of polymer foils for electret production, in the research of the charge stability and charging/injection processes in dielectric materials, principally in film/foil form and in electrostatic separation processes. Corona-based electrostatic precipitators have found widespread application in the treatment of contaminated gases and also in the separation of metals and non-metal components. It has, among others, the advantages not to require the deposition of an electrode on the sample surface exposed to the discharge, allowing the reversal of the discharge polarity (positive or negative), to pole/charge samples with complex non-planar geometries and it is well suited for large scale film poling/charging. A new a corona triode system developed in our facilities is presented, including some theoretical background behind this technique. This system can operate on a more traditional method and also on a more sophisticated principle based on a feedback circuit that continuously adjusts the voltage applied to the metallic grid in order to maintain the charging current flowing through the sample constant. Thus, the sample surface potential buildup can be monitored in real-time by the metallic grid voltage. Charging results on bioactive hydroxyapatite [$Ca_{10}(PO_4)_6(OH_2)$ – Hap] pellets, prepared from commercial Hap powders, are presented and discussed.

P. R. dos Santos Prezas (✉) · M. J. de Araújo Pereira Soares · M. P. F. Graça (✉)
I3N and Physics Department, University of Aveiro, Aveiro, Portugal
e-mail: pedro.rafael@ua.pt; mpfg@ua.pt

M. M. Costa
Physics Department, Federal University of Mato Grosso, UFMT, Cuiabá, Brazil

P. Petkov et al. (eds.), *Nanoscience and Nanotechnology in Security and Protection against CBRN Threats*, NATO Science for Peace and Security Series B: Physics and Biophysics, https://doi.org/10.1007/978-94-024-2018-0_3

Keywords Corona triode system · Corona discharge · Electrical charging · Hydroxyapatite

3.1 Introduction

The roots and development of the corona triode charging technique are strongly connected to Brazilian researchers and universities, who contributed in the seventies and the eighties decisively to its development and understanding. Consequently, names such as R.A. Moreno, B. Gross (born in Germany) and later J.A. Giacometti (born in Brazil) became intimately associated with the corona triode [1–3].

The corona discharge is a stable, self-sustainable, atmospheric electrical discharge that occurs when a sufficiently high potential difference is applied between two asymmetric electrodes, such as a point and plane ones. DC corona voltages in the 10–15 kV range under a "normal" or low-humidity atmosphere environment are frequently applied [4]. The threshold potential difference to start the corona discharge depends upon the availability of free electrons which are able to ionize the surrounding gas molecules, being around 5 kV in a "normal" atmosphere [5]. Two different regions are defined in a corona discharge: the ionization and the drift regions. The ionization region is confined to a region close to the point electrode while the drift region extends to the plane electrode. Figure 3.1 schematizes both regions, including the electric field and ion flow lines [5]. The drift region comprises ionic species with the same polarity, and their mobility is relatively low, in the order of a few cm^2/Vs. The current magnitude in the drift region is in the range of a few μA for potentials between 10 and 15 kV. The corona current always increases with the increase of the corona potential (the potential applied to the point electrode), making the discharge controllable and therefore applicable to generate thermalized ions in order to charge dielectric samples [5].

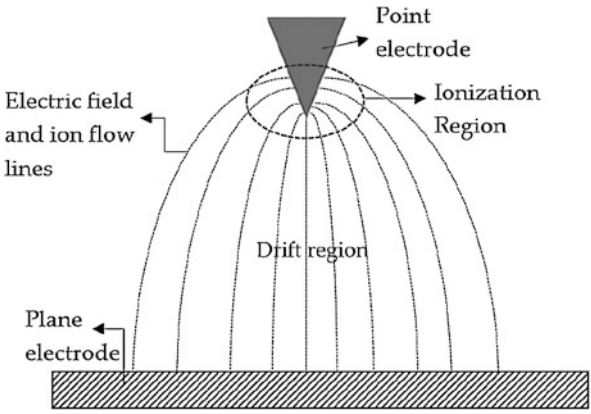

Fig. 3.1 The corona discharge in a point and plane electrode system. Two regions are defined: the ionization region, confined close to the point electrode, and the drift region, extending up to the plane electrode

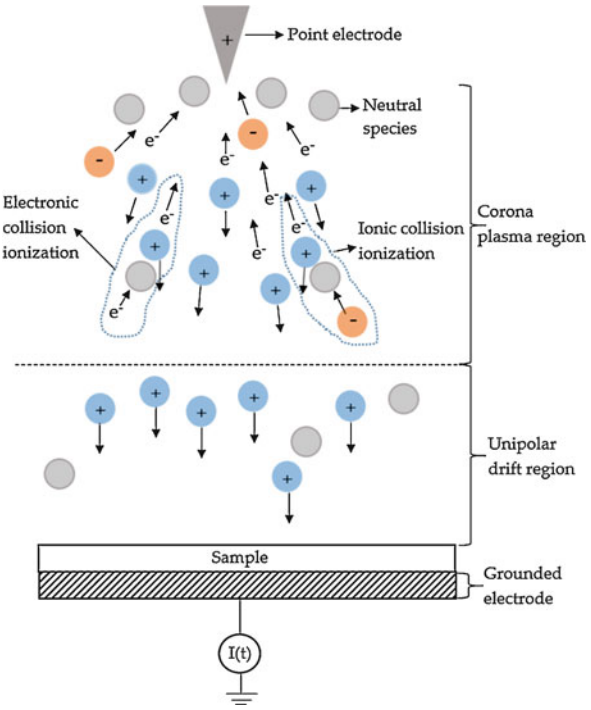

Fig. 3.2 Model of a positive corona discharge. The discharge comprises two main regions: the corona plasma and the unipolar drift regions. The plasma region includes the ionization region. The sample thickness is exaggerated in this figure. (Adapted from [6])

Figure 3.2 displays a model of a positive corona discharge (the sample thickness is exaggerated) [6]. The corona plasma region, containing the ionization region, is maintained by processes such as electron and ionic collisions, and photoionization. The drift region contains ionic species of the same polarity, which are driven towards the surface of the sample covering the grounded electrode. The drift region may also contain neutral species. In negative corona discharge, the electrons are generated by photoemission at the point electrode and captured to form negative ionic species. A very important characteristic of the corona discharge is that the thermal energy of the ionic species in the drift region reaching the sample surface is comparable to that of the environment. For this reason, these ions do not penetrate the sample or damage the surface, they just transfer their excess charge to the surface of the sample [7].

The corona discharge has been widely applied in the electrical charging of polymer foils intended to be used in electret microphones, in the investigation of electret formation and charge stability in dielectric materials, especially in film/foil form, in the study of polarization phenomena in dielectrics and ferroelectrics, in electro-photographic processes, in the charging of polymer wires to be used in electrostatic filters and electrical separation of particles from gases (corona-based electrostatic precipitators have found widespread application in the treatment of contaminated gases in heavy industries) [5, 8].

The first corona systems had only two electrodes, the point and plane ones, and some information would be lost during the charging process, particularly the final

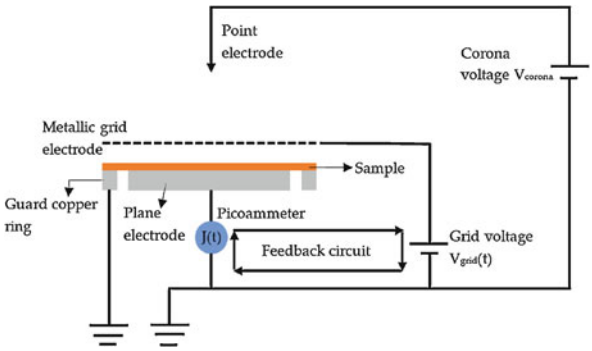

Fig. 3.3 Scheme of a corona triode. As the name suggests, three electrodes are used: the point, grid and plane (or measurement) electrodes

surface potential of the sample. Considering this limitation and also the necessity of an improved charging current radial uniformity reaching the sample, the corona triode was developed and introduced in 1976 [1]. Three electrodes are used instead of two, as the name suggests. The introduction of a metallic grid electrode between the point and the plane electrodes allows to follow the surface potential buildup of the sample during the charging process and to improve significantly the charging current radial uniformity below the grid [1, 7]. The constant current corona triode can be used to evaluate the phase transition in polymers as well as to evaluate the polarization value using only the surface potential vs time curves [9].

Figure 3.3 depicts a technical scheme of a corona triode. One of the voltage sources is connected to the point electrode, and therefore is responsible for producing the corona discharge. The other source is connected to the metallic grid, controlling the grid potential. A picoammeter is connected to the plane electrode (also designated as the measurement electrode) to measure the charging current that flows through the sample. The guard copper ring prevents eventual surface currents from reaching the measurement electrode. The sample (the thickness is exaggerated) is placed on the top of the measurement electrode and the guard ring. Typical point/measurement electrode and grid/measurement electrode distances reported in the literature are in the range of 5–10 cm and 2–5 mm, respectively [2, 7].

The theory behind this technique is now going to be presented, in order to understand the meaning of the "feedback circuit" in Fig. 3.3. Consider Fig. 3.4, which shows the air gap between the metallic grid and the sample, as well as the relevant physical quantities to be considered for this problem [8].

For simplicity, the physical quantities are assumed to be independent of the lateral position coordinate in the air gap, depending only on the vertical coordinate x perpendicular to the sample and grid surfaces [8]. The air gap conduction current is due to the transport of a unipolar ionic charge density $\rho_{gap}(x,t)$, and the current density J(t) reaching the sample surface ($J(t) = I(t)/A$, where A is the sample area) is given by Eq. 3.1 [8, 10]:

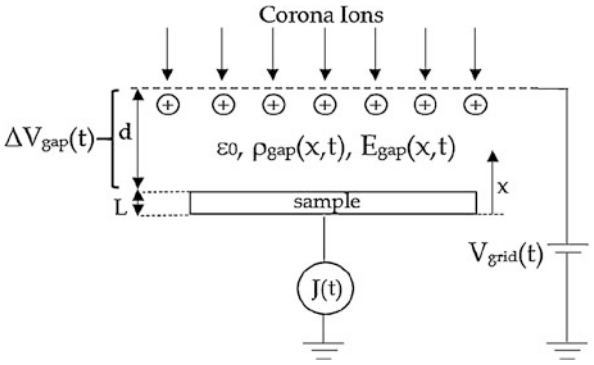

Fig. 3.4 The air gap between the metallic grid and the sample, with the relevant physical quantities. ε_0 is the vacuum dielectric permittivity, $E_{gap}(x,t)$ the gap electric field, $\rho_{gap}(x,t)$ the gap ionic charge density, L and d are the sample and gap thicknesses, $V_{grid}(t)$ the grid voltage and J(t) is the charging current density flowing through the sample. During the discharge, there is a potential difference $\Delta V_{gap}(t)$ between the grid and the sample surface

$$J(t) = \left[v + \mu E_{gap}(x,t)\right]\rho_{gap}(x,t) + \frac{\varepsilon_0 \partial E_{gap}(x,t)}{\partial t} \tag{3.1}$$

where the term $v\rho_{gap}(x,t)$ is the current density due to gas movements produced by the discharge, known as corona wind and $\mu E_{gap}(x,t)\rho_{gap}(x,t)$ is the ionic conduction term, where μ is the mobility. The corona wind term has a small influence on the magnitude of J(t), the ionic conduction term is much more relevant. Equation 3.1 also shows that J(t) depends on the time derivative of $E_{gap}(x,t)$ multiplied by ε_0. This is actually what is known as a displacement current density: a time-varying electric field in a dielectric medium will produce a displacement current contribution. This was discovered by Maxwell and led to the generalization of the Ampère law, producing the well-known Maxwell-Ampère equation, which is included in the Maxwell equations. The integration of Eq. 3.1 over the air gap thickness d, yields Eq. 3.2 [8]:

$$J(t) = \frac{1}{d}\int_{L}^{L+d} \left[v + \mu\, E_{gap}(x,t)\right] \rho_{gap}(x,t)\, dx + \frac{\varepsilon_0}{d}\frac{d}{dt}\left[V_{grid}(t) - V_{sample}(t)\right] \tag{3.2}$$

where $V_{sample}(t)$ is the sample surface potential. $V_{sample}(t)$ can be written according to Eq. 3.3 [7, 8]:

$$V_{sample}(t) = V_{grid}(t) - \Delta V_{gap}(t) \tag{3.3}$$

where $\Delta V_{gap}(t)$ is the potential difference between the grid and the surface of the sample. Analyzing Eqs. 3.2 and 3.3, it is reported that if the current density J (t) flowing through the sample is controlled to be constant $J(t) = J_0$, stationary states

for the gap ionic charge density $\rho_{gap}(x,t)$ and for the gap electric field $E_{gap}(x,t)$ are reached, i.e., these quantities become independent of the time [$\rho_{gap}(x)$ and $E_{gap}(x)$]. In such a case, the second term in Eq. 3.2 is null and J_0 is equal to the medium value of the first term, the conduction current. Furthermore, $\Delta V_{gap}(t)$ becomes independent of the time. Equation 3.3 can be rewritten as [8, 11]:

$$V_{sample}(t) = V_{grid}(t) - \Delta V_{gap} \tag{3.4}$$

Note that in Eq. 3.4 ΔV_{gap} is a constant. Experimentally, ΔV_{gap} is kept constant through the feedback circuit between the current flowing through the sample J(t) and the voltage applied to the grid. During the discharge, as the ionic species transfer their excess charge to the surface of the dielectric sample, its surface potential builds up. The feedback circuit forces J(t) to be at a constant defined value J_0 by increasing the voltage applied to the grid in order to follow the potential build-up of the surface of the sample so that ΔV_{gap} is constant. Therefore, during the corona charging, the potential of the surface of the sample can be directly calculated from the potential applied to the metallic grid through Eq. 3.4, it is just required to subtract the constant gap potential drop [7, 8].

The ΔV_{gap} constant is determined by calibration curves, i.e., the potential drop is determined for different experimental conditions of the system, for example, the distances between point/measurement electrode and grid/measurement electrode, the polarity of the discharge, the discharge potential applied to the point electrode, the temperature and relative humidity of the system. The calibration curves consist of J_0 vs V_{grid} plots, which are performed without any sample covering the measurement electrode. In this situation, it is easy to see that $V_{grid} = \Delta V_{gap}$ the potential applied to the grid is exactly the gap potential drop, because there is no sample.

Another important factor is the atmosphere relative humidity, which should be a variable to be considered in the determination of the calibration curves. Nonetheless, if one finds a way to get a reproducible atmosphere the humidity can be ignored in the calibration curves since it would be similar for all the experiments. As it will be shown, in the system developed we achieve that by having a container with silica gel placed in an adapted furnace where the corona triode is inserted, yielding a reproducible low-humidity atmosphere.

Summing up, in a corona triode charging experiment the user chooses a constant charging current density J_0 (or current I_0) to charge the sample. Through the calibration curves, the user knows the constant value of ΔV_{gap} for the defined charging current I_0 and for the particular experimental conditions. Therefore, the user can apply Eq. 3.4 to directly calculate and follow the potential buildup of the sample. The feedback circuit has to be programmed to maintain the charging current approximately constant at the defined value I_0.

Several advantages of the corona charging with respect to the conventional contact polarization techniques can be mentioned: it does not require the deposition of an electrode on the sample surface exposed to the corona charges, it allows to polarize/charge samples up to higher surface potentials, even if localized dielectric breakdowns occur (because of the absence of two electrodes); it is a well-suited technique for large scale film charging/poling; it is possible to charge/pole samples with complex, non-planar geometries (even materials with porosity) and it allows to

control the polarity of the discharge and thus the sign of the injected charges in the sample [4, 11]. The lack of electrode deposition on the sample surface exposed to the corona charges is a very important advantage regarding the potential application of this technique on the charging/ of bioactive coatings in orthopaedic implants. The strict regulations required to be complied for the introduction of a new implant to the medical market, as defined by the ISO and ASTM standards that regulate this market, could cause serious complications for the acceptance of electrically polarized materials where metallic electrodes had been previously deposited, even with a posterior electrode removal step, polishing for example. In contact polarization methods, Hap has to be heated up to considerable temperatures, typically in the 250–500 °C range. Some diffusion of metallic atoms or ions from the electrode into the sample has to be regarded as a very likely possibility, and even if such diffusion does not occur into the bulk of the sample, a polishing step could not be enough to remove the contaminants, which could also interfere the bioactivity and the *in vivo* cellular behavior. Such an electrically polarized Hap coated implant would certainly face a high degree of resistance to be approved for marketing, contrarily to the corona charged Hap coated implant. Moreover, to polarize conventionally a Hap coated orthopaedic implant would be a daunting task, due to the simple fact that it is not a flat surface and has a considerable surface roughness of few or dozen micrometers. Hence, the corona triode technique contains the requirements which confer it a strong potentiality to be applied in the field of orthopaedics.

3.2 Experimental

A corona triode system was developed "from scratch" for new applications. The main requirements which we defined for our experimental system were (i) to be able to polarize materials with a planar geometry (coatings, bulk samples with planar parallel faces, e.g. pellets, etc.); (ii) to allow the reversal of the corona discharge polarity; (iii) to be able to follow the surface potential buildup of the samples; (iv) to be able to change the discharge temperature. Furthermore, the system must be contained in a reproducible atmosphere, in terms of relative humidity, so that all the discharges occur approximately under the same conditions.

Figure 3.5 presents an overview of the corona triode individual components and of the assembled system. A metallic ring stretches the grid so that it is parallel relative to the measurement electrode surface. The grid is made of stainless steel and has 40 mesh per inch (as defined by the supplier), with a wire diameter of 0.2 mm. One of the requisites of the grid is to have a considerably higher surface area than the sample, which is achieved by the mesh structure and the thin-diameter wire. The distance between the grid and the measurement electrode, without a sample, is 5 mm. Since our Ti substrates have a thickness of 1 mm, the grid/sample distance is 4 mm (the Hap coating thicknesses are in the micrometric range, therefore negligible compared to the Ti substrates thickness).

Fig. 3.5 Photographs of the developed corona triode. In the left, the single components can be observed and, in the right, the assembled system

Fig. 3.6 Photograph of the experimental corona triode system

The central teflon lid (Fig. 3.5), is actually a two-piece structure, allowing to introduce the discharge point electrode and close to the lid. The point electrode is a ceriated tungsten electrode (containing 2 wt% of cerium) with a length of 15 cm and a diameter of 3.2 mm (except on the tip, obviously). The distance between the point and the sample can be easily changed, by just controlling how deep the electrode is inserted in the central teflon lid. When the total electrode length is inserted in the lid, the distance between the point and the measurement electrodes is 7 cm. Thus, the distance between point/sample is approximately 7 cm, disregarding the sample thickness of 1 mm.

Figure 3.6 presents an overview of the developed experimental system. The corona triode is inside a furnace, where the maximum controlled temperature that can be reached is 200 °C, mostly because of the teflon components used in the

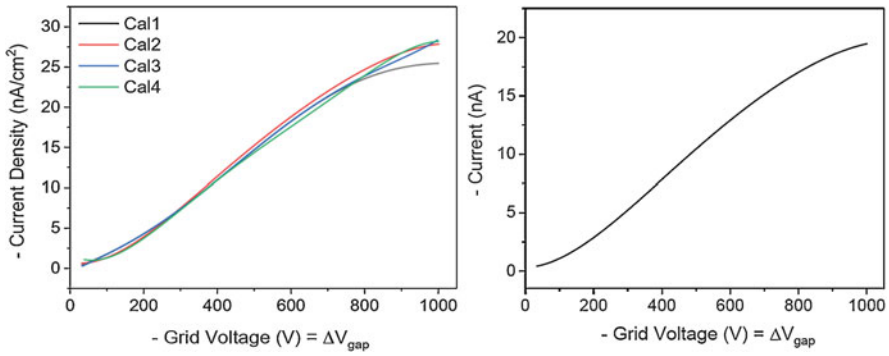

Fig. 3.7 Calibration curves obtained for a negative discharge at 200 °C. In the left: four calibrations were performed, labelled as Cal1, (. . .), Cal4. In the right: the calibration average curve obtained from the four individual calibrations. The corona discharge potential was set at – 15 kV and the point/measurement electrode and grid/measurement electrode distances are 7 cm and 5 mm, respectively

corona triode. Inside the furnace we use thermal resistant silicone electrical cables. Additionally, we have introduced a silica-gel container inside the furnace. We concluded that the silica-gel container allows to obtain a low-humidity, reproducible atmosphere so that we do not have to consider it for the calibration curves since all the discharges are performed in essentially the same relative humidity conditions. Measurements performed with a Fluke 971 Temperature and Humidity Meter show that the relative humidity values of the system at 200 °C (the defined temperature to charge our samples) are below 10%.

It was decided to perform the corona charging of the Hap samples at 200 °C, the maximum service temperature of our experimental system. Moreover, the samples were subjected to a discharge with negative polarity. The calibration curves of the system obtained at 200 °C and for a negative discharge are shown in Fig. 3.7. Four individual calibrations were performed, as the plots in the left show. Each curve is a polynomial fit of the data points. The calibration average curve is shown in the right plot. The average curve refers to the measurement electrode surface area (0.71 cm^2), therefore it is not a current density. The corona discharge potential was set at – 15 kV, and the point/measurement electrode and the grid/measurement electrode distances are 7 cm and 5 mm, respectively. These values, the discharge potential and the electrode distances, are well within the common range of values reported in the literature, as discussed before. It is interesting to note that the information which is requested from the calibration curve in Fig. 3.7 is essentially just a single point. To charge our samples we have to choose a constant charging current value and through the calibration curve, we know the approximate constant gap potential drop for that particular current. Hence, when we charge a sample with that particular current value, we are able to follow the surface potential buildup of the sample directly through the grid voltage: the sample surface potential is the grid voltage minus the constant gap potential drop. Moreover, as Fig. 3.7 shows, low charging current

values imply lower gap potential drops. If the particular sample being charged with a low current value reaches a high surface potential saturation value, some authors even disregard the gap potential drop and directly assume the grid voltage to be approximately the surface potential of the sample. Either way, the sample surface potential buildup can be followed through the grid potential.

Control software routines were developed in order to allow the performance of the calibration experiments and also for the constant charging current method. The grid voltage source and the picoammeter, visible in the bottom shelf on Fig. 3.6, are connected to a computer through a GPIB protocol. The feedback program, as discussed, tries to maintain the charging current flowing through the sample constant at a user-defined value by updating continuously the grid voltage.

3.3 Results and Discussion

Pellets were prepared from Hap commercial powder. The pellets with diameter of 20 mm were prepared using a hydraulic press. The mass of powder used was always 700 mg, leading to a thickness of about 1 mm when applying a tension of 9 tons for 5 min. The pellets were subsequently sintered at 1150 °C for 2 h. One of the prepared pellets is shown in Fig. 3.8. The rationale behind the application of the corona triode in Hap is that it was found in the middle of the nineties that electrical polarization/charging of Hap bioceramics enables the storage of a large charge density magnitude which significantly enhances the bioactivity level [12]. The possibility of charging Hap materials without the necessity of applying electrodes would be very promising, considering the *in vivo* orthopaedic applications and the regulations that such materials have to comply. Thus, the corona triode technique may constitute an excellent opportunity.

The constant current method was applied to charge the samples. Three different charging current values were defined: −1, −3 and − 3.5 nA. Figure 3.9 shows an example of the surface potential buildup curve for a Hap pellet charged with −3 nA.

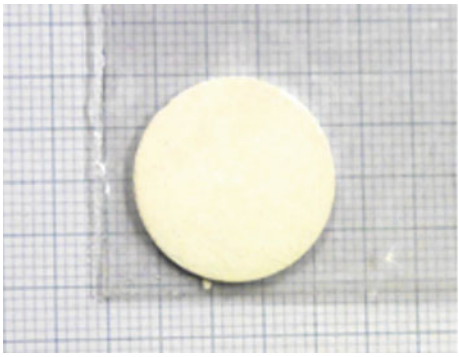

Fig. 3.8 Photograph of one of the Hap pellets prepared from the Hap commercial powder used to test this corona system

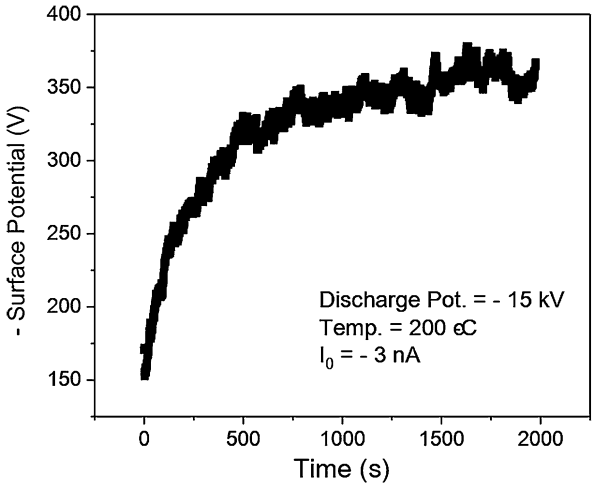

Fig. 3.9 The surface potential buildup curve for a Hap pellet charged with a constant current of −3 nA. The other samples, charged with −1 and − 3.5 nA, present the same characteristic shape

We show the raw data exactly as received through the feedback software, not smoothened or manipulated.

All samples display surface potential buildup curves with the same characteristic shape shown in Fig. 3.9. They start with approximately linear behaviour and subsequently a sublinear behaviour is observed, where the surface potential increases at a slower rate up to the saturation value. This potential buildup characteristic shape is explained as follows: the first approximately linear behaviour suggests that charge trapping is occurring essentially at a surface level; subsequently, the sublinear behaviour, where the potential buildup rate decreases, indicates that charge trapping is occurring predominantly at a bulk level. Finally, when the surface potential tends to reach the saturation value, the current through is essentially purely conductive, no charge trapping is taking place. Additional information regarding this analysis, including some physical background, can be consulted in references [7, 8].

All samples display surface potential buildup curves with the same characteristic shape shown in Fig. 3.9. They start with approximately linear behaviour and subsequently a sublinear behaviour is observed, where the surface potential increases at a slower rate up to the saturation value. This potential buildup characteristic shape is explained as follows: the first approximately linear behaviour suggests that charge trapping is occurring essentially at a surface level; subsequently, the sublinear behaviour, where the potential buildup rate decreases, indicates that charge trapping is occurring predominantly at a bulk level. Finally, when the surface potential tends to reach the saturation value, the current through is essentially purely conductive, no charge trapping is taking place. Additional information regarding this analysis, including some physical background, can be consulted in references [7, 8].

TSDC (thermally stimulated depolarization currents) were undertaken on the charged pellets in order to calculate the stored charge density in the samples and to estimate the temporal stability (discharge time) of the stored charge. Theoretical background behind the TSDC technique is provided in reference [13]. Figure 3.10

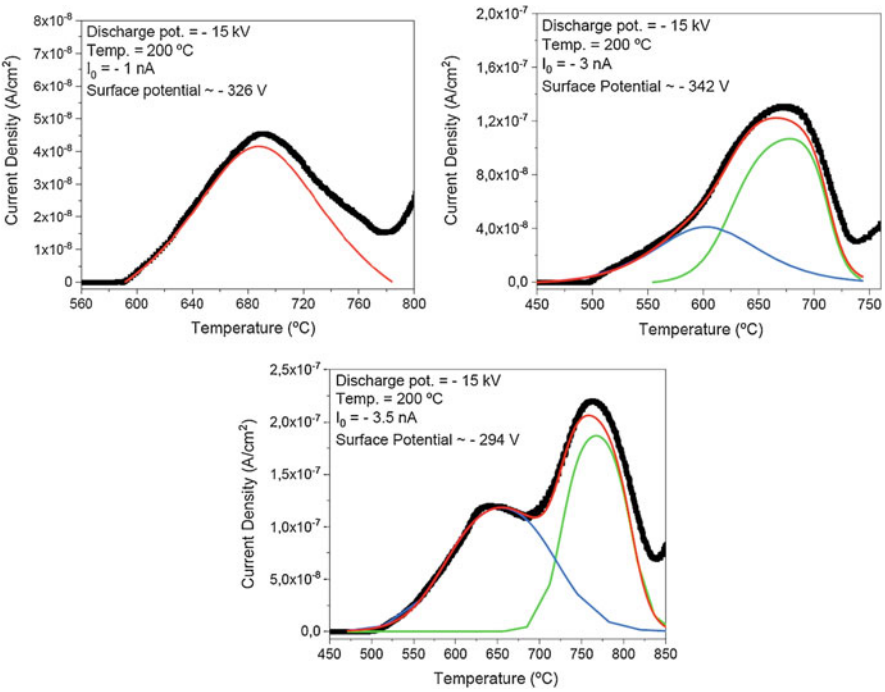

Fig. 3.10 TSDC spectra of the Hap pellets charged with different charging current of −1, −3 and − 3.5 nA, as indicated in each individual spectrum. The surface potential values saturated at about −326, −342 and − 294 V, respectively. The fitting curves of the spectra are also presented

displays the TSDC spectra of the pellets charged with −1, −3 and − 3.5 nA. The fitting curves of the spectra are also shown. The red curve, the cumulative fitting curve, does not coincide with the experimental data because a baseline correction is performed in order to remove the small contribution if the intrinsic exponential ionic conductivity which starts to be significant right after the depolarization peaks (the beginning of this exponential conductivity is visible in Fig. 3.10). While the sample charged with −1 nA presents a spectrum with one clear depolarization process, the samples charged with higher currents present two depolarization peaks. The peak centered at lower temperatures seems to be especially favoured for higher charging current values, comparing the −3 and − 3.5 nA samples.

It is interesting to note that the sample charged with the highest current presents the lowest saturation surface potential. Consider Table 3.1, which presents the stored charge density and the discharge time at room temperature (RT) for the pellets. The sample charged with −3.5 nA has the highest stored charged density although it reaches the lowest surface potential, meaning that the increase of the charging current promotes charge trapping at a bulk level and not at a surface level. For the pellet charged with −3 nA this behaviour is not observed, suggesting that the charge trapping at a bulk might not be yet dominating for this particular charging current

Table 3.1 The stored charge density and discharge time at room temperature (RT) for the Hap pellets charged with −1, −3 and − 3.5 nA

	Constant current value		
	−1 nA	−3 nA	−3.5 nA
Stored charge density ($\times 10^{-4}$ C/cm^2)	1.00	1.81	4.05
Discharge time at RT (months)	~15	~22	~13

value. Observing Table 3.1, the stored charge density values for all the samples are very encouraging. The literature demonstrates that the significant increase of the bioactivity level of Hap is observed both *in vitro* and *in vivo* for stored charge densities in the 10^{-6} C/cm^2 magnitude [14]. Our samples are well above, in the 10^{-4} C/cm^2 range. The stored charge temporal stability values, presented in Table 3.1 as an estimate of the required time for complete discharge at RT, are also highly encouraging providing more than enough time for the stored charge to take its effect *in vivo*.

3.4 Conclusions

A functional corona triode experimental system was developed "from scratch". The system is able to produce a positive or negative discharge; thus, it allows the user to define the charge polarity to be injected in the sample, an important feature and advantage. Compared to more conventional systems, our system offers the possibility of applying the more complex constant charging current method, where the charging current through the sample can be controlled and the sample surface potential buildup can be followed in real-time during a charging experiment. Moreover, the temperature of the experimental system can be controlled up to 200 °C and low humidity, reproducible atmosphere is maintained in all the charging experiments, an important feature to be considered in the development of a corona triode system. Pellets produced from commercial Hap powder were successfully charged through the constant charging current method. The TSDC measurements of the pellets charged with −1, −3 and − 3.5 nA revealed stored charge densities in the 10^{-4} C/cm^2 range. These are extremely interesting values, considering that they are well above the 10^{-6} C/cm^2 magnitude, reported as necessary to produce significant *in vitro* and *in vivo* bioactivity enhancements in Hap biomaterials [14]. The stored charge temporal stability (time for complete discharge at room temperature) estimates are also very encouraging, with values $\geq$13 months, providing more than enough time for the stored charge to take its effect by *in vivo* orthopaedic applications.

References

1. Moreno RA, Gross B (1976) Measurement of potential buildup and decay, surface charge density, and charging currents of corona-charged polymer foil electrets. J Appl Phys 47(8):3397
2. Giacometti JA (1987) Radial current-density distributions and sample charge uniformity in a corona triode. J Phys D Appl Phys 20:675–682
3. Gross B (1987) Radiation-induced charge storage and polarization effects. In: Sessler GM (ed) Electrets. Springer, Berlin/Heidelberg
4. Sessler GM (1994) Poling and properties of polarization of ferroelectric polymers and composites. Key Eng Mater 92–93:249–274
5. Giacometti JA, Oliveira NO Jr (1992) Corona charging of polydmers. IEEE Trans Electr Insul 27(5):924–943
6. Dhima P, Vila F (2017) Determination of volume conductivity of polyethylene using positive corona, when the current through the sample depends linearly on grid potential. J Mater Sci Chem Eng 5:40–51
7. Giacometti JA, Fedosov S, Costa MM (1999) Corona charging of polymers: recent advances on constant current charging. Braz J Phys 29(2):269–279
8. Giacometti JA, Campos JSC (1990) Constant current corona triode with grid voltage control. Application to polymer foil charging. Rev Sci Instrum 61(3):1143–1150
9. Costa MM, Giacometti JA (1993) Electric-field-induced phase changes in polyvinylidene fluoride: effects from corona polarity and moisture. App Phys Lett 62(10):1091–1093
10. Oliveira ON, Ferreira GFL (1985) Grid-to-plate current-voltage characteristics of a corona triode. Rev Sci Instrum 56(10):1957–1961
11. Giacometti JA, Ribeiro PA, Raposo M, Marat-Mendes JN, Campos JSC, DeReggi AS (1995) Study of poling behavior of biaxially stretched poly(vinylidene fluoride) films using the constant-current corona triode. J Appl Phys 78(9):5597
12. Yamashita K, Oikawa N, Umegaki T (1996) Acceleration and deceleration of bone-like crystal growth on ceramic hydroxyapatite by electric poling. Chem Mater 8:2697–2700
13. Prezas PR, Graça MPF (2018) Thermally stimulated depolarization and polarization currents. In: Graça MPF (ed) Electrical measurements: introduction, concepts and applications. Nova Science Publishers, New York
14. Bodhak S, Bose S, Bandyopadhyay A (2010) Electrically polarized HAp-coated Ti: in vitro bone cell-material interactions. Acta Biomater 6:641–651

Chapter 4
Transparent Organic-Inorganic Hybrids Obtained from Covalently Bonded Ureasilicate Monomers: Optical and Mechanical Properties

Vania Ilcheva, Victor Boev, Galina Zamfirova, Valentin Gaydarov, Vanya Lilova, and Tamara Petkova

Abstract Flexible optically clear ureasil monoliths were synthesized by hydrolysis and condensation of two hybrid organic-inorganic ureasilicate monomers (precursors) with different lengths of the polymer segments. The monomer with a longer polymer chain length was obtained by reaction of 1 mol of silicon modified alkoxyde (ICPTES) and 2 mol of double terminated polyetheramine (Jeffamine), and that with a shorter length by reaction of 1 mol of ICPTES and 1 mol of 3-aminopropyl triethoxysilane (APTES), which provides stoichiometric ratio between the initial ingredients. The obtained materials were characterized by optical UV-VIS spectroscopy and depth-sensing indentation method (DSI). The influence of the molar ratio between the ureasilicate monomers on the optical and mechanical properties of the samples was investigated.

Keywords Ureasilicates · Ureasil · Organic-inorganic hybrids · Sol-gel · Microhardness

V. Ilcheva (✉) · V. Boev · T. Petkova
Institute of Electrochemistry and Energy Systems, Bulgarian Academy of Sciences, Sofia, Bulgaria
e-mail: vania.ilcheva@iees.bas.bg

G. Zamfirova · V. Gaydarov
Transport University "T. Kableshkov", Sofia, Bulgaria

V. Lilova
University of Chemical Technology and Metallurgy, Sofia, Bulgaria

P. Petkov et al. (eds.), *Nanoscience and Nanotechnology in Security and Protection against CBRN Threats*, NATO Science for Peace and Security Series B: Physics and Biophysics, https://doi.org/10.1007/978-94-024-2018-0_4

4.1 Introduction

Nowadays, the interest in hybrid organic-inorganic nanocomposites is rapidly growing due to their improved properties and new features in comparison with the traditional materials as metals, polymers and ceramics [1]. It has been known for a long while that mixing organic and inorganic components at the nanometer scale makes possible to control the basic characteristics of the final polymer (such as optical transparency and surface hardness) through the composition and preparation conditions [2]. Well-known representatives of organic-inorganic hybrid polymer nanocomposites are the so-called ureasilicates: polymer/siloxane materials, in which rigid siliceous backbone is covalently bonded to softer organic segments by urea (-NHCONH-) linkages [3, 4]. The versatile properties of these materials make them potential candidates for applications in medicine as biomaterials for bone regeneration [5] and biofilms with bioactive agents [6], in lighting technologies for fabrication of planar doped luminescent solar concentrators [7], in environmental technology for purification of contaminated water and also biosensors for water pollutants [8], in solid state electrochemistry for production of solid state electrochromic devices (smart windows) [9], electrolytes for lithium batteries [10], in optics for manufacturing of full-color displays [11], hosts for organic dyes, semiconductor and metal nanoparticles, etc.

The aim of this work is the preparation of ureasilicate monoliths by hydrolysis and condensation of two hybrid organic-inorganic ureasilicate monomers (precursors) with different lengths of the polymer segments. We suggest that the variation of the length of the polymer chains could influence the mechanical properties, provoked by a change of the molar ratio between the two ureasilicate precursors. Furthermore, and more importantly, the possibility to tailor chemically the composition, the structure and the functionalities of the inorganic building block and of the polymer matrix could attribute to the wider practical application of this type of materials.

4.2 Experimental Details

3-(Triethoxysilyl)propyl isocyanate (ICPTES), O´-bis(2-aminopropyl)- polypropylene glycol-block-polyethylene glycol-block-polypropylene glycol-500, (Jef-famine ED-600) and 3-(aminopropyl) triethoxysilane (APTES) were purchased from Aldrich and applied without further purification. Ethanol (96%, Alfa Aesar) and concentrated ammonia solution (25%, Alfa Aesar) were used as received. Double distilled water was used for the preparation of ammonia solution with appropriate concentration.

Two ureasil precursors with different lengths of the polymer segments were chosen for the preparation of sol-gel materials that includes two moieties blended on the molecular scale. The first monomer (Precursor 1) was obtained by reaction

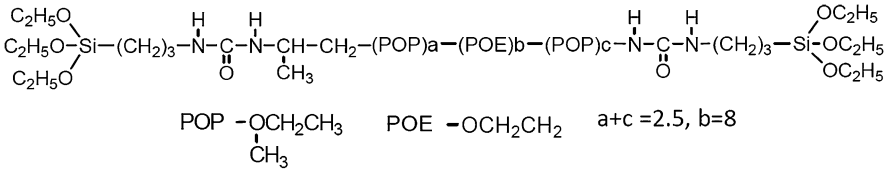

Precursor 1

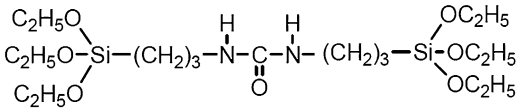

Precursor 2

Fig. 4.1 Chemical structures of Precursor 1 and Precursor 2

Table 4.1 Volume and molar ratios of the precursors used for the preparation of ureasilicate samples

	vol % Precursor 1	vol % Precursor 2	mol % Precursor 1	mol % Precursor 2
Sample 1	100	0	100	0
Sample 2	75	25	56,6	43,4
Sample 3	50	50	30,8	69,2
Sample 4	25	75	12,7	87,3
Sample 5	0	100	0	100

between Jeffamine ED-600 (1 mol) and ICPTES (2 mol), and the second one (Precursor 2) – between APTES (1 mol) and ICPTES (1 mol). These molar contents provide mixing of the components in stoichiometric amounts. Figure 4.1 shows the structures of the resulting precursors. The length of the organic segment of the first precursor synthesized was longer than that of the second one with the length of POE/POP chains and a urea bridge.

The ureasil precursors were mixed at different molar ratios in presence of ethanol, playing the role of homogenizing agent. The sol-gel transition was catalyzed by addition of ammonia solution with appropriate concentration. The mixture was stirred for 20 min and poured into polystyrene Petri dish, tightly sealed with Parafilm, and pin-holed after gelling at room temperature. The duration of the process of gelling was 24 h under these experimental conditions. During the final step the obtained gels were kept in an oven for 24 h at 40 °C with silicagel allowing a completion of the hydrolysis/condensation reactions and an evaporation of the residual liquid. The molar and volume percentages of the reagents used for the synthesis are presented in Table 4.1.

UV-visible transmission spectra of the samples were measured in the wavelength range from 350 to 800 nm at room temperature using a double-beam computer-controlled JASCO spectrophotometer with an accuracy of ±0.5 nm.

Depth-sensing indentation method (DSI) was applied for the measurements of the mechanical characteristics of the samples. The measurements were performed with a

Dynamic Ultra Micro Hardness Tester DUH-211S from Shimadzu (Japan) according to ISO 14577-1. The tests were made in a "load – hold – unload" mode with a holding time at load of 30 s, a loading speed of 0.2439 mN/s and a preset controlled indentation depth of 10 μm. The calculated percent error is in the frame of 3%, which indicates relatively good sample homogeneity.

4.3 Results and Discussion

Pictures of the obtained ureasilicates are shown in Fig. 4.2. It is obvious that all samples demonstrate an excellent transparency in the visible range.

Optical transmission spectra of the samples are presented in Fig. 4.3. An extended spectral transmission window in the UV region with increase of the content of Precursor 2 is detected. The shift of the absorption edge at T = 50% as a function of the molar percent of Precursor 2 is shown in the inset. The maximum blue shift is established for the samples with 100 mol% content of Precursor 2. The improvement of transmission could be explained with the absence of native pale-yellow coloration, inherent to polyetheramines and diamines.

The indentation curves obtained for all measured samples are plotted in Fig. 4.4. Examination of the experimental curves shows that the mechanical behavior of the

Fig. 4.2 Photograph of the samples with different molar ratios of Precursor 1 and Precursor 2

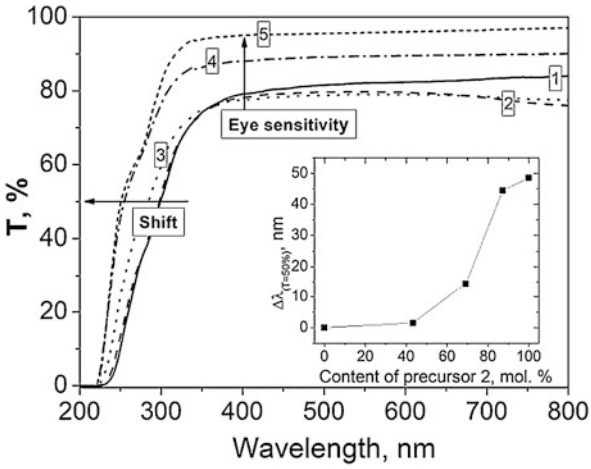

Fig. 4.3 Optical transmission UV-VIS spectra of the samples. Inset: shift of the absorption edge at T = 50% as a function of the molar percentage of Precursor 2

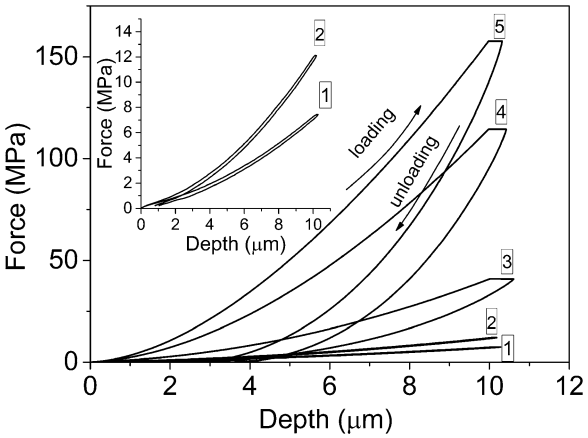

Fig. 4.4 Indentation curves for all measured samples

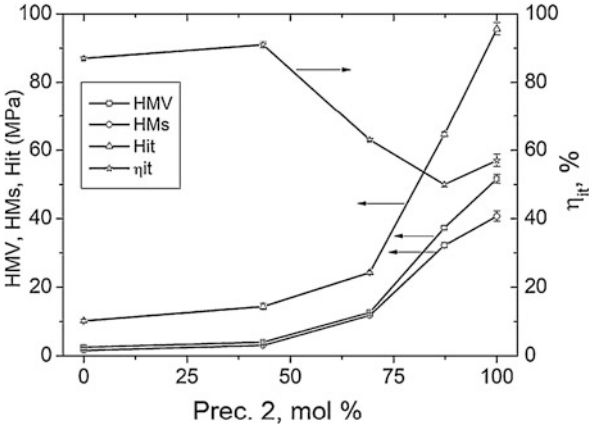

Fig. 4.5 Dependences of Dynamic hardness (HMV), Martens hardness (HMs), Indentation hardness (H_{it}) and Elastic part of the indentation work (η_{it}) on the molar percentage of Precursor 2

samples is clearly distinct. As could be seen in the inset, Samples 1 and 2 do not demonstrate any indentation creep, which is typical for an elastic solid.

The dependences of different parameters (Dynamic hardness, Martens hardness, Indentation hardness and Elastic part of the indentation work) that can be derived from the depth-force curves on the molar content of Precursor 2 are shown in Fig. 4.5. The obtained results reveal that at lower content of Precursor 2 (Sample 1 and Sample 2) the Dynamic hardness, the Martens hardness and the Indentation hardness display a minor increment. At the same time these samples indicate very high elasticity according to the values, obtained for the Elastic part of the indentation work.

Further addition of Precursor 2 leads to drastic change in the parameters. The Dynamic hardness, the Martens hardness and the Indentation hardness increase significantly and grow consistently for Samples 3, 4 and 5. The Elastic part of the indentation work shows an opposite behavior. Thus, Sample 1 and Sample 2 are very elastic and soft, whereas the other three samples are much harder. The obtained results demonstrate that the studied mechanical parameters depend mainly on the silica content which contributes significantly to the total hardness of the material.

4.4 Conclusions

Novel ureasil hybrid structure was obtained by co-condensation of two ureasilicate precursors with different lengths of the organic segments. The synthesized materials exhibit excellent transparency in the visible range. The addition of second precursor leads to significant blue-shift of their absorption edge. It opens a prospect for extending the light-harvesting window in device performance of light solar concentrators. The mechanical properties of the ureasilicate organic-inorganic hybrids, obtained by co-condensation of two ureasilicate precursors, are easily controllable by variation of their molar ratio.

Acknowledgments The authors are grateful for the financial support of this work by the Bulgarian Ministry of Education and Science (NSF DN09/12).

References

1. Borovin E (2015) NMR characterization of sol-gel derived hybrid nanomaterials: insight on organicinorganic interfaces. PhD thesis
2. Gómez ML, Fasce DP, Williams RJJ, Previtali CM, Montejano HA (2010) Transparent polysilsesquioxane films obtained from bridged ureasil precursors: tunable photoluminescence emission in the visible region and filtering of UV-radiation. Macromol Mater Eng 295:1042
3. Armand M, Poinsignon C, Sanches JV, Bermudez VZ (1994) U. S. Patent 5283310
4. Bermudez VZ, Carlos LD, Duarte MC, Silva MM, Silva CJR, Smith MJ, Assunção M, Alcácer L (1998) A novel class of luminescent polymers obtained by the sol–gel approach. J Alloys Compd 275–277:21
5. Oshiro JA Jr, Scardueli CR, Lopes de Oliveira GJP, Marcantonio RAC, Chiavacci LA (2017) Development of ureasil-polyether membranes for guided bone regeneration. Biomed Phys Eng Express 3:015019
6. de Jesus NAM, de Oliveira AHP, Tavares DC, Furtado RA, de Silva MLA, Cunha WR, Molina EF (2018) Biofilm formed from a tri-ureasil organic−inorganic hybrid gel for use as a cubebin release system. J SolGel Sci Technol 88:192
7. Kaniyoor A, McKenna B, Comby S, Evans RC (2016) Design and response of high-efficiency, planar, doped luminescent solar concentrators using organic–inorganic di-ureasil waveguides. Adv Opt Mater 4:444
8. Bekiari V, Lianos P (2006) Ureasil gels as a highly efficient adsorbent for water purification. Chem Mater 18:4142

9. Barbosa PC, Fernandes M, Vilela SMF, Gonçalves A, Oliveira MC, Fortunato E, Silva MM, Smith MJ, Rego R, de Zea Bermudez V (2011) Di-ureasil hybrids doped with LiBF4: attractive candidates as electrolytes for "smart windows". Int J Electrochem Sci 6:3355
10. Nunes SC, de Zea Bermudez V, Ostrovskii D, Silva MM, Barros S, Smith MJ, Carlos LD, Rocha J, Morales E (2005) Diurea cross-linked poly(oxyethylene)/siloxane ormolytes for lithium batteries. J Electrochem Soc 152:A429
11. Carlos LD, Sá Ferreira RA, De Zea Bermudez V, Ribeiro SJL (2001) Full-color phosphors from amine-functionalized crosslinked hybrids lacking metal activator ions. Adv Funct Mater 11:111

Chapter 5
Sol-Gel Technique to Design Hybrid Materials and their Application in Water Purification

Inna V. Melnyk, Veronika V. Tomina, Nataliya V. Stolyarchuk, and Miroslava Václavíková

Abstract The reaction of hydrolytic polycondensation underlying the sol-gel method is extensively applied in the production of inorganic and hybrid organic-inorganic materials. Its advantages include variable synthesis conditions, the possibility to use multi-component systems (considering precursors, e.g. alkoxysilanes), multiformity of the final products (monoliths, films, coatings, or powders of different dispersion). In our research, we focused on the design of functionalized hybrid materials using silane with amino group. The current report presents the synthesis of silica nano- and microparticles, magnetic core-shell particles and ceramic membranes using the same sol containing structure-forming agent tetraethoxysilane (TEOS) or 1,2-bis(triethoxysilyl)ethane (BTESE) and 3-aminopropyltriethoxysilane (APTES). The synthesized materials were tested for the sorption of pollutants, such as ions of Cu, Pd, Pb, Ag, some organic dyes, as well as biomolecules of albumin and urease. These results may be interesting for scientists and engineers from different areas, such as materials science, nanotechnology, life sciences, medicine, and environmental chemistry.

Keywords Sol-gel method · Polyorganosiloxanes · Bridged polysilsesquioxanes · Silica particles · Magnetite/silica composites · Ceramic membranes · Environmental technologies

I. V. Melnyk (✉)
Institute of Geotechnics, SAS, Kosice, Slovakia

Chuiko Institute of Surface Chemistry, NAS of Ukraine, Kyiv, Ukraine
e-mail: melnyk@saske.sk

V. V. Tomina · N. V. Stolyarchuk
Chuiko Institute of Surface Chemistry, NAS of Ukraine, Kyiv, Ukraine

M. Václavíková
Institute of Geotechnics, SAS, Kosice, Slovakia

P. Petkov et al. (eds.), *Nanoscience and Nanotechnology in Security and Protection against CBRN Threats*, NATO Science for Peace and Security Series B: Physics and Biophysics, https://doi.org/10.1007/978-94-024-2018-0_5

5.1 Introduction

Silica-based materials with different functional groups and structures have progressed significantly over the recent years due to their multifunctional applications in sorption technologies, catalysis, nanomedicine, ecoanalytical chemistry, biotechnology and separation technology [1–3].

The sol-gel process based on the reaction of hydrolytic polycondensation of alkoxysilanes is a simple and convenient method for the preparation of silica materials. To begin with, in the presence of water the alkoxy groups in the alkoxysilanes hydrolyze to ≡Si–OH silanol groups. The latter easily interact with each other to form siloxane bonds ≡Si–O–Si≡, thus composing oligomers. Further condensation of these oligomers fabricates inorganic polymers of different structures. As a result of the growth of the polymers, colloidal particles appear, followed by their enlargement and aggregation causing the sol-gel transition. The majority of the alkoxysilanes are easily mixable fluids, and such syntheses are often conducted in ethanol to decrease the influence of coproducts on the reaction process.

The following research summarizes the results from hydrolytic polycondensation reactions of alkoxysilanes for the production of hybrid materials with amino groups in their surface layers. Generally, we used two-component reaction systems regarding the alkoxysilanes (Fig. 5.1). The first component acting as a structuring agent was either tetraethoxysilane (TEOS), $Si(OC_2H_5)_4$, or 1,2-bis (triethoxysilyl)ethane (BTESE), $(H_5C_2O)_3Si–C_2H_4–Si(OC_2H_5)_3$, while the second component was

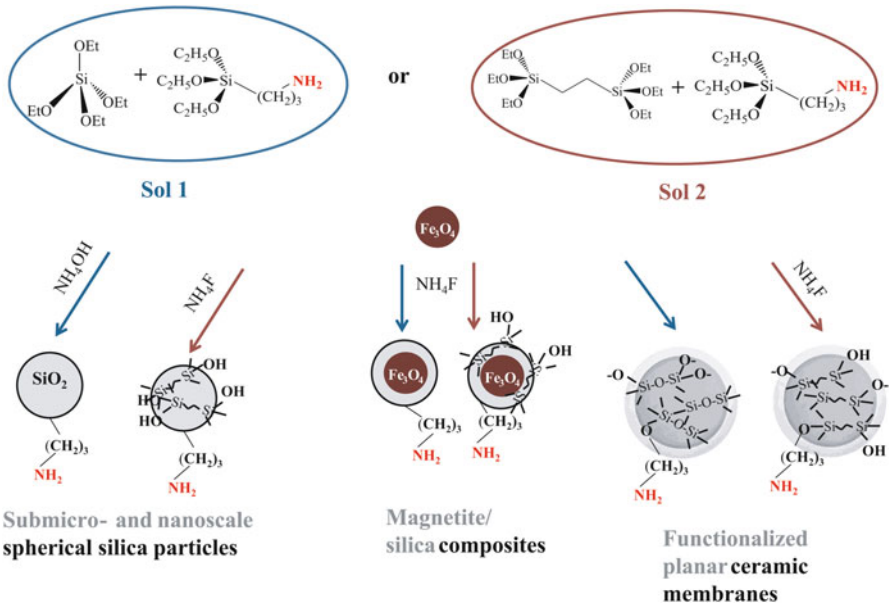

Fig. 5.1 Sol-gel routes to prepare different types of materials from the same sols

trifunctional silane containing functional amino group 3-aminopropyltriethoxysilane (APTES), $(H_5C_2O)_3Si–C_3H_6NH_2$. Applying these two types of sols we produced spherical silica particles, magnetically sensitive materials and ceramic membranes with amino groups on the surface.

5.2 Submicro– and Nanoscale Spherical Silica Particles

The silica spheres are promising materials for application in chromatography, drug delivery, adsorption, and biocatalysis due to their controllable size, porosity, and surface layer composition. There are two most commonly used techniques for the synthesis of functionalized spherical silica particles. The first one is based on the post-synthetic surface modification of silica spheres with trifunctional silanes. The second technique relates to the one-pot synthesis when the structuring (TEOS or BTESE) and the functionalizing (APTES) agents are added to the reaction solution under some order. The latter is economically and energy-efficient technique. Moreover, the reaction is catalyzed by an "internal" catalyst, the amino groups of APTES itself. However, there are many factors affecting the shape and size of the particles, the content of functional groups, the hydrolytic stability of the surface layer, and even the yield of the final product. In order to obtain spherical particles, the synthesis must be conducted in an alkaline medium with a large amount of the solvent. As mentioned, such a medium can be created by the amino groups of APTES, but it leads to wide size distribution of the particles; therefore, it is necessary to add ammonium hydroxide after the beginning of the reaction. The amount of added ammonium hydroxide affects to a certain extent the particle size. Increasing the ammonia concentration decreases the average size of the particles; though, it also decreases the number of functional groups due to the destruction of siloxane and ≡Si–C bonds at high pH values. Thus, the amount of ammonia and the time of synthesis influence the yield of the final product. The size of the TEOS-based particles is also affected by the synthesis temperature: the smallest particles of 100 nm with amino groups can be prepared in an ice bath during one-step synthesis, while raising the temperature can increase diameter of the particles to 300 and 700 nm [4]. The hydrolytic stability of the surface amino groups is influenced by the presence of silanol and additional organic groups. The bifunctional silica particles are characterized by faster adsorption kinetics than the monofunctional aminosilica particles due to the fact that the additional organic groups can prevent the formation of hydrogen bonds between the amino groups and the surface silanol groups or water molecules [5, 6]. In addition, during the one-step synthesis, it is possible to adjust the porosity of the particles using bissilanes and varying the ratio between the bissilane and APTES [7]. Thus, knowing the regularities of the reaction between TEOS (BTESE) and APTES, it is possible to program the required characteristics of the final materials in a certain way. As a result, the particle size can be 50–720 nm, the content of amino groups 0.3–3.8 mmol/g, the specific surface area from 15–543 m^2/g, and additional methyl or phenyl groups can be attached

[4, 8]. The sorption properties of such particles also vary: adsorption of copper (II) ions can occur in the range of 19–203 mg/g, methylene blue in the range of 55–114 mg/g and acid red in the range of 81–161 mg/g. Also very interesting were the antibacterial properties of the aminosilica particles with phenyl groups and adsorbed copper(II) ions. The survival indexes of the bacterial cells after 120 min contact with the 1% particle suspension were as follows for various bacterial species: *S. aureus* – 1.3%, *E. coli* – 0.02%, *P. aeruginosa* – 0% [9].

5.3 Magnetite/Silica Composites

Recently, magnetic composites have been used in many areas, including sorption [10]. In order to prevent the oxidation of the magnetite, its dissolution in the acidic medium or aggregation, and to provide it with specificity, silica precursors can be applied to cover the magnetite nanoparticles with polysiloxane layers. We proposed a one-stage synthesis of magnetic functional materials (Fig. 5.1) during which it is possible to regulate the size of the particles and the thickness of the polysiloxane layer [11], the number of functional groups [11, 12], the porosity of the polysiloxane shell [13], and to introduce other groups simultaneously with the complexing [12]. According to the XRD data, the functionalized materials retain their magnetite structure and magnetic properties.

Using TEOS as a structuring agent together with APTES and additional trifunctional silane with methyl or propyl groups, it is possible to prepare magnetic particles with a specific surface area of 16–180 m^2/g and 0.8–2.2 mmol/g content of amino groups. Such composites can adsorb 16.8 mg/g of palladium(IV) [14], up to 26.7 mg/g of copper(II) [15], and 32.3 mg/g of silver(I) ions [16], as well as up to 214 mg/g of albumin [12] and 95.4 mg/g of urease (while the residual activity of the immobilized urease is up to 84%) [17]. Moreover, the attachment of additional organic groups promotes the adsorption of biomolecules from aqueous solutions. Interestingly, when the amino functionalized magnetic samples are prepared using BTESE as a structuring agent, their specific surface area increases to 400–750 m^2/g, and the content of amino groups is 0.8–2.8 mmol/g. Such materials have proven to be very powerful adsorbents of heavy metal ions and dyes, apparently due to the well-developed porous structure and the presence of a large number of silanol groups along with the aminopropyl ones. Thus, the adsorption of copper(II) ions reached 214 mg/g, of lead(II) 165.6 mg/g, of silver(I) 321 mg/g, of acid red 118 mg/g and of methylene blue 62 mg/g [13].

5.4 Functionalized Ceramic Membranes

Organosilica membranes have been increasingly applied in gases and liquids-phase separation [18]. The functionalization of the inorganic membrane is important to enhance the separation or the interaction with specific chemicals. Loading with amino groups (using APTES) was shown to improve the performance of silica membranes in gas separation [19]. Meanwhile, the deposition of NH_2-functional silica layer on ultrafiltration membranes endows them affinity to heavy metal ions [20, 21] and better anti-fouling properties [20]. Thus, we used sol-gel method of hydrolytic polycondensation of TEOS or BTESE with APTES to prepare amino-silica sols for deposition of selective layers with amino groups on the surfaces of planar ceramic alumina membranes [22] (Fig. 5.1). To prepare a continuous coating, structuring/ functionalizing silanes with a ratio of 4/1 was applied and the sol required additional dilution with ethanol to decrease the viscosity. TEOS-based polysiloxane layer was about 0.35 μm thick and consisted of particles with 80–100 nm diameter and with amino group content of 2.6 mmol/g. For comparison, the BTESE-based polysilsesquioxane layer was thicker, about 4.4 μm, and consisted of smaller particles, 50–80 nm in diameter with lower amino groups content of 1.3 mmol/g. The hydrophilicity of the active layer is independent of the type of the structuring agent but increases with the introduction of additional methyl group. Such functionalized membranes are capable of retaining copper(II) ions during filtration of diluted solutions due to the complexation of the amino groups in the selective layer with these ions (from 10.2 to 23 mg/g) [22].

5.5 Conclusions

The current review summarizes the possibility of preparing different types of materials from the same sol, using the sol-gel method and the one-stage approach. Such synthesis is green and environmentally friendly. As a result of the development of the synthesis method, the obtained silica materials with amino groups can be used as adsorbents of heavy metals, dyes, antibacterial agents, as well as serve as precursors for materials produced by the reaction with an amino group.

Acknowledgments The research is financed by the project VEGA 2/0156/19.

References

1. Ciriminna R, Fidalgo A, Pandarus V, Beland F, Ilharco LM, Pagliari M (2013) The sol–gel route to advanced silica-based materials and recent applications. Chem Rev 113:6592–6620
2. Pillai SC, Hehir S (2017) Sol-gel materials for energy, environment and electronic applications. Springer, Cham. ISBN:978-3-319-50144-4

3. Laskowski L, Laskowska M, Schabikowski M, Walcarius A (2019) Mesoporous silica-based materials for electronics-oriented applications. Molecules 24(13):2395
4. Melnyk IV (2014) Aminosilica nano- and submicrospheres: study of influence factors on morphology, structure and properties. Chem J Mold 9(1):123–127
5. Tomina V, Melnyk I, Zub Y, Kareiva A, Vaclavikova V, Seisenbaeva G, Kessler V (2017) Tailoring bifunctional hybrid organic-inorganic nanoadsorbents by the choice of functional layer composition probed by adsorption of Cu^{2+} ions. Beilstein J Nanotech 8:334–347
6. Kotsyuda SS, Tomina VV, Zub YL, Furtat IM, Lebed AP, Vaclavikova M, Melnyk IV (2017) Bifunctional silica nanospheres with 3-aminopropyl and phenyl groups. Synthesis approach and prospects of their applications. Appl Sur Sci 420:782–791
7. Stolyarchuk NV, Barczak M, Melnyk IV, Zub YL (2016) Amine-functionalized nanospheres, synthesized using 1,2-bis(triethoxysilyl)ethane. In: Fesenko O, Yatsenko L (eds) Nanophysics, nanophotonics, surface studies, and applications, vol 183. Springer, Cham, pp 415–425. ISBN:978-3-319-30737-4
8. Tomina V, Furtat I, Stolyarchuk N, Yu Z, Kanuchova M, Vaclavikova M, Melnyk I (2019) Surface and structure design of aminosilica nanoparticles for multifunctional applications: adsorption and antimicrobial studies. In: Biocompatible hybrid oxide nanoparticles for human health: from synthesis to applications. Elsevier, Amsterdam, pp 15–31
9. Melnyk IV, Tomina VV, Stolyarchuk NV, Lebed AP, Furtat IM, Kanuchova M, Vaclavikova M (2018) Effect of synthesis conditions on the formation of spherical silica particles with amino groups and their investigation in sorption and as antibacterial agents. In: Bokányi L (ed) Proceedings of the international V4 waste recycling 21 conference. Miskolci Egyetem: 76, ISBN:978–963–358-173-5
10. Mehta D, Mazumdar S, Singh SK (2015) Magnetic adsorbents for the treatment of water/wastewater – a review. J Water Process Eng 7:244–265
11. Melnik IV, Zub YL, Alonso B, Abramov NV, Gorbik PP (2012) Creation of a functional polysiloxane layer on the surface of magnetic nanoparticles using the sol-gel method. Glas Phys Chem 38(1):96–104
12. Melnyk IV, Zub YL (2012) Preparation and characterisation of magnetic nanoparticles with bifunctional surface layer $\equiv Si(CH_2)_3NH_2/\equiv SiCH_3$ (or $\equiv SiC_3H_{7-n}$). Micropor Mesopor Mat 154:196–199
13. Melnyk IV, Tomina VV, Stolyarchuk NV, Bespalko OV, Vaclavikova (2019) Functionalization of the magnetite nanoparticles with polysilsesquioxane bearing N- and S-complexing groups to create solid phase adsorbents, Appl Nanosci https://doi.org/10.1007/s13204-019-01087-1
14. Zavoiura O, Zaporozhets O, Volovenko O, Melnyk I, Yu Z (2015) Silica-coated magnetite nanoparticles modified with 3-aminopropyl groups for solid phase extraction of Pd(II) ions from water solutions. Adsorpt Sci Technol 33(3):297–306
15. Melnyk IV, Gdula K, Dąbrowski A, Zub YL (2016) Magneto-sensitive adsorbents modified by functional nitrogen-containing groups. Nanoscale Res Lett 11:61
16. Gdula K, Skwarek E, Dabrowski A, Melnyk I (2017) Amine-functionalized silica particles with magnetic core as magnetically removable adsorbents of ag(I) ions. Adsorpt Sci Technol 35 (5–6):432–438
17. Pogorilyi RP, Melnyk IV, Zub YL, Seisenbaeva GA, Kessler VG, Shcherbatyik MM, Kosak A, Lobnik A (2013) Urease adsorption and activity on magnetite nanoparticles functionalized with monofunctional and bifunctional surface layers. J Sol-Gel Sci Technol 68:447–454
18. Ren X, Tsuru T (2019) Organosilica-based membranes in gas and liquid-phase separation. Membranes 9(9):107. https://doi.org/10.3390/membranes9090107
19. McCool BA, DeSisto WJ (2005) Amino-functionalized silica membranes for enhanced carbon dioxide permeation. Adv Funct Mater 15(10):1635–1640. https://doi.org/10.1002/adfm.200400293
20. Bao Y, Yan X, Du W, Xie X, Pan Z, Zhou J, Li L (2015) Application of amine-functionalized MCM-41 modified ultrafiltration membrane to remove chromium (VI) and copper (II). Chem Eng J 281:460–467. https://doi.org/10.1016/j.cej.2015.06.094

21. Tomina VV, Stolyarchuk NV, Melnyk IV, Zub YL, Kouznetsova TF, Prozorovich VG, Ivanets AI (2017) Composite sorbents based on porous ceramic substrate and hybrid amino- and mercapto-silica materials for Ni(II) and Pb(II) ions removal. Sep Purif Technol 175:391–398
22. Tomina VV, Stolyarchuk NV, Melnyk IV, Kochkodan VM, Zub YL, Chodosovskaja A, Kareiva A (2016) Surface functionalization of ceramic membranes with 3-aminopropyl groups using the sol- gel method. Prot Met Phys Chem Surf 52(1):55–60

Chapter 6
$BaTiO_3$ Structure as a Function of the Preparation Method

Denitza Nicheva, Ruzha Harizanova, Vania Ilcheva, Irena Mihailova, Tamara Petkova, and Plamen Petkov

Abstract Barium titanate is synthesized by sol-gel and hydrothermal methods. The sol-gel technique allows the preparation of amorphous powders which are subsequently subjected to appropriate time-temperature programs and barium titanate is precipitated. The allotropic modification of the barium titanate from the obtained sol-gel powder depends on the temperature applied. It is cubic for heat treatment at 900 °C for 4 h, while in case of crystallization at 1100 °C for 3 h the tetragonal modification occurs as witnessed by X-ray diffraction analyses. Barium titanate is also successfully prepared by the hydrothermal method which results in the crystallization of the cubic allotrope as observed by X-ray diffraction. The microstructure of the formed barium titanate powders is imaged by scanning electron microscopy and reveals the formation of large fraction of crystals which are polydispersed for the samples prepared via sol-gel method and tend to agglomerate in case of hydrothermal synthesis. The infrared spectroscopy investigation of the powders obtained by both synthesis methods shows the presence of the absorption peak characteristic for the barium titanate phase in the range 540–580 cm^{-1}.

Keywords Barium titanate · Sol-gel · Hydrothermal method · Crystallization · Allotropy

D. Nicheva (✉)
University of Chemical Technology and Metallurgy, Sofia, Bulgaria

Institute of Electrochemistry and Energy Systems, Bulgarian Academy of Sciences, Sofia, Bulgaria
e-mail: d.vladimirova@iees.bas.bg

R. Harizanova · I. Mihailova · P. Petkov
Department of Physics, University of Chemical Technology and Metallurgy, Sofia, Bulgaria

V. Ilcheva · T. Petkova
Institute of Electrochemistry and Energy Systems, Bulgarian Academy of Sciences, Sofia, Bulgaria

P. Petkov et al. (eds.), *Nanoscience and Nanotechnology in Security and Protection against CBRN Threats*, NATO Science for Peace and Security Series B: Physics and Biophysics, https://doi.org/10.1007/978-94-024-2018-0_6

6.1 Introduction

Nanomaterials containing metals are subject of scientific interest because they exhibit size-dependent optical, magnetic, electronic as well as catalytic properties which are a prerequisite for the development of next generation devices. One promising material whose electrical and optical properties have been widely investigated in the last few decades is $BaTiO_3$ (BT) [1]. Recently, there has been a renewal of interest in nano- and microscale BT because of the existing strong correlation between the physical properties and material structure. For instance, the tetragonal structure of $BaTiO_3$ is applicable as ferroelectric in different piezo- and pyroelectric sensors, in detectors and high-capacity systems due to its high dielectric constant and domain structure. The cubic $BaTiO_3$ owing to its paraelectric properties and the possibility also to achieve high dielectric constant is suitable for the preparation of multilayered ceramic capacitors finding application in electronic circuits [2]. In general, BT could exist in four allotropic modifications: orthorhombic (stability range up to −90 °C), rhombohedral (stable between −90 and 0 °C), tetragonal (existing between 0 and 120 °C) and cubic with stability region above 120 °C. The occurrence of one or another allotrope of BT at room temperature depends on the preparation technique and the size of the precipitated crystals [3]. In literature there is a variety of different synthesis methods reported: sol-gel [4], hydrothermal method [5], sintering [6], as well as utilizing controlled crystallization from glasses [7–10]. Using relatively simple and inexpensive methods like sol-gel and hydrothermal synthesis could allow the preparation of monophase BT powders or even monolith materials with controllable sizes and size-distribution, as well as in high volume fraction. The broad range of possible applications of BT determines the necessity to investigate thoroughly the phase composition, thermal and physico-chemical properties of the prepared materials and also to characterize their structure and microstructure.

The main objective of the present work is to prepare $BaTiO_3$ by two different techniques, namely sol-gel and hydrothermal methods, and to study the influence of the preparation technique on the structure and phase composition of the obtained materials. The as-prepared powders were characterized by X-ray diffraction (XRD), Fourier transform infrared spectroscopy (FTIR), and scanning electron microscopy (SEM).

6.2 Experimental

6.2.1 Preparation of the Samples

BT powders with cubic and tetragonal phases were synthesized via sol-gel and hydrothermal methods. $Ti(OC_4H_9)_4$ and $Ba(CH_3COO)_2$ were used as starting materials. By the sol-gel method initially 0.1 mol $Ti(C_4H_9O)_4$ was dissolved in 0.3 mol

acetic acid and 0.3 mol absolute ethanol under continuous stirring for 30 min. Further, 0.1 mol $Ba(CH_3COO)_2$ was added in portions in 90 ml 36% acetic acid while stirring at room temperature. For the preparation of $BaTiO_3$, these two solutions were mixed with a Ba/Ti molar ratio 1:1. After stirring vigorously for 1 h, a homogenous, transparent sol was obtained. A clear gel was formed after leaving the sol undisturbed for 48 h at room temperature. The clear gel was then treated at 100 °C for 10 h in a drying oven to produce a dry gel. For sol-gel method the obtained gel precursor was calcined at 900 °C for 4 hours and at 1100 °C for 3 h. By the hydrothermal method the obtained gel precursor was introduced into 2 M KOH to form a suspension. Then, the achieved suspension was transferred into Teflon-lined stainless-steel autoclave at 120 °C for 8 h. After the hydrothermal reaction, the obtained solution was vacuum-filtered and washed with distilled water, acetic acid and absolute ethanol several times. Finally, the powder was dried for 8 h to obtain pure $BaTiO_3$.

6.2.2 Characterization Methods

XRD analyses were performed using X-ray diffractometer Philips APD-15. The data were collected at ambient temperature with a constant step of 0.02 deg. from 2θ angles in the range of 10°–90° using a CuKα tube (wavelength $\lambda = 1.54178$ Å). The infrared spectroscopy (IR) investigations were carried out with a FTIR spectrophotometer Tenzor27-Brucker on powdered samples pressed in KBr in the wavenumber range of 400–4000 cm^{-1}. The morphology of the materials was determined with a scanning electron microscope Philips 515, digitalized, with secondary electrons detector at acceleration voltage 30 kV and magnification 40,000x.

6.3 Results and Discussion

The sol-gel powder subjected to heat treatment at 900 °C for 4 h and 1100 °C for 3 h was examined by X-ray diffraction to establish the BT structure. The phases of the powders obtained by sol-gel and hydrothermal techniques reveal the formation of BT in large amounts (Figs. 6.1, 6.2 and 6.3). In the sample heated at 1100 °C the BT phase occurs in its tetragonal modification, whereas in the sol-gel sample heat-treated at 900 °C and in the hydrothermally synthesized sample cubic modification is present. The XRD pattern of the sol-gel sample crystallized at 900 °C shows presence of a second crystalline phase in minor quantity detected at about 28°, whereas in the 1100 °C sol-gel sample and the hydrothermally synthesized sample this peak is missing.

SEM images of the BT powdered materials are presented in Figs. 6.4, 6.5 and 6.6. The microstructure of the sol-gel samples are characterized by the presence of fine dispersed particles attributed to the BT tetragonal phase. The microstructure of the

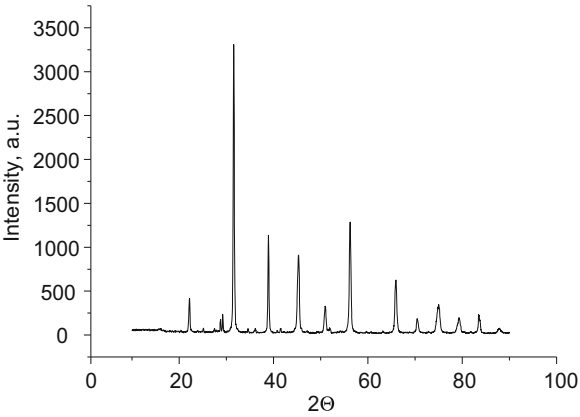

Fig. 6.1 XRD patterns of barium titanate obtained from the thermal treatment of sol-gel powder at 900 °C for 4 h – crystallization of cubic phase

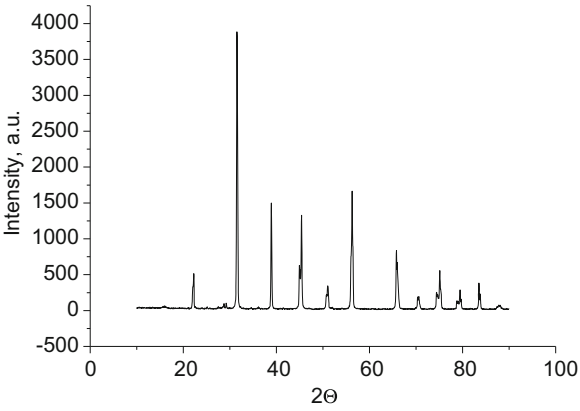

Fig. 6.2 XRD patterns of barium titanate obtained from the thermal treatment of sol-gel powder at 1100 °C for 3 h – crystallization of tetragonal phase

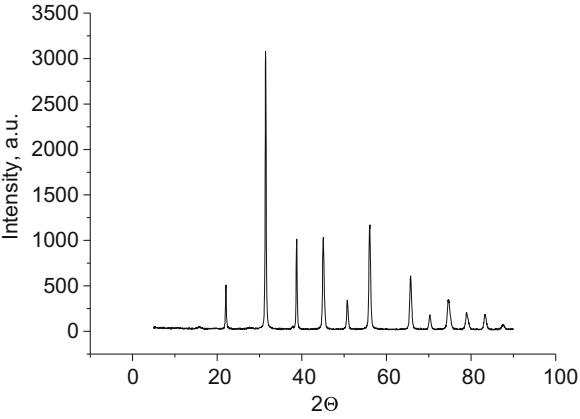

Fig. 6.3 XRD patterns of BT obtained via the hydrothermal method crystallized in cubic phase

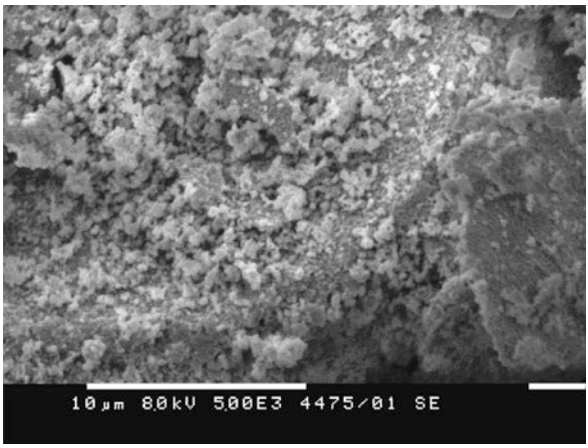

Fig. 6.4 SEM micrograph of BT obtained after thermal treatment at 900 °C for 4 h

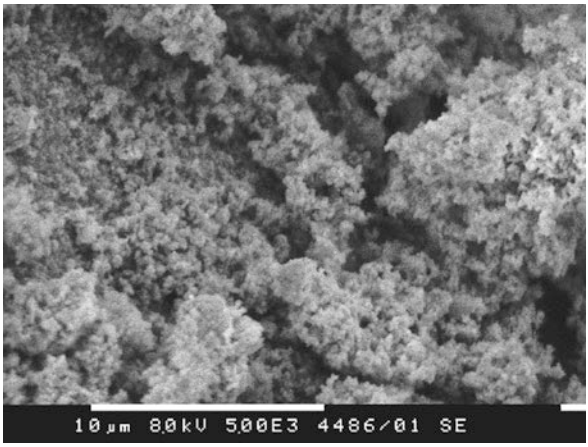

Fig. 6.5 SEM micrograph of BT obtained after thermal treatment at 1100 °C for 3 h

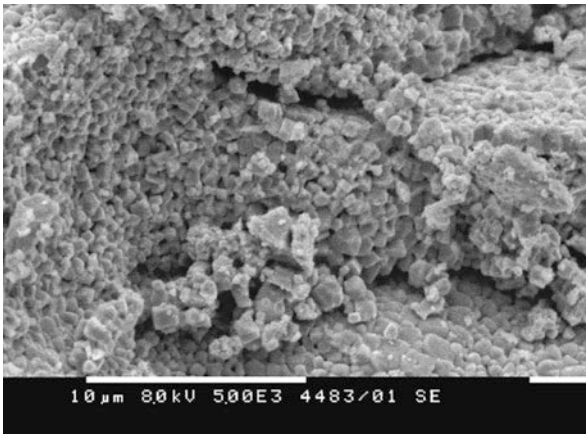

Fig. 6.6 SEM micrograph of BT obtained via the hydrothermal method

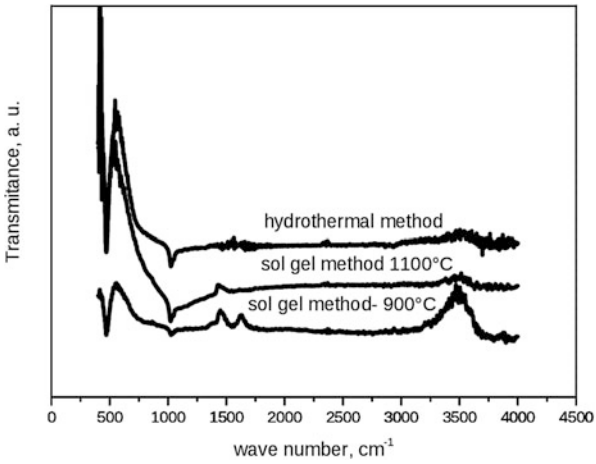

Fig. 6.7 FTIR spectra of $BaTiO_3$ obtained via sol-gel and hydrothermal methods

hydrothermally synthesized BT powder shows tendency for building of agglomerates and thus, larger particles are formed which results in a coarser microstructure (Fig. 6.7).

The IR spectroscopic investigations of BT show that in the wave number range of 400–4000 cm^{-1} the barium titanate phase has a single peak at about 540–580 cm^{-1} for both cubic and tetragonal modifications [11, 12]. This makes the identification of the BT allotrope based solely on FTIR spectra unreliable. However, the data from the XRD patterns, as shown in Figs. 6.1, 6.2 and 6.3, allow to conclude that in the 900 °C sol-gel and in the hydrothermal synthesized samples BT is present in its cubic modification, whereas in the 1100 °C sol-gel sample the tetragonal modification occurs. The peaks around 1400 cm^{-1} correspond to the carboxylic groups and the absorption in the range of 1600 cm^{-1} should be attributed to the hydroxyl groups present in the samples (the bending vibration of H-O-H) [13].

6.4 Conclusions

Monophase $BaTiO_3$ particles in the form of powder are successfully prepared by utilizing two different techniques: sol-gel and hydrothermal methods. The XRD patterns of the powdered samples reveal that the sol-gel samples calcined at 900 °C as well as the hydrothermally obtained barium titanate correspond to the cubic modification while the sol-gel sample crystallized at 1100 °C is tetragonal. The SEM imaging of the sol-gel $BaTiO_3$ witnesses the occurrence of polydispersed spherical particles while the hydrothermal method results in significant agglomeration of the formed particles. The FTIR spectra of the barium titanate powders show the presence of the characteristic absorption peak for $BaTiO_3$ in the range 540–580 cm^{-1} but also of vibrations of the Ti-O bonds at approximately

850 cm^{-1}, as well as of carboxylic and hydroxyl groups at 1400 cm^{-1} and 1600 cm^{-1}, respectively.

Acknowledgments This work is financially supported by contract KP-06-N28/1 with the Bulgarian National Scientific Fund.

References

1. Zhu X, Zhu J, Zhou S, Liu Z, Ming N, Hesse D (2005) $BaTiO_3$ nanocrystals: Hydrothermal synthesis and structural characterization. J Cryst Growth 283:553–562
2. Chen C, Hao H, Wang T, Cheng J, Luo Z, Zhang L, Cao M, Yao Z, Liu H (2019) Nano-$BaTiO_3$ phase transition behavior in coated $BaTiO_3$-based dielectric ceramics. Ceram Int 45:7166–7172
3. Capsal JF, Dantras E, Laffont L, Dandurand J, Lacabanne C (2010) Nanotexture influence of $BaTiO_3$ particles on piezoelectric behaviour of PA 11/$BaTiO_3$ nanocomposites. J Non-Cryst Solids 356:629–634
4. Joshi U, Yoon S, Baik S, Lee JS (2006) Surfactant-free hydrothermal synthesis of highly tetragonal barium titanate nanowires: a structural investigation. J Phys Chem B 110:12249
5. Vijatović MM, Bobić JD, Stojanović BD (2008) History and challenges of barium titanate: Part II. Sci Sinter 40:235–244
6. Du GP, Hu ZJ, Han QF, Qin XM, Shi WZ (2010) Effects of niobium donor doping on the phase structures and magnetic properties of Fe doped $BaTiO_3$ ceramics. J Alloys Comp 492:L79–L81
7. Maiti RP, Basu S, Bhattacharya S (2009) Multiferroic behavior in silicate glass nanocomposite having a core–shell microstructure. J Non-Cryst Solids 355:2254–2259
8. Harizanova R, Mazhdrakova A, Vladislavova L, Avdeev G, Bocker C, Gugov I, Rüssel C (2015) Crystallization behaviour of the systems $Na_2O/BaO/TiO_2/SiO_2/B_2O_3/Al_2O_3$ and $Na_2O/BaO/TiO_2/SiO_2/B_2O_3/Fe_2O_3/Al_2O_3$. J Chem Technol Metall 50:375-380
9. Harizanova R, Tatchev D, Avdeev G, Bocker C, Karashanova D, Mihailova I, Gugov I, Rüssel C (2017) Investigation on the crystallization behaviour of sodium-aluminoborosilicate glasses with high concentrations of Ba and Ti. Bulg Chem Comm 49:119–125
10. Buscaglia V, Buscaglia MT, Viviani M, Mitoseriu L, Nanni P, Trefiletti V, Piaggio P, Gregora I, Ostapchuk T, Pokorny J, Petzelt J (2006) Grain size and grain boundary-related effects on the properties of nanocrystalline barium titanate ceramics. J Eur Ceram Soc 26:2889–2898
11. Wada S, Suzuki T, Noma T (1996) Role of lattice defects on size effect of barium titanate particles. J Ceram Soc Jpn 104:383–392
12. Wada S, Chikamori H, Noma T, Suzuki T, Tsurimi T (2000) Synthesis and characterization of nanometer-order barium titanate single crystal particles using an improved low temperature direct synthesis method. J Ceram Soc Jpn 108:728–735
13. Wang W, Cao L, Liu W, Su G, Zhang W (2013) Low-temperature synthesis of $BaTiO_3$ powders by the sol–gel-hydrothermal method. Ceram Int 39(6):7127–7134

Part III
Characterization

Chapter 7
Impedance Spectroscopy: Concepts and Applications

Bruno M. G. Melo, Dona Blaskova-Kochnitcharova, Silvia Soreto Teixeira, Tamara Petkova, and Luis C. Costa

Abstract Impedance spectroscopy is a technique that allows to characterize electrically materials, in particular the polarization mechanisms, that is, the charge migration and the orientation of permanent dipoles. To obtain a complete characterization of the dielectric response, a huge range of frequencies and temperatures must be used. The different regimes of the dielectric function can be observed and the dynamics of the relaxations can be found. In this chapter, different examples of using impedance spectroscopy to characterize materials are presented, showing the capability of this technique. Grains and grain boundaries can be identified, and several equivalent circuits are discussed. Performances that permit to investigate the fundamental aspects of the electrical properties are presented, yielding a wealth of information about the molecular motions and relaxation processes present in different materials.

Keywords Impedance spectroscopy · Dielectric relaxation · Cole-Cole plot · Equivalent circuits

7.1 Introduction

To obtain the dielectric response of a material, a broadband frequency of measurement must be used, from a few mHz to hundreds of GHz [1–3], requiring the applications of different methods, based on several measurement techniques. Bridges [4], oscilloscopes methods [5] or lock-in amplifiers [6] are frequently used for low frequency measurements. For radio frequencies, impedance analysers and

B. M. G. Melo · S. S. Teixeira · L. C. Costa (✉)
I3N and Physics Department, University of Aveiro, Aveiro, Portugal
e-mail: kady@ua.pt

D. Blaskova-Kochnitcharova · T. Petkova
Institute of Electrochemistry and Energy Systems Acad. Evgeni Budevsky, Bulgarian Academy of Sciences, Sofia, Bulgaria

P. Petkov et al. (eds.), *Nanoscience and Nanotechnology in Security and Protection against CBRN Threats*, NATO Science for Peace and Security Series B: Physics and Biophysics, https://doi.org/10.1007/978-94-024-2018-0_7

transformer ratio arm bridges [7] have applicability. Resonant cavities can be used for the microwave range, based on the small perturbation theory [8]. Several advantages and limitations can be associated to these methods. Nevertheless, many systematic studies on different materials are reported in several articles [9–12].

Petrus Debye described the simplest condition of a relaxation phenomenon [4], based on a physical model consisting of dipoles immersed in a viscous medium, with the assumption that they did not interact with each other. Under the action of an electric field, those dipoles were oriented, returning to the equilibrium position after switching off the field. Then, the depolarization function presents an exponential decay with time,

$$\Phi(t) = \Phi_0 \exp\left(-\frac{t}{\tau_D}\right) \tag{7.1}$$

where Φ_0 is the initial polarization and τ_D the relaxation time.

Fourier transform can be used to transfer from time to frequency domain. For the Debye model, we can obtain an expression,

$$\varepsilon^*(\omega) = \varepsilon_\infty + \frac{\varepsilon_s - \varepsilon_\infty}{1 + i\omega\tau_D} \tag{7.2}$$

where ε^* is the complex permittivity, $\varepsilon^* = \varepsilon'$-i$\varepsilon''$, ω the angular frequency, and ε_∞ and ε_s the dielectric constants at high and low frequencies, respectively. This equation can be solved in order to obtain, the real and imaginary parts,

$$\varepsilon'(\omega) = \varepsilon_\infty + \frac{\varepsilon_s - \varepsilon_\infty}{1 + \omega^2\tau_D{}^2} \tag{7.3}$$

$$\varepsilon''(\omega) = \frac{(\varepsilon_s - \varepsilon_\infty)\ \omega\tau_D}{1 + \omega^2\tau_D{}^2} \tag{7.4}$$

To make a measurement, the general approach is to apply an electrical stimulus and observe the response of the material. From a practical point of view, the complex impedance$Z^*(\omega) = Z'(\omega)$-i$Z''(\omega)$ is measured. Based on it, other physical entities can be calculated that can eventually be more useful to understand the reaction of the material, e.g. macroscopic properties like the admittance, $Y^* = (Z^*)^{-1} = Y'(\omega) + iY''$ (ω), or intrinsic properties, such as the dielectric permittivity, $\varepsilon^*(\omega) = \varepsilon'(\omega)$-i$\varepsilon''(\omega)$, and the dielectric modulus [13], $M^* = (\varepsilon^*)^{-1} = M'(\omega) + iM''(\omega)$.

7.2 Relaxation Models

The Debye model, the simplest one, is represented in Fig. 7.1. The real and imaginary parts of the complex permittivity are shown as a function of the frequency in the range between 10^{-1} and 10^5 Hz.

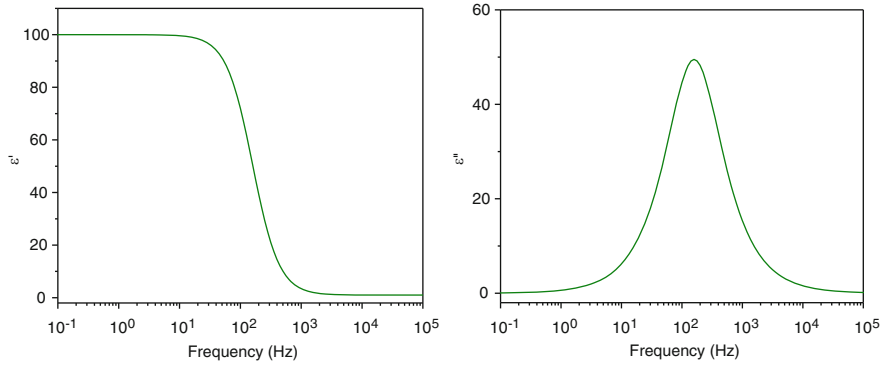

Fig. 7.1 Real (left panel) and imaginary (right panel) parts of the complex permittivity for the Debye model in a semi-logarithmic representation

As it can be seen, both functions exhibit a symmetric behavior. The inflection point of ε' corresponds to the maximum of ε'', which can be demonstrated using the Kramers-Kronig relations [14]. This point corresponds to the relaxation frequency f_r,

$$f_r = \frac{1}{2\pi\tau_D} \tag{7.5}$$

A mathematical development of Eqs. (7.3) and (7.4) leads to the expression,

$$\left(\varepsilon'(\omega) - \frac{\varepsilon_s + \varepsilon_\infty}{2}\right)^2 + \left(\varepsilon''(\omega)\right)^2 = \left(\frac{\varepsilon_s - \varepsilon_\infty}{2}\right)^2 \tag{7.6}$$

which is an equation of a circle. Then, representing ε'' versus ε', known as Cole-Cole plot, we obtain a semi-circle with radius $(\varepsilon_s - \varepsilon_\infty)/2$, and center in the point with coordinates $((\varepsilon_s + \varepsilon_\infty)/2, 0)$. Figure 7.2 shows the data of Fig. 7.1 in this new representation.

Nevertheless, a great part of relaxations that are identified in materials do not follow this behavior. Then, new empirical models were considered, in particular the Cole-Cole, the Cole-Davidson and the Havriliak-Negami. This means that there is no more a single relaxation time, but a distribution of relaxation times [15]. By choosing an appropriate distribution function, it should be possible to fit the experimental dielectric response of many different materials.

Cole-Cole model [16] is described by the expression

$$\varepsilon^*(\omega) = \varepsilon_\infty + \frac{\varepsilon_s - \varepsilon_\infty}{1 + (i\omega\tau_{cc})^{1-\alpha}} \tag{7.7}$$

where τ_{cc} is the relaxation time and α a parameter ($0 < \alpha \leq 1$) that leads to a broadening of the relaxation function. In this case, the curve in the Cole-Cole plot is

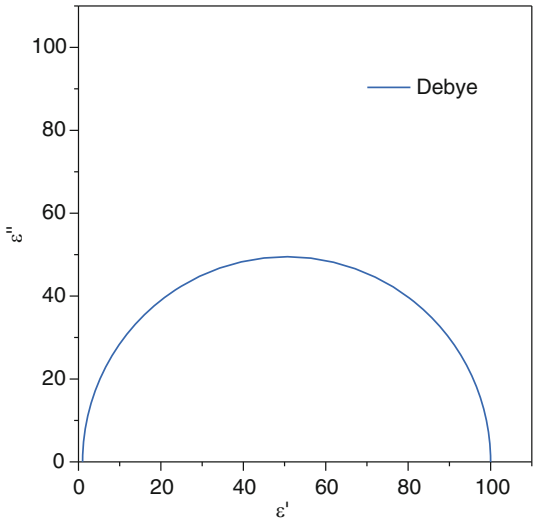

Fig. 7.2 Cole-Cole plot for the data of Fig. 7.1 (Debye model)

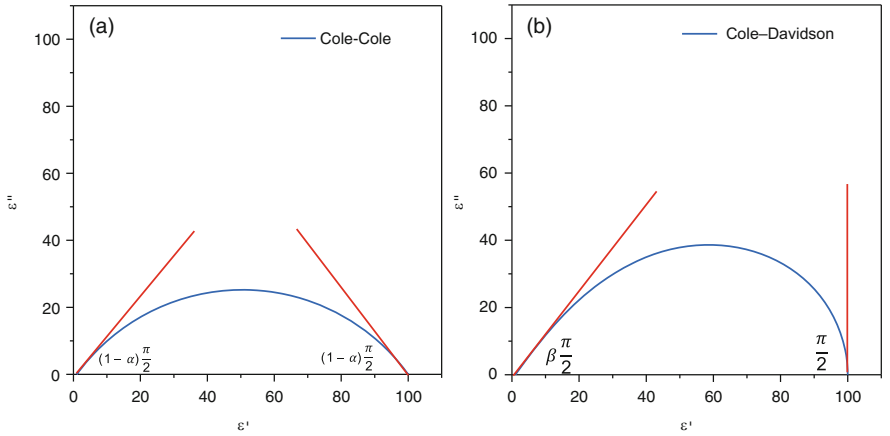

Fig. 7.3 (**a**) Cole-Cole (symmetric) and (**b**) Cole-Davidson (asymmetric) models

also symmetric, but the center of the semi-circle is not on the abscissa, but below it, as shown in Fig. 7.3a. The angle of the asymptotes in the limits of high and low frequencies is the same, namely (1-α)π/2.

Cole-Davidson model [17] is an alternative, quite often used in complex materials, expressed by

$$\varepsilon^*(\omega) = \varepsilon_\infty + \frac{\varepsilon_s - \varepsilon_\infty}{(1 + i\omega\tau_{cd})^\beta} \tag{7.8}$$

where again the exponent β ($0 < \beta \leq 1$) reflects the broadening of the relaxation function and τ_{cd} is the relaxation time. In this case, the curve in the Cole-Cole plot is no more symmetric, as it can be seen in Fig. 7.3b. In the low frequency regime, the asymptote has an angle of $\pi/2$, in the high frequency regime the angle is $\beta\pi/2$.

An even more general model function was introduced by Havriliak and Negami [18], which is a combination of Cole-Cole and Cole-Davidson functions:

$$\varepsilon^*(\omega) = \varepsilon_\infty + \frac{\varepsilon_s - \varepsilon_\infty}{\left(1 + (i\omega\tau_{hn})^{1-\alpha}\right)^\beta} \tag{7.9}$$

This model, depending on the values of α and β can lead to one of the previous models. If $\alpha = 0$ and $\beta = 1$, it represents the Debye model, for $\alpha \neq 0$ and $\beta = 1$ the Cole-Cole model, and for $\alpha = 0$ and $\beta \neq 1$ the Cole-Davidson model.

7.3 Case Study 1

Figure 7.4 shows the real part of the dielectric permittivity of lead borate glass with the composition $xGd_2O_3.PbO.2B_2O_3$ ($x = 0.05$) at a constant temperature of 300 K. Two relaxation processes can be observed. Figure 7.5 presents the Cole-Cole plots of these two relaxations, where it is visible that the Cole-Davidson model can be applied to fit the experimental data. Table 7.1 summarizes the β parameter, which is a measure of the dipole interaction, at low and high frequency relaxations, for two different glass matrixes (lead borate and lead silicate), and two different ion dopings (oxides of Gd and Nd). The low frequency relaxation is dependent on the matrix, whereas the high frequency relaxation depends only on the doping oxide.

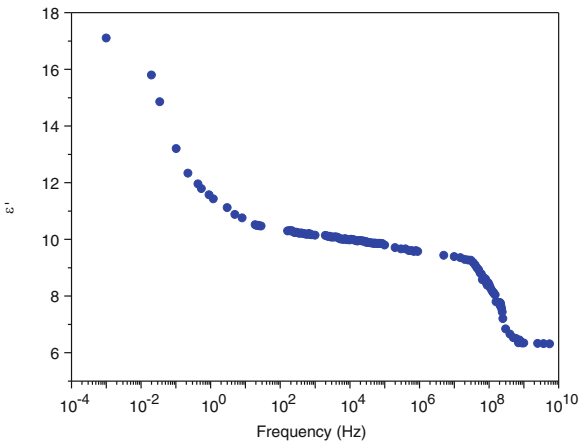

Fig. 7.4 ε' versus frequency, at T =300 K, for a lead borate glass

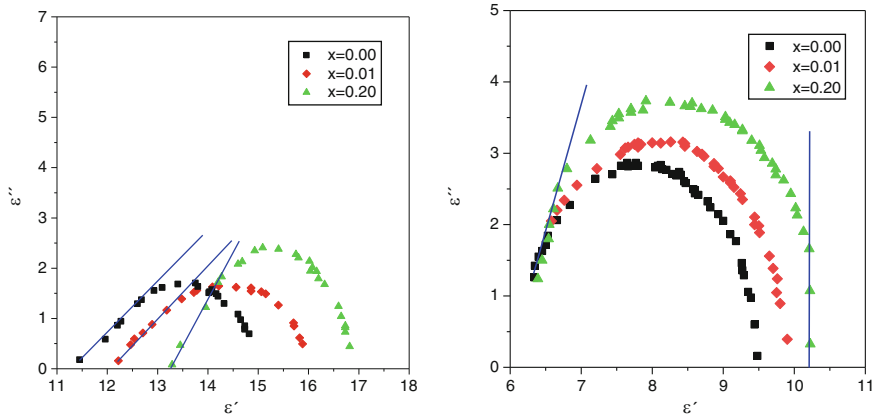

Fig. 7.5 Cole-Cole plots for the two relaxations observed in Fig. 7.4

Table 7.1 β parameter (Cole-Davidson model) for lead borate (LB) and lead silicate (LS) matrixes and different doping ion oxides

	LB + xGd_2O_3		LB + xNd_2O_3		LS + xGd_2O_3	
x	β_{LF}	β_{HF}	β_{LF}	β_{HF}	β_{LF}	β_{HF}
0.00	0.45	0.89	0.45	0.88	0.65	0.90
0.01	0.51	0.88	0.45	0.87	0.65	0.88
0.05	0.51	0.86	0.50	0.83	0.66	0.86
0.10	0.51	0.85	0.48	0.78	0.66	0.85
0.20	0.50	0.84	0.48	0.77	0.66	0.84

7.4 Case Study 2

A bulk sample with composition $(TiO_2)_{10}(V_2O_5)_{60}$ $(P_2O_5)_{30}$ was synthesized by melt-quenching method, and impedance spectroscopy was used to study the dielectric properties. Figure 7.6 shows the Nyquist plot (Z'' versus Z') at a constant temperature T = 120 °C.

Three relaxation processes can be observed, corresponding to the electrodes, to the grain boundaries and to the grains (the last one seen in the inset). This morphology was observed by scanning electron microscopy, as shown in Fig. 7.7.

The Havriliak-Negami model was used to fit the three relaxation processes. Actually, for this model the equivalent circuit can be simulated by a series of resistances in parallel with a constant phase element, as presented in Fig. 7.8a. The constant phase element (CPE) is a component whose impedance is defined as

$$Z_{CPE} = \frac{1}{Q(iw)^{1-\alpha}} \tag{7.10}$$

When α is 0, this impedance corresponds to a capacitor, that is the ideal Debye model.

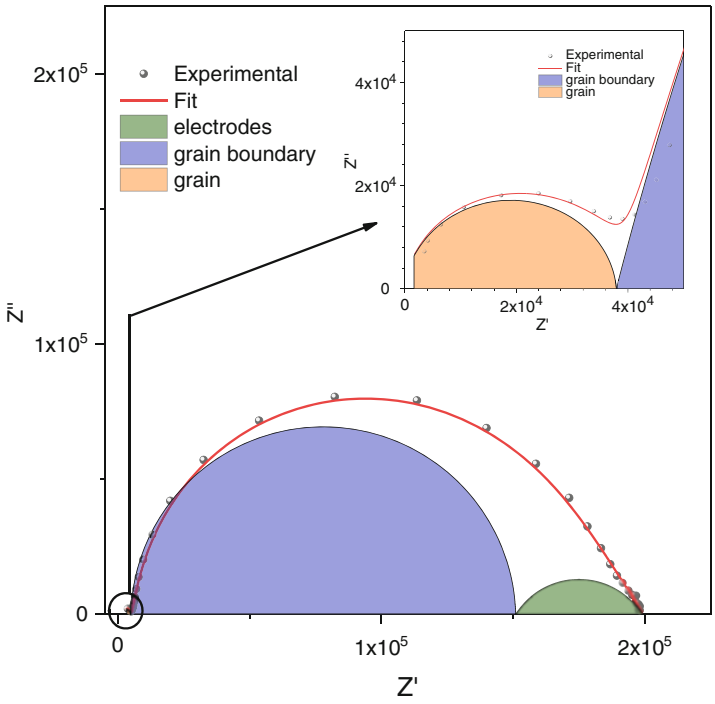

Fig. 7.6 Nyquist plot for a sample of the system $(TiO_2)_{10}(V_2O_5)_{60}$ $(P_2O_5)_{30}$ at constant temperature T = 120 °C

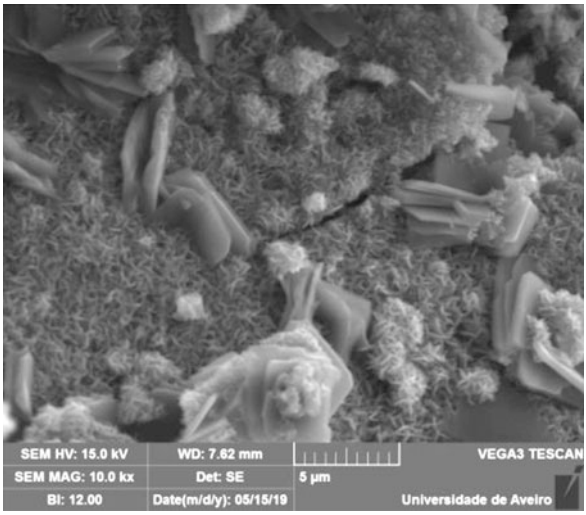

Fig. 7.7 SEM image for a sample of the system $(TiO_2)_{10}(V_2O_5)_{60}$ $(P_2O_5)_{30}$

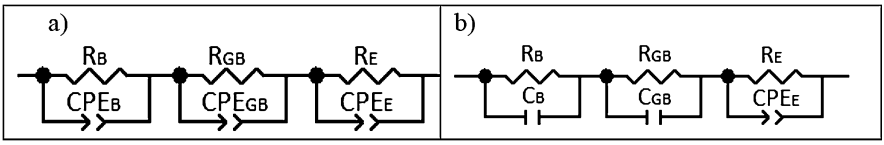

Fig. 7.8 Equivalent circuits for (**a**) Havriliak-Negami model and (**b**) present case study

Table 7.2 Calculated relaxation parameters α and β using Havriliak-Negami function

	α	β
Electrodes	0.36	1.00
Grain boundary	0.01	1.00
Grain	0.02	1.00

The relaxation parameters α and β were calculated for T = 120 °C and the results are summarized in Table 7.2.

As can be seen, for the grain and grain boundary relaxation processes, the parameters indicate that they can be described by the Debye models. Then, Eq. (7.10) corresponds to a single capacitor. For the electrode process, the results indicate that the Cole-Cole model should be used. This behavior can be simulated by the equivalent circuit in Fig. 7.8b. The grain and the grain boundaries are simulated by R-C and the electrode by R-CPE parallel circuits.

Figure 7.6 gives also an important information about the conductivity of the different components, which is related with the radius of the semi-circles. The highest conductivity can be contributed to the grains, corresponding to the smallest radius. The grain boundaries are more resistive, presented by the largest radius, as it can be expected.

7.5 Conclusion

Impedance spectroscopy is a powerful technique that can be used to understand materials, allowing the characterization of the migration of the charges and the orientation of permanent dipoles inside them. The different regimes of the dielectric function can be observed, and the dynamics of the relaxations processes can be described.

Several relaxation models can be used, the simplest one, corresponding to a single relaxation time, is the Debye model. Nevertheless, for a great part of materials, this is not common, and an alternative empirical model must be applied, such as the Cole-Cole, Cole-Davidson and Havriliak-Negami models.

The presentation of equivalent circuits is also useful to fit the experimental results. However, the ambiguity of using this approach can lead to several problems and only the implementation of other characterization techniques, such as scanning electron microscopy (SEM), Raman spectroscopy, X-ray diffraction (XRD) and nuclear magnetic resonance spectroscopy (NMR) can be helpful and solve them.

Acknowledgments D. B-K. acknowledges the financial support of INFRAMAT (National Roadmap for Scientific Infrastructure, CMD No. 354 from 29.06.2017). D. B-K and T. P. thank Assoc. Prof. Dr. I. Kanazirski for the impedance spectroscopy measurements. B. M. G. M. thanks National Funds FCT – Fundação para a Ciência e a Tecnologia, for the financial support through the grant SFRH/BD/117487/2016.

References

1. Kremer F, Arndt M (1997) In: Runt JP, Fitzgerald JJ (eds) Dielectric spectroscopy of polymeric materials. American Chemical Society, Washington,DC
2. McCrun NG, Read BE, Willians G (1991) Anelastic and dielectric effects in polymeric solids. Wiley, New York
3. Westphal WB, von Hippel AR (1954) Dielectric materials and applications. MIT Press/Wiley, New York
4. Amstrong D, Race WP, Thirsk HR (1968) Determination of electrode impedance over an extended frequency range by alternating current bridge methods. Electrochem Acta 13:215
5. Macdonald JR (1992) Impedance spectroscopy. Ann Biom Eng 20:289
6. Costa LC (1995), Propriedades eléctricas de vidros com alguns iões de terras raras, PhD Thesis, University of Aveiro
7. Calvert R (1948) A new technique in bridge measurements. Electron Eng 20:28
8. Henry F (1961), Développement de la métrologie hyperfréquences et application à l'étude de l'hydratation et la diffusion de l'eau dans les matériaux macromoléculaires, PhD Thesis, University of Paris
9. Karasz FE (1972) Dielectric properties of polymers. Plenum Press, New York
10. Costa LC (2011) Double relaxation processes in the glass system $xEu_2O_3.PbO.2B_2O_3$ studied by Broadband Dielectric Spectroscopy. J Non Cryst Sol 357:2178
11. Ku CC, Liepins R (1987) Electrical properties of polymers. Hanser, Munich
12. Adachi K (1997) In: Runt JP, Fitzgerald JJ (eds) Dielectric spectroscopy of polymeric materials. American Chemical Society, Washington, DC
13. Tsangaris GM, Psarras GC, Kouloumbi N (1998) Electric modulus and interfacial polarization in composite polymeric systems, J Mater Sci 33:2027
14. Jonscher AK (1983) Dielectric relaxation in solids. Chelsea Dielectric Press, London
15. Barsoukov E, Macdonald JR (2005) Impedance spectroscopy. Wiley, New Jersey
16. Cole KS, Cole RH (1941) Dispersion and absorption in dielectrics-I Alternating current characteristics. J Chem Phys 9(4):341
17. Davidson DW, Cole RH (1951) Dielectric relaxation in glycerol, propylene glycol and n-propanol. J Chem Phys 19:1484
18. Havriliak S, Negami S (1966) A complex plane analysis of α-dispersions in some polymer systems. J Polym Sci C 14:99

Chapter 8
Undesirable Aspects of Fatigue on Stretchable Elastomer Sensors

Evghenii Harea, Sanjoy Datta, Martin Stěnička, and Radek Stoček

Abstract Flexible electronics is a rapidly developing branch of modern economy. Flexing, bending and stretching of elastic components leads to inevitable changes in the internal structures which brings undesirable variation in their electrical behaviors. The present work was focused on investigation of undesirable aspects of fatigue on functionality of stretchable elastomer sensors based on natural rubber composites containing multi-walled carbon nanotubes (MWCNT) and carbon black hybrid filler systems at various weight combinations. Conductive elastomer containing all common additives, curatives and a fixed amount of hybrid fillers were prepared and tested before and after 10^5 dynamic loading cycles at three different strain amplitudes. Although the increased loading of MWCNT in the hybrid filler system improved progressively the conductivity of the fabricated composites and tended to prevent conductivity degradation during fatigue test, continued cyclic deformation led to decreased conductivity of all studied samples. Besides the conductivity degradation, other undesirable feature found were the time dependent increase of the conductivity during measurements at a constant applied voltage and the prolonged stress induced softening of the composites.

Keywords Conductive rubber · Fatigue · Hybrid fillers · Sensors

E. Harea (✉) · S. Datta · M. Stěnička · R. Stoček
Centre of Polymer Systems, University Institute, Tomas Bata University in Zlín, Zlín, Czech Republic
e-mail: harea@utb.cz

P. Petkov et al. (eds.), *Nanoscience and Nanotechnology in Security and Protection against CBRN Threats*, NATO Science for Peace and Security Series B: Physics and Biophysics, https://doi.org/10.1007/978-94-024-2018-0_8

8.1 Introduction

Stretchable strain sensors are usually designed for accurate detection of different mechanical deformations or of stress necessary to achieve such deformations. Conventional metal-based stress/strain sensors show maximum strain around 5% [1]. This is why polymer-based stretchable sensors have attracted great interest. Conductive particles/nanofibers/layers coated on or embedded into polymeric substrate surfaces have a good sensitivity, a high gauge factor [2], well reproducible results [3] and are easily fabricated [4]. Another group of stretchable sensors are fabricated by blending conductive particles with insulating elastomer [5–7]. These composites are also promising materials for transducers and flexible electrodes [8–10] because of their ability to be elastically deformed while still providing some degree of electrical conductivity [11].

Along with accessible, low-cost types of conductive fillers such as carbon black (CB) [12], in the last few decades more expensive multi-walled carbon nanotubes (MWCNT) fillers are largely used in various studies and prototype devices due to their outstanding electrical, mechanical and thermal properties. The high aspect ratio and intrinsic conductivity allow production of nanocomposites with enhanced bulk electrical conductivity [13, 14].

The carbon black combined with carbon nanotubes, so called hybrid fillers, also became a promising cost-efficient option to produce conductive elastomers. For example, the natural rubber-based composites with MWCNT+CB hybrid fillers encompassed noticeable enhancements in the mechanical properties such as fracture, fatigue resistance [15], friction and wear [16]. Here, the CB particles bridge the MWCNT, surrounded by the nonconductive polymer and contribute to the formation of new electron pathways [8, 17, 18]. Consequently, higher conductivity of the composite at lower percolation threshold can be obtained [8]. The electrical conductivity of the filled elastomers is affected by macroscopic deformation because of the variation of distances between the conductive particles, which is the basic mechanism used in stretchable sensors. During long term usage the flexible electrodes, sensors and transducers endure millions of fatigue cycles, which can lead to internal micro-failure [19] and undesirable change in device accuracy.

The present work was focused on the preparation of natural rubber (NR) composites with 30 parts per hundred rubber (phr) of various ratios of MWCNT and CB hybrid fillers (Table 8.1) via simple mixing method [16, 20] and the investigation of undesirable effects which may affect the proper functionality of stretchable sensors after 10^5 fatigue cycles at different deformation amplitudes.

Table 8.1 Notation of samples based on hybrid filler composition

	NR0	NR1	NR3	NR5
NR, phr	100	100	100	100
MWCNT, phr	0	1	3	5
CB, phr	30	29	27	25

8.2 Experimental

8.2.1 Materials

Natural rubber used in this research was supplied by the Astlett Rubber Inc. (type SMR 20 CV/BP1). Sulphur used as curing agent, and zinc oxide (ZnO) and stearic acid used as activators were supplied by Sigma-Aldrich®. The hybrid filler system consisted of CB of type N220 supplied by Cabot Corporation and MWCNT with average diameter of 10–20 nm provided by Chuiko Institute of Surface Chemistry, National Academy of Sciences of Ukraine [21]. CBS (N-cyclohexyl-2-benzothiazolesulfenamide) was employed as curing accelerator. The complete composition of the compounds is listed in Table 8.2 and is identical with that in Ref. [20].

8.2.2 Rubber Compounding

The rubber compounds based on NR filled with CB and hybrid CB + MWCNT fillers were mixed in a Brabender Plastograph. The compounding was performed at 60 °C with 50 rpm and at a fill factor of 80%. The chemicals in the proportion listed in Table 8.2 were successively added as follows: NR was masticated for 3 min followed by mixing of ZnO and stearic acid activators both for 1 min successively. The hybrid fillers were consecutively added and mixed for 15 min. Finally, CBS and sulphur were added in batches, and the total mixing time in each case was 22 min. After 24 h conditioning at ambient temperature of 20 °C and a relative humidity of 40%, the blends were molded into 125 × 125 × 2 mm^3 sheets and cured in an electrically heated hydraulic press at 160 °C under 200 kN force in accordance with the optimum curing time obtained from a moving die rheometer.

8.2.3 Testing

The cure characteristics of the natural rubber nanocomposite were studied using a Monsanto Moving Die Rheometer (MDR 3000 MonTec, Germany) according to

Table 8.2 Batch composition of the studied samples ($x^* = 0.0, 1.0, 3.0, 5.0$)

$NR_{(MWCNTx + CB30-x)}$	NR, phr	100
	MWCNT, phr	x^*
	Carbon Black, phr	$30\text{-}x^*$
	CBS, phr	1.0
	Sulphur, phr	2.5
	ZnO, phr	5.0
	Stearic Acid, phr	2.0

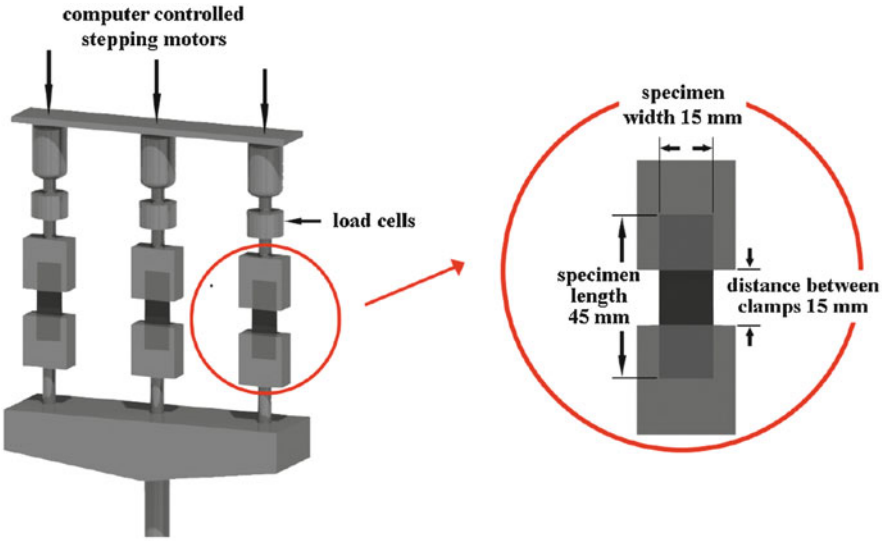

Fig. 8.1 Sketch of the loading engine, clamping system and specimen dimensions

ISO 3417 at 160 °C. Each molded sheet of about 2 mm thickness was cut into rectangular strips of 45 × 15 mm^2.

The DC conductivity was calculated from the current passed through the sample measured at 3 V during 300 s in the geometrical center of the strip in a two-point setup using brass plate electrodes of 15 mm diameter (described in Ref. [20]) with a programmable electrometer (Keithley 6517 A, USA) as:

$$\sigma = \frac{I}{U} * \frac{t}{S} \tag{8.1}$$

where I is the current, U the voltage, t the sample thickness (in cm) and S – the area of the electrodes (in cm^2).

Fatigue measurements were carried out using Tear and Fatigue Analyzer (Coesfeld GmbH, Germany). The detailed description can be found in Ref. [22]. The analyses were done on the device with implemented 3 independent loading engines, where 3 specimens were simultaneously analyzed at each of the engines. Each upper part of clamp attachment of the test specimens was fixed to the load cell and its corresponding sample clamp attachment was connected to a separate computer-controlled stepper motor to ensure constant pre-stress during the whole time of testing (Fig. 8.1). A set of 3 samples per compound was analyzed at each of the three strain amplitudes using a frequency of 5 Hz and 10^5 cycles. Strain amplitudes were set to 10%, 25% and 50% with an initial distance of 15 mm between the clamps. Fatigue loading was applied using sinusoidal waveform, where the pre-stress was set to 0 MPa.

8.3 Results and Discussion

8.3.1 Undesirable Long Lasting Mullins Effect

Effect of fatigue in dynamic loading on stress/strain relation of materials is a very important parameter for the real devices based on elastomers. NR based composites for strain sensor application is a topic of many studies and articles and, as stated in the introduction, the goal of the present work was to study the undesirable effects of dynamic fatigue on functionality of NR based nanocomposite materials filled with hybrid fillers. Figure 8.2 denotes the stress magnitude applied for consequent 10^5 cycles to achieve 10%, 25% and 50% of the strain for the investigated samples. The data was collected after each 100 cycles.

It is certainly observed that lower strain amplitude requires lower stress for all samples. CNT loading increased the stress necessary to reach the fixed strain amplitude. An undesirable and not expected result was the Mullins effect (softening of rubber during cyclic deformation [23]) which was observed at 50% elongation up to approximately 6000 cycles for the CNT containing samples. Properly working device is supposed to achieve every time a similar deformation amplitude, being subjected to comparable mechanical load and vice versa. As can be seen from Fig. 8.2, the stabilization of stress-strain relations depends on the strain amplitude

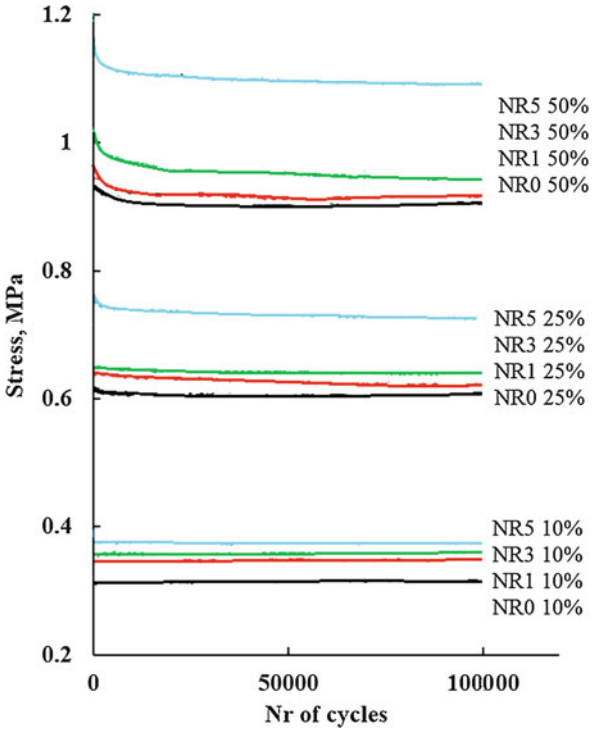

Fig. 8.2 Stress applied to deform samples up to the set strain amplitude (10%, 25% and 50%) vs. number of fatigue cycles. (Reprinted with permission of eXPRESS Polymer Letters [20])

and the composition of the fillers. Hence, for 10% strain amplitude, stabilization was observed from the beginning (up to 100 tensile cycles) for all studied compositions. At 50% strain testing amplitude, rubber softening lasted up to 6000 cycles. So, comparable stress/strain output of sensors should be expected only after suitable dynamic strain conditioning.

8.3.2 *Undesirable Electric Field Driven Conductive Path Reorganization*

Figure 8.3 shows the DC volume electrical conductivity of NR based composites filled with different ratios of CNT + CB hybrid fillers.

Gradual replacement of predefined amount of CB with same quantity (by weight) of MWCNT, namely 1.0, 3.0, and 5.0 phr, led to very fast increase of the conductivity, best represented by the logarithmic scale in Fig. 8.3. Current flow through filled polymers is mainly governed by percolation threshold of matrix-filler system and tunneling effect between conductive fillers. Since, the density of CB (~2.2 g/cm^3) is close to those of MWCNT (2.1–2.6 g/cm^3, depending on manufacturing process), the volume fraction of the hybrid fillers was considered more or less similar. The key factors here were the difference between the conductivities of CB and MWCNT and also the difference between their aspect ratios, which resulted in different resistivity of the rubber composites.

A pure CB N220 exhibits moderate electrical conductivity $\sigma \sim 2$ S/cm. The NR containing 30 phr of CB N220 (samples NR0) showed a conductivity of only $\sim 10^{-5}$ S/cm. Replacing 5% of CB by MWCNT with conductivity of about $\sim 10^{3}$ S/cm increased the electrical conductivity of the nanocomposite up to $\sim 10^{-3}$ S/cm.

Figure 8.3 reveals an increment of the conductivity as a function of time, which reflects another undesirable factor for sensitivity and accuracy of sensors based on

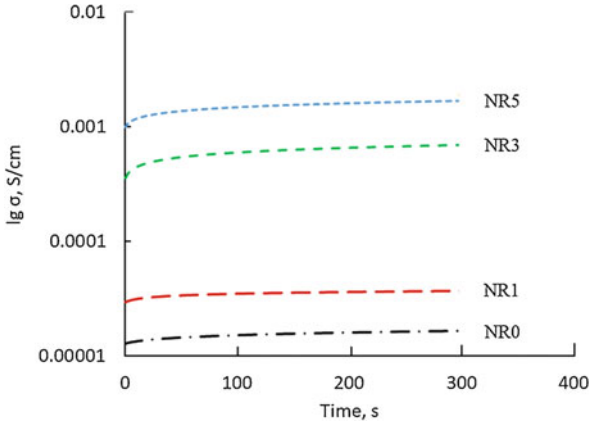

Fig. 8.3 Electrical conductivity of samples before fatigue test. (Reprinted with permission of eXPRESS Polymer Letters [20])

CB or hybrid filled NR composites. The current passed through the sample increased with time, initially very rapidly, then more slowly, approaching a quasi-equilibrium value. This phenomenon is also described in [24]. According to the authors, the carbon black particles are connected to each other by the flexible long rubber molecules. In unstretched state, the rubber molecules are curled up, in accordance with the kinetic theory of rubber elasticity. The flexibility of the rubber molecules permits almost free translational kinetic (Brownian) motion of the carbon black particles up to the limit given by the length of the rubber molecules.

In addition to the aforementioned arguments, in the present work a hypothesis was propounded which pointed to the existence of conductive pathway segments separated by nonconductive polymer insets. During electrical measurements, electromagnetic field charged the segments and made them to attract or repel each other, leading to reorganization of the conductive paths and consequent increase of conductivity.

In case of hybrid fillers, MWCNT are much more limited in their kinetic motion inside of rubber matrix due to their much higher aspect ratio. Hence, the motion of the carbon black particles was mostly responsible for the variation of resistivity as a function of time.

8.3.3 Undesirable Electrical conductivity degradation After Long Term Usage

The electrical conductivity measurements (mean value) after cyclic deformation of the samples at different strain amplitudes are exhibited in Fig. 8.4. For all investigated samples, the fatigue reduced essentially the conductivity.

Similar to the nanocomposites before the fatigue test, the conductivity was time dependent process and it was assumed that it was influenced by the electric field driven conductive pathway reorganization discussed above.

More informative than Fig. 8.4 and also easier to analyze is Fig. 8.5. Keeping in mind that the resistivity $\rho = 1/\sigma$, this figure reflects how many times the resistivity of the samples increased after the fatigue test. The highest change of conductivity was observed for samples NR0 where MWCNT were absent, and the higher fatigue stress amplitude produced higher sample resistivity. This trend was generally revealed for all sample compositions. However, the increased quantity of MWCNT in the hybrid fillers preserved the electrical properties of the nanocomposites subjected to fatigue processes in a much better way.

It can be generalized that the decrease of the conductivity after cyclic stretching of the samples is definitely caused by internal changes in the material and surely will affect the electrical output of the sensor during long term usage. Even if there are no visible defects in the polymer matrix at nano-level, the distribution of the fillers is subjected to important transformations [20], which leads to significant destruction of the conductive paths.

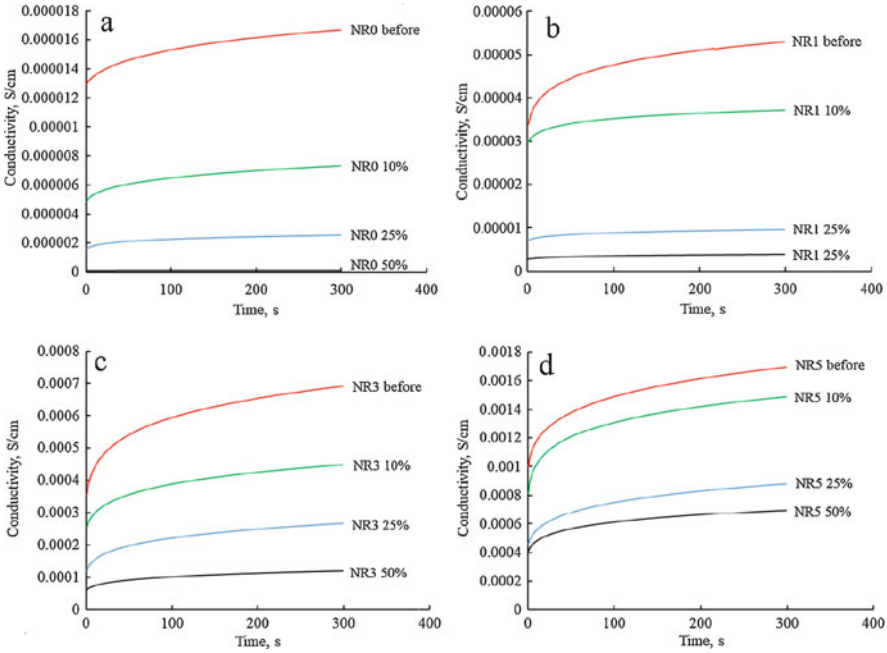

Fig. 8.4 Conductivity vs. time before and after fatigue test at 10%, 25% and 50% strain amplitude for (**a**) samples NR0, (**b**) samples NR1, (**c**) samples NR3 and (**d**) samples NR5

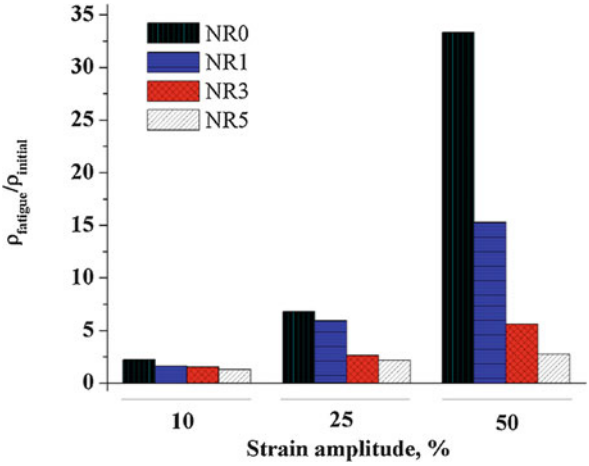

Fig. 8.5 Normalized resistivity after fatigue test

8.4 Conclusions

Natural rubber based electro-conductive composites can be conditionally accepted for flexible electronics. Long lasting Mullins effect (especially at high deformation amplitude) results in a change of the conductivity after the fatigue test and time dependent conductivity should be carefully taken into consideration and some restrictions for application of NR filled with CNT and CB hybrid fillers are to be imposed. Addition of CNT definitely improved the volume conductivity and tended to preserve the dramatic changes of the conductivity after cyclic deformation. Increasing of deformation amplitude significantly enhanced the electrical resistivity of the studied samples. Time dependent conductivity phenomenon was observed for all investigated samples before and after the fatigue test.

Summarizing the presented work, the following suggestions are framed:

- Elastomer based active elements for stress/strain sensors should be prestrained before calibration at strain amplitudes greater or equal to those expected to be encountered in real life applications.
- Number of prestrain cycles is recommended to be enough to achieve the equilibrium of stress-strain relations.
- Electrical output of sensors should be carefully analyzed and processed only after stabilization. For "fast" reacting sensors it is recommended to calculate the stabilized output signals using fitting equations.

Acknowledgments This article was written with the support of Operational Program Research and Development for Innovations co-funded by the European Regional Development Fund and national budget of the Czech Republic, within the framework of the project CPS—strengthening research capacity (reg. Number: CZ.1.05/2.1.00/19.0409) as well as supported by the Ministry of Education, Youth and Sports of the Czech Republic—Program NPU I (LO1504).

References

1. Yamada T, Hayamizu Y, Yamamoto Y, Yomogida Y, Najafabadi AI, Futaba DN, Hata K (2011) A stretchable carbon nanotube strain sensor for human-motion detection. Nat Nanotech 6:296–301. https://doi.org/10.1038/nnano.2011.36
2. Eswaraiah V, Balasubramaniam K, Ramaprabhu S (2011) Functionalized graphene reinforced thermoplastic nanocomposites as strain sensors in structural health monitoring. J Mater Chem 21:12626–12628. https://doi.org/10.1039/C1JM12302E
3. Xu F, Zhu Y (2012) Highly conductive and stretchable silver nanowire conductors. Adv Mater 24:5117–5122. https://doi.org/10.1002/adma.201201886
4. Noh JS (2013) Cracked titanium film on an elastomeric substrate for highly flexible, transparent, and low-power strain sensors. Nanoscale Res Lett 8:441. https://doi.org/10.1186/1556-276X-8-441
5. Gong S, Schwalb W, Wang Y, Chen Y, Tang Y, Si J, Shirinzadeh B, Cheng W (2014) A wearable and highly sensitive pressure sensor with ultrathin gold nanowires. Nat Commun 5:3132. https://doi.org/10.1038/ncomms4132

6. Wang SL, Wang P, Ding TH (2009) Piezoresistivity of silicone-rubber/carbon black composites excited by AC electrical field. J Appl Polym Sci 113:337–341. https://doi.org/10.1002/app.29685
7. Hwang J, Jang J, Hong K, Kim KN, Han JH, Shin K, Park CE (2011) Poly(3-hexylthiophene) wrapped carbon nanotube/poly(dimethylsiloxane) composites for use in finger-sensing piezoresistive pressure sensors. Carbon 49:106–110. https://doi.org/10.1016/j.carbon.2010.08.048
8. Natarajan TS, Eshwaran SB, Stöckelhuber KW, Wießner S, Pötschke P, Heinrich G, Das A (2017) Strong strain sensing performance of natural rubber nanocomposites. ACS Appl Mater Interfaces 9(5):4860–4872. https://doi.org/10.1021/acsami.6b13074
9. Liu P, Liu CX, Huang Y, Wang WH, Fang D, Zhang YG, Ge YJ (2016) Transfer function and working principle of a pressure/temperature sensor based on carbon black/silicone rubber composites. J Appl Polym Sci 133(42979). https://doi.org/10.1002/app.42979
10. Ciselli P, Lu L, Busfield J, Peijs T (2010) Piezoresistive polymer composites based on EPDM and MWNTs for strain sensing applications. e-Polymers 014:1–13. https://doi.org/10.1515/epoly.2010.10.1.125
11. De Focatiis DSA, Hull D, Sanchez-Valencia A (2012) Roles of prestrain and hysteresis on piezoresistance in conductive elastomers for strain sensor applications. Plast Rubber Compos 41(7):301–309. https://doi.org/10.1179/1743289812Y.0000000022
12. Salaeh S, Nakason C (2012) Influence of modified natural rubber and structure of carbon black on properties of natural rubber compounds. Polym Compos 33(4):489–500. https://doi.org/10.1002/pc.22169
13. Moniruzzaman M, Winey KI (2006) Polymer nanocomposites containing carbon nanotubes. Macromolecules 39:5194–5205. https://doi.org/10.1021/ma060733p
14. Kummerlöwe C, Vennemann N, Pieper S, Siebert A, Nakaramontri Y (2014) Preparation and properties of carbon-nanotube composites with natural rubber and epoxidized natural rubber. Polimery 59(11–12):811–818. https://doi.org/10.14314/polimery.2014.811
15. Dong B, Liu C, Lu Y, Wu Y (2015) Synergistic effects of carbon nanotubes and carbon black on the fracture and fatigue resistance of natural rubber composites. J Appl Polym Sci 42075. https://doi.org/10.1002/app.42075
16. Harea E, Stoček R, Storozhuk L, Sementsov Y, Kartel N (2019) Study of tribological properties of natural rubber containing carbon nanotubes and carbon black as hybrid fillers. Appl Nanosci 9(5):899–906. https://doi.org/10.1007/s13204-018-0797-6
17. Nakaramontri Y, Pichaiyut S, Wisunthorn S, Nakason C (2017) Hybrid carbon nanotubes and conductive carbon black in natural rubber composites to enhance electrical conductivity by reducing gaps separating carbon nanotube encapsulates. Eur Polym J 90:467–448. https://doi.org/10.1016/j.eurpolymj.2017.03.029
18. Ma PC, Liu MY, Zhang H, Wang SQ, Wang R, Wang K, Yiu-Kei W, Ben-Zhong T, Soon-Hyung H, Kyung-Wook P, Jang-Kyo K (2009) Enhanced electrical conductivity of nanocomposites containing hybrid fillers of carbon nanotubes and carbon black. ACS Appl Mater Interfaces 1(5):1090–1096. https://doi.org/10.1021/am9000503
19. Huneau B, Masquelier I, Marco Y, Le Saux V, Noizet S, Schiel C, Charrier P (2016) Fatugue crack initiation in a black filled natural rubber. Chem Technol 89(1):126–141. https://doi.org/10.5254/rct.15.84809
20. Harea E, Datta S, Stěnička M, Stoček R (2019) Electrical conductivity degradation of fatigued carbon black reinforced natural rubber composites: effects of carbon nanotubes and strain amplitudes. Express Polym Lett 13(12):1116–1124. https://doi.org/10.3144/expresspolymlett.2019.96
21. Yanchenko VV, Sementsov Y, Melezhyk AV (2007) Process of preparation of carbon nanotubes. U.A. Patent 69292, Ukraine (in Russian)
22. Eisele U, Kelbch SA, Engels HW (1992) The tear analyzer – a new tool for quantitative measurements of the dynamic crack growth of elastomers. Kautschuk und Gummi Kunststoffe 45(1064–1069)

23. Mullins L (1969) Softening of rubber by deformation. Rubber Chem Technol 42:339–362. https://doi.org/10.5254/1.3539210
24. Wack PE, Anthony RL, Guth E (1947) Electrical conductivity of GR-S and natural rubber stocks loaded with Shawinigan and R-40 blacks. J Appl Phys 18:456–469. https://doi.org/10.1063/1.1697676

Chapter 9
Dielectric Characterization of $(Bi_{1-x}Fe_x)NbO_4$ Ceramics Prepared by Wet-Chemical Route

Susana Devesa, Manuel P. Graça, and Luis C. Costa

Abstract $(Bi_{1-x}Fe_x)NbO_4$ powders with $0.00 \leq x \leq 0.75$ were prepared by a wet-chemical route. Pellets from these powders were made and sintered at temperatures between 500 and 1100 °C. The dielectric properties were analyzed as a function of the thermally activated structural and morphologic evolution. The structure was studied by X-ray diffraction (XPD) and the morphology by scanning electron microscopy (SEM). The XRD results revealed that the substitution of bismuth by iron was successful for $x = 0.25$ and 0.50, with the formation of the non-stoichiometric phases $Bi_{1.34}Fe_{0.66}Nb_{1.34}O_{6.35}$ and $Bi_{1.721}Fe_{1.056}Nb_{1.134}O_7$. The dielectric properties were measured by impedance spectroscopy method in the frequency range of 10^2–10^6 Hz as a function of temperature (200–330 K). For the samples with $x \geq 0.25$ treated at 800 and 1100 °C, the dielectric constant and the dielectric losses remain practically constant with the frequency and temperature. The dielectric relaxation mechanisms were studied using the complex modulus formalism.

Keywords Bismuth niobate · Iron · Impedance spectroscopy · Dielectric relaxation

9.1 Introduction

With the progress of the modern communication systems, where the wireless equipment is indispensable, the compactness, power efficiency and affordability are considered basic requirements for equipment that are produced by the telecommunication industry [1, 2]. To achieve this purpose, the development of dielectric materials for electronic applications has been focused on reducing the size and weight of radiofrequency (RF) and microwave (MW) components in telecommunication [3].

S. Devesa (✉) · M. P. Graça · L. C. Costa
I3N and Physics Department, University of Aveiro, Aveiro, Portugal

P. Petkov et al. (eds.), *Nanoscience and Nanotechnology in Security and Protection against CBRN Threats*, NATO Science for Peace and Security Series B: Physics and Biophysics, https://doi.org/10.1007/978-94-024-2018-0_9

Amongst the dielectrics, the ceramic materials, in particular low temperature co-fired ceramics (LTCC), have been extensively used in multilayer RF and MW components [1, 3] namely the bismuth-containing oxides. They have rich structural diversity and promising physical properties for applications in catalysis, optics, nanophotonics and nanoelectronics [4]. There are several works that highlight the interest in bismuth oxides, since bismuth based compounds would possess low operating voltage, fast switching speed, negligible fatigue values up to 10^{12} switching cycles, excellent retention characteristics and low leakage current density on Pt electrodes for integrated device applications in non-volatile ferroelectric random access memories (FRAM) [5].

Even though bismuth is a relatively rare element (64th in abundance in the Earth's crust), large quantities of bismuth are produced every year as a by-product [6]. Furthermore, in spite of its heavy metal status, bismuth is considered to be safe, due to its non-toxic and non carcinogenic nature [6, 7].

Bismuth niobate ($BiNbO_4$) has been evaluated to be a novel material, cofired at low temperatures and with potential for dielectric applications [3, 5, 8]. It exists in two polymorph structures, an orthorhombic (α) phase (space group P_{nna}) and a triclinic (β) phase (space group P_1) [9]. According to previous studies, the transition of low temperature β-$BiNbO_4$ to α-$BiNbO_4$ occurs at temperatures between 600 and 750 °C, with the opposite, and supposed irreversible, transition occurring at 1020/1050 °C [10, 11]. In 2007, Zhou et al. [12] reported the transformation of high temperature β-$BiNbO_4$ to α-$BiNbO_4$ in bulk samples.

In 1992 Kagata et al. [13] reported the microwave dielectric properties of bismuth niobate for the first time, using as sintering aids CuO and V_2O_5 to obtain higher densification without compromising the dielectric properties. Since then, several researchers attempted to improve the physical and the dielectric properties of $BiNbO_4$ ceramics, either by the addition of sintering aids (oxides), or by the substitution of bismuth or niobium by other cations, or even by the combination of the two techniques [14]. Most of these studies are focused on the dielectric characterization in the microwave frequency range, and very few reported the dielectric properties in the radiofrequency regime. Furthermore, the papers concerning the stability of the dielectric permittivity with temperature are even less, despite the importance of the temperature coefficient of capacitance (TCC) for RF components. Some deviation in component specifications with temperature can adversely affect the channel/frequency selection characteristics of filter/resonator circuits in an RF module [2].

In this work, $(Bi_{1-x}Fe_x)NbO_4$ ($0.00 \leq \times \leq 0.75$) samples were prepared by sol-gel method through the citrate route. The fine particles were pressed into pellets and heat-treated at four different temperatures between 500 and 1100 °C, established in accordance with the differential thermal analysis (DTA) results. The dielectric characterization in the RF regime was performed by impedance spectroscopy in the frequency range from 100 Hz to 1 MHz. The analysis of the results from the electrical measurements analysis was made in agreement with the changes in the micro-structure (XRD) and morphology (SEM) due to the content of iron and the heating process.

9.2 Experimental

9.2.1 Samples Preparation

$(Bi_{1-x}Fe_x)NbO_4$ powders were prepared by the sol-gel method through the citrate route. $Bi(NO_3)_3.5H_2O$ and $Fe(NO_3)_3.9H_2O$ were dissolved in a solution of previously prepared citric acid, $NbCl_5$ was dissolved in minor amount of H_2O_2 (3% V/V) and then added to the citric acid solution. The use of hydrogen peroxide in processes with niobium chloride, even in small amounts, prevents the formation of undesirable precipitates and removes most of the chlorine from the gel [15].

Ethylene glycol was added to the starting materials in the corresponding molar ratio in order to promote the polymerization phase. The obtained mixtures were stirred for 7 days to promote the solubility, until transparent colloidal suspensions were obtained. I order to establish the period of stirring, the viscosity of the mixture with $x = 0.00$ was monitored with an AND Vibro Viscosimeter. The viscosity varied between 2.61 and 3.30 mPa.s and it tended to stabilize after 7 days of stirring. To evaporate the solvent, the obtained gels were dried. The mixture with $x = 0.00$ was dried at 400 °C for 48 h and the mixtures with $0.25 \leq x \leq 0.75$ were dried at 300 °C for 60 h. This heating process promoted the expansion of the material with the formation of a fragile material similar to a foam that was milled until a fine powder was obtained. Subsequently, the obtained powders were thermally analysed by differential thermal analysis performed with a *Lynseis Apparatus type L92/095*, in the temperature range of 20–1200 °C with a heating rate of 5 °C/min and using Al_2O_3 as a reference.

The DTA of the powders is shown in Fig. 9.1. For the powders with $x = 0.00$ one can see three exothermic phenomena at 649, 1043 and 1129 °C. When $x = 0.25$, the thermal phenomena are also exothermic and centred at 519, 637 and 1054 °C. The powder with $x = 0.50$ exhibited three exothermic phenomena as well – at 489, 556

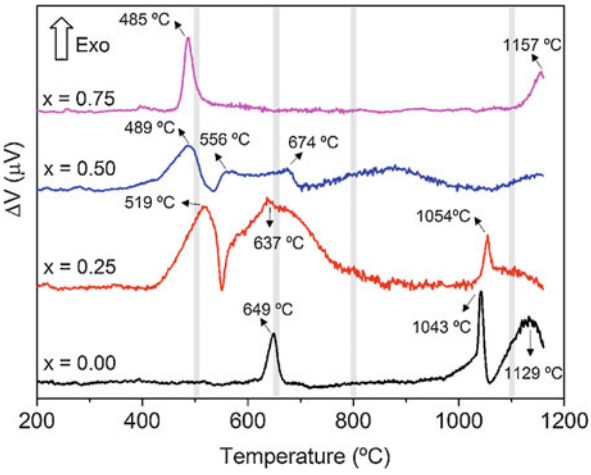

Fig. 9.1 DTA of $(Bi_{1-x}Fe_x)NbO_4$ powders heated with rate of 5 °C/min

and 674 °C. Finally, two exothermic phenomena were identified for $x = 0.75$ – at 485 and 1157 °C.

The different powders were pressed into pellets and heat-treated, according to the DTA results, at 500, 650, 800 and 1100 °C using a dwell time of 4 h with a heating rate of 5 °C/min. The heat-treatment performed at 1200 °C promoted the fusion of the samples.

9.2.2 Characterization Methods

The structural characterization was performed by X-ray diffraction. The patterns were obtained with a X'Pert MPD Philips diffractometer (CuKα radiation, λ = 1.54060 Å) at 45 kV, and 40 mA, with a curved graphite monochromator, an automatic divergence slit (irradiated length 20.00 mm), a progressive receiving slit (height 0.05 mm) and a flat plane sample holder in a Bragg-Brentano parafocusing optics configuration. Intensity data was collected by the step counting method (step 0.02° in 1 s) in the 2θ angle range of 10–60°.

The morphology of the obtained samples on the free and fractured surfaces was analyzed by scanning electron microscopy using a TESCAN-Vega III. The samples were covered with carbon before the microscopic observation.

For the electrical measurements, the opposite sides of the pellets were painted with silver conducting paste. During the measurements, the samples were maintained in a helium atmosphere in order to improve the heat transfer and eliminate the moisture. The impedance spectroscopy measurements were performed in the frequency range from 100 Hz to 1 MHz and in the temperature range from 200 to 330 K using an Agilent 4294A precision impedance analyzer in the $C_p{}^{-}R_p$ configuration.

The complex dielectric permittivity of the material can be written as [16]:

$$\varepsilon^* = \varepsilon' - i\varepsilon'' \tag{9.1}$$

The real ε' and the imaginary ε'' parts of the complex permittivity can be calculated from C_p and R_p [17]:

$$\varepsilon' = C_p \frac{d}{A\varepsilon_0} \tag{9.2}$$

$$\varepsilon'' = \frac{d}{\omega R_p A \varepsilon_0} \tag{9.3}$$

where d represents the sample thickness, A the electrode area, ε_0 the empty space dielectric constant and ω the angular frequency.

The loss tangent $tg\delta$ is given by the ratio between ε'' and ε'.

The stability of the dielectric constant with temperature can be evaluated through the temperature coefficient of capacitance (TCC). This is a very important parameter and can be written as [16–18]:

$$TCC = \frac{C_{T2} - C_{T1}}{C_{T1}(T_2 - T_1)} \times 10^6 \ ppm/^\circ C \tag{9.4}$$

where C_{T1} and C_{T2} are the measured capacitance at temperatures T_1 and T_2, respectively.

For applications demanding precise capacitance control, nearly zero TCC is required. This can be achieved with a mixture of materials with positive and negative TCC [18].

9.3 Results and Discussion

9.3.1 Structural Characterization

The crystalline phases presented in the sintered pellets were identified by X-ray diffraction patterns and are shown in Fig. 9.2 and Table 9.1. In the samples with $x = 0.00$ heat-treated at 500 °C, it is possible to identify Bi_2O_3 and BiOCl phases, as well as the beginning of the formation of orthorhombic α-$BiNbO_4$ and triclinic bismuth niobate (β-$BiNbO_4$). The sample treated at 650 °C has a combination of α and β-$BiNbO_4$. As the treatment temperature increases to 800 °C, the diffractogram reveals the formation of pure α-$BiNbO_4$ and, as the temperature increases further, this phase is converted to triclinic $BiNbO_4$. The information extracted from the X-ray diffraction results is consistent with the differential thermal analysis showed in Fig. 9.1.

9.3.2 Morphological Characterization

The micrographs of the samples with $x = 0.00$ treated at 500 and 650 °C reveal particles with spherical shape with diameters of about 0.2 μm (Fig. 9.3). Increasing the treatment temperature to 800 °C increases the size, as well as the shape of the particles to rod-shaped grains of about 1 μm long. However, when the treatment temperature reaches 1100 °C more significant transformation occurs with a remarkable grain growth. This sample shows particles with variable shapes and dimensions and very well-defined boundaries.

The micrographs of the samples with $x = 0.25$ show the same trend as the reference samples (Fig. 9.4). The samples treated at 500 and 650 °C consist of particles with spherical shape, which after heat-treatment at 800 °C tend to lengthen and increase in size. Again, the treatment at higher temperature promotes the major

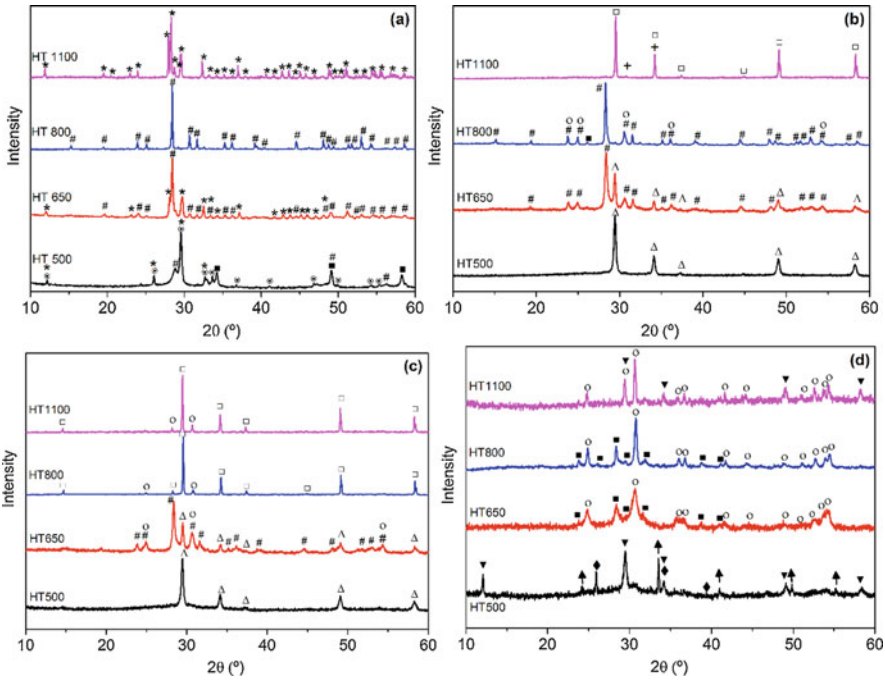

Fig. 9.2 X-ray diffraction patterns of $(Bi_{1-x}Fe_x)NbO_4$ samples treated at four different temperatures (HT) for: (**a**) $x = 0.00$; (**b**) $x = 0.25$; (**c**) $x = 0.50$; (**d**) $x = 0.75$

changes with a significant grain growth. The samples with $x = 0.50$ and 0.75 showed the same trend.

9.3.3 Dielectric Characterization

The frequency dependence of the dielectric constant at a constant temperature (300 K) is shown in Fig. 9.5. For the samples with $x = 0.00$, the dielectric constant is practically constant with the frequency. The sample heat-treated at 500 °C showed higher values of ε'. For the samples with $x > 0.00$, the dielectric constant of the samples heat-treated at 800 and 1100 °C remains practically constant with the frequency, whereas for the samples treated at lower temperatures, the dielectric constant decreases with the frequency. For the samples with $0.25 \leq x \leq 0.75$ it is possible to analyze the cases where the same crystalline phases were identified:

- samples with $x = 0.25$ and 0.50 treated at 500 °C: at low frequencies the sample with the higher iron content presents higher values of ε', however, with the increase of the frequency, this is also the sample with the sharper decrease of the dielectric constant;

Table 9.1 Identification of the crystalline phases of $(Bi_{1-x}Fe_x)NbO_4$ samples, heat-treated at 500, 650, 800 and 1100 °C

	HT 500	HT 650	HT 800	HT 1100
$x = 0.00$	α-$BiNbO_4$ (#)	α-$BiNbO_4$ (#)	α-$BiNbO_4$ (#)	β-$BiNbO_4$ (*)
	β-$BiNbO_4$ (*)	β-$BiNbO_4$ (*)		
	Bi_2O_3 (■)			
	BiOCl (⊙)			
$x = 0.25$	$Bi_{1.34}Fe_{0.66}Nb_{1.34}O_{6.35}$ (Δ)	α-$BiNbO_4$ (#)	α-$BiNbO_4$ (#)	$Bi_{1.721}Fe_{1.056}Nb_{1.134}O_7$ (□)
		$Bi_{1.34}Fe_{0.66}Nb_{1.34}O_{6.35}$ (Δ)	$FeNbO_4$ (○)	$BiFeO_3$ (+)
			Bi_2O_3 (■)	
$x = 0.50$	$Bi_{1.34}Fe_{0.66}Nb_{1.34}O_{6.35}$ (Δ)	α-$BiNbO_4$ (#)	$Bi_{1.721}Fe_{1.056}Nb_{1.134}O_7$ (□)	$Bi_{1.721}Fe_{1.056}Nb_{1.134}O_7$ (□)
		$Bi_{1.34}Fe_{0.66}Nb_{1.34}O_{6.35}$ (Δ)	$FeNbO_4$ (○)	$FeNbO_4$ (○)
$x = 0.75$	$Bi_{15}NbO_{25}$ (▼)	$FeNbO_4$ (o)	$FeNbO_4$ (○)	$FeNbO_4$ (○)
	Fe_2O_3 (↑)	Bi_2O_3 (■)	Bi_2O_3 (■)	$Bi_{15}NbO_{25}$ (▼)
	$Fe_{0.33}Nb_{0.67}O_2$ (◆)			

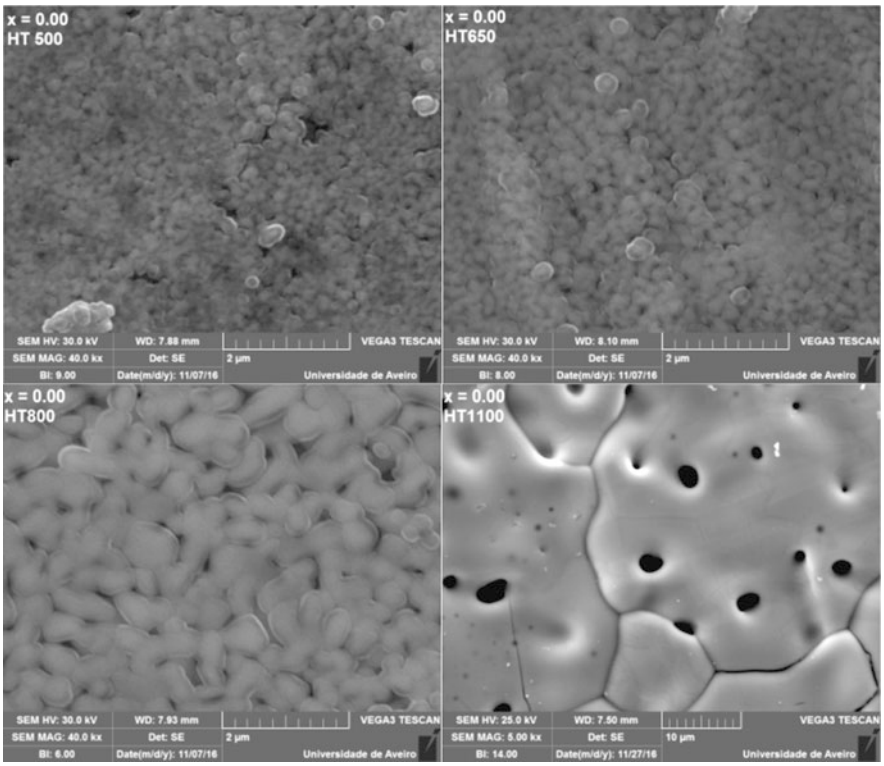

Fig. 9.3 SEM micrographs of $(Bi_{1-x}Fe_x)NbO_4$ samples with $x = 0.00$ with magnification of 40,000 (500, 650 and 800 °C) and 5000 (1100 °C)

- samples with $x = 0.25$ and 0.50 treated at 650 °C: in this case the increase of the iron content causes a marked decrease of the dielectric constant when measured at low frequencies. With the increase of the frequency, these values tend to stabilize;
- samples with $x = 0.75$ treated at 650 and 800 °C: at low frequencies the sample treated at 650 °C has much higher values of ε', however, with the increase of the frequency, this is also the sample with sharper decrease of these values;
- samples with $x = 0.50$ treated at 800 and 1100 °C: it can be seen that the increase of the treatment temperature promotes a significant increase of the dielectric constant, justified by the increased size of the grains and/or increased density.

The frequency dependence of the dielectric losses at constant temperature (300 K) is shown in Fig. 9.6. For the samples with $x = 0.00$ the dielectric losses are relatively low, except for the sample heat-treated at 650 °C, particularly at lower frequencies. For the samples with $x > 0.00$ we can observe the same trend identified for the dielectric constant. The dielectric losses of the samples heat-treated at 800 and 1100 °C remain practically constant with the frequency, while for the samples treated at lower temperatures the dielectric losses decrease with the frequency.

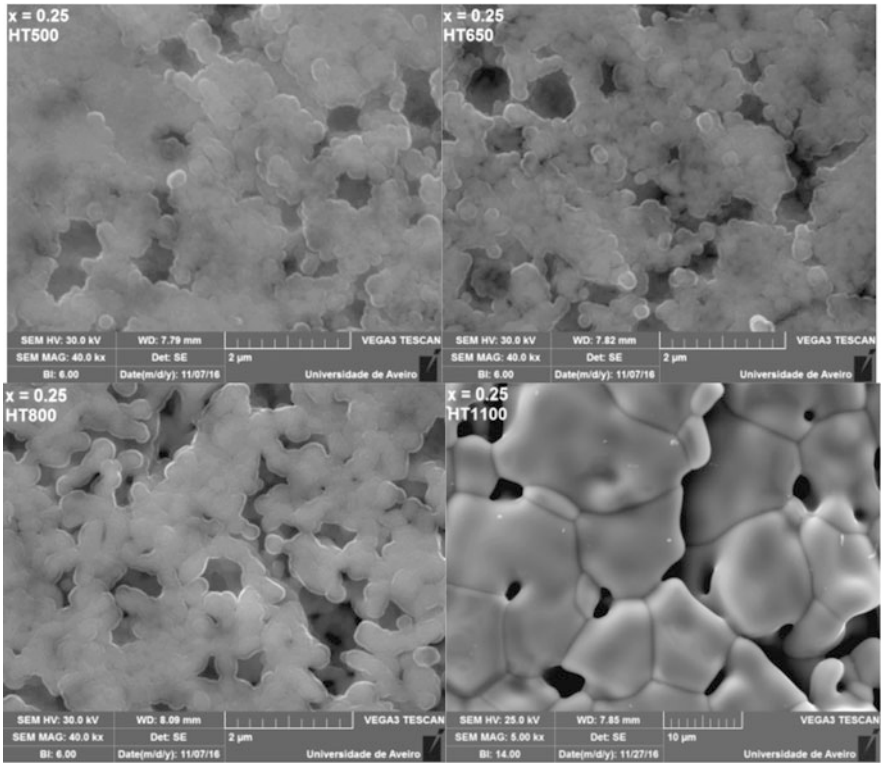

Fig. 9.4 SEM micrographs of $(Bi_{1-x}Fe_x)NbO_4$ samples with $x = 0.25$ with magnification of 40,000 (500, 650 and 800 °C) and 5000 (1100 °C)

Figure 9.7 shows the TCC values, obtained through the Eq. (9.4), for all studied samples at 100 kHz, where C_{T1} was measured at 300 K and C_{T2} at 330 K. For the samples with $x = 0.00$ the TCC values are not significantly influenced by the treatment temperature, a behavior that is not verified for the samples with $x > 0.00$. For these samples, the lowest TCC values occur for the heat-treatments at 800 and 1100 °C, and the TCC values of the samples treated at 500 °C increase with the increase of the iron content.

Considering the samples with $x = 0.25$ and 0.50, we can observe that the TCC signal changes from the samples treated at 800 °C (2548 and 102 ppm/°C) to the samples treated at 1100 °C (−570 and −122 ppm/°C). This signal change can indicate that an intermediate treatment temperature exists where TCC is 0 ppm/°C. Considering now the samples treated at 1100 °C, the TCC signal changes from the sample with $x = 0.00$ (584 ppm/°C) to the sample with $x = 0.25$ (−570 ppm/°C), and from the sample with $x = 0.50$ (−122 ppm/°C) to the sample with $x = 0.75$ (182 ppm/°C). We can infer that it is possible to find x values between 0.00 and 0.25 and between 0.50 and 0.75 where TCC = 0 ppm/°C, which is important for temperature stable applications [16, 18].

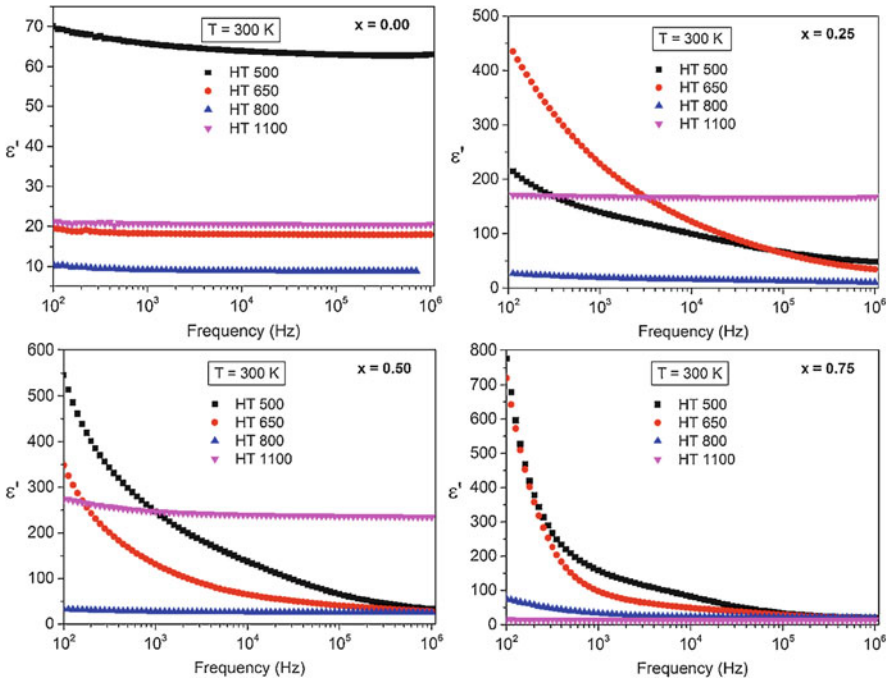

Fig. 9.5 Frequency dependence of the dielectric constant ε' at $T = 300$ K

The real and imaginary parts of the dielectric permittivity can be fitted using the general Havriliak-Negami (HN) function (Eq. 9.5):

$$\varepsilon(\omega) = \varepsilon_\infty + \frac{\varepsilon_s - \varepsilon_\infty}{(1 + (i\omega\tau_\varepsilon)^\alpha)^\gamma} \tag{9.5}$$

where ε_s and ε_∞ are the dielectric constant values at the limits of low and high frequency range, respectively, τ_ε the relaxation time, and α and γ are shape parameters.

When space-charge relaxation phenomena are not clearly detected using the complex permittivity formalism, the use of complex modulus formalism can be a solution [19, 20], which is the present experimental case. It is known that the graphic representation of M'' versus M' is very useful for materials with similar bulk and grain boundary capacitances [19, 21]. Using this representation, the relaxation process, τ_M, appears at a higher frequency than the corresponding process in the permittivity representation, indicating that τ_M is, in general, faster than τ_ε. In a simple Debye-like relaxation $\tau_M/\tau_\varepsilon \approx \varepsilon_\infty/\varepsilon_s$ [22, 23]. However, in non-Debye systems the difference between τ_M and τ_ε becomes more pronounced, but the ratio τ_M/τ_ε should remain constant.

Figure 9.8a presents the real part of the dielectric modulus M' as a function of the frequency and temperature for the sample with $x = 0.25$ treated at 650 °C. Typical

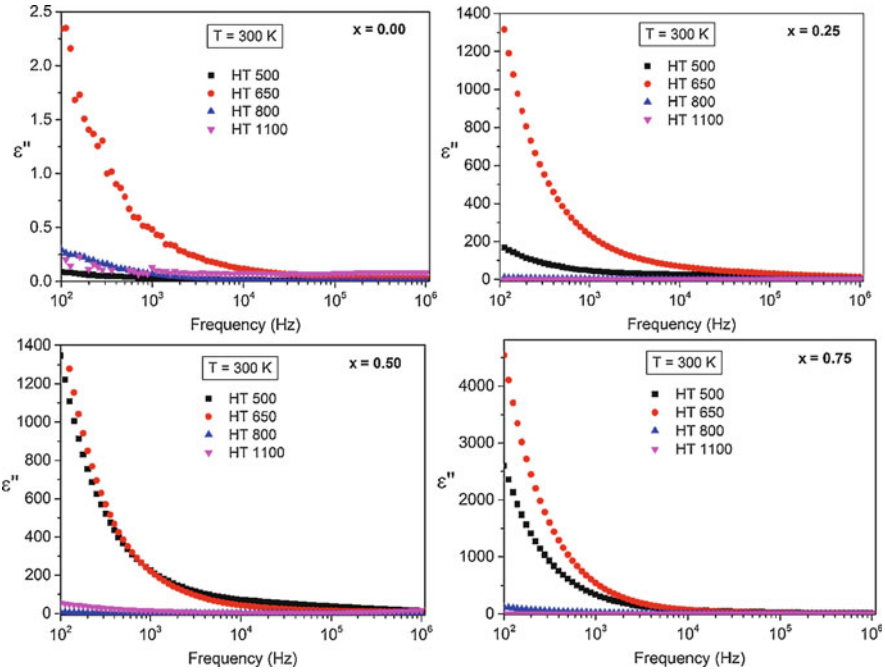

Fig. 9.6 Frequency dependence of the dielectric losses ε'' at $T = 300$ K

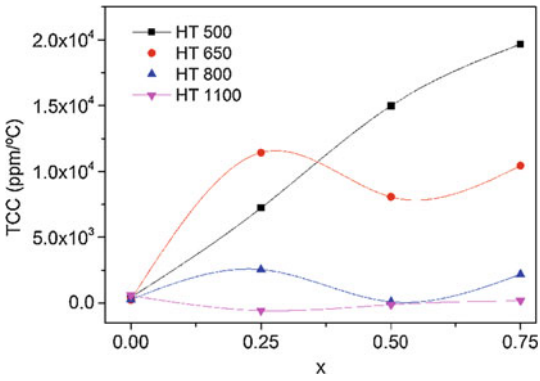

Fig. 9.7 TCC of the $(Bi_{1-x}Fe_x)NbO_4$ samples as function of x

dispersion behavior for polarizations in the relaxation regime is distinguished in this representation. Figure 9.8b shows the imaginary part of the dielectric modulus M'' as a function of the frequency and temperature for the same sample. The existence of two relaxation processes can be observed.

Figure 9.9 shows the frequency dependence of the imaginary parts of the permittivity and dielectric modulus for the sample with $x = 0.25$ sintered at 800 °C. It can be seen that the frequency of the M'' maximum is shifted to higher values in

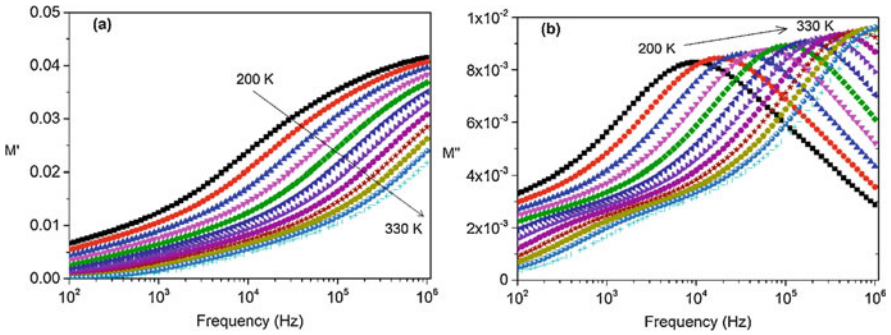

Fig. 9.8 (**a**) Real part of the complex modulus M'; (**b**) imaginary part of the complex modulus M'' for the sample with $x = 0.25$ treated at 650 °C

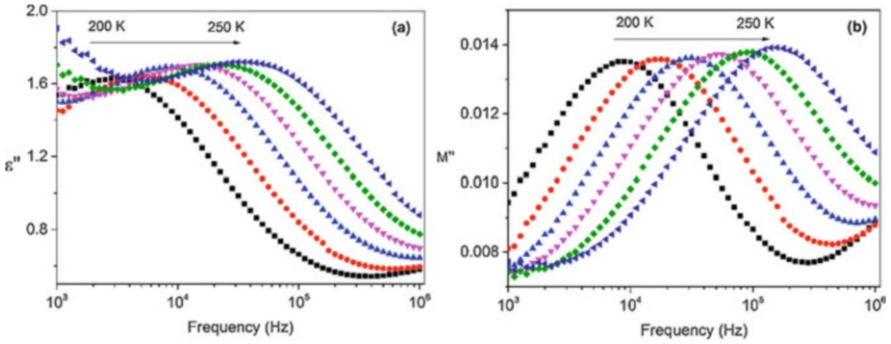

Fig. 9.9 (**a**) Imaginary part of the permittivity and (**b**) imaginary part of the modulus for the sample with $x = 0.25$ treated at 800 °C

comparison with the frequency of the ε'' maximum. This behavior was expected since $\tau_M < \tau_\varepsilon$, like it is predicted in the literature [23].

9.4 Conclusion

In this work, the structural, morphological and dielectric properties of $(Bi_{1-x}Fe_x)NbO_4$ powders sintered at different temperatures were investigated. The obtained results suggest that the addition of iron inhibits the formation of low temperature triclinic bismuth niobate and retards, or even inhibits the formation of the high temperature triclinic bismuth niobate. Also, the addition of iron leads to an increase of the ε' values and, despite the increase of the dielectric losses, the obtained values are still acceptable for electronic applications. The dielectric relaxation mechanisms were studied using the complex modulus formalism, with all iron-containing samples presenting at least one relaxation process in the frequency range studied.

References

1. Filho RC, Araújo JH, Ginani MF, D'Assunção AG Jr, Martins RA, D'Assunção AG, Mendonça LM (2010) Simulation and measurement of inset-fed microstrip patch antennas on $BiNbO_4$ substrates. Microw Opt Technol Lett 52:1034
2. Freire FNA, Santos MRP, Pereira FMM, Sohn RSTM, Almeida JS, Medeiros AML, Sancho EO, Costa MM, Sombra ASB (2009) Studies of the temperature coefficient of capacitance (TCC) of a new electroceramic composite: $Pb(Fe_{0.5}Nb_{0.5})O_3$ (PFN)–$Cr_{0.75}Fe_{1.25}O_3$(CRFO). J Mater Sci Mater Electron 20:149
3. Butee S, Kulkarni AR, Prakash O, Aiyar RPRC, Sudheendran K, Raju KCJ (2010) Effect of lanthanide ion substitution on RF and microwave dielectric properties of $BiNbO_4$ ceramics. J Alloys Compd 492:351
4. Savina AA, Atuchin VV, Solodovnikov SF, Solodovnikova ZA, Krylov AS, Maximovskiy EA, Molokeev MS, Oreshonkov AS, Pugachev AM, Khaikina EG (2015) Synthesis, structural and spectroscopic properties of acentric triple molybdate $Cs_2NaBi(MoO_4)_3$. J Solid State Chem 225:53
5. Rao KS, Buddhudu S (2010) Structural, Thermal and Dielectric Properties of $BiNbO_4$ Ceramic Powder. Ferroelectr Lett 37:101
6. Mohan R, Leonard N, Wieland L (2002) Applications of bismuth (III) compounds in organic synthesis. Tetrahedron 58:8373
7. Yang N, Sun H (2007) Biocoordination chemistry of bismuth: Recent advances. Coord Chem Rev 251:2354
8. Shihua D, Xi Y, Yu M, Puling L (2006) Microwave dielectric properties of $(Bi_{1-x}R_x)NbO_4$ ceramics (R=Ce, Nd, Dy, Er). J Eur Ceram Soc 26:2003
9. Litimein F, Khenata R, Gupta SK, Murtaza G, Reshak AH, Bouhemadou A, Omran SB, Yousaf M, Jha PK (2014) Structural, electronic, and optical properties of orthorhombic and triclinic $BiNbO_4$ determined via DFT calculations. J Mater Sci 49:7809
10. Radha R, Muthurajan H, Koteswara Rao N, Sivaram, Pradhan, Gupta UN, Jha RK, Mirji SA, Ravi V (2008) Low temperature synthesis and characterization of $BiNbO_4$ powders. Mater Charact 59:1083
11. Xu C, He D, Liu C, Wang H, Zhang L, Wang P, Yin S (2013) High pressure and high temperature study the phase transitions of $BiNbO_4$. Solid State Commun 156:21
12. Zhou D, Wang H, Yao X, Wei X, Xiang F, Pang L (2007) Phase transformation in $BiNbO_4$ ceramics. Appl Phys Lett 90:172910
13. Kagata H, Inoue T, Kato J, Kameyama I (1992) Low-fire bismuth-based dielectric ceramics for microwave use. Jpn J Appl Phys 31:3152
14. Devesa S, Graça MP, Costa LC (2018) Dielectric Properties of Bismuth Niobate Ceramics. In: Zhou Y, Dong F, Jin S (eds) Bismuth: advanced applications and defects characterization. IntechOpen, London, p 93
15. Alquier C, Vandenborre MT, Henry M (1986) Synthesis of niobium pentoxide gels. J Non-Cryst Solids 79:383
16. Almeida JS, Fernandes TS, Sales AJ, Silva MA, Júnior GF, Rodrigues HO, Sombra AS (2011) Study of the structural and dielectric properties of Bi_2O_3 and PbO addition on $BiNbO_4$ ceramic matrix for RF applications. J Mater Sci Mater Electron 22:978
17. Devesa S, Graça MP, Henry F, Costa LC (2016) Dielectric properties of $FeNbO_4$ ceramics prepared by the sol-gel method. Solid State Sci 61:44
18. Lee BW, Abothu IR, Raj PM, Yoon CK, Tummala RR (2006) Tailoring of temperature coefficient of capacitance (TCC) in nanocomposite capacitors. Scr Mater 54:1231
19. Czekaj D, Czekaj AL, Adamczyk M (2014) Influence of bismuth content on complex Immittance characteristics of Pressureless sintered $BiNbO_4$ ceramics. Arch Metall Mater 59:225
20. Belattar CBJ, Graça MPF, Costa LC, Achour ME (2010) Electric modulus-based analysis of the dielectric relaxation in carbon black loaded polymer composites. J Appl Phys 107:124111

21. Tsangaris NKGM, Psarras GC (1998) Electric modulus and interfacial polarization in composite polymeric systems. J Mater Sci 33:2027
22. Saltas V, Triantis D, Manios T, Vallianatos F (2007) Biomonitoring of environmental pollution using dielectric properties of tree leaves. Environ Monit Assess 133:69
23. Wojnarowska Z, Knapik J, Díaz M, Ortiz A, Ortiz I, Paluch M (2014) Conductivity Mechanism in Polymerized Imidazolium-Based Protic Ionic Liquid [HSO_3–BVIm][OTf]: Dielectric Relaxation Studies. Macromolecules 47:4056

Part IV
Thin Films

Chapter 10
Study of In_2O_3 Thin Films Doped with As as Active Layer in Position Sensitive Structures

Veselin Zhelev, Plamen Petkov, Georgi Avdeev, Vanya Lilova, and Tamara Petkova

Abstract Transparent and conductive thin films of As-doped In_2O_3 have been deposited on glass and silicon substrates by spray pyrolysis technique using $InCl_3$ and $3As_2O_5.5H_2O$ as starting materials. The films obtained were characterized by X-ray diffraction, UV-VIS spectroscopy, scanning electron microscopy and atomic force microscopy. The effects of As concentration on the resistivity and optical transmission of the films have been investigated. The application of the films in position sensitive structures Si-SiO_2-In_2O_3 acting on the base of lateral photoeffect has been examined.

Keywords Thin films · Metal oxide layers · Spray pyrolysis · Position sensitive photodetector

10.1 Introduction

Transparent and conductive In_2O_3 thin films are suitable for various applications, such as transparent electrodes in solar cells, flat panel displays, heat reflecting mirrors, anodes for solar cell structures and elements in optoelectronic devices [1–7], due to their high optical transmission in the visible region, high reflection in the near-infrared region and good electrical conductivity. Transparent conducting metal oxide thin films can be prepared by different methods: reactive evaporation [8], DC

V. Zhelev · T. Petkova (✉)
Institute of Electrochemistry and Energy Systems, Bulgarian Academy of Science, Sofia, Bulgaria
e-mail: tpetkova@bas.bg

P. Petkov · V. Lilova
Department of Physics, University of Chemical Technology and Metallurgy, Sofia, Bulgaria

G. Avdeev
Institute of Physical Chemistry, Bulgarian Academy of Sciences, Sofia, Bulgaria

P. Petkov et al. (eds.), *Nanoscience and Nanotechnology in Security and Protection against CBRN Threats*, NATO Science for Peace and Security Series B: Physics and Biophysics, https://doi.org/10.1007/978-94-024-2018-0_10

and RF sputtering [9], pulsed laser ablation [10], chemical vapor deposition [11], and recently by sol-gel [12] and spray pyrolysis technique [13, 14]. A major advantage of the spray pyrolysis method is the simple and inexpensive experimental arrangement, high growth rate and capability of uniform large area coatings.

Pure stoichiometric In_2O_3 is n-type semiconductor with poor electrical conductivity. To obtain thin films with high conductivity and transparency it can be doped with donor impurities. In our recent paper [15] we have established that As-doped SnO_2 thin films deposited on monocrystalline silicon substrates are transparent and conductive making them suitable for preparation of large area position sensitive photodetectors acting on the base of lateral photoeffect [16, 17].

In the present study we focused on arsenic (As) as a dopant in In_2O_3 films. The information about films doped with As is very rare, covered mainly by chemical vapor deposition (CVD) method for preparation of the films [18]. The idea is that the substitution of In^{+3} with As^{+5} in the lattice of In_2O_3 films would affect the film behaviors. The aim of the work is to study how the As doping revises the physical properties (transmission, conductivity) of the films and to investigate the possibility to apply these coatings as an active layer in two dimensional position sensitive n-Si-SiO_2-In_2O_3 photodetectors acting on the base of lateral photoeffect.

10.2 Experimental Details

The In_2O_3 thin films were prepared using a conventional spray pyrolysis set-up consisting of a reactor, a nozzle giving droplets with very small size and good distribution, a heating substrate holder with electronic control of the substrate temperature and a system for control of the solution and carrier gas flow rates. The doped films were deposited on Corning glass or n-Si (111) (1.61 Ω.cm) substrates heated at 450 °C by spraying 0.25 M water-alcoholic solutions of $InCl_3$, containing As_2O_5 as a source of As dopant. The concentration of As_2O_5 in the solutions of $InCl_3$ was varied between 0.5 and 5 mol%.

The properties of the films are dependent on the technological parameters: substrate temperature, concentration of the ingredients in the solutions, distance between the nozzle and the substrate, spraying rate and angle of spraying. The parameters were varied in a wide range to achieve films with the lowest resistivity and the highest transparency in the visible and near infrared spectrum. UV-visible transmission spectra of the samples were measured in the wavelength range from 300 nm to 1400 nm at room temperature using a double-beam computer-controlled JASCO spectrophotometer with an accuracy of ±0.5 nm. The structure, morphology and microstructure of the films were examined by X-ray diffraction (XRD, Philips APD-15), by scanning electron microscopy (SEM, Philips 515, digitalized, with secondary electrons detector, acceleration voltage 30 kV, magnification 40,000×) and by atomic force microscopy (AFM, scanning probe microscope Multimode V, Bruker, ex Veeco Santa Barbara CA). The film thickness was measured by the gravimetric method and from the cross-section SEM images. The measurements of

the electrical resistivity were carried out by the standard four-probe method, using silver paste as electrical contact to the films.

10.3 Results and Discussion

When the aerosol of the solution reaches the heated substrate two processes take place on the surface: hydrolysis (1) and pyrolysis (2):

$$InCl_3 + 3H_2O = In(OH)_3 + 3HCl \quad (10.1)$$

$$2In(OH)_3 = In_2O_3 + 3H_2O \quad (10.2)$$

The estimated optimal technological conditions were as follows: substrate temperature 450 °C, concentration of In_2O_3 0.25 M, concentration of As_2O_5 in the solution 0.5–5 mol% and flow rate 6–8 ml/min. These conditions allowed the deposition of uniform, highly adherent and homogeneous films over the entire surface (Si wafer with diameter of 76.2 mm and glass plates 40 × 40 mm), with film thickness in the range 90–300 nm.

The sheet resistance of the films decreases with the concentration of As_2O_5 in the spray solution till certain amount and increases after that (Fig. 10.1).

The trend in the resistivity can be explained as follows: at low arsenic concentration (< 5 mol% As_2O_5) the As^{5+} ions can substitute indium (In^{3+}) ions in the In_2O_3 lattice leading to generation of additional electrons responsible for the sheet resistance decrease. At higher concentrations as the arsenic ion radius is larger than that of indium the doping produces electrical and structural defects, creating traps in the band gap of In_2O_3, hindering consequently the conductivity. When the concentration of As in the solution increases, the number of defects arises and As atoms act as traps

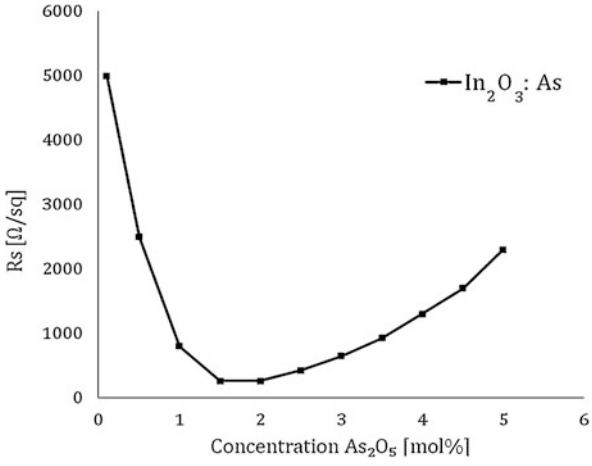

Fig. 10.1 Dependence of the sheet resistance on the molar concentration of As_2O_5 in the solution

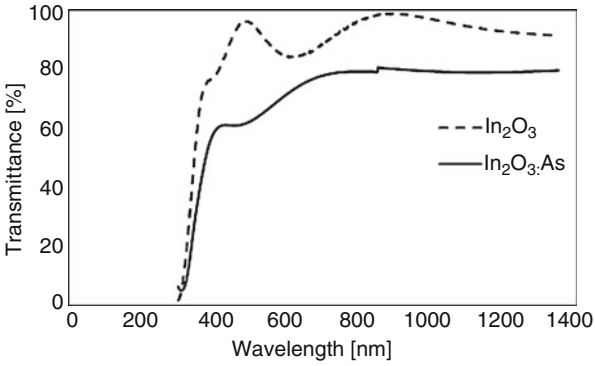

Fig. 10.2 Optical transmittance of undoped and doped (1.5 mol% As_2O_5) films of In_2O_3

rather than donors. The lowest resistance of about 70 Ω/sq. is obtained for the film deposited from a solution with 1.5 mol% As_2O_5. Therefore, this film composition is used in our further study.

Figure 10.2 presents optical transmittance spectra of undoped and doped In_2O_3 films recorded in the spectral range 300–1400 nm.

The undoped film of In_2O_3 shows high transparency (>90%) in the visible and near infrared range of the spectra; however, this film possesses very high resistivity. The doping with As decreases considerably the permeability of the film in the visible spectrum. In the near infrared region of the spectrum the transparency reaches values of 80%.

The optical absorption coefficient α and the optical band gap of the In_2O_3 films E_g are determined from the transmission spectra by the relations:

$$\alpha = -\ln(T)/t \tag{10.3}$$

$$\alpha h\nu = A\left(h\nu - E_g\right)^{1/2} \tag{10.4}$$

where α is the optical absorption coefficient, T – the transmission, t – the thickness of the film, A is a constant, (hν) – the photon energy and Eg – the optical band gap.

Figure 10.3 shows the plot of $(\alpha h\nu)^2 = f(h\nu)$ for pure and doped with In_2O_3 As films. The value of the optical band gap obtained by extrapolation of the linear part of the curve to zero absorption value ($\alpha = 0$) is 3.6 eV for the doped and 3.8 eV for pure In_2O_3. The smaller band gap is attributed to the creation of levels in the band gap due to the doping.

The XRD spectrum of doped In_2O_3 thin film deposited on silicon substrates shown on Fig. 10.4 reveals that the film is polycrystalline. All diffraction peaks belong to In_2O_3 cubic structure (JCPDS 41–1445). The diffraction peaks at 21.5, 30.5, 35.5, 50.9 and 60.8 match with the diffraction lines due to the (211), (222), (400), (440) and (622) planes of the In_2O_3 cubic phase.

The SEM image of the In_2O_3 thin film deposited at 450 °C and doped with 1.5 mol% As_2O_5 in the solution reveals a smooth and homogeneous surface

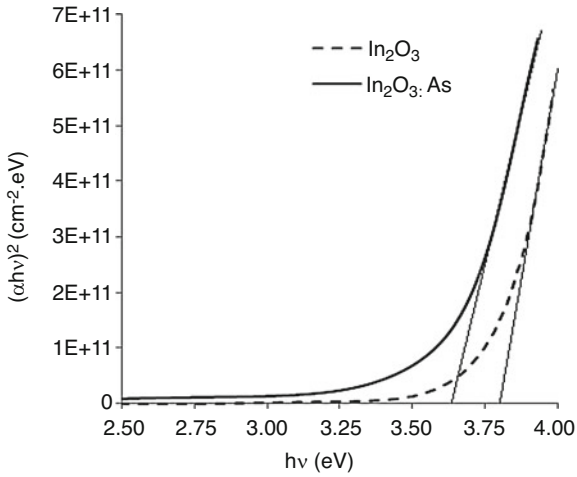

Fig. 10.3 Plot of $(\alpha h\nu)^2 = f(h\nu)$ for undoped and doped (1.5 mol% As_2O_5) films of In_2O_3

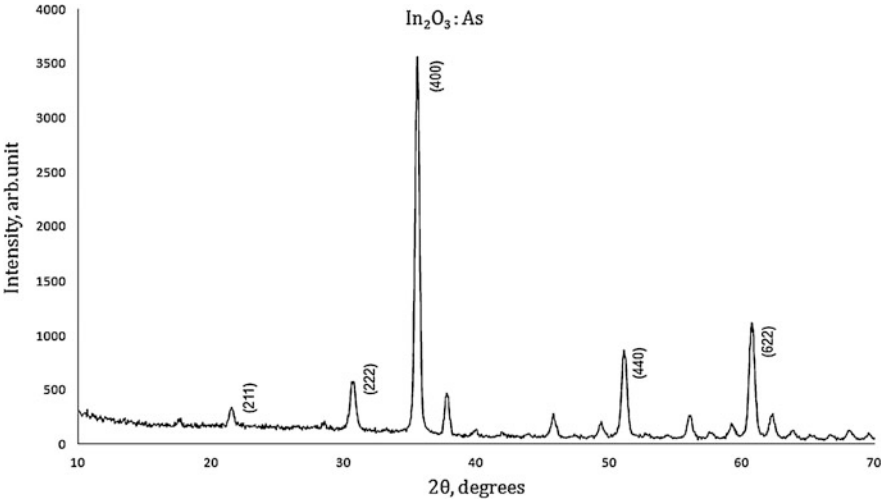

Fig. 10.4 XRD spectrum of In_2O_3 thin film doped with 1.5 mol% As_2O_5

morphology. The nanocrystalline particles are identical in size and shape and are densely packed in a uniform structure (Fig. 10.5).

The microstructure and surface roughness of the films were examined by atomic force microscopy (two dimensional and 3D topographic views) as shown in Fig. 10.6. They revealed granular uniform microstructure with average size of the particles about 50–70 nm, determined from the AFM from 1 μm^2 film area.

The results from the microscopic study demonstrate that the films prepared by spray pyrolysis are smooth and uniform which is an important prerequisite for their practical application. The optical and electrical behaviors of In_2O_3 film deposited at 450 °C from a solution with 1.5 mol% As_2O_5 are appropriate to explore the film as

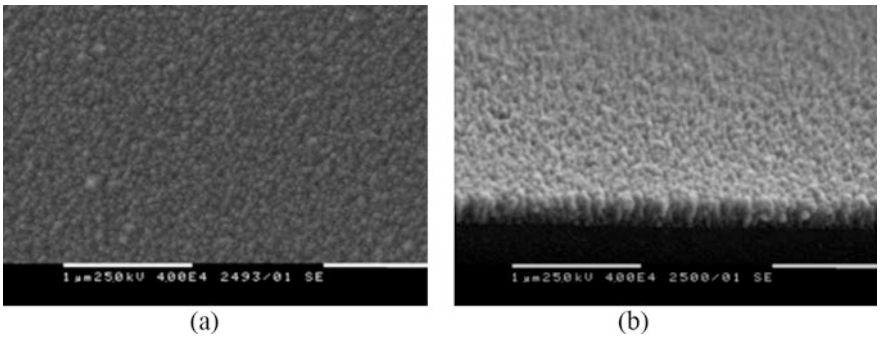

Fig. 10.5 SEM micrographs of As-doped In_2O_3 with 1.5 mol% As_2O_5 and thickness of 210 nm: (**a**) surface morphology and (**b**) cross-section at 45° tilt

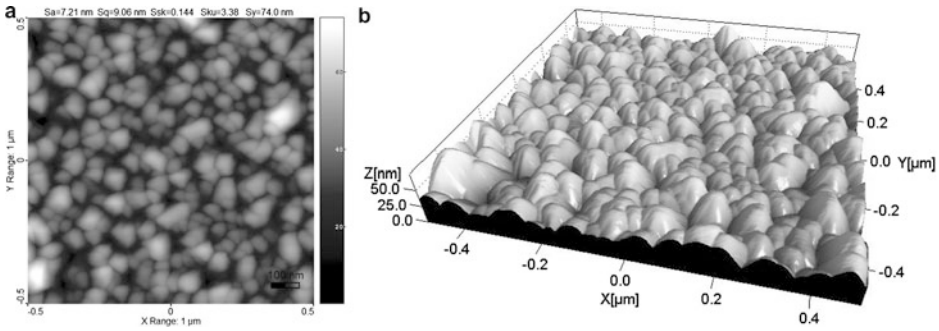

Fig. 10.6 Two dimensional (**a**) and 3D (**b**) topographic views of As-doped In_2O_3 film deposited at 450 °C and 1.5 mol% As_2O_5 in the solution

an active layer in position sensitive structures. The lateral photoeffect is examined over two dimensional position sensitive structure Si-SiO_2-In_2O_3:As. The samples were cut into rectangles and silver (Ag) was used as contact metal. The distance between the contacts was 5–7 mm. The samples are scanned by laser with 5 mW power and 532 nm wavelength. The diameter of the spot focused on the surface of the metal oxide was 100 µm. The induced lateral photovoltage (LPV) as a function of the laser beam position is shown in Fig. 10.7.

A symmetric curve for the In_2O_3 film with 1.5 mol% As_2O_5 deposited on silicon substrates is obtained for film thickness of 210 nm. The LPV sensitivity is about 17 mV/mm. The good linearity of the curve demonstrates the uniformity of the metal oxide films and the opportunity of practical application.

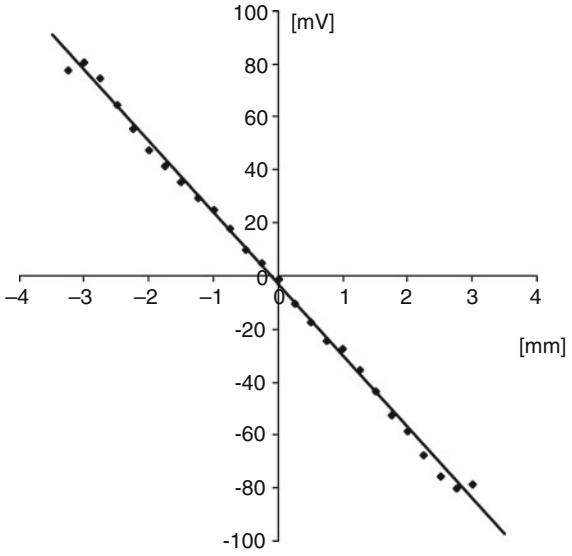

Fig. 10.7 LPV as a function of the laser beam position on the As-doped In_2O_3 films

10.4 Conclusions

Thin film Si-SiO_2-In_2O_3:As structures have been prepared by spray pyrolysis technique. The films were doped with As included into the spray solution as 0.25 M As_2O_5. The doping with As significantly reduces the sheet resistance of the layers but adversely affects their optical transmission in the visible region of the spectrum. High optical transmission (about 80%) is observed in the near infrared region demonstrating that these thin films could be used in position sensitive structures acting on the base of lateral photoeffect.

References

1. Elangovan E, Ramamurthi K (2003) Optoelectronic properties of spray deposited SnO_2:F thin films for window materials in solar cells. J Optoelectr Adv Mater 5(1):45–54
2. Mustapha N, Hennashe A, Fekkai Z (2014) Deposition of conducting oxide thin films as anode for solar cell device. Br J Appl Sci Technol 4(5):739–748
3. Calnan S, Tiwari AN (2010) High mobility transparent conducting oxides for thin film solar cells. Thin Solid Films 518:1839–1849
4. Fortunato E, Ginley D, Hosono H, Paine D (2007) Transparent conducting oxides for photovoltaics. MRS Bull 32:242–247
5. Fekkai Z (2014) Deposition of conducting oxide thin films as anode for solar cell device. Br J Appl Sci Technol 4:739–748
6. Hosono H, Paine DC (2010) Handbook of transparent conductors. Springer, Heidelberg/Dordrecht/London
7. Frank G, Kauer E, Kostlin H, Schmitte FJ (1983) Transparent heat-reflecting coatings for solar applications based on highly doped tin oxide and indium oxide. Sol Energy Mater 8:387–398

8. Thilakan P, Kalainathan S, Kumar J, Ramasamy P (1995) Deposition and characterization of indium oxide and indium tin oxide semiconducting thin films by reactive thermal deposition technique. J Electron Mater 24(6):719–724
9. Kurdesau F, Khripunov G, da Cunha AF, Kaelin M, Tiwari AN (2006) Comparative study of ITO layers deposited by DC and RF magnetron sputtering at room temperature. J Non-Crystall Solid 352:9–20
10. Preiss EM, Rogge T, Krauss A, Seidel H (2015) Gas sensing by SnO_2 thin films prepared by large-area pulsed laser deposition. Proc Eng 120:88–91
11. Olopade MA, Awe OE, Awobode AM, Alu N (2012) Characterization of SnO_2:F films deposited by atmospheric pressure chemical vapor deposition for optimum performance solar cells. Afr Rev Phys 7:177–180
12. Lee S-Y, Park B-O (2005) Electrical and optical properties of In_2O_3-ZnO thin films prepared by sol-gel method. Thin Solid Films 484:184–187
13. Thanachayanont C, Yordsri V, Boothroyd C (2011) Microstructural investigation and SnO nanodefects in spray-pyrolyzed SnO_2 thin films. Mater Lett 65:2610–2613
14. Udayakumar R, Kahanaa V, Saravanan T (2013) Synthesis and structural characterization of thin films of SnO2 prepared by spray pyrolysis technique. Int J Adv Res 1:666–669
15. Zhelev V, Petkov P, Shindov P, Bineva I, Vasilev S, Ilcheva V, Petkova T (2018) As-doped SnO_2 thin films for use as large area position sensitive Photodetector. Thin Solid Films 653:19–23
16. Wallmark JT (1957) A new semiconductor photocell using lateral photoeffect. Proc IRE 45 (4):474–483
17. Jing L, Wang H (2011) Large lateral photovoltaic effect observed in nano Al-doped ZnO films. Opt Express 19(15):13806–13807
18. Hsu YS, Chandhi SK (1979) The preparation and properties of arsenic – doped thin oxide films. J Electrochem Soc 126(8):1434–1435

Chapter 11
Design of Mesoscopic Ordered Titania and Silica Hybrid Sol-Gel Films as Planar Waveguide

Yevhen Leonenko, German Telbiz, Vasil Yashchuk, Taras Kavetskyy, Nickolay Kukhtarev, and Anatoliy Glushchenko

Abstract We report of the successful design of waveguide based on formed on a glass substrate mesoscopic ordered organic-inorganic SiO_2 and TiO_2 films doped with Rhodamine 6G formed on a glass substrate that allowed mode lasing. The designed films had a refractive index lower (1.499) and higher (1.565) than the index of the glass substrate. The laser oscillation was observed on the quasi modes of the waveguide which possess radiative losses in a substrate and was accompanied by radiation of substrate radiative mode.

Keywords Mesoscopic · Sol-gel · Hybrid films · Titania and silica · Planar waveguide

Y. Leonenko (✉) · G. Telbiz
L.V. Pisarzhevsky Institute of Physical Chemistry, National Academy of Sciences of Ukraine, Kyiv, Ukraine

V. Yashchuk
Physics Department, Kyiv Taras Shevchenko National University, Kyiv, Ukraine

T. Kavetskyy
Drohobych Ivan Franko State Pedagogical University, Drohobych, Ukraine

The John Paul II Catholic University of Lublin, Lublin, Poland

Joint Ukraine-Azerbaijan International Research and Education Center of Nanobiotechnology and Functional Nanosystems, Drohobych, Ukraine

N. Kukhtarev
University of Colorado at Colorado Spring, Colorado Spring, CO, USA

A. Glushchenko
Alabama A&M University, Normal, AL, USA

P. Petkov et al. (eds.), *Nanoscience and Nanotechnology in Security and Protection against CBRN Threats*, NATO Science for Peace and Security Series B: Physics and Biophysics, https://doi.org/10.1007/978-94-024-2018-0_11

11.1 Introduction

Recently, there has been growing interest in optically transparent film materials with embedded luminescent dyes, which are promising for recording and processing information, for solar concentrators and especially as laser optics materials, and which represent a new class of solid-state active media for waveguide (WG) lasers [1–4]. The advantages of solid state laser active media over dye solutions in liquid systems can significantly expand the field of the practical applications of dye lasers that have the ability to tune the radiation frequency and have found a practical application for laser separation of isotopes, in spectroscopy, forensics, medicine, etc. At the same time, solid state hybrids are significantly superior to polymer analogs and crystals in laser strength and stability under the influence of powerful optical radiation (laser pumping). Therefore, the realization of all the possibilities for application of dye lasers in solid-state matrices is associated with an improvement of the characteristics of the hybrid films, and primarily, of their photochemical stability. With a selected laser dye, the efficiency of laser-active media is determined by the chemical structure and composition of the solid-state matrix. Major advances of integrated optoelectronics now are related to preparation of light sources with submicron dimensions. Most appropriative for this purpose are waveguide (WG) lasers which confine lasing emission in the host medium resulting in increased optical gain and decreased lasing threshold. These lasers may be easily assembled on the same chip with other optoelectronic devices such as transmission lines, modulators, filters, etc. The organic/inorganic hybrid films prepared by the sol-gel approach have become a new field of research in materials for WG laser [4]. This method allows the deposition of a film of some hundreds of nanometers thickness as a result of self-organization and allows managing independently the two most important parameters of planar WG laser: gain value and the refractive index of the matrix material. In the formed hybrid film, the inorganic component determines the refractive index and the dye incorporated in micelles specifies the value and contour of the gain. In this way, the film will act as a waveguide, if its refractive index is higher than that of the substrate. Therefore, one should use high refractive dielectric materials such as dioxides of titanium or zirconium. The hybrid film may be significantly thinner than the other ones because the dye cross-section is four orders higher. Fabrication of ultra-thin WG laser based on hybrid films requires to solve two principal problems. The first one is ensuring of high concentration of dye molecules, without concentration quenching of luminescence, in order to provide sufficient absorbance of the pumping radiation in thin and hence the gain. The second one is to provide a higher refractive index of the film relative to the substrate to ensure waveguide conditions at film/substrate interface. These problems have been solved by the fabrication of hybrid organic-inorganic mesostructured films doped with Rhodamine 6G (Rh6G) by sol-gel approach using triblock copolymer Pluronic P123 and tetraethoxysilane or tetra isopropoxide as a precursor of the inorganic matrix. The sol solution was deposited on a glass substrate by

spin-coating technique. The common details of preparation of the films are described previously in papers [5–7].

11.2 Experimental

The films formatted on the substrate by spin coating procedure represent a mesoscopic ordered inorganic matrix of silicon or titanium dioxide with oriented channels with a diameter of 12 nm filled with hybrid micelles surfactant (P123) containing Rh6G molecules [5]. The mean thickness of the films was 200–300 nm and the value of the refractive index varied in the range of 1.499–1.68, depending on the type of the inorganic precursor and the conditions of formation. For laser experiments, we have chosen the films with refractive indexes $n_{f1} = 1.499$ (SiO_2 film) and $n_{f2} = 1.565$ (TiO_2 film). The concentration of Rh6G in films was 1 mmol/l. The problem of luminescence quenching in the hybrid was thus overcome by elaborated methods of confining of Rh6G in P123 micelles situated in the channels of the matrix pores that prevent planar packing of the dye molecules in H-type dimers [8]. The fabricated films on the glass substrate together with air as cover material form asymmetric waveguides having the order of interlacing layers with refractive indices of $1/n_f/n_s$, where $n_f = 1.499$ (1.565) is the refractive index of the SiO_2 (TiO_2) films and $n_s = 1.515$ the refractive index of the glass substrate.

Lasing of the films was excited by the second-harmonic radiation of a Q-switched YAG-Nd^{3+} laser (wavelength of 532 nm, pulse duration of 12 ns). The pumping radiation was focused on the film plane in the strip with two cylindrical lenses. The intensity was varied with grey glass filters. Spatial distribution of the emitted radiation was observed on a screen spaced 80 mm from edge of the film. The spectra of this radiation were single-shot registered by a spectrograph and a CCD camera with a total spectral resolution of 0.3 nm.

11.3 Results and Discussion

The emitted radiation of the hybrid films was visualized on a screen as two hyperbolic-like bright arcs. They are formed by the radiation emitted from the film edge which propagates under angle of 26°. The intensity of the arcs depends non-linearly on the pumping intensity; they become visible only when its value overcomes 0.04 MW/mm^2. In this case, the main power is concentrated in the last arc, as the brightness of the radiation spectrum in 26° direction is much higher than in the other directions. Considering the substantial difference of the divergence, we can assume that these components are emitted from different parts of the sample edge. The first component should be attributed to radiation just from the film edge which strongly diverged due to diffraction on small (200 nm) aperture of this edge. The other one may be related to radiation from the edge of the glass substrate which

diffraction must be much less because of the greater aperture (h = 1.1 mm) of the edge. The radiation power of the substrate is significantly higher than that emerging from the film. Considering that the condition of total internal reflection (TIR) on the film-substrate interface is not fulfillment ($n_f < n_s$) one should consider the second arc as the radiative substrate mode of the WG formed by the SiO_2 film on the glass. So, the radiation coming out from the film edge may be attributed to a waveguide mode which takes place due to partial reflection at this interface as a result of the indexes difference. It is not a true waveguide mode but may be called conditionally quasi WG mode – a waveguide mode with energy loss owing to the radiative mode coming out of the substrate. This quasi mode is able to survive only due to light amplification in the WG core (film) that compensates its radiative loss and therefore may arise only under high intensity of pumping.

In the case of SiO_2 film two radiations may really arise: quasi WG mode and radiative mode of the substrate. These radiations have equal angles of incidence, which we evaluated. For the main mode, m = 0 the evaluated angle of propagation outer the SiO_2 film with taking into account refraction on the film-substrate interface is about 28° which is rather close to experimentally observed angle of 26°. The spectrum components of the radiation show quite different behavior. The spectrum of the first component (Fig. 11.1a) narrows sharply from 31 nm to 4.5 nm width under pumping intensity above 0.04 MW/mm^2. This spectrum contains a narrow lasing component of 4.5 nm FWHM and a component of amplified spontaneous emission (ASE) of 16 nm FWHM which disappears under higher pumping. The spectrum of the second component narrows much less in the same pumping range (Fig. 11.1b) from 32 to 23 nm. The different spectral behavior of these components is caused by their different origin. The sharp spectral narrowing of the first component appears since the radiation of the quasi WG mode is confined in the film, where the optical gain is high and therefore, it may develop as lasing. The radiation of the second component spreads over the substrate, where there is no gain and therefore the effective gain of it is much less. As a result, this radiation develops as ASE.

One should note that this radiation consists of many parallel plane waves coming out from the film to the substrate and undergoes TIR (Fig. 11.1b). The radiative mode of the substrate which appears under lasing onset in the film may be called Lummer-Gehrke mode [4]. Thus, the present radiation mode of the substrate is not just a part of the radiation that is lost by the quasi WG mode, but it is created as a result of interference. These modes are situated in the common area (hybrid film) of their propagation but they may take place independently. The lasing quasi mode can develop independently of the radiative mode of the substrate owing to amplification in the core of WG. The radiative mode of the substrate exists alone but under lasing the WG core originates from ASE.

Figure 11.2 shows the spectra of radiation from the film edge (quasi WG mode) depending on the direction of propagation relative to the track. In this case, the spectrum of radiation from track edge is independent of the angle of propagation at least in the range ±26°, where this radiation does not overlap with a lateral beam of the radiative mode of the substrate. This property fits well with the strong diffraction divergence of the radiation of the quasi WG mode on the small-size aperture of the

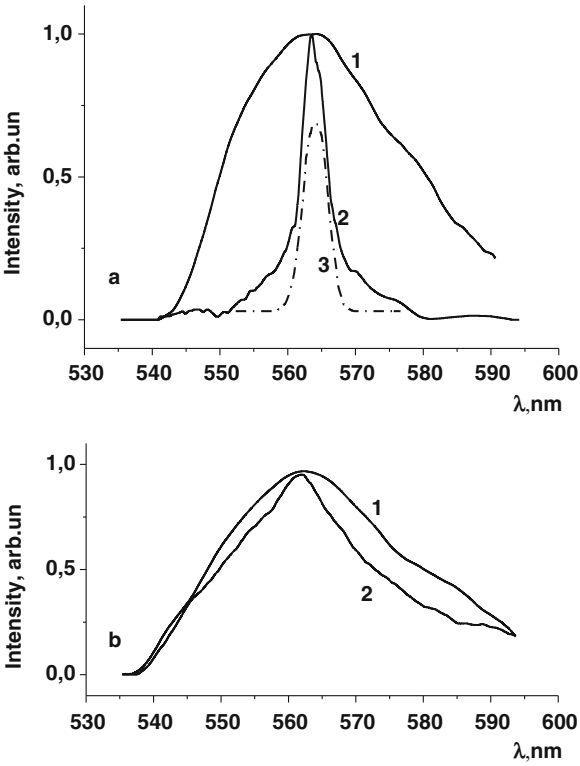

Fig. 11.1 Emission spectra of the radiation from the track edge in the SiO_2 film (**a**) and of the lateral beam at 26° to this track (**b**) under pumping intensity Ip = 0.03 (1) and 0.3 (2) MW/mm^2; 3 – lasing component of the emission from the track edge

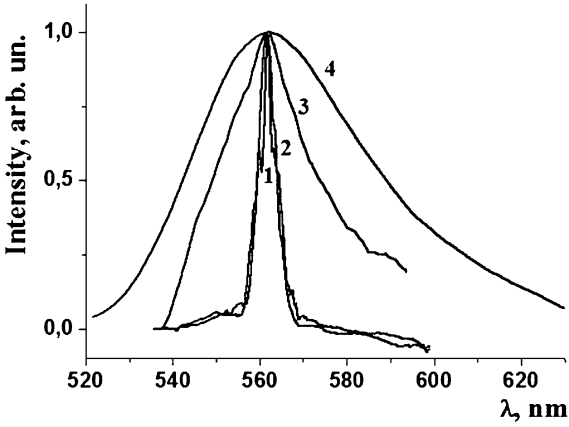

Fig. 11.2 Spectra of the lasing component of the emission propagated at 0° (*1*) and 12° (*2*) to the track under pumping (Ip = 0.3 MW/mm^2); *3* – emission spectrum of lateral emission at 26° to the track under 0.3 MW/mm^2 pumping; *4* – luminescence spectrum of Rh6G in SiO_2 film

film edge. The latter can be considered as an important proof of the occurrence of this radiation. Its lasing nature was apparent from the comparison of the spectra with a luminescence spectrum of Rh6G confined in the film. The FWHM (4.5 nm) of the radiation is about one order narrower than the FWHM of the luminescence (46.5 nm) and as noted above, this narrowing is more sharply. In TiO_2 film with refractive index n = 1.565, the necessary condition for TIR is available. The thickness of the film of 200 nm is smaller than the cut-off thickness of the lowest mode m = 0 (300 nm). Therefore, in this film true WG modes cannot exist. For their existence the refractive index of the film or its thickness must be higher. However, lasing radiation in this film arises as well. Moreover, in this film lasing arose under pumping with intensity of one order less and its radiation brightness was nearly one order higher. The radiation spectrum had the same width with FWHM of 5 nm.

According to the above mentioned conception, the lower threshold of lasing and the higher brightness of emitted radiation from TiO_2 film in comparison with the SiO_2 film can be as a result of physicochemical design explained by higher reflectivity on the film-substrate interface conditioned by the higher refractive index of the first one. Therefore, it should be expected that the formation of the TiO_2 film of higher refractive index and the optimal thickness will provide lasing in a true WG mode in which all emitted radiation will be confined in the WG core. This can be a starting point for further decrease of the threshold and increase of radiation brightness.

11.4 Conclusion

The possibility of lasing from Rhodamine 6G confined in smart designed mesostructured hybrid sol-gel film waveguides has been shown. It was established that lasing true waveguide mode in SiO_2 and TiO_2 films with refractive indexes lower (1.499) or higher (1.565) than the index of the glass substrate under these conditions cannot be implemented because of low refractive index or high cut-off thickness. The lasing in these films arises in quasi waveguide modes due to radiative losses in the substrate. Lasing radiations emerge from the film edge and are high diverged due to diffraction. This lasing is accompanied by substrate radiative mode which forms a low diverge lateral beam at direction about 26° related to the film plane. Lasing in the film with higher refractive index has by order lower threshold accompanied by an increase of the radiation brightness.

References

1. Innocenzi P, Malfatti L (2009) Mesoporous thin films: properties and applications. Chem Soc Rev 42:4198–4216
2. Guyvel X, Schutzmann S, Stella L, Matteis F (2008) Effect of titania content on the optical properties of dye-doped hybrid sol-gel coatings. Opt Mater 31:451–454

3. Tikhonov E, Telbiz G (2011) Spectroscopic manifestation of dye pair interactions at high concentrations in structurally organized SiO_2 films. Mol Cryst Liq Cryst 535:82–90
4. Tikhonov E, Telbiz G, Yashchuk V (2018) Planar waveguide nanolaser configured by dye-doped hybrid nanofilm on substrate. Laser Phys 28(045801):1–6
5. Telbiz G, Leonenko E, Dvoynenko M (2017) Optical properties of Rh6G molecules ordering in the sil-ica- and titanium dioxide mesoscopic sol-gel films. Mol Cryst Liq Cryst 642:74–80
6. Kazakevičius A, Peckus D, Boiko O, Valkunas L, Leonenko E, Telbiz G, Gulbinas V (2015) Insights into the mechanism of enhanced rhodamine 6G dimer fluorescence in mesoscopic pluronic-silica matrixes. J Phys Chem C 119:19126–19133
7. Telbiz G, Leonenko E, Gulbinas V, Manoryk P (2018) Nanocomposites for optoelectronic devices manufactured by the sol-gel method. In: Advanced nanotechnologies for detection and defense against CBRN agents. Springer, Dordrecht, pp 37–42
8. Kasha M, Rawls H, El-Bayoumi A (1965) The exciton model in molecular spectroscopy. Pure Appl Chem 11:371–392

Part V
Carbon-Based Materials

Chapter 12
CVD Diamond and Nanodiamond: Versatile Materials for Countering a Wide Range of CBRN Threats

Paul W. May

Abstract Fabrication of thin films of diamond by chemical vapour deposition (CVD) has now developed into a mature technology, with high-quality diamond readily available from multiple vendors at relatively low cost. As such, scientists and engineers now have access to the wide range of outstanding mechanical, thermal, optical and electronic properties that diamond has to offer. In this review, we shall discuss a range of applications in which CVD diamond films and nanodiamond particles can help to reduce, remove or mitigate the threats from chemical, biological, radiological and nuclear (CBRN) incidents or attacks. Some of these applications are commercially available today, others may require further research or modification of existing diamond-based devices for the unusual requirements of CBRN events, while others are currently only ideas which have yet to be developed.

Keywords Diamond · Nanodiamond · CBRN threats · Water purification · Chemical reagent detection and analysis · Antimicrobial surfaces · Bioimplants · Radiation detectors · Radiation dosimeters · Radiation-hard electronics · Targeted 'magic bullet' treatments · Telecommunications · Reliable power supplies · Nuclear batteries

12.1 Introduction

Diamond has a unique set of extreme properties (Table 12.1) that make it useful for a wide range of thermal, electronic, optical and mechanical applications [1]. However, for much of recent history, diamond was available only in the form of single-crystal natural stones which limited its use to expensive jewellery. The situation began to change in the 1950s, when the high-pressure high-temperature (HPHT) method of synthesising diamond in a laboratory was developed and commercialised by the

P. W. May (✉)
School of Chemistry, University of Bristol, Bristol, UK
e-mail: Paul.May@bristol.ac.uk

P. Petkov et al. (eds.), *Nanoscience and Nanotechnology in Security and Protection against CBRN Threats*, NATO Science for Peace and Security Series B: Physics and Biophysics, https://doi.org/10.1007/978-94-024-2018-0_12

Table 12.1 A selection of some of the outstanding properties of diamond

Extreme mechanical hardness (~90 GPa) and wear resistance
Highest bulk modulus (1.2×10^{12} N m^{-2})
Lowest compressibility (8.3×10^{-13} m^2 N^{-1})
Highest room temperature thermal conductivity (2×10^3 W m^{-1} K^{-1})
Very low thermal expansion coefficient at room temperature (1×10^{-6} K^{-1})
Optical transparency from the deep ultraviolet to the far infrared
Highest sound propagation velocity (17.5 km s^{-1})
Very good electrical insulator (room temperature resistivity is ~10^{13} Ω cm)
Doped diamond is a semiconductor with a wide bad gap of 5.4 eV
Very resistant to chemical corrosion
Biologically compatible
Some surfaces exhibit very low or 'negative' electron affinity
The NV centre defect acts as a single-photon source

General Electric Company. This HPHT process originally produced mm-sized stones which were yellowy-brown in colour due to unwanted nitrogen incorporation, making them unsuitable for gemstones. The ready availability and low cost of these so-called 'industrial diamonds' led to a number of applications that exploited diamond's hardness, such as drilling, sawing or milling, and prompted the beginning of a multi-million-dollar industry which continues to this day [2]. Since ~2015, advances in the HPHT process have allowed colourless gemstone-quality HPHT diamonds to be manufactured which are now good enough for the jewellery market. However, HPHT diamond is only produced in the form of stones or particles, meaning that a large contingent of diamond's exceptional properties still cannot be exploited.

This problem was finally solved with the advent of diamond grown by chemical vapour deposition (CVD) in the 1980s, because this method produces diamond in the form of a thin coating or layer conformally attached to a surface (or as a freestanding diamond plate if removed from the substrate) [3]. Diamond coatings such as these allow almost all of the superlative properties of diamond to be accessed, and as a result, the number of applications for CVD diamond has increased hugely over the past few years. Advances in deposition technology, driven by the burgeoning market in CVD diamond gemstones [4], have allowed thicker diamond films to be deposited at faster rates, and therefore more cheaply. Another factor has been the large increase in the number of companies producing lab-grown diamond (both for gems and as coatings), increasing the availability and supply of diamond material. Nowadays, the previous commonly held perception that diamond is a rare and expensive product only useful for gems or niche applications is rapidly being dispelled, and finally diamond is becoming regarded as a truly useful, affordable, engineering material.

12.2 The CVD Process

In the CVD process [3], a diamond coating is deposited onto the surface of a suitable substrate, such as a smaller diamond seed in the case of gemstone growth, a Si wafer for electronics, a quartz window for optics, or an engine component for mechanical-wear applications. The substrate is placed onto a heated stage inside a vacuum chamber. The substrate is heated to 700–1000 °C while process gases (a carbon source such as methane diluted to just a few percent input mole fraction in hydrogen) are passed over the substrate at a pressure of 20–200 torr. The gases are typically energised using either a heated metal (W, Ta, or Re) filament placed a few mm above the substrate surface, or by application of a microwave discharge in the form of a stable 'plasma ball' which sits above the substrate surface. In either case, the thermal or electrical energy deposited into the process gases causes the molecules to fragment and form a chemical 'soup' of atoms, radicals, ions and clusters near to the substrate surface. Reactive species (mainly H atoms and CH_3 radicals) from this hot gas mixture diffuse to the surface, and if the conditions are optimal, they deposit onto the surface as a continuous layer of diamond [5]. The diamond coating can remain on the surface after growth and be utilised *in situ*, or the substrate can be removed by a suitable etch process (e.g. conc. nitric acid to dissolve a Si wafer) to create a freestanding diamond 'wafer'.

12.3 Types of CVD Diamond

If diamond is grown homoepitaxially [6] onto an existing HPHT or natural diamond seed crystal, then the enlarged single-crystal diamond (SCD) that results can either be cut and polished into a gemstone (which is the basis for the flourishing CVD diamond gemstone market [4]) or laser cut into flat SCD substrates usually a few mm in size, suitable for advanced applications.

In contrast, heteroepitaxial diamond growth on a non-diamond substrate begins from numerous individual, isolated nucleation sites, e.g. from micro- or nanodiamond seed crystals scattered on the surface, or surface defects such as scratches, impurities or dislocations [7]. The individual diamond nuclei grow and fuse with their immediate neighbours to form a coalesced (or closed) two-dimensional film that then continues to grow normal to the surface. The resulting material will usually be polycrystalline, composed of almost pure diamond crystallites (or grains) joined together by grain boundaries that contain varying amounts of impurities and non-diamond carbon. By choosing the appropriate process conditions [8], the morphology and the average crystallite size can be tuned [9], as shown in Fig. 12.1. Diamond films are usually grouped into categories depending upon their crystallite size and morphology.

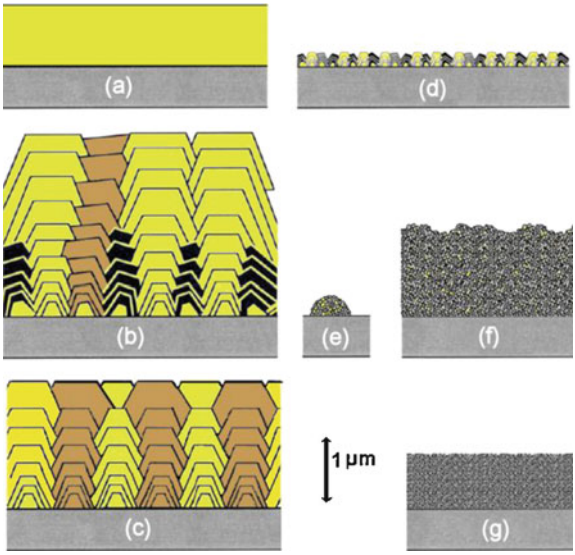

Fig. 12.1 Schematic representation of various forms of diamond film growth. (**a**) SCD film grown epitaxially on a SCD substrate. (**b**) MCD columnar growth from randomly sited nuclei, where the slowest growth face determines the overall film texture, in this case (100). (**c**) Highly oriented 'textured' MCD obtained following special nucleation procedures. (**d**) Faceted NCD, which is really just thin MCD with high nucleation density. (**e**) Cauliflower NCD before it has coalesced into a continuous film. (**f**) Cauliflower NCD film. (**g**) UNCD

- Microcrystalline diamond (MCD) films [3] exhibit faceted crystallites of size 0.5 µm to a few 100 µm, with a columnar growth structure that produces anisotropic properties which vary with film thickness.
- Nanocrystalline diamond (NCD) films [10] contain more rounded crystallites (sometimes referred to as 'cauliflower' diamond) ranging in size from ~10–100 nm.
- Ultrananocrystalline diamond (UNCD) films [11, 12] have crystallite sizes <10 nm embedded in a sp^2 carbon matrix, and although their properties are somewhat degraded compared to MCD and NCD, they have the advantage of being smooth on the nm scale.

12.4 Doping

Undoped CVD diamond of any grain size is highly electrically insulating. However, doping by incorporation of a suitable impurity atom, can increase the conductivity of the film in a controllable manner. The dopant atoms are usually added to the input gas mixture in gaseous form, e.g. B_2H_6 for boron, NH_3 or N_2 for nitrogen and PH_3 for phosphorus. Adding boron into diamond at low-to-medium concentrations creates a p-type semiconductor [13], while at high concentrations ($>1 \times 10^{20}$ cm^{-3}) the conductivity becomes near-metallic, and even superconducting at temperatures <10 K [14]. B-doped diamond (BDD) can, therefore, be used in a variety of simple electronic devices, sensors, and especially as

electrochemical electrodes [15] (see Sect. 12.8). In contrast, n-type semiconductivity is much harder to achieve, because most potential n-type dopants (P, As, Li) are too large to easily replace a small C atom in the diamond lattice, and thus have a low solid-state solubility in diamond [16]. Some degree of success has been achieved with phosphorus doping [17], but a reliable n-type dopant with useful electronic properties remains the 'Holy Grail' of diamond semiconductor research.

12.5 The NV Centre

Nitrogen atoms, however, are small enough to substitute for carbon [18], however the energy levels of the N donor in diamond are too deep and so the material is electrically useless for most applications. Nevertheless, N in diamond, when situated next to a vacancy, forms the so-called 'NV centre' [19], as shown in Fig. 12.2. This defect is causing a great deal of excitement in the scientific community because NV centres located within a diamond lattice behave as isolated 'chromophores', with a set of energy levels distinct from those of the surrounding diamond. When exposed to a stream of photons from a laser, each NV defect will absorb only *one* photon.

When they subsequently relax, each NV centre will re-emit only a single photon (with reduced energy), and each photon emerges with a specific optically readable spin [20]. The photons can then be individually collected in suitable optical waveguides and transported where required. After a suitable delay, the NV resets, and can absorb and re-emit another photon. Thus, NV centres act as excellent single-photon sources [21], underpinning a host of applications involving quantum computing and quantum information processing [22–24].

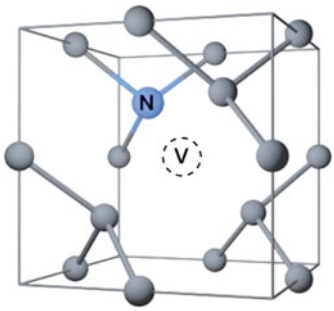

Fig. 12.2 Schematic diagram of the NV defect centre in the diamond lattice

12.6 CVD Reactors and Systems

Turning now to the practicalities of deposition, hot filament (HF) CVD reactors can usually only deposit diamond at rates of ~0.5–1 μm h^{-1}, but they can be scaled up to coat large areas (such as 12-inch-diameter wafers) and can coat non-flat shapes such as wires and substrates with complex 3D morphology [3]. In contrast, microwave (MW) plasma CVD reactors can deposit diamond at rates as high as a few 100 μm h^{-1} depending on the MW power used, but only over smaller areas (typically 3-inch-diameter samples) and predominantly flat substrates. However, these limitations to growth rates and substrate area are rapidly being overcome, with continuing improvements in reactor technology and more widespread use of CVD diamond in various applications. Currently, there are over 200 research groups worldwide studying growth or applications of CVD diamond, and perhaps 100 commercial companies either making diamond (for gemstone or other applications) or utilising CVD diamond in high-tech devices. As a result, the cost of diamond has fallen rapidly over the past decade; at the time of writing, the typical costs for a freestanding single-crystal diamond sample (4 × 4 × 0.5 mm) from a company such as Element Six is ~$1700, while that for a larger (10 × 10 × 0.5 mm) polycrystalline sample is only ~$50–200 depending on quality, while the number of suppliers has increased accordingly (see Table 12.2).

12.7 Nanodiamond

Together with diamond in the form of single-crystal gemstones or thin films, diamond particles of different sizes are another area of considerable current scientific interest [26]. Here, we shall focus only upon nanodiamond (ND) particles, which typically have sizes 2–10 nm [27]. The most common ND production method is via detonation of explosives (such as TNT and hexogen) in an inert atmosphere or in water/ice, inside a steel chamber [28]. The detonation produces a shockwave which propagates through the reaction mixture at supersonic speeds. In the transient shockwave, the prevailing pressure and temperature can be $p \sim 10$–20 GPa and $T \sim 2000$–4000 K. Under these conditions diamond is the thermodynamically favoured phase of carbon, while at all other times, the pressure and temperature conditions favour other forms of carbon. Thus, the explosion produces a mixture of diamond particles, soot and other sp^2 carbon material.

The powdery mixture of products from the detonation is cleaned with various acids and reagents to remove unwanted metallic impurities and soot, and the diamond component extracted. The resulting material, often called ‘detonation nanodiamond’ (DND) is commercially available from many suppliers worldwide (see Table 12.2) as a powder (see Fig. 12.3) or as a suspension in water, and is currently produced at a rate of several tons per year and sold for as little as $100/kg. Unfortunately, the DND particles tend to fuse into aggregates ~100 nm in size, and

Table 12.2 Selected suppliers of diamond gems, HPHT grit, CVD diamond substrates and nanodiamond powders

Supplier	Diamond product	Country	Refs.
Element Six, Ltd	CVD substrates, HPHT	UK, USA	[36]
DiamFab	CVD diamond films	France	[37]
Ceratonia	Diamond grit, CVD substrates	Germany	[38]
Yorkshire Bioscience	Nanodiamond	UK	[39]
Carbodeon	Nanodiamond	Finland	[40]
Diamond Materials	CVD substrates	Germany	[41]
Microdiamant	Nanodiamond	Switzerland	[42]
Nanodiamond.com	Nanodiamond	Switzerland	[43]
Ray Techniques, Ltd	Nanodiamond	Israel	[44]
Advanced Diamond Technologies	UNCD substrates	USA	[45]
Applied Diamond, Inc.	CVD substrates	USA	[46]
Crystallume	CVD substrates	USA	[47]
Diamond Foundry	Gems	USA	[48]
Gemesis	Gems	USA	[49]
SCIO diamond	Gems	USA	[50]
EDP Corporation	CVD substrates	Japan	[51]
NanoCarbon Research Institute, Co., Ltd.	Nanodiamond	Japan	[52]
Crysdiam Technology	Gems, CVD substrates and nanodiamond	China	[53]
Pam-Xiamen	CVD wafers	China	[54]
WEC Superabrasives	Gems	Taiwan	[55]
New Diamond Technology	Gems, CVD substrates	Russia	[56]
2a Technologies	Gems, CVD substrates	Singapore	[57]
Diamond Elements	Gems, substrates	India	[58]

A more comprehensive and continually updated list of diamond suppliers can be found in Ref. [35]

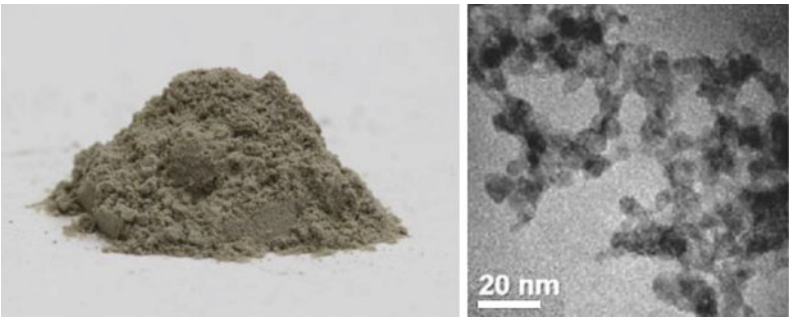

Fig. 12.3 Left: DND powder. Right: transmission electron microscopy image of DND [25]. (Copyright © R. Hamers research group, University of Wisconsin, used with permission)

thus the as-supplied material usually requires de-aggregation before subsequent processing. This can be achieved in many ways, including ball milling, pulverisation, high-power sonication, acid treatments, controlled heating in O_2 or H_2, or combinations of these methods [29]. The resulting DND particles are best described as having a diamond core surrounded by a (partially) graphitic or fullerene-like shell – and are sometimes described as 'bucky-diamonds' [30].

As a result of the various cleaning processes applied following detonation synthesis, the surfaces of DND particles are usually terminated with oxygen-containing groups like carboxyl, hydroxyl or bridging-ether groups. DND particles are therefore usually hydrophilic, which helps their stability when in aqueous suspensions. This oxygenated surface can be modified by standard chemical methods, replacing the O-groups with H (producing a mildly hydrophobic surface), with F (which is superhydrophobic), or with NH_2. Both O-terminated and NH_2-terminated ND are of particular interest because they enable the subsequent binding of a large variety of functional molecules, such as bioactive compounds (proteins, enzymes, antibodies, DNA), catalysts, drug molecules, or polymer building-blocks by amide bond formation or other standard chemical procedures [31].

ND particles containing fluorescent NV centres exhibit bright luminescence, which, combined with a readily modifiable surface and biocompatibility, make them extremely promising for biomedical applications [32], and, in particular, for use as a biomarker to 'tag' biomolecules of interest as they travel around within living organisms [33, 34].

In this short review we shall concentrate on applications of CVD diamond and nanodiamond that may help to mitigate the effects of a chemical, biological, radiological or nuclear (CBRN) threat. The aim is to identify potential applications where CVD diamond is a key component that counter a diverse range of CBRN threats. In some cases, these applications may reduce the likelihood of a particular threat happening, or even prevent it altogether. In others, they may simply help to mitigate the damage following a successful CBRN attack. However, the number of applications involving diamond that could be brought to bear on CBRN issues is huge, so we limit ourselves here to a few examples from each threat type. In some cases, the technology is already being developed, although perhaps only on a small scale; in others it hasn't yet been invented.

12.8 Chemical Threats

Although there are many potential chemical threat scenarios, we shall only consider two here: poisoning of a water supply, such as a reservoir or river, and detection of chemical agents in smuggled items.

12.8.1 Poisoning of a Water Supply

The drinking-water supply to a city or region may become contaminated by toxic chemicals, either accidentally as the result of, say, an industrial leak, or deliberately due to a terrorist attack. In the latter case, there are two scenarios. In the first option, the perpetrator could seek to cause maximum casualties as quickly as possible. In this case, the attack might take the form of dumping a large volume of a highly toxic chemical into a river, reservoir or aquifer, with the aim that by the time it is detected the damage would have already been done. This is quite a challenge, however, because most developed counties have detectors that continuous monitor the water supply, and any sudden spike in toxin concentration would automatically shut down the supply. This strategy might work in less-developed countries without sophisticated monitoring systems, but the perpetrators still have the problems of how to obtain large amounts (perhaps 100 s of litres) of toxic chemicals without alerting the authorities, and then how to transport them undetected to the dump site.

A more subtle approach might be to go for 'little and often'; use much smaller amounts of a toxic substance such that it falls below the detection limit of most current sensors, and add it to the reservoir repeatedly over a long period. A systemic poison like dimethylmercury or thallium, which accumulate in the body, might be piped to a population for many weeks or months, undetected, before the first symptoms of poisoning started to appear – and by then it may be too late.

For the authorities, the challenge here, is in detecting minute concentrations of the toxin, and identifying it unambiguously amongst many other chemicals also present in the water [59]. One possible solution is to use boron-doped diamond (BDD) electrodes to detect the electrochemical oxidation and/or reduction peaks characteristic of known poisons. BDD has a number of advantages over conventional electrodes made from silver, platinum or glassy carbon [15]. It has a wide potential window, from −1 to +1.8 V, allowing detection of redox species that would normally fall outside the operating range of conventional electrodes, including heavy metals (mercury [60], cadmium, lead, nickel [61], arsenic [62]), polycyclic aromatics (PCAs) and pesticides [63], hormones and estrogenic compounds, explosives [64], neurotransmitters such as dopamine [65], drugs (paracetamol, cyanides, narcotics, pharmaceuticals) [66], and water-soluble nerve agents [64]. Within this operating window, the response is flat, so there is no background, making the BDD electrodes highly sensitive. This enables them to detect some compounds at nanomolar (ppb) levels, even in the presence of similar chemical species (see Fig. 12.4a). Furthermore, the BDD electrodes can be nanostructured into needle shapes ('black diamond'), increasing the available surface area by many 100-fold, along with a concomitant increase in sensitivity [65] (see Fig. 12.4b, c). BDD electrodes are robust, have far less tendency to foul than other electrodes, and can be electrochemically cleaned *in situ*.

Although there are perhaps 50 research groups worldwide studying BDD electrochemistry, there are few, if any, commercially available BDD water monitors on the market, although a number of companies (e.g. Element Six (UK), Windsor

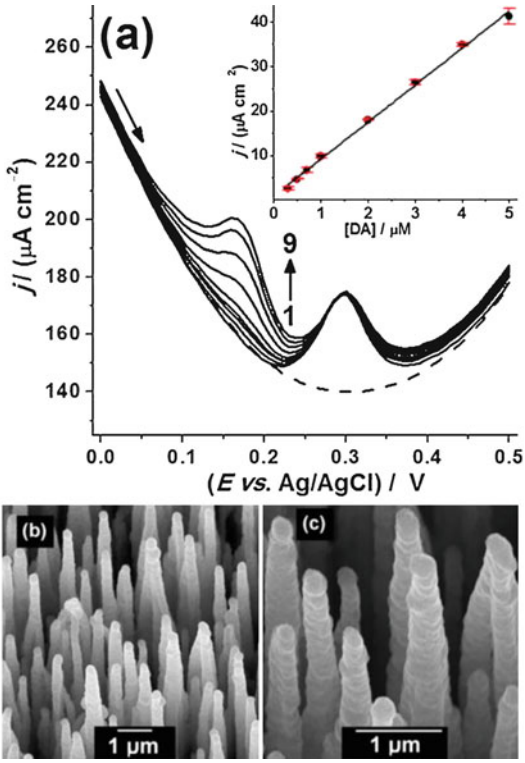

Fig. 12.4 An example of the sensitivity and selectivity of BDD electrodes used for electrochemical trace analysis in water. (**a**) Differential pulse voltammograms recorded for different dopamine concentrations ($1–9 = 0.0–5.0 \times 10^{-6}$ M) in the presence of a chemically similar analyte (uric acid 3.0×10^{-5} M). Inset: Current density j (μA cm^{-2}) vs. concentration of dopamine (μM) showing a linear response with concentration. (**b**) and (**c**) SEM images of 'black diamond', nanostructured BDD needles on the surface of an electrode. Figures reprinted under CC BY 4.0 licence from Ref. [65]. (Published by The Royal Society of Chemistry)

Scientific (UK), Adamant Technologies (Switzerland), Condias (Germany), Sumitomo (Japan) and sp3 Diamond Technologies (USA)) sell BDD electrode material for use in detectors.

Whether the water-supply was contaminated by accident or deliberately, the next issue would be to clean up the water as quickly and efficiently as possible. One method that would be particularly effective for removal of organic toxins (chemical agents or bacteria/viruses) is electrolytic destruction. This is an electrochemical technique which involves passing a high current (often many tens of amps) through the contaminated water via a series of electrodes. The current fragments any dissolved or suspended molecules, converting the organic components to CO_2 and rendering the toxin harmless. Unfortunately, the high currents sustained for long periods of time cause degradation and erosion of the electrodes, which must be replaced periodically at high cost in money and time. BDD electrodes have proven to be more robust than most alterative materials, allowing higher currents to be used for longer periods between replacements [67].

A number of commercial companies offer water purification systems based on BDD electrode technology, such as Proaqua (Austria), CSEM (Switzerland), and WaterDiam (France). These systems may be suitable for household supplies, or perhaps a small factory, but not for emergency rapid clean-up of an entire reservoir following an attack. However, in principle, to do so, this technology just needs to be scaled up and made portable. One might imagine an emergency response team composed of a fleet of trucks, each carrying a BDD water-purification system, that could drive rapidly to the site of a reservoir-poisoning event to begin clean-up within hours.

12.8.2 Detection of Chemical Reagents

Many chemical reagents, such as nerve agents or poison gases, that might be used in an attack upon a military or civilian population are very difficult to detect, and even tiny amounts can be devastating. The Novichok attack in Salisbury in 2018 used only ~2–10 mL of Novichok A234, smuggled into the UK in a modified perfume bottle [68]. It killed 1 person and severely injured 4 others – but caused an estimated £10–30 M in clean-up costs, plus untold economic damage to this major commercial city, devastating their tourist industry for nearly a year [69]. Most airports use random swab tests to spectroscopically detect chemical residues on the clothes or baggage of travellers. But determined terrorists or government agents can defeat these measures easily. The failure to detect the disguised perfume bottle containing Novichok when it passed through Gatwick Airport border highlights the urgent need to develop new and more sensitive methods to selectively detect these types of reagents at very low levels (ppb).

One solution is a so-called 'electronic nose' (EN), which can 'sniff' out illicit substances. Some airports have these fitted as full body scanners, but they are often large, and create extra queueing time for passengers. A better answer would be an EN that is inexpensive, portable, lightweight, and highly sensitive – but only to the molecules of interest. Many competing gas-sensor technologies are candidates for the next generation of EN [70], including those based on semiconductor-metal-oxides, conducting polymers, surface acoustic waves, QCM, and optical-fibres, but CVD diamond ENs offer a number of advantages. They can use smaller gas volumes, have smaller detection surfaces, and offer shorter detection times.

An example of a diamond-based EN developed by *CEA* (France) is shown in Fig. 12.5 [71]. It uses microelectromechanical systems (MEMS) technology in the form of freestanding diamond cantilevers etched onto a silicon substrate. The cantilevers can be made to resonate using an attached piezo-electric layer. The resonant frequency, f, depends upon the dimensions of the cantilever, the material it is made from, and its mass. Because the cantilever is made from diamond, the resonant frequency is very high (20–150 kHz), making it extremely sensitive to

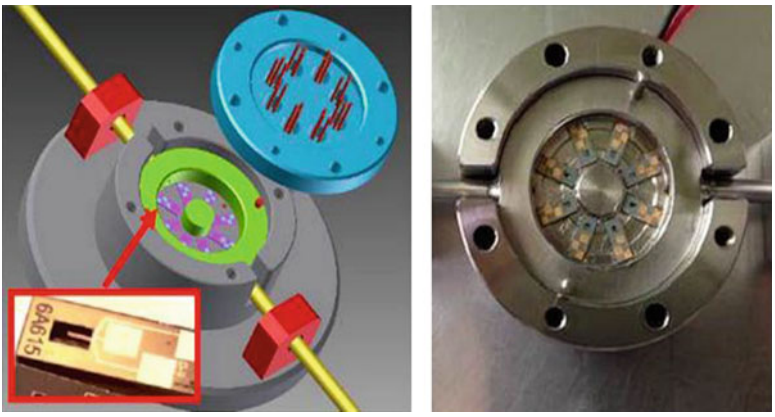

Fig. 12.5 Left: Three-dimensional drawing of an EN gas sensor showing the 8 MEMS cantilevers inside. Right: Photograph of the sensor. (Figure reproduced from Ref. [71] under CC BY 4.0 licence)

changes in mass. When gas molecules adsorb onto the cantilever, its total mass changes, which lowers the resonant frequency. This frequency change Δf provides an indication of the gas concentration. Selectivity for different gas molecules is achieved by chemically functionalising the diamond electrode surface using a specific binding molecule (protein, antibody, inorganic reagent) which is covalently bonded to the diamond surface. The French group reported successful trials of an 8-cantilever array sensor, each one functionalised to detect a different molecule. Such systems are still in development, but the next stage would be to scale these up to detect simultaneously perhaps 100 different molecules of interest. They could then be deployed at train stations, airports and other critical buildings.

12.9 Biological Threats

Although there are many types of threats posed by different biological incidents, accidental or otherwise, here we shall concentrate only upon two – the first application is preventative, while the second aims to help victims after the event.

12.9.1 Antimicrobial Surfaces

Bioweapons can spread harmful bacteria over large areas; as well as the immediate infection problem and risk of epidemics, the infectious agent may coat the surfaces,

walls, floors, etc. for km around the initial site. These areas may remain infectious until the pathogen finally dies, which maybe days or even weeks. Moreover, surfaces which were clean can become contaminated by contact with people that have been exposed to the bacteria, or via the air. Thus, along with the immediate casualties, a bioweapon attack might also deliver a 'denial of services' effect, because military or emergency services cannot enter the affected areas without special protective clothing and equipment. Furthermore, in an emergency situation, disinfectants or other antibacterial chemical agents might run out or be in short supply, making decontamination even more of a problem.

So, the question is: Can we equip critical equipment (e.g. those used by hospitals, Emergency services, military, etc.) with antimicrobial coatings that kill bacteria mechanically rather than chemically? One possible answer comes from the study of the microstructure of the wings of dragonflies and cicadas [72]. The wings are covered with micropillars a few 100 nm tall, which biologists believe act as a protective antimicrobial surface. A surface with properties similar to these was fabricated using black silicon – a synthetic nanostructured material that contains high-aspect-ratio nanoprotrusions, such as nanospikes or nanoneedles, on its surface produced through plasma etching. Black Si acts as an effective bactericidal surface for both Gram-negative and Gram-positive bacteria [72], but the nanostructured surface is rather delicate and easily damaged or scratched – even a human fingernail dragged across the surface breaks and dislodges the needles. A solution to this is to coat the needles with a conformal layer of diamond, 50–100 nm thick (see Fig. 12.4b, c). The advantage of the diamond coating is that the structures become far more robust and less likely to become damaged. As well as having excellent electrochemical properties (see Sect. 12.4), the diamond-coated spikey surface (called 'black diamond'), generated a mechanical bactericidal effect, killing bacteria efficiently and effectively [65, 73], see Fig. 12.6. When the surfaces of the

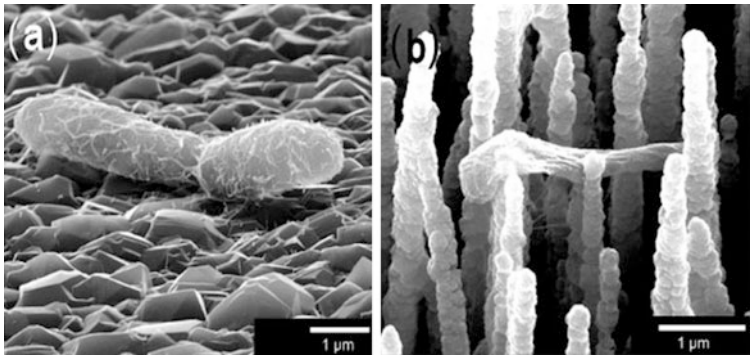

Fig. 12.6 SEM images of *E. coli* bacteria, showing (**a**) healthy, turgid bacterial cells on MCD control samples, but (**b**) deformed and flaccid dead bacteria on a black diamond surface. (Figures reprint from Ref. [74] under CC BY 4.0 licence)

black-diamond needles were fluorinated by exposure to an SF_6 plasma, they became superhydrophobic, further increasing their antimicrobial properties, as well as hindering the growth of biofilm [74].

For applications in the real world, bioresistant surfaces will realistically never be coated with exotic materials, such as black diamond. Instead, similar nanostructured surfaces could be fabricated from more conventional materials like stainless steel, titanium, or polymers such as medical-grade rubber or PTFE. Nevertheless, the general findings from studies such as those on black diamond, optimising biocidal activity in terms of types, shapes and densities of surface morphology and chemical nature, will provide important information for the development of next-generation antibacterial surfaces made from more practical materials.

12.9.2 Diamond-Based Bioimplants

One of the long-term after-effects of a CBRN incident may be a large number of civilian and military personnel with chronic medical conditions that might require treatment for years. Neurological conditions and/or nerve damage can be brought about by mechanical trauma, or by exposure to chemicals such as nerve agents, but whatever the cause, there would be a requirement to treat these victims as effectively as possible.

Diamond may again become the material of choice for studying and achieving these treatments [75, 76], mainly because it is bioinert, i.e. it does not provoke an immune response when implanted inside the body. This advantage means that diamond-based implants produce less or even zero inflammation, and can therefore survive and function for years, or even decades, within the body, with no need for the cost and trauma of surgical replacement, probably within the patient's lifetime. Diamond is also corrosion resistant, so is not chemically attacked by the body's fluids. Thus, it can be used to protect non-biologically inert components (such as Si microprocessor circuitry) within hermetically sealed diamond boxes. An example of this is the 'bionic eye' project from Melbourne University [77, 78], that uses an artificial retina chip sealed inside a protective diamond shell, implanted into the eye, to provide some degree of sight for patients with a malfunctioning retina.

Diamond can be heavily doped with boron to increase its electrical conductivity to near-metallic, and this makes it useful as biosensor, allowing signals to be transferred to and from cells. This is especially useful for neurons situated in the brain, the central nervous system, or in the periphery such as arms and legs. There have recently been two major EU-funded research consortia (DREAMS [79] and NEUROCARE [80]) to study the function of diamond-based implants that interface with living human neurons, with the aim of finding treatments for neurological disorders, such as Alzheimer's, Parkinson's, stroke, epilepsy, paralysis due to trauma, and many others. An example is artificial retinas that use a conducting diamond film grown onto a flexible polyimide substrate that can wrap around the back of the eyeball and transfer signals from the retina to the optic nerve [81]. Other

examples currently being researched are diamond sensors embedded into the spinal cord of paraplegic patients, which pick up signals from the brain and transfer them wirelessly to an external computer. Interpretation of these signals using special software may allow robotic legs to be moved at will by the patient. Such treatments for paralysis have already been demonstrated using multiple external sensors placed on the scalp [82], but with a diamond implant, the sensor would be portable and remain *in situ* for perhaps 30 years.

Such two-way communication opens up other possibilities too, such as direct brain-computer interfaces (BCIs) [82]. Here, the diamond sensors would be permanently implanted into the brain, picking up the neural impulses and transferring them wirelessly to an external computer. With suitable software to interpret the signals (a difficult problem in itself), it may, in time, be possible to develop thought-controlled equipment (TVs, cars, drones, etc.), or mind-to-mind communication ('telepathy') to other people with BCI implants linked via the internet. Although this may seem rather far away, the implications of BCI technology for medical applications, military applications, and society as a whole, are huge.

Another approach for using diamond medicinally is as a bioinert culture plate upon which to grow human cells [76]. These cells are then available as *in vitro* test subjects for determining the efficacy of new drug treatments, or for studying the toxic effects of chemical or neurological agents –- without the cost and controversy of using *in vivo* tests or animal experiments. Cells cultured on diamond plates can survive for many months, unlike those on traditional glass or plastic substrates which typically die after a few weeks. This means that long-term testing is possible, as are inheritance tests that require multiple generations of cells. Studies at University College London [83] and Bristol University [84] have demonstrated that human stem cells thrive on diamond culture-plates, and that they can later be transformed into other cell types (kidney, liver, and especially neurons) using suitable chemical treatments. When BDD is used as the substrate, then the cells growing on its surface can be electrically interrogated or stimulated via the conducting substrate. The substrate can be patterned or treated such that areas of the surface are amenable to cell growth, while other areas are not. In this way cells, such as neurons, can be persuaded to grow only in certain areas, allowing two-dimensional neuron networks to be fabricated [85], as shown in Fig. 12.7. These 'brains-on-a-plate' act as models that mimic to some degree the behaviour of a real 3D brain, allowing neuroscientists to study how different types of stimuli propagate through the neural network. Such studies pave the way for future development of organic computers. Diamond is also being used as a scaffold upon which to grow human bone cells or cartilage tissue for subsequent transplant procedures [86, 87].

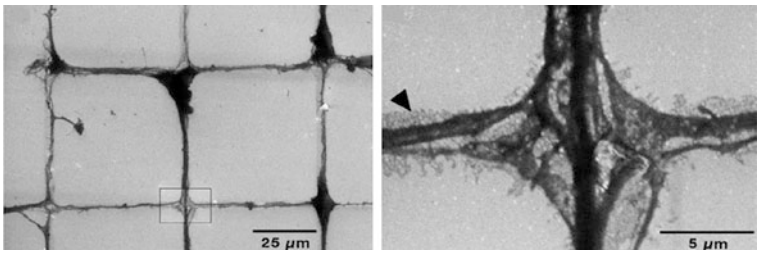

Fig. 12.7 Ordered growth of mice neurons on a patterned laminin-coated hydrophilic CVD diamond surface. The neurons only grow along the patterned areas, and then form connections at the crossing points. (Figures reprinted with permission from Ref. [85])

12.10 Radiological/Nuclear Threats

12.10.1 Radiation Detectors

One way to prevent a CBRN nuclear incident is to detect the presence of nuclear material before it enters the country or crosses a city threshold. Thousands of passive radiation detectors may need to be employed as screening devices at ports, airports, and on highways entering cities, and as air-flow meters in hospitals, or in waste incineration. Such detectors need to be cheap, portable and reliable.

Diamond has a number of advantages compared to competing materials and technologies in relation to detecting and measuring radiation levels [88]. First, diamond radiation detectors can be designed to detect and analyse most forms of ionising and non-ionising radiation, including neutrons, protons, alpha, beta, and gamma radiation, and X-rays, so long as the energies involved are greater than the band gap of diamond (5.4 eV). Diamond-based detectors are very robust and therefore have no need for frequent replacements. They have a high mobility of free charges (~4500 $cm^2\ V^{-1}\ s^{-1}$ for electrons, 3800 $cm^2\ V^{-1}\ s^{-1}$ for holes [89]) which gives a very fast response (<100 ps) and they can be operated at room temperature with no need for cooling. They have a resistivity several orders of magnitude greater than Si-based detectors, with extremely low leakage currents which makes them highly sensitive. Unlike Si detectors, diamond detectors do not require p-type or n-type junctions to connect the detector to the control electronics. Because such junctions are often a point of failure, the diamond detectors are more robust, allowing them to be used in extreme environmental conditions, e.g. high temperature, high humidity, very high radiation, and highly corrosive environments.

These features, combined with the intrinsic properties of diamond, give diamond detectors perhaps their most important advantage over other materials – they are resistant to extremely high radiation levels – values at which most other detectors stop functioning. Indeed, the main Atlas detector used on the Large Hadron Collider at CERN is made from diamond, as no other material could survive the huge radiation levels in the beam (proton fluences of $1 \times 10^{15}\ cm^{-2}$ and instantaneous

Fig. 12.8 Photograph of a large area (46 mm diameter by 100 μm thick) diamond radiation detector. (Image reprint under CC BY 3.0 license from Ref. [93])

rates of at least 1×10^9 cm^2 s^{-1} [90]). The intense beams of X-rays from synchrotron sources at ESRF (Grenoble) and the Diamond Light Source (Harwell, UK) are monitored using diamond detectors and focused using diamond compound refractive lenses [91], while the Joint European Torus nuclear fusion facility at Culham (UK) uses diamond detectors for UV and neutron detection.

The diamond research group at CEA Saclay in France have developed a number of different diamond-based radiation detectors [92], and there are several companies worldwide that produce them commercially, including PTW-Freiburg (Germany), St. Gobain/Norton Diamond Film (Northboro, MA, USA), and Element Six, Ltd. (Harwell, UK). An example of such a detector is shown in Fig. 12.8.

12.10.2 Radiation Dosimeters

Similarly, diamond can also be used as a radiation dosimeter, to detect and monitor the total radiation dosage of humans exposed to a radiation incident [94, 95]. Most dosimeters are designed for medical and therapeutic use (X-rays, CAT scans), but these often only work at low radiation levels. Moreover, many existing technologies have limitations: Si dosimeters suffer from radiation damage and low lifetime, whereas ionisation chambers have low spatial resolution and low sensitivity. To overcome these, dosimeters that utilise natural diamond have been developed recently, but these tend to be expensive. Therefore, multiple research groups worldwide are actively developing dosimeters that instead use cheap CVD diamond. Examples include the EU project *MAESTRO* (Methods & Advanced Equipment for Simulation & Treatment in Radiation Oncology) [96] and two projects funded by the Italian National Institute of Nuclear Physics called *CANDIDO* and *CONRAD*, on natural and synthetic diamond-based dosimeters for clinical radiotherapy [97].

However, in the event of widespread contamination, e.g. following a dirty bomb or nuclear accident (such as those that occurred at Chernobyl and Fukushima), clean-up crews, emergency services and the general population will need to wear portable dosimeters to monitor their radiation exposure. These dosimeters may need to be far more sensitive than standard medical devices, and also be able to withstand far higher radiation dosage than might be expected clinically.

Diamond has a low atomic number ($Z = 6$) while the mean value for soft tissue is $Z \sim 6.5$–7.5, thus, diamond is described as being 'tissue equivalent'. This means diamond dosimeters have fewer calibration errors or offsets than, say, Si ($Z = 14$) detectors, and do not over-estimate the dosage at lower energies [98]. The CVD diamond detectors that are in development for therapeutic use could easily be adapted to the more extreme conditions of a CBRN incident. Because diamond detectors are highly sensitive, the dosimeters could be made very small, and thus cheap, portable and even disposable. Moreover, they would work at low and high radiation levels, with a long lifetime, and with little/no damage or deterioration of performance over time – which is vital, as clean-up operations following a CBRN incident may take months or even years.

12.10.3 Radiation-Hard Electronics

Ever since the loss of the Telstar 1 satellite in 1962 after a high-altitude nuclear test, scientists have been aware that delicate electronic circuits can be damaged or destroyed by exposure to radiation. Unfortunately, most electronics based on Si, GaAs, GaN or similar semiconductor materials, are not radiation hard [99]. Ionising radiation (alpha and beta) is a particular problem with semiconductor substrates; even a single high-energy particle can create thousands of electron-hole pairs as it passes through the substrate. The resulting large transient currents can disperse through the conducting substrate, damaging circuit components and transistors over a large area, leading to irreversible failure of the device. Some devices can be improved by clever design (e.g. by adding extra error-correcting circuitry) or by using insulating substrates (e.g. silicon-on-sapphire (SoS) and silicon-on-insulator (SoI) wafers). Devices can also be shielded (often by encapsulating the circuitry inside metal boxes), but shielding is large, heavy, and not always viable, for instance, in aerospace applications. Generally, due to the extra cost, complexity and time required for extra testing, radiation-hard devices usually perform poorly compared to standard devices [100].

Diamond can play a vital role, here, too. A variation of SoI technology involves depositing the active semiconductor layer (e.g. Si or GaN) on top of an insulating CVD diamond substrate. Silicon-on-diamond (SoD) [101] or GaN-on-Diamond (GoD) [102] technologies are currently being developed for thermal management in high-power devices (see Sect. 12.11). Studies have shown that SoD devices outperform their SoI equivalents, while being significantly more radiation hard [103].

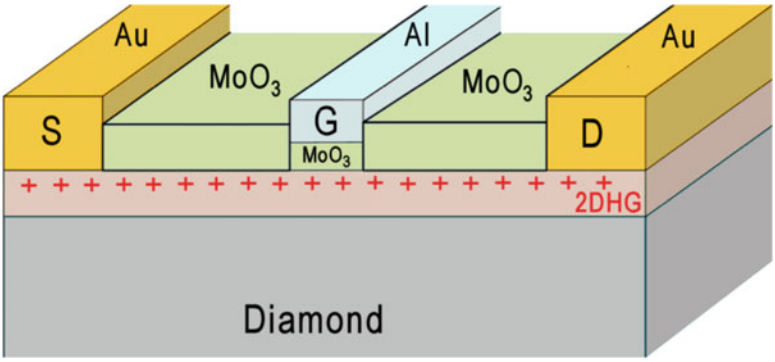

Fig. 12.9 Schematic cross-sectional view of a diamond-based MOSFET device utilising the 2DHG conduction channel in H-terminated diamond protected by a MoO_3 capping layer, based on the design proposed in Ref. [104]. S, G, and D refer to source, gate and drain, respectively

One promising new avenue of research involves a new type of field-effect transistor (FET) design based on an unusual property of the diamond surface called 'surface transfer doping' [105]. Hydrogen-terminated diamond exhibits a surface dipole due to the difference in electronegativity between the carbon atoms in the bulk and the H atoms on the surface. Electron-accepting molecules from the ambient air adsorb onto this polar surface and electrons are transferred from the bulk to the adsorbates. As a result, the adsorbates become negatively charged, and a stable two-dimensional hole-gas (2DHG) layer a few nm thick is formed just below the surface [106]. This thin layer is electrically conducting, with both a high hole mobility (100–200 $cm^2\ V^{-1}\ s^{-1}$) and high hole concentration (10^{12}–$10^{13}\ cm^{-2}$), but the conductivity can be altered or even destroyed simply by changing the atmosphere (pressure, humidity, etc.) above the surface. To stabilise this conductive layer, the diamond can be capped with a protective layer of V_2O_3, MoO_3 or Al_2O_3, which hermetically seals the surface as well as providing additional surface acceptors helping to generate the 2DHG layer.

Many research groups, such as those at Glasgow University [107] and Waseda University (Tokyo) [108], have been exploiting these ideas to produce novel FET devices in which the conduction from source to drain, moderated via a gate electrode as usual, is through this conductive layer, rather than through the semiconducting substrate (see Fig. 12.9). Not only do these 2DHG FETs exhibit excellent device performance, but because they are fabricated directly onto an insulating diamond substrate, they should be considerably radiation more hard compared to standard Si-based devices. If this is proven experimentally, such 2DHG diamond FETs may herald a new paradigm in radiation-hard electronics for space, military, and CBRN applications.

12.10.4 Targeted 'Magic Bullet' Treatments

The aftermath of any successful CBRN incident may require hundreds, thousands, or even millions of people requiring medical attention. As well as short-term injures and trauma, there may well be much longer-term treatments required for chronic problems such as different forms of cancer induced by radiation exposure. Moreover, bulk medicines to treat these chronic ailments may be in short supply, or insufficient to treat the potentially large number of patients that require them. One solution is to use targeted treatments that affect only the afflicted part of the body, such as an organ or a tumour. So-called 'magic bullet' treatments require far fewer drugs and have fewer side-effects – but most are still under development.

Targeted treatments use a delivery vehicle, which is usually some sort of nanoparticle, which has had its surface chemically functionalised to allow other molecules to attach to it. Many different nanoparticles have been used for this purpose (metals, carbon nanotubes, lipids, polymers, etc.), but 4–10 nm nanodiamond (see Sect. 12.7) is particularly suitable for this purpose [109] because (a) it is cheap, and readily available as a suspension in water (recall Table 12.2), (b) its surface can be readily functionalised with a wide range of chemical groups, (c) many studies have shown that nanodiamond is bioinert and non-toxic [76], and (d) after its job is done, the nanodiamond will simply be excreted harmlessly from the body.

To make the nanodiamond specific to only the chosen cell type, a molecule (e.g. a reagent, protein, antibody, DNA strand, etc.) known to be a specific binding agent for the chosen cell type is chemically bonded to the ND surface [110]. When the functionalised ND particles are administered into the patient, often intravenously, they travel around the bloodstream until they meet the targeted cell type, at which point they recognise the cell and attach to it.

What happens next depends upon what extra functionalisation the ND has experienced. As mentioned previously, NDs can be treated so that they contain fluorescent NV centres which emit light when illuminated with a laser. These then act as fluorescent biolabels or biotags, revealing the location of the ND along with the cell to which it is attached, thus identifying the regions of interest, such as cancerous cells, within the living organism [32]. Recently, real-time tracking of single florescent ND particles inside a cell has been reported [112]. Such studies are starting to provide valuable insights into the movement of fluids within cells, as well as the mechanisms by which metabolic products are transported around living cells [113].

To convert a ND into a 'magic bullet' requires bonding a second molecule to the ND surface alongside the binding agent. This second molecule interacts with the chosen cell, either killing it in the case of a cancer cell (see Fig. 12.10), or curing/treating it in the case of malfunctioning cells. This drug molecule is usually bound weakly to the ND in such a way that it detaches when activated by an external stimulus such as UV light, or falls off automatically after a few hours to be excreted from the body. Although these sorts of treatments are still under development, they

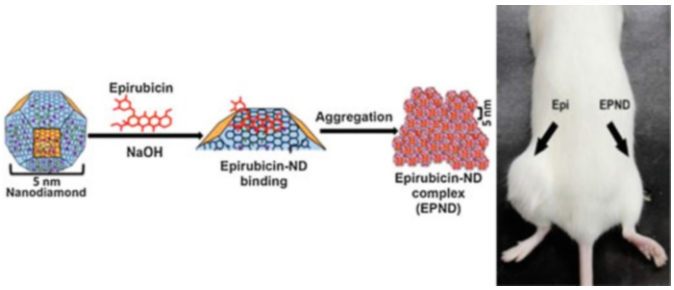

Fig. 12.10 Schematic diagram showing 5 nm nanodiamond (ND) being functionalised using the anti-cancer drug epirubicin (Epi) which then aggregate to form an epirubicin-ND complex (EPND). The photo on the right shows a tumour-bearing mouse following treatment with either Epi or EPND. The tumour treated with the EPND was significantly reduced compared to that treated with the Epi control. (Figure reproduced with permission from the ACS, taken from Ref. [111]. Further permissions related to reproducing this figure should be directed to the ACS)

may be a realistic method to treat the mass casualties that may result from a large-scale successful CBRN attack.

12.11 General Infrastructure

In this section we shall discuss applications that don't counter a specific CBRN threat type, but instead sustain or improve the response of emergency services to a CBRN incident, and in particular maintain the country's power grid, telecommunications network, transport links, and the general infrastructure. We shall focus on two of these aspects: power and telecommunication.

12.11.1 Reliable Fast Communications

In a major CBRN incident the communication networks often fail due to overload, with people frantically trying to use the mobile-phone network to contact family members who may have been caught up in the attack. Failure of these networks due to lack of bandwidth capacity helps to spread fear and panic among the general population. During the 9/11 attacks in New York in 2001 the mobile phone networks in both the US and UK jammed for several hours, while during the London Bridge attacks in June 2017, 'communication issues' between emergency services meant

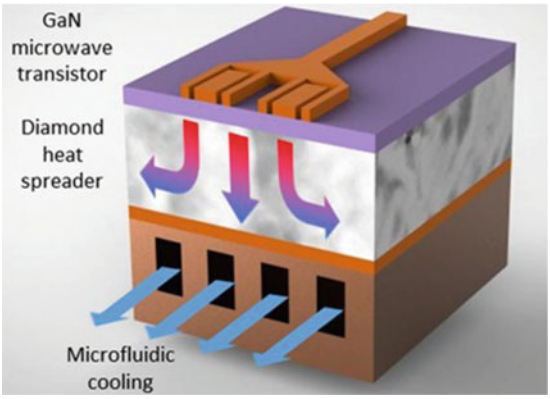

Fig. 12.11 Concept for a GaN-on-Diamond device. The heat flows from the hot device into the diamond (in this case with no interface layer between them), which then spreads it rapidly into the underlying substrate cooled by microfluidic channels. (Copyright © University of Bristol 2017)

that paramedics did not know which areas were safe and which areas were hot zones, and so were not allowed into these areas to help injured people for up to 1 h [114].

One solution to this problem would be to develop telecom networks that are many times faster than those currently in use (4G & 5G), and which could cope easily with excess demands in an emergency. Current RF power amplifiers and microwave transmitters use GaN as the device material in high electron-mobility transistors (HEMTs). But these devices can only be operated at ~50% max power due to overheating and reduced lifetimes [115]. The next generation transmitters, either HEMTs or monolithic microwave integrated circuits (MMICs), being developed for beyond 5G will be even more power-hungry. In order for these to work effectively, efficient heat extraction is essential. Studies have shown that most of the thermal resistance occurs at the interface between the active GaN device layer and the substrate, which is usually made from Si or SiC [115]. Manufacturers have tried to lower this thermal barrier using thin interface layers, made of materials such as SiC or SiN, between the GaN and substrate, but the results are not ideal.

Diamond has one of the highest thermal conductivity values known (see Table 12.1) and so is ideal for use as a heat spreader. Placing a thin (few μm) layer of CVD diamond between the GaN and Si/SiC substrate should allow the localised heat to be rapidly transported away from the hot device and into the substrate. This heat could then be removed using a suitable heat sink, radiator or microfluidic cooling pipes (see Fig. 12.11). A number of research groups and commercial companies are actively studying this approach, one of the largest of which is a project called *GaN-DAME* [116], a UK six-university consortium based at the University of Bristol funded by a £4.3 M grant in 2017. However, the technical problems are not easy. The CVD conditions for diamond growth (Sect. 12.2) are not compatible with GaN [117], so it is tricky to achieve an adherent diamond coating with good thermal contact. One possible solution is to use a thin 'glue' layer between the diamond and the Si substrate [118]. A promising option for the layer is AlN [119]. Although it has a smaller thermal conductivity (400 W m^{-1} K^{-1}) than

diamond, so long as the AlN layer is thin (200 nm) the thermal resistance at this interface is acceptable.

Another problem, which is exacerbated with larger wafer sizes, is the mismatch in thermal expansion coefficients between diamond and the Si substrate, which results in the wafers bowing.

Despite these problems, the ultimate aim is to develop HEMTs with a spectacular >5 times increase in RF power compared to the current commercially available GaN-on-SiC devices. Equally valuably, a dramatic shrinkage in MMIC or power-amplifier size should be possible, delivering an increase in efficiency through the removal of combining networks as well as a reduction in cost. This would be a disruptive change in capability allowing the realisation of new system architectures and thus enabling the bandwidths needed to deliver 5G and beyond. This would deliver a telecom network that works reliably both for day-to-day activities and during emergency situations.

12.11.2 Emergency Power for Critical Equipment – Nuclear Batteries

In a CBRN incident the power grid may fail, either locally or city-wide, depending on the type of attack. It is vital that some power is maintained for critical services, e.g. hospitals, police, communications, etc, or for essential equipment, such as radiation detectors, gas sniffers, lighting, and so on. Some of these pieces of equipment are battery operated, but most batteries won't last more than a day or so of continual operation without being recharged. Others may have a generator back-up, but these, too, may only work for as long as the fuel lasts, perhaps a few days.

What is required is a power source which does not require charging from the mains supply, and which has a very long lifetime – such as a 'nuclear battery' or 'betavoltaic battery'. In simple terms, a nuclear battery turns radioactivity into electricity. Many different types of nuclear battery exist, developed mainly for powering spacecraft as they travel to distant planets over periods of many years. However, a new type of nuclear battery based on ^{14}C diamond is currently gaining a lot of interest [120] (see Fig. 12.12). In these proposed devices, radioactive graphite

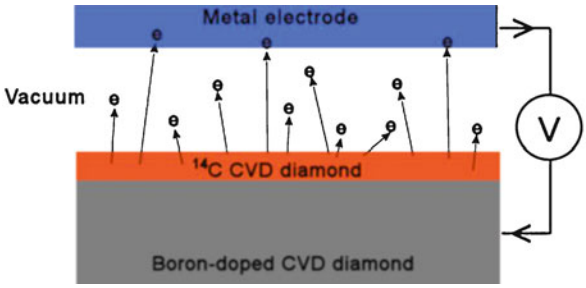

Fig. 12.12 Schematic diagram of a concept for a diamond-based nuclear battery

(a waste product from many nuclear power stations) containing ^{14}C is converted into $^{14}CH_4$ by burning in hydrogen gas. This methane is then used as the carbon source in a CVD reactor, which deposits a layer of ^{14}C diamond onto a conducting substrate. ^{14}C is a beta emitter, so it emits high-energy electrons with a half-life of ~8000 years. A second 'collector' electrode is placed a few 100 μm away from the diamond layer, with a vacuum gap between the two. The electrons emitted from the ^{14}C-diamond layer travel ballistically across the gap and are absorbed by the collector. Thus, the collector gradually becomes more negative while the emitting electrode more positive, and a self-bias develops between the two electrodes. Connecting the two electrodes with a wire allows current to flow back to the emitter, driving an external load, if required. Other designs based on layers of alternating p- or n-doped diamond sandwiched between ^{14}C diamond emitting layers [121], that utilise ^{63}Ni or tritium as the radioactive sources [122], or which combine beta radiation and thermionic emission [123], have also been proposed.

Such devices would produce electrical power almost indefinitely (thousands of years), and can be made into small, portable, sealed solid-state packages, with no moving parts and which require zero maintenance. The output power per device would be tiny, perhaps only a few μW, but hundreds or thousands of devices could be joined together in series to produce higher powers if required. Because the battery is always on, it could continuously trickle-charge a capacitor ready for intermittent high-power use, e.g. a burst transmitter on a spacecraft that sends all its data back to Earth in a short high-frequency pulse once a day. As well as spacecraft and satellites, other uses include areas where changing a battery is difficult, costly or impossible, such as military applications (e.g. remote surveillance), aerospace applications (e.g. sensors inside jet engines) or medical applications (perpetual pacemakers). There are numerous commercial applications, such as for domestic use (watches, calculators, mobile phone chargers, etc.), and powering 'smart' devices for the 'Internet of Things' [124]. A great many household devices, from kettles to fridges, may soon be connected to the internet, and these will require a small but continual supply of power. It would be impractical for all these appliances to be mains-powered, whilst normal batteries would need changing continually, but a nuclear battery could supply the small power levels required indefinitely.

In terms of CBRN applications, diamond-based nuclear batteries might provide the power for a maintenance-free network of radiation detectors or biosensors distributed around a city or country. They might also provide a back-up power supply for emergency-service equipment, portable detectors, phones, torches, defibrillators, etc.

12.12 Summary

In this short review, we have attempted to think the unthinkable – if a CBRN attack were to succeed, what might be some of the consequences, and how could advanced materials, and in particular, the new technological applications involving CVD

diamond, be used to mitigate the damage? Although we have covered a rather diverse range of threat scenarios, there are still a multitude of applications for diamond which have been omitted. Examples include: diamond NV centres for quantum computing and quantum information processing (unbreakable codes) [125], spintronics and magnetic field sensing [126], thermionic emission from diamond (cheap solar power) [127], high-power electronics [128], field emission displays (radiation-hard displays) [129], radiation-hard optics (windows, lenses, prisms) and laser windows [130], diamond-fibre reinforced composite materials (lightweight, very stiff materials for aerospace) [131, 132], diamond microplasma arrays (large area UV sources, chemical reactors) [133], secondary electron emission detectors (night-vision goggles, photomultiplier tubes) [134], to name but a few. Although CVD diamond technology is only just over 30 years old, the range of applications made possible by this remarkable material is truly astonishing, many of which may hopefully help to make the world a safer place.

References

1. Field JE (1992) The properties of natural and synthetic diamond. Academic, London
2. de Vries RC (1987) Synthesis of diamond under metastable conditions. Annu Rev Mater Sci 17:161–187
3. May PW (2000) Diamond thin films: a 21st century material. Philos Trans R Soc Lond A 358:473–495
4. Onstad E, Clarke D (2018) How man-made diamonds have grown to threaten natural gems. Reuters Business News. Online at: https://uk.reuters.com/article/uk-diamonds-debeers-synthetic/how-man-made-diamonds-have-grown-to-threaten-natural-gems-idUKKCN1OK0NB
5. Ashfold MNR, May PW, Petherbridge JR, Rosser KN, Smith JA, Mankelevich YA, Suetin NV (2001) Unravelling aspects of the gas phase chemistry involved in diamond chemical vapour deposition. Phys Chem Chem Phys 3:3471–3485
6. Tallaire A, Achard J, Silva F, Brinza O, Gicquel A (2013) Growth of large size diamond single crystals by plasma assisted chemical vapour deposition: recent achievements and remaining challenges. C R Phys 14:169–184
7. Dischler CW (ed) (1998) Low-pressure synthetic diamond: manufacturing and applications. Springer, Berlin
8. Butler JE, Sumant AV (2008) The CVD of nanodiamond materials. Chem Vap Depos 14:145–160
9. May PW, Ashfold MNR, Mankelevich YA (2007) Microcrystalline, nanocrystalline and ultrananocrystalline diamond chemical vapor deposition: experiment and modeling of the factors controlling growth rate, nucleation and crystal size. J Appl Phys 101:053115
10. Williams OA (2011) Nanocrystalline diamond. Diam Relat Mater 20:621–640
11. Gruen DM (1999) Nanocrystalline diamond films. Annu Rev Mater Sci 29:211–259
12. Shenderova OA, Gruen DM (2012) Ultrananocrystalline diamond: synthesis, properties and applications. Elsevier, Burlington
13. May PW, Ludlow WJ, Hannaway M, Heard PJ, Smith JA, Rosser KN (2008) Raman and conductivity studies of boron doped microcrystalline diamond, facetted nanocrystalline diamond and cauliflower diamond films. Diam Relat Mater 17:105–117
14. Zhang G, Zeleznik M, Vanacken J, May PW, Moshchalkov VV (2013) Metal-bosonic insulator-superconductor transition in boron-doped granular diamond. Phys Rev Letts 110:077001

15. Macpherson JV (2015) A practical guide to using boron doped diamond in electrochemical research. Phys Chem Chem Phys 17:2935–2949
16. Kalish R (2001) The search for donors in diamond. Diam Relat Mater 10:1749–1755
17. Pinault-Thaury MA, Temgoua S, Gillet R, Bensalah H, Stenger I, Jomard F, Issaoui R, Barjon J (2019) Phosphorus-doped (113) CVD diamond: a breakthrough towards bipolar diamond devices. Appl Phys Lett 14:112106
18. Ashfold MNR, Goss JP, Green BL, May PW, Newton ME, Peaker CV (2019) Nitrogen in diamond. Chem Rev. in press
19. Schirhagl R, Chang K, Loretz M, Degen CL (2014) Nitrogen-vacancy centers in diamond: nanoscale sensors for physics and biology. Ann Rev Phys Chem 65:83–105
20. Gruber A, Dräbenstedt A, Tietz C, Wrachtrup J, von Borczyskowski C (1997) Scanning confocal optical microscopy and magnetic resonance on single defect centers. Science 276:2012–2014
21. Kurtsiefer C, Mayer S, Zarda P, Weinfurter H (2000) Stable solid-state source of single photons. Phys Rev Lett 85:290–293
22. Prawer S, Greentree AD (2008) Diamond for quantum computing. Science 320:1601–1602
23. Dobrovitski VV, Fuchs GD, Falk AL, Santori C, Awschalom DD (2013) Quantum control over single spins in diamond. Ann Rev Cond Matter Phys 4:23–50
24. Jelezko F, Wrachtrup J (2006) Single defect centres in diamond: a review. Phys Status Solidi 203:3207–3225
25. Hamers R (2014) Nuclear proliferation and sustainability: the history of nanodiamonds. Sustain Nano. Available online at: http://sustainable-nano.com/2014/01/23/nuclear-proliferation-sustainability-the-history-of-nanodiamonds/
26. Nunn N, Torelli M, McGuire G, Shenderova O (2017) Nanodiamond: a high impact nanomaterial. Curr Opin Solid State Mater Sci 21:1–9
27. Mochalin VN, Shenderova O, Ho D, Gogotsi Y (2012) The properties and applications of nanodiamonds. Nat Nanotechnol 7:11–23
28. Dolmatov V, Veretennikova M, Marchukov V, Sushchev V (2004) Currently available methods of industrial nanodiamond synthesis. Phys Solid State 46:611–615
29. Krueger A, Ozawa M, Jarre G, Liang Y, Stegk J, Lu L (2007) Deagglomeration and functionalisation of detonation diamond. Phys Status Solidi A 204:2881–2887
30. Barnard AS, Russo SP, Snook IK (2003) Coexistence of bucky diamond with nanodiamond and fullerene carbon phases. Phys Rev B 68:073406
31. Krueger D (2012) Lang, functionality is key: recent progress in the surface modification of nanodiamond. Adv Funct Mater 22:890–906
32. Say JM, van Vreden C, Reilly DJ, Brown LJ, Rabeau JR, King NJC (2011) Luminescent nanodiamonds for biomedical applications. Biophys Rev 3:171–184
33. Fu C-C, Lee H-Y, Chen K, Lim T-S, Wu H-Y, Lin P-K, Wei P-K, Tsao P-H, Chang H-C, Fann W (2007) Characterization and application of single fluorescent nanodiamonds as cellular biomarkers. Proc Natl Acad Sci U S A 104:727–732
34. Barnard AS (2009) Diamond standard in diagnostics: nanodiamond biolabels make their mark. Analyst 134:1751–1764
35. http://www.chm.bris.ac.uk/pt/diamond/othergps.htm
36. https://e6cvd.com
37. http://diamfab.eu/
38. https://ceratonia.com/startseite-ceratonia/
39. http://www.york-bio.com/index.htm
40. http://www.carbodeon.com/
41. http://www.diamond-materials.com/
42. http://www.microdiamant.com/
43. http://www.nanodiamond.com/
44. http://www.nanodiamond.co.il/
45. http://www.thindiamond.com/

46. http://usaplieddiamond.com/
47. http://crystallume.com/
48. https://diamondfoundry.com/
49. http://www.gemesis.com/
50. http://sciodiamond.com/
51. http://www.d-edp.jp/
52. http://nano-carbon.jp/english/category_14/
53. http://www.cn-jingzuan.com/en/products.asp?cataID=139
54. https://www.powerwaywafer.com/Diamond-wafers.html
55. http://www.wec.com.tw/
56. http://ndtcompany.com/
57. http://2atechnologies.com/
58. http://www.diamondelements.com/
59. Rodriguez-Narvaez OM, Peralta-Hernandez JM, Goonetilleke A, Bandala ER (2017) Treatment technologies for emerging contaminants in water: a review. Chem Eng J 323:361–380
60. Manivannan MS, Seehra DA, Tryk A (2002) Fujishima, electrochemical detection of ionic mercury at boron-doped diamond electrodes. Anal Lett 35:355–368
61. Zazoua A, Khedimallah N, Jaffrezic-Renault N (2018) Electrochemical determination of cadmium, lead, and nickel using a polyphenol–polyvinyl chloride—boron-doped diamond electrode. Anal Lett 51:336–347
62. Ivandini TA, Sato R, Makide Y, Fujishima A, Einaga Y (2006) Electrochemical detection of arsenic(III) using iridium-implanted boron-doped diamond electrodes. Anal Chem 78:6291–6298
63. Barek J, Fischer J, Navrátil T, Pecková K, Yosypchuk B, Zima J (2007) Nontraditional electrode materials in environmental analysis of biologically active organic compounds. Electroanalysis 19:2003–2014
64. Wang J, Chen G, Chatrathi MP, Fujishima A, Tryk DA, Shin D (2003) Microchip capillary electrophoresis coupled with a boron-doped diamond electrode-based electrochemical detector. Anal Chem 75:935–939
65. May PW, Clegg M, Silva TA, Zanin H, Fatibello-Filho O, Celorrio V, Fermin DJ, Welch CC, Hazell G, Fisher L, Nobbs A, Su B (2016) Diamond-coated 'black silicon' as a promising material for high-surface-area electrochemical electrodes and antibacterial surfaces. J Mater Chem B 4:5737–5746
66. Rivera-Utrilla J, Sánchez-Polo M, Ferro-García MÁ, Prados-Joya G, Ocampo-Pérez R (2013) Pharmaceuticals as emerging contaminants and their removal from water: a review. Chemosphere 93:1268–1287
67. Li D, Qu J (2009) The progress of catalytic technologies in water purification: a review. J Environ Sci 21:713–719
68. May PW. (2019) Novichok – The notorious nerve agent. Molecule of the month (August 2019). https://doi.org/10.6084/m9.figshare.7177919. Available online at: http://www.chm.bris.ac.uk/motm/novichok/novichokh.htm
69. Thompson T. Police professional (August 28th 2018). Available online at: https://www.policeprofessional.com/news/response-to-novichok-poisoning-cost-30-million/
70. Wilson AD, Baietto M (2009) Applications and advances in electronic-nose technologies. Sensors 9:5099–5148
71. Possas-Abreu M, Ghassemi F, Rousseau L, Scorsone E, Descours E, Lissorgues G (2017) Development of diamond and silicon MEMS sensor arrays with integrated readout for vapor detection. Sensors 17:1163
72. Ivanova EP, Hasan J, Webb HK, Gervinskas G, Juodkazis S, Truong VK, Wu AHF, Lamb RN, Baulin VA, Watson GS, Watson AJ, Mainwaring DE, Crawford RJ (2013) Bactericidal activity of black silicon. Nat Commun 4:2838
73. Hazell G, May PW, Taylor P, Nobbs AH, Welch CC, Su B (2018) Studies of black silicon and black diamond as materials for antibacterial surfaces. Biomater Sci 6:1424–1432

74. Dunseath O, Smith EJW, Al-Jeda T, Smith JA, King S, May PW, Nobbs AH, Hazell G, Welch CC, Su B (2019) Studies of black diamond as an AntiBacterial surface for gram negative bacteria: the interplay between chemical and mechanical bactericidal activity. Sci Rep 9:8815
75. Barriga-Rivera L, Bareket J, Goding UA, Aregueta-Robles GJ (2017) Suaning, visual prosthesis: interfacing stimulating electrodes with retinal neurons to restore vision. Front Neurosci 11:620
76. Nistor PA, May PW (2017) Diamond thin films: giving biomedical applications a new shine. J R Soc Interface 14:20170382
77. Bionic Eye Project. University of Melbourne, Australia. Available online at: https://biomedical.eng.unimelb.edu.au/neuroengineering/bionic-eye/
78. Hadjinicolaou AE, Leung RT, Garrett DJ, Ganesan K, Fox K, Nayagam DA et al (2012) Electrical stimulation of retinal ganglion cells with diamond and the development of an all diamond retinal prosthesis. Biomaterials 33:5812–5820
79. Bergonzo P (2006) DREAMS project – final activity report. Available online at: https://cordis.europa.eu/docs/publications/1235/123542961-6_en.pdf
80. Bergonzo P (2015) Final report summary – NEUROCARE (Neuronal NanoCarbon Interfacing Structures). Available online at: https://cordis.europa.eu/project/rcn/102485/reporting/en
81. Bergonzo P, Bongrain A, Scorsone E, Bendali A, Rousseau L, Lissorgues G, Mailley P, Li Y, Kauffmann T, Goy F, Yvert B, Sahel JA, Picaud S (2011) 3D shaped mechanically flexible diamond microelectrode arrays for eye implant applications: the MEDINAS project. IRBM 32:91–94
82. Braingate: https://www.braingate.org/
83. Thalhammer RJ, Edgington LA, Cingolani R, Schoepfer RB (2010) Jackman, the use of nanodiamond monolayer coatings to promote the formation of functional neuronal networks. Biomaterials 31:2097–2104
84. Nistor PA, May PW, Tamagnini F, Randall AD, Caldwell MA (2015) Long-term culture of pluripotent stem cell derived human neurons on diamond – a substrate for Neurodegeneration research and therapy. Biomaterials 61:139–149
85. Specht CG, Williams OA, Jackman RB, Schoepfer R (2004) Ordered growth of neurons on diamond. Biomaterials 25:4073–4078
86. Fox K, Palamara J, Judge R, Greentree AD (2013) Diamond as a scaffold for bone growth. J Mater Sci Mater Med 24:849–861
87. Aversa R, Petrescu RV, Apicella A, Petrescu FI (2016) Nano-diamond hybrid materials for structural biomedical application. Am J Biochem Biotechnol 13:34–41
88. Kania DR, Landstrass MI, Plano MA, Pan LS, Han S (1993) Diamond radiation detectors. Diam Relat Mater 2:1012–1019
89. Isberg J, Hammersberg J, Johansson E, Wikström T, Twitchen DJ, Whitehead AJ, Coe SE, Scarsbrook GA (2002) High carrier mobility in single-crystal plasma-deposited diamond. Science 297:1670–1672
90. Meier D et al (1999) Proton irradiation of CVD diamond detectors for high-luminosity experiments at the LHC. Nucl Instrum Method Phys Res A 426:173
91. Alianelli L, Sánchez del Rio M, Fox OJL, Korwin-Mikke K (2015) Aberration-free short focal length X-ray lenses. Opt Lett 40:5586–5589
92. Bergonzo P, Tromson D, Mer C, Guizard B, Foulon F, Brambilla A (2001) Particle and radiation detectors based on diamond. Phys Status Solidi A 185:167–181
93. Liu L, Ouyang X, Zhang J, Zhang X, Zhong Y (2014) Polycrystalline CVD diamond detector: fast response and high sensitivity with large area. AIP Adv 4:017114
94. Whitehead AJ, Airey R, Buttar CM, Conway J, Hill G, Ramkumar S, Scarsbrook GA, Sussmann RS, Walker S (2001) CVD diamond for medical dosimetry applications. Nucl Instrum Method Phys Res A 460:20–26
95. Davis JA, Petasecca M, Guatelli S, Lerch MLF, Rosenfeld AB (2019) Evolution of diamond based microdosimetry. J Phys Conf Ser 1154:012007

96. Haas O, Burnham K, Skworcow P, Sahih A (2009) Methods and advanced equipment for simulation and treatment in radiation oncology. Project report, University of Coventry. Available online at: https://pureportal.coventry.ac.uk/en/projects/methods-and-advanced-equipment-for-simulation-and-treatment-in-ra
97. Bucciolini M, Borchi E, Bruzzi M, Casati M, Cirrone P, Cuttone G et al (2005) Diamond dosimetry: outcomes of the CANDIDO and CONRAD INFN projects. Nucl Instrum Method Phys Res A 552:189–196
98. Ravichandran R, Binukumar JP, Al Amri I, Davis CA (2016) Diamond detector in absorbed dose measurements in high-energy linear accelerator photon and electron beams. J Appl Clin Med Phys 17:291–303
99. Messenger GC (2014) Radiation hardening. In: AccessScience. McGraw-Hill Education, Boston
100. Dawes WR Jr (1990) Overview of radiation hardening for semiconductor detectors. Nucl Instrum Method Phys Res A 288:54–61
101. Mazellier JP, Faynot O, Cristoloveanu S, Deleonibus S, Bergonzo P (2008) Integration of diamond in fully-depleted silicon-on-insulator technology as buried insulator: a theoretical analysis. Diam Relat Mater 17:1248–1251
102. Francis D, Faili F, Babic D, Ejeckam F, Nurmikko A, Maris H (2010) Formation and characterization of 4-inch GaN-on-diamond substrates. Diam Relat Mater 19:229–233
103. Aleksov JM, Gobien X, Li JT, Prater Z (2006) Sitar, silicon-on-diamond – an engineered substrate for electronic applications. Diam Relat Mater 15:248–253
104. Ren Z, Zhang J, Zhang J, Zhang C, Chen D, Yang P, Li Y, Hao Y (2017) Polycrystalline diamond MOSFET with MoO_3 gate dielectric and passivation layer. IEEE Electron Dev Lett 38:1302–1304
105. Strobel P, Riedel M, Ristein J, Ley L (2004) Surface transfer doping of diamond. Nature 430:439–441
106. Nebel CE (2007) Surface-conducting diamond. Science 318:1391–1392
107. Crawford KG, Qi D, McGlynn J, Ivanov TG, Shah PB, Weil J, Tallaire A, Ganin AY, Moran DAJ (2018) Thermally stable, high performance transfer doping of diamond using transition metal oxides. Sci Rep 8:3342
108. Kawarada H, Yamada T, Xu D (2017) Durability-enhanced two-dimensional hole gas of C-H diamond surface for complementary power inverter applications. Sci Rep 7:42368
109. Ho D, Wang C-HK, Chow EK-H (2015) Nanodiamonds: the intersection of nanotechnology, drug development, and personalized medicine. Sci Adv 1:e1500439
110. Mochalin VN, Pentecost A, Li X-M, Neitzel I, Nelson M, Wei C, He T, Guo F, Gogotsi Y (2013) Adsorption of drugs on nanodiamond: toward development of a drug delivery platform. Mol Pharm 10:3728–3735
111. Wang X, Low XC, Hou W, Abdullah LN, Toh TB, Rashid MMA, Ho D, Chow EK-H (2014) Epirubicin-adsorbed nanodiamonds kill chemoresistant hepatic cancer stem cells. ACS Nano 8:12151–12166. https://doi.org/10.1021/nn503491e
112. Faklaris O, Garrot D, Joshi V, Boudou J-P, Sauvage T, Curmi PA, Treussart F (2009) Comparison of the photoluminescence properties of semiconductor quantum dots and non-blinking diamond nanoparticles. Observation of the diffusion of diamond nanoparticles in living cells. J Eur Optic Soc 4:090325
113. Claveau S, Bertrand J-R, Treussart F (2018) Fluorescent nanodiamond applications for cellular process sensing and cell tracking. Micromachines 9:247
114. Fairlie M. ITV news report. Chaos and poor communication saw emergency services take 'too long' to help London Bridge terror attack victims. Available online at: https://www.itv.com/news/2019-06-17/emergency-services-hampered-by-communication-problems-in-london-bridge-attack/
115. Meneghesso G, Meneghini M, Zanoni E (2014) Breakdown mechanisms in AlGaN/GaN HEMTs: an overview. Jap J Appl Phys 53:100211

116. Kuball M et al. EPSRC grants: integrated GaN-diamond microwave electronics: from materials, transistors to MMICs. Available online at: https://gow.epsrc.ukri.org/NGBOViewGrant.aspx?GrantRef=EP/P00945X/1
117. May PW, Tsai HY, Wang WN, Smith JA (2006) Deposition of CVD diamond onto GaN. Diam Relat Maters 15:526–530
118. Yates L, Anderson J, Gu X, Lee C, Bai T, Mecklenburg M et al (2018) Low thermal boundary resistance interfaces for GaN-on-diamond devices. ACS Appl Mater Interfaces 10:24302–24309
119. Mandal S, Cuenca J, Massabuau F, Yuan C, Bland H, Pomeroy J et al (2019) Thick adherent diamond films on AlN with low thermal barrier resistance. https://arxiv.org/abs/1907.02481
120. South West Nuclear Hub. The diamond battery. Available online at: https://southwestnuclearhub.ac.uk/research/case-studies/diamond-battery/
121. Delfaure C, Pomorski D, de Sanoit J, Bergonzo P, Saada S (2016) Single crystal CVD diamond membranes for betavoltaic cells. Appl Phys Lett 108:252105
122. Bormashov VS, Troschiev SY, Tarelkin SA, Volkov AP, Teteruk DV, Golovanov AV et al (2018) High power density nuclear battery prototype based on diamond Schottky diodes. Diam Relat Mater 84:41–47
123. Croot G, Wan A, Rowan HD, Andrade JA, Smith NA (2017) Fox, beta radiation enhanced thermionic emission from diamond thin films. Front Mech Eng 3:17
124. Gubbi J, Buyya R, Marusic S, Palaniswami M (2013) Internet of things (IoT): a vision, architectural elements, and future directions. Futur Gener Comput Syst 29:1645–1660
125. Aharonovich I, Greentree AD, Prawer S (2011) Diamond photonics. Nat Photon 5:397–405
126. Markham ML, Dodson JM, Scarsbrook GA, Twitchen DJ, Balasubramanian G, Jelezko F, Wrachtrup J (2011) CVD diamond for spintronics. Diam Relat Mater 20:134–139
127. Koeck FAM, Nemanich RJ, Balasubramaniam Y, Haenen K, Sharp J (2011) Enhanced thermionic energy conversion and thermionic emission from doped diamond films through methane exposure. Diam Relat Mater 20:1229–1233
128. Koizumi S, Umezawa H, Pernot J, Suzuki M (eds) (2018) Power electronics device applications of diamond semiconductors. Woodhead Publishing, San Diego. ISBN:9780081021835
129. Zhou S, Chen K, Cole MT, Li Z, Chen J, Li C, Dai Q (2019) Ultrafast field-emission electron sources based on nanomaterials. Adv Mater:1805845
130. Muhr A, Twitchen D, de Wit H (2018) Diamond meta-surfaces for high power laser applications. In: 2018 IEEE Research and Applications of Photonics in Defense Conference (RAPID). Miramar Beach, FL, pp 1–4
131. Partridge PG, May PW, Rego CA, Ashfold MNR (1994) Potential for diamond fibres and diamond fibre composites. Mater Sci Technol 10:505–512
132. May PW, Portman R, Rosser KN (2005) Thermal conductivity of CVD diamond fibres and diamond fibre reinforced epoxy composites. Diam Relat Mater 14:598–603
133. Truscott BS, Turner C, May PW (2016) High-pressure DC glow discharges in hollow diamond cathodes. Plasma Sources Sci Technol 25:025005
134. Vaz R, May PW, Fox NA, Harwood CJ, Chatterjee V, Smith JA, Horsfield CJ, Lapington JS, Osbourne S (2015) Measurement of the secondary electron emission from CVD diamond films using phosphor screen detectors. JINST 10:P03004

Chapter 13
Fabrication of Diamond AFM Tips for Quantum Sensing

Alexander Schmidt, Tzach Jaffe, Meir Orenstein, Johann Peter Reithmaier, and Cyril Popov

Abstract Diamond attracts an ever-increasing scientific interest not only due to its outstanding properties, but also as host material for the so-called color centers. In particular, the nitrogen-vacancy (NV) center is a promising candidate for applications in quantum sensing on a nanoscale. Incorporating such centers in sharp diamond tips, allows the fabrication of a controllable sensor for magnetic and electric fields. In this regard, we present two different ways to fabricate diamond atomic force microscope (AFM) probes. One approach is based on a bottom-up method, first structuring a silicon substrate by photolithography and anisotropic wet etching and subsequently depositing a nanocrystalline diamond (NCD) film onto the pre-patterned silicon substrate. The second approach is based on electron beam lithography (EBL) and reactive ion etching (RIE), which is also applicable to monocrystalline diamond (MCD). To this end we show our first results in fabricating NV-containing MCD tips by He^+ ion implantation and annealing. We demonstrate the fabrication of bottom-up NCD probes with tip radii in the range of ca. 25 nm, and top-down fabricated NCD AFM probes with tip radii even below 10 nm.

Keywords NV centers · Diamond · AFM tips · Bottom-up techniques · Top-down techniques

A. Schmidt · J. P. Reithmaier · C. Popov (✉)
Institute of Nanostructure Technologies and Analytics, Center for Interdisciplinary Nanostructure Science and Technology, University of Kassel, Kassel, Germany
e-mail: popov@ina.uni-kassel.de

T. Jaffe · M. Orenstein
Andrew & Erna Viterbi Department of Electrical Engineering, Technion – Israel Institute of Technology, Haifa, Israel

P. Petkov et al. (eds.), *Nanoscience and Nanotechnology in Security and Protection against CBRN Threats*, NATO Science for Peace and Security Series B: Physics and Biophysics, https://doi.org/10.1007/978-94-024-2018-0_13

13.1 Introduction

Over the last decade diamond has attracted an ever-increasing scientific interest as platform for components in quantum information technology (QIT), like single photon sources, quantum repeaters, quantum memories, but also in quantum sensing applications. Therefore, distinct quantum mechanical properties of certain defects in the diamond lattice are utilized. The so-called color centers in diamond are based on e.g. vacancies and impurity atoms. One promising candidate among these luminescent defects is the nitrogen-vacancy (NV) center, showing outstanding properties even at room temperature like high photostability, easy electron spin initialization, manipulation and readout, high sensitivity to magnetic and electric fields at the nanoscale and many more. In order to develop new QIT components and devices, those colors centers should be incorporated in photonic structures, allowing for better control of light – matter interactions. Especially in the case of quantum sensing, it is also important to bring the color center in close proximity to the sample surface, which can be accomplished by integrating the color center in the apex of a diamond nanotip. Realizing such a NV-based scanning probe magnetometer is of significant technological and scientific interest, because of its broad spectrum of possible applications [1, 2].

13.2 Nanoscale Sensing with Nitrogen-Vacancy (NV) Centers in Diamond Scanning Probes

The utilization of single NV centers in nanoscale scanning-probe magnetometry was first demonstrated in 2008, showing initial proof-of-principle experiments [3]. The main idea of realizing a NV-based magnetometer is illustrated in Fig. 13.1a, showing a combination of an atomic force microscope (AFM) with a single NV center within the end of a diamond tip and a confocal microscope on top of it. Figure 13.1b exhibits an electron scanning microscope (SEM) image of a fabricated monocrystalline diamond (MCD) cantilever with an integrated nanopillar as a probe, glued on a quartz tip [4].

Optically detected magnetic resonance (ODMR) can be monitored when the NV center is scanned over the surface of a magnetic target by applying a resonant microwave driving field, as illustrated in Fig. 13.1c. An additional scheme of the electronic ground state spin configuration of the NV^- center indicates the spin-dependent fluorescence intensities, which allows for an easy optical read out. Since only the negatively charged state of the NV center possesses the fundamental properties suitable for magnetometry applications, it will be simply denoted as NV center henceforward. In addition to its single photon source characteristics, which can be demonstrated with the photon autocorrelation curve in Fig. 13.1d, the NV center shows high photostability and does not suffer from photobleaching or blinking, which is also an important property for the implementation as a sensor.

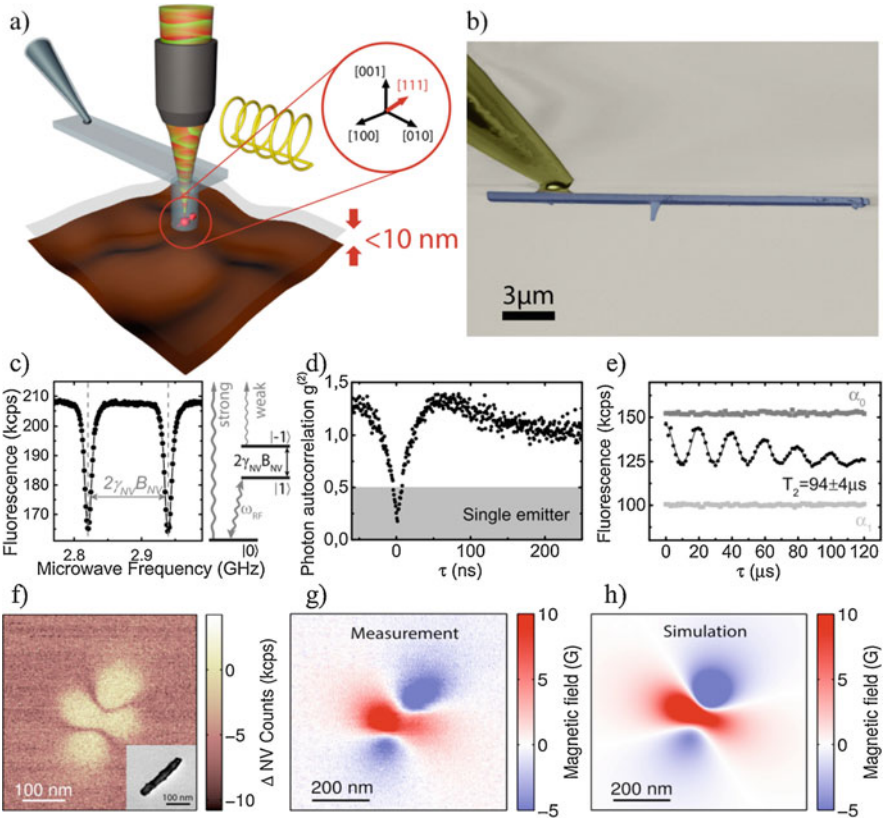

Fig. 13.1 (**a**) Schematic model of a NV-based magnetometer: A single NV center is incorporated close to the end of a monocrystalline diamond nanopillar, combined with a confocal setup on top of it. (**b**) SEM image of the monocrystalline diamond AFM probe glued to the end of a quartz tip. (**c**) Optically detected magnetic resonance and schematic illustration of the electronic ground state spin configuration, showing spin-dependent fluorescence intensities, since the spin triplet ground state $|0\rangle$ exhibits a higher fluorescence rate compared to $|\pm 1\rangle$. (**d**) Photon autocorrelation curve and (**e**) Hahn echo measurement for a single NV at the apex of the AFM probe. (**f**) Iso-magnetic-field image and SEM image (inset) of a single Ni nanorod. (**g**) Full field map of the Ni nanorod and (**h**) simulation of the magnetic field from a point dipole ($m = 3.75 \times 10^{-17}$ A m^{-2}) projected onto the NV axis for an NV center located 80 nm above the dipole. Single images reprinted with permission from [4]. Copyright 2016, AIP Publishing LLC

Furthermore, depending on the coherence time T_2, a sensitivity to ac magnetic fields of up to 4 nT Hz$^{-1/2}$ can be reached [5], which is high enough to image the magnetic field from a single electron spin [6] at room temperature, using a single-NV magnetometer. The coherence time can be derived from Hahn echo measurements, as indicated in Fig. 13.1e [4].

An exemplary application of single NV-magnetometry is depicted in Fig. 13.1f, imaging the stray field of a single Ni nanorod. A SEM image of such a typical nanorod can be seen in the inset of Fig. 13.1f (ca. 24 nm in diameter and 230 nm in

length). Imaging an isomagnetic field, when the MW frequency is fixed to the NV spin transition frequency in the absence of a sample and in the presence of a magnetic field the NV spin transition frequency gets detuned from the MW frequency leading to an increased NV fluorescence, is a fast way to probe magnetic structures and their dynamics on a nanoscale. A completely quantitative magnetic stray field map is depicted in Fig. 13.1g. Therefore, the Zeeman shift needs to be measured, which can be achieved by using a feedback loop to lock the MW frequency to the NV spin transition frequency. A simulation for the expected stray field map for a single dipole is calculated onto the NV axis and presented in Fig. 13.1h.

13.3 Fabrication of Diamond AFM Probes

Many fabrication techniques are used implementing a bottom-up or top-down approach to structure diamond atomic force microscope (AFM) tips. The bottom-up approach usually utilizes selective growth of diamond on a pre-patterned substrate, [7–15] whereas the top-down approach relies on lithographic techniques to structure a hard mask on top of diamond, followed by its transfer into the diamond via reactive ion etching (RIE) [4, 16–21]. Recently, first proof-of-principle experiments have been demonstrated in 2019 by Jaffe et al., using a combination of both approaches. In this hybrid approach, initially nanopillars are structured in a typical top-down manner into monocrystalline diamond which are overgrown afterwards to form nanopyramids along the crystal facets [22].

In our group a bottom-up approach for nanocrystalline diamond (NCD) AFM probes and a top-down approach, which is also applicable on monocrystalline diamond, are currently investigated and will be presented in the following sections. Subsequently, a brief overview of the combined top-down and bottom-up approach for monocrystalline diamond pyramids will be given.

13.3.1 Bottom-Up Fabrication Method

For the fabrication of ready-to-mount diamond AFM probes, we apply a bottom-up method based on photolithography and growth of nanocrystalline diamond (NCD) films via hot filament chemical vapor deposition (HFCVD) [12]. The advantages of this method are the easy and cheap accessibility for mass production of sharp diamond AFM probes with radii in the range of 20–30 nm (approximated from the SEM images). The fabrication process is schematically shown in Fig. 13.2.

Starting from a standard three-inch (100) silicon wafer, covered with a 2 µm thermal silicon dioxide layer, a photoresist (AZ1518) is spin-coated on top of the oxide. Conventional photolithography is used to open a square window (width $d = 20$ µm) into the resist, which defines the basis of the future tip.

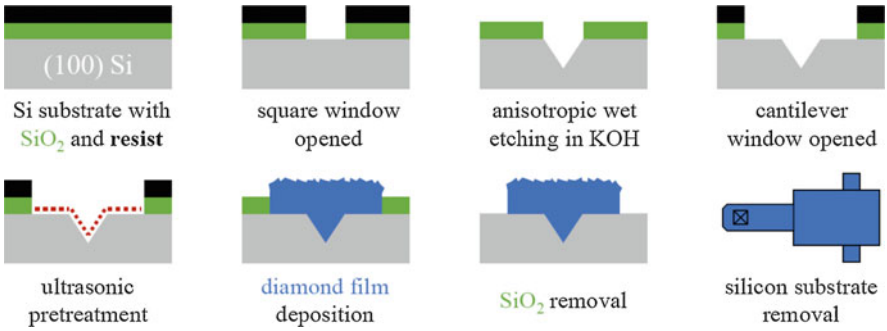

Fig. 13.2 Scheme of the bottom-up fabrication process of NCD AFM probes

Fig. 13.3 SEM micrographs showing the NCD AFM probe (left) and a magnification (right) of the integrated pyramidal tip

This window is transferred into the oxide layer by wet chemical etching in buffered hydrofluoric acid 7:1 ($HF:NH_4F = 12.5:87.5\%$) for 19 min at room temperature. Afterwards, a hollow pyramid with a depth of ca. 0.7 d and a top angle of 70.6° is etched into the opened window by anisotropic wet etching in potassium hydroxide (44% KOH at 85 °C). Subsequently, a window for the future cantilever (150 µm width and 650 µm length) is opened in a second photolithography in a similar way. Then the exposed silicon surface is pretreated ultrasonically in a suspension of diamond powders of different sizes in n-pentane to achieve a nucleation density of ca. 1×10^{10} cm^{-2} according to [23]. The main growth parameters applied in our self-built HFCVD are as following: 1% CH_4 in H_2 with a total gas flow of 505 sccm, a working pressure of 25 mbar, seven tungsten filaments heated to a temperature of ca. 2000 °C and a substrate temperature of 890 °C. Further details and full investigations of the resulting NCD films can be found in the literature [23]. After 8 h deposition the film thickness was around 3 µm and the average crystallite size on the order of 700 nm, exceeding typical length scales of NCD, more approaching to polycrystalline nature. An overview of the final device can be seen in the scanning electron microscope (SEM) images in Fig. 13.3.

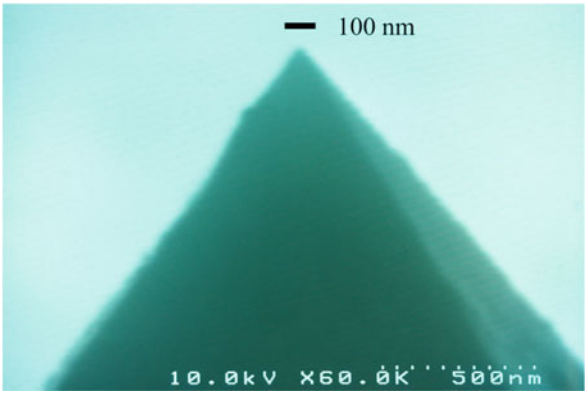

Fig. 13.4 Magnified SEM view of a NCD pyramid (AFM tip)

A magnification of the pyramid is shown in Fig. 13.4, revealing a fully closed diamond film up to the very apex of the tip. The radius of the tip can be approximated from the SEM image to be on the order of 20–30 nm. Further examination and first mechanical measurements of those NCD AFM probes are still under investigation. For easier operability of the cantilevers the film thickness can be increased by longer deposition times and for convenient probe handling a holder chip (e.g. Si holder chips) can be glued on the cantilever basis [11, 14, 20].

In order to incorporate NV centers in the apex of the tip, NV-containing nanocrystallites, which are commercially available, can be used for the ultrasonic pretreatment prior the growth. It has been shown that the pretreatment step has a crucial role in growing fully filled apex pyramids and that a seed directly at the apex mold could influence the pyramid properties [13], i.e. in our case incorporating NV centers in the apex of the tip. Another approach for incorporating NV centers in the apex, which we will investigate, is the addition of nitrogen gas into the reaction chamber at the first moments of the diamond growth.

13.3.2 Top-Down Fabrication Method

For the top-down fabrication of full diamond AFM probes we rely on electron beam lithography (EBL) and reactive ion etching (RIE). Integrating the structures on NCD membranes via anisotropic etching of the Si substrate in KOH, as shown in one of our previous studies [24], makes the AFM probes also easily accessible for further processing and mounting. The process is schematically depicted in Fig. 13.5. Using a Raith EBL system, cantilever structures (3 µm width, 20 µm length, connected by small 500 nm bridges) and a supporting scaffold are defined into a negative e-beam resist (ARN 7520.18), followed by a hard mask deposition (5 nm of titanium as adhesive layer and 200 nm of gold). The structures are opened in a following lift-off process and transferred into the diamond by an inductively coupled O_2 plasma (ICP) RIE step.

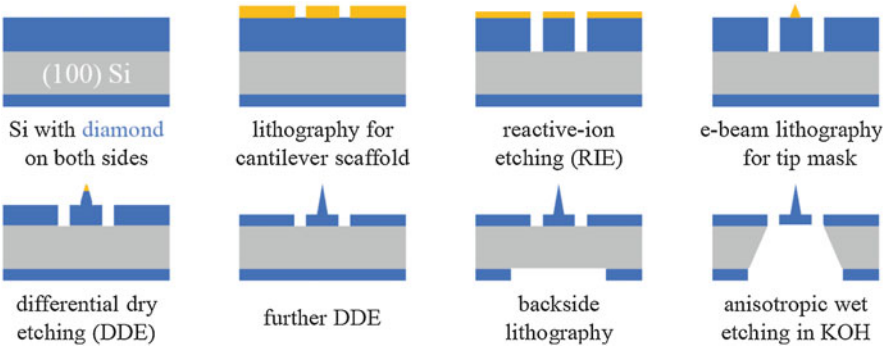

Fig. 13.5 Scheme of the top-down fabrication process of NCD AFM probes

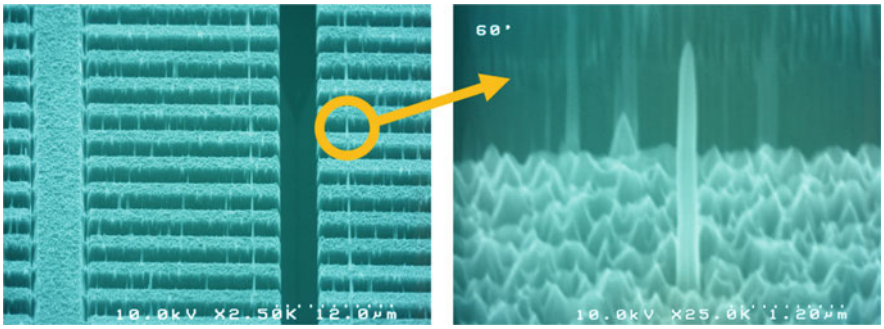

Fig. 13.6 Overview of suspended NCD cantilevers (left) and magnification of a tip (right)

The main parameters of our standard O_2 ICP RIE recipe can be found in [24], which can be summarized as follows: 1000 W ICP power, 200 W RF power, 10 sccm O_2 flow, 5 mTorr working pressure, 30 °C substrate temperature, which was kept constant by He-backing and an etch duration of 25 min with a typical etch rate of ~110 nm min^{-1}. An overview of the resulting cantilever structures can be seen in Fig. 13.6.

Afterwards, a second EBL with a positive e-beam resist (ARP 617.08) is performed in alignment to the first one, in order to structure the future tip on top of the cantilevers. Therefore, small circles with a diameter of 200 nm are defined into the resist. Subsequently, mask deposition, lift-off and RIE as described above lead to the formation of sharp diamond tips on top of the cantilever structures. For this purpose, it is beneficial if the mask shape for the future tip already exhibits a tip-like shape, which will then lead preferentially to the formation of sharp tips rather than pillars. Therefore, typical overexposure of the resist was used to create tip-like mask shapes, as can be seen in Fig. 13.7. Please note that the wave-like shape of the apices of the tips in the right column of Fig. 13.7 appears from SEM distortions due to a charging effect. The images were taken at an acceleration voltage of 10 kV and a

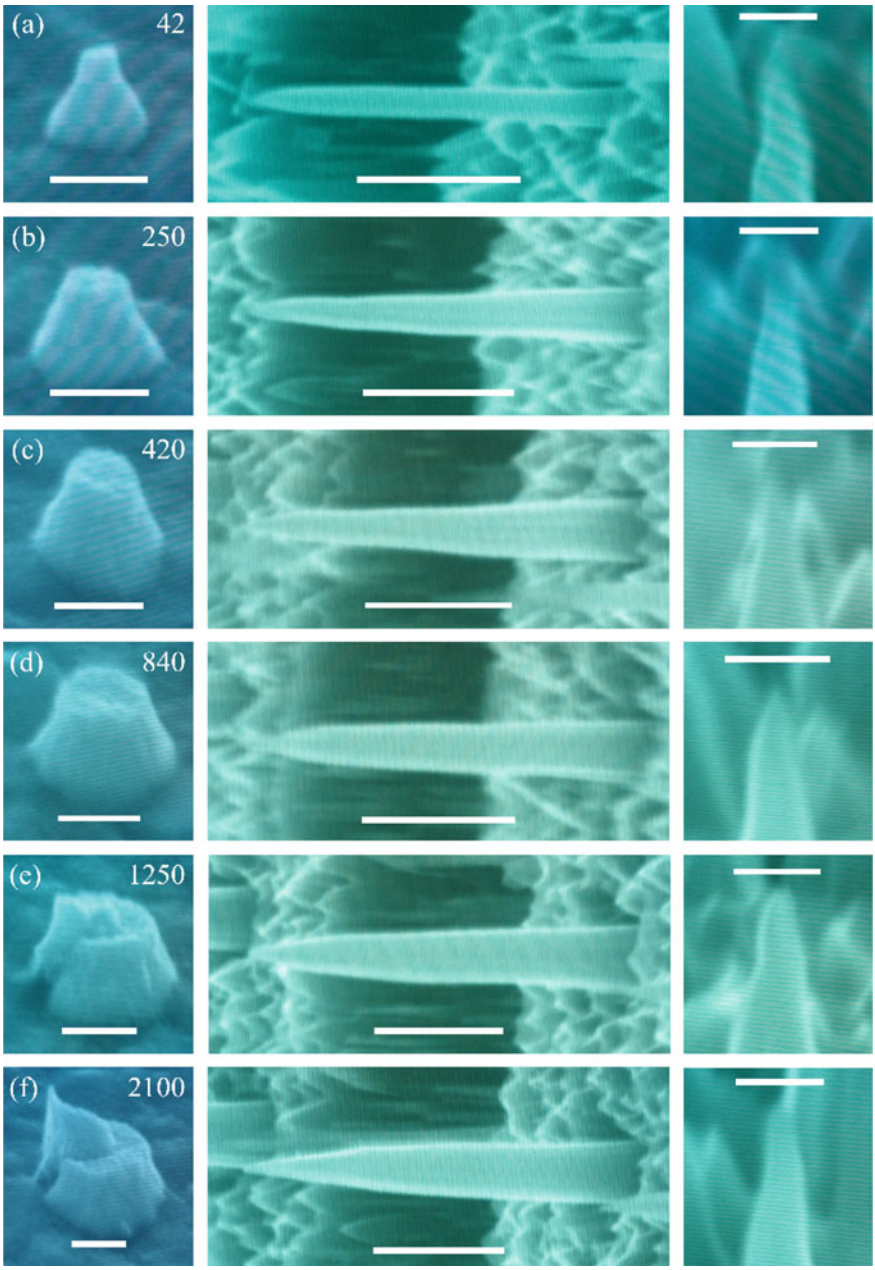

Fig. 13.7 SEM images of the tip mask before etching (first column with indicated exposure dose μC cm^{-2} in EBL, scale bar 300 nm); the resulting tip shape after differential dry etching (middle column, scale bar 1 μm) and a magnification of the apex (right column, scale bar 200 nm)

Fig. 13.8 Magnified SEM image of an overetched NCD AFM tip, revealing slope amplification and sharpening

tilting angle of 65°. The tips are shown directly after differential dry etching (DDE) including the remaining mask material.

The first column exhibits the resulting tip mask shape with increasing exposure doses in the EBL step from top to bottom. Starting from an exposure dose of 42 μC cm^{-2} (Fig. 13.7a), the resulting mask possesses a conical shape and is broadened (ca. 300 nm) compared to the initially defined 200 nm. This effect increases with increasing the exposure dose as revealed by the SEM images, reaching the mask depicted in Fig. 13.7f, which was defined with an exposure dose of 2100 μC cm^{-2}. The second column in Fig. 13.7 shows the resulting diamond tip after 11 min of ICP RIE with the parameters described above. Such an etching process purposely makes use of mask erosion and removal in order to dry etch differentially the mask material and the diamond beneath it, as illustrated in Fig. 13.5 [17]. This leads to the formation of long and sharp diamond tips, either with completely etched off tip masks or residual mask material on top of the tip, which will be important for a future application for the incorporation of shallow NV centers.

It is possible to fabricate diamond AFM probes with tips of various diameters, ranging from ca. 200–400 nm (measured at the half of the original tip length). The tips are shown without any further processing, so possible mask material may remain on top of the tips, which can be indicated by the slight contrast difference at the apex of the tip (e.g. Figure 13.7c). This will be advantageous for further processing of the tips, because usually shallow NV centers are created by ion implantation and annealing before structuring [4, 16]. Consequently, the initial surface is kept intact, which ensures the presence of the implanted NV centers. Furthermore, it is possible to fine-tune the tip sharpness via the etch duration and the exposure dose in EBL. Additionally, other parameters can be adjusted and fine-tuned for tip shape and size, like the ICP and RF powers, as shown in the literature [18]. Figure 13.8 shows slope amplification and tip sharpening by further dry etching of a tip and therefore the ultimate limit of this fabrication approach.

After the fabrication of the AFM probes, the backside of the silicon wafer is structured as shown in Fig. 13.5. The NCD film with the AFM probes is suspended in air by anisotropic wet etching (44% KOH at 85 °C) of the silicon wafer in a

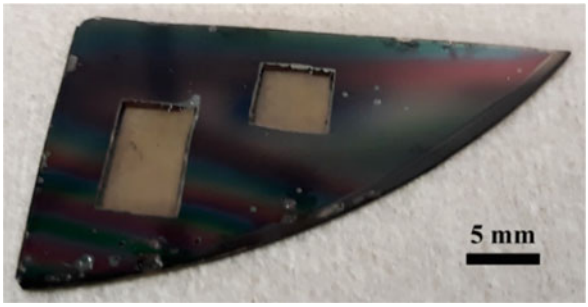

Fig. 13.9 Photo of an exemplary sample with nanostructured suspended NCD membranes

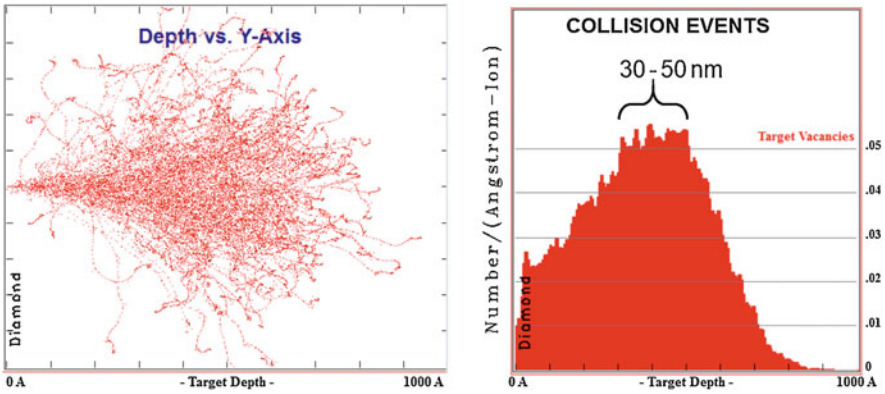

Fig. 13.10 SRIM simulations for the creation of vacancies by He^+ ion implantation, showing a typical depth profile for the implanted ion tracks (left) and a bar chart (right) with the statistical formation of vacancies along the depth profile

defined window below the structures. Further details can be found in Ref. [24]. A typical sample with two opened membranes, which contain the structured AFM probe areas, is shown in Fig. 13.9. Integrating the AFM probes on membranes makes them easily accessible for further processing and mounting. They can be transferred to an AFM head by ion assisted metal deposition and focused ion beam (FIB) milling [16] or with a UV curable glue applied through a quartz micropipette and micromanipulators under ambient conditions [4].

Another advantage of the shown fabrication method is the possibility to transfer it as well on monocrystalline diamond (MCD) samples. Therefore, the main steps of the process can be transferred directly on MCD. To that end we show our initial results in regard to fabrication of NV-containing MCD tips. The fabrication method has been applied on a typical nitrogen-rich Ib MCD sample. In order to create vacancies, He^+ ion implantation with an acceleration voltage of 10 kV and a dose of 10^{14} cm^{-2} has been performed before structuring of the tips. Thus, shallow vacancies should be formed by the crystal damage during the implantation process, which can be demonstrated with the SRIM simulations in Fig. 13.10. During an

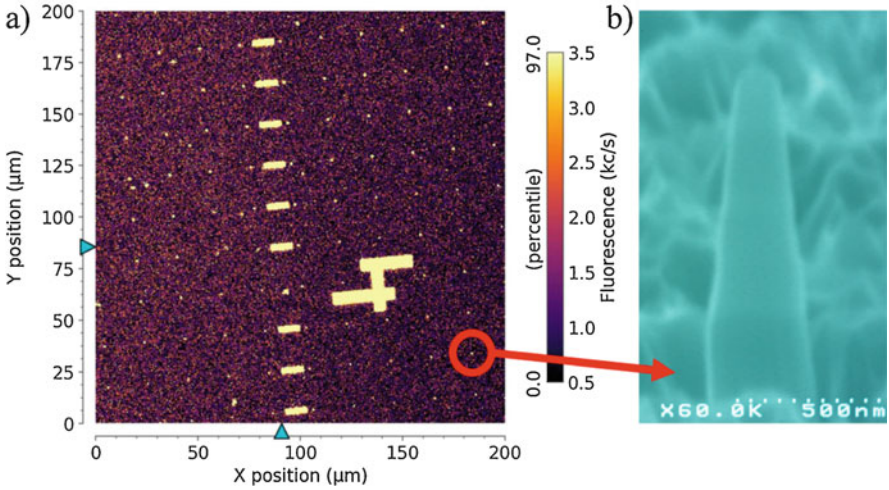

Fig. 13.11 (**a**) Fluorescence mapping of an array of MCD AFM tips; (**b**) exemplary SEM image of a tip from the sample (10 kV acceleration voltage, 75° tilting angle)

annealing step, vacancies will able to migrate to the inherently present nitrogen impurities and form NV centers [25–27].

A fluorescence map of the resulting structures after a top-down fabrication process, as described above, can be seen in Fig. 13.11a, which shows well-aligned bright spots from the diamond tips and some bright marker structures for better orientation.

Since the tips can be clearly distinguished from the background signal and preliminary photoluminescence measurements confirm a peak at the zero-phonon line of the NV center at 637 nm, we assume the successful formation of NV centers within a depth of 80 nm and a maximal density around 30–50 nm according to the SRIM simulations in Fig. 13.10. Usually very shallow NV centers ($\leq$10 nm from the surface) are desired for magnetometry applications, since the NV-to-sample distance is one of the most important factors for high quality measurements. Thus, the depth profile of NV centers in our case may be even advantageous, because the tips can be subjected to further DDE for sharpening and slope amplification, which would also further remove some material from the surface. This would not only lead to sharper tips, but also possibly to NV centers closer to the surface, if one does not overetch the tips. As shown before, different parameters in the fabrication process have been used to fabricate various tip shapes and diameters. One exemplary tip can be seen in Fig. 13.11b. Further processing of those NV-containing tips is still under investigations. Compared to our fabrication method for NCD AFM probes shown in Fig. 13.5, the last step integrating the nanostructured areas on a membrane for better accessibility can be achieved by thinning down the MCD plates from the unstructured backside with extensive RIE [4, 16].

General routes to incorporate NV centers in such top-down fabrication methods, beside the shown He^+ ion implantation in nitrogen-rich Ib diamond, would be nitrogen ion implantation in high purity IIa diamond, also followed by an annealing step. This process can either be performed before structuring of the tips [4, 16, 28] or afterwards [28].

13.3.3 Combined Top-Down and Bottom-Up Fabrication Method

This method is capable of producing monocrystalline diamond pyramids with tip radii on the order of 10 nm, as demonstrated in [29]. One major advantage of this fabrication technique could be the high quality of the overgrown monocrystalline diamond [22], which is usually degraded by crystal damage in a top-down RIE approach. Additionally, the process of overgrowth allows for incorporation of color centers in situ during the growth, which has been demonstrated for silicon-vacancy centers in our former study [22]. In a similar way NV centers could also be incorporated in situ during the overgrowth, e.g. as delta-doped layer close to the surface. Compared to the inherent crystal damage during typical ion implantation for the creation of color centers, this could also be advantageous leading to high crystal quality up to the very apex of the tip.

This combined top-down and bottom-up fabrication method applies typical EBL and RIE to structure nanopillars into monocrystalline diamond. Subsequently, the nanopillars are subjected to chemical vapor deposition (CVD) to allow diamond growth along the crystal facets. The fabrication is schematically summarized in Fig. 13.12 (left). A typical overgrown nanopillar after CVD overgrowth can be seen in Fig. 13.12 (right), showing a faceted nanopyramid at the top. Since the growth rates of the different crystal planes not only depend on the growth conditions

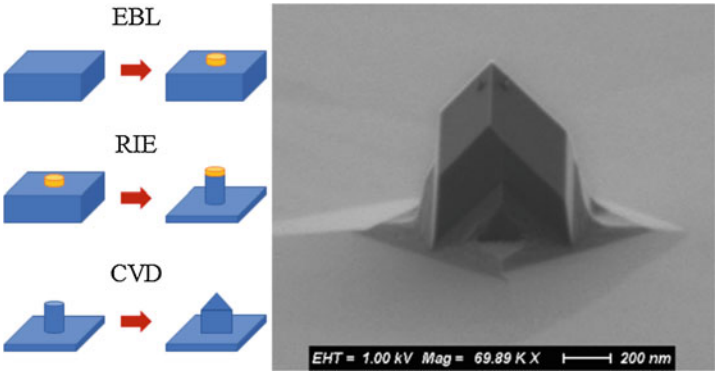

Fig. 13.12 Scheme of the combined top-down & bottom-up fabrication method (left) and an exemplary SEM image of a resulting, faceted monocrystalline diamond nanotip (right)

(e.g. methane concentration and substrate temperature) but also on the substrate orientation, different shaped diamond nanostructures can be formed. Further information regarding the overgrowth process and the quality of the overgrown diamond can be found in Ref. [22]. Integrating such a monocrystalline diamond nanopyramid as a NV-based AFM probe can be achieved by the methods mentioned in the sections above. In a recent publication we have demonstrated a novel approach for delta-doping resulting in a deterministic and nanometer-thin layer of negatively charged NV centers in diamond [30]. The pristine quality of diamond was preserved after the incorporation of NV delta layer with the highest reported nitrogen content. The exhibited possibility for NV topographic patterning and the large measured ODMR contrast can pave the pathway for the realization of NV-based nano-magnetometers with very high sensitivity [30].

13.4 Summary

We presented three different methods for the fabrication of diamond AFM probes with potential routes of incorporating NV centers in the apices of the tips. Such devices are promising candidates for quantum sensing magnetic fields at a nanoscale. The bottom-up approach for NCD AFM probes is based on conventional photolithography and anisotropic wet etching of the Si substrate in KOH to create inverted pyramid molds into silicon wafers, which are subjected afterwards to HFCVD diamond growth. Relying on EBL and RIE, we demonstrate a top-down fabrication approach suitable for both NCD and monocrystalline diamond. We implemented such NCD AFM probes on suspended NCD membrane windows for better accessibility via anisotropic wet etching of Si substrate in KOH. In the case of monocrystalline diamond (MCD), we demonstrate our first results regarding NV-containing tips via He^+ ion implantation in nitrogen-rich Ib diamond and annealing. The fabricated MCD AFM tips can be integrated also on membranes by extensive RIE from the backside. Estimated from the SEM images, our bottom-up fabricated NCD tips show radii in the range of 20–30 nm and in the case of the top-down approach 10–40 nm, which can be even further decreased by fine-tuning the process parameters, leading to tip radii in the range of ca. 5 nm. Finally, we described a hybrid top-down & bottom-up approach, which combines the advantages of both methods.

Acknowledgments The authors would like to thank the group of Prof. Dr. A. Ehresmann (University of Kassel) for the He^+ ion implantation and Christian Osterkamp from the group of Prof. Dr. F. Jelezko (University of Ulm, Institute for Quantum Optics) for the annealing and preliminary optical characterizations of the MCD sample. This work was supported by the Volkswagen Stiftung under the project “Quantum coins and nano sensors” (Az. 91001).

References

1. Rondin L, Tetienne J-P, Hingant T, Roch J-F, Maletinsky P, Jacques V (2014) Magnetometry with nitrogen-vacancy defects in diamond. Rep Prog Phys 77:056503
2. Bernardi E, Nelz R, Sonusen S, Neu E (2017) Nanoscale sensing using point defects in single-crystal diamond: recent progress on nitrogen vacancy center-based sensors. Crystals 7(5):124
3. Balasubramanian G, Chan IY, Kolesov R, Al-Hmoud M, Tisler J, Shin C, Kim C, Wojcik A, Hemmer PR, Krueger A, Hanke T, Leitenstorfer A, Bratschitsch R, Jelezko F (2008) Nanoscale imaging magnetometry with diamond spins under ambient conditions. Nature 455:648–651
4. Appel P, Neu E, Ganzhorn M, Barfuss A, Batzer M, Gratz M, Tschöpe A, Maletinsky P (2016) Fabrication of all diamond scanning probes for nanoscale magnetometry. Rev Sci Instrum 87:063703
5. Balasubramanian G, Neumann P, Twitchen D, Markham M, Kolesov R, Mizuochi N, Isoya J, Achard J, Beck J, Tissler J, Jacques V, Hemmer PR, Jelezko F (2009) Ultralong spin coherence time in isotopically engineered diamond. Nat Mater 8:383–387
6. Grinolds MS, Hong PMS, Luan L, Lukin MD, Walsworth RL, Yacoby A (2013) Nanoscale magnetic imaging of a single electron spin under ambient conditions. Nat Phys 9:215–219
7. Aharonovich I, Lee JC, Magyar AP, Bracher DO, Hu EL (2013) Bottom-up engineering of diamond micro- and nano-structures. Laser Photonics Rev 7:61–65
8. Kölling S, Hantschel T, Vandervorst W (2007) Conductive diamond probes with electroplated holder chips. Microelectron Eng 84:1178–1181
9. Hantschel T, Niedermann P, Trenkler T, Vandervorst W (2000) Highly conductive diamond probes for scanning spreading resistance microscopy. Appl Phys Lett 76(12):1603
10. Park J, Lee S, So B, Jung Y, Kawasegi N, Morita N, Lee D (2007) J Mater Process Technol 187–188:321–325
11. Mihalcea C, Scholz W, Malave A, Albert D, Kulisch W, Oesterschulze E (1998) Fabrication of monolithic diamond probes for scanning probe microscopy applications. Appl Phys A Mater Sci Process 66:87–90
12. Oesterschulze E, Scholz W, Mihalcea C, Albert D, Sobisch B, Kulisch W (1997) Fabrication of small diamond tips for scanning probe microscopy application. Appl Phys Lett 70(4):435–437
13. Tsigkourakos M, Hantschel T, Arstila K, Vandervorst W (2013) Diamond nano-particle seeding for tip moulding application. Diam Relat Mater 35:14–18
14. Hantschel T, Tsigkourakos M, Zha L, Nuytten T, Paredis K, Majeed B, Vandervorst W (2016) Diamond scanning probes with sub-nanometer resolution for advanced nanoelectronics device characterization. Microelectron Eng 159:46–50
15. Obraztsov N, Kopylov PG, Loginov BA, Dolganov MA, Ismagilov RR (2010) Single crystal diamond tips for scanning probe microscopy. Rev Sci Instrum 81:013703
16. Maletinsky P, Hong S, Grinolds MS, Hausmann B, Lukin MD, Walsworth RL, Loncar M, Yacoby A (2012) A robust scanning diamond sensor for nanoscale imaging with single nitrogen-vacancy centres. Nat Nanotechnol 7:320–324
17. Moldovan N, Divan R, Zeng H, Carlisle JA (2009) Nanofabrication of sharp diamond tips by e-beam lithography and inductively coupled plasma reactive ion etching. J Vac Sci Technol B 27(6):3125–3131
18. Mehedi H-A, Mille V, Achard J, Brinza O, Gicquel A (2014) Effect of the process parameters of inductively coupled plasma reactive ion etching on the fabrication of diamond nanotips. Phys Status Solidi A 211(10):2343–2346
19. Uetsuka H, Yamada T, Shikata S (2008) ICP etching of polycrystalline diamonds: fabrication of diamond nano-tips for AFM cantilevers. Diam Relat Mater 17:728–731
20. Arstila K, Hantschel T, Demeulemeester C, Moussa A, Vandervorst W (2009) Microfabricated diamond tip for nanoprobing. Microelectron Eng 86:1222–1225
21. Wang Z, Gu C, Li J, Cui Z (2005) A novel method for making high aspect ratio solid diamond tips. Microelectron Eng 78–79:353–358

22. Jaffe T, Felgen N, Gal L, Kornblum L, Reithmaier JP, Popov C, Orenstein M (2019) Deterministic arrays of epitaxially grown diamond nanopyramids with embedded silicon-vacancy centers. Adv Opt Mater 7(2):1800715
23. Kulisch W, Petkov C, Petkov E, Popov C, Gibson PN, Veres M, Merz R, Merz B, Reithmaier JP (2012) Low temperature growth of nanocrystalline and ultrananocrystalline diamond films: a comparison. Phys Status Solidi A 209(9):1664–1674
24. Schmidt A, Bernardoff J, Singer K, Reithmaier JP, Popov C (2019) Fabrication of nanopillars on nanocrystalline diamond membranes for the incorporation of color centers. Phys Status Solidi A 216(21):1900233
25. de Oliveira FF, Momenzadeh SA, Antonov D, Fedder H, Denisenko A, Wrachtrup J (2016) On the efficiency of combined ion implantation for the creation of near-surface nitrogen-vacancy centers in diamond. Phys Status Solidi A 213(8):2044–2050
26. Kleinsasser EE, Stanfield MM, Banks JKQ, Zhu Z, Li W-D, Acosta VM, Watanabe H, Itoh KM, Fu K-MC (2016) High density nitrogen-vacancy sensing surface created via He^{+} ion implantation of ^{12}C diamond. Appl Phys Lett 108(20):202401
27. Schwartz J, Michaelide P, Weis CD, Schenkel T (2011) In situ optimization of co-implantation and substrate temperature conditions for nitrogen-vacancy center formation in single-crystal diamonds. New J Phys 13:035022
28. Hausmann BJM, Babinec TM, Choy JT, Hodges JS, Hong S, Bulu I, Yacoby A, Lukin MD, Lončar M (2011) Single-color centers implanted in diamond nanostructures. New J Phys 13:045004
29. Batzer M, Shields B, Neu E, Widmann C, Giese C, Nebel C, Maletinsky P (2019) Single crystal diamond pyramids for applications in nanoscale quantum sensing. arXiv:1910.10737 [cond-mat.mes-hall]
30. Jaffe T, Attrash M, Kuntumalla MK, Akhvlediani R, Michaelson S, Gal L, Felgen N, Fischer M, Reithmaier JP, Popov C, Hoffman A, Orenstein M (2020) Novel ultra localized and dense nitrogen delta-doping in diamond for advanced quantum sensing. Nano Lett. https://doi.org/10.1021/acs.nanolett.9b05243

Chapter 14
Nanostructured Biochar: Production Pathways and Applications

Abderrahman Mellalou, Abdelkader Outzourhit, and Abdelaziz Bacaoui

Abstract Hydrochar/biochar represents the solid yield of the hydrothermal carbonization and the pyrolysis processes of biomass. It is a nanostructured carbon-rich material with a high specific energy and density, high hydrophobicity and high friability. This coal-like material might appear like a very low-tech product. However, its physicochemical properties make it potentially useful in variety of fields such as energy storage, in environmental field as a sustainable way to mitigate anthropogenic CO_2 by CO_2 sorption and sequestration, in waste-water pollution remediation, as soil amendment, as a precursor for activated carbon, in the advanced material field as a primary material for nano-structured material generation (nanocomposites), in building insulation and bioenergy production. Biochar has H/O and O/C ratios similar to those of coal and a comparable caloric value with low ash and oxygen content. The production of hydrochar/biochar using either hydrothermal carbonization or pyrolysis techniques will be fully described. The potential applications of biochar and hydrochar will be presented and discussed.

Keywords Biochar · Hydrochar · Biomass · Pyrolysis · Hydrothermal carbonization · Biofuel · Supercapacitors · Environmental applications

14.1 Introduction

Biomass and its derivates represent a sustainable alternative to fossil fuels [1, 2]. The valorization of this form of energy requires adequate conversion technologies and techniques, in order to benefit the most from this environmentally friendly renewable feedstock. Several processing methods exist, such as biological (fermentation,

A. Mellalou (✉) · A. Outzourhit
LNEE, Department of Physics, FSSM, Cadi Ayyad University, Marrakech, Morocco

A. Bacaoui
LCA, Department of Chemistry, FSSM, Cadi Ayyad University, Marrakech, Morocco

P. Petkov et al. (eds.), *Nanoscience and Nanotechnology in Security and Protection against CBRN Threats*, NATO Science for Peace and Security Series B: Physics and Biophysics, https://doi.org/10.1007/978-94-024-2018-0_14

esterification and anaerobic digestion), thermochemical (pyrolysis, liquefaction and gasification) and hydrothermal (hydrothermal carbonization, hydrothermal liquefaction and hydrothermal gasification) conversion technologies. Biomass can be processed into an array of valuable products via these conversion methods.

Thermochemical conversion process received a lot of attention in the last decade as an alternative to treat and upgrade biomass waste to produce valuable products [3]. Biomass wastes such as sewage sludge, municipal, industrial and pharmaceutical wastes present a threat to the environment and have a dangerous impact on soil and life with all its forms if they are not well stored or treated [2]. Heavy metals, pathogens and a range of toxic compound represent the biggest part of biomass wastes composition. Thermochemical conversion is recommended as the appropriate treatment methods due to the benefits of heat used to kill and dissociate the toxic compound; by far it is an environmentally friendly and safe method of biomass waste conversion [3].

Pyrolysis and hydrothermal carbonization, among the other thermochemical conversion technologies, have attracted a great interest as a valuable biomass waste management methods, due to their yield in biochar and hydrochar respectively [1–3]. These products might seem to be low-tech components; however, their physicochemical and structural properties enhance their potential use in a variety of fields. Different studies have comprehensively characterized biochar and hydrochar produced from diverse raw biomass feeds under different process conditions [4–6].

14.2 Pyrolysis

Pyrolysis represents one of the most studied technologies in the last decades and it is a promising conversion method to reduce pollution and recover materials from biomass waste [3, 7–9]. It is one of the efficient and effective techniques to get energy from biomass in the form of charcoal. Pyrolysis refers to the deterioration of biomass waste and the cleavage of its chemical bonds in an inert medium, free from oxygen or with an oxygen percentage that avoids biomass combustion, under temperatures ranging from 400 °C to 1200 °C [5, 8–11]. Oxygen free atmosphere has the advantage of heating the biomass to a high temperature over its limit of thermal stability resulting in valuable compounds and solid residues of high stability [9]. A large number of reactions taking place during the pyrolysis conversion have been identified either in series or in parallel, such as depolymerization, dehydration, decarboxylation, aromatization isomerization and charring [9, 12].

The temperature, the heating rate, the pressure, the residence time and the heating route determine the types and the modes of pyrolysis [8]. Depending on those parameters the pyrolysis can be categorized into 5 types or modes: slow pyrolysis, intermediate pyrolysis, fast or flash pyrolysis, microwave pyrolysis and vacuum pyrolysis [8, 9]. Each one of these modes leads to different product distribution.

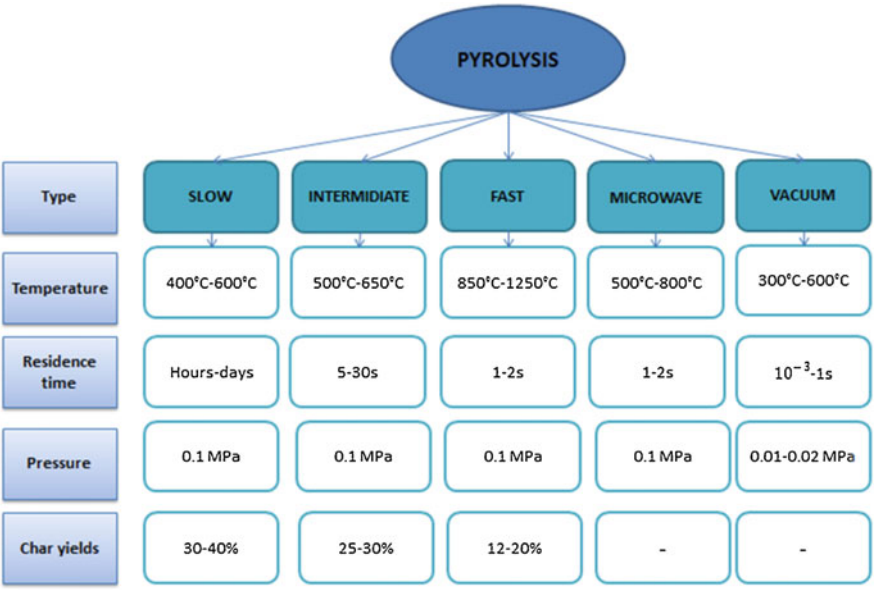

Fig. 14.1 Types of pyrolysis, their operation conditions and biochar yield

Figure 14.1 illustrates the different types of pyrolysis, their operation conditions and biochar yield.

The pyrolysis has the advantage to be optimized to get the desired products. Slow pyrolysis comes in the first place for high biochar production. It is characterized by its slow heating rates and long residence times which provide the adequate and suitable environment for secondary reactions to complete and as a consequence maximize the biochar yield [8, 9]. This biochar is a carbonaceous compound with a high potential for application in a variety of fields. Its hydrogen and oxygen contents are reduced by dehydration and decarboxylation, respectively, which enhances the formation of a porous structure on its surface that can be used as adsorbent [13]. Moreover soil treatment, water improvement, water decontamination and carbon sequestration represent the most and powerful applications of this biochar [13–16].

14.3 Hydrothermal Carbonization (HTC)

Hydrothermal carbonization (HTC) is a thermochemical process for high moisture biomass treatment and upgrade. It converts the biomass waste into viable products dedicated to several applications. HTC is carried out in a temperature range between 180 °C and 350 °C [2, 5, 6]. During this process, the biomass is totally submerged in water and heated under pressure of 2–6 MPa for a period varying between 5 min and

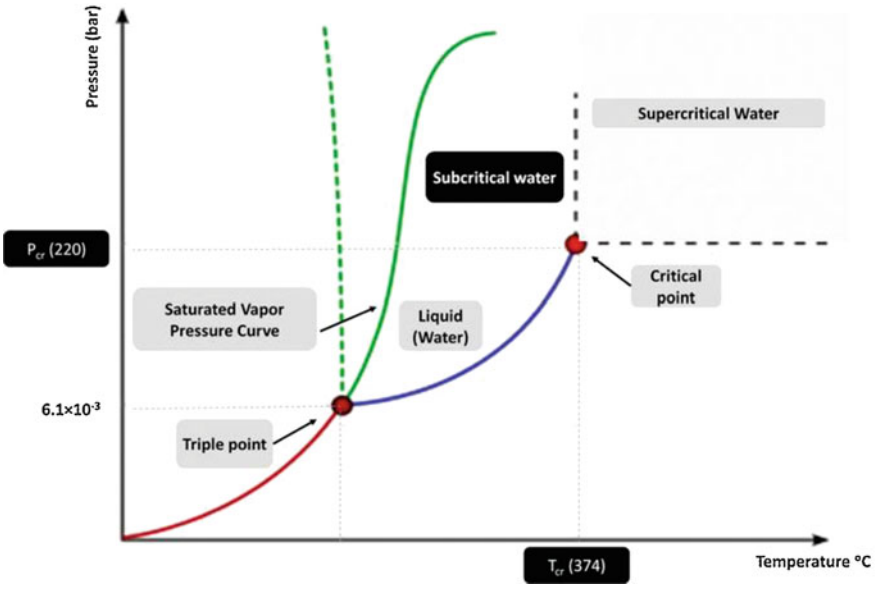

Fig. 14.2 Water phase diagram highlighting its subcritical and supercritical region

240 min [2, 5]. The main product of HTC is a solid substance named hydrochar. It also produces liquid (water-soluble) and gaseous (mainly CO_2) by-products. The hydrothermal carbonization is an efficient conversion method, capable of converting up to 80% of the raw biomass into hydrochar [5].

The hydrothermal carbonization has several advantages, starting by processing in aqueous medium, which makes it suitable for biomass with high moisture content, without need of pre-drying, which consequently reduces the thermal cost of the overall process [1, 2]. This option offers the possibility of processing a large variety of biomass feedstocks of different types and characteristics. The HTC process takes place in the subcritical region as shown in Fig. 14.2. Subcritical water refers to liquid water with a temperature between 100 °C and 374 °C and a pressure higher than the corresponding saturation pressure [17]. In this region, the properties of water (miscibility, density, dielectric constant, ionic product, viscosity and diffusion coefficients) change in a significant positive way, therefore enhancing the conversion process and increasing its efficiency [17].

Several reactions occur during the hydrothermal carbonization process, the detailed nature of the reaction pathways and the kinetics are not yet fully understood. Based on several studies [6, 12, 15, 18–20], it can be stated that hydrochar can be obtained by three main reaction pathways: (1) direct solid-solid conversion of biomass waste through the reactions of hydrolysis, dehydration, decarboxylation, devolatilization and condensation; (2) polymerization of dissolved by-products of the initial feedstocks to a variety of polyfuranes; (3) direct carbonization of lignin and formation of aromatic stable structures.

14.4 Properties of Hydrochar and Biochar

The characteristics of biochar and hydrochar differ from each other. Biochar is produced at temperatures ranging between 400–600 °C in an inert medium, whereas the hydrochar production occurs in an aqueous medium at moderate temperatures (180–250 °C). Gascó et al. [10] performed both hydrothermal carbonization and pyrolysis process of pig manure, and characterized the char produced. They found that the pyrolysis led to biochar characterized by high thermal stability and high amount of aromatic structures, whereas the hydrochar contained more aliphatic structures. The oxygen content of the hydrochar was the highest, and its surface had micropores with size ranging from 200 to 30,000 nm. The ash content of the biochar is much higher than that of the hydrochar, due to the processing medium. The majority of the ash during the HTC process is dissolved in water, while during the pyrolysis the ash remains in the feedstock. The higher heating values (HHVs) of both hydrochar and biochar were found to be almost similar with value of 12.03 and 9.98 MJ/kg, respectively. On the other hand, Al Afif et al. [12] found that the HHV value of biochar produced by pyrolysis process of cotton stalks was 5.845 MJ/kg, while Zhu et al. [21] found that the HHV of hydrochar of cotton stalks was in the range from 19.66 to 25.68 MJ/kg. Table 14.1 illustrates the characteristics of biochar and hydrochar produced from various raw biomass types under different process parameters.

Table 14.1 Properties of biochar and hydrochar obtained from different initial biomass feeds under distinct process parameters

Conversion technics	Raw biomass	Processing conditions	Biochar/Hydrochar	References
Pyrolysis	Pig manure	600 °C	High content of aromatic structures High thermal stability High ash content	[10]
	Apple tree branches	400–600 °C	High surface area Large pore volume	[11]
Hydrothermal carbonization	Pig manure	200–240 °C 2 h	High amount of aliphatic structures leading to more labile carbon structures Low porous structure	[10]
	Lignocellulosic and non-lignocellulosic	300 °C 5 °C/min 30 min	High aromatization degree High hydrophobicity Low H/C and O/C ratios Good combustion quality	[18]
	Waste eucalyptus bark	220–300 °C 2 h	Low oxygen containing functional groups Low H/C and O/C ratios HHV of hydrochar is in the range of 20.2–29.2 MJ/kg	[20]

14.5 Potential Applications of Hydrochar

14.5.1 Energy Field

14.5.1.1 Solid Biofuel

Biomass waste is a valuable and renewable source of energy. Its physicochemical properties make it suitable for direct use as a fuel. However, its ash, metal and moisture contents limit such applications. HTC and pyrolysis process lower these contents, and further increase the fixed carbon, decrease the oxygen and hydrogen contents, and as a consequence produce a char with upgraded properties that is suitable for direct combustion. Kim et al. [4] performed thermogravimetric analysis to characterize the hydrochar produced from cellulose. The fuel properties of the cellulose have been enhanced by increasing the fixed carbon value, and by the increase of the HHV of the hydrochar produced. Moreover, the external structure of the hydrochar was full of fissures, which facilitates its combustion. He et al. [22] evaluated the fuel characteristics and the combustion behavior of hydrochar produced by the conversion of sewage sludge. The fuel ratio (fixed carbon/volatile matter), which ranks the hydrochar as an alternative to coal, has increased. Moreover, the ignition temperature has increased, which minimizes the explosion of the hydrochar during combustion. Furthermore, the maximum combustion temperature also increased, thus improving the efficiency of the biofuel.

In summary, both hydrochar and biochar are characterized by low O/C and H/C ratios, low volatile matter and high heating value similar to that of coal, a high fixed carbon value and a low metal and inorganic compound contents. These properties fit exactly the requirements of a highly efficient, environmental, eco-friendly source of energy, which makes both materials very competitive with coal and fossil fuels.

14.5.1.2 Building Insulation

Biochar has been found to be an eco-friendly building material and an environmental solution to pollution problems caused by fossil fuels. This nanostructured material is considered as a novel bio-compound, which can be mixed with other products and be useful for building applications. Several studies have shown that the mechanical strength of the biochar is increased by about 20% compared to the raw biomass. Yang et al. [23] tried to produce an eco-friendly material with improved thermal and mechanical performances by mixing biochar and red clay. In this study, the authors found that the biochar integration lowers the thermal conductivity of the composite. Moreover, the compressive strength of the mixture increased. Biochar is also a cheaper filler material which has good effect on the properties of bio-composite materials, due to its high carbon content and relatively high surface area, allowing the matrix to transmit readily load to the reinforcement. Dahal et al. [24] studied the effect of biochar integration in glass fiber on the fire retardancy. They reported that

the use of biochar as a filler in glass fiber had significant impact on its stiffness and fire retardancy properties. Moreover, the thermal stability of the composite has increased with higher biochar contents. The acoustic and thermal properties of standard concrete modified by biochar were studied by Cuthberson et al. [25]. They found that the biochar addition creates pore networks within the concrete, which increases the sound adsorption coefficient of the concrete in the range of 200–2000 Hz. Furthermore, the thermal conductivity of the concrete decreased upon addition of biochar.

14.5.1.3 Supercapacitor

Capacitor applications represent also one of the other potential uses of biochar and hydrochar. Due to the number of functional groups, their wettability and the presence of high surface area with porous structure, hydrochar and biochar are attractive carbon materials for fabricating sustainable and eco-friendly electrodes. Moreover, these properties enhance their capacitance and energy density and improve their pseudo-capacitance. Pontiroli et al. [19] used super-activated biochar derived from purity litter, and evaluated its performance as electrode material for supercapacitors. The authors reported that this porous compound allows to reach high specific capacitance up to 229 F/g, and to supply high current density of 10 A/g without the need of using any conducting additive. In another study [26], activated carbon derived from Cucumis melo fruit peel showed almost the same properties in supercapacitors, with an excellent specific capacitance value of 404 F/g at 1 A/g and a good cycle life performance, as the specific capacitance decreased only 9% after 8000 charge and discharge cycles. On the other hand, hydrochar was evaluated as a novel anode material for supercapacitors. Ding et al. [27] combined hydrochar with nickel and studied its performances. The degree of graphitization of hydrochar has dramatically changed due to the fact that the nickel acted as a graphitization catalyst. Moreover, the specific capacity of the couple hydrochar/nickel has significantly increased by 149% revealing a value of 174.5 F/g.

14.5.2 Environmental and Agricultural Field

14.5.2.1 Soil Amendment, Remediation and Amelioration

Several studies have introduced biochar and hydrochar as multi-functional soil amendments. They have great impact on both the physical and the chemical properties of the soil. They are also a sustainable way to mitigate anthropogenic CO_2 and are used for long-term carbon storage. Heikkinen et al. [28] studied the impact of both biochar and hydrochar on the clay soil aggregate stability. The hydrochar had a significant impact on the wettability of the clay soil. Its high hydrophobicity reduces the wetting rate and aggregate slaking of the soil, thus reducing the soil erosion and

maintaining its porous structure. The soil remediation is achieved by the adsorption property of the biochar, which is provided by its morphological structure, rich in micropores, its pH, specific surface area, active functional groups, organic carbon and mineral contents. The adsorption mechanism of heavy metals by the biochar relies on the surface complexation, electrostatic interaction, precipitation, cation exchange, chemical reduction and electrostatic attraction. Incorporating biochar as a high porous material not only improves the soil quality but can also boost the remediation efficiency of contaminated soil, thus allowing land reclamation. Zeng et al. [29] evaluated the effect of the biochar on the remediation efficiency and the reduction of the ecological risk in the wetland soils. The results showed that the biochar integration reduces the bioavailability and the mobility of Cd, Cu, Zn and Pb in the soil. Moreover, it improved the soil microbial biomass. On the other hand, Gasco et al. [30] evaluated the effect of the combination of biochar and phytoextraction by *Brassica napus* on the remediation of mining soils in Spain. They found that the mixture of those two materials reduced the amount of As, Cu, Co, Cr, Se and Pb in the soil, thus improving the soil quality.

In addition to amendment and remediation, biochar and hydrochar can also increase the soil fertility. Both hydrochar and biochar are rich in carbon and nutrients. Bento et al. [15] evaluated the nutrient and carbon release from hydrochar derived from sugarcane bagasse and vinasse, and its impact on the soil fertility and quality. Their results clearly revealed the role of the soil type on the behavior of hydrochar, and also the impact of hydrochar on the soil. The addition of 4% hydrochar in the soil provided the greatest release of nutrients and organic carbon. Moreover, sandy soils tend to release high concentration of nutrients, while clay soils tend to retain more nutrients and organic carbon. On the other hand, Abel et al. [14] studied the impact of hydrochar and biochar on water retention characteristics and on the wettability of sand soils. The addition of biochar and hydrochar leads to a decrease of the bulk density and an increase of the total porosity. In addition, the variation of available water capacity (AWC) depends on the soil characteristics. The AWC increases for all sandy soils, while it does not change for highly humic sands. Furthermore, the biochar and hydrochar particle size had impacts on the pore size distribution of the soil matrix.

14.5.2.2 Water and Waste Water Treatment

Hydrochar and biochar have been tested for their ability to adsorb a range of organic and inorganic pollutants, such as dyes, pesticides, pharmaceutical compounds and pathogens. Several parameters are involved during the waste water treatment with char. The physicochemical properties of biochar and hydrochar, their surface structure, pore size, in addition to the type and characteristics of the targeted pollutants, play a fundamental role in waste water decontamination. Activated biochar was the subject of a study on the removal of phenols, petroleum based compounds and polyaromatic hydrocarbons (PAHs) from contaminated liquids [16]. The activated biochar is able to remove carcinogenic PAHs, gasoline and diesel from water. This

offers an effective way to treat and clean up water from petroleum spills, thus preventing the pollution of the environment. Jiang et al. [13] modified corn straw hydrochar (HC) with H_3PO_4 (H_3PO_4-HC) and with polyethyleneimine (PEI) (PEI-HC) and tested their abilities to adsorb Pb (II) from aqueous solution. Both materials demonstrated high performance for Pb (II) adsorption with an adsorption capacity of 353.4 mg/g and 214.0 mg/g for H_3PO_4-HC and PEI-HC respectively, which are higher than the initial adsorption capacity of the original hydrochar (32.67 mg/g).

14.6 Conclusion

In summary, hydrochar, biochar and their derivatives are promising materials which have a huge potential of use in a variety of fields. From the above discussed applications, it is important to know the targeted field for biochar and hydrochar use. Moreover, upgrade and modification of their physicochemical characteristics and surface structure may be required for an efficient and effective implementation.

References

1. Nizamuddina BS, Balochb HA, Griffina GJ, Mubarakc NM, Bhuttob AW, Abrod R, Mazarib SA, Ali BSA, Si S (2017) An overview of effect of process parameters on hydrothermal carbonization of biomass. Renew Sust Energ Rev 73(December 2015):1289–1299
2. Wang T, Zhai Y, Zhu Y, Li C, Zeng G (2018) A review of the hydrothermal carbonization of biomass waste for hydrochar formation: process conditions, fundamentals, and physicochemical properties. Renew Sust Energ Rev 90(March):223–247
3. Kambo HS, Dutta A (2015) A comparative review of biochar and hydrochar in terms of production, physico-chemical properties and applications. Renew Sust Energ Rev 45:359–378
4. Kim D, Yoshikawa K, Park KY (2015) Characteristics of biochar obtained by hydrothermal carbonization of cellulose for renewable energy. Energies 8(12):14040–14048
5. Fang J, Zhan L, Ok YS, Gao B (2018) Minireview of potential applications of hydrochar derived from hydrothermal carbonization of biomass. J Ind Eng Chem 57:15–21
6. Missaoui A, Bostyn S, Belandria V, Cagnon B, Sarh B, Gökalp I (2017) Hydrothermal carbonization of dried olive pomace: energy potential and process performances. J Anal Appl Pyrolysis 128(April):281–290
7. Zhang S, Hu B, Zhang L, Xiong Y (2016) Effects of torrefaction on yield and quality of pyrolysis char and its application on preparation of activated carbon. J Anal Appl Pyrolysis 119:217–223
8. Tripathi M, Sahu JN, Ganesan P (2016) Effect of process parameters on production of biochar from biomass waste through pyrolysis: a review. Renew Sust Energ Rev 55:467–481
9. Akhtar J, Saidina N, Wood P (2012) A review on operating parameters for optimum liquid oil yield in biomass pyrolysis. Renew Sust Energ Rev 16(7):5101–5109
10. Gascó G, Paz-Ferreiro J, Álvarez ML, Saa A, Méndez A (2018) Biochars and hydrochars prepared by pyrolysis and hydrothermal carbonisation of pig manure. Waste Manag 79:395–403

11. Wang X-D, Zhao S-X, Ta N (2017) Effect of temperature on the structural and physicochemical properties of biochar with apple tree branches as feedstock material. Energies 10(9):1293
12. Al Afif R, Anayah SS, Pfeifer C (2019) Batch pyrolysis of cotton stalks for evaluation of biochar energy potential. Renew Energy 116:9
13. Jiang Q, Xie W, Han S, Wang Y, Zhang Y (2019) Enhanced adsorption of Pb(II) onto modified hydrochar by polyethyleneimine or H3PO4: an analysis of surface property and interface mechanism. Colloids Surf A Physicochem Eng Asp 583(August):123962
14. Abel S, Peters A, Trinks S, Schonsky H, Facklam M, Wessolek G (2013) Impact of biochar and hydrochar addition on water retention and water repellency of sandy soil. Geoderma 202–203:183–191
15. Bento LR, Castro AJR, Moreira AB, Ferreira OP, Bisinoti MC, Melo CA (2019) Release of nutrients and organic carbon in different soil types from hydrochar obtained using sugarcane bagasse and vinasse. Geoderma 334(June 2017):24–32
16. Sullivan GL, Prigmore RM, Knight P, Godfrey AR (2019) Activated carbon biochar from municipal waste as a sorptive agent for the removal of polyaromatic hydrocarbons (PAHs), phenols and petroleum based compounds in contaminated liquids. J Environ Manag 251 (August):109551
17. Möller M, Nilges P, Harnisch F, Schröder U (2011) Subcritical water as reaction environment: fundamentals of hydrothermal biomass transformation. ChemSusChem 4(5):566–579
18. Zhuang CWX, Zhanb H, Songa Y, Hed C, Huanga Y, Yina X (2019) Insights into the evolution of chemical structures in lignocellulose and non-lignocellulose biowastes during hydrothermal carbonization (HTC). Fuel 236(July 2018):960–974
19. Pontirolia MRD, Scaravonatia S, Magnania G, Fornasinia L, Bersania D, Bertonib G, Milanesed C, Girellad A, Ridie F, Verucchif R, Mantovanig L, Malcevschig A (2019) Super-activated biochar from poultry litter for high-performance supercapacitors. Microporous Mesoporous Mater 285(February):161–169
20. Pin Gao GX, Zhou Y, Menga F, Zhang Y, Liu Z, Zhang W (2016) Preparation and characterization of hydrochar from waste eucalyptus bark by hydrothermal carbonization. Energy 97:238–245
21. Zhu CZG, Yangb L, Gaob Y, Xua J, Chena H, Zhua Y, Wangb Y, Liaoa C, Lub C (2019) Characterization and pelletization of cotton stalk hydrochar from HTC and combustion kinetics of hydrochar pellets by TGA. Fuel 244(January):479–491
22. He C, Giannis A, Wang JY (2013) Conversion of sewage sludge to clean solid fuel using hydrothermal carbonization: hydrochar fuel characteristics and combustion behavior. Appl Energy 111:257–266
23. Yang S, Wi S, Lee J, Lee H, Kim S (2019) Biochar-red clay composites for energy efficiency as eco-friendly building materials: thermal and mechanical performance. J Hazard Mater 373 (March):844–855
24. Dahal RK, Acharya B, Saha G, Bissessur R, Dutta A, Farooque A (2019) Biochar as a filler in glassfiber reinforced composites: experimental study of thermal and mechanical properties. Compos Part B Eng 175(March):107169
25. Cuthbertson D, Berardi U, Briens C, Berruti F (2019) Biochar from residual biomass as a concrete filler for improved thermal and acoustic properties. Biomass Bioenergy 120(November 2018):77–83
26. Elaiyappillaia PMJE, Srinivasana R, Johnboscod Y, Devakumarb P, Murugesanc K, Kesavanb K (2019) Low cost activated carbon derived from Cucumis melo fruit peel for electrochemical supercapacitor application. Appl Surf Sci 486(December 2018):527–538
27. Ding L, Wang Z, Li Y, Du Y, Liu H, Guo Y (2012) A novel hydrochar and nickel composite for the electrochemical supercapacitor electrode material. Mater Lett 74:111–114
28. Heikkinena KRJ, Keskinena R, Soinnea H, Hyväluomaa J, Nikamaa J, Wikbergb H, Källib A, Siipolab V, Melkiorc T, Dupontd C, Camparguee M, Larssonf SH, Hannulag M (2019) Possibilities to improve soil aggregate stability using biochars derived from various biomasses

through slow pyrolysis, hydrothermal carbonization, or torrefaction. Geoderma 344 (March):40–49
29. Zeng YHG, Wu H, Liang J, Guo S, Huang L, Xu P, Liu Y, Yuana Y, Hea X (2015) Efficiency of biochar and compost (or composting) combined amendments for reducing Cd, Cu, Zn and Pb bioavailability, mobility and ecological risk in wetland soil. RSC Adv 5(44):34541–34548
30. Gascó G, Álvarez ML, Paz-Ferreiro J, Méndez A (2019) Combining phytoextraction by Brassica napus and biochar amendment for the remediation of a mining soil in Riotinto (Spain). Chemosphere 231:562–570

Part VI
Nanowires and Nanoparticles

Chapter 15
Nanowires for NEMS Switches

Jelena Kosmaca, Liga Jasulaneca, Raimonds Meija, Raitis Sondors, and Donats Erts

Abstract Nanoelectromechanical systems (NEMS) are a promising novel technology for operation in extreme conditions (e.g. high temperature and radiation levels), where complementary semiconductor technology devices might fail due to electronic instability. An example for a NEMS device is a nanowire-based switch, which employs mechanical deflection of a nanowire to open and close an electrical circuit. To date, assembly and operation of individual nanowire based NEMS switches have been successfully demonstrated at laboratory level, but their further technological development remains a challenge. This chapter gives an insight into the current advances in applications of nanowires for NEMS switches. Synthesis, electrical and mechanical tests of the nanowires, their assembly in nanodevices, investigation of nanocontacts and optimization of switching parameters are discussed. Particular attention is devoted to characterization of mechanical properties of various semiconductor, such as germanium (Ge), bismuth selenide (Bi_2Se_3) and copper oxide (CuO) nanowires, and their operation as NEMS switches.

Keywords Nanowires · Nanodevice · NEMS · Switch · Mechanical resonance · *In-Situ* SEM

15.1 Introduction

In NEMS nanodevices, flexible and electrically conductive nanomaterials act as sensors and transducers. In contrast to semiconductor devices which operate purely electrically, a NEMS utilizes electrical and mechanical functionality of the material. This can give an advantage for operation under extreme conditions [1, 2]. For example, reliable NEMS switch operation at temperatures up to 500 °C has been demonstrated [3]. Potentially, NEMS devices would be able to operate until physical

J. Kosmaca (✉) · L. Jasulaneca · R. Meija · R. Sondors · D. Erts
Institute of Chemical Physics, University of Latvia, Riga, Latvia
e-mail: jelena.kosmaca@lu.lv

P. Petkov et al. (eds.), *Nanoscience and Nanotechnology in Security and Protection against CBRN Threats*, NATO Science for Peace and Security Series B: Physics and Biophysics, https://doi.org/10.1007/978-94-024-2018-0_15

breakdown of the active element at the melting temperature. Thanks to nearly infinite OFF-state resistance, NEMS switches can offer better energy efficiency than the electronic transistors. However, several challenges must be addressed to bring NEMS technology to industrial level.

The switch performance is usually determined by its switching speed, range of operational voltage and current, reliability and durability. Operational characteristics can be significantly affected by surface wear of contacting materials, permanent deformation of the switching element, dielectric breakdown or irreversible closure of the switch due to adhesion. The role of adhesion at the nanoscale becomes crucial and significantly affects the operation of NEMS compared to MEMS. The outlined challenges define the relevant material properties necessary for the NEMS switches – low surface energy, high Young's modulus and electrical conductivity [2].

Electrical and mechanical properties of the synthesized nanowires should be characterized prior their application in devices. They may significantly differ from that of the bulk material, exhibit size-dependence influenced by changes in crystalline structure and surface effects [4–6], therefore characterization of individual nanowires is advantageous.

Due to ultra-small dimensions tests on individual nanowires and fabrication of NEMS switches present a challenge. Experimental investigation on NEMS switches utilizes either device microfabrication and testing on chip, or measurements by *in-situ* electron microscopy [7]. The latter enables real-time observation of the nanostructure response to physical stimuli, monitoring evolution of the nanocontacts and evaluation of the forces acting on the nanowire during switching. This is advantageous for fundamental research on specific parts and simulation of processes in a NEMS, where the construction of the complete device is not required.

The first application of one-dimensional nanostructures as nanoelectromechanical switching elements was demonstrated for carbon nanotube nanorelays [8]. However, the use of carbon nanotubes in NEMS switches can be limited due to instable electrical properties and mechanical brittleness [1]. Semiconductor Ge nanowires were found to be more reliable than the carbon nanotubes due to the higher mechanical stability, while their lower conductivity provided opportunity to implement high-voltage devices [9]. Several semiconductor materials, such as Si, SiC, Ge, GeSn, Bi_2Se_3, CuO were found to fit the requirements for NEMS.

15.2 Nanowire Synthesis and Characterization

The synthesis of nanowires usually follows either a top-down or a bottom-up approach. Generally, the bottom-up nanowire growth outperforms the top-down fabrication (e.g. lithography) in terms of costs of materials and ability to produce crystalline vertically aligned nanostructures in large quantities. The yield and morphology of the nanowires can be controlled during the synthesis by selecting the substrates and growth parameters (e.g. pressure, temperature, gas flow rate). For example, CuO nanowires (Fig. 15.1a) can be grown by simply heating a copper

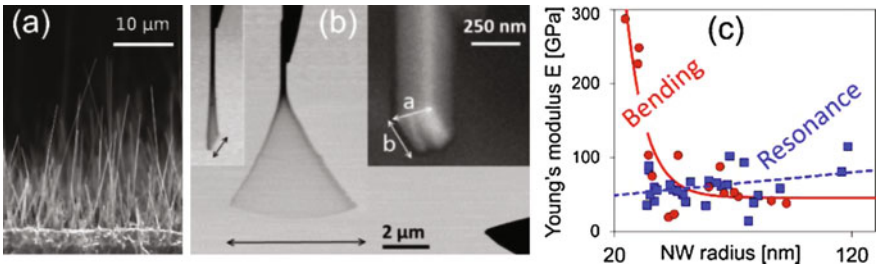

Fig. 15.1 (**a**) Electron microscopy image of CuO nanowires grown on foil substrate; (**b**) A single-clamped nanowire, its cross-section and resonance in two directions (arrows). Adapted from Ref. 15 with permission from Beilstein Journal of Nanotechnology; (**c**) Size-dependent Young's moduli of GeSn nanowires obtained from bending and resonance tests. Adapted from Ref. [6] with permission from The Royal Society of Chemistry

substrate in air. The yield of Bi_2Se_3 nanowires synthesized by physical vapor deposition from Bi and Se precursors can be enhanced by choosing a specific substrate [10]. The composition and properties of Ge nanowires can be modified by incorporation of Sn atoms during the synthesis, yielding alloy GeSn nanowires with a direct bandgap, highly crystalline structure and good mechanical properties [6, 11].

Mechanical resonance and three-point bending tests are commonly used measurement approaches suitable for characterization of individual nanowires. Nanowire vibrations can be excited by a combined AC + DC electric field and detected visually by *in-situ* electron microscopy (Fig. 15.1b). Resonance is observed, when the excitation frequency matches the natural frequency of the nanowire: $\omega = (\beta/L)^2(EI/\rho A)^{1/2}$, where β is a constant determined by the resonance mode and boundary conditions, L the length, E the Young's modulus, I the moment of inertia of the nanowire cross-sectional area A, and ρ the mass density of the nanowire material. Calculations of E from the resonance frequency have been successfully applied for the characterization of Ge nanowires with Young's moduli of about hundred GPa, which is close to that of the bulk material [12–14].

Investigation of nanowire resonance modes can also be used to characterize their morphology. Nanowires with rectangular cross-sections have split resonance modes, and increased amplitude vibrations can be observed in two directions at different frequencies [15, 16]. The ratio of these frequencies is close to the ratio of the width and thickness of the cross-section. Comparison of the two resonant frequencies of Bi_2Se_3 nanowires was used to distinguish rectangular cross-section ones from nanowires with cut-outs [16]. This is especially convenient for quality control of free-standing nanowires during their assembly in NEMS switches.

Three-point bending tests use nanowire response to a point load, which can be performed in atomic force microscopy setup. The Young's moduli extracted from stress-strain curves of CuO nanowires suggested their suitability for NEMS, although they showed dependence on nanowire crystallinity and surface effects [5].

Size-dependent Young's moduli were observed for GeSn nanowires, which were measured by a combination of *in-situ* SEM resonance and AFM three-point bending tests. The size dependence was prominent for nanowires with radii smaller than 30 nm; moreover, the results from resonance and bending showed two opposite trends (Fig. 15.1c). This outlines the importance of choosing the measurement approach and the consideration of nanowire boundary conditions [6].

For electrical tests, individual nanowires are either assembled *in-situ* using nanomanipulations or aligned on an insulating substrate with metallic electrodes for two-point and four-point measurements. The nanowires may exhibit relatively high contact resistances, which is evident in two-point measurements [17]. The electrical resistances of the nanowires extracted from current-voltage characteristics typically span from hundreds kΩ up to GΩ, corresponding to nanowire material conductivities of 0.01–100 S/m. Nanowires with high conductivities can be used as low-voltage signal transmitters, while low conductivities provide potential for application in high-voltage devices. It is important to note that the electrical properties of semiconductor nanomaterials are influenced by the ambient conditions such as temperature, pressure, humidity, etc.

15.3 Investigation of Nanowire Based NEMS Switches

Common configurations of NEMS switches use single-clamped and double-clamped nanowires [1, 2]. A schematic of a NEMS switch with a single-clamped nanowire, in which a nanowire is attached to one electrode and positioned above another electrode is shown in Fig. 15.2a. When voltage is applied between the nanowire in OFF state and the bottom electrode, potential difference results in an attractive electrostatic force, balanced by an elastic restoring force of the nanowire.

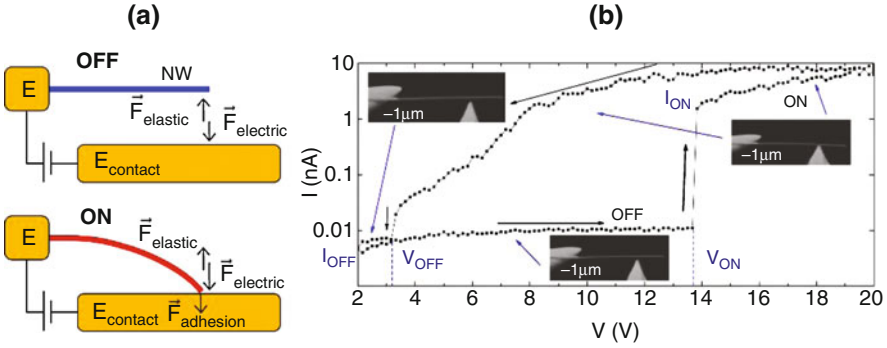

Fig. 15.2 (**a**) Schematics of a nanowire based NEMS switch being in OFF and ON states; (**b**) Current in the NEMS switch circuit vs. applied voltage and scanning electron microscopy images of a nanowire switching. Reprinted and adapted from Ref. [20] with permission from IOP Publishing 2019

When a critical voltage is reached, and $F_{electric} > F_{elastic}$, the nanowire deflects and comes into contact with the electrode (Fig. 15.2a). In the ON state this leads to a sharp increase of the current from I_{OFF} up to I_{ON} (Fig. 15.2b). The elastic force is balanced by the attractive adhesion and electric forces that hold the NEMS contact. The nanowire switching to the OFF state occurs, when the restoring forces overcome the attractive forces, e.g. when the voltage is diminished to V_{OFF}. Consequently, the circuit current drops down. Usually this V_{OFF} voltage value is lower than V_{ON} due to adhesion force in the contact. If adhesion at the nanowire-electrode interface exceeds the restoring force, the nanowire remains in contact with the electrode even with no voltage applied between the electrodes. This case refers to non-volatile operation switches. One way to achieve switch operation in reversible ON-OFF regime, is to increase the distance between the nanowire and electrode in OFF state. Consequently, the elastic force of the nanowire would increase. On the other hand, this would also lead to increase of V_{ON} voltage, which requires nanowires to be electrically stable.

Therefore, the demonstrated Ge-nanowire based NEMS devices operated at relatively high V_{ON} voltages of 14–37 V in reversible ON-OFF regime [9]. Switching of molybdenum-sulfur-iodine nanowires with similar sizes and mechanical properties was performed in the same range [18]. However, high operation voltages are disadvantageous due to increased power in the device. For example, Joule heating caused by high current densities in nanowire-electrode interface lead to increased adhesion and nanocontact stiffening [13]. In this case, the adhesion force in the nanocontact may be opposed by high amplitude vibrations of the nanowires. Precise alignment of the electrodes and careful adjustment of DC amplitude and AC frequency were used to induce resonant oscillations of the nanowire. The voltage levels required to operate the NEMS switch dynamically by electrostatically induced resonance were about 10 times smaller compared to equivalent static-only switches [19].

Resonance assisted switching may also be used to decrease the V_{ON} voltage and control of switching direction, as demonstrated recently for GeSn and Bi_2Se_3 nanowire few-terminal devices [20]. Monitoring the resonance frequencies of the nanowires in NEMS switches can be used also for accurate sensing of changes in the nanocontacts [13, 14].

Practical applications of nanoelectromechanical switching of the nanowires is not limited to single-nanowire NEMS switches. For example, gradual nanoelectromechanical switching in arrays of Bi_2Se_3 nanowires was used to tune up the number of functional interconnections between flat electrodes in a sandwich-like optoelectronic device and consequently to increase its efficiency [17]. Further, functionality of nanowires can be combined with the NEMS switching towards hybrid devices, such as nano-opto-electromechanical systems (NOEMS).

15.4 Conclusions

Semiconductor nanowires are promising candidates for NEMS switch active elements as their properties are tunable during synthesis. The electrical and mechanical behavior of bottom-up synthesized semiconductor (Ge, GeSn, Bi_2Se_3, and CuO) nanowires demonstrate their suitability for applications in NEMS devices. The operational parameters of the demonstrated nanowire based NEMS switches can be further improved using electrically induced resonant vibrations. For scalability and integration, current technological development is aimed at investigation of nanocontacts and optimization of switching parameters, as well as fabrication of devices on chip.

Acknowledgments The authors acknowledge the support from European Regional Development Fund (project no. 1.1.1.1/16/A/256, "Creation of nanoelectromechanical switches").

References

1. Loh OY, Espinosa HD (2012) Nanoelectromechanical contact switches. Nat Nanotechnol 7:283
2. Jasulaneca L, Kosmaca J, Meija R, Andzane J, Erts D (2018) Electrostatically actuated nanobeam-based nanoelectromechanical switches - materials solutions and operational conditions. Beilstein J Nanotechnol 9:271
3. Lee T-H, Bhunia S, Mehregany M (2010) Electromechanical computing at 500 C with silicon carbide. Science 329:1316
4. Park HS, Cai W, Espinosa HD, Huang H (2009) Mechanics of crystalline nanowires. MRS Bull 34:178
5. Tan EPS, Zhu Y, Yu T, Dai L, Sow CH, Tan VBC, Lim CT (2007) Crystallinity and surface effects on Young's modulus of CuO nanowires. Appl Phys Lett 90:163112
6. Kosmaca J, Meija R, Antsov M, Kunakova G, Sondors R, Iatsunskyi I, Coy E, Doherty J, Biswas S, Holmes JD, Erts D (2019) Investigating the mechanical properties of GeSn nanowires. Nanoscale 11:13612
7. Erts D, Lohmus A, Lohmus R, Olin H (2001) Instrumentation of STM and AFM combined with transmission electron microscope. Appl Phys A Mater Sci Process 72:S71
8. Lee SW, Lee DS, Morjan RE, Jhang SH, Sveningsson M, Nerushev OA, Park YW, Campbell EEB (2004) A three-terminal carbon nanorelay. Nano Lett 4:2027
9. Andzane J, Petkov N, Livshits AI, Boland JJ, Holmes JD, Erts D (2009) Two-terminal nanoelectromechanical devices based on germanium nanowires. Nano Lett 9:1824
10. Kunakova G, Meija R, Andzane J, Malinovskis U, Petersons G, Baitimirova M, Bechelany M, Bauch T, Lombardi F, Erts D (2019) Surface structure promoted high-yield growth and magnetotransport properties of Bi_2Se_3 nanoribbons. Sci Rep 9:1
11. Biswas S, Doherty J, Saladukha D, Ramasse Q, Majumdar D, Upmanyu M, Singha A, Ochalski T, Morris MA, Holmes JD (2016) Non-equilibrium induction of tin in germanium: towards direct bandgap $Ge_{1-x}Sn_x$ nanowires. Nat Commun 7:11405
12. Smith DA, Holmberg VC, Lee DC, Korgel BA (2008) Young's modulus and size-dependent mechanical quality factor of nanoelectromechanical germanium nanowire resonators. J Phys Chem C 112:10725

13. Meija R, Kosmaca J, Jasulaneca L, Petersons K, Biswas S, Holmes JD, Erts D (2015) Electric current induced modification of germanium nanowire NEM switch contact. Nanotechnology 26:195503
14. Livshits AI, Jasulaneca L, Kosmaca J, Meija R, Holmes JD, Erts D (2017) Extra tension at electrode-nanowire adhesive contacts in nano-electromechanical devices. Eur J Mech 66:412
15. Jasulaneca L, Meija R, Livshits AI, Prikulis J, Biswas S, Holmes JD, Erts D (2016) Determination of Young's modulus of Sb_2S_3 nanowires by in situ resonance and bending methods. Beilstein J Nanotechnol 7:278
16. Kosmaca J, Jasulaneca L, Meija R, Andzane J, Romanova M, Kunakova G, Erts D (2017) Young's modulus and indirect morphological analysis of Bi_2Se_3 nanoribbons by resonance measurements. Nanotechnology 28:325701
17. Kosmaca J, Andzane J, Baitimirova M, Lombardi F, Erts D (2016) Role of nanoelectromechanical switching in the operation of nanostructured Bi_2Se_3 interlayers between conductive electrodes. ACS Appl Mater Interfaces 8:12257
18. Andzane J, Prikulis J, Dvorsek D, Mihailovic D, Erts D (2010) Two-terminal nanoelectromechanical bistable switches based on molybdenum–sulfur–iodine molecular wire bundles. Nanotechnology 21:125706
19. Andzane J, Meija R, Livshits AI, Prikulis J, Biswas S, Holmes JD, Erts D (2013) An AC-assisted single-nanowire electromechanical switch. J Mater Chem C 1:7134
20. Meija R, Livshits AI, Kosmaca J, Jasulaneca L, Andzane J, Biswas S, Holmes JD, Erts D (2019) Resonance assisted jump-in voltage reduction for electrostatically actuated nanobeam-based gateless NEM switches. Nanotechnology 30:385203

Chapter 16
Modification of TiO_2 and ZnO Particles Under Mechanical Stress with Polypropylene

Olha Skurikhina, Erika Tothova, Smilja Markovic, and Mamoru Senna

Abstract Solid-state process of introducing oxygen vacancies into the structure of TiO_2 and ZnO particles was studied. The phase transformations of metal oxides throughout the process were examined by X-ray diffraction (XRD). The influence of the loaded mechanical stress on the band gap was studied by diffuse reflectance spectroscopy (DRS). Mechanism of elimination of oxygen atoms from the surface of the oxides by co-milling with polyolefins, which can lead to creation of more effective materials for waste water treatment, was proposed.

Keywords High-energy ball milling · TiO_2 · ZnO · Oxygen vacancies

16.1 Introduction

Metal oxides such as TiO_2 and ZnO were extensively studied during the last decades because of their unique intrinsic properties and a wide range of possible applications as photocatalysts, photoelectrodes, antibacterial agents or gas sensors [1, 2]. One of the limiting factors of their practical application as photocatalysts is the width of the band gap, which corresponds to the required photon energy, necessary for the creation of electron-hole pairs. Both titanium dioxide and zinc oxide have wide

O. Skurikhina (✉)
Institute of Geotechnics, Kosice, Slovakia

Technical University of Kosice, Košice, Slovakia

E. Tothova
Institute of Geotechnics, Kosice, Slovakia

S. Markovic
Institute of Technical Sciences of SASA, Belgrade, Republic of Serbia

M. Senna
Department of Applied Chemistry, Faculty of Science and Technology, Keio University, Yokohama, Japan

P. Petkov et al. (eds.), *Nanoscience and Nanotechnology in Security and Protection against CBRN Threats*, NATO Science for Peace and Security Series B: Physics and Biophysics, https://doi.org/10.1007/978-94-024-2018-0_16

band gaps (ZnO ~3.3 eV; TiO_2 ~3.2 eV) that enable photocatalysis only under UV light within the energy range 3–124 eV [3, 4]. With the aim of increasing the photocatalytic efficiency of these materials under solar light for degradation of organic pollutants, tuning of the band gaps is desirable.

Changes in metal oxides which accompany the process of high-energy ball milling (HEBM) have been previously investigated [5]. The process of HEBM, in contrast to the standard grinding used for comminution of materials, is aimed at accumulation of energy in the materials for further chemical transformations by introducing various defects such as dilation/shrinking of the lattice, vacancies, interstitial ions and atoms, dislocations [6]. These defects in turn alter the width of band gap of the material, which enables the employment of HEBM method for tuning of the material properties toward higher energy harvest.

16.2 Inducing Defects in Structure of Metal Oxides Under Mechanical Stress

An attempt to induce oxygen vacancies in TiO_2 (anatase) and ZnO was done in a planetary ball mill Pulverisette 7 premium line. The time of milling was varied from 60 min up to 180 min. As an oxygen subtracting agent polypropylene (PP) was used, since it is known that anion-containing polyolefins can decompose concurrently acting as reductants [7]. In Fig. 16.1, XRD patterns of samples co-milled with PP are shown. The formation of defects due to plastic deformations is one of the relaxation pathways under mechanical treatment, the others are heating, reduction of particles, amorphisation along with possible formation of polymorph. The last ones are observed in our case as well. During milling, TiO_2 transforms from anatase phase to rutile with the high-pressure phase of TiO_2, called TiO_2-II, as intermediate [5]. As seen from the XRD patterns, the percent of rutile phase is increasing with prolongation of the milling time which has a negative effect on the photocatalytic efficiency

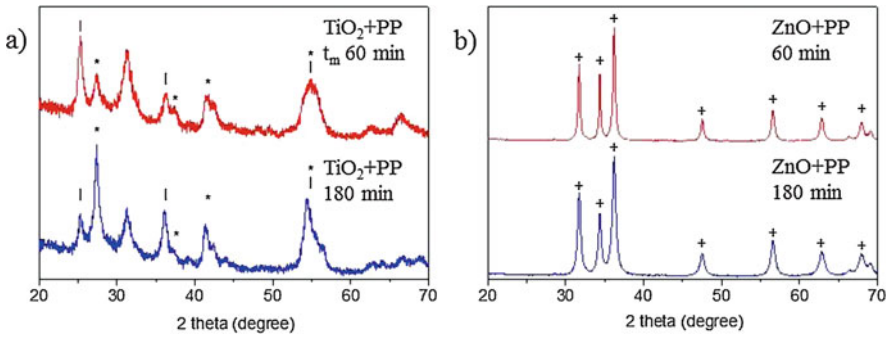

Fig. 16.1 XRD patterns of (**a**) TiO_2 (l – anatase; ∗ – rutile) and (**b**) ZnO (+ – wurtzite ZnO), milled with PP for 60 and 180 min

of the materials. Together with the transition between different polymorphs, amorphisation process occurs which is seen from the broadening of the XRD peaks for both materials. In the case of ZnO, no peaks of new phase are observed which is in conformity with previous investigations of the structural changes during HEBM process [8]. As investigated by several researchers [9–11], ZnO crystals usually do not undergo reconstructions to other polymorphs during milling, except for small shrinkage of the lattice even when the presence of surface defects, particularly oxygen vacancies is shown by other techniques such as high resolution transmission electron microscopy (HRTEM) or by behavioral change revealed by photoluminescence (PL), Raman spectra, etc.

By XRD the structural changes in long-range order can be seen but it is impossible to identify defects in short-range order. Since it is known that the impact of defects on photocatalysis is not unequivocal and the distribution of point defects plays a role, the surface oxygen vacancies are usually considered as favoring the photocatalysis preventing electron-hole recombinations and acting as active sites for adsorption, whereas the bulk oxygen vacancies have an opposite effect serving as recombination centers [1]. For investigations of the influence of HEBM on the electron structures of the materials, DRS measurements were performed.

16.3 Abstraction of Oxygen by Organic Constituent

As mentioned above, PP does not contain any anions for anionic exchange as, for example, polytetrafluoroethylene (PTFE) or polyvinylidene fluoride (PVDF). However, the process of subtraction of oxygen from the surface of the metal oxide can take place because of destruction of bonds. The ability of mechanical stress to destruct chemical bonds in polymer was studied earlier [12]. So we suggested mechanochemically induced destruction of hydrocarbon polymer with subsequent formation of reactive species that can react with the surface oxygen, creating oxygen vacancies without concomitant anion exchange [13]. The process of oxygen abstraction from the surface has greater impact on the band gap width than the reduction of Ti^{4+} [14]. In Fig. 16.2, DRS spectra show a distinct shift towards visible light range for the milled samples. From these spectra the width of the band gaps was calculated by Kubelka-Munk function and the narrowing from 3.56 eV to 3.39 eV and from 3.27 eV to 3.16 eV for titanium dioxide and zinc oxide, respectively, was observed.

Because of the afore-mentioned possible presence of bulk defects which have lower impact on the band gap state [15] but can significantly change the photocatalytic properties of material, photocatalytic degradation of methylene blue was performed. Dye degradation upon irradiation is an indirect method for examination of the present defects. The increased efficiency of the process confirms the improved separation of e-h pairs. Prolonged milling led to decrease of the photocatalytic activity, whereas the sample of TiO_2 co-milled with PP for 60 min exhibited an increase in the activity during the first 60 min with subsequent decline after comparing to the pristine titanium dioxide.

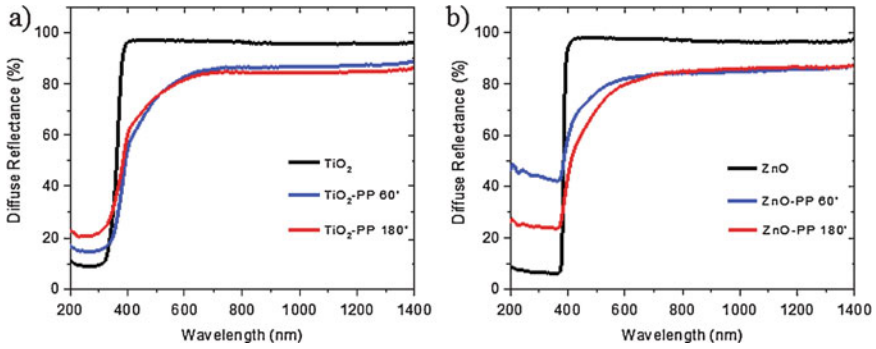

Fig. 16.2 DRS spectra of (**a**) TiO_2 and (**b**) ZnO milled with PP for 60 and 180 min

16.4 Conclusions

The introduction of oxygen vacancies in ZnO and TiO_2 by solid-state process was demonstrated as a consequence of HEBM. The increased milling time revokes the positive effect of HEBM on the band gap state and the photocatalytic activity because of the unwanted process of amorphisation and polymorph transitions. However, this method is very attractive due to its simplicity for preparation of photocatalytic materials with enhanced efficiency for degradation of different organic pollutants.

Acknowledgments The work was realized within the frame of the project „Research Centre of Advanced Materials and Technologies for Recent and Future Applications „PROMATECH", ITMS 26220220186.

References

1. Kong M, Li YZ, Chen X, Tian TT, Fang PF, Zheng F, Zhao XJ (2011) Tuning the relative concentration ratio of bulk defects to surface defects in TiO_2 nanocrystals leads to high photocatalytic efficiency. J Am Chem Soc 133:16414–16417. https://doi.org/10.1021/ja207826q
2. Wang J, Chen RS, Xiang L, Komarneni S (2018) Synthesis, properties and applications of ZnO nanomaterials with oxygen vacancies: a review. Ceram Int 44:7357–7377. https://doi.org/10.1016/j.ceramint.2018.02.013
3. Ozgur U, Alivov YI, Liu C, Teke A, Reshchikov MA, Dogan S, Avrutin V, Cho SJ, Morkoc H (2005) A comprehensive review of ZnO materials and devices. J Appl Phys 98. https://doi.org/10.1063/1.1992666
4. Dette C, Perez-Osorio MA, Kley CS, Punke P, Patrick CE, Jacobson P, Giustino F, Jung SJ, Kern K (2014) TiO_2 anatase with a bandgap in the visible region. Nano Lett 14:6533–6538. https://doi.org/10.1021/nl503131s
5. Sepelak V, Begin-Colin S, Le Caer G (2012) Transformations in oxides induced by high-energy ball-milling. Dalton T 41:11927–11948. https://doi.org/10.1039/c2dt30349c

6. Boldyrev VV (2006) Mechanochemistry and mechanical activation of solids. Russ Chem Rev 75:203–216. https://doi.org/10.1070/RC2006v075n03ABEH001205
7. Senna M, Noda H, Xin YZ, Hasegawa H, Takai C, Shirai T, Fuji M (2018) Solid- state reduction of silica nanoparticles via oxygen abstraction from SiO_4 units by polyolefins under mechanical stressing. RSC Adv 8:36338–36344. https://doi.org/10.1039/c8ra07271j
8. Glushenkov AM, Zhang HZ, Zou J, Lu GQ, Chen Y (2007) Efficient production of ZnO nanowires by a ball milling and annealing method. Nanotechnology 18. https://doi.org/10.1088/0957-4484/18/17/175604
9. Vojisavljevic K, Scepanovic M, Sreckovic T, Grujic-Brojcin M, Brankovic Z, Brankovic G (2008) Structural characterization of mechanically milled ZnO: influence of zirconia milling media. J Phys Condens Matter 20. https://doi.org/10.1088/0953-8984/20/47/475202
10. Giri PK, Bhattacharyya S, Singh DK, Kesavamoorthy R, Panigrahi BK, Nair KGM (2007) Correlation between microstructure and optical properties of ZnO nanoparticles synthesized by ball milling. J Appl Phys 102. https://doi.org/10.1063/1.2804012
11. Chen DM, Wang ZH, Ren TZ, Ding H, Yao WQ, Zong RL, Zhu YF (2014) Influence of defects on the photocatalytic activity of ZnO. J Phys Chem C 118:15300–15307. https://doi.org/10.1021/jp5033349
12. Delogu F, Gorrasi G, Sorrentino A (2017) Fabrication of polymer nanocomposites via ball milling: present status and future perspectives. Prog Mater Sci 86:75–126. https://doi.org/10.1016/j.pmatsci.2017.01.003
13. Dadali AA, Lastenko IP, Kojushner MA (1993) Kinetics of radical processes in organic-crystals during high-pressure shearing. J Solid State Chem 102:289–298. https://doi.org/10.1006/jssc.1993.1037
14. Li GW, Blake GR, Palstra TTM (2017) Vacancies in functional materials for clean energy storage and harvesting: the perfect imperfection. Chem Soc Rev 46:1693–1706. https://doi.org/10.1039/c6cs00571c
15. Yim CM, Pang CL, Thornton G (2010) Oxygen vacancy origin of the surface band-gap state of TiO_2(110). Phys Rev Lett 104. https://doi.org/10.1103/Physrevlett.104.036806

Chapter 17
Use of Magnetic Susceptibility Measurement for Analysis of Self-Organized Magnetic Nanoparticles in Biological Systems

Taras Kavetskyy, Oksana Zubrytska, Lyudmyla Pan'kiv, Rovshan Khalilov, Aygun Nasibova, Abolfazl Akbarzadeh, Andriy Pryima, Nataliia Stebeletska, and Svitlana Voloshanska

Abstract Magnetic susceptibility (MS) measurements for analysis of superparamagnetic iron oxide nanoparticles (SPIONs) in various biological systems were applied. The MS measurements by the Faraday method were carried out at room temperature. On the basis of the MS experimental data and the model based on the Langevin function, the concentrations of magnetically ordered clusters N_{cl} and paramagnetic centers per magnetic cluster N_0 for Fe_3O_4 SPIONs and superoxide

T. Kavetskyy (✉)
Drohobych Ivan Franko State Pedagogical University, Drohobych, Ukraine

The John Paul II Catholic University of Lublin, Lublin, Poland

Joint Ukraine-Azerbaijan International Research and Education Center of Nanobiotechnology and Functional Nanosystems, Drohobych, Ukraine

O. Zubrytska · L. Pan'kiv · A. Pryima
Drohobych Ivan Franko State Pedagogical University, Drohobych, Ukraine

R. Khalilov
Joint Ukraine-Azerbaijan International Research and Education Center of Nanobiotechnology and Functional Nanosystems, Drohobych, Ukraine

Baku State University, Baku, Azerbaijan

Institute of Radiation Problems of NAS Azerbaijan, Baku, Azerbaijan

A. Nasibova
Joint Ukraine-Azerbaijan International Research and Education Center of Nanobiotechnology and Functional Nanosystems, Drohobych, Ukraine

Institute of Radiation Problems of NAS Azerbaijan, Baku, Azerbaijan

P. Petkov et al. (eds.), *Nanoscience and Nanotechnology in Security and Protection against CBRN Threats*, NATO Science for Peace and Security Series B: Physics and Biophysics, https://doi.org/10.1007/978-94-024-2018-0_17

dismutase with manganese (Mn-SOD) in biological systems taken from environmentally "green" and polluted regions of Azerbaijan are found to be in a good agreement with electron spin resonance spectroscopy results.

Keywords Superparamagnetic iron oxide nanoparticles · Superoxide dismutase with manganese · Magnetic susceptibility · Electron spin resonance spectroscopy

17.1 Introduction

Recently, an innovative approach based on the effect of bio-mineralization as a response reaction of cells to decrease their damage upon stress was applied for biomaterials represented by *Juniperus communis* [1]. Using electron spin resonance (ESR) technique, the formation of self-organized magnetic nanoparticles such as superparamagnetic iron oxide nanoparticles (SPIONs) was found in the *J. communis* shell, while the antioxidant activity due to Mn-containing enzymes (e.g., superoxide dismutase with manganese, Mn-SOD) was detected in the *J. communis* seeds. In the present work, magnetic susceptibility (MS) measurements were applied for analysis of SPIONs in various biological systems.

17.2 Experimental

Samples of two types of biomaterials – called as "Babek" and "Ahmadli" (leaf of pine), taken respectively from polluted and environmentally "green" regions of Azerbaijan, were used for the current research. The MS measurements of the investigated biological systems by the Faraday method were carried out at room temperature in the magnetic field range of 0.3–5.0 kOe. The advantage of this technique is the possibility to measure samples with optimal mass and length of

A. Akbarzadeh
Joint Ukraine-Azerbaijan International Research and Education Center of Nanobiotechnology and Functional Nanosystems, Drohobych, Ukraine

Stem Cell Research Center, Tabriz University of Medical Sciences, Tabriz, Iran

Universal Scientific Education and Research Network (USERN), Tabriz, Iran

N. Stebeletska
Separated Subdivision of NULES of Ukraine "Berezhany Agrotechnical Institute", Berazhany, Ukraine

S. Voloshanska
Drohobych Ivan Franko State Pedagogical University, Drohobych, Ukraine

Joint Ukraine-Azerbaijan International Research and Education Center of Nanobiotechnology and Functional Nanosystems, Drohobych, Ukraine

120–150 mg and 8–10 mm, respectively. The main parameters of the equipment for the MS measurements were: diameter of quartz capillary of 0.5 mm, length of 950 mm, distance from sample to axis of the quartz capillary of 12 mm, and own frequency of torque balance without sample of 140 Hz. An automated equipment for removal of the error of the MS measurement related to deformation of current supplies due to addition of new assemblies of control, i.e., device with comparator, was used [2]. In this way, the accuracy of the obtained experimental data was essentially increased, giving a relative error less than 1%, and sensitivity of $5 \cdot 10^{15}$ Bohr magnetons.

On the basis of the MS experimental data and the model based on the Langevin function, the concentrations of magnetically ordered clusters and paramagnetic centers per magnetic cluster were evaluated for the investigated samples [3, 4]. In this model, the dependence of the magnetic susceptibility on the external magnetic field strength $\chi(H)$ is presented by the expression: $\chi(H) = \chi_L + \chi^{par} + N_{cl} m_{cl} L'(m_{cl} H/kT)$, where N_{cl} is the concentration of the magnetically ordered clusters, m_{cl} the magnetic moment of the cluster (it is suggested that all the clusters have identical magnetic moment), and $L'(x)$ the derivative of the Langevin function ($L = (\coth\alpha - 1/\alpha)$, where $\alpha = MH/kT$, with M the magnetization, k the Boltzmann constant, and T the temperature). The magnetic moment of the cluster follows the equation: $m_{cl} = N_0 \mu_B g(s(s+1))^{1/2}$, where N_0 is the concentration of the paramagnetic centers per magnetic cluster, μ_B the Bohr magneton, g the g-factor and s the spin of paramagnetic center composing the magnetic cluster.

The electron spin resonance (ESR) spectra of the biomaterials studied were registered with an X-range ESR spectrometer ECS-106 (Bruker, Germany) at the following conditions: magnetic field HF-modulation amplitude of 0.5 mT, field center of 260 mT, field scanning of 290 mT, temperature of 293 K, and gain of 10^4.

17.3 Results and Discussion

Figure 17.1 shows the dependences of the magnetic susceptibility χ on the external magnetic field strength H for the investigated biomaterials ("Babek" – polluted and "Ahmadli" – environmentally "green" samples) at $T = 293$ K. Fitting of the $\chi(H)$ curves within the model based on the Langevin function gives a possibility to evaluate the concentrations of magnetically ordered clusters N_{cl} and paramagnetic centers per magnetic cluster N_0, as shown in Fig. 17.2.

The results obtained for the "Babek" sample are following: (i) for Mn-SOD at $g = 2.01$ and $s = 3/2$ – $N_{cl} = 7.3 \times 10^{13}$ cm^{-3}; $N_0 = 18.57 \times 10^5$ 1/cluster; $(N_{cl} \times N_0)_{Mn} = 135.56 \times 10^{18}$ cm^{-3}; and (ii) for Fe_3O_4 SPIONs at $g = 2.28$ and $s = 1/2$ – $N_{cl} = 7.3 \times 10^{13}$ cm^{-3}; $N_0 = 36.51 \times 10^5$ 1/cluster; $(N_{cl} \times N_0)_{Fe3O4} = 266.52 \times 10^{18}$ cm^{-3}. Thus, $(N_{cl} \times N_0)_{\Sigma}^{Babek} = (N_{cl} \times N_0)_{Mn} + (N_{cl} \times N_0)_{Fe3O4} = 402.08 \times 10^{18}$ cm^{-3}.

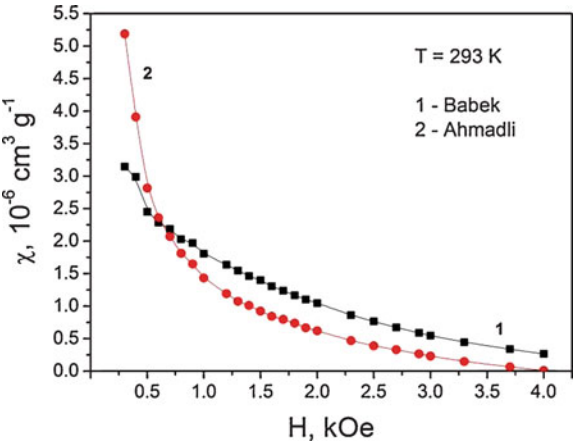

Fig. 17.1 Dependences of the magnetic susceptibility χ on the external magnetic field strength H for the investigated biomaterials

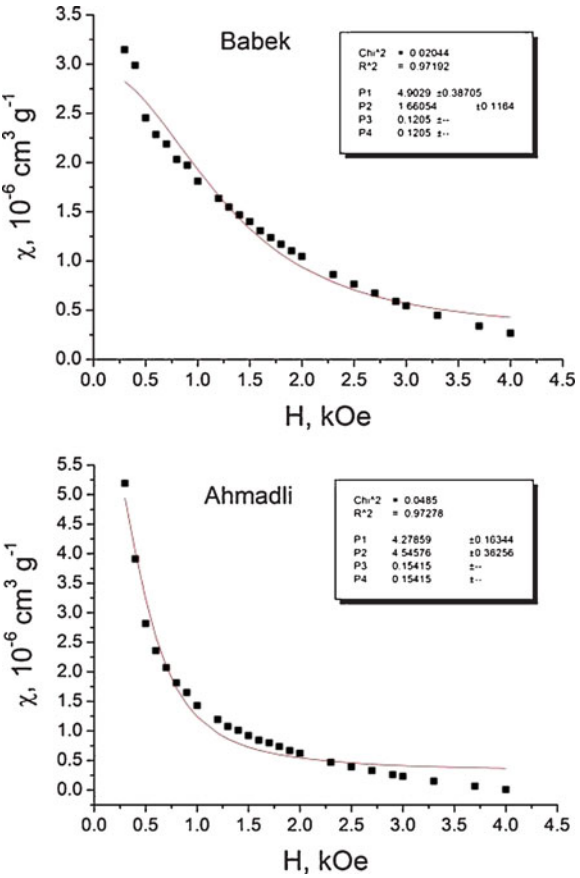

Fig. 17.2 Fitting of the $\chi(H)$ curves within the model based on the Langevin function for the "Babek" sample (upper panel) and "Ahmadli" sample (lower panel)

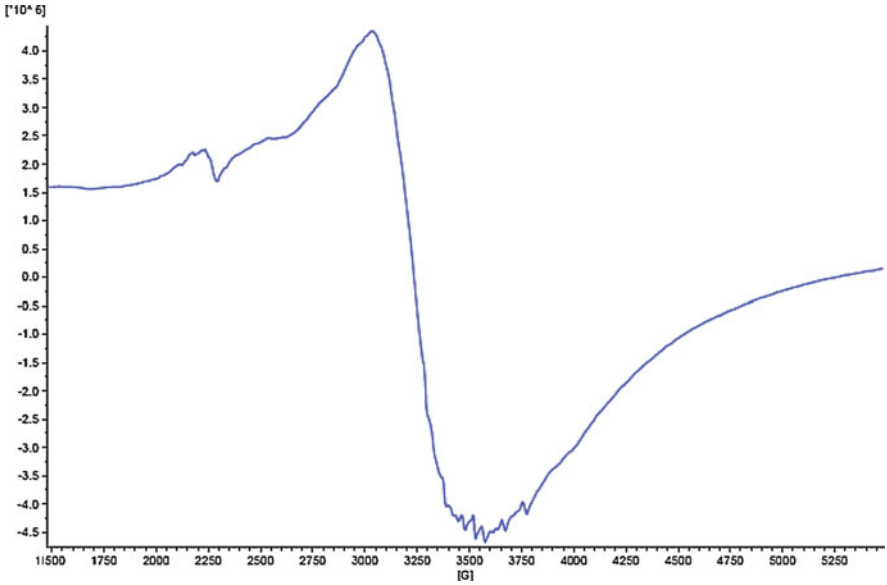

Fig. 17.3 ESR spectrum for the "Babek" sample at $T = 293$ K

The results obtained for the "Ahmadli" sample are following: (i) for Mn-SOD at $g = 2.01$ and $s = 3/2$ – $N_{cl} = 2.3 \times 10^{13}$ cm^{-3}; $N_0 = 50.85 \times 10^5$ 1/cluster; $(N_{cl} \times N_0)_{Mn} = 116.96 \times 10^{18}$ cm^{-3}; and (ii) for Fe_3O_4 SPIONs at $g = 2.28$ and $s = 1/2$ – $N_{cl} = 2.3 \times 10^{13}$ cm^{-3}; $N_0 = 99.96 \times 10^5$ 1/cluster; $(N_{cl} \times N_0)_{Fe3O4} = 229.91 \times 10^{18}$ cm^{-3}. Thus, $(N_{cl} \times N_0)_{\Sigma}^{Ahmadli} = (N_{cl} \times N_0)_{Mn} + (N_{cl} \times N_0)_{Fe3O4} = 346.87 \times 10^{18}$ cm^{-3}.

Figures 17.3 and 17.4 show the ESR spectra for the "Babek" and "Ahmadli" samples at $T = 293$ K, respectively. A broad ESR signal is detected from Fe_3O_4 SPIONs ($g = 2.28$) in the polluted "Babek" sample [1, 5–10]. At the same time, in the case of the environmentally "green" "Ahmadli" sample, the ESR signal from Mn-containing compounds [1, 5–10], e.g. Mn-SOD ($g = 2.01$, characterized by six-component hyperfine structure) is observed as a dominant one.

It is clearly seen that the evaluated values of N_{cl} and N_0 for the Fe_3O_4 SPIONs and Mn-SOD, $(N_{cl} \times N_0)_{\Sigma}^{Babek}$ and $(N_{cl} \times N_0)_{\Sigma}^{Ahmadli}$, in the biological systems used correlate well with the ESR results obtained. Namely, in the case of the polluted "Babek" sample, the presence of Fe_3O_4 SPIONs is dominant as detected from the both MS and ESR experiments carried out.

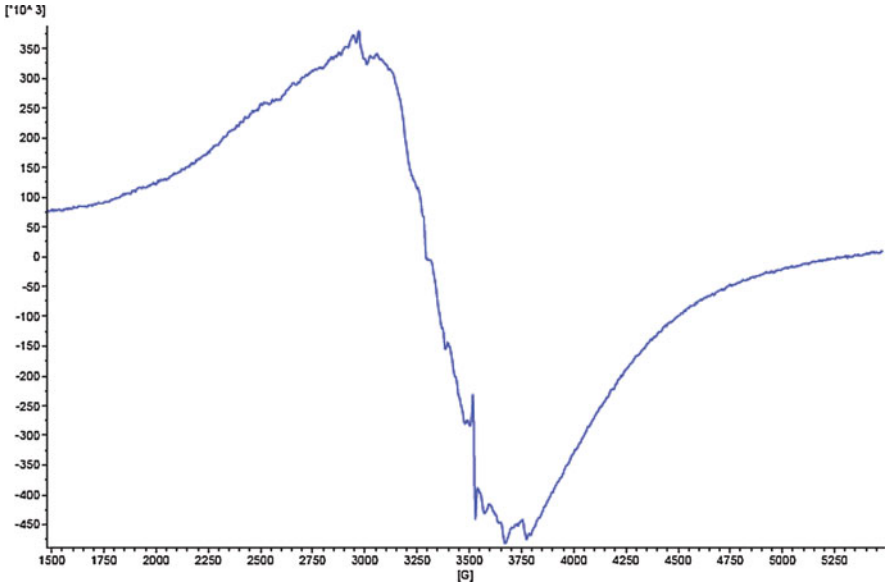

Fig. 17.4 ESR spectrum for the "Ahmadli" sample at $T = 293$ K

17.4 Conclusion

The evaluated concentrations of magnetically ordered clusters N_{cl} and paramagnetic centers per magnetic cluster N_0 for Fe_3O_4 SPIONs and Mn-SOD in the biological systems used as taken from environmentally "green" and polluted regions of Azerbaijan are found to be in a good agreement with the ESR results obtained for these systems. The observed correlation in the MS and ESR data supports the advantage of combining these both complementary techniques as a promising experimental approach for monitoring the environmental pollution.

Acknowledgments The authors would like to thank Dr. V.A. Serezhenkov and N.A. Tkachev (Semenov Institute of Chemical Physics of RAS) for their help with ESR measurements. This work was supported in part by the Ministry of Education and Science of Ukraine (projects Nos. 0117 U007142, 0118 U000297, and 0119 U100671).

References

1. Khalilov RI, Kavetskyy TS, Serezhenkov VA, Akbarzadeh A, Davaran S, Nasibova AN, Pourhassan-Moghaddam M, Tkachev NA, Milani M, Kouhi M, Šauša O, Voloshanska SY (2018) Detection of manganese-containing enzymes and magnetic nanoparticles in *Juniperus Communis* and related biomaterials by ESR spectroscopy. Adv Biol Earth Sci 3:167

2. Tsmots VM, Pankiv IS, Pankiv LI, Pavlovskyy YuV, Petrenko VV, Kavetskyy S, Labovka DV, Luchkevych MM, Okhrymovych RV, Salan VP, Tsyuper MV (2006) Equipment for measurement of magnetic susceptibility of materials. Patent of Ukraine, 77284
3. Tsmots VM, Litovchenko PG, Pavlovska NT, Pavlovskyy YV, Ostrovskyy IP (2010) Study and simulation of magnetic susceptibility of Si and $Si_{0.95}Ge_{0.05}$ whiskers. Semiconductors 44:623
4. Kavetskyy TS, Tsmots VM, Pankiv LI, Dubyk-Pihur OM, Petkova T, Petkov P, Eckert H, Stepanov AL (2014) On the concentrations of magnetically ordered clusters and paramagnetic centers per magnetic cluster in Ag/AgI-As_2S_3 glasses. J Optoelectron Adv M 16:1317
5. Khalilov RI, Nasibova AN (2010) The endogenous EPR-detectable iron nanoparticles in plants. News Baku University 3:35
6. Khalilov RI, Nasibova AN, Gasimov RJ (2011) Magnetic nanoparticles in plants: EPR researches. News Baku University 4:56
7. Khalilov RI, Nasibova AN, Serezhenkov VA, Ramazanov MA, Kerimov MK, Garibov AA, Vanin AF (2011) Accumulation of magnetic nanoparticles in plants grown on soils of Apsheron peninsula. Biophysics 56:316
8. Khalilov RI, Nasibova AN, Youssef N (2015) The use of EPR signals of plants as bioindicative parameters in the study of environmental pollution. Int J Pharm Pharm Sci 7:172
9. Nasibova AN, Khalilov RI (2016) Preliminary studies on generating metal nanoparticles in pomegranates (Punica Granatum) under stress. Int J Dev Res 6:7071
10. Kavetskyy TS, Khalilov RI, Voloshanska OO, Kropyvnytska LM, Beyba TM, Serezhenkov VA, Nasibova AN, Akbarzadeh A, Voloshanska SY (2018) Self-organized magnetic nanoparticles in plant systems: ESR detection and perspectives for biomedical applications. Chapter 48: NATO science for peace and security series B: physics and biophysics. In: Petkov P, Tsiulyanu D, Popov C, Kulisch W (eds) Advanced nanotechnologies for detection and defence against CBRN agents. Springer, Dordrecht, pp 487–492

Part VII
Nanocomposites

Chapter 18
Solvent Dispersible Nanocomposite Based on RGO Surface Decorated with Au Nanoparticles for Electrochemical Genosensors

Chiara Ingrosso, Michela Corricelli, Alessia Disha, Francesca Bettazzi, Evgenia Konstantinidou, Elisabetta Fanizza, Giuseppe Valerio Bianco, Nicoletta Depalo, Marinella Striccoli, Angela Agostiano, Maria Lucia Curri, and Ilaria Palchetti

Abstract A novel hybrid nanocomposite, formed of Reduced Graphene Oxide (RGO) flakes surface functionalized with 1-pyrene carboxylic acid (PCA) and decorated by Au nanoparticles (NPs), has been synthesized for the electrochemical detection of the miRNA-221 cancer biomarker. The hybrid material has been prepared by a facile approach, relaying on the *in situ* synthesis of the Au NPs onto the PCA carboxylic groups in presence of 3,4-dimethylbenzenethiol (DMBT) and $NaBH_4$. The short aromatic thiol DMBT acts as reducing and coordinating agent, and hence, enables the dispersion of the nanocomposite in organic solvents. Concomitantly, DMBT favors the non-covalent anchoring of the Au NPs onto RGO, potentially allowing an efficient particle/RGO and interparticle π-π mediated electron coupling, which enhances the electron conductivity and charge transfer. PCA-RGO flakes, densely and uniformly decorated with a multilayer network of DMBT-coated Au NPs, 2.8 ± 0.6 nm in size, have been obtained, overcoming limitations previously reported for similar hybrid materials in terms of coating

C. Ingrosso (✉) · M. Corricelli · N. Depalo · M. Striccoli
CNR-IPCF S. Bari, c/o Dipartimento di Chimica, Università di Bari, Bari, Italy
e-mail: c.ingrosso@ba.ipcf.cnr.it

A. Disha · E. Fanizza
Dipartimento di Chimica, Università di Bari, Bari, Italy

F. Bettazzi · E. Konstantinidou · I. Palchetti
Dipartimento di Chimica Ugo Schiff, Università degli Studi di Firenze, Firenze, Italy

G. V. Bianco
CNR-NANOTEC, c/o Università di Bari, Bari, Italy

A. Agostiano · M. L. Curri
CNR-IPCF S. Bari, c/o Dipartimento di Chimica, Università di Bari, Bari, Italy

Dipartimento di Chimica, Università di Bari, Bari, Italy

P. Petkov et al. (eds.), *Nanoscience and Nanotechnology in Security and Protection against CBRN Threats*, NATO Science for Peace and Security Series B: Physics and Biophysics, https://doi.org/10.1007/978-94-024-2018-0_18

density and NP size distribution. Screen-Printed Carbon Electrodes (SPCEs), modified by the hybrid material and then functionalized with a thiolated DNA capture probe, have been tested for the determination of miRNA-221 in spiked human serum samples.

Keywords Colloidal gold nanoparticles · Reduced graphene oxide · Hybrid nanocomposite · Electrochemical genosensors

18.1 Introduction

Hybrid nanocomposites based on graphene and Au nanoparticles (NPs) have attracted wide interest for electrochemical biosensing, thanks to their enhanced sensitivity and selectivity, stemming from the synergistic combination of the peculiar properties of both the components. Graphene based electrodes show high electrochemical stability and electrocatalytic activity, large potential window and fast heterogeneous electron transfer kinetics for diverse analytes [1–4]. In addition, the high chemical reactivity of the graphene platform allows its hybridization with NPs and biomolecules, leading to the manufacturing of highly functional nanocomposites. When decorated with Au NPs, the characteristics of graphene are combined with the capability of such NPs of binding biomolecules by diverse chemical groups, as well as the high rate of electron transfer kinetics of the NPs at the electrode/electrolyte interface, and the excellent surface redox electrocatalytic activity [1]. Thus, electrodes modified by hybrid nanocomposites formed of Au NPs and graphene have demonstrated a rapid and sensitive current response [2].

In this work, a novel hybrid nanocomposite formed of Reduced Graphene Oxide (RGO) flakes, surface decorated with 3,4-dimethylbenzenethiol (DMBT)-capped Au NPs, has been prepared and tested as active material in a genosensing platform. The hybrid nanostructures have been synthesized by means of a flexible *in situ* Au precursor reduction, that has been carried out in presence of the aromatic ligand DMBT, and $NaBH_4$, and by using 1-pyrenecarboxylic acid as linker [5]. The RGO flakes have been surface functionalized with PCA by means of π-π interactions, and the carboxylic groups of PCA have been exploited as heteronucleation and coordination sites for the *in situ* synthesis of the Au NPs, being concomitantly able to couple electronically both components [5]. Finally, the aromatic thiol molecules control the Au NPs morphology and are also effective in providing a further anchoring group for Au NPs immobilization onto the flakes by π-π interactions, granting Au interparticle coupling that results in a conductive network onto the flakes [5].

Thanks to their solution processability, the colloidal PCA-RGO/Au NPs hybrid nanostructures have been used to modify disposable and cost-effectively obtained Screen-Printed Carbon Electrodes (SPCEs) that have been tested for the detection of miRNA-221, a circulating non coding small RNA overexpressed in lung cancer [6].

The hybrid modified SPCEs have shown, compared to the PCA-RGO modified and bare SPCEs, faster heterogeneous electron transfer (ET) kinetics at the interface

with the electrolyte, an increase of the conductivity, and an overall enhancement of the electrocatalytic properties [7].

A thiol-tethered DNA-capture probe has been immobilized onto the PCA-RGO/Au NPs modified SPCEs, and differential pulse voltammetry (DPV) has been applied to estimate the extent of the hybridization reaction with a biotinylated target miRNA-221 sequence by detecting 1-naphthol, originating via the enzymatic reaction on 1-naphthyl phosphate assisted by streptavidin-alkaline phosphatase. The hybrid modified SPCEs have shown diagnostic feasibility and reliability in the determination of miRNA-221 in spiked human blood serum samples, resulting in a LOD (0.7 pM) comparable with those reported for the state-of-art sensors [8].

18.2 Experimental

A PCA-RGO/Au NPs hybrid nanocomposite with Au NPs 2.8 ± 0.6 nm in size was synthesized as reported elsewhere [5], starting with 7×10^{-3} M in $HAuCl_4 \cdot 3H_2O$, synthesized with the 17:1 PCA:RGO w/w and 1:10 $HAuCl_4 \cdot 3H_2O$:$NaBH_4$ molar ratio, at the HAuCl4·$3H_2O$:DMBT molar ratio and $HAuCl_4 \cdot 3H_2O$:PCA-RGO w/w of 1:2 and 23:1, respectively.

1 μL of the PCA-RGO/Au NPs hybrid suspensions were drop casted onto Screen-Printed Carbon Electrodes (SPCEs), which were then incubated with the DNA-SH capture probe. Hybridization experiments were carried out using the biotinylated target miRNA-221 sequence in a direct assay format [9]. The biotinylated hybrid at the electrode surface was reacted with 8 μL of a solution containing 0.8 U mL^{-1} of the streptavidin–alkaline phosphatase conjugate and 10 mg mL^{-1} of BSA blocking agent in DEA buffer. The modified SPCEs were incubated with 150 μL of 1 mg mL^{-1} 1-naphthyl phosphate solution in DEA buffer and the electrochemical signal of 1-naphthol, oxidized by the enzyme, was measured by DPV with a modulation time of 0.05 s, an interval time of 0.15 s, a step potential of 5 mV, a modulation amplitude of 70 mV and a potential scan between 0 to 600 mV.

Human serum type AB was diluted 1:100 (v/v) in a phosphate buffer (PB) and filtered by a 0.45 μm pore filter in polyethersulfone (PES). Spiked samples were prepared by adding known quantities (10 and 100 nM) of miRNA-221 to diluted serum.

Steady state UV–Vis absorption spectra were recorded with a Cary 5000 (Varian) UV/Vis/NIR spectrophotometer, at room temperature. Raman spectra were collected with a LabRAM HR Horiba-Jobin Yvon spectrometer with a 532 nm excitation laser source under ambient condition and at a low laser power (1 mW), by using the Raman band recorded from a silicon wafer at 520 cm^{-1} to calibrate the spectrometer with an accuracy of ca. 1 cm^{-1}.

TEM analyses were performed by using a Jeol Jem-1011 microscope, operating at 100 kV and equipped by a high-contrast objective lens, a W filament as electron source, and an ultimate point resolution of 0.34 nm. Images were collected with a Quemesa Olympus CCD 11 Mp Camera. Size statistical analyses of the NP average

size and size distribution were performed by counting 200 NPs by the freeware ImageJ analysis program.

FE-SEM images were recorded with a Zeiss Sigma microscope operating in the range of 0–10 keV and equipped with an in-lens secondary electron detector and an INCA Energy Dispersive Spectroscopy (EDS) detector.

Electrochemical measurements were carried out at room temperature (25 °C) with a three-electrode system and an AUTOLAB PGSTAT 10 digital potentiostat/galvanostat. The GPES 4.9004 software (Eco Chemie BV, Utrecht, The Netherlands) was used for Cyclic Voltammetry (CV) and Differential Pulse Voltammetry (DPV). The FRA2 module was used for faradaic impedance experiments. All potentials were referred to the screen-printed silver pseudo-reference electrode and the experiments were carried out at room temperature. CV was performed by a planar electrochemical cell covered by 150 μL of an electrolyte solution, and the electroactive areas (A_{ele}) have been determined as reported in [7].

Faradaic impedance measurements were carried out in presence of the 5 mM $[Fe(CN)_6]^{3/4-}$ redox probe (equimolecular mixture in 0.1 M KCl). A sinusoidal voltage of 10 mV in amplitude (peak-to-peak) was superimposed to the applied bias potential within the frequency range of 100 kHz–10 mHz. The dc potential was set up at the potential value observed at the Open Circuit Potential (O.C.P.) before each measurement. Experimental spectra presented in the form of complex plane diagrams (i.e. Nyquist plots) were fitted with proper equivalent circuits by using the FRA2 software 4.9004 (EcoChemie) to estimate charge transfer resistance values. The Randles equivalent circuit was successfully applied to fit the acquired data.

18.3 Results and Discussion

The Au NPs surface modified PCA-RGO flakes have been prepared by means of the *in situ* reduction of the $HAuCl_4 \cdot 3H_2O$ precursor, in presence of the aromatic 3,4-dimethylbenzenethiol (DMBT) capping ligand. The Au(III) precursor is reduced to Au(I) by DMBT, and then to Au(0) by $NaBH_4$ [5]. The Au NPs have been found to heteronucleate and grow at the oxygen containing functionalities of the PCA-RGO sheets [5], while DMBT controls the NP morphology and size distribution during the synthesis by coordination to the NP surface [5]. Figure 18.1a shows the RGO flakes surface functionalized with PCA by means of π-π interactions, and bearing carboxylic groups available for the heteronucleation and coordination of the Au NPs, which are coated by DMBT that further favors their anchorage onto the sheets by π-π interactions [5].

TEM micrographs of PCA-RGO show μm large sheet-like structures, almost electron transparent, characterized by higher contrast areas, reasonably due to folded edges and wrinkles, explained by mechanical lattice deformations (Fig. 18.1b). The

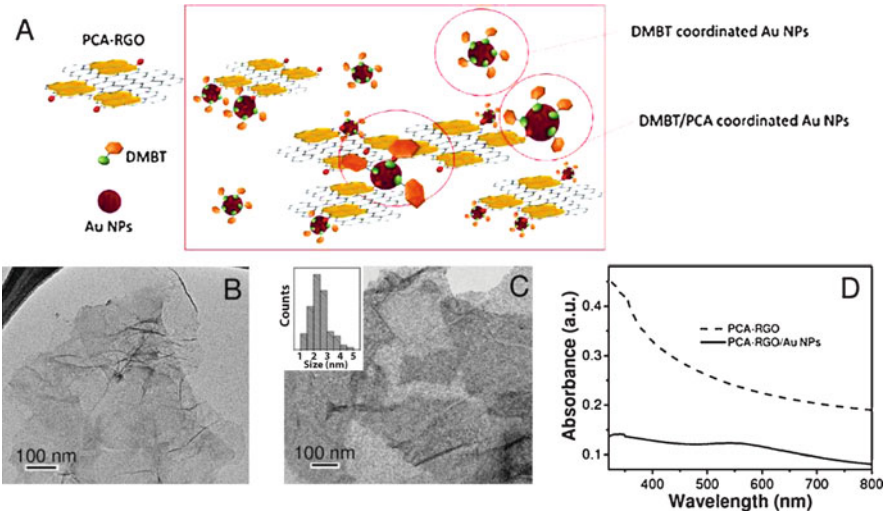

Fig. 18.1 (**a**) Sketch of the anchoring of the DMBT-capped Au NPs onto the PCA-RGO flakes. (The schemes do not show proper the proportions of the reported structures). TEM of (**b**) PCA-RGO complex and (**c**) PCA-RGO/Au NPs sample deposited onto carbon coated copper grid. (D) UV-Vis absorption spectra of 0.15 mg mL^{-1} PCA-RGO and PCA-RGO/Au NPs sample in toluene

surface morphology of the PCA-RGO/Au NPs hybrid nanocomposite is, instead, characterized by sheet-like structures, densely and uniformly coated by higher contrast round shaped nano-objects, 2.8 ± 0.6 nm in mean diameter, reasonably accounted for by the Au NPs, grown onto the flakes with a uniform morphology and a narrow size distribution (inset of Fig. 18.1c). The UV-Vis absorption spectrum of the hybrid nanocomposite (Fig. 18.1d) presents scattering phenomena originating from the RGO flakes, with superimposed the absorption signals of PCA in the near UV region, namely at 329 nm and 346 nm, ascribed to the π-π∗ transition of the –C=C– bonds, and the Localized Surface Plasmon Resonance (LSPR) peak of the Au NPs at 564 nm [5].

Screen-Printed Carbon Electrodes (SPCE), fabricated by the procedure reported in [10], have the typical surface morphology presented in Fig. 18.2a. After modification by casting 1 μl of toluene dispersions of PCA-RGO, the electrodes are coated by flakes having a smooth surface with bright contrast wrinkles and folded edges (Fig. 18.2b). In the PCA-RGO/Au NPs hybrid sample, such flakes appear uniformly coated by bright grain type structures ascribed to the Au NPs (Fig. 18.2c), expected to increase the available surface area of the electrode [7].

Figure 18.2d shows the CVs of the SPCEs, either as bare or modified with PCA-RGO and PCA-RGO/Au NPs, respectively, recorded in presence of $[Fe(CN)_6]^{3-/4-}$. The CVs recorded on the bare SPCEs present the couple of quasi-reversible redox peaks of $[Fe(CN)_6]^{3-/4-}$ and ΔE_p which decreases passing to the PCA-RGO coated SPCEs, and further to the PCA-RGO/Au NPs modified SPCEs

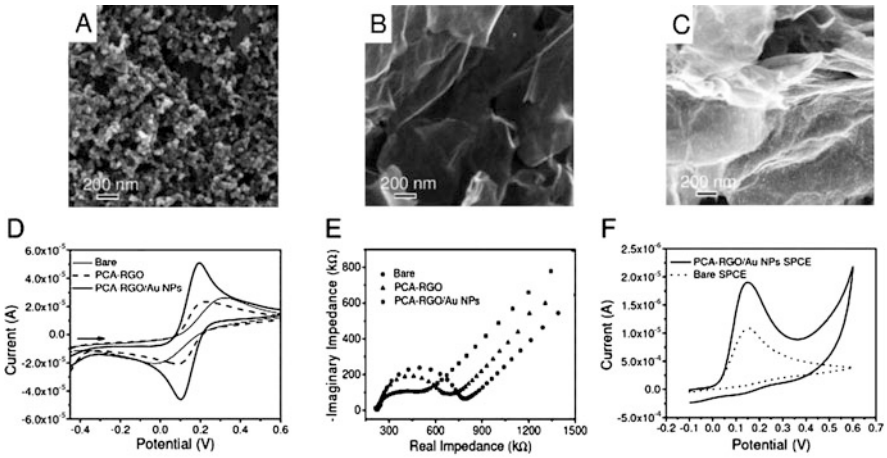

Fig. 18.2 SEM micrographs of SPCEs as bare (**a**), coated by PCA-RGO (**b**) and PCA-RGO/Au NPs flakes (**c**), recorded at 5 kV with the magnifications of 102.16 kX (**a**), 101.67 kX (**b**) and 123 kX (**c**). (**d**) CVs of SPCEs, as bare, modified by PCA-RGO and PCA-RGO/Au NPs in 0.1 M KCl and 5 mM $[Fe(CN)_6]^{3-/4-}$ at 10 mV s^{-1}. (**e**) EIS spectra (Nyquist plots) before (●) and after SPCE modification with (▲) PCA-RGO and (■) PCA-RGO/Au NPs in 5 mM $[Fe(CN)_6]^{3-/4-}$ and 0.1 M KCl. (**f**) CVs of 500 μM 1-napthol at PCA-RGO/Au NPs SPCEs and bare SPCEs in 0.1 M DEA buffer at pH 9.6 and scan rate of 50 mV s^{-1}

(Fig. 18.2d). This evidence accounts for the higher conductivity and for the enhancement of the electron transfer capability at the electrode/electrolyte interface upon the hybrid modification of the SPCE surface [7]. The peak current of the PCA-RGO/Au NPs hybrid modified SPCEs increases with respect to that of the bare counterpart, and of the PCA-RGO modified SPCEs (Fig. 18.2d), likely due to the increase of the electroactive surface area, attesting for the higher electrochemical reactivity of the hybrid modified SPCEs [7].

The electroactive areas (A_{ele}) of both the bare and PCA-RGO/Au NPs modified SPCEs have been estimated using the Randles-Sevcik equation, and for the modified one it is almost twice the geometric area of the native SPCE (7 mm^2), namely 14 ± 2 mm^2 [7].

The apparent heterogeneous electron transfer rate constant (k_0) has been calculated by using the method applied for quasi-reversible systems [11] and it is $9.3 \pm 0.7 \times 10^{-4}$ cm s^{-1}, threefold higher than that of the bare SPCEs, which is $2.7 \pm 0.5 \times 10^{-4}$. This evidence indicates that the electrode modification with the hybrid nanostructures results in an increased conductivity and faster heterogeneous electron transfer.

EIS spectra, reported in Fig. 18.2e as Nyquist plots, include a semicircle portion at higher frequencies, where the diameter of the semi-circle corresponds to the electron transfer resistance (R_{et}) at the electrode interface and a linear portion at lower frequencies, which represents the diffusion process. R_{et} of ca. 0.5 ± 0.1 kΩ can be estimated for the bare SPCEs, ca. 0.4 ± 0.1 kΩ for the PCA-RGO modified SPCEs and ca. 0.30 ± 0.08 kΩ for the electrode modified with the PCA-RGO/Au

NPs hybrid flakes [7]. In case of the hybrid modified electrodes a much lower resistance is found, reasonably due to the high surface area of the hybrid nanostructures coating the SPCE and the excellent electrical conductivity of the nanocomposite, accelerating the electron transfer at the electrode/electrolyte interface [7], and hence, confirming the indication coming from the CV results.

Figure 18.2f shows the CV scans of a 500 μM solution of 1-naphthol, the product resulting from the Alkaline Phosphatase (AP) catalyzed electrochemical assay and designed for detecting the miRNA-221 biomarker. The CVs are recorded on the PCA-RGO/Au NPs modified and unmodified SPCEs in di-ethanol amine buffer (DEA) at pH 9.6 in the potential range between – 0.2 and + 0.6 V, keeping the geometrical area of the electrode constant (7 mm^2).

The PCA-RGO/Au NPs modified SPCEs show the largest current response, being about 1.5 and 3 times higher than that recorded for the unmodified SPCEs, with a potential negatively shifted with respect to the bare SPCEs of ca. 20 mV (Fig. 18.2f). No cathodic peak is observed for 1-naphthol during the reverse scan, because of its irreversible oxidation. The increase of the anodic peak current of the 1-naphthol oxidation, and the decrease of the overpotential of the PCA-RGO/Au NPs hybrid modified SPCEs, show that such electrodes are efficient electrocatalysts for a sensitive determination of 1-naphthol.

The sketch in Fig. 18.3(a–c) exhibits the proposed enzyme amplified genosensor assay. DNA CP has been immobilized onto the Au NPs surface of the hybrid modified SPCEs in self-organized layers, subsequently backfilled with 6-mercapto-1 hexanol (MCH). Such a short alkanethiol is used to remove any competing nonspecific adsorption of other species and favors the organization of the DNA strand [12] in layers not too closely packed, which can limit the steric hindrance and electrostatic repulsion during the hybridization with the miRNA-221 target.

The biotinylated target miRNA-221 sequence has been allowed to react with the DNA CP and subsequently exposed to the streptavidin-Alkaline Phosphatase (AP) enzyme. After incubation in 1-naphthyl phosphate, the production of 1-naphthol catalyzed by AP has been detected by monitoring its oxidation peak current by DPV. Figure 18.3d displays the Nyquist plots of the PCA-RGO/Au NPs SPCEs, before and after modification with CP (PCA-RGO/AuNPs/CP), and after hybridization with the target (T) miRNA-221 (PCA-RGO/AuNP/CP/T). The plot of the PCA-RGO/Au NPs modified SPCEs is semicircular and has R_{et} of about 0.30 ± 0.08 kΩ, which increases up to 0.6 ± 0.1 kΩ after CP immobilization (Fig. 18.3d), due to the repulsion of the $[Fe(CN)_6]^{3-/4-}$ caused by the negatively charged phosphoric acid backbones of the CPs, inhibiting the electron transfer [7]. An enhancement of R_{et} up to 1.2 ± 0.2 kΩ is observed after the hybridization of DNA-CP with the target miRNA-221 due to an increase of the negative charge originated from the double-stranded RNA/DNA formation [7].

The analytical performance of the hybrid modified SPCEs in the assay has been estimated by a calibration experiment. The current has been found to increase with the target miRNA-221 concentration from 1 pM to 5 nM (Fig. 18.3e), and the limit of detection (LOD) has been determined to be 0.7 pM (0.7 amol in 10 μL), considering it as the value of the background signal, added of three times its standard deviation. The found LOD is lower than other LODs recently reported for other

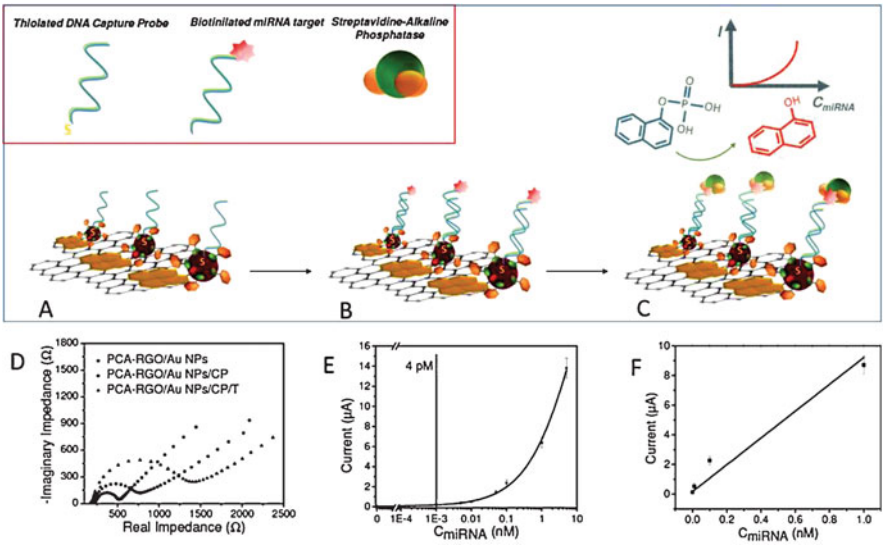

Fig. 18.3 Sketch of the preparation of the PCA-RGO/Au NPs modified SPCEs for the electrochemical genosensor assay. (The schemes do not show proper the proportions of the reported structures). (**a**) Immobilization of the DNA capture probe (CP) on the PCA-RGO/Au NPs modified SPCEs. (**b**) Hybridization of the DNA CP with the miRNA-221 target. (**c**) Exposure of the SPCEs to AP, incubation of the substrate in 1-naphthyl phosphate, generation of 1-naphthol detected by DPV. (**d**) Faradaic impedance spectra (in form of Nyquist plots) in 0.1 M KCl and 5 mM $[Fe(CN)_6]^{3-/4-}$(1:1) solution of (■) PCA-RGO/Au NPs SPCEs, (●) DNA CP functionalized SPCEs (PCA-RGO/Au NPs/CP) and (▲) PCA-RGO/Au NPs/CP SPCEs after incubation with the 10 nM miRNA-221 target (PCA-RGO/Au NPs/CP/T). (E) miRNA-221 calibration plots in PB, achieved by PCA-RGO/Au NPs SPCEs. The error bar corresponds to the standard deviation and the vertical bar points at the minimum detected concentration value. (**f**) Calibration curve of miRNA-221 in spiked serum samples

graphene-Au NPs nanocomposite electrode modifiers, still using AP as enzymatic label, and comparable with the LODs reported for other electrochemical methods for miRNA analysis [13]. Such an enhanced analytical performance is accounted for by the high conductivity of the hybrid nanocomposite modified electrodes, the fast electron transfer kinetics, the high electroactivity of the electrode towards 1-naphthol oxidation and the high electroactive area and morphology [8] of the nanostructured surface. Indeed, such a morphology offers convenient geometry for the hybridization process, providing a high extent of the DNA CP immobilization, and hence amplified hybridization events with the miRNA target [1].

The operational reliability and feasibility of the developed assay have been finally assessed by analyzing diluted human blood serum samples, added with different concentrations of miRNA-221, namely 10 and 100 pM (Fig. 18.3f) and the determined recovery values, namely 103% and 117%, respectively, seem to be affected by unspecific physisorption of serum proteins at the electrode surface.

18.4 Conclusions

A novel colloidal hybrid material based on RGO sheets, surface modified by pyrene-carboxylic acid (PCA), and highly densely modified by Au NPs (PCA-RGO/Au NPs) coated by the aromatic thiol DMBT, has been synthesized. PCA anchors the RGO platform by π-π interactions and behaves as linker and coupling agent between the RGO flakes and the NPs. The PCA carboxyl moieties act as coordinating active sites for the *in situ* colloidal reduction of the Au precursor, promoted by DMBT and $NaBH_4$. DMBT controls the Au NPs growth, ultimately resulting in a narrow size distribution of the NPs, 2.8 ± 0.6 nm in size, and in providing their π-π stacking into assemblies onto the PCA-RGO platform, as well as mutual electron coupling interactions. SPCEs modified by the hybrid nanocomposite show an increased electroactive surface area, higher electrical conductivity, faster heterogeneous electron transfer kinetics at the electrode interface, higher electron transfer constant and a decreased resistance at the electrode-electrolyte interface with respect to the PCA-RGO modified and pristine SPCEs. The hybrid modified SPCEs have been applied in an AP amplified electrochemical bioassay for the detection of the miRNA-221 cancer biomarker in spiked human blood serum samples, with a LOD of 0.7 pM (7 amol in 10 μL) and RSD% of 13% in a range of 1–5000 pM. The obtained hybrid nanocomposite modified electrodes can be applied in diverse affinity assays for the detection of other biomolecules in point of care devices.

Acknowledgments This work was partially supported by Ministero dell'Istruzione, dell'Università e della Ricerca (MIUR) in the framework of PRIN 2012 (Grant No. 20128ZZS2H).

References

1. Turcheniuk K, Boukherroub R, Szunerits S, Mater J (2015) Gold–graphene nanocomposites for sensing and biomedical applications. Chem B 3:4301
2. Zhang Y, Bai X, Wang X, Shiu K-K, Zhu Y, Jiang H (2014) Highly sensitive graphene–Pt nanocomposites amperometric biosensor and its application in living cell H2O2 detection. Anal Chem 86:9459
3. Peng H-P, Hu Y, Liu P, Deng Y-N, Wang P, Chen W, Liu A-L, Chen Y-Z, Lin X-H (2015) Label-free electrochemical DNA biosensor for rapid detection of mutidrug resistance gene based on Au nanoparticles/toluidine blue–graphene oxide nanocomposites. Sensors Actuators B Chem 207:269
4. Kilic T, Erdem A, Ozsoz M, Carrara S (2018) microRNA biosensors: Opportunities and challenges among conventional and commercially available techniques. Biosens Bioelectron 99:525
5. Ingrosso C, Corricelli M, Disha A, Fanizza E, Bianco GV, Depalo N, Panniello A, Agostiano A, Striccoli M, Curri ML (2019) Solvent dispersible nanocomposite based on Reduced Graphene Oxide and in-situ decorated gold nanoparticles. Carbon 152:777
6. Voccia D, Sosnowska M, Bettazzi F, Roscigno G, Fratini E, De Franciscis V, Condorelli G, Chitta R, D'Souza F, Kutner W, Palchetti I (2017) Direct determination of small RNAs using a biotinylated polythiophene impedimetric genosensor. Biosens Bioelectron 87:1012

7. Ingrosso C, Corricelli M, Bettazzi F, Konstantinidou E, Bianco GV, Depalo N, Striccoli M, Agostiano A, Curri ML, Palchetti I, Mater J (2019) Au nanoparticle in situ decorated RGO nanocomposites for highly sensitive electrochemical genosensors. Chem B 7:768
8. Kong D, Bi S, Wang Z, Xia J, Zhang F (2016) Anal Chem 88:10667. In Situ Growth of Three-Dimensional Graphene Films for Signal-On Electrochemical Biosensing of Various Analytes
9. Voccia D, Bettazzi F, Fratini E, Berti D, Palchetti I (2016) Improving impedimetric nucleic acid detection by using enzyme-decorated liposomes and nanostructured screen-printed electrodes. Anal Bioanal Chem 408:7271
10. Laschi S, Palchetti I, Marrazza G, Mascini M (2006) Development of disposable low density screen-printed electrode arrays for simultaneous electrochemical measurements of the hybridisation reaction. J Electroanal Chem 593:21
11. Nicholson RS (1965) Theory and application of cyclic voltammetry for measurement of electrode reaction kinetics. Anal Chem 37:1351
12. Palchetti I, Laschi S, Marrazza G, Mascini M (2007) Electrochemical imaging of localized sandwich DNA hybridization using scanning electrochemical microscopy. Anal Chem 79:7206
13. Campuzano S, Torrente-Rodríguez RM, López-Hernández E, Conzuelo F, Granados R, Sánchez-Puelles JM, Pingarrón JM (2014) Magnetobiosensors based on viral protein p19 for microRNA determination in Cancer cells and tissues. Angew Chem Int Ed 53:6168

Chapter 19
Electrical Properties in PMMA/ Carbon-Dots Nanocomposite Films Below the Percolation Threshold

Zakaria El Ansary, Ilham Bouknaitir, Silvia Soreto Teixeira, Lamyaa Kreit, Annamaria Panniello, Paola Fini, Marinella Striccoli, Mohamed El Hasnaoui, Luís Cadillon Costa, and Mohammed Essaid Achour

Abstract An investigation of the thermal, electrical and dielectric properties of original nanocomposite materials based on the incorporation of carbon dots, synthesized in organic solvents, in a poly(methyl methacrylate) (PMMA) is presented. Thermal analysis was performed using differential scanning calorimetry. Electrical and dielectric measurements were carried out in the frequency range from 100 Hz to 1 MHz and at temperatures between 200 and 400 K. The data were analyzed using two formalisms: (i) AC conductivity that has been found to follow the Jonscher's power law with double exponents, and (ii) electric modulus that permits to identify two dielectric relaxation processes. The first one, appearing at low-frequency, was attributed to the conduction effect which is consistent with the Havriliak-Negami model, and the second one, appearing at high-frequency was associated with the interfacial polarization effect. Furthermore, the analysis of the temperature dependence of AC conductivity using the Arrhenius representation indicated the existence of two mechanisms basically governing the conductivity.

Keywords Carbon dots · Composites · AC conductivity · Havriliak-Negami model · Activation energy

Z. El Ansary · I. Bouknaitir · L. Kreit · M. El Hasnaoui · M. E. Achour (✉)
LASTID Laboratory, Physics Department, Faculty of Sciences, Ibn Tofail University, Kenitra, Morocco
e-mail: achour.me@univ-ibntofail.ac.ma

S. S. Teixeira · L. C. Costa
I3N and Physics Department, University of Aveiro, Aveiro, Portugal

A. Panniello · P. Fini · M. Striccoli
CNR-IPCF S. Bari, c/o Dipartimento di Chimica, Università di Bari, Bari, Italy

P. Petkov et al. (eds.), *Nanoscience and Nanotechnology in Security and Protection against CBRN Threats*, NATO Science for Peace and Security Series B: Physics and Biophysics, https://doi.org/10.1007/978-94-024-2018-0_19

19.1 Introduction

In recent years, a significant effort has been devoted to the design and fabrication of new materials in the nanometric size range. The nanoparticles can be prepared by a top-down or bottom-up approach, the last one with the advantage of having the nano-objects dispersed in an organic solvent. Such peculiarity easily allows the preparation of original nanocomposites by incorporation of different kinds of nanoparticles into polymer matrixes using a common solvent, opening the way toward many emerging applications [1]. Indeed, the dispersed particles are mainly used to enhance some properties of the composite material, such as conductivity, mechanical and rheological features, optical properties and others. One of the main reasons for using nanoparticles is their large surface to volume ratio, which increases the number of particle-matrix interactions, thus enhancing the effects on the overall material properties [2]. The properties of the nanocomposites depend on both the inherent characteristics of the components (such as nanoparticle size, ligands on their surface, molecular weight of the polymer, crystallinity, etc.) and the distribution of the nano-objects inside the polymer matrix [3]. Carbon-based nanostructures are currently object of great interest in nanotechnology [4]. Recently, carbon nanodots (C-Dots) have emerged as an effective alternative to the classical inorganic semiconductor quantum dots (QDs) for a wide range of interesting applications comprising sensors, photovoltaics, catalysis, bioimaging, drug delivery, and optoelectronics. Compared to QDs, C-Dots combine intense and tunable photoluminescence (PL) with good biocompatibility, low toxicity, high resistance to photobleaching, and inexpensive cost [5]. C-Dots have attracted extensive attention as a novel zero-dimensional carbon-based nanomaterial, particularly as a promising material for energy storage as reported by Bhattacharya et al. [6]. Owing to their high surface area, more active edge sites, good electrochemical conductivity and dispersion in various solvents, C-Dots were used by Yaru et al. [7] to prepare C-Dots/TiO_2 composites to be applied for the first time in photoreduction of Cr(VI) under sunlight illumination. In other works [8–11], it was demonstrated that C-Dots can considerably improve the electrochemical performance of supercapacitors, especially for the application in high-performance electrodes [12, 13].

Electrical and dielectric relaxation phenomena were used to study the transport mechanisms of several series of composite materials based on a PMMA matrix loaded with conducting charges. For instance, Logakis et al. [14] analyzed the dielectric relaxation appearing in PMMA/CNT percolating system, in consistence with differential scanning calorimetry and dynamic-mechanical analysis, finding a weak interaction between the macromolecular chains and the CNT particles and that the absence of crystallinity facilitates the achievement of high conductivity levels in the nanocomposites. Maji et al. [15] studied the effect of temperature and frequency on the dipolar motion of the polymeric chains of PMMA/$Zn(NO_3)_2$ composite, finding that it is one of the appropriate candidates for numerous technical applications such as supercapacitors, high-speed computers and gate dielectric material for organic FETs. The results of electrical and dielectric properties of PMMA/PPy

composites published by Aribou et al. [16] and El Hasnaoui et al. [17] revealed that the response of these materials, for the loading above the percolation threshold, has an abnormal low-frequency dispersion due to the hopping of charge carriers between localized states.

As a relaxation process and related phenomena are expected in PMMA/C-Dots nanocomposites, their investigation is essential not only from the practical point of view, because of their potential applications, but also for the insight information regarding charge mobility, polarization, and conduction mechanisms. The optical properties of PMMA/C-Dots composite have been already presented by Bouknaitir et al. [18], who found that the absorption increases with increasing of the C-Dots fraction, indicating that the nanoparticles preserve their individuality in the polymer matrix and do not undergo a strong aggregation. In addition, the photoluminescence spectra of the composites show a large emission band that shifts towards lower energy as the excitation wavelength increases, characteristic of the embedded C-Dots. Thus, in order to complete this study, the electrical and thermal properties of these composites were investigated in the current work.

19.2 Experimental Procedures

19.2.1 Materials and Sample Preparation

Poly (methyl methacrylate) (PMMA) was supplied by BHD Chemicals Ltd. Poole, England. $CHCl_3$ was purchased from Sigma-Aldrich, Germany, and the carbon-dots (C-Dots) were synthesized in the laboratory of CNR–IPCF, Bari, Italy. The luminescent nanoparticles were prepared by a one-step method consisting of the carbonization of citric acid (CA), carried out in a mixture of octadecene (ODE) as non-coordinating solvent and hexadecylamine (HDA) as coordinating agent [19]. The citric acid was injected in a mixture of HDA and ODE at 200 °C (473 K), followed by a growth step at 300 °C (573 K) for 3 h. Then, a purification procedure by an extraction step, adding a mixture 1:1 $CHCl_3/CH_3OH$, a precipitation step with acetone and a concentration step using a rotary evaporator were carried out. Finally, the C-dots were dispersed in chloroform. The synthesized nanoparticles have a diameter of about 5 nm and consist of an amorphous core with sp^3 and sp^2 carbon and an outer oxidized carbon shell, which is functionalized by different molecules, particularly by amide derivatives, responsible for their emission [20]. The polymeric matrix solution was prepared by dissolving 0.5 g of PMMA powder in 10 ml of chloroform. The solution was stirred for few hours at room temperature, then PMMA/C-Dots nanocomposite solutions were prepared by incorporation of adequate volumes of C-dots into the polymer solution, in order to achieve loadings in the range from 0% to 4%. Finally, the prepared composites were poured on a glass substrate and let the solvent evaporate at room temperature for 48 h to obtain freestanding films that were peeled off from the substrate.

19.2.2 DSC Measurements

Differential scanning calorimetry (DSC) analyses were carried out on a Q200 TA Instruments calibrated with indium, with 10 K/min under inert atmosphere: First, we made a heating scan from 303 to 503 K to investigate thermal transition to the drop-casted material and, in order to erase the thermal history of the samples, we stabilized the temperature at 503 K for 5 minutes. Then we started the measurements of cooling scan till 303 K to identify the thermal transition of relaxed nanocomposites material at the different C-Dots loading. A reheating scan from 303 to 503 K allowed recognizing the thermal transitions with the same thermal history [21]. Glass transitions are evident in the cooling and in the second heating scan.

19.2.3 Electrical Measurements

For the electrical measurements the samples were prepared as discs with a thickness of about 3 mm and a diameter of 12 mm with aluminum electrodes on the opposite sides of the sample. The electrical contacts were formed by silver conductive paint. Impedance spectroscopy measurements were performed as a function of frequency in the range from 100 Hz to 1 MHz, and at temperature between 200 and 400 K, using a bath cryostat system where the samples are maintained in a controlled helium atmosphere, in order to avoid moisture and to homogenize the sample temperature. The stabilization of the temperature was better than 0.1 K over the electrical measurement periods. This was achieved using an Agilent 4292A impedance analyzer, in the C_p-R_p configuration. Since the samples have a disk geometry with a considerably larger diameter compared with their thickness, the parallel plate capacitor model can be applied, and the AC electrical conductivity $\sigma_{AC}(\omega)$ can be calculated through the measured complex impedance by:

$$\sigma_{AC}(\omega) = \frac{d}{A}\frac{1}{R_p} \tag{19.1}$$

where d and A are the sample thickness and electrode surface area, respectively. The real (M') and imaginary (M'') parts of electric modulus $M*(\omega) = M'(\omega) - jM''(\omega)$, were calculated through C_p-R_p using Eqs. (19.2) and (19.3). The estimated relative error of the electrical measurements was less than 5%.

$$M'(\omega) = \frac{A}{d}\frac{\varepsilon_0 C_P(\omega R_P)^2}{1 + (\omega R_P C_P)^2} \tag{19.2}$$

$$M''(\omega) = \frac{A}{d} \frac{\varepsilon_0 R_P \omega}{1 + (\omega R_P C_P)^2} \tag{19.3}$$

19.3 Results and Discussion

19.3.1 DSC Analysis

Heat flow measured during cooling and heating of neat PMMA and two samples of nanocomposites with 2.5% and 4% loading are shown in Fig. 19.1. As can be seen, each curve shows an endothermic peak at a particular temperature that corresponds to a reversible phase transition of second order from a glassy state to an elastic one. Table 19.1 illustrates the estimated values of glass transition temperatures of cooling (T_{gc}) and heating (T_{gh}). Analysis of the results yields the two following observations: (i) the values of T_{gc} and T_{gh} for the neat PMMA are found to be in good agreement with those reported by Kumar and co-workers [22] and (ii) the addition of C-Dots nanofillers causes in both cases a decrease of the glass transition temperature, more pronounced at higher loading of C-Dots filler. These results indicate that C-Dots nanofillers have a plasticizing effect on the polymer structure, giving rise to an increase of the charge mobility inside PMMA chains [23]. PMMA based nanocomposites, mainly prepared using solvent-based methods, point out a decrease

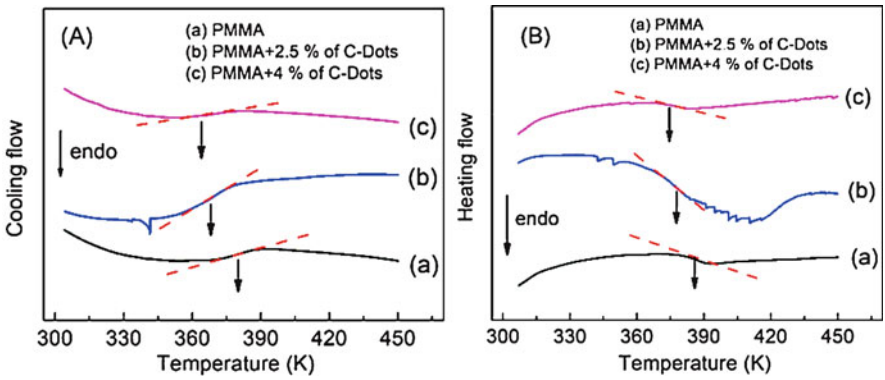

Fig. 19.1 DSC measurements of cooling (**A**) and heating (**B**) scans of the PMMA matrix and PMMA/C-dots nanocomposites

Table 19.1 Glass transition temperatures obtained during cooling (T_{gc}) and heating (T_{gh}) scans of neat PMMA and PMMA/C-Dots nanocomposites

ϕ(%)	0.0	2.5	4.0
T_{gh} (K)	385	377	374
T_{gc} (K)	380	367	363

of the glass transition temperature [24]. An explanation of this behavior, based on thermodynamic model developed by Lee et al. [25] for binary polymer/nanoparticles systems, states that the increases or decreases of T_g depend on the negative or positive change of the total configurational entropy. Among the four contributions considered in the total configurational entropy, namely the disorientation entropy of the polymer, the confinement entropy of the nanoparticle, the mixing and the specific interaction entropies of the polymer/nanoparticle, the most important component in determining the T_g value is the intensity of the specific interaction entropy between the polymer and the nanofillers. This entropy is quantitatively identified by a physical parameter γ_{spe} in the model of Lee, which represents the specific interaction between the polymer and the nanofillers. A decrease of T_g is possible only when γ_{spe} is zero, the case when no specific interaction occurs between the polymeric chains and the nanofillers. In concordance to our results, we considered that, even for the increased C-Dots concentrations inside PMMA matrix, the specific interactions between these constituents are weak.

19.3.2 AC Electrical Conductivity Analysis

It is proven that the analysis of temperature effect on frequency-dependence of the electrical conductivity is a powerful method for studying the charge-transport mechanisms occurring in heterogeneous materials. Figure 19.2 shows the log-log representations of the frequency dependence of the AC conductivity of neat PMMA (Fig. 19.2A), sample with 2.5% (Fig. 19.2B), and 4% (Fig. 19.2C) of C-Dots loaded PMMA matrix, while in Fig. 19.3, we associated three curves of electrical conductivity corresponding to the different samples at a constant temperature ($T = 380$ K). Analysis of these figures allows to identify three interesting remarks. First, for all samples the AC conductivity increases with the temperature, this behavior will be interpreted in terms of activation energies. Second, the log-log variation of AC conductivity versus frequency shows a linear increase with a change in slope at a specific value of frequency noted F_c (Figs. 19.2 and 19.3), suggesting a superposition of different electrical transport mechanisms [26, 27]. Third, the loading of C-Dots nanofillers increases the AC conductivity of the composites (Fig. 19.3). Different types of hopping and carrier species are then involved in the transport behavior.

The AC conductivity in the two frequency domains can be described by the power law with double exponents expressed by the following equation [28]:

$$\sigma_{ac}(\omega, T) = \sigma(\omega, T) - \sigma_{dc}(T) = \sigma_1 \omega^{s1(T)} + \sigma_2 \omega^{s2(T)} \tag{19.4}$$

where $\sigma(\omega,T)$ represents the total electrical conductivity, $\sigma_{dc}(T)$ is the direct current conductivity that represents the frequency independent part of the AC conductivity, not shown in our data (Fig. 19.2), σ_1 and σ_2 are constants, the exponent s1 ($0 < s1$

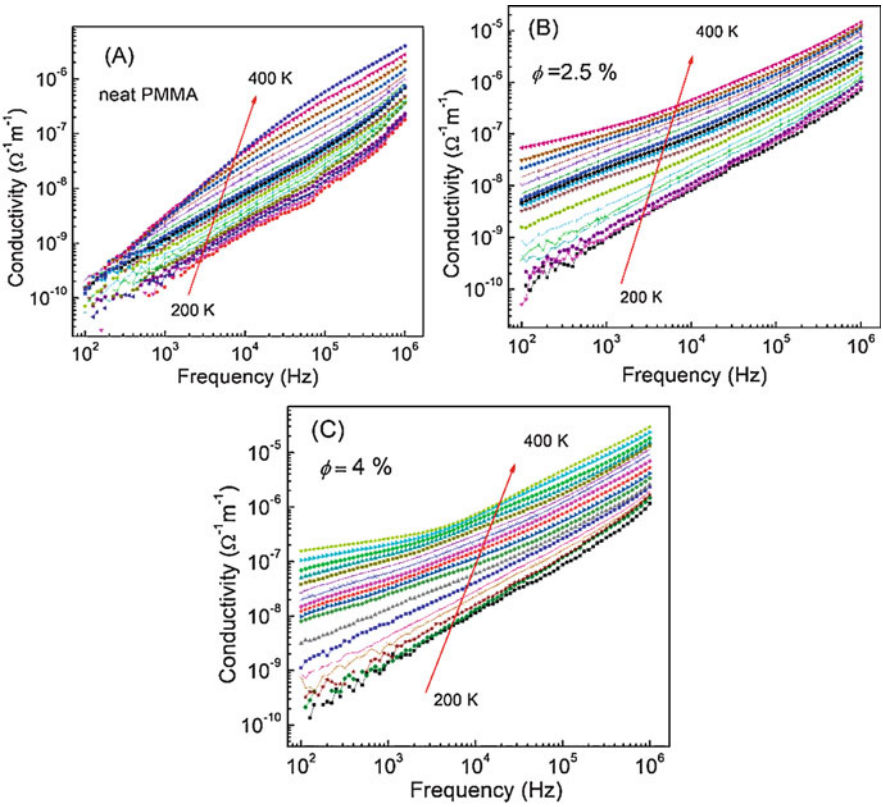

Fig. 19.2 Frequency dependence of AC conductivity of neat PMMA (**A**) and PMMA/C-Dots nanocomposites ($\Phi = 2.5\%$ (**B**) and $\Phi = 4\%$ (**C**)) in the range of 200–400 K

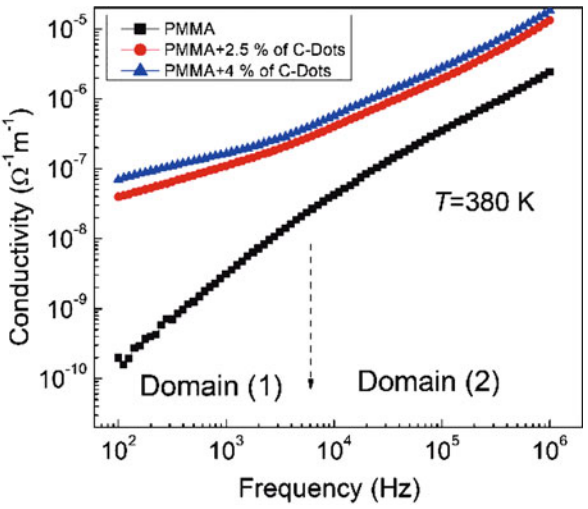

Fig. 19.3 Comparative curves of frequency dependence of AC electrical conductivity of each sample at 380 K

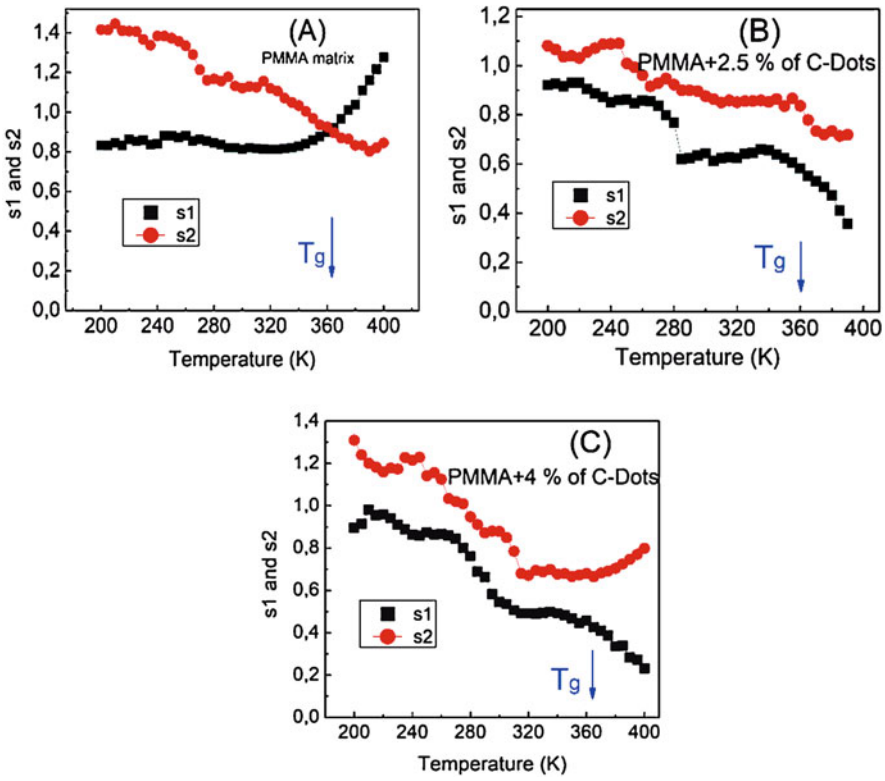

Fig. 19.4 Temperature effect on s1 and s2 (low and high frequency exponents, respectively) of neat PMMA and two samples of PMMA/C-Dots nanocomposites

(T) < 1) characterizes the translational hopping in the low frequency domain, while the exponent s2 (s2(T) < 2) characterizes the existence of localized relaxation, or reorientaional hopping process in the high frequency domain [29].

Figure 19.4 shows the evolution of the obtained values of s1 and s2 as a function of the temperature for neat PMMA (Fig. 19.4A), PMMA loaded with 2.5% C-Dots (Fig. 19.4B), and PMMA loaded with 4% C-Dots (Fig. 19.4C).

For the neat PMMA, the value of the exponent s2 is constant at about 0.85 and the exponent s1 decreases from 1.4 to about 0.9 for temperatures below $T_r = 300$ K (room temperature). Above T_r, s2 continues to decrease to 0.8 but s1 increases to 1.3. When C-Dots particles are added to the PMMA matrix, the obtained values of s2 are higher than those of s1 in the whole range of temperatures and both of them decrease with decreasing of temperature. The temperature dependence of s1 and s2 exponents gives information about the mechanism involved in the AC conductivity. Due to localization of charge carriers, which results in the formation of polarons in this case, hopping conduction can occur between the nearest neighboring sites. For small polaron hopping conduction, the exponent s increases with temperature, whereas for large polaron hopping conduction it decreases [30]. Applying these descriptions

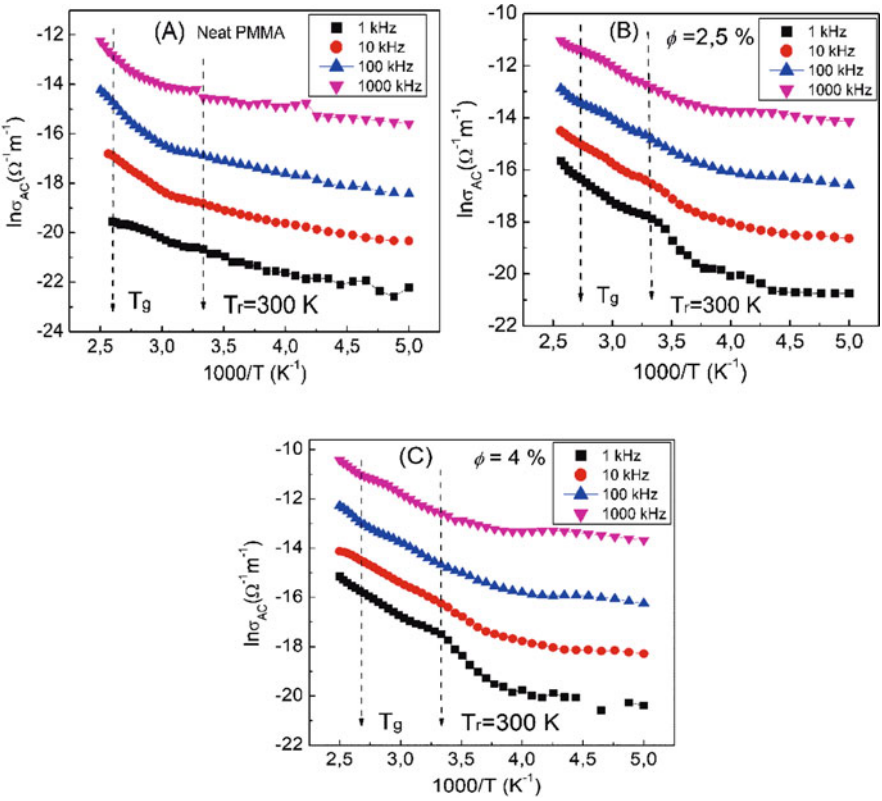

Fig. 19.5 $\ln\sigma_{AC}$ vs. the inversed temperature at different values of frequency: (**A**) neat PMMA; (**B**) and (**C**): samples with $\phi = 2.5\%$ and $\phi = 4\%$ C-Dots, respectively

to our case, we have come to the following conclusions: (i) the conduction in PMMA is related to large polaron hopping at high frequencies for temperatures below room temperature T_r, whereas it is related to small polaron hopping at low frequencies for temperatures above T_r [31], and (ii) when C-Dots are added to PMMA matrix, both s1 and s2 decrease with increasing the temperature, showing the dominance of large polaron hopping mechanism.

In order to investigate the frequency and temperature effects on the activation energies, we have represented in Fig. 19.5 $ln\sigma_{AC}$ vs. 1000/T according to the Arrhenius law:

$$\sigma_{AC}(F,T) = \sigma_o \exp\left(-\frac{W_a}{k_b T}\right) \tag{19.5}$$

where k_b is the Boltzmann's constant, σ_o a pre-exponential factor, and W_a represents the activation energy. It can be observed that there is a change in the slopes at about room temperature, indicating a transition in the conduction mechanism. The

Table 19.2 Frequency dependence of the activation energy of neat PMMA and two samples of PMMA/C-Dots nanocomposites at temperatures below and above the room point $T_r = 300$ K

	W_a (meV) 1 kHz		W_a (meV) 10 kHz		W_a (meV) 100 kHz		W_a (meV) 1 MHz	
ϕ(%)	$T < T_r$	$T > T_r$	$T < T_r$	$T > T_r$	$T < T_r$	$T > T_r$	$T < T_r$	$T > T_r$
0.0	80	180	82	300	83	390	70	400
2.5	79	290	47	230	38	210	36	200
4.0	54	270	47	240	35	230	27	220

activation energies characterizing each domain of temperature, $T < T_r$ and $T > T_r$, at different values of the frequency have been calculated and summarized in Table 19.2. The values of W_a increase from 27–83 meV at low temperatures to 180–400 meV at high temperatures. These changes could be attributed to more energy required to overcome the thermal fluctuation by the charge carriers in high temperature domain. It is also noticed that the activation energy increases with increasing the frequency for the neat PMMA, while when C-Dots are added to PMMA, the behavior has changed, i.e. W_a decreases with the frequency. This may be due to the fact that in the low-frequency domain the conductivity is due to the hopping mobility of charge carriers over a large distance [32], while in the high-frequency domain the hopping is restricted to only the nearest neighboring defect sites.

19.3.3 Electrical Modulus Analysis

The formalism of the electrical modulus has been used in several works to interpret the relaxation processes appearing in the dielectric responses of heterogeneous materials based on conductive nanoparticles loaded into polymeric matrix [33, 34]. The real $M'(\omega)$ and imaginary $M''(\omega)$ parts of the electric modulus are shown in Fig. 19.6.

It can be observed that, for the neat PMMA (Figs. 6A_1 and A_2), M'' shows a relaxation peak in the spectra, whose value and intensity increase with the temperature due to faster charge movements, leading to decrease of the relaxation times [35]. When C-Dots nanoparticles are added to PMMA matrix with two concentrations (Figs. 6B_1, B_2, C_1 and C_2), M'' spectra show the presence of two dielectric relaxation peaks. Comparing these behaviors with that of similar materials [34, 36, 37], we attribute the dielectric relaxation appearing in PMMA matrix to the conductivity effect (the same that appeared in the low frequency domain in the composites, relaxation 1). The dielectric relaxation that appeared in the high frequency domain in the composites (relaxation 2) is attributed to the interfacial polarisation or Maxwell-Wanger-Sillars (MWS) effect that results in charge accumulations inside the PMMA matrix. We note that for all prepared samples, the value of M' tends to zero at low frequencies, indicating that the electrode polarization has a negligible contribution [38, 39].

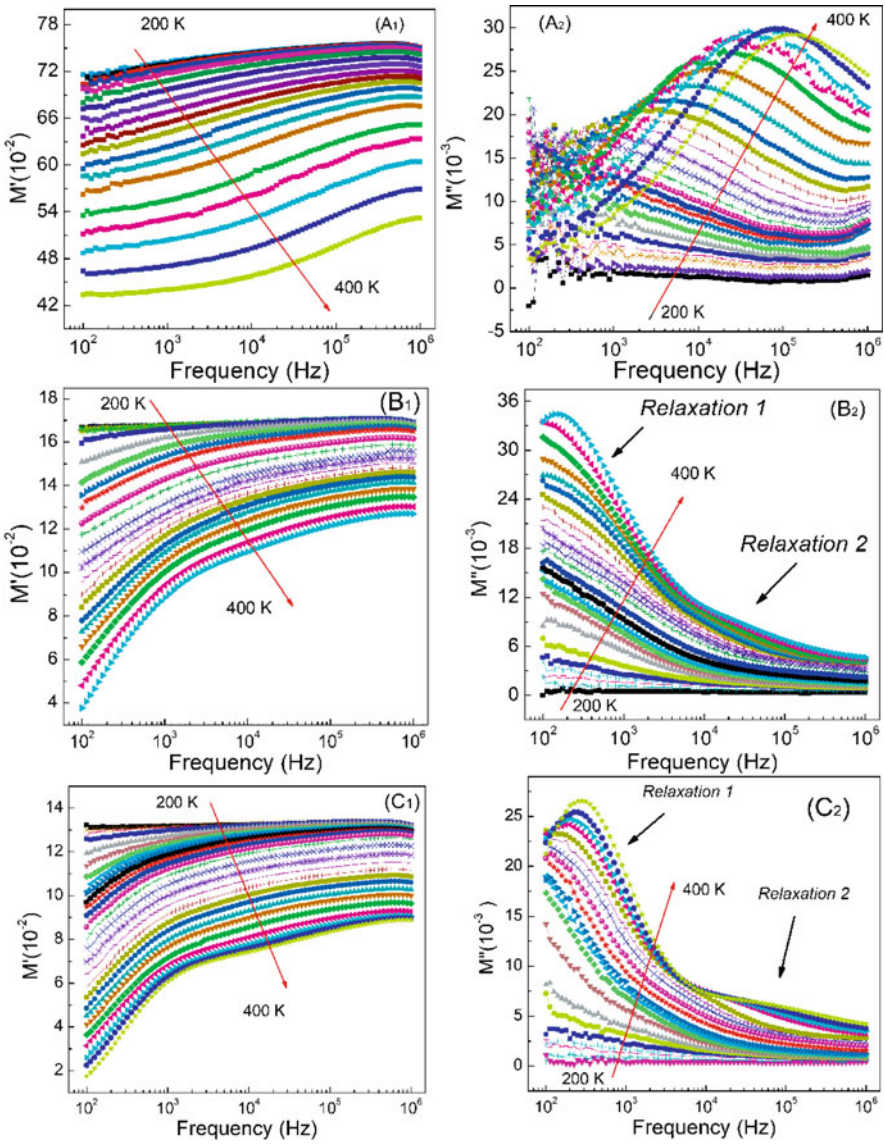

Fig. 19.6 Frequency dependence of real M' and imaginary M'' parts of electric modulus for the neat PMMA (A_1 and A_2), $\phi = 2.5\%$ (B_1 and B_2), and $\phi = 4\%$(C_1 and C_2) in the temperature range from 200 to 400 K

19.3.4 Havriliak-Negami Modeling

The asymmetrical spectra of $M''(\omega)$ indicate that the Debye model is inappropriate to describe the relaxation occurring in these materials and should be replaced by a frequency-dependent electric modulus given as [40]:

$$M^*(\omega) = M'_\infty[1 - \int_0^\infty e^{j\omega t}(-\frac{d\phi(t)}{dt})dt] \tag{19.6}$$

where $\phi(t)$ denotes the electric field relaxation function. The real and imaginary parts of the complex modulus according to the Havriliak-Negami model are given by the following expressions [41]:

$$M'(\omega) = M_\infty \frac{\left(M_s r^\beta + (M_\infty - M_s)\cos(\beta\varphi)\right)r^\beta}{M_s^2 r^{2\beta}(M_\infty - M_s)M_s\cos(\beta\varphi) + (M_\infty - M_s)^2} \tag{19.7}$$

$$M''(\omega) = M_s M_\infty \frac{(M_\infty - M_s)\sin(\beta\varphi)r^\beta}{M_s^2 r^{2\beta}(M_\infty - M_s)M_s\cos(\beta\varphi) + (M_\infty - M_s)^2} \tag{19.8}$$

where M_s and M_∞ are the values of the real part of the electric modulus at low- and high-frequency sides of the relaxation, respectively, and the two parameters r and φ are defined as:

$$r = \left(1 + 2(\omega\tau)^{1-\alpha}\sin\left(\frac{\alpha\pi}{2}\right) + (\omega\tau)^{2(1-\alpha)}\right)^{1/2} \tag{19.9}$$

$$\varphi = \text{arctg}\left(\frac{(\omega\tau)^{1-\alpha}\cos(\alpha\pi/2)}{1 + (\omega\tau)^{1-\alpha}\sin(\alpha\pi/2)}\right) \tag{19.10}$$

where τ is the relaxation time, α and β are fractional shape parameters describing the skewing and broadening of the dielectric function, respectively. Both α and β range between 0 and 1, and they represent the deviation from the Debye model. When $\alpha = 0$ and $\beta = 1$, this equation reduces to the Debye model. We made a fit of the experimental data in the low frequency range (relaxation 1) using the above Eqs. (19.7, 19.8 and 19.10) from which we extracted the parameters α, β, τ, and $\Delta M = M_\infty - M_s$.

Figure 19.7 shows an example of M'' versus M' data for neat PMMA and PMMA/C-Dots composite (ϕ= 4%) (together with a simulation (solid lines) according to Havriliak-Negami model. The obtained values of all studied samples are presented in Table 19.3. The values of α are in the range 0.5–0.77 and increases with the temperature, indicating increase of interactions between the particles and the segment of PMMA as the temperature increases. In addition, the values of β are greater

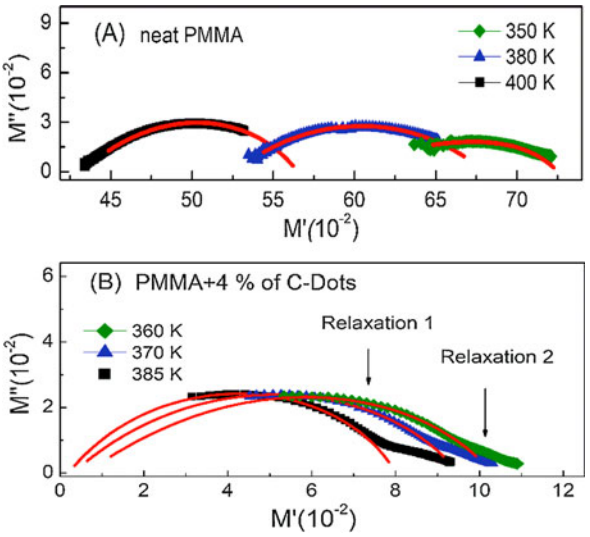

Fig. 19.7 M'' vs. M' plots for neat PMMA and PMMA/C-Dots nanocomposite ($\phi = 4\%$). Solid lines represent the Havriliak-Negami model fitting

Table 19.3 Parameters obtained by fitting the data according to the Havriliak–Negami model of neat PMMA and two samples of PMMA/C-Dots composites at different temperatures

ϕ (%)	T (K)	ΔM	α	β	τ (10^{-5} s)
0.0	350	0.12	0.50	0.55	1.7
	380	0.13	0.50	0.72	1.5
	400	0.14	0.55	0.76	1.2
2.5	350	0.14	0.43	0.70	5.0
	370	0.13	0.52	0.80	3.5
	390	0.10	0.74	0.98	2.0
4.0	360	0.10	0.63	0.71	4.0
	370	0.09	0.65	0.82	3.6
	385	0.07	0.77	0.90	2.8

than 0.55 and increases with the temperature up to 0.98. This indicates that the dielectric relaxation appearing at low frequency is best fitted according to the Havriliak-Negami model in the intermediate range of temperatures and according to the Cole-Cole model for high temperatures, where β is close to 1. We note that, first, the relaxation times reveal a steadily decrease behavior due to an increase of molecular dipole mobility as the temperature increases [42]. Second, the values of the relaxation time increase as C-Dots are added to the PMMA matrix, leading to a significant effect on the dielectric relaxation characterizing the conduction effects.

19.4 Conclusion

This work presents a study of thermal, electrical, and dielectric properties of neat poly(methyl methacrylate) (PMMA) and composites based on PMMA matrix loaded with two concentrations of carbon dots. DSC spectra revealed that the glass

transition temperature of the matrix decreases with the loading of fillers. The electrical conductivity versus frequency was found to follow a double power law, showing two conducting mechanisms contributing to the conductivity. The frequency dependence of the electric modulus showed the existence of two dielectric relaxation processes due to the dipolar interactions related to these composites: the first one appearing at low frequencies attributed to conduction effect, and the second one, appearing at high frequencies, associated with interfacial polarization. The temperature dependence of AC conductivity was found to follow the Arrhenius law with a change of the activation energy at room temperature.

Acknowledgments This work is supported by the Italian (CNR)-Moroccan (CNRST) bilateral project, Ref. (Italy): Prot. CNR Ammin Centr. 24477 del April 24, 2016, Ref. (Morocco): Contrat N: 406/2016. The authors also thank FEDER funds through the COMPETE 2020 Program and National Funds through FCT–Portuguese Foundation for Science and Technology under the project UID/CTM/50025/2019.

References

1. Fengge G (2012) Handbook of advances in polymer nanocomposites. Science Direct, Nottingham
2. Supova M, Martynková GS, Barabaszová K (2011) Effect of nanofillers dispersion in polymer matrices: a review. Sci Adv Mater 3:1
3. Bhattacharya M (2016) Polymer nanocomposites - a comparison between carbon nanotubes, graphene, and clay as nanofillers. Materials 9:262
4. Balasubramanian K, Kern K (2014) 25th Anniversary article: label-free electrical biodetection using carbon nanostructures. Adv Mater 26:1154
5. Wang Y, Hu A (2014) Carbon quantum dots: synthesis, properties and applications. J Mater Chem C 2:6921
6. Bhattacharya K, Deb P (2015) Hybrid nanostructured C-dot decorated Fe_3O_4 electrode materials for superior electrochemical energy storage performance. Dalton Trans 44:9221
7. Yaru L, Zhongmin L, Yongchuan W, Chen J, Jingyu Z, Fengmin J, Ping N (2018) Carbon dots-TiO_2 nanosheets composites for photoreduction of Cr(VI) under sunlight illumination: favorable role of carbon dots. Appl Catal B Environ 224:508
8. Li HT, Kang ZH, Liu Y, Lee ST (2012) Carbon nanodots: synthesis, properties and application. J Mater Chem 22:24230
9. Li XM, Rui MC, Song JZ, Shen ZA, Zeng HB (2015) Carbon and graphene quantum dots for optoelectronic and energy devices: a review. Adv Funct Mater 25:4929
10. Zhang ZP, Zhang J, Chen N, Qu LT (2012) Graphene quantum dots: an emerging material for energy-related applications and beyond. Energy Environ Sci 5:8869
11. Bak S, Kim D, Lee H (2016) Graphene quantum dots and their possible energy applications: a review. Curr Appl Phys 16:1192
12. Zhu YR, Ji XB, Pan CC, Sun QQ, Song WX, Fang LB, Chen QY, Banks CE (2013) A carbon quantum dot decorated RuO_2 network: outstanding supercapacitances under ultrafast charge and discharge. Energy Environ Sci 6:3665
13. Wei JS, Ding H, Zhang P, Song YF, Chen J, Wang YG, Xiong HM (2016) Carbon dots/$NiCo_2O_4$ nanocomposites with various morphologies for high performance supercapacitors. Small 12:5927

14. Logakis E, Pandis C, Pissis P, Pionteck J, Pötschke P (2011) Highly conducting poly(methyl methacrylate)/carbon nanotubes composites: investigation on their thermal, dynamic-mechanical, electrical and dielectric properties. Compos Sci Technol 71:854
15. Maji P, Pande PP, Choudhary RB (2015) Effect of $Zn(NO_3)_2$ filler on the dielectric permittivity and electrical modulus of PMMA. Bull Mater Sci 38:417
16. Aribou N, Elmansouri A, Achour ME, Costa LC, Belhadj Mohamed A, Oueriagli A, Outzourhit A (2012) Thermal and spectral dielectric properties of polypyrrole/polymethylmethacrylate composites. Spectro Lett 45:477
17. El Hasnaoui M, Abazine K, Achour ME, Costa LC (2016) Mott-hopping processes in polymethylmethacrylate matrices filled with polypyrrole particles. J Optoelectron Adv Mater 18:389
18. Bouknaitir I, Striccoli M, Panniello A, Costa LC, Teixeira SS, Achour ME, Kreit L, Corricelli M (2019) Optical and dielectric properties of PMMA poly(methylmethacrylate)/carbon dots composites. Polym Compos 40:E1312
19. Wang F, Pang S, Wang L, Li Q, Kreiter M, Lui CY (2010) One-step synthesis of highly luminescent carbon dots in noncoordinating solvents. Chem Mater 22:4528
20. Panniello A, Mauro AED, Fanizza E, Depalo N, Agostiano A, Curri ML, Striccoli M (2018) Luminescent oil-soluble carbon dots toward white light emission: a spectroscopic study. J Phys Chem C 122:839
21. Iorio M, Teno J, Nicolás M, García-González R, Peláez VH, González-Gaitano G, González-Benito J (2018) Conformational changes on PMMA induced by the presence of TiO_2 nanoparticles and the processing by solution blow spinning. Colloid Polym Sci 296:461
22. Kumar M, Chakraborty S, Upadhyaya P, Pugazhenthi G (2018) Morphological, mechanical, and thermal features of PMMA nanocomposites containing two-dimensional Co–Al layered double hydroxide. Appl Polym Sci 135:45774
23. Alekseeva OV, Noskov AV, Guseynov SS (2016) Features of the thermal behavior of PMMA/C60 film composites. Prot Met Phys Chem Surf 52:1019
24. Eriksson M, Goossens H, Peijs T (2015) Influence of drying procedure on glass transition temperature of PMMA based nanocomposites. Nano 1:36
25. Lee KJ, Lee DK, Kim YW, Choe WS, Kim JH (2007) Theoretical consideration on the glass transition behavior of polymer nanocomposites. Polym Sci Part B Polym Phys 45:2232
26. El Hasnaoui M, Graca MPF, Achour ME, Costa LC, Outzourhit A, Oueriagli A, El Harfi A (2010) Effect of temperature on the electrical properties of copolymer/ carbon black mixtures. J Non-Cryst Solids 356:1536
27. El Hasnaoui M, Kreit L, Costa LC, Achour ME (2017) Investigations of temperature effect on the conduction mechanism of electrical conductivity of copolymer/carbon black composite. Appl Microsc 47:121
28. Phan BT, Eom KT, Lee J (2017) AC Electrical conduction of Cr-Doped SrTiO thin films with an oxygen-deficient interface layer. Electron Mater 46:3796
29. Dussan S, Kumar A, Scott JF, Katiyar RM (2012) Effect of electrode resistance on dielectric and transport properties of multiferroic superlattice: a impedance spectroscopy study. AIP Adv 2:032136
30. Ortega N, Kumar A, Bhattacharya P, Majumdar SB, Katiyar RS (2008) Impedance spectroscopy of multiferroic $PbZr_xTi_{1-x}O_3/CoFe_2O_4$ layered thin films. Phys Rev B 77:014111
31. Sumi S, Prabhakar RP, Deepa M, Koshy P (2010) Electrical conductivity and impedance spectroscopy studies of cerium based aeschynite type semiconducting oxides $CeTiMO_6$ (M=Nb or Ta). J Appl Phys 108:063718
32. Melianas A (ed) (2017) Non-equilibrium charge motion in organic solar cells. Linköping University Electronic Press
33. Yusof Y, Ng ZY, Wong YH, Johan MR (2018) The tunable permittivity of multi-walled carbon nanotubes/silver nanoparticles reinforced polyvinyl alcohol (PVA) nanocomposites at low frequency. Mater Res Express 5:085604

34. El Hasnaoui M, Triki A, Graça MPF, Achour ME, Costa LC, Arous M (2012) Electrical conductivity studies on carbon black loaded ethylene butylacrylate polymer composites. J Non-Cryst Solids 358:2810
35. Tsangaris GM, Psarras GC, Kontopoulos AJ (1991) Dielectric permittivity and loss of an aluminum-filled epoxy resin. J Non-Cryst Solids 131:1164
36. Triki A, Guicha M, Ben Hassen M, Arous M, Fakhfakh Z (2011) Studies of dielectric relaxation in natural fibres reinforced unsaturated polyester. J Mater Sci 46:3698
37. Karray M, Triki A, Poilâne C, Picart P, Gargouri M (2016) Dielectric relaxation phenomena in flax fibers composite. Fiber Polym 17:88
38. Rao KS, Prasad DM, Murali Krishna P, Latha TS, Lee JH (2007) Electrical and electromechanical studies on tungsten-bronze electroceramic: lead potassium dysprosium niobate. Optoelectron Adv Mater Rapid Commun 1:510
39. Nanda M, Tripathy DK (2008) Physico-mechanical and electrical properties of conductive carbon black reinforced chlorosulfonated polyethylene vulcanizates. Exp Polym Lett 2:855
40. Provenzano V, Boesch LP, Volterra V, Moynihan CT, Macedo PB (1972) Electrical Relaxation in $Na_2O{\cdot}3SiO_2$ Glass. J Am Ceram Soc 55:492
41. Havriliak S, Negami S (1966) A complex plane analysis of α-dispersions in some polymer systems. J Polym Sci Part C Polym Lett 14:99
42. El Hasnaoui M, Triki A, Achour ME, Arous M (2014) Modelling of dielectric relaxation processes of epoxy-resin filled with carbon black particles. Phys B Condens Matter 433:62

Chapter 20
Microwave Characteristics (Reflection Losses) of Composite Materials Consisting of Magnetic Nanoparticles

Svetoslav Kolev and Tatyana Koutzarova

Abstract Magnetic materials find numerous applications in various devices, such as absorbers in the mm range. Depending on their purpose, soft or hard magnetic materials are used in a bulk, film or composite form. The object of the work presented was to investigate the microwave (MW) absorbing properties of nanocomposite bulk samples. We used magnetite (Fe_3O_4) with a particle size of about 30 nm as a filler in a silicone rubber matrix and investigated the influence of an applied external magnetic field during the process of polymerization of the samples measuring the reflection losses in the frequency range of 1–20 GHz. It was found that the external magnetic field increased the reflection losses and slightly changed the matching frequencies at which they appeared.

Keywords Nanosized ferrites · Magnetite · External magnetic field · Shielding · Absorption · MW radiation · Antireflection properties

20.1 Introduction

Protection from electromagnetic radiation (EMR) in the MW range has recently become a problem of pressing interest due to the world-wide spread of many technologies, such as cellular phones, to name but one. MW radiation shielding in medical research and in MW domestic appliances has also focused the attention of the researchers. Over the last 30 years, the transmission density has doubled every 4 years, meaning that the electromagnetic pollution has increased by a factor of about 100. The wavelengths used are getting shorter; we have now entered the MW era where we are dealing with minuscule dimensions. However, the shorter the waves, the more energy they produce.

S. Kolev (✉) · T. Koutzarova
Institute of Electronics, Bulgarian Academy of Sciences, Sofia, Bulgaria

P. Petkov et al. (eds.), *Nanoscience and Nanotechnology in Security and Protection against CBRN Threats*, NATO Science for Peace and Security Series B: Physics and Biophysics, https://doi.org/10.1007/978-94-024-2018-0_20

The health consequences of EMR exposure vary in intensity from mild symptoms to serious diseases. Some symptoms are termed as "radio-wave sickness". EMR from transmission towers and mobile phones is suspected of initiating cancer because of interfering with the electric field inside the human cells. People working or living in continuous exposure to EMR are under the greatest risk.

A solution to the above problem may be provided by the new scientific branch of nanoscience and nanotechnology, which has undergone an extraordinarily fast development in the last three decades. Tools were created that allow us to obtain materials with very small dimensions and unique physical and chemical properties. The aim of this work was to prepare and investigate composite materials consisting of nanosized ferrites to be used as shields and absorbers of electromagnetic radiation in the MW range.

20.2 Results and Discussion

In this study we aimed specifically to clarify the contribution of a Fe_3O_4 ferrite filler with a particle size of 30 nm and the influence of an external magnetic field on the microwave characteristics of composite absorbing structures.

A large variety of absorbing materials exists that can be used for suppressing electromagnetic radiation, depending on the requirements for a narrow or wide absorbing frequency band, or for low- or high-frequency application of the absorber. Concerning the MW range, the absorbing materials most often used are rubbers, plastics, thermoplastics etc. These are non-magnetic substances resistant to atmospheric influences, which often contain magnetic fillers, such as ferrites, iron, or cobalt-nickel alloys. The additives alter the values of the dielectric constant and the magnetic permeability in a way to achieve a maximal absorption of the electromagnetic radiation.

The current interest in MW absorbing materials concerns mainly studies on ferrimagnetic composites in order to avoid radar detection in the GHz range [1–12]. These materials dissipate efficiently the electric and magnetic energy of an incident magnetic field. A widely applied way of preparing such absorbing media is dispersing an electrically conductive powder in an insulating matrix. In the study reported here, we dealt with magnetite, which, unlike most ferrites, is a semiconductor exhibiting a high electrical conductivity. As a consequence, the bulk magnetite behaves as a reflector when irradiated by an electromagnetic wave. One can avoid this problem by homogeneously dispersing magnetite powder in an insulating matrix. The experiments on studying the material properties consist of irradiating them with a plane electromagnetic wave of a given frequency and detecting the transmitted and reflected signals. The latter are processed appropriately to obtain the dielectric constant and magnetic permeability of the material, and to attempt to clarify the mechanisms giving rise to the magnetic losses.

In our study we prepared composite samples with 30 nm Fe_3O_4 particles as a filler. With the advances of the nanotechnologies allowing the preparation of

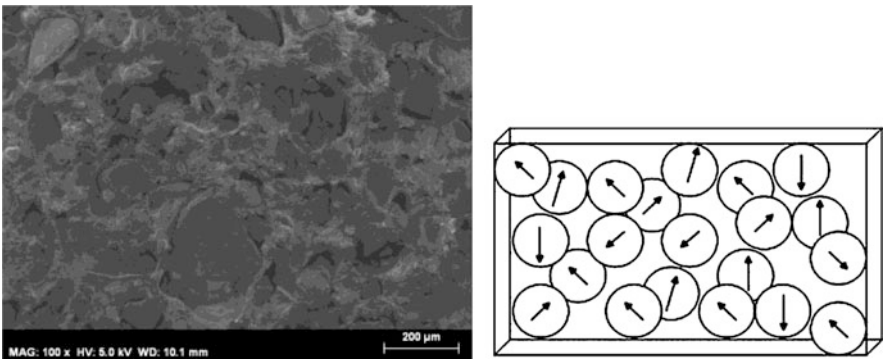

Fig. 20.1 Surface morphology of the sample and a schematic representation of the random orientation of the filler's magnetic moments

nanostructured Fe_3O_4, its use as a filler has attracted growing interest due to its larger effective surface and, thus, a potentially higher efficiency.

To characterize the composite structures prepared, we used to short-circuit measurement as follows. A transverse electromagnetic wave (TEM) was directed normally to a one-layer absorber, with a perfect conductor placed behind it (short circuit) [13, 14]. This is a fast and accurate technique, allowing one to measure directly the reflection losses R_L (the ratio of the incident and the reflected power in dB).

The experimental setup employed to find the relationship between the sample absorption properties, the influence of the external magnetic field and the MW frequency range consisted of a scalar network analyzer (Hewlett Packard 8756 A, frequency band 1–20 GHz) and a sample mounted perpendicularly to the incident MW signal and short-circuited by a perfect conductor.

We evaluated the MW performance of magnetite powder dispersed in a polymer matrix (silicon rubber). The samples characterized contained magnetite powders with an average particle size of 30 nm (prepared by a soft-chemistry technique in the Microwave Magnetics Laboratory of IE BAS). The ferrite powders were dispersed homogeneously in the polymer matrix. Two types of samples were prepared. The first type had an outer diameter of 7 mm, an inner diameter of 3 mm and a thickness of 4 mm and contained 1.5 g of monodomain magnetite dispersed in 1 cm^3 of silicon rubber. In this case, the monodomain particles are with randomly oriented magnetic moments in the volume. Figure 20.1 shows the surface morphology of the sample and the schematically presented orientation of the filler's magnetic moments.

The second type of samples had the same preparation parameters, but during the process of polymerization the sample was placed in a magnetic field with strength of 0.4 T. The monodomain particles are thus oriented along the magnetic force lines of the external magnet. The surface morphology of the sample and the schematically presented orientation of the magnetic moment of the particles are shown in Fig. 20.2.

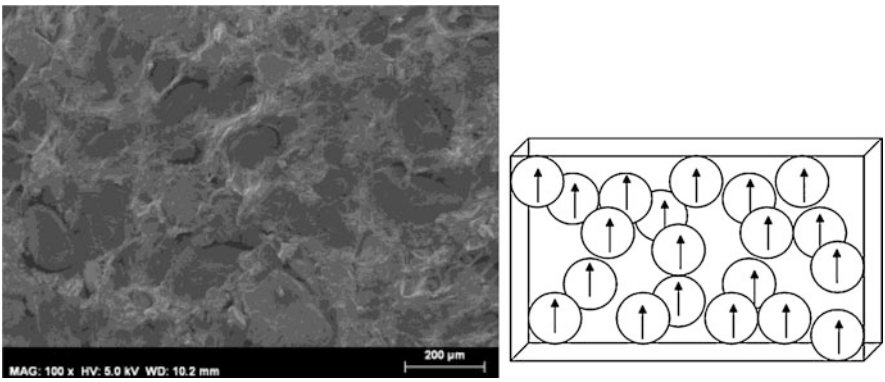

Fig. 20.2 The surface morphology of the sample and a schematic representation of the filler's oriented magnetic moments

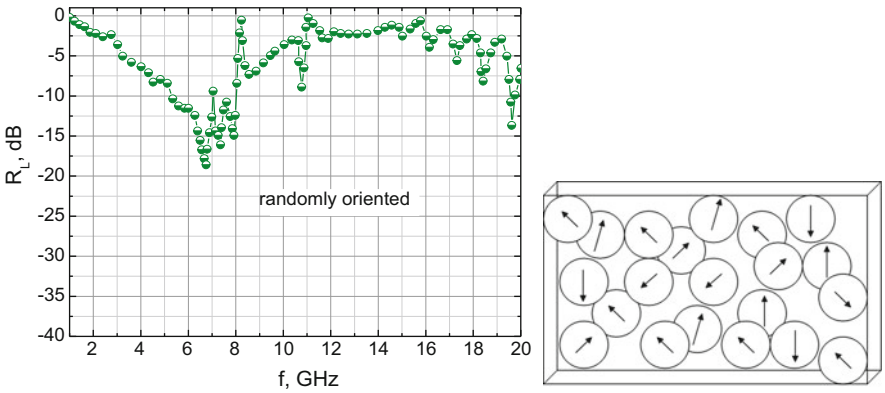

Fig. 20.3 Frequency dependence of the reflection losses R_L of a nanocomposite sample with a filler with randomly oriented magnetic moments

The frequency dependence of the reflection losses of a nanocomposite absorber in which the monodomain particles have randomly oriented magnetic moments is shown in Fig. 20.3.

Figure 20.4 illustrates the frequency dependence of the reflection losses of a nanocomposite absorber with monodomain particles with uniformly oriented magnetic moments.

As can be seen for the case of the composite absorber with a filler with uniformly oriented magnetic moments, the matching frequencies are the same as for the sample with a filler with randomly oriented magnetic moments, but the value of the reflection losses is higher. The values of the matching frequencies are related to the thickness t_m, the dielectric constant ε_r and the magnetic permeability μ_r of the samples [15, 16,]:

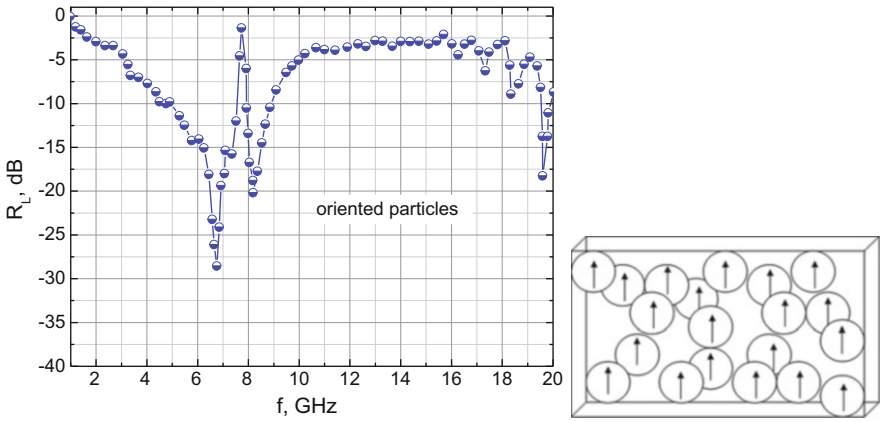

Fig. 20.4 Frequency dependence of the reflection losses R_L of a nanocomposite sample with a filler with oriented magnetic moments

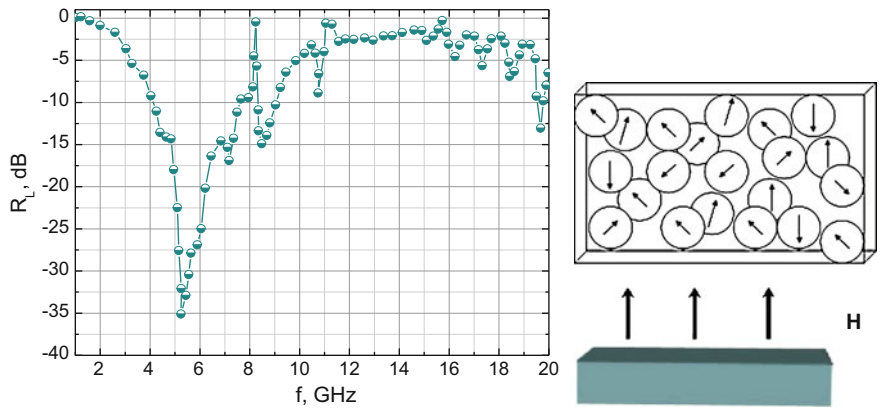

Fig. 20.5 Frequency dependence of the reflection losses R_L of a nanocomposite sample with a filler with randomly oriented magnetic moments and applied external magnetic field

$$f_m = \frac{nc}{4t_m\sqrt{|\varepsilon_r\mu_r|}}(n = 1, 3, 5, \ldots\ldots)$$

We continued our investigation with experiments applying an external magnetic field with strength of 0.4 T during the measurement of the reflection losses. Figure 20.5 illustrates how the external magnetic field changed the reflection losses for a sample with a filler with randomly oriented magnetic moments.

Figure 20.6 provides information on the variation of the matching frequency values due to the external magnetic field for a sample whose filler consists of particles with oriented magnetic moments. We observed that this case was the best one exhibiting the highest reflection losses namely, $R_L = -35$ dB. As also seen in the

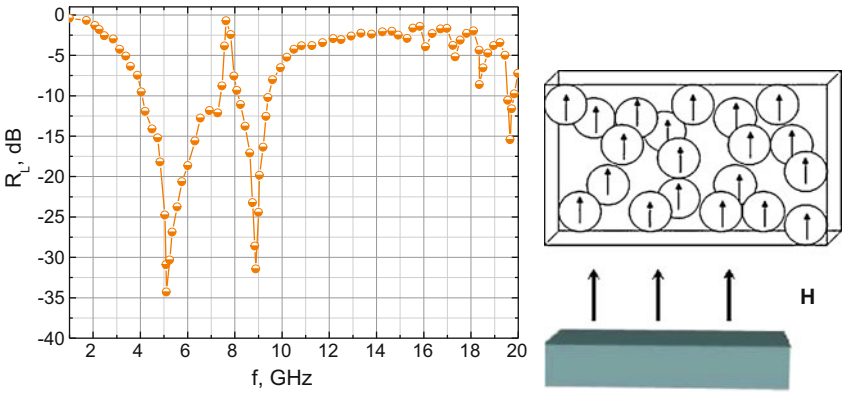

Fig. 20.6 Frequency dependence of the reflection losses R_L of a nanocomposite sample with a filler with oriented magnetic moments and applied external magnetic field

figure, applying an external magnetic field alters slightly the matching frequency values.

The results presented demonstrate that the technique used by us to determine the MW parameters of composite materials (in our case, a ferrite filler in a polymer matrix) offers a fast and efficient way of measuring the reflection losses and evaluating the applicability of the material as an antireflection coating.

20.3 Conclusions

Our results prove the possibility of varying the reflection losses of a nanocomposite sample in a controlled way by varying the degree of orientation of the magnetic moments of the ferrite filler, while keeping the sample thickness and filler-polymer weight ratio constant. This could happen in two ways, either by applying an external magnetic field during the sample formation or during the measurement of the reflection losses. The nanocomposite structures prepared could find applications as absorbers of MW electromagnetic waves or as antireflection coatings for metal surfaces.

References

1. Kolev S, Yanev A, Nedkov I (2006) Microwave absorption of ferrite powders in a polymer matrix. Phys Status Solidi C 3:1308
2. Kolev S, Koutzarova T Yanev A, Ghelev C, Nedkov I (2008) Microwave properties of polymer composites containing combinations of micro- and nanosized magnetic fillers. J. Nanosci Nanotechno 8:650

3. Lin Y, Liu Y, Dai J, Wang L, Yang H (2018) Synthesis and microwave absorption properties of plate-like $BaFe_{12}O_{19}$@Fe_3O_4 core-shell composite. J Alloy Compd 739:202
4. Abbas SM, Dixit AK, Chatterjee R, Goel TC (2007) Complex permittivity, complex permeability and microwave absorption properties of ferrite–polymer composites. J Magn Magn Mater 309:20
5. Harris VG, Geiler A, Chen Y, Yoon SD, Wu M, Yang A, Chen Z, He P, Parimi PV, Zuo X, Patton CE, Abe M, Acher O, Vittoria C (2009) Recent advances in processing and applications of microwave ferrites. C Vittoria J Magn Magn Mater 321:2035
6. Ting TH, Wu KH (2010) Synthesis, characterization of polyaniline/$BaFe_{12}O_{19}$ composites with microwave-absorbing properties. J Magn Magn Mater 322:2160
7. Kong I, Ahmad SH, Abdullah MH, Hui D, Yusoff AN, Puryanti D (2010) Magnetic and microwave absorbing properties of magnetite–thermoplastic natural rubber nanocomposites. J Magn Magn Mater 322:3401
8. Chang S, Kangning S, Pengfei C (2012) Microwave absorption properties of Ce-substituted M-type barium ferrite. J Magn Magn Mater 324:802
9. Wang Y, Chen Y, Wu X, Zhang W, Luo C, Li J (2018) Fabrication of MoS_2-graphene modified with Fe_3O_4 particles and its enhanced microwave absorption performance. Adv Powder Technol 29:744
10. Tyagi S, Pandey VS, Baskey HB, Tyagi N, Garg A, Goel S, Shami TC (2018) RADAR absorption study of $BaFe_{12}O_{19}$/$ZnFe_2O_4$/CNTs nanocomposite. J Alloy Compd 731:584
11. Sharma V, Kumari S, Kuanr BK (2018) Exchange-coupled hard-soft ferrites; A new microwave material. J Alloy Compd 736:266
12. Han Q, Meng X, Lu C (2018) Exchange-coupled $Ni0.5Zn0.5Fe_2O_4$/$SrFe_{12}O_{19}$ composites with enhanced microwave absorption performance. J Alloy Compd 768:742
13. Kim SS, Jo SB, Gueon KI, Choi KK, Kim JM, and Churn KS (1991) Complex permeability and permittivity and microwave absorption of ferrite-rubber composite at X-band frequencies. IEEE Trans Magn 27:5462
14. Shin JY and Oh JY (1993) The microwave absorbing phenomena of ferrite microwave absorbers. IEEE Trans Magn 29:3437
15. Qiao L, Wang T, Mei ZL, Li XL, Sui WB, Tang LY, Li FS (2016) Analyzing Bandwidth on the Microwave Absorber by the Interface Reflection Model. Chin Phys Lett 33:027502
16. Zhao H, Xu SY, Tang DM, Yang Y, Zhang BS (2014) Thin magnetic coating for low-frequency broadband microwave absorption. J Appl Phys 116:243911

Chapter 21
Dielectric Properties of PMMA/PPy Composite Materials

Sanae Barnoss, Najoia Aribou, Yassine Nioua, Mohamed El Hasnaoui, Mohammed E. Achour, and Luís C. Costa

Abstract This work presents a study of the structural, electrical, and dielectric properties of polymethylmethacrylate/polypyrrole composites. Structural analysis was performed using X-ray diffraction, showing an increase in the crystallinity index with the increasing of filler concentrations. The electrical conductivity mechanism and the dielectric relaxation process of these composites were studied in the frequency range from 100 Hz to 1 MHz and temperature range from 290 to 380 K, using impedance spectroscopy. The frequency-dependence of the conductivity is analyzed using the Jonscher power law. The values of the *n* exponent in this law are superior to 1, which is an indication that electron hopping occurs between neighboring sites. The Nyquist representations of the complex impedance spectra are modeled using the Cole-Cole model. The temperature dependence of both DC conductivity and relaxation process behaviors, using the Arrhenius equation, indicates that the conduction process is thermally activated.

Keywords Percolation · Electrical conductivity · Impedance spectroscopy

21.1 Introduction

Conducting polymers have attracted considerable interest from researchers in material sciences due to industrial demands [1–3]. These materials are still subject of much research today for both fundamental and potential applications. These composites present high interest for industry due to their potential for applications in different fields [4–6]. In general, the addition of conducting charges such as carbon

S. Barnoss · N. Aribou · Y. Nioua · M. El Hasnaoui · M. E. Achour (✉)
LASTID Laboratory, Physics Department, Faculty of Sciences, Ibn Tofail University, Kenitra, Morocco
e-mail: achour.me@univ-ibntofail.ac.ma

L. C. Costa
I3N and Physics Department, University of Aveiro, Aveiro, Portugal

P. Petkov et al. (eds.), *Nanoscience and Nanotechnology in Security and Protection against CBRN Threats*, NATO Science for Peace and Security Series B: Physics and Biophysics, https://doi.org/10.1007/978-94-024-2018-0_21

black [7, 8], and copper [9] into the insulating matrix ensures the electrical conductivity of the composites. But the presence of this type of filler considerably modifies the mesostructural characteristics when compared to the uncharged materials [10]. The use of conductive polymers has resulted in composites with high electrical conductivity and preserving the good mechanical and often optical properties of the host polymer [11, 12].

The analysis of frequency dependence of the electrical conductivity and impedance spectra have been used in several works to provide new properties related to conducting polymers based on polymethylmethacrylate (PMMA) filled with conducting charges. For example, Elimat [13] analyzed the AC electrical conductivity spectra of PMMA/carbon black composite, finding that the electrical conduction mechanism is related to the transfer of electrons through the carbon black aggregations distributed in the polymer matrix. Dixit et al. [14] studied the temperature effect on the dielectric relaxations of PMMA/CdS composite, finding that the addition of CdS particles revealed two dielectric relaxations which were attributed to α and β processes.

This work presents a study on the electrical and dielectric properties of composites based on polypyrrole doped particles (PPy-doped) loaded into an insulating matrix of polymethylmethacrylate (PMMA), using impedance spectroscopy. Frequency dependence of the electrical conductivity and impedance spectra were analyzed using the Jonscher power law and the Cole-Cole model, respectively. Temperature dependence of various relaxation parameters was exploited to identify the conduction mechanisms that occur in these conducting polymers.

21.2 Experimental

21.2.1 Preparation of Composites

PPy powder was obtained by doping intrinsic PPy with tosylate anion TS^-. The doping rate was controlled by X-ray photoelectron spectroscopy (XPS) and a ratio of one sulphur (S) for four nitrogen (N) was found, i.e. one tosylate ion TS^- for four pyrrole monomers [15]. The average grain size of PPy is in the range of 10–15 μm. A series of samples has been prepared by mixing the desired volume fraction ϕ of PPy. The two powders, PMMA and PPy, were mixed in several proportions and pressed at 5000 kg/cm^2 at 423 K. After pressing, the samples cooled down freely to room temperature resulting in solid disc shaped samples for measurements. All discs had a diameter of 13 mm and 3–4 mm thickness. The DC conductivities of the PPy and the PMMA matrix are 54 and 3.10^{-5} $(\Omega.m)^{-1}$, respectively [16] and their densities 1.20 and 1.14–1.20 g.cm^{-3}. The percolation threshold ϕ_c for this series of samples is about 3.24%. The glass transition temperature of PMMA polymer is $T_g \sim 388$ K [17].

21.2.2 Measurements

X-ray diffraction (XRD) was carried out using a Philips X'pert MPD diffractometer operating at 40 kV and 30 mA, equipped with a Cu anticathode of wavelength $\lambda = 1.5406$ Å. The scans were recorded in the range of 2θ values from 6° to 52° at room temperature.

DC electrical resistivity ρ was measured at room temperature using a 617 Keithley electrometer. The samples were prepared with aluminum electrodes of 10 mm diameter on the opposite sites. The electrical contacts were made with silver paint.

Dielectric measurements were carried out in the frequency range from 100 Hz to 1 MHz and temperature range from 290 to 380 K using a HP network analyser Agilent 4192A (CA, USA). First, we measured the real $G(\omega)$ and the imaginary $B(\omega)$ parts of the complex admittance $Y^*(\omega) = G(\omega) + jB(\omega)$ of each sample. Then, we calculated the real $\sigma'(\omega)$ and imaginary $\sigma''(\omega)$ parts of the complex conductivity $\sigma^*(\omega) = \sigma'(\omega) - j\sigma''(\omega)$ using the following expressions:

$$\sigma'(\omega) = \frac{d}{A\varepsilon_0} G(\omega) \tag{21.1}$$

$$\sigma''(\omega) = \frac{d}{A\varepsilon_0} B(\omega) \tag{21.2}$$

in which, $G(\omega)$ is the susceptance, $B(\omega)$ the conductance, ε_0 the vacuum permittivity, A and d the surface area and the diameter of the sample, respectively. The real $Z'(\omega)$ and imaginary $Z''(\omega)$ parts of the complex impedance $Z^*(\omega) = Z'(\omega) - jZ''(\omega)$ were calculated using the following relations:

$$Z'(\omega) = \frac{G(\omega)}{G^2(\omega) + B^2(\omega)} \tag{21.3}$$

$$Z''(\omega) = \frac{B(\omega)}{G^2(\omega) + B^2(\omega)} \tag{21.4}$$

21.3 Results and Discussion

21.3.1 XRD Spectra Analysis

Figure 21.1 shows the results of X-ray diffraction (XRD) measurements of the PMMA/PPy composite samples. In comparison with the diffractogram of the neat

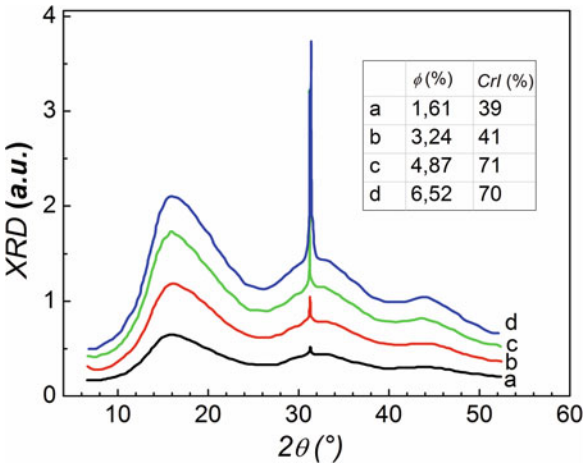

Fig. 21.1 X-ray diffractograms of PMMA/PPy composites. The insert table shows the corresponding crystallinity index fraction *CrI* for each PPy fraction

PMMA [16,18], we attributed the diffraction peak observed at 31.2° to TS^- anion doped PPy structure. It is obvious that the intensity of the peak increases with filler concentration, meaning that the crystallinity of the PMMA/PPy composite increases. According to Segal empirical method [19], the crystallinity index (*CrI*) can be calculated from the X-ray diffraction spectra using the following expression:

$$CrI = \frac{I_f - I_s}{I_f} \times 100 \tag{21.5}$$

in which, I_f is the intensity of both crystalline and amorphous peak corresponding to TS^--doped PPy particles at $2\theta = 31.2°$ and I_s the intensity of the minimum between two peaks at about $2\theta = 26°$. We notice that the peak at about $2\theta = 15°$ represents the amorphous PMMA phase [20].

The crystallinity index of PMMA/PPy composites has been calculated for all concentrations of PPy particles taking the amorphous and crystalline contributions to the diffraction intensity. The insert table in Fig. 21.1 illustrates the obtained values of *CrI* corresponding to each PPy concentration. It is clear that *CrI* increases with PPy fraction indicating a good dispersion of fillers resulting in the increase in the crystallinity of the PMMA/PPy composite. In addition, the obtained values of *CrI* are between 40 and 70% which are greater than those obtained for other composites: for PMMA/CdS composites they are between 39 and 42% [21] and for PMMA/TiO_2 composites between 10 and 19% [22]. These differences are related to the type of conducting charges used in each composite, i.e., PPy doped with TS^- has more pronounced effect on the PMMA crystallinity than cadmium sulfide (CdS) and titanium dioxide (TiO_2) semiconductor particles. We can also notice that there is a

significant change of the crystallinity index value below and above the percolation threshold, which will be determined in "DC electrical resistivity analysis" section. Above the percolation threshold, *CrI* exhibits the highest values, showing the significant effect of the PPy particles on the electrical transport mechanisms governing this conducting composite.

21.3.2 DC Electrical Resistivity Analysis

Figure 21.2 shows the semi-logarithmic curve of the resistivity ρ as a function of the PPy fraction embedded in the PMMA polymer matrix, measured at T = 300 K. As it can be seen, the resistivity is high at low concentrations indicating that the charge transport is governed by the PMMA matrix. Above the percolation threshold ϕ_c the resistivity begins to decrease abruptly. For $\phi > \phi_c$, the behavior of ρ can be modelled by the percolation model written as $\rho = \rho_0 (\phi - \phi_c)^{-t}$ [23, 24], in which t is a parameter related to dimensionality of the composite and ρ_0 a pre-exponent factor.

In our recent paper [25], we estimated the percolation threshold of $\phi_c = 3.24\%$ and calculated the values of the two parameters t and ρ_0, found to be 1.69 and 34.7 (Ω.m), respectively. The value of exponent t is comparable with the value 1.6 found by Ou et al. for PMMA/carbon black composites [26]. The value $\phi_c = 3.24\%$ is greater than the values obtained for series of composites based on PMMA reinforced with nanographite, graphene oxide, and graphite [27]. The difference is related to the particle size, knowing that a filler with small particle size gives a lower percolation threshold and a better transfer of properties to the polymer [28].

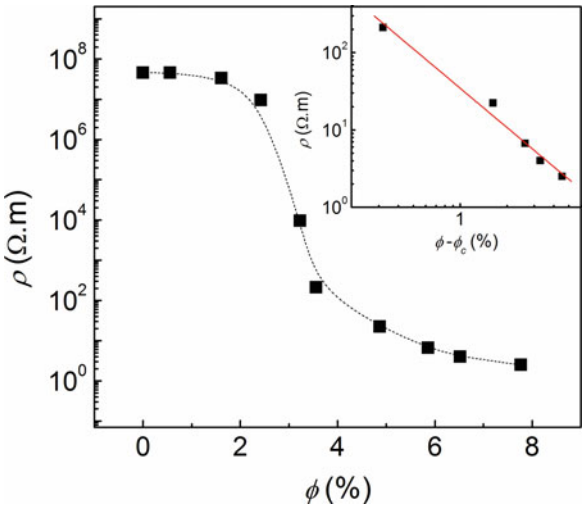

Fig. 21.2 Semi-log plot of the electrical resistivity ρ versus PPy concentration at T = 300 K. The inset figure represents the fit of data corresponding to the percolation model

21.3.3 Complex Conductivity Analysis

Figures 21.3 and 21.4 show the frequency dependence of the real $\sigma'(\omega)$ and imaginary $\sigma''(\omega)$ parts of the complex electrical conductivity $\sigma^*(\omega)$ at different temperatures for $\phi > \phi_c$. It is clearly seen that $\sigma'(\omega)$ exhibits two distinct domains. In the first one, it shows a plateau at low frequencies, while in the second domain, i.e. above a critical frequency F_c, it exhibits a frequency-dependent behavior. Below F_c, the conductivity represents the DC conductivity $\sigma_{dc}(T)$. This behavior can be explained by the fact that the conducting charges scan a large distance inside the material before the direction of the electric field is changed. Then, the mean distance covered by the conducting charge for $F < F_c$ is greater than the correlation length, hence, the conductivity is independent of the frequency [29]. For $F > F_c$, the

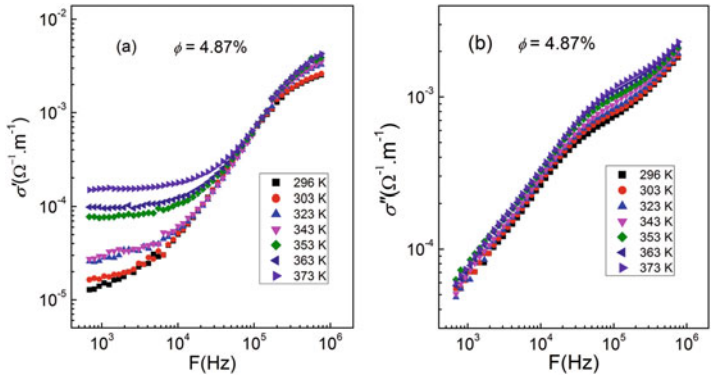

Fig. 21.3 Real $\sigma'(\omega)$ and imaginary $\sigma''(\omega)$ parts of the complex electrical conductivity $\sigma^*(\omega)$ of PMMA/PPy composites at different temperatures for $\phi = 4.87\%$

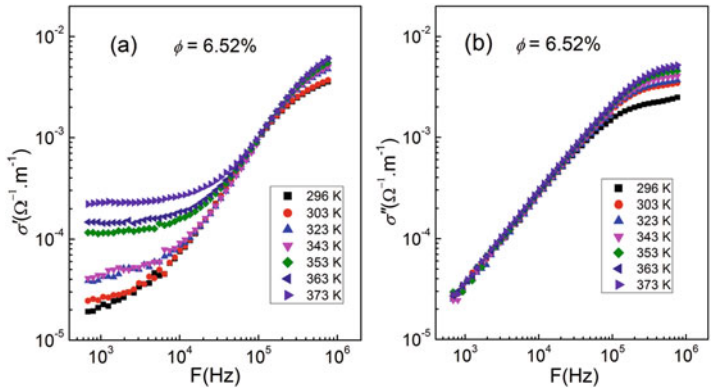

Fig. 21.4 Real $\sigma'(\omega)$ and imaginary $\sigma''(\omega)$ parts of the complex electrical conductivity $\sigma^*(\omega)$ of PMMA/PPy composites at different temperatures for $\phi = 6.52\%$

Table 21.1 DC conductivity σ_{dc} and exponent n as functions of temperature for PPy concentrations above the percolation threshold

ϕ (%)	4.87		6.52	
T(K)	σ_{dc} (Ω^{-1} m^{-1})	n	σ_{dc} (Ω^{-1} m^{-1})	n
296	$1.27\ 10^{-5}$	1.13	$1.91\ 10^{-5}$	1.12
303	$1.63\ 10^{-5}$	1.13	$2.44\ 10^{-5}$	1.13
323	$2.52\ 10^{-5}$	1.15	$3.86\ 10^{-5}$	1.08
343	$2.76\ 10^{-5}$	1.15	$4.22\ 10^{-5}$	1.05
353	$7.67\ 10^{-5}$	1.04	$1.15\ 10^{-4}$	1.03
363	$9.82\ 10^{-5}$	1.04	$1.47\ 10^{-4}$	0.99
373	$1.51\ 10^{-4}$	0.99	$2.32\ 10^{-4}$	0.84

displacement of the conducting charge occurs by hopping between the localized states, resulting in a significant increase of $\sigma'(\omega)$ [30].

The log-log representation of frequency dependence exhibits universal power law, that can be described by the Jonscher law [31].

$$\sigma'(\omega, T) = \sigma_{dc}(T) + \sigma_o \omega^{n(T)} \tag{21.6}$$

in which, $\sigma_{dc}(T)$ is the DC conductivity, σ_o the pre-exponential factor, and $n(T)$ the fractional exponent, which represents the degree of interaction between the charge carriers and the surrounding environment. According to the results of Funke [32], when the values of $n(T)$ are lower than 1, the electron hopping involves a translational motion with a sudden hopping, whereas when $n(T)$ is greater than 1, the motion involves localized hopping between neighboring sites. Table 21.1 summarizes the obtained values of $\sigma_{dc}(T)$ and $n(T)$ for the PMMA/PPy composites. It is clear that σ_{dc} increases with the temperature, showing thermal behavior of static conduction which will be used to calculate the activation energy related to static conduction in "Activation energy"section below. On the other hand, the exponents n decrease with increasing temperature. As mentioned, the temperature dependence of n gives information regarding the suitable mechanism involved in the electrical conductivity. In our case, the values of n are temperature-dependent with a linear relationship, showing a good agreement with the correlated barrier-hopping CBH mechanism [33]. In addition, for temperatures below the glass transition T_g the values of n are superior to 1, indicating that the electron hopping of TS^- anion occurs between neighboring sites.

The imaginary part of conductivity $\sigma''(\omega)$ for two concentrations of PPy exhibited frequency-dependent behavior (Figs. 21.3b and 21.4b). From Eqs. 21.2 and 21.4, we can conclude that σ'' was proportional to Z''; hence, it is associated with the energy-dissipation effects of the material. As can be observed, $\sigma''(\omega)$ is independent of the temperature for the range of frequency below 10^5 Hz. However, it increases with increasing the frequency of the alternating electrical field, showing the contrary behavior of the study performed by Bairlein et al. [34], finding that σ'' depends strongly on the temperature. We suggest that the main reason for this difference is that the mobility of the ions in fluid is increased with the temperature. In addition, $\sigma''(\omega)$ increased with the increase of the PPy concentration at each value of the

frequency; this behavior is related to a high number of charge carriers during conduction.

21.3.4 Complex Impedance Analysis

Figure 21.5 and its inset show the real Z' and imaginary Z'' parts of the complex impedance versus frequency for the PMMA/PPy composites with $\phi > \phi_c$ at various temperatures. It can be seen that the spectra of Z'' are characterized by appearance of peaks which shift to higher frequencies with increasing temperature, indicating a decrease of dielectric relaxation time. The dielectric relaxation is a thermally activated process. The maximum amplitude of the relaxation peak decreases and the relaxation time decreases as PPy concentration increases, at constant temperature. This behavior is attributed to the injection of TS^- ions that exist on PPy particles into the PMMA matrix.

In addition, the observed plots are not symmetric on the frequency axis, indicating that a single relaxation described by the Debye model [35] cannot be applied for interpreting this experimental data. Instead, we have used the Cole-Cole model [36]:

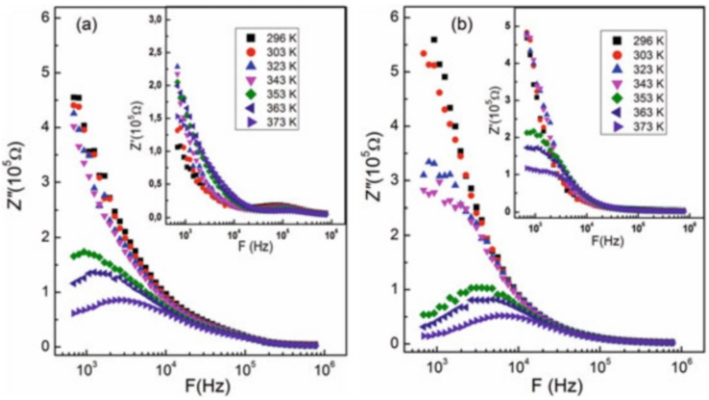

Fig. 21.5 Frequency dependence of the real Z' and imaginary Z'' parts of the complex impedance Z^* for $\phi = 4.87\%$ (**a**) and $\phi = 6.52\%$ (**b**) at different temperatures

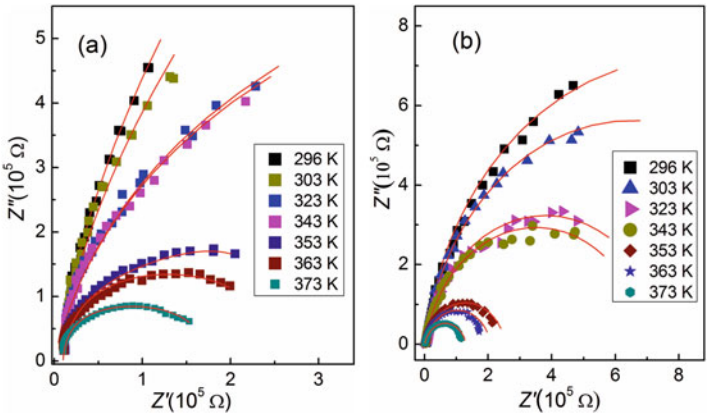

Fig. 21.6 Cole–Cole plots (solid lines) according to the experimental data (symbols) for $\phi = 4.87\%$ (**a**) and $\phi = 6.52\%$ (**b**) concentrations at different temperatures

$$Z^*(\omega) = Z_\infty + \frac{Z_0 - Z_\infty}{1 + (j\omega\tau)^{1-\alpha}} \tag{21.7}$$

in which, Z_o is the low frequency resistance, Z_∞ the high frequency resistance, τ the relaxation time ($\tau = 2\pi F_r$), and α a parameter between 0 and 1 that reflects the dipole interaction.

In Fig. 21.6 the Nyquist diagrams of the PMMA/PPy composites with concentrations above the percolation threshold are shown at different temperatures. The solid curves were produced by the best fitting of the experimental points using the Cole-Cole model (Eq. 21.7).

The evaluated parameters are represented in Fig. 21.7. The values of α (Fig. 21.7a) are close to 0, showing that we are close to a single relaxation process, with values increasing from 0.08 at 296 K to 0.14 at 373 K, indicating a transition from Debye model to Cole-Cole model with the temperature. We note that the values of α for $\phi = 6.52\%$ are greater than those for $\phi = 4.87\%$ at high temperatures, showing increased heterogeneity of the composites with higher PPy concentration.

21.3.5 Activation Energy

The effect of temperature on the electrical properties of PMMA/PPy has been analyzed using DC conductivity σ_{dc} and relaxation frequency f_r. Activation energies were calculated using the Arrhenius equations expressed as $\sigma_{dc} = \sigma_0 \exp(-E_{dc}/k_bT)$ and $f_r = f_0 \exp(-E_r/k_bT)$, in which k_b is the Boltzmann's constant, σ_0 and f_0 are pre-exponential factors, E_{dc} and E_r the activation energies related to static conductivity and relaxation process, respectively. Figure 21.8 depicts the plots of $ln(\sigma_{dc})$ and $ln(f_r)$ vs. 1000/T along with linear fits to the Arrhenius equations. The calculated values of E_{dc} and E_r as well as their pre-exponential factors are shown in Table 21.2.

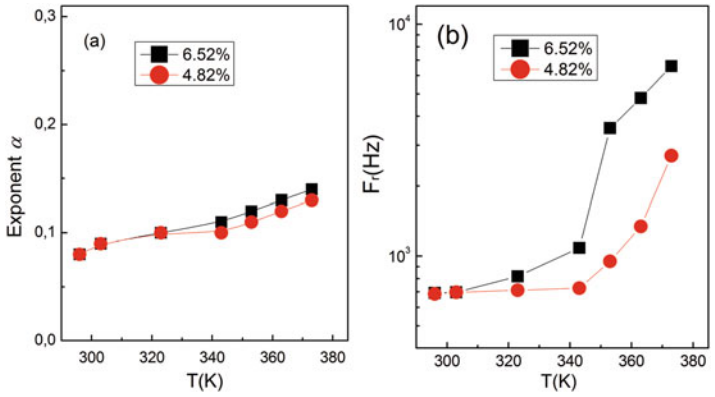

Fig. 21.7 Cole-Cole relaxation parameters versus temperature of the two studied samples. Solid lines are drawn to guide the eye only

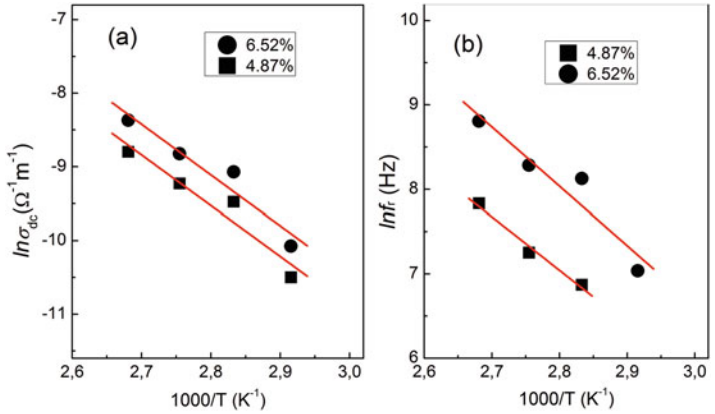

Fig. 21.8 Arrhenius plots of relaxation frequency obtained from the imaginary parts of the DC electrical conductivity (**a**) and the complex impedance (**b**) for the two studied samples

Table 21.2 Activation energies obtained from the DC electrical conductivity and relaxation processes

ϕ (%)	E_{dc} (eV)	$ln\sigma_o$	E_r (eV)	lnf_o
4.52	0.59 ± 0.11	9.73	0.54 ± 0.07	24.7
6.87	0.60 ± 0.11	10.18	0.60 ± 0.13	27.7

As can be observed, the activation energies obtained from both two methods are approximately the same, showing a small increase with the concentration of the PPy particles. This is probably due to TS^- anions that exist in PPy particles, i.e. TS^- anions can block the PMMA polymer chain in a way that prevents the chains from moving out of the pathway. That is hindering the movement of ions and other conducting impurities which leads to an increase of the activation energy. These results are in accordance with those of Clayton et al. [37] who reported a study of the DC electrical conductivity of PMMA/carbon nanotube composites and are significantly greater than those of ethylene butylacrylate/carbon black composites [38, 39]. These disagreements are related to the difference of conduction mechanisms occurring in these two types of composites.

21.4 Conclusion

A study on conducting polymer composite based on PMMA loaded with PPy particles has been presented. The X-ray diffraction patterns showed the increase of crystallinity index with PPy concentration. The dependence of the electrical resistivity with PPy fraction exhibited a percolation threshold at which the behavior of transport mechanism changes. The frequency-dependence of the electrical conductivity and impedance spectra were modeled using the Jonscher power law and Cole-Cole model, respectively. The variations of n and α exponents as functions of the temperature give an idea about the transport mechanisms occurring in the PMMA/PPy composites. Whereas, the temperature dependence of DC conductivity and relaxation frequency indicates that the conduction process is thermally activated.

References

1. Kaur G, Adhikari R, Cass P, Bown M, Gunatillake P (2015) Electrically conductive polymers and composites for biomedical applications. RSC Adv 5:37553
2. Bouknaitir I, Aribou N, Elhad Kassim SA, El Hasnaoui M, Melo BMG, Achour ME, Costa LC (2017) Electrical properties of conducting polymer composites: experimental and modeling approaches. Spectro Lett 50:196
3. Mishra AK (2018) Conducting polymers: concepts and applications. J Atom Mol Cond Nano Phys 5:159
4. Bhadra S, Khastgir D, Singha NK, Lee JH (2009) Progress in preparation, processing and applications of polyaniline. Prog Polym Sci 34:783
5. Halik M, Klauk H, Zschieschang U, Schmid G, Ponomarenko S, Kirchmeyer S, Weber W (2003) Relationship between molecular structure and electrical performance of oligothiophene organic thin film transistors. Adv Mater 15:917
6. Soto-Oviedo MA, Araujo OA, Faez R, Rezende MC, De Paoli M-A (2006) Antistatic coating and electromagnetic shielding properties of a hybrid material based on polyaniline/organoclay nanocomposite and EPDM rubber. Synth Met 156:1249
7. El Hasnaoui M, Triki A, Achour ME, Arous M (2014) Modeling of dielectric relaxation processes of epoxy-resin filled with carbon black particles. Phys B Consens Matter 433:62

8. Aribou N, Nioua Y, Bouknaitir I, El Hasnaoui M, Achour ME, Costa LC (2019) Prediction of filler/matrix interphase effects on AC and DC electrical properties of carbon reinforced polymer composites. Polym Compos 40:346
9. Putson C, Lebrun L, Guyomar D, Muensit N, Cottinet P-J, Seveyrat L, Guiffard B (2011) Effects of copper filler sizes on the dielectric properties and the energy harvesting capability of nonpercolated polyurethane composites. J Appl Phys 109:024104
10. Evingür GA, Pekcan Ö. (2016) Carbon nanotubes –current progress of their polymer composites (MR Berber, IH Hafezeds), p 125. https://doi.org/10.5772/63054
11. Aliofkhazraei M (2019) Advances in nanostructured composites: volume 1: carbon nanotube and graphene composites. CRC Press
12. Bouknaitir I, Striccoli M, Panniello A, Costa LC, Teixeira SS, Achour ME, Kreit L, Corricelli M (2019) Optical and dielectric properties of PMMA (poly(methyl methacrylate))/carbon dots composites. Polym Compos 40:E1312
13. Elimat ZM (2006) AC electrical conductivity of poly(methyl methacrylate)/carbon black composite. J Phys D Appl Phys 39:2824
14. Dixit M, Gupta S, Mathur V, Rathore KS, Sharma K, Saxena NS (2009) Study of glass transition temperature of PMMA and CdS-PMMA composite. Chalcogenide Lett 6:131
15. Belhadj AM, Miane JL, Zangar H (2001) Radiofrequency and microwave (10 kHz–8 GHz) electrical properties of polypyrrole and polypyrrole–poly(methyl methacrylate) composites. Polym Int 50:773
16. Tripathi SN, Saini P, Gupta D, Choudhary V (2013) Electrical and mechanical properties of PMMA/reduced graphene oxide nanocomposites prepared via in situ polymerization. J Mater Sci 48:6223
17. Achour ME, Droussi A, Zoulef S, Gmati AF, Belhadj MA, Zangar H (2008) Electrical conductivity of polypyrrole-polymethylmethacrylate composites determined by impedance spectroscopy. Spectrosc Lett 41:328
18. Thomas P, Ernest Ravindran RS, Varma KBR (2014) Fabrication and characterization of poly (methyl methacrylate)/$CaCu_3Ti_4O_{12}$ composites. Polym Eng Sci 54:551
19. Segal L, Creely JJ, Martin AE Jr, Conrad CM (1959) An empirical method for estimating the degree of crystallinity of native cellulose using the X-ray diffractometer. Text Res J 29:786
20. Kumar M, Chakraborty S, Upadhyaya P, Pugazhenthi G (2017) Morphological, mechanical, and thermal features of PMMA nanocomposites containing two-dimensional Co–Al layered double hydroxide. J Appl Polym Sci 135:45774
21. Patel AK, Jain N, Patel P, Das K, Bajpai R (2018) Crystalline and absorption studies on PMMA/CdS composite using XRD & UV-Vis techniques. AIP Conf Proc 1942:070029
22. El-Zaher NA, Melegy MS, Guirguis OW (2014) Thermal and structural analyses of PMMA/TiO_2 nanoparticles composites. Nat Sci 6:859
23. Stauffer D, Aharony A (1992) Introduction to percolation theory. Taylor and Francis, London
24. Kirkpatrick S (1973) Percolation and conduction. Rev Mod Phys 45:574
25. Aribou N, Barnoss S., El Hasnaoui M, Achour ME, Costa LC (2019). Structural, electrical and thermal properties of composites based on conducting polymer. Jordan J Phy Accepted
26. Ou R, Gupta S, Parker CA, Gerhardt RA (2006) Fabrication and electrical conductivity of poly (methyl methacrylate) (PMMA)/carbon black (CB) composites: comparison between an ordered carbon black nanowire-like segregated structure and a randomly dispersed carbon black nanostructure. J Phys Chem B 110:22365
27. Kausar A (2019) Interpenetrating polymer network and nanocomposite IPN of polyurethane/epoxy: a review on fundamentals and advancements. Polym -Plast Polym Plast Technol Mater 58:691
28. Deepa KS, Kumari Nisha S, Parameswaran P, Sebastian MT, James J (2009) Effect of conductivity of filler on the percolation threshold of composites. Appl Phys Lett 94:142902
29. Kilbride BE, Coleman JN, Fraysse J, Fournet P, Cadek M, Drury A, Hutzler S, Roth S, Blau WJ (2002) Experimental observation of scaling laws for alternating current and direct current conductivity in polymer-carbon nanotube composite thin films. J Appl Phys 92:4024

30. Sinha S, Chatterjee SK, Ghosh J, Meikap AK (2015) Analysis of the dielectric relaxation and ac conductivity behavior of polyvinyl alcohol-cadmium selenide nanocomposite films. Polym Compos 38:287
31. Jonscher AK (1983) Dielectric relaxation in solids. Chelsea Dielectric, London
32. Funke K (1993) Jump relaxation in solid electrolytes. Prog Solid State Chem 22:111
33. Elliott SR (1987) A.c. conduction in amorphous chalcogenide and pnictide semiconductors. Adv Phys 36:135
34. Bairlein K, Bücker M, Hördt A, Hinze B (2016) Temperature dependence of spectral induced polarization data: experimental results and membrane polarization theory. Geophys J Int 205:440
35. Debye P (1945) Polar molecules. Dover, New York
36. Cole KS, Cole RH (1941) Dispersion and absorption in dielectrics I. alternating current characteristics. J Chem Phys 9:341
37. Clayton LM, Knudsen B, Cinke M, Meyyappan M, Harmon JP (2007) DC conductivity and interfacial polarization in PMMA/nanotube and PMMA/soot composites. J Nanosci Nanotechnol 7:3572
38. El Hasnaoui M, Graça MPF, Achour ME, Costa LC (2011) Electric modulus analysis of carbon black/copolymer composite materials. Mater Sci Appl 2:1421
39. El Hasnaoui M, Graça MPF, Achour ME, Costa LC, Lahjomri F, Outzourhit A, Oueriagli A (2011) Electrical properties of CB/ copolymer composites above and below the melting temperature. J Mater Environ Sci 2:1

Part VIII
Polymer-Based Materials

Chapter 22
Recent Advances of Electrospinning and Multifunctional Electrospun Textile Materials for Chemical and Biological Protection

Didem Demir, Ashok Vaseashta, and Nimet Bölgen

Abstract The primary task of protective clothing is to maximize the user's survival, sustainability and effectiveness against cold, heat, fire, ballistic, biological, radiological, nuclear and chemical agents. The protective textiles made of many different fabric materials have been widely used to provide effective protection for various specific applications. With the recent and ongoing advancements in nanotechnology, it is desirable that protective textiles have multifunctional properties. Thus, the newly developed composite materials gained various features such as flame retardancy, UV protection, pollutant capturing, antibacterial property, decontamination, detoxification and self-cleaning ability as well as providing wearing comfort. These properties can be achieved by incorporating functional agents (specific functional ligands or molecules, nanoparticles and drugs) into fabricated materials. Therefore, a new generation of protective fabrics has been produced in recent years. Electrospun textile materials are suitable for use as new protective clothing due to their easy production method, breathable, lightweight, comfortable and functionalizable properties. The electrospun membranes can be fabricated with diverse morphologies (core-shell, side-by-side, multilayer, hollow interior and with high porosity) by regulating the operating conditions and modifying the needle device. Electrospun nanofibers can be used in various application areas including filtration, sensing, wastewater treatment, biomedicine and protective textiles due to their extraordinary physicochemical features at nano level. This chapter aims to review recent advances of the electrospinning technique and the use of multifunctional electrospun materials for protection against chemical and biological agents.

D. Demir · N. Bölgen (✉)
Engineering Faculty, Chemical Engineering Department, Mersin University, Mersin, Turkey
e-mail: nimet@mersin.edu.tr

A. Vaseashta
International Clean Water Institute, Manassas, VA, USA

NJCU – State University of New Jersey, New Jersey, NJ, USA

P. Petkov et al. (eds.), *Nanoscience and Nanotechnology in Security and Protection against CBRN Threats*, NATO Science for Peace and Security Series B: Physics and Biophysics, https://doi.org/10.1007/978-94-024-2018-0_22

Keywords Electrospinning · Nanofibers · Multifunctional properties · Protective clothing · Chemical agents · Biological agents

22.1 Introduction

Protective clothing materials that protect the user from physical, chemical, biological, radiological and nuclear hazards are required for professional activities of specific work environments including battlefields, hospitals, police stations, fire and other occupational departments [1]. People working in these environments are at high risk of exposure to various types of hazardous environments including nanoparticles, explosives, chemical and biological agents, including pathogens that may pose a serious risk to human health. Nanofibrous structures fabricated by electrospinning are excellent candidates for the construction of protective textile materials due to their comfort in long-term operations, adsorptive, lightweight, low-cost and easy functionalization properties. Up to now, many studies have reported protective clothing materials produced by electrospinning to protect the wearer against chemical and biological agents. With the recent advances in nanotechnology, new multifunctional materials are produced by combining nanoparticles with electrospun nanofibers. Thus, the newly developed composite materials gained functional properties such as flame retardancy, gas sensing, self-detoxifying, UV protectivity, self-cleaning and antimicrobial ability. In this chapter, the recent developments in the electrospinning technique and the use of electrospun protective textile materials in preventing the harmful effects of chemical and biological agents are summarized.

22.2 Electrospinning

Electrospinning is a process governed by the electrohydrodynamic phenomena in which the fibers are made from polymer solutions or molten polymers [2]. The typical electrospinning set-up consists of three major components: a polymer solution placed in a reservoir (typically a syringe or a spinneret), a high voltage power supply and a grounded collector [3]. Figure 22.1 shows the schematic illustration of a conventional electrospinning set-up. First, the fluid for electrospinning is prepared by dissolving the selected polymer in a suitable solvent or by melting the polymer. The prepared solution is then loaded into the syringe and fed at a constant rate with the aid of a syringe pump. Meanwhile, the ambient conditions such as humidity and temperature should also be kept constant to ensure a reproducible and well-controlled electrospinning process. Afterward, a high voltage is applied to the polymer solution in order to charge it electrically, the solvent evaporates as the polymer jet advances towards the collector and polymeric fibers with diameters

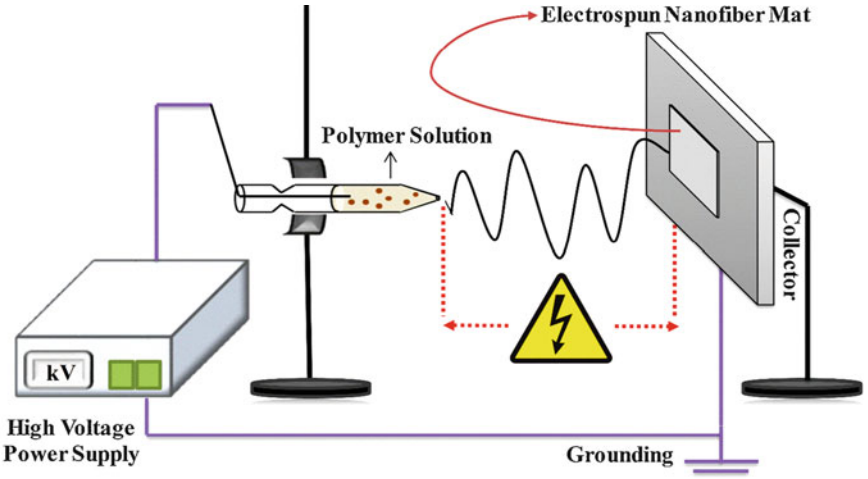

Fig. 22.1 Schematic illustration of conventional electrospinning set-up

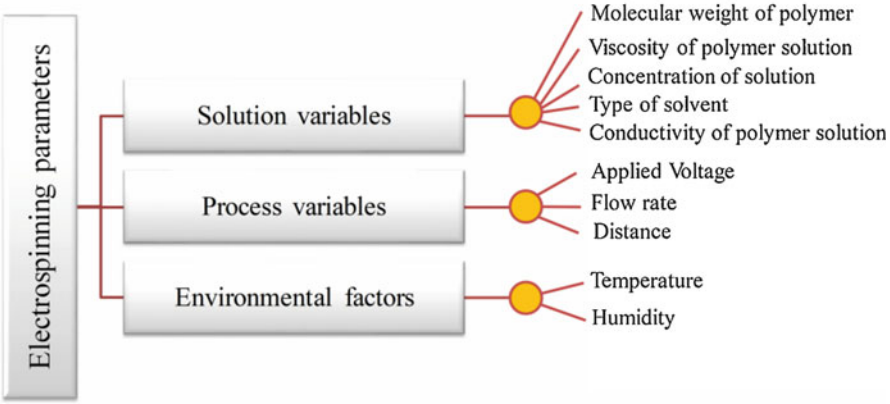

Fig. 22.2 The major factors affecting electrospinning process

ranging from nanometers to a few micrometers are formed on the grounded collector [4].

The surface and inner morphology of the resulting electrospun mats can be changed by the process variables such as polymer type and concentration, type of solvent, needle to collector distance, flow rate, applied electric field, temperature, humidity, etc. Since the properties (porosity, length and diameter) of the electrospun nanofibers are significantly affected by the fabrication parameters, many studies have been carried out to clarify the relationship between the properties of the resultant nanofibers and the process parameters. These parameters can be classified into three main groups as demonstrated in Fig. 22.2.

22.3 Latest Technological Advances of Electrospinning

The electrospinning method was first patented in 1934 in the USA [5]. Until the 1970s, many patents for improvement of the process and system parameters were continuously published. In the last decade, electrospinning technique attracted the attention of many scientists due to a surge of interest in nanofiber technology [6]. Because of the unique features of the electrospun materials, including their large surface *area*, tunable porosity, superior mechanical properties and ease of surface modification, the use of nanofibers made from synthetic and natural polymers, and composite systems has been drastically increased in recent years for numerous application areas.

Among all potential applications, one of the most common application area of electrospun nanofibers is tissue engineering and regenerative medicine [7]. Electrospun nanofibrous structures are used as scaffolds in tissue engineering applications, since they simulate the natural extracellular matrix and enhance new tissue formation or tissue reconstruction by providing the cells a favourable environment for adhesion, growth, proliferation, migration and differentiation [8]. The fibers produced by electrospinning in nanoscale, can improve cellular interactions of a wide variety of cell types [9]. In addition to the use of electrospun materials as scaffolds in tissue engineering, they are also utilized in targeted drug delivery systems [10, 11].

Filtration system for wastewater treatment is another application field of electrospun nanofibrous membranes [12]. These filtration membranes prepared by electrospinning are good candidates for removal or separation of pathogenic microorganisms, chemical residues, dyestuffs and antibiotics from potable water to wastewater sources. The properties of the membranes can be tailored for filtration of different kinds of residues by tuning the pore size and fiber diameter through adjustment of the electrospinning parameters [13].

Another area that has made significant progress in recent years is the use of electrospun materials as protective clothing. Efficient protective materials, that prevent the hazardous effects of nanoparticles, toxic industrial chemicals, aerosols, pesticides and chemical warfare agents, such as clothing, gloves, masks, shoe covers and filters, have been successfully produced by using electrospinning technique [14]. Due to comfortable wearing and lightweight properties, high surface area and open porous morphology of electrospun nanofibers, these materials are promising to overcome the problems of the traditional protective clothing [15]. Nanoscience and nanotechnology provided the development of advanced materials that could make human life easier, safer and more comfortable in different application areas such as tissue engineering, protective clothing, filtration and sensors. In recent years, researchers focused on the development of diverse electrospun materials by tuning the process parameters or by functionalization of the nanofibers to produce materials with superior properties. Lately, new electrospun nanofibrous materials have been developed by tuning the fiber fineness, surface morphology, orientation and cross-sectional configuration of the nanofibers by modifying the electrospinning set-up.

Some of these techniques can be summarized as (a) multiaxial electrospinning, (b) multiple needles and (c) wet electrospinning.

22.3.1 Multiaxial Electrospinning

Multilayer nanofiber structures can be produced by coaxial or triaxial electrospinning. In these techniques, two or three different solutions can be electrospun simultaneously through a spinneret composed of two or more syringes to produce core-shell or core-intermediate-shell structured nanofibers [16, 17]. Schematic diagrams of the multiaxial electrospinning set-up and the resulting structure of the produced nanofibers are shown in Fig. 22.3. With these methods, various combinations of natural and synthetic polymers can be produced in different layers to provide heterogeneous structures with desirable properties. In addition, numerous hydrophilic and lipophilic components, including growth factors, DNA, inhibitors, drugs, hormones and antibodies, can be incorporated into multiaxial fibers during the spinning process [18].

Pakravan et al. used coaxial electrospinning to fabricate core-shell structured nanofibers from polyethylene oxide (PEO) and chitosan. They co-electrospun the PEO and chitosan solutions as core and sheath materials, respectively. The detailed morphology of the fabricated coaxial PEO/chitosan nanofibers is shown in a TEM micrograph in Fig. 22.3c. The dark and bright regions represent the core and the shell of the nanofiber, respectively [17].

In another study, Habibi et al. used triaxial electrospinning to produce tri-layer structured nanofibers for the sustained release of Doxorubicin (DOX), Paclitaxel (PTX) and 5-fluorouracil (5-FU) anticancer drugs from multilayered nanofibers. The different combinations of chitosan (CS), polyvinyl alcohol (PVA) and poly (lactic acid) (PLA) solutions were used to prepare CS/PVA/5FU as core, PLA/CS as middle and graphitic carbon nitride (g-C_3N_4)/DOX and g-C_3N_4/PTX nanosheets incorporated PLA/CS as shell layer. They determined different release profiles of the drugs that are separately loaded either in the sheath or in the core of the nanofibers [16].

22.3.2 Multiple Needles

In recent years, a lot of research has been done on different types of needle electrospinning spinnerets. The purpose of using multiple needles is to overcome the limitation of commercial production by increasing the rate and yield of electrospinning. Because of the increased spinning solution mass and electrostatic interference between the needles, higher voltage is required in the multiple needle systems compared to the single needle system, to maintain continuous electrospinning [20, 21]. This system is designed not only with needles but also with different types of nozzles such as channels, tips and holes [22].

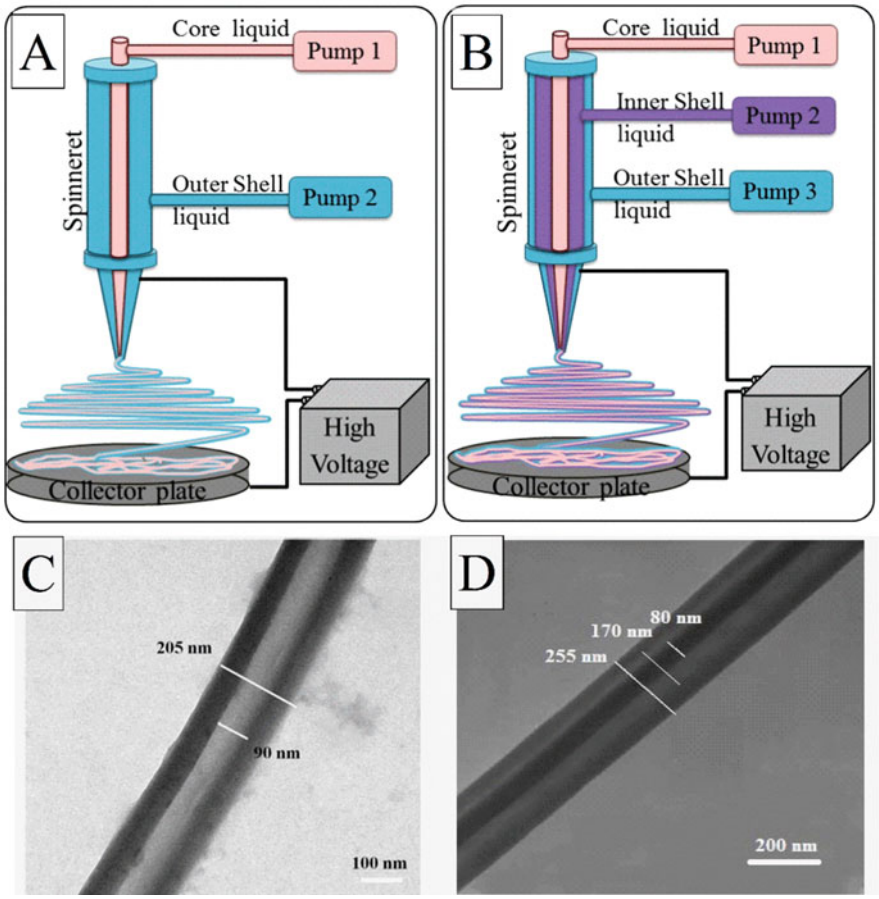

Fig. 22.3 Coaxial (**a**) and triaxial (**b**) electrospinning set-ups, where bi- (**c**) and tri-layered (**d**) nanofibers were obtained. (**a**) and (**b**) Reprinted with permission from Ref. [19] Copyright 2018 Elsevier. (**c**) Reprinted with permission from Ref. [17] Copyright © 2012, American Chemical Society (**d**) Reprinted with permission from Ref. [16] Copyright 2018 Elsevier

For example, Zhu et al. designed a multi-needle electrospinning head to obtain more uniform and enhanced deposition of nanofibers. They found that even when they increased the number of needles in the trapezoidal wave arrangement to 32 needles, the electrospinning jet was still stable and the nanofibers were uniform without formation of droplets [23].

Liu et al. installed tiny needle tips around a circular disk and then axially assembled these disks to form a multi-needle disk electrospinning device as shown in Fig. 22.4a–c. This device significantly enhanced the nanofiber production with a uniform fiber diameter distribution (Fig. 22.4d) [24].

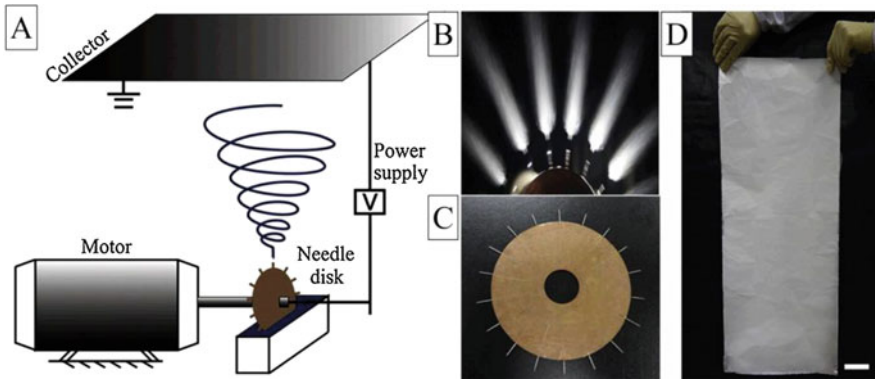

Fig. 22.4 The multi-needle disk apparatus arrangement of electrospinning head (**a** and **c**), the image of needle-helix slice spinneret (**b**) and large scale produced nanofibers (**d**). (Reprinted with permission from Ref. [24] Copyright © 2016 Elsevier Ltd.)

22.3.3 Wet Electrospinning

Wet electrospinning also called "hydrospinning" or "liquid-bath electrospinning" is a modified technique based on the use of a liquid collector instead of a solid metal collector [25]. During wet electrospinning, the polymer solution is spun directly from the nozzle to a coagulation bath. Polymeric fibers are collected in liquid (such as water, ethanol and methanol) in the coagulation bath which is a non-solvent system for the electrospun polymer. The main advantage of wet electrospinning is that it allows the spinning of natural polymers without denaturation since they are not subjected to higher voltage compared to the conventional system [26]. Moreover, the use of a coagulation bath is very essential for removing less volatile solvents from the produced fibers.

In one of the recent studies, Sonseca et al. fabricated 3D helically coiled structures by conventional electrospinning with a flat metal collector and by wet electrospinning with a system, in which methanol was used as non-solvent in the coagulation bath. Many parameters of both electrospinning methods including the solution and operational parameters, and the type of non-solvent liquid in the coagulation bath were varied in order to determine their synergetic effect on the morphology of the resulting fibers. By adjusting these parameters, it was demonstrated that a range of architectures could be obtained, from the flatter, ribbon-like coils to spring-like coils [27].

In another study, Majidi et al. reported the fabrication of alginate (Alg) and alginate/gelatin hydrogel (Alg/GelF-MA) nanofibers for 3D cell culture using wet electrospinning in the presence of a supporting polymer, polyethylene oxide and a surfactant Pluronic®F127. Figures 22.5b, e show SEM images of electrospun scaffolds obtained by conventional electrospinning with a solid collector (Fig. 22.5a) and by wet electrospinning (Fig. 22.5d) with ethanol, used as non-solvent in the coagulation bath containing 2% (w/v) $CaCl_2$, respectively. The collected nanofibers

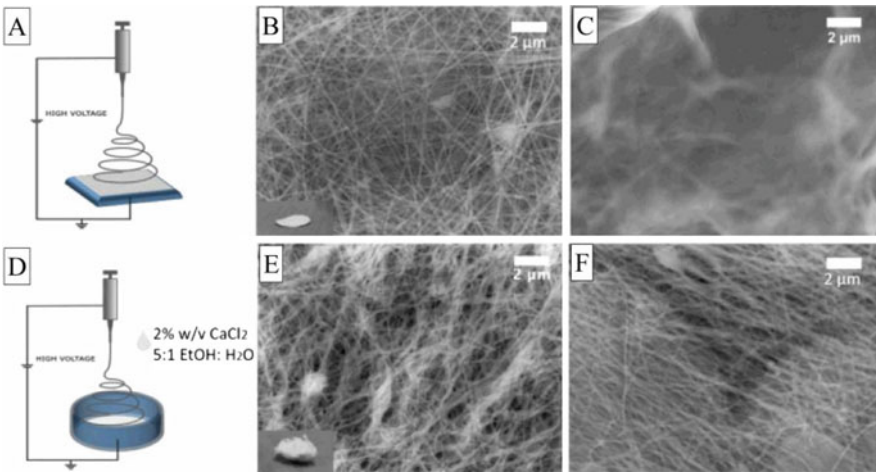

Fig. 22.5 Conventional (**a**) and wet (**d**) electrospinning set-ups, SEM images of electrospun Alg/PEO/F127/GelF-MA 2D nanofibers before (**b**) and after exposure to a water droplet (**c**), SEM images of wet electrospun 3D Alg/PEO/F127 nanofibers (E) and UV crosslinked Alg/PEO/F127/GelF-MA nanofibers (**f**) after exposure to water for 2 days. Insets, images of 2D and 3D fibrous electrospun scaffolds produced via conventional (**b**) and wet (**e**) electrospinning methods. (Reprinted with permission from Ref. [28] Copyright 2018 Elsevier)

were crosslinked via UV exposure. After crosslinking, the stability of the nanofibers was tested against water. The fibrous structure using conventional electrospinning was not stable enough to withstand exposure to water for 1 min (Fig. 22.5c), however the cotton-like nanofibrous membrane produced by wet electrospinning was stable enough to endure water washing and being held in water for 2 days (Fig. 22.5f) [28].

22.4 Electrospun Nanofibers for Protective Clothing

One of the most important application areas of nanofibrous structures is their use as protective clothing materials. Protective clothing, including helmets, goggles and shoe covers or other garments that are designed to protect the wearer's body from injury, harsh environmental effects or chemical, physical, nuclear and biological hazards. Protective textile materials can be used for ballistic protection, for protection against chemical and biological agents, as face masks, smart textiles or sport wear [1]. Chemical and biological protective clothing can protect emergency workers, healthcare providers, military personnel and potential victims of terrorist attacks against dangerous agents. Chemical and biological agents that are exposed by the related activities can be considerably complicated that no protective clothing alone can be sufficient for protection. Therefore, the development of new barrier equipment, devices and multifunctional personal protective clothing is required to

protect the health of military personnel and the people working under hazardous environmental conditions.

Fabrication of nanofibrous matrices by electrospinning is a promising approach. Filtration, detoxification, degradation and separation of harmful agents can be successfully achieved by electrospun nanofibers due to their large surface area, high porosity and appropriateness for functionalization. In addition, the textiles produced by electrospinning are flexible, lightweight and breathable, which provide suitable comfort to the wearer. The superiority of electrospinning over the other methods is that it is a fast, simple, and economically feasible method for converting various polymers or their composites into nanofibrous structures having fibers with diameters ranging from nanometers to several micrometers [14].

The potential application of electrospun fiber mats as protective barrier materials was first suggested by Gibson et al. The electrospun nanofiber mats that they produced have demonstrated a high filtration efficiency against aerosol particles [29]. Starting with this research, a variety of studies have been reported about the use of electrospun nanofibrous materials for protection against chemical and biological agents. The researchers are currently focused on the fabrication of electrospun nanofibrous textile materials which can be functionalized to increase their efficiency in adsorption. The recently developed protective clothing have antimicrobial properties, sensing, self-cleaning and self-detoxifying abilities.

22.4.1 Self-Detoxifying Nanofibers

Self-detoxifying electrospun fabrics are newly developed textile materials for protection against chemical and biological warfare agents, especially encountered in military applications and terrorist attacks. In recent years, studies focused on the achievement of detoxification of the toxic and hazardous chemicals/chemical weapons such as sarin, soman, nerve, blister, choking, tear, vomit and blood agents [30, 31]. Actually, activated carbon has been widely used for years for protection against these kinds of chemicals. Although it is an excellent adsorbent, it has some disadvantages such as being heavy (a full garment weighs about 2.5 kg), and difficulty in disposal of the contaminated clothing [31]. Modifying electrospun nanofibers with functional groups and combining nanofibers with metal oxides to detoxify the chemical warfare agents, have been considered as possible alternatives to activated carbon.

Lee et al. produced polyacrylonitrile nanofibers through electrospinning and chemical vapor deposition, in order to develop functional non-woven nanofiber mats for detoxifying simulant of chemical warfare agents. They prepared and modified nanofibers with a series of amines. These fiber mats effectively degraded di-isopropyl fluorophosphate which is a simulant of G-series chemical warfare agent [31].

In another study, Liang et al. developed electrospun ZrO_2 nanofibers-based metal-organic framework filters (Zr-MOFilters) including UiO-66, UiO-67 and

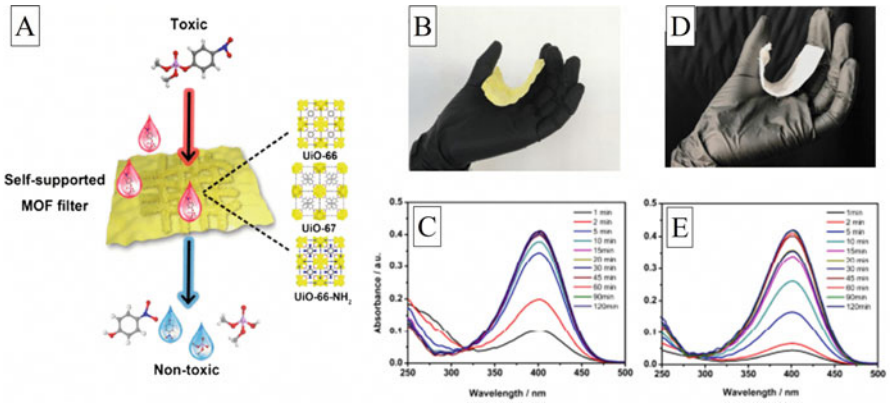

Fig. 22.6 General overview (**a**), optical photographs and kinetic analysis of DMNP degradation of the prepared Zr-MOFilters: UiO-66-NH_2 (**b** and **c**) and UiO-67 (**d** and **e**). (Reproduced with permission from Ref. [32] Copyright © 2018, American Chemical Society)

UiO-66-NH_2 for fast detoxification of chemical warfare agent simulants (Fig. 22.6a). The catalytic activity of Zr-MOFilters was found to be continuous at long-term exposure to dimethyl 4-nitrophenyl phosphate (DMNP) (Figs. 22.6c, e). In addition, the produced samples showed good structural integrity and flexibility (Figs. 22.6b, d) [32].

In yet another study, a series of metal hydroxide catalysts ($Ti(OH)_x$, $Zr(OH)_4$, and $Ce(OH)_4$) were incorporated into three different polymeric nanofiber networks (polyvinylidene fluoride, polymethylmethacrylate and polystyrene). The catalytic activities of the prepared materials against a nerve agent simulant were evaluated. Two methods were used to incorporate the metal hydroxides into the nanofibers. In the first method, the catalyst was directly added to the polymer solution before electrospinning. In the second method, a precursor molecule of $Ti(OH)_x$ was added to the polymer solution. Surface with uniform hydroxyl distribution and high wettability was achieved by the second method, which provided higher reaction rates and catalytic activity against a nerve agent simulant [33].

22.4.2 Antimicrobial Nanofibers with Multifunctional Properties

Current developments in the use of electrospun nanofibers in protective garments include the production of antimicrobial nanofibers. Antibacterial and antiviral properties can be achieved by incorporating functional agents (nanoparticles, drugs, and photo-catalytic materials or biocidal agents) into nanofiber mats to prevent infections caused by microorganisms. Inorganic metal and metal oxide additives such as silver, gold and gallium nanoparticles; or ZnO, MgO and CuO have been known to have

effective bactericidal properties [34]. In addition, nanofibers prepared from polysaccharides such as chitin and chitosan have also shown good antibacterial functionality [35].

Recent reports present the development of effective protective clothing with multi-functional properties that has antimicrobial activities against biological agents as well as decontaminating, detoxifying and self-cleaning properties against certain chemicals. In particular, contamination can damage the protective layers mounted on garments and cause decay in their performance in a short time duration. For this reason, it is important to produce self-cleaning coatings to remove inorganic and organic contaminants [36].

Sinha et al. coated polypropylene (PP) non-woven fabric with electrospun chitosan nanofibers by utilizing nanospider technology. Then, the prepared web was functionalized with ZnO nanoparticles by electrospraying technique in order to disintegrate sulfur mustard chemical warfare agent. The chitosan nanofiber coated PP web prevented the mustard agents to pass. The ZnO functionalized chitosan nanofibrous layer acted as a semipermeable barrier that prevented the penetration of mustard chemical particles, providing at the same time water vapor and air transportation. In addition, the produced materials showed antimicrobial activity against both gram-positive (*Staphylococcus aureus*) and gram-negative (*Escherichia coli*) bacteria [37].

In another study, Khan et al. fabricated multifunctional electrospun ZnO nanoparticles incorporated polyvinyl alcohol (PVA) nanofibrous membranes (PVA/ZnO) with antibacterial, self-cleaning and UV protection properties. ZnO nanoparticles added self-cleaning ability, antibacterial property and photocatalytic activity to the matrice. PVA/ZnO electrospun matrices showed 98% self-cleaning performance for methylene blue dye under UV light within 3 h, while neat PVA nanofibers did not show any self-cleaning ability. In addition, the composite nanofibers showed nearly zero UV transmission, where the neat PVA nanofibers showed high UV transmission. Antibacterial activities of the membranes against *Staphylococcus aureus* and *Escherichia coli* model bacteria were also assessed. It was observed that the antibacterial efficiency of the membranes increased with increasing the amount of ZnO nanoparticles. Plain PVA did not have any antibacterial property [38, 39].

22.4.3 Gas Sensing Nanofibers

Flexible, sensitive and lightweight electrospun nanofibers can be applied as portable and wearable sensors for the detection of harmful agents. Due to the unique features of electrospun nanofibers including large surface area, they can be used in sensor systems with high sensing ability. The electrospun nanofibers can be implemented for gas sensing [40].

The development of sensor technology has received considerable attention in recent years especially for colorimetric sensors. In a recent study, Phos-3-embedded

electrospun poly(ethylene oxide) nanofibrous structures were prepared to be used as a colorimetric chemosensor for the detection of phosgene in the gas phase. The produced membrane exhibited a golden yellow color under both colorimetric and fluorescent conditions prior to exposure to phosgene, while it emitted cyan color after exposure to gaseous phosgene. In addition, after the gas treatment the morphological structure of the fibers changed as a result of the reaction between Phos-3 and phosgene. Wang et al. prepared test strips to develop an easy and fast method to detect phosgene gas. Test strips exposed to various concentrations of gas gradually became colorless under room light, while the color changed from yellow to cyan under fluorescence. Moreover, they investigated the selective detectability of phosgene in the case of exposure of test strips to a mixture of phosgene and various other analytes. On exposure to phosgene, the test strips exhibited the same color change and high selectivity toward phosgene over other gaseous analytes [41].

Supraja et al. developed electrospun manganese oxide nanofibers (MNF) as an anti-atrazine-antibody based immunosensor to detect atrazine, a toxic chemical that severely affects the human endocrine system. The developed fibers were able to detect atrazine in the concentration range of 10^{-21} g/mL, with a limit of 0.22×10^{-21} g/mL and a sensitivity of 52.54 (kΩ/μg·mL^{-1})/cm^2 which is the lowest detection limit for any atrazine sensors reported in the literature. In addition, they tested the sensor performance against water samples to determine the usability of the sensor for real-time atrazine detection. The results show that the proposed platform is suitable for real-time applications [42].

22.5 Conclusions

In recent years, there has been a significant growth in the number of studies demonstrating the modification of the conventional electrospinning process. The modifications made in the electrospinning equipment provide the production of nanofibers with various structures and properties. Nanofiber based multifunctional materials can be integrated into protective clothing systems. Multifunctional electrospun materials open up new opportunities for the development of advanced devices for effective protection against both chemical and biological agents. Electrospun protective clothing is still in the development phase and has some limitations in commercial production and difficulty in establishment of the bridge between the researchers and the industry. The development of advanced multifunctional protective clothing that can protect the user from any chemical or biological agents is a requirement. Combining the antimicrobial, self-cleaning and self-detoxifying properties of functional electrospun materials with textile fabrics can create new horizons in the protective garment industry under the light of multidisciplinary research which will help to bridge the gap between researchers and manufacturers.

References

1. Gorji M, Bagherzadeh R, Fashandi H (2017) Electrospun nanofibers in protective clothing. In: Woodhead publishing series in textiles, vol 186. Woodhead publishing, pp 571–598
2. Reneker DH, Yarin AL (2008) Electrospinning jets and polymer nanofibers. Polymer 49:2387–2425. https://doi.org/10.1016/J.POLYMER.2008.02.002
3. Xie J, Li X, Xia Y (2008) Putting electrospun nanofibers to work for biomedical research. Macromol Rapid Commun 29:1775–1792. https://doi.org/10.1002/MARC.200800381
4. Wang C, Wang J, Zeng L et al (2019) Fabrication of electrospun polymer nanofibers with diverse morphologies. Molecules 24:1–33. https://doi.org/10.3390/molecules24050834
5. Anton F (1934) Process and apparatus for preparing artificial threads. US Patent 1,975,504 (2 Oct 1934)
6. Garg K, Bowlin GL (2011) Electrospinning jets and nanofibrous structures. Biomicrofluidics 5:1–19. https://doi.org/10.1063/1.3567097
7. Bölgen N, Menceloğlu YZ, Acatay K et al (2005) In vitro and in vivo degradation of non-woven materials made of poly(ε-caprolactone) nanofibers prepared by electrospinning under different conditions. J Biomater Sci Polym Ed 16:1537–1555. https://doi.org/10.1163/156856205774576655
8. Smith LA, Ma PX (2004) Nano-fibrous scaffolds for tissue engineering. Colloid Surface B 39:125–131. https://doi.org/10.1016/J.COLSURFB.2003.12.004
9. Liu H, Ding X, Zhou G et al (2013) Electrospinning of nanofibers for tissue engineering applications. J Nanomater 2013:1–11. https://doi.org/10.1155/2013/495708
10. Demir D, Güreş D, Tecim T et al (2018) Magnetic nanoparticle-loaded electrospun poly(ε-caprolactone) nanofibers for drug delivery applications. Appl Nanosci 8:1461–1469. https://doi.org/10.1007/s13204-018-0830-9
11. Yeniay E, Öcal L, Altun E et al (2019) Nanofibrous wound dressing material by electrospinning method. Int J Polym Mater Polym Biomater 68:11–18. https://doi.org/10.1080/00914037.2018.1525718
12. Mirjalili M, Zohoori S (2016) Review for application of electrospinning and electrospun nanofibers technology in textile industry.J nanostructure Chem 6:207–213. https://doi.org/10.1007/s40097-016-0189-y
13. Tlili I, Alkanhal TA (2019) Nanotechnology for water purification: electrospun nanofibrous membrane in water and wastewater treatment. J Water Reuse Desalin 9:232–248. https://doi.org/10.2166/wrd.2019.057
14. Faccini M, Vaquero C, Amantia D (2012) Development of protective clothing against nanoparticle based on electrospun nanofibers. J Nanomater 2012:1–9. https://doi.org/10.1155/2012/892894
15. Raza A, Li Y, Sheng J et al (2014) Protective clothing based on electrospun nanofibrous membranes. Electrospun nanofibers for energy and environmental applications, Springer, Heidelberg, In
16. Habibi Jouybari M, Hosseini S, Mahboobnia K et al (2019) Simultaneous controlled release of 5-FU, DOX and PTX from chitosan/PLA/5-FU/g-C3N4-DOX/g-C3N4-PTX triaxial nanofibers for breast cancer treatment in vitro. Colloid Surface B 179:495–504. https://doi.org/10.1016/J.COLSURFB.2019.04.026
17. Pakravan M, Heuzey M-C, Ajji A (2012) Core–shell structured PEO-chitosan nanofibers by coaxial electrospinning. Biomacromolecules 13:412–421. https://doi.org/10.1021/bm201444v
18. Khalf A, Madihally SV (2017) Modeling the permeability of multiaxial electrospun poly(ε-caprolactone)-gelatin hybrid fibers for controlled doxycycline release. Mater Sci Eng C 76:161–170. https://doi.org/10.1016/J.MSEC.2017.03.093
19. Khalf A, Madihally SV (2017) Recent advances in multiaxial electrospinning for drug delivery. Eur J Pharm Biopharm 112:1–17. https://doi.org/10.1016/J.EJPB.2016.11.010

20. Begum HA, Khan MKR (2017) Study on the various types of needle based and needleless electrospinning system for nanofiber production. Int J Text Sci 6:110–117
21. Tian L, Zhao C, Li J et al (2015) Multi-needle, electrospun, nanofiber filaments: effects of the needle arrangement on the nanofiber alignment degree and electrostatic field distribution. Text Res J 85:621–631. https://doi.org/10.1177/0040517514549990
22. SalehHudin HS, Mohamad EN, Mahadi WNL et al (2018) Multiple-jet electrospinning methods for nanofiber processing: a review. Mater Manuf Process 33:479–498. https://doi.org/10.1080/10426914.2017.1388523
23. Zhu Z, Xu G, Chen R et al (2018) Uniform electric field enabled multi-needles electrospinning head based on trapezoid arrangement. AIP Adv 8:1–9. https://doi.org/10.1063/1.5026908
24. Liu Z, Chen R, He J (2016) Active generation of multiple jets for producing nanofibres with high quality and high throughput. Mater Des 94:496–501. https://doi.org/10.1016/j.matdes.2016.01.075
25. Sensini A, Cristofolini L (2018) Biofabrication of electrospun scaffolds for the regeneration of tendons and ligaments. Materials (Basel) 11:1–43. https://doi.org/10.3390/ma11101963
26. DeFrates KG, Moore R, Borgesi J et al (2018) Protein-based fiber materials in medicine: a review. Nano 8:1–26. https://doi.org/10.3390/nano8070457
27. Sonseca A, Sahay R, Stepien K et al (2018) Architectured helically coiled scaffolds from elastomeric poly(butylene succinate) (PBS) copolyester via wet electrospinning. ChemRxiv 1–23. https://doi.org/10.26434/chemrxiv.6353402
28. Majidi SS, Slemming-Adamsen P, Hanif M et al (2018) Wet electrospun alginate/gelatin hydrogel nanofibers for 3D cell culture. Int J Biol Macromol 118:1648–1654. https://doi.org/10.1016/j.ijbiomac.2018.07.005
29. Gibson P, Schreuder-Gibson H, Rivin D (2001) Transport properties of porous membranes based on electrospun nanofibers. Colloids Surfaces A Physicochem Eng Asp 187:469–481. https://doi.org/10.1016/S0927-7757(01)00616-1
30. Jang YJ, Kim K, Tsay OG et al (2015) Destruction and detection of chemical warfare agents. Chem Rev 115:1–76. https://doi.org/10.1021/acs.chemrev.5b00402
31. Lee J, Seo E, Yoo M et al (2019) Preparation of non-woven nanofiber webs for detoxification of nerve gases. Polymer 179:1–9. https://doi.org/10.1016/j.polymer.2019.121664
32. Liang H, Yao A, Jiao X et al (2018) Fast and sustained degradation of chemical warfare agent simulants using flexible self-supported metal-organic framework filters. ACS Appl Mater Interfaces 10:20396–20403. https://doi.org/10.1021/acsami.8b02886
33. Dwyer DB, Liu J, Gomez JC et al (2019) Metal hydroxide/polymer textiles for decontamination of toxic organophosphates: an extensive study of wettability, catalytic activity, and the effects of aggregation. ACS Appl Mater Interfaces 11:31378–31385. https://doi.org/10.1021/acsami.9b10440
34. Gold K, Slay B, Knackstedt M et al (2018) Antimicrobial activity of metal and metal-oxide based nanoparticles Adv Ther:1. https://doi.org/10.1002/adtp.201700033
35. Jayakumar R, Prabaharan M, Nair SV et al (2010) Novel chitin and chitosan nanofibers in biomedical applications. Biotechnol Adv 28:142–150. https://doi.org/10.1016/j.biotechadv.2009.11.001
36. Gugliuzza A, Drioli E (2013) A review on membrane engineering for innovation in wearable fabrics and protective textiles. J Memb Sci 446:350–375. https://doi.org/10.1016/j.memsci.2013.07.014
37. Sinha MK, Das BR (2018) Chitosan nanofibrous materials for chemical and biological protection. J Text Fibrous Mater 1:1–13. https://doi.org/10.1177/2515221118788370
38. Khan MQ, Kharaghani D, Nishat N et al (2019) Preparation and characterizations of multifunctional PVA/ZnO nanofibers composite membranes for surgical gown application. J Mater Res Technol 8:1328–1334. https://doi.org/10.1016/j.jmrt.2018.08.013
39. Vaseashta A (2007) Controlled formation of multiple Taylor cones in electrospinning process Appl Phys Lett:90. https://doi.org/10.1063/1.2709958

40. Aliheidari N, Aliahmad N, Agarwal M et al (2019) Electrospun nanofibers for label-free sensor applications. Sensors 19:1–27. https://doi.org/10.3390/s19163587
41. Wang SL, Zhang CL, Song QH (2019) Selectively instant-response nanofibers with a fluorescent chemosensor toward phosgene in gas phase. J Mater Chem C 7:1510–1517. https://doi.org/10.1039/C8TC05281F
42. Supraja P, Tripathy S, Krishna Vanjari SR et al (2019) Label free, electrochemical detection of atrazine using electrospun Mn2O3 nanofibers: towards ultrasensitive small molecule detection. Sensors Actuators B Chem 285:317–325. https://doi.org/10.1016/j.snb.2019.01.060

Chapter 23
Temperature Effect on Dielectric Properties of Heterogeneous Material Based on Carbon Black Loaded Copolymer Nanocomposite

Mohamed El Hasnaoui, Mohammed E. Achour, and Luis C. Costa

Abstract In this work, we report an experimental study of the thermal and electrical properties of heterogeneous materials based on ethylene butylacrylate copolymer filled with carbon black nanoparticles. For this study, a series of samples were prepared with filler fractions above the percolation threshold. Their thermal characterization was performed using differential scanning calorimetry, thermogravimetric analysis, and differential thermal analysis which allowed to observe significant changes in the spectrum at melting and degradation temperatures of composites. Dielectric measurements were carried out in the frequency domain 40 Hz–2 MHz and temperature domain 300–400 K. Using the impedance spectrum, it has been found that the Cole-Cole model is capable to describe quantitatively the experimental data from which we extract the relaxation time and exponent that gauges the broadening of the loss spectrum. The obtained values of α exponent are near zero, suggesting a behavior close to a model of single relaxation time. Furthermore, the relaxation time versus temperature follows an Arrhenius behavior for temperatures above the melting point. The activation energies and the pre-exponential factors decrease with carbon black concentrations, indicating that the relaxation mechanism does not result simply from thermally activated dipolar interactions, but it is a collective cooperative effect of the mesostructured particles.

Keywords Composite materials · Degradation · Percolation · Impedance spectroscopy · PTCR effect

M. El Hasnaoui (✉) · M. E. Achour
LASTID Laboratory, Physics Department, Faculty of Sciences, Ibn Tofail University, Kenitra, Morocco
e-mail: med.elhasnaoui@uit.ac.ma

L. C. Costa
I3N and Physics Department, University of Aveiro, Aveiro, Portugal

P. Petkov et al. (eds.), *Nanoscience and Nanotechnology in Security and Protection against CBRN Threats*, NATO Science for Peace and Security Series B: Physics and Biophysics, https://doi.org/10.1007/978-94-024-2018-0_23

23.1 Introduction

Nowadays, the research on innovative materials became an important subject of the scientists. Composites based on polymeric matrices loaded with conducting charges, such as graphite (Gt), carbon nanotubes (CNT) and carbon black (CB), play an important role in improvement the performance of industrial materials in different areas such as radio-frequency shielding, self-regulator heating and static charging. It is known that the addition of conductive filler in insulating polymer matrix produces a composite with conductive behaviour when the fraction of conducting phases is above a specific concentration, the percolation threshold (ϕ_c) [1–3]. According to percolation theory, when the concentration of conductive filler is above ϕ_c, a continuous conductive path of loaded particles is built throughout the polymer matrix; in this case, the electrical properties of composites are controlled by filler type. Several works found that ϕ_c is largely dependent on the shape of the conducting particles and can be extremely low in composites including highly anisotropic filler. For example, carbon nanotubes loaded polyester possesses a percolation threshold of 0.6% [4]; it can be also low in composites with thermosetting matrix. For instance, CB loaded diglycidylic ether of bisphenol F (DGEBF) epoxy gave a percolation threshold of 2.7–3.6% [5]. In addition, a filler with low particle size will have a lower percolation threshold and better transfer of properties to the polymer [6]. It is established also that under the application of an electric field, a composite can be driven to an insulator-conductor transition if the conducting fraction is below ϕ_c [7, 8] supporting the idea that conductivity increase can be emulated by changing the connectivity of the conducting particle aggregates. In our previous works [9–11], we performed a systematic investigation of CB concentration effect on electrical conductivity of nanocomposites based on ethylene butylacrylate (EBA) copolymer loaded CB particles. The results showed that the value of percolation threshold is near to 11%, and this behaviour was attributed to the formation of an infinite agglomerate pathway which allows electrons to travel a macroscopic distance through the polymer matrix.

Impedance spectroscopy has proven to be a powerful tool for studying conduction mechanisms, phase transitions and dielectric relaxation in polymer composites and heterogeneous systems [12]. It can provide valuable information on thermal and frequency behaviour related to composite polarization. In this paper, we report an analysis of experimental data to extract new information about the thermal properties of CB/EBA percolating nanocomposites for concentrations above the percolation threshold using differential scanning calorimetry (DSC), thermogravimetric analysis (TGA), and differential thermal analysis (DTA), and the dielectric properties related to relaxation process occurring in the frequency range from 40 Hz to 2 MHz and over the temperature range from 300 to 400 K.

23.2 Experimental

23.2.1 Materials

In this study, we used a copolymer matrix of ethylene butylacrylate (EBA), with approximately 4 mol% of butylacrylate, supplied by Borealis AB, Sweden. The butylacrylate monomer contains butylester side groups providing a certain polarity and a relatively low crystallinity (≈20 vol%). The glass transition temperature and dc conductivity of EBA are respectively $T_g = 198$ K and $\sigma_{dc} = 10^{-12}$ $(\Omega.\mathrm{m})^{-1}$. Carbon black (CB) particles were used as a conducting filler obtained from Borealis AB, Sweden. The average size of the primary CB particles is about 30 nm and the mean size of the primary aggregates is on the order of 150 nm. CB fillers have a density of 1.89 g/cm^3, a specific surface area (SSA) of 63 m^2/g and a dc conductivity of 1 $(\Omega.\mathrm{m})^{-1}$. A series of four samples with nominal carbon black concentrations 13, 16, 19, and 22% were fabricated by mechanical mixing above the percolation threshold $\phi_c \approx 11\%$ [10]. Reference [13] presented the experimental details of the sample preparation procedure.

Figure 23.1 shows SEM micrographs of the composites with CB concentrations of 19% and 22%. We can observe that the CB is well dispersed into the EBA matrix, having in mind that the aggregation of CB fillers is not only a critical parameter influencing the electrical properties but also an important parameter accounting for the thermal stability of the composites [14]. Several works have demonstrated that the state of aggregation can be controlled by the processing conditions and by the structure of the CB fillers [15–18].

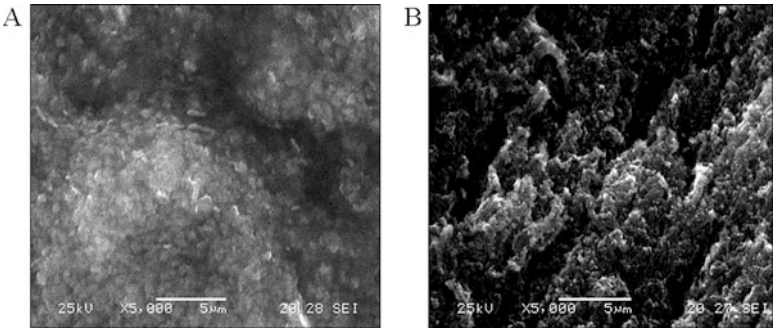

Fig. 23.1 SEM images of CB/EBA composite samples: (**A**) $\phi = 19\%$ of CB and (**B**) $\phi = 22\%$ of CB

23.2.2 Thermal Characterizations

Differential scanning calorimetry (DSC) measurements were performed with a Shimatzu DSC-50 system. The spectra were recorded with a heating rate of 10 K/min in the temperature range from 300 to 473 K. Each sample was placed in a platinum cell with an aluminum lid, while an empty platinum cell was used as a reference.

Thermogravimetric analysis (TGA) for thermal degradation and differential thermal analysis (DTA) of our composites were performed using a Setaram Labsys™ TG-DTA16 instrument with a heating rate of 20 K/min from 293 to 873 K. Samples of 31–50 mg were place and sealed in aluminum pans. The instrument was calibrated according to the manufacturer's recommendations.

23.2.3 Dielectric Impedance Measurements

Dielectric measurements were performed in the frequency range from 40 Hz to 2 MHz using an impedance analyzer Agilent 4294A. Isothermal measurements were carried out between 300 and 400 K with a temperature step of 5 K. In order to improve the heat transfer and to homogenize the temperature, the sample holder was maintained in a helium atmosphere during the measurements. Each sample is realistically represented by a parallel combination of a capacitor C_p and a resistance R_p, which permits the calculation of the real (Z') and imaginary (Z'') parts of the complex impedance, $Z^* = Z' - jZ''$, using the following relations:

$$Z'(\omega) = \frac{R_p}{1 + \left(\omega R_p C_p\right)^2} \tag{23.1}$$

$$Z''(\omega) = \frac{\omega C_p {R_p}^2}{1 + \left(\omega R_p C_p\right)^2} \tag{23.2}$$

where ω represents the angular frequency. The estimated relative error of the measurements is 5%.

23.3 Results and Discussion

23.3.1 DSC Spectrum Analysis

Heating DSC thermograms of several samples are shown in Fig. 23.2. A clear endothermic peak is observed at about 360 K and has no significant change with increasing the CB loaded to the EBA copolymer. This peak is attributed to

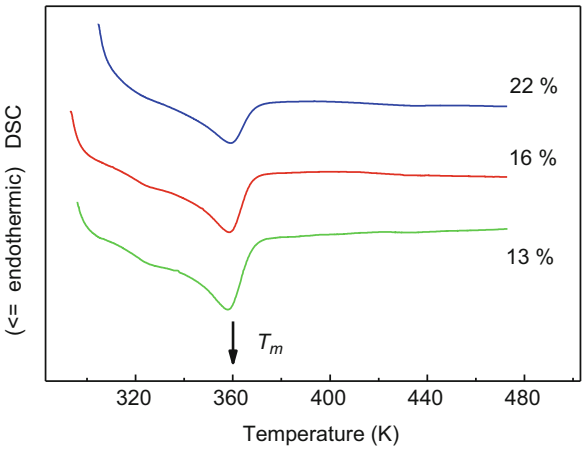

Fig. 23.2 DSC curves of CB/EBA composites. An endothermic peak at about 360 K is attributed to the melting temperature of the composites

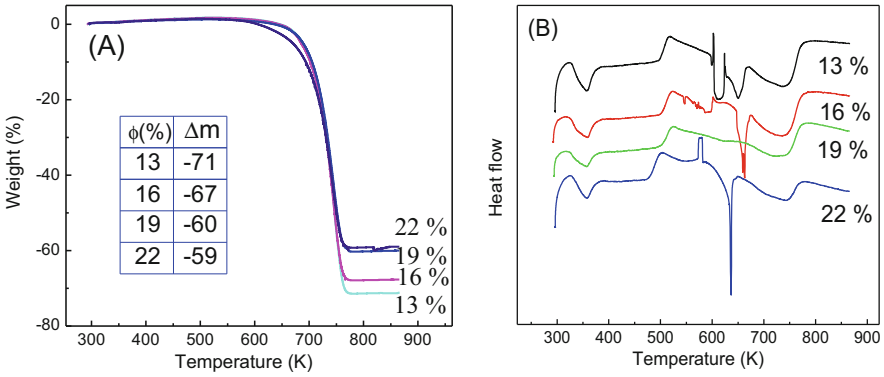

Fig. 23.3 TGA (**A**) and DTA (**B**) curves of CB/EBA composites for different concentrations of CB above the percolation threshold

disordering in the structure associated with the melting temperature T_m. The approximate value was mentioned by Jager et al. [17] who studied the AC conductance and capacitance of the same type of composite during thermal cycling and isothermal annealing.

23.3.2 DTA and TGA Spectra Analyses

The transition phases and thermal degradation were analyzed by DTA and TGA under standard atmosphere. The obtained results are illustrated in Fig. 23.3. In order to analyze the evolution of these curves, we combined in Fig. 23.4 DTA and TGA plots for the case of 16% CB. Examination of these figures yields the following observations: (i) the appearance of first endothermic peak at about 360 K in DTA

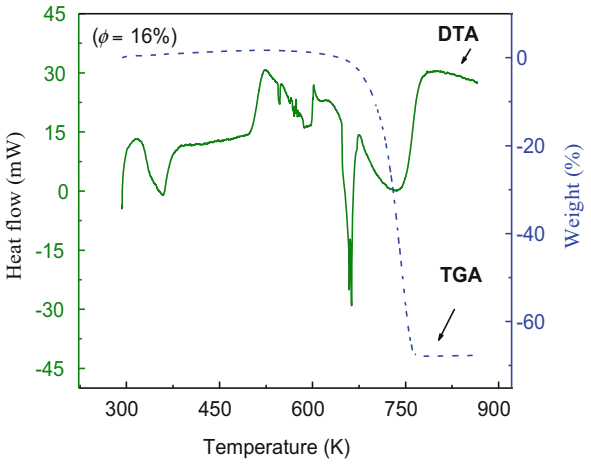

Fig. 23.4 Comparative curves of TGA and DTA of CB/EBA composite with 16% CB

curves which confirm the melting temperature also determined in the DSC spectra; (ii) a second endothermic peak at about 653 K in DTA curves that corresponds to a small decrease in TGA curves attributed to the beginning of composite degradation, and (iii) a third endothermic peak at around 723 K in DTA curves that corresponds to sharp decreases in TGA curves (weight loss), attributed to the degradation temperature of CB/EBA composites. It is interesting to remark that the percentage of residual sample that is stable up to 873 K increases with increasing the CB fraction (Fig. 23.3A). This may arise from the strong particle-matrix interactions at high CB concentrations [19]. Moreover, it indicates that the loading of CB particles into the EBA matrix has improved the thermal stability of the CB/EBA composite [20–22].

23.3.3 Temperature and CB Fraction Effects on the Complex Impedance

The frequency dependence of real Z' and imaginary Z'' parts of the complex impedance of the composites for CB concentration $\phi = 13\%$, is presented in Fig. 23.5. Analysis of this figure yields the following observations: (i) Z'' shows a relaxation peak at a specific frequency F_r and (ii) with increasing the temperature, the value of low frequency impedance, and intensity of relaxation peak increase for $T < T_m$, showing a positive temperature coefficient in resistivity (PTCR) and decrease for $T > T_m$, showing a negative temperature coefficient in resistivity (NTCR). Figure 23.6 presents the Nyquist plot of impedance for the same CB concentration for temperatures below T_m (Fig. 23.6A), and above T_m (Fig. 23.6B). We note that the high frequency impedance is constant with temperature, and the evolution of the obtained curves versus temperature confirms the PTCR and NTCR effects.

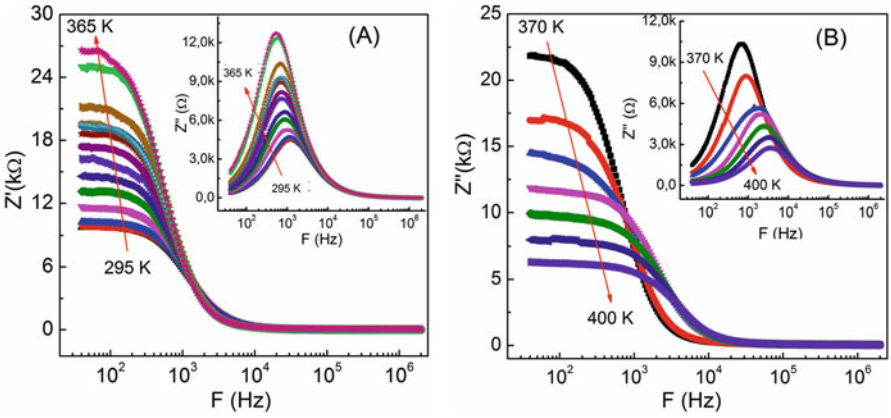

Fig. 23.5 Frequency dependence of the real Z' (**A**) and imaginary Z'' (**B**) parts of the complex impedance ($\phi = 13\%$) for temperatures $T < T_m$ and $T > T_m$

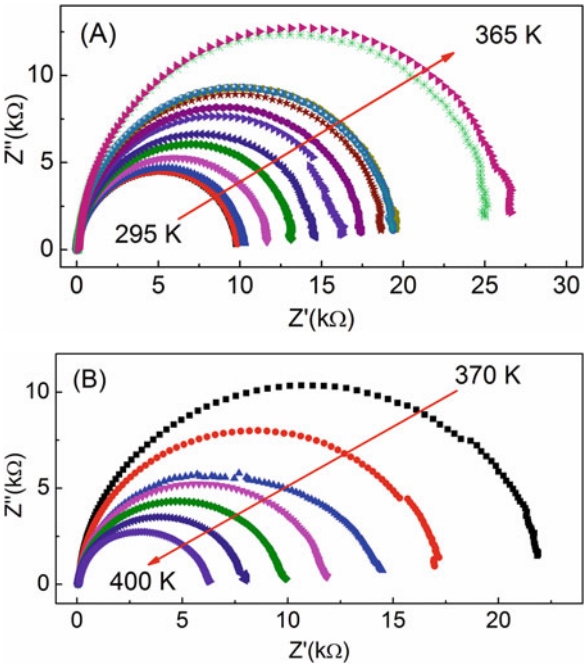

Fig. 23.6 Z'' vs. Z' ($\phi = 13\%$) for temperatures $T < T_m$ (A) and $T > T_m$ (B)

23.3.4 Cole-Cole Modeling

All samples revealed the same behaviour as in the case of 13% CB (Figs. 23.5 and 23.6). The asymmetrical curves of $Z''(\omega)$ (Fig. 23.5) and the arcs in Fig. 23.6, not centred on the Z' axis, indicate that a single relaxation time, as described by the

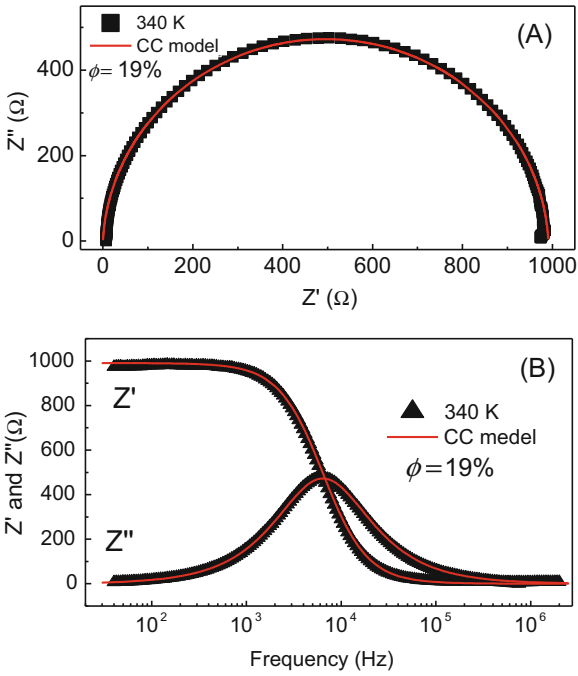

Fig. 23.7 (**A**) Nyquist representation of the complex impedance of CB/EBA ($\phi = 19\%$) at 340 K. The solid line is a fit to the Cole-Cole model, the fit parameters are $\Delta Z = 991\ \Omega$, $\alpha = 0.03$ and $\tau = 2.1\ 10^{-4}$ s. (**B**) Frequency dependence of Z' and Z'' for the same sample

Debye equation [23], is inappropriate to fit the relaxation process, and should be replaced by another model, such as the Cole-Cole function [24] given by:

$$\frac{Z^*(\omega) - Z_\infty}{Z_o - Z_\infty} = \frac{1}{1 + (\ j\omega\tau)^{1-\alpha}} \tag{23.3}$$

where τ is the characteristic relaxation time, Z_∞ and Z_o are the high and low frequency resistances, respectively, and α is a parameter between 0 and 1 that reflects the dipolar interaction. Using the theoretical expressions given in eqs. 4 and 5, we can calculate the relaxation parameters. Figure 23.7 shows an example of Z'' versus Z' and frequency dependence of Z' and Z'' at 340 K ($\phi = 19\%$).

$$\frac{Z'(\omega) - Z_\infty}{Z_o - Z_\infty} = \frac{1 + (\omega\tau)^{1-\alpha} \sin(\alpha\pi/2)}{1 + 2(\omega\tau)^{1-\alpha} \sin(\alpha\pi/2) + (\omega\tau)^{2(1-\alpha)}} \tag{23.4}$$

$$\frac{Z''(\omega)}{Z_o - Z_\infty} = \frac{(\omega\tau)^{1-\alpha} \cos(\alpha\pi/2)}{1 + 2(\omega\tau)^{1-\alpha} \sin(\alpha\pi/2) + (\omega\tau)^{2(1-\alpha)}} \tag{23.5}$$

The analysis of the effect of temperature and CB concentration on the relaxation parameters yields the following results:

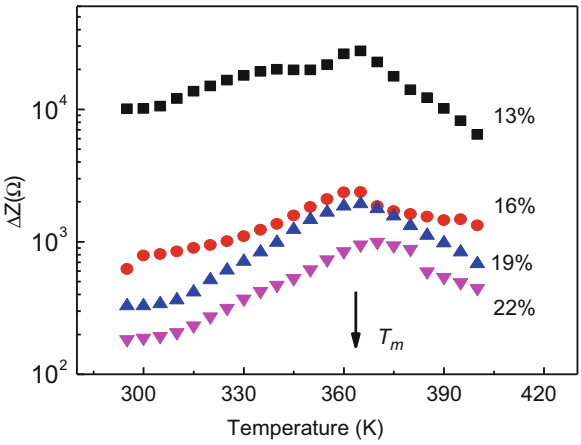

Fig. 23.8 Temperature effect on strength resistance for all concentrations of CB above the percolation threshold

- The values of the parameter α that measures the broadening of Z'', are between 0.03 and 0.17, suggesting that the behavior is close to a single relaxation time. These results are in complete accordance with those of Belattar and co-workers [25] who reported a study of the electrical modulus of the same composites.
- The strength in resistance, $\Delta Z = Z_o - Z_\infty$, increases with the temperature below the melting point and decreases above of this point (Fig. 23.8), confirming the PTCR and NTCR effects already shown by Ding and co-workers [26]. An explanation based on the tunneling effect was broadly accepted to evaluate the electrical transport mechanism. The crystallites began to melt when the temperature reaches the melting point of EBA, leading to the formation of new amorphous zones. The gaps between the CB particles in the EBA matrix increase significantly due to the thermal expansion [17, 18]. The appearance of NTCR effect above the melting temperature is related to the reagglomeration of the CB fillers in the high temperature range that leads to the formation of a new conductive CB network, thus decreasing ΔZ.
- The relaxation time strongly depends on the temperature for all CB concentrations. For the temperatures above the melting point ($T > T_m$), it increases with the temperature, which allows to calculate the activation energy W_a using the Arrhenius equation expressed by:

$$\tau(T) = \tau_o \exp\left(\frac{W_a}{k_b T}\right) \tag{23.6}$$

where τ_o is a pre-exponential factor, k_b the Boltzmann constant. Figure 23.9 depicts the plots of $ln(\tau)$ vs. 1000/T along with a linear fit to the above equation. The values of W_a and the pre-exponential factor with their correlation coefficients were calculated and given in Table 23.1. As shown, the values of the activation energy decreased from 0.69 eV for $\phi = 13\%$ to 0.21 eV for $\phi = 22\%$. The obtained W_a

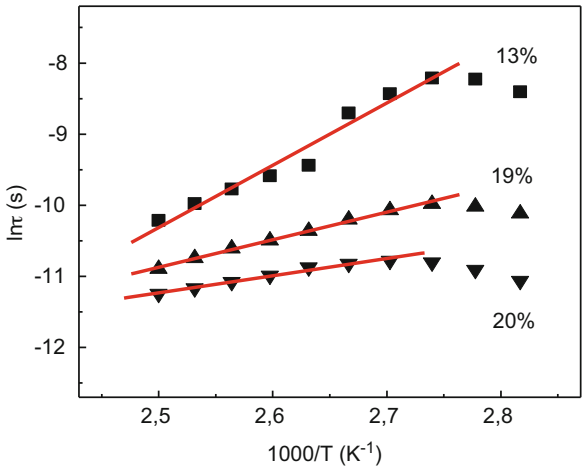

Fig. 23.9 Arrhenius representation of the relaxation time. The solid lines represent the best linear fits

Table 23.1 Values of the activation energy and the Arrhenius pre-exponential factor related to the relaxation processes for the impedance spectra, as well as their correlation coefficient R_{co}

ϕ (%)	W_a (eV)	ln(τ_o) s	R_{co}
13	0.69	−32	0.95
19	0.33	−20	0.99
22	0.21	−17	0.98

and Arrhenius pre-exponential factor τ_o decrease with increasing the CB concentration, reflecting the fact that the relaxation mechanism does not result simply from thermally activated dipolar interactions but it is a collective cooperative effect of the CB mesostructure.

23.4 Conclusion

Summarizing, we have studied thermal transitions and dielectric relaxation in CB loaded EBA copolymer composites. Melting transition and thermal degradation were identified by DSC and TGA spectra, respectively, and confirmed by DTA measurements. It was found that the melting temperature does not depend on the CB fraction. However, the degradation rate depends on it. The complex impedance spectra were used to interpret the relaxation processes for CB concentrations above the percolation threshold. The Cole-Cole model fits correctly the experimental data, the relaxation parameters showed that our case is close to the Debye relaxation model. The calculated activation energy and Arrhenius pre-exponential factor were found to be dependent on the CB concentration, indicating that for temperatures above the melting point, the relaxation mechanism does not result simply from

thermally activated dipolar interactions but it is a collective cooperative effect of the CB mesostructure.

Acknowledgments The authors are grateful to Prof. F. Carmona (Paul Pascal Research Centre – CNRS, University of Bordeaux I, France) for supplying the composite materials and Prof. M. Mansori (Faculty of Sciences and Technics, Cadi Ayyad University, Morocco) for realizing the thermal measurements. This work is partially supported by the Morocco-Portugal cooperation program (No. Physique/04/08/09).

References

1. Bauhofer W, Kovacs JZ (2009) A review and analysis of electrical percolation in carbon nanotube polymer composites. Combust Sci Technol 69:1486
2. Mamounya YP (1999) Morphology and percolation conductivity of polymer blends containing carbon black. J Macromol Sci B 38:615
3. Costa LC, Valente M, Sá F, Henry A (2006) Electrical and magnetic properties of polystyrene doped with iron nanoparticles. Polym Bull 57:881
4. Abazine K, Anakiou H, El Hasnaoui M, Graça MPF, Fonseca MA, Costa LC, Achour ME, Oueriagli A (2016) Electrical conductivity of multiwalled carbon nanotubes/polyester polymer nanocomposites. J Compos Mater 50:3283
5. Aribou N, Nioua Y, Bouknaitir I, El Hasnaoui M, Achour ME, Costa LC (2019) Prediction of filler/matrix interphase effects on AC and DC electrical properties of carbon reinforced polymer composites. Polym Compos 40:346
6. Deepa KS, Kumari Nisha S, Parameswaran P, Sebastian MT, James J (2009) Effect of conductivity of filler on the percolation threshold of composites. Appl Phys Lett 94:142902
7. Stauffer D, Aharony A (eds) (1992) Introduction to percolation theory. Taylor and Francis, London
8. Gefen Y, Aharony A, Alexander S (1983) Anomalous diffusion on percolation clusters. Phys Rev Lett 50:77
9. El Hasnaoui M, Triki A, Graça MPF, Achour ME, Costa LC, Arous M (2012) Electrical conductivity studies on carbon black loaded ethylene butylacrylate polymer composites. J Non-Cryst Solids 358:2810
10. El Hasnaoui M, Graça MPF, Achour ME, Costa LC, Lahjomri F, Outzourhit A, Oueriagli A (2011) Electrical properties of CB/ copolymer composites above and below the melting temperature. J Mater Environ Sci 2:1
11. El Hasnaoui M, Graça MPF, Achour ME, Costa LC, Outzourhit A, Oueriagli A, El Harfi A (2010) Effect of temperature on the electrical properties of copolymer/carbon black mixtures. J Non-Cryst Solids 356:1536
12. Kremer F, Schonhals A (2004) Broadband dielectric measurement techniques (10^{-6} Hz to 10^{12} Hz). In: Kremer F, Schonhals A (eds) Broadband dielectric spectroscopy. Springer, Berlin, p 35
13. Mdarhri A, Brosseau C, Zaghrioui M, El Aboudi I (2012) Electronic conduction and microstructure in polymer composites filled with carbonaceous particles. J Appl Phys 112:034118
14. Houang JC (2002) Carbon black filled conducting polymers and polymer blends. Adv Polym Technol 2:299
15. Brosseau C, Boulic F, Queffelec P, Bourbigot P, Le Mest Y, Loaec J (1997) Dielectric and microstructure properties of polymer carbon black composites. J Appl Phys 81:882
16. Boulic F, Brosseau C, Le Mest Y, Loaec J, Carmona F (1998) Absorbency properties and electron paramagnetic resonance characterization of polymeric carbon black composites. J Phys D Appl Phys 31:1904

17. Jager KM, McQueen DH, Vilcakova J (2002) Ac conductance and capacitance of carbon black polymer composites during thermal cycling and isothermal annealing. J Phys D 35:1068
18. Leblanc JL, Jager KM (2006) Investigating nonlinear viscoelastic properties of molten carbon black/poly(ethylene-co-butyl acrylate) composites, using fourier transform rheometry and other test techniques. J Appl Polym Sci 101:4071
19. Saleem A, Frormann L, Iqbal A (2007) Mechanical, thermal and electrical resistivity properties of thermoplastic composites filled with carbon fibers and carbon particles. J Polym Res 14:121
20. Omastova M, Podhradska S, Prokes J, Janigova I (2003) Thermal ageing of conducting polymeric composites. J Stejskal Polym Degrad Stab 82:251
21. Zhang J, Feng S, Ma Q (2003) Kinetics of the thermal degradation and thermal stability of conductive silicone rubber filled with conductive carbon black. J Appl Polym Sci 89:1548
22. Long D, Lequeux F (2001) Heterogeneous dynamics at the glass transition in van der Waals liquids, in the bulk and in thin films. Eur Phys J E 4:371
23. Debye P (ed) (1945) Polar molecules. Dover, New York
24. Cole KS, Cole RH (1941) Dispersion and absorption in dielectrics I. alternating current characteristics. J Chem Phys 9:341
25. Belattar J, Graça MPF, Costa LC, Achour ME, Brosseau C (2010) Electric modulus-based analysis of the dielectric relaxation in carbon black loaded polymer composites. J Appl Phys 107:124111
26. Ding X, Wand J, Zhang S, Wang J, Li S (2016) Carbon black-filled polypropylene as a positive temperature coefficient material: effect of filler treatment and heat treatment. Polym Bull 73 (2):369

Chapter 24
Novel Photocross-Linked Polymers for Construction of Laccase-Based Amperometric Biosensors

Taras Kavetskyy, Khrystyna Zubrytska, Oleh Smutok, Olha Demkiv, Helena Švajdlenková, Ondrej Šauša, Sigita Kasetaite, Jolita Ostrauskaite, and Mykhailo Gonchar

Abstract The procedure of enzyme immobilization in biosensorics has a purpose to induce maximal activity of biological element with sufficient stability and reusability of the bioelectrodes. The entrapment of the biomaterial with a porous solid matrix looks most promising in this respect due to minimal alteration of enzyme structure and behavior. On the other hand, the method needs pore-size control to reduce the diffusional limitation of the substrate to the enzyme. We propose the use of photocross-linked polymers consisted of epoxidized linseed oil (ELO) as a matrix for immobilization of fungal laccase. The network properties of the polymer matrixes, holding the biosensing element, were studied by positron annihilation lifetime spectroscopy measurements. The correlation between the operational

T. Kavetskyy (✉)
Drohobych Ivan Franko State Pedagogical University, Drohobych, Ukraine

The John Paul II Catholic University of Lublin, Lublin, Poland

Joint Ukraine-Azerbaijan International Research and Education Center of Nanobiotechnology and Functional Nanosystems, Drohobych, Ukraine

K. Zubrytska
Drohobych Ivan Franko State Pedagogical University, Drohobych, Ukraine

O. Smutok
Drohobych Ivan Franko State Pedagogical University, Drohobych, Ukraine

Institute of Cell Biology, National Academy of Sciences of Ukraine, Lviv, Ukraine

O. Demkiv · M. Gonchar
Institute of Cell Biology, National Academy of Sciences of Ukraine, Lviv, Ukraine

H. Švajdlenková
Polymer Institute, Slovak Academy of Sciences, Bratislava, Slovak Republic

O. Šauša
Institute of Physics, Slovak Academy of Sciences, Bratislava, Slovak Republic

S. Kasetaite · J. Ostrauskaite
Kaunas University of Technology, Kaunas, Lithuania

P. Petkov et al. (eds.), *Nanoscience and Nanotechnology in Security and Protection against CBRN Threats*, NATO Science for Peace and Security Series B: Physics and Biophysics, https://doi.org/10.1007/978-94-024-2018-0_24

parameters of the constructed biosensor and the microscopical free volume of the holding photocross-linking matrixes was established.

Keywords Photocross-linking · Positron annihilation · Laccase · Amperometric biosensor

24.1 Introduction

The development of new approaches for monitoring of dangerous substances in the environment is a topical nowadays problem to improve human life quality. During the past two decades bioelectrochemistry has received increased attention. In this respect, the laccase-based biosensors look the most promising approaches due the effective biocatalysis of the enzyme without the requirement of hydrogen peroxide as a co-substrate or any other cofactors. This results in a simple procedure for their application for the quantitative determination of toxic phenolic compounds, asides, pesticides, etc. in groundwater or in technogenic wastewaters [1, 2]. One of the most important problems of the existing biosensor technologies is the formation of a biorecognition membrane on the physical transducer which contains immobilized bioelements, in particular enzymes. A large number of laccase-based biosensors are described using various methods for immobilization of the enzyme: covalent binding, adsorption, cross-linking and entrapment in the gel [3]. By the entrapment of the biomaterial into a porous solid matrix, the enzyme suffers minimum alteration and this immobilization approach looks the most promising in sensor technologies. The method needs pore-size control to reduce the diffusional limitation of the substrate to the enzyme. For laccase-based bioelectrodes, it has been demonstrated that the immobilization of the enzyme has an important effect on the sensitivity of the biosensor [4]. Recently, it was additionally approved using organic-inorganic ureasil-based composites as host polymer matrix for laccase immobilization on the surface of different transducers (carbon-rod and gold planar electrodes) [5, 6]. It was shown that the biosensor constructed with ureasil-chalcogenide glass composite exhibited extremely high sensitivity of 67,540 $A \cdot M^{-1} \cdot m^{-2}$ [5]. Thus, the screening of new suitable matrixes for effective laccase immobilization is a crucial part in the construction of improved laccase-based amperometric biosensors.

In the present study, we report the construction and the results from the characterization of a biosensor based on laccase and two photocross-linked polymers (ELO/10RD and ELO/30RD) as holding matrixes. The network properties of the polymer matrixes were studied by positron annihilation lifetime spectroscopy (PALS) measurements. The enzyme biosensor parameters were evaluated using cyclic voltamperometric and chronoamperometric analysis. A correlation between the operational parameters of the constructed biosensor and the hole volume of the holding matrixes was established. This finding demonstrates a way to control the functionality of amperometric enzyme biosensor using the knowledge about the microstructure of the holding polymer matrix.

24.2 Experimental

The photocross-linked polymers ELO/RD were synthesized by the reaction of ELO (epoxidized linseed oil, having an average number of six epoxy groups per molecule) and RD (bisphenol A diglycidyl ether), using PI (50% mixture of triarylsulfonium hexafluorophosphate in propylene carbonate) as photoinitiator [7]. The measurements of positron and positronium lifetime with a PALS spectrometer with time resolution FWHM of ~220–320 ps cover the time range from 1 up to 142 ns. From the lifetimes the free-volume pore sizes [8, 9] as well as their thermal expansion characteristics were determined. The spherical void size R was determined from the *ortho*-positronium (*o*-Ps) lifetime in a simple approach by an semi-empirical relation Eq. (24.1), where $\Delta R = 0.166$ nm is the empirical constant [9]:

$$\tau_{\text{o-Ps}} = 0.5 \times [1 - R/(R + \Delta R) + (1/2\pi) \times \sin(2\pi R/(R + \Delta R))]^{-1} \quad (24.1)$$

The corresponding hole volume V_h is given by the equation:

$$V_h = 4/3(\pi R^3) \quad (24.2)$$

Important characteristics such as the glass transition temperatures T_g (or temperatures of crystallization in some cases) and the coefficients of thermal expansion for the free-volume holes, $\alpha_F = 1/V_h(T_g^{PALS})(\Delta V_h/\Delta T)$ below (α_{F1}) and above (α_{F2}) T_g were revealed from $V_h(T)$ dependences.

Amperometric biosensors were evaluated using constant-potential amperometry in a three-electrode configuration with an Ag/AgCl/KCl (3 M) reference electrode, a Pt-wire counter electrode and a graphite rod (type RW001, 3.05 mm diameter, Ringsdorff Werke, Bonn, Germany) a working electrode. Amperometric measurements were carried out with a potentiostat CHI 1200A (IJ Cambria Scientific, Burry Port, UK) connected to a personal computer and performed in a batch mode under continuous stirring in a standard 40 ml electrochemical cell at room temperature. The laccase immobilization included the following stages: (1) dropping of 5 μl of laccase solution (1 mg·ml^{-1} with an activity 13 U·mg^{-1}) on the working electrode surface and drying for 5 min at 15 °C; (2) covering the dried enzyme by 0.3 mm thick layer of photocross-linked polymer ELO/10RD or ELO/30RD; and (3) fixation of the formed enzyme-polymer matrix by net cap using plastic "O"-ring. The formed bioelectrode was washed by 50 mM acetic buffer, pH 4.5 and stored at 8 °C till usage.

24.3 Results and Discussion

Annihilation of a positron is a very sensitive tool for the examination of local regions with low electron density, local free-volumes, i.e. intermolecular spaces, voids or pores with different size. In the organic materials a bound state of positron-electron, positronium (Ps), can be created. This atomic probe in triplet spin state (*ortho*-Positronium) annihilates in vacuum with characteristic lifetime of 142 ns. The typical annihilation of *o*-Ps in organic materials is the pick-off process at which e^+ from *o*-Ps annihilates with e^- from the void surface which results in a reduced lifetime $\tau_{o\text{-Ps}}$ compared to the vacuum value. The value of that reduced lifetime depends on the hole size. The advantage of this technique – positron annihilation lifetime spectroscopy – is the relatively simple arrangement, the ability to measure the lifetime under different external conditions (temperature, pressure, etc.) and the sensitivity of the lifetime to the microstructural free-volume size. Thus, lifetime measurements provide important information about the local free volume and the arrangement of the polymeric structure on the range of 0.2–50 nm [10]. For a simple explanation, we can define total specific volume V as a sum of the specific (by atoms) occupied volume V_{occ} and the specific free volume V_f. This specific free volume can be presented as $V_f = V_h N_h$, where V_h the hole volume (local free volume) determined by PALS and N_h is the number of free-volume holes per unit mass. The hole volumes of the photocross-linked polymers ELO/10RD and ELO/30RD in heating and cooling cycles are shown in Fig. 24.1.

A significant difference in $V_h(T)$ dependences between the temperature cycles of heating and cooling for both samples, especially for polymer ELO/10RD, was observed. The temperature at which the free-volume (*o*-Ps lifetime) changes its slope is assigned as glass transition temperature T_g. The determination of the glass transition temperature T_g is complicated due to the different points, where the slopes of $V_h(T)$ dependences change by different cycles. The value of T_g is about 230 K for both samples. If we suppose a "relaxed structure" with lower V_h values by slow

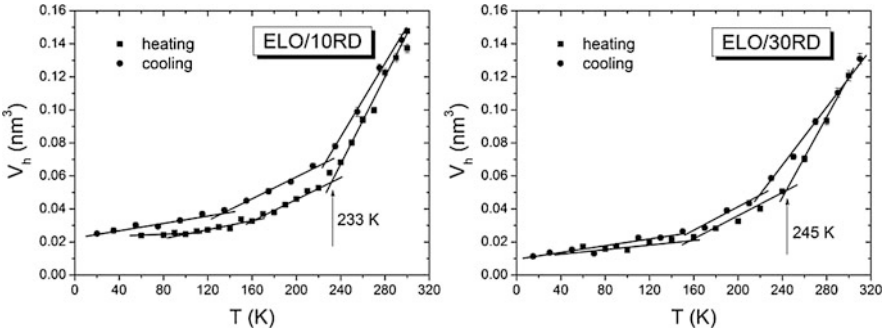

Fig. 24.1 Hole volume of the photocross-linked polymers ELO/10RD (left) and ELO/30RD (right) in heating and cooling cycles. Adapted from [7]

Table 24.1 Hole volume V_h at T_g, swellability S in EtOH, and slopes α_{F1}, α_{F2} of the $V_h(T)$ dependences in the regions below and above T_g, respectively, as well as their differences (values for heating and cooling cycles are in top and bottom parts of the boxes, respectively) [7]

Polymers	V_h (nm^3)	T_g (K)	S (%)	α_{F1} (10^{-4} K^{-1})	α_{F2} (10^{-4} K^{-1})	$\alpha_{F2} - \alpha_{F1}$ (10^{-4} K^{-1})
ELO/ 10RD	0.057 ± 0.002 0.068 ± 0.002	233	24.09	3.53 ± 0.30 3.31 ± 0.32	13.02 ± 0.60 11.16 ± 0.55	9.49 ± 0.67 7.85 ± 0.64
ELO/ 30RD	0.051 ± 0.002 0.049 ± 0.002	245	24.81	3.47 ± 0.33 3.87 ± 0.83	12.42 ± 0.64 8.96 ± 0.48	8.95 ± 0.72 5.09 ± 0.96

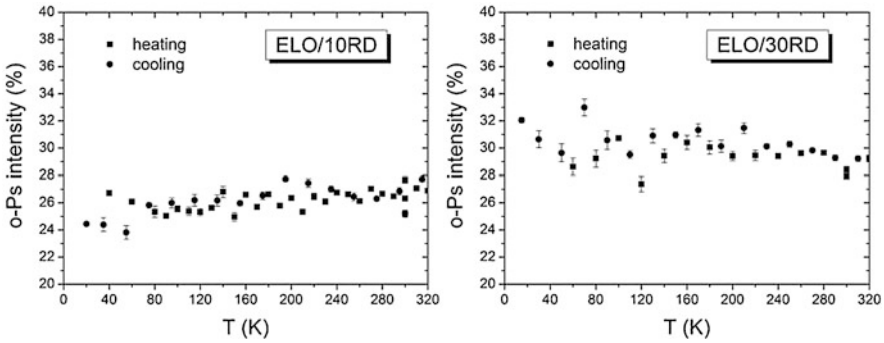

Fig. 24.2 *o*-Ps intensity temperature dependences for the polymers ELO/10RD (left) and ELO/30RD (right) in the heating and cooling cycles. Adapted from [7]

heating cycles, then T_g should be 233 K and 245 K for the polymers ELO/10RD and ELO/30RD, respectively (Fig. 24.1, Table 24.1).

Figure 24.2 shows the *o*-Ps relative intensities for the investigated samples as a function of the temperature in the range of 15–350 K. Assuming that this quantity is related only to the concentration of free-volume holes in the material, the polymer ELO/10RD has lower hole concentration compared to ELO/30RD. Any changes in hole volume depend on the cooling or heating rate. After heating to room temperature, the hole volume is reproduced.

It can be noted that the average sizes of the free-volume holes in the polymer ELO/10RD are larger than that of ELO/30RD. Lifetime measurements showed the reproducible lifetime values at room temperature after heating over T_g. Values of V_h in the third heating cycle (after first heating and second cooling runs) are very similar to the first heating cycle. These facts indicate the chemical network stability during the PALS measurements.

For the immobilization of laccase, 0.3 mm thick layer of photopolymer ELO/10RD or ELO/30RD was held on the laccase-adsorbed surface of the graphite-rod electrode by means of "O"-ring fixed net cap [7]. The principle of biosensor detection of ABTS as a typical substrate for laccase is based on the reduction of intermediary oxidation product of the monoradical ($ABTS^{+}\cdot$) or biradical ($ABTS^{(2+)}$), resulting in the generation of redox current (Fig. 24.3, left).

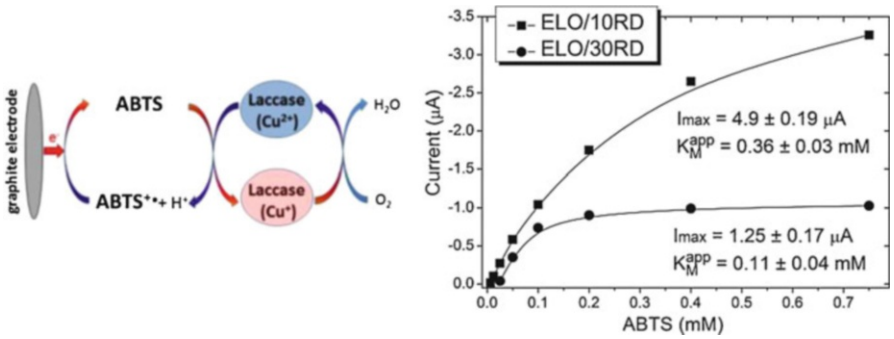

Fig. 24.3 The principal scheme of electron transfer in the biorecognition layer of laccase-based biosensor using ABTS as analyte (left). Calibration curves of the responses to increasing concentrations of ABTS for the bioelectrodes based on the photocross-linked matrixes (right). Adapted from [7]

Cyclic voltamperometric analysis was applied for estimation of the optimal working potential of this process, which corresponds to −100 mV *vs* Ag/AgCl (*data not shown*). The bioelectrodes constructed by ELO/10RD or ELO/30RD demonstrated a difference in their operational properties (Fig. 24.3, right). The bioelectrode based on ELO/10RD showed a fourfold higher maximal current at substrate saturation (I_{max}) versus the bioelectrode based on ELO/30RD (4.9 μA *vs* 1.25 μA, respectively). The ELO/10RD-based bioelectrode exhibited a threefold higher apparent Michaelis-Menten constant (K_M^{app}) [11] than ABTS as a substrate (0.36 *vs* 0.11 mM of ABTS). It is known from literature that the K_M value of ABTS for laccase from *Trametes versicolor* in solution is 0.29 mM [12].

Thus, the obtained K_M^{app} values for the constructed bioelectrodes in the range between 0.11 and 0.36 mM indicate a native configuration of laccase in the photopolymeric matrixes. The sensitivity of the bioelectrodes was calculated using the slope of the calibration curve *B* in the linear part and the area of the electrode used (7.3 mm^2). The sensitivity of the ELO/10RD-based bioelectrode was 1.3-fold higher compared to the ELO/30RD-based one: 1.673 $A \cdot M^{-1} \cdot m^{-2}$ *vs* 1.234 $A \cdot M^{-1} \cdot m^{-2}$, respectively. On the other hand, the linear part of the calibration curve of the ELO/10RD-based bioelectrode was 1.5-fold wider compared to ELO/30RD-based one (from 0.006 to 0.15 mM *vs* 0.025–0.1 mM toward ABTS). The wider linear parts and the higher sensitivity of the bioelectrodes based on ELO/10RD make them more perspective for the analysis of real samples of wastewater due to outhitting the dilution step.

According to the comparative analysis of the biosensor's operational parameters, it is seen that the laccase-based amperometric biosensor constructed using holding polymer ELO/10RD matrix has better sensitivity characteristics as well as extended range of linearity to ABTS, than that constructed using holding polymer ELO/30RD matrix.

24.4 Conclusion

Summarizing the obtained PALS-results for two photocross-linked polymer samples, it may be concluded that ELO/10RD has compared to the ELO/30RD: (i) the higher crosslink density, (ii) the larger free-volume holes, (iii) the lower concentration of free-volume holes, and (iv) the larger difference in the coefficients of thermal expansion of free-volume holes in the regions below and above T_g. At the same time, the laccase-based amperometric biosensor constructed using the polymer ELO/10RD as a biosensor holding matrix shows improved biosensor parameters compared to ELO/30RD. It seems that the microstructural network properties of the polymer holding matrix are crucial for the determination of the biofunctionality of the constructed amperometric biosensors.

Acknowledgments This work was supported in part by the Ministry of Education and Science of Ukraine (projects Nos. 0117U007142, 0118U000297, and 0119U100671), National Academy of Sciences of Ukraine in the frame of the Scientific-Technical Program "Smart sensor devices of a new generation based on modern materials and technologies" (project No. 13), Slovak Grant Agency VEGA (project No. 2/0157/17) and Slovak Research and Development Agency (project No. APVV-16-0369).

References

1. Majid D, Gholamreza B, Amir A, Seyed J (2017) Biotechnological and industrial applications of laccase: a review. J Appl Biotechnol Rep 4:675
2. Kavetskyy T, Smutok O, Demkiv O, Matko I, Svajdlenkova H, Sausa O, Novak I, Berek D, Cechova K, Pecz M, Nykolaishyn-Dytso O, Wojnarowska-Nowak R, Broda D, Gonchar M, Zgardzinska B (2020) Microporous carbon fibers as electroconductive immobilization matrixes: effect of their structure on operational parameters of laccase-based amperometric biosensor. Mater Sci Eng C 109:110570
3. Fernandez-Fernandez M, Sanroman M, Moldes D (2013) Recent developments and applications of immobilized laccase. Biotechnol Adv 31:1808
4. Freire RS, Duran N, Kubota LT (2015) Effects of fungal laccase immobilization procedures for the development of a biosensor for phenol compounds. Talanta 54:681
5. Kavetskyy T, Smutok O, Gonchar M, Demkiv O, Klepach H, Kukhazh Y, Sausa O, Petkova T, Boev V, Ilcheva V, Petkov P, Stepanov AL (2017) Laccase-containing ureasil-polymer composite as the sensing layer of an amperometric biosensor. J Appl Polym Sci 134:45278
6. Kavetskyy T, Stasyuk N, Smutok O, Demkiv O, Kukhazh Y, Hoivanovych N, Boev V, Ilcheva V, Petkova T, Gonchar M (2019) Improvement of amperometric laccase biosensor using enzyme-immobilized gold nanoparticles coupling with ureasil polymer as a host matrix. Gold Bull 52:79
7. Kavetskyy T, Smutok O, Demkiv O, Kasetaite S, Ostrauskaite J, Svajdlenkova H, Sausa O, Zubrytska K, Hoivanovych N, Gonchar M (2019) Dependence of operational parameters of laccase-based biosensors on structure of photocross-linked polymers as holding matrixes. Eur Polym J 115:391
8. Tao S (1972) Positronium annihilation in molecular substances. J Chem Phys 56:5499
9. Eldrup M, Lightbody D, Sherwood J (1981) The temperature dependence of positron lifetimes in solid pivalic acid. Chem Phys 63:51

10. Svajdlenkova H, Sausa O, Matko I, Koch T, Gorsche C (2018) Investigating the free-volume characteristics of regulated dimethacrylate networks below and above glass transition temperature. Macromol Chem Phys:1800119
11. Sundaram P (1978) An analysis and interpretation of the Michaelis-Menten kinetics of immobilized enzymes perturbed by film diffusion. J Solid-Phase Biochem 3:241
12. Mishra A, Kumar S (2009) Kinetic studies of laccase enzyme of Coriolus versicolor MTCC 138 in an inexpensive culture medium. Biochem Eng J 46:252

Part IX
Oxide and Non-oxide Glasses

Chapter 25
Surface Phenomena in Glassy Chalcogenides by Gas Sensing

Dumitru Tsiulyanu, Marina Ciobanu, and Olga Mocreac

Abstract The surface phenomena in glassy chalcogenides (GCh), including those caused by gas adsorption, are reviewed and discussed. A detailed quantitative analysis is made on experimental data taken on glassy and nanocrystalline chalcogenide based thin films of $As_2S_3Ge_8$ – Te system, physically grown in vacuum. Particularly the measurements of the frequency dependence of the AC conductivity of these films in the frequency range 5 Hz–13 MHz are reported, in both dry air and its mixture with a controlled concentration of different gases. The behavior of AC conductivity fits the generally accepted model of charge transport in disordered materials that implies both the extended states above mobility edges and the localized states in the gap, but the variation of the environmental conditions by applying of even very small amount (ppm) of toxic gases, dramatically influences the AC conductivity spectra. This is evidence that for some chalcogenide materials the surface phenomena disturb the energetic distribution of the states adjacent to the surface leading to modifications of the transport mechanisms by the surface. The modification of the surface transport mechanism by adsorption of gas species alters the physical parameters of the surface, i.e. the work function, the diffusion and the dipolar potential, the screening length, etc., which lead to variation of both surface and total electrical conductivity, impedance and its spectral distribution, as well as of electric capacity of functional structures based on these materials. The examples are given of the development of room temperature operating functional structures designed to detect nitrogen dioxide and hydrogen sulfide in dry and humid media via variation of their impedance or capacitance.

Keywords Surface phenomena · Chalcogenide films · Gas sensors

D. Tsiulyanu (✉) · M. Ciobanu · O. Mocreac
Department of Physics, Technical University, Chisinau, Moldova

P. Petkov et al. (eds.), *Nanoscience and Nanotechnology in Security and Protection against CBRN Threats*, NATO Science for Peace and Security Series B: Physics and Biophysics, https://doi.org/10.1007/978-94-024-2018-0_25

25.1 Introduction

The influence of the surface of the glassy calcogenides on their physical properties has been observed at the early stage of investigation of these materials. Firstly, the effect of surface was exanimated for the glassy As_2Se_3 via studying the kinetics and spectral distribution of surface photoconductivity under the conditions of mechanical and chemical treatment of the bulk samples [1, 2]. The impact of the surface conditions was shown to be impressive: The surface photoconductivity increases as the quality of the surface improves, moving from samples with abrasive surfaces to those treated chemically, and further to those with polished surface. Later attempts were made to clarify the influence of gas adsorption on the electrophysical properties of this calcogenide glass by applying water vapor, ammonia, carbon oxide or carbon dioxide, as well as molecular oxygen [3]. It has been found that both surface conductivity and photoconductivity exhibit some sensitivity to gases, especially to H_2O and NH_3 vapors. On the other hand, it was pointed out that the variation of the electrophysical parameters of the As_2Se_3 samples with the polished surfaces is insignificant under application of any of the mentioned gases. The real interest in the surface phenomena in structures based on glassy or nanostructured calcogenides has appeared after publications dedicated to the process of detection of propylamine ($C_3H_7NH_2$) and nitrogen dioxide with films of artificial dimorphite (As_4S_3) and Te [4–6]. Later, gas sensitive films based on different compositions in binary, ternary and quaternary chalcogenide systems have been reported [7–10], along with a number of extensive reviews on fundamental and applicative aspects of the interaction of gases with chalcogenide materials, including the elemental tellurium [11, 12]. From the mentioned publications it turns out that the sensitization of the surface phenomena, that is their influence on the electrophysical parameters of the materials in question, increases dramatically with the increase of the spatial (and possibly the compositional) disorder of the surface. Although the study of the surface phenomena in either glassy or nanocrystalline chalcogenides is still at the early stage, such behavior can be explained in terms of interaction between the lone pair electrons of the chalcogen atoms and their “dangling” bonds at the surface, as namely at the surface the maximum concentration of dangling bonds (unshared electrons) occurs. This interaction means the capture of electrons from the valence band, which results in formation of region adjacent to the surface enriched (accumulation) in holes, so that the bands bend up [13]. Consequently one reason for the surface phenomena in chalcogenide materials, caused by gas adsorption, can be the formation of new surface states, i.e. the donor or acceptor like levels, which control the band – bending at the surface, owing to variation of the hole density in the accumulation region. Another reason can be the variation of the hole mobility in the accumulation (surface) region in the presence of gaseous media as a result of a possible modification of the charge transport mechanism. As the last effect must be essential in the case of AC conductivity, the present work is conducted to analyze the surface processes in chalcogenide thin films by gas adsorption, considering their AC

conductivity in large frequency and temperature ranges, along with the fabrication and characterization of AC operating gas sensitive devices based on such films.

25.2 Materials, Morphology and Structure of the Films

The study was performed using two materials: pure (99.99%) tellurium and quaternary alloy $As_2Te_{13}Ge_8S_3$. The latter has been prepared by melt-quenching method of pure (99.99%) As, S, Te and Ge in quarts ampoules evacuated to 5 10^{-5} Torr. The melting was performed at 900 °C. The ampoules were rotated around the longitudinal axis at velocity of 7–8 rotations/min and were agitated for homogenization during the synthesis time (24 h), then they were quenched on a copper refrigerator with running water. The chalcogenide thin films based on these materials have been prepared by their thermal evaporation from a tantalum boat onto ceramic Al_2O_3, at a working pressure of 10^{-4} Pa. The substrates contained the previously deposited platinum interdigital electrodes with an electrode width of 15 μm and interelectrode distances of 45 μm. The growth velocity of the films was in the order of 30 nm/s, the area of deposition was around 5 mm^2. The thickness of the films was about 60 nm, being determined using a microinterferometer MII – 4. Structural investigations of the grown films were carried out by scanning electron microscopy (SEM) and X –ray analyses. The surface morphology of the films was revealed with a VEGA TESCAN TS 5130 MM scanning electron microscope at an acceleration voltage of 30 kV, whereas X-ray analyses using a DRON –YM1 diffractometer with FeK $_\alpha$ radiation was applied for phase-structural investigations. The rotation velocity of the scintillation counter was 2 (or 4) degrees/min. Figure 25.1 shows SEM images of the guaternary $As_2Te_{13}Ge_8S_3$ and elemental Te films, grown on sintered alumina substrates, using deposition rate of 30 nm/s. As can be seen, the films consist of agglomerated islands, resulting in great surface roughness. In all cases no crystallites are observed.

Figure 25.2 shows XRD patterns of quaternary $As_2Te_{13}Ge_8S_3$ and pure Te films deposited on alumina substrates. No peaks of crystalline Te are observed in the $As_2Te_{13}Ge_8S_3$ films (Fig. 25.2a) that is an evidence of their vitreous state.

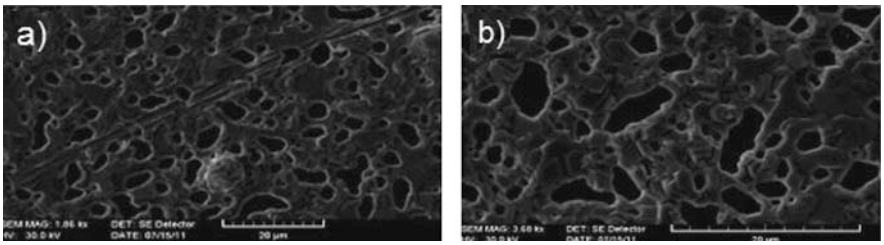

Fig. 25.1 SEM images of (**a**) $As_2Te_{13}Ge_8S_3$ and (**b**) pure tellurium thin films grown on sintered alumina (Al_2O_3) substrates

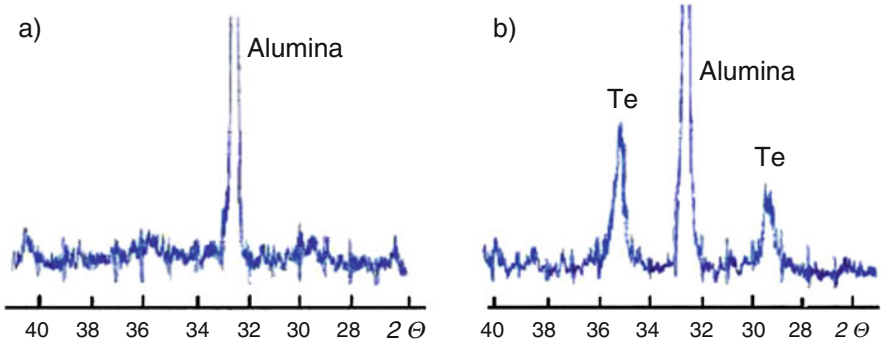

Fig. 25.2 XRD diffraction patterns of (**a**) $As_2Te_{13}Ge_8S_3$ and (**b**) pure tellurium thin films grown on sintered alumina substrates

On the other hand, the pure Te films (Fig. 25.2b) exhibit very small peaks corresponding to crystalline phases of Te, indicating their nearly amorphous nature. No peaks corresponding to oxides of tellurium are visible in the XRD patterns. These results are in agreement with the SEM observations.

25.3 Experimental Procedures

Thin film devices were put into a test cell (of 10 ml volume) in which the gases were injected parallel to the film surface. Constant flow (100 ml/min) was maintained by mass flow controllers. The NO_2 vapor with a concentration of 1.5 *ppm* was obtained using a calibrated permeation cylinder (Vici Metronics, USA), which was incorporated into the experimental set-up. The measurements were carried out at different temperatures in either dry air or its mixture with NO_2 vapor.

DC conductivity measurements have been performed at temperatures between 20 and 200 °C. The thin film device was fixed onto an electrical refrigerator, allowing cooling of the sample down to 10 °C, then both pieces, the film and the refrigerator, were placed into a stove for subsequent heating. A platinum resistance temperature detector PT – 100 close to the film has been used for assisting the temperature control. The processing of the data was performed with a PC and a data acquisition board manufactured by National Instruments Inc. In all cases the applied voltage was varied between –5 V and +5 V with a step of 20 mV and the respective values of the current were measured. The delay time between the measurements was 2 s. Additional test experiments, conducted to clarify the influence of molecular hydrogen, were performed at room temperature. For this purpose, mixtures of H_2 with dry synthetic air, obtained from cylinders (Linde, Germany) have been used. AC conductivity, impedance and electrical capacity have been measured using a HP 4192A impedance analyzer. The experiments were carried out in the frequency range from 5 Hz to 13 MHz.

25.4 Impact of Adsorbed Gases on the Surface Charge Transport

25.4.1 Dynamic Conductivity

Figure 25.3 shows the dynamic conductivity of the films measured in the 5 Hz–13 MHz frequency range at room temperature. It is seen that the AC conductivity does not depend on the frequency up to ~ 10^4 Hz and ~ 10^5 Hz for the quaternary $As_2Te_{13}Ge_8S_3$ and pure Te films, respectively.

Then, the AC conductivity increases as $\sigma(\omega) \sim \omega^n$, with n dependent both on the composition and the frequency range. For the $As_2Te_{13}Ge_8S_3$ films in the frequency range $10^4 < \omega < 10^6$ Hz the exponent n ≈ 0.7. For the pure Te films the exponent n ≈ 0,7 ÷ 0,8 has been observed only in a narrow frequency range close to 10^5 Hz. At higher frequencies after a shoulder at ~10^6 Hz (for $As_2Te_{13}Ge_8S_3$), the dynamic conductivity increases more sharply with an exponent n ≈ 1,8. This behavior means that in the applied frequency range different transport mechanisms are realized, due to either the carriers excited to mobility band edges or their hopping via localized states in the gap. When the carriers are excited to mobility edges no frequency dependent conductivity is expected, at least up to frequencies of 10^8 Hz. For $As_2Te_{13}Ge_8S_3$, our results show the increase of the conductivity already above 10^3 Hz, which is five orders of magnitude lower. So, we can assume that at

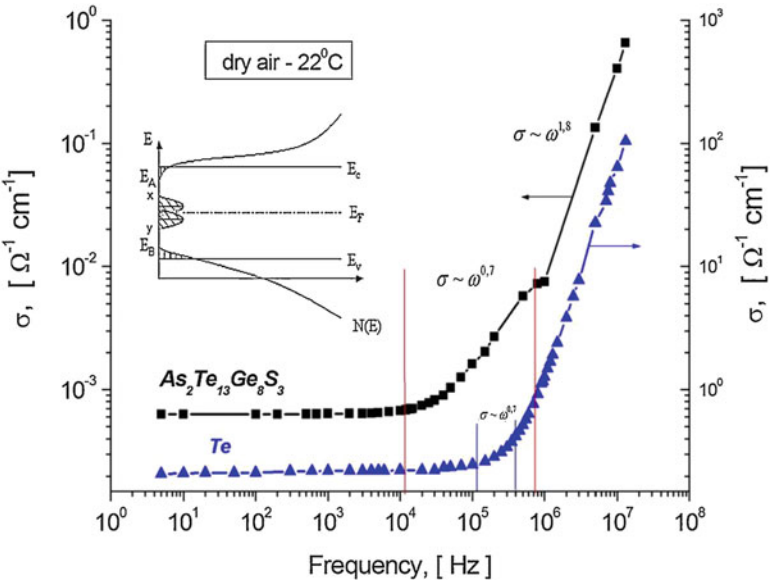

Fig. 25.3 Frequency dependence of the AC conductivity at room temperature in normal air environment. Inset shows the applied model of the density of states as a function of the energy in an amorphous semiconductor

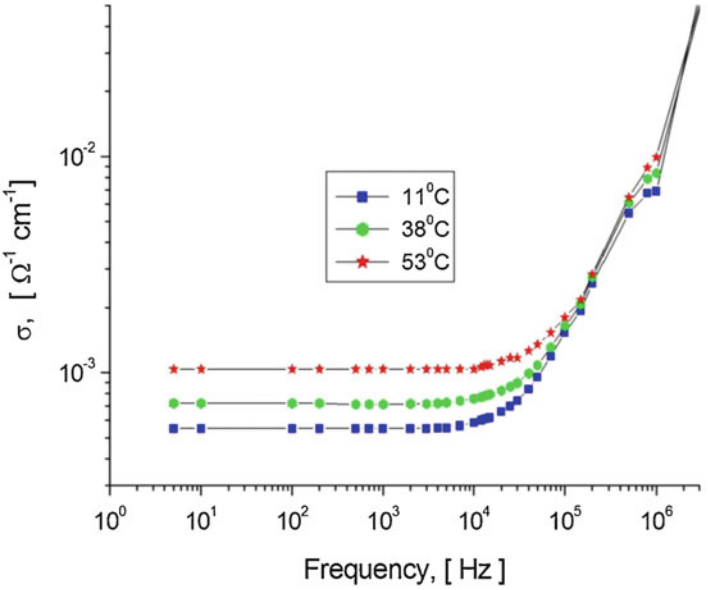

Fig. 25.4 Effect of the temperature on the frequency dependent AC conductivity

frequencies above 10^3 Hz, the conductivity $\sigma(\omega)$ is due to hopping of charge carriers via localized states. On the other hand, the frequency dependent conductivity can be realized by hopping of charge carriers both via localized states of the band tails and via states localized close to the Fermi level, as shown in the inset of Fig. 25.3. The difference between these two kinds of hopping conductivities, both described as $\sigma(\omega) \sim \omega^{0,7}$, can be viewed from the temperature dependence of $\sigma(\omega)$.

The effect of the temperature on the AC conductivity of $As_2Te_{13}Ge_8S_3$ based films is shown in Fig. 25.4, where $\log\sigma$ is plotted as a function of $\log\omega$ for several temperatures. Figure 25.5 shows $\ln\sigma$plotted versus the reciprocal temperature at different frequencies, together with the DC conductivity. It can be observed (curves for 0,5 kHz and 3 kHz with experimental points presented by crosses and squares, respectively) that up to approximately 3 kHz, the slope of $\ln\sigma - \frac{10^3}{T}$ is frequency independent, giving an activation energy of $E = 0,12eV$. Then in the 10^3–10^6 Hz frequency range, $\sigma(\omega)$ increases with the temperature, but this increase is strongly dependent on the frequency of applied electric field. Note, that in the frequency range higher than 10^6 Hz, where $n \approx 1,8$ (not shown in the picture), $\sigma(\omega)$ was found to be nearly independent on the temperature.

The weak dependence of $\sigma(\omega)$ on the frequency in the range up to approximately $5 \cdot 10^3$ Hz, accompanied by its exponential increase with temperature (Fig. 25.5) let us assume that in this frequency range the dynamic conductivity is due to charge hopping between the tail localized states, so its dependence on the temperature can be described as [14]:

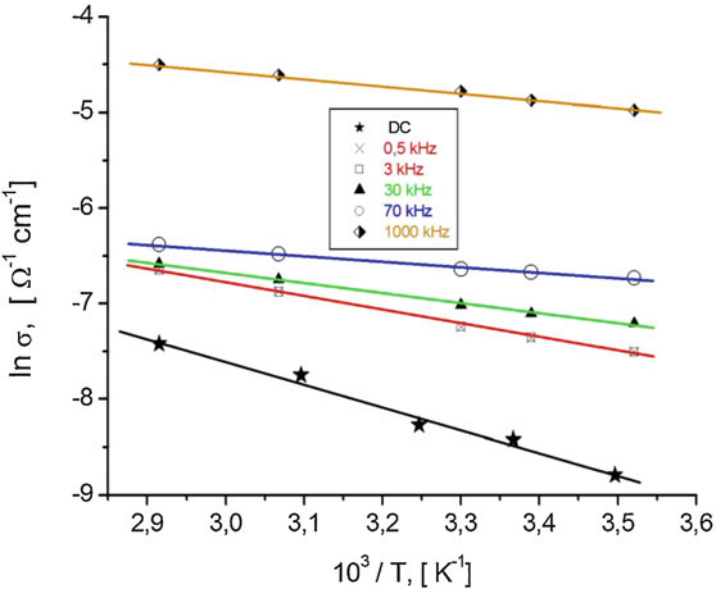

Fig. 25.5 lnσ versus the reciprocal temperature at different frequencies in an air environment

$$\sigma(\omega, T) = C_\omega \exp\left(-\frac{E}{kT}\right) = C_0 k T \exp\left(-\frac{E_F - E_B}{kT}\right) \tag{25.1}$$

where C_0 is a frequency dependent coefficient. The values of the parameters that match the above expression are: $C_\omega = 0,\ 14\Omega^{-1}\text{cm}^{-1}$ and $E = 0,\ 12\text{eV}$.

At frequencies up to $5{\bullet}10^3$ Hz, the AC conductivity is higher than the DC conductivity, at room temperature their ratio is $\sigma(\omega)/\sigma_0 \approx 3$. This ratio increases with the frequency, but at the same time it becomes less and less temperature dependent. Such a behavior is interpretable in terms of transition to a mechanism of hopping that includes the localized states N (E_F) in the middle of the mobility gap. Using the equation given by Austin and Mott (1969) as reported by Davis & Mott [15] and Mott & Davis [16] the conductivity can be presented as:

$$\sigma(\omega) = \frac{\pi}{3} e^2 kT[N(E_F)]^2 \alpha^{-5} \omega \left[\ln\left(\frac{\nu}{\omega}\right)\right]^4 \tag{25.2}$$

where ν is the phonon frequency ($\sim 10^{13}$ Hz), and α describes the spatial extension of the wave function associated with the localized states. It is seen from this expression that, due to logarithmic term $\left[\ln\left(\frac{\nu}{\omega}\right)\right]^4$, the slope of the curves $\ln\sigma(\omega)$ vs. $\ln\omega$ evidences a slight decrease with the frequency increase. Figures 25.3 and 25.4 clearly illustrate a decrease of the slope of $\ln\sigma(\omega) \propto \ln\omega$ dependences in the surrounding of 10^6 Hz, where this decrease looks like a shoulder. Using Eq. (25.2) we have estimated the density of the states at the Fermi level as:

$$N(E_F) = \sqrt{\frac{3\alpha^5}{\pi kTe^2}} \cdot \sqrt{\frac{\sigma(\omega)}{\omega\{\ln(\frac{\nu}{\omega})\}^4}} \tag{25.3}$$

Taking $\nu = 10^{13}$ Hz and $\alpha = 8$ Å [15] at T = 295 K and different frequencies between 10^5 and 10^6 Hz we have obtained $N(E_F) \approx 1{,}3 \cdot 10^{21}$ $eV^{-1} \cdot cm^{-3}$, not much dependent on the frequency. This value of $N(E_F)$ is quite large, but it appears to be typical for complex telluride glasses [15]. For pure Te films this analysis could not be done due to very short frequency interval with $\sigma(\omega) \sim \omega^{0,7}$ (Fig. 25.3). For this reason it can be assumed that in the Te films the dynamic conductivity, being independent on the frequency up to $\sim 10^5$ Hz, goes directly to exponent law with $n \approx 1{,}8$, meaning that the current transport at least up to $\omega \approx 10^5$ Hz occurs only via extended states above the mobility edges.

25.4.2 Effect of Gas Adsorption

Figure 25.6 shows the frequency dependent AC conductivity of the $As_2Te_{13}Ge_8S_3$ films obtained in pure dry air and upon exposure to NO_2 at room temperature (22 °C). It is seen that the addition of nitrogen dioxide to dry air leads to both increase of the dynamic conductivity by approximately one order of magnitude and extension of its independence on the frequency also by approximately one order of

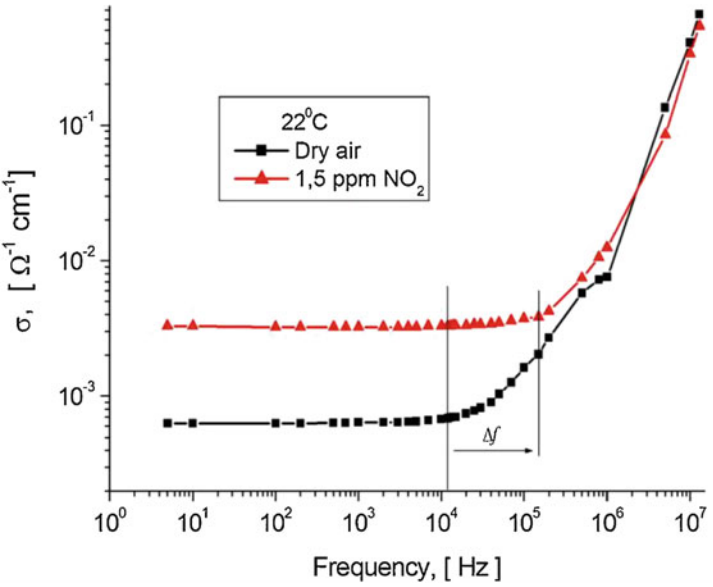

Fig. 25.6 Frequency dependence of the conductivity of $As_2Te_{13}Ge_8S_3$ films in different gaseous environments at room temperature

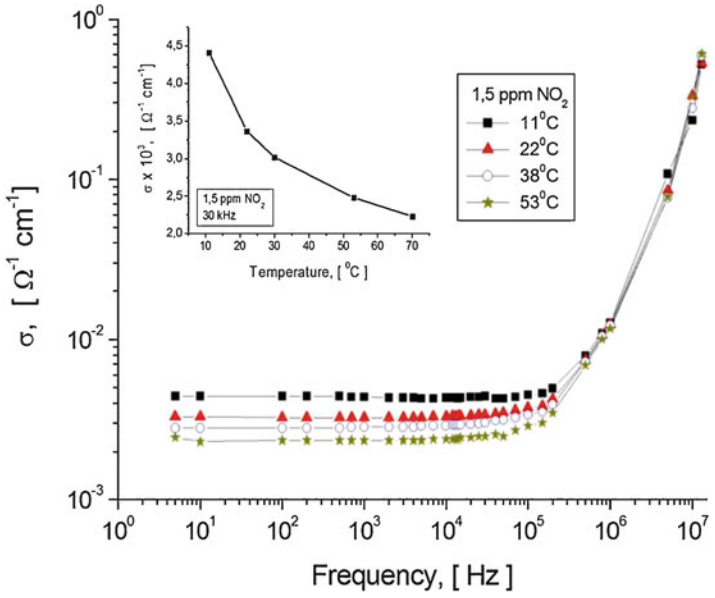

Fig. 25.7 The spectral distribution of the dynamic conductivity of $As_2Te_{13}Ge_8S_3$ in mixture of dry air with 1,5 ppm NO_2 at various temperatures. Inset shows the conductivity at $3•10^4$ Hz vs. temperature in these environmental conditions

magnitude, i.e. up to ~ 10^5 Hz. At higher frequencies the gas adsorption does not much affect the spectrum of the AC conductivity. Figure 25.7 shows the dynamic conductivity of $As_2Te_{13}Ge_8S_3$ films at different temperatures in an environment of dry air with addition of 1,5 ppm of NO_2.

Figure 25.7 reveals that the heating does not affect the general shape of the spectra, but the effect of temperature on dynamic conductivity becomes opposite to that observed in samples studied in an environment of pure air (Fig. 25.4). The inset of Fig. 25.7 illustrates how the conductivity at a definite frequency ($3•10^4$ Hz) decreases with the temperature increase upon such environmental conditions. In the frequency range higher than 10^6 Hz (with $n \approx 1{,}8$) the dynamic conductivity becomes nearly independent on the temperature, i.e. exhibits the same behavior as in an environment without nitrogen dioxide.

The essential modification of the AC conductivity under gas (NO_2) adsorption (Fig. 25.6) gives an evidence for a modification of the dominant mechanism of charge transport at the surface. If the conductivity via extended states without NO_2 covers the frequency range up to 10^4 Hz, the addition of nitrogen dioxide to the dry air prolongs this range by approximately one order of magnitude, up to ~ 10^5 Hz. Thus, within $10^4 < \omega < 10^5$ Hz frequency range, the effect of the gas (NO_2) adsorption consists in a modification of the charge transport mechanism from hopping between the tail localized states to the drift via extended states of the valence band.

Obviously, this means that the adsorption of NO_2 molecules results in a strong increase of the concentration of free holes at the surface. The gas induced mechanism of conductivity via extended states remains the major one up to frequencies $\omega > 10^5$ Hz, at which the transport mechanism due to hopping via localized states in the vicinity of the Fermi level becomes already predominant. It seems evident that the increase of the main carrier (holes) concentration by the gas adsorption is due to creation of new acceptor levels at the surface that control the charge transport. The surface conductivity generated by adsorption can be expressed as $\Delta\sigma = e\mu_p\Delta p$, where Δp is the excess of hole concentration at the surface and μ_p – their drift mobility. The type and concentration of the adsorbed molecules, as well as the temperature, control the induced surface conductivity. Using the experimental results from Fig. 25.6 and taking $\mu_p \approx 10^2 \text{cm}^2/\text{V} \times \text{s}$ [14], we have assessed the excess of holes concentration induced by the gas adsorption at the given conditions as $\Delta p \approx 2 \cdot 10^{15} \text{cm}^{-3}$. Such enhanced value makes evident the high concentration of acceptor levels induced by NO_2 adsorption. Unfortunately, the energetic positions of these levels cannot be assessed from the temperature dependence of the DC conductivity or AC conductivity at low frequencies due to temperature – dependent desorption processes. Langmuir's theory [17] gives for adsorption equilibrium at low pressures (Henry's isotherm) the relation:

$$N = \frac{N^* P \chi s}{\nu\sqrt{2\pi MkT}} \exp\left(\frac{q}{kT}\right) \tag{25.4}$$

where N is the surface concentration of adsorbed molecules, N∗ the surface concentration of adsorption centers, P the pressure, M the mass of the adsorbed molecule, s the effective surface area, χ the sticking probability, ν is a constant, q the building energy, k is Boltzmann constant and T the absolute temperature. From this equation it is seen that the number of adsorbed molecules, which controls the release of additional holes into the valence band, strongly diminishes with the temperature increase according to an exponent power factor. Hence, a decrease of the surface conductivity should be expected when the sample is heated. As shown in Fig. 25.7, the dynamic conductivity really decreases with the temperature increase, but not via a definite law. The aspect of this law cannot be determined exactly because two contradictory processes occur at the surface: the heating of the sample leads to the increase of the dynamic electric conductivity owing to the increase of the concentration of free holes, while the desorption of the gas molecules reduces the concentration of free holes, that diminishes the conductivity. It is important to note that the adsorption of the target gas (NO_2), as well as the temperature variation practically does not affect the transport mechanism, based on hopping via localized states in the vicinity of the Fermi level. As can be seen from Figs. 25.6 and 25.7, by adsorption of nitrogen dioxide this mechanism could be realized in a narrow range of frequencies $3{\bullet}10^5 \div 10^6$ Hz. The respective calculations of the density of states at the Fermi level have given the same values as for environment of dry air, i.e. $N(E_F) \approx 1{,}3{\cdot}10^{21}\ \text{eV}^{-1}\ \text{cm}^{-3}$.

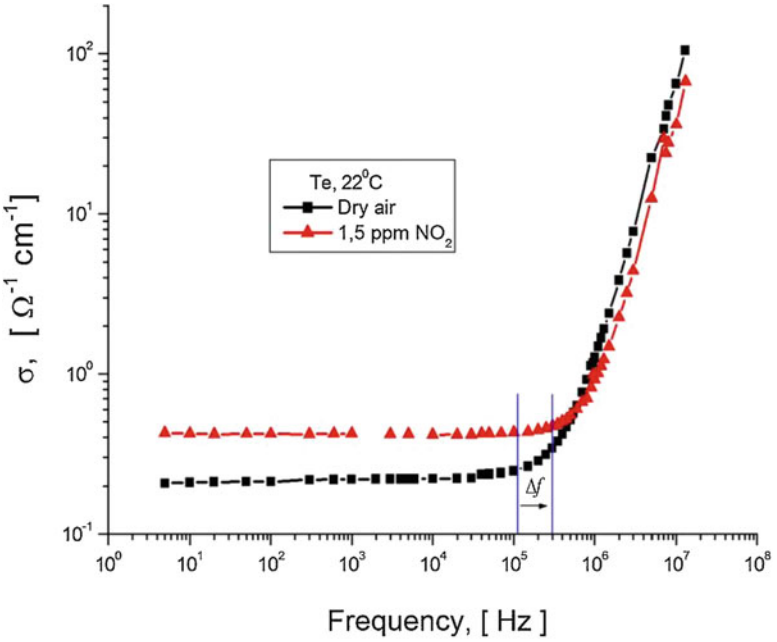

Fig. 25.8 Frequency dependence of the dynamic conductivity of vitreous Te films in dry air and its mixture with nitrogen dioxide at room temperature

Figure 25.8 shows the effect of nitrogen dioxide on the dynamic conductivity spectra of pure Te films at room temperature. It can be seen that the adsorption of NO_2 on the surface of vitreous Te affects the dynamic conductivity spectra in the same manner as for glassy $As_2Te_{13}Ge_8S_3$ films. The AC conductivity increases, but only in a very narrow frequency range around 10^5 Hz, where modification of the mechanism of charge transport occurs.

25.5 Impedance and Capacitive Operating Gas sensors Based on Glassy Chalcogenides

Variation of the charge state of the surface, as well as modification of the mechanism of the surface charge transport of glassy and nanocrystalline chalcogenides caused by gas adsorption, allow to develop gas sensitive functional structures operating via variation of their impedance or capacitance [10, 18]. The gas sensitivity of such thin film devices can be defined as relative variation of measured value (impedance or capacitance for a selected frequency) in a mixture of carrier gas with target one (X_g) and in pure carrier gas (X_a), divided by the target gas concentration (C) in percent/ppm:

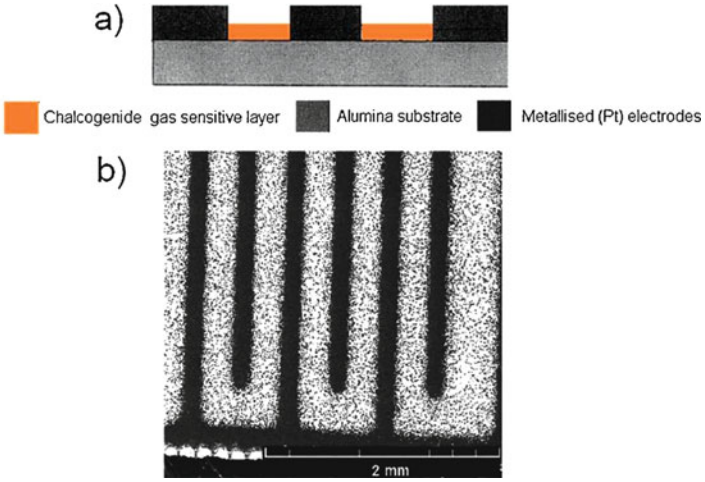

Fig. 25.9 (**a**) Schematic representation of GCh based functional structure and (**b**) its SEM image

$$\eta_{Z,C} = \frac{|X_a - X_g|}{X_a C} \bullet 100\% \tag{25.5}$$

The schematic and the real view of a gas sensitive functional structure are shown in Fig. 25.9a and b, respectively. The active chalcogenide layers are grown between interdigital Pt electrodes in such a way that the lateral parts form metal–semiconductor junctions (GCh/Pt) but the upper surface of GCh layers is exposed directly to the gaseous environment. The functional structures have been encapsulated in standard TO – 16 sockets and their contacts were thermally bonded to socket pins with copper wires.

25.5.1 Impedance Gas Sensitive Devices

Figure 25.10 shows the effect of nitrogen dioxide on the spectral distribution of the impedance of gas sensitive functional structure based on vitreous Te film. It is seen that the effect of the gas adsorption on impedance is frequency dependent, which obviously is caused by the above-mentioned surface processes, that are the variation of the charge state of the surface and modification of the charge transport mechanism. Using the impedance spectra measured in both dry air and its mixture with 1,5 ppm of NO_2, as well as Eq. (25.5), the spectral distribution of sensitivity to nitrogen dioxide can be carried out and the frequency at which the maximum sensitivity occurs can be determined. Figure 25.10 shows the frequency dependent sensitivity of Te films towards NO_2 at room temperature. It is observed that the

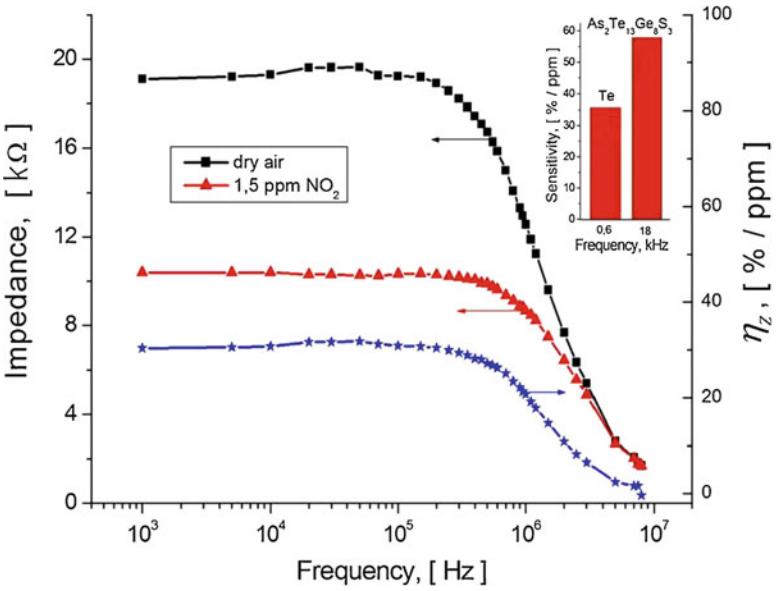

Fig. 25.10 Spectral distribution of impedance and sensitivity to nitrogen dioxide of functional structure based on vitreous Te films at room temperature. Inset shows the comparison of the maximum sensitivities at respective frequencies for both materials of this work

sensitivity of the film decreases with the frequency increase but tends to saturation already at approximately 3 MHz.

Recently, we have shown that functional structures based on glassy $As_2Te_{13}Ge_8S_3$ exhibit similar sensitivity spectra but the sensitivity itself decreases more sharply with the frequency increase and tends to saturation already at approximately 500 kHz [10]. Consequently, the spectral edge of the sensitivity depends on the composition of the active glassy material and, furthermore, it depends also on the nature of the adsorbed gaseous species. In our previous paper [13] it has been shown that the spectra of sensitivity to NO_2, H_2S and H_2 of films in question are similar, while the spectral position of the sensitivity edge is rather different for different target gases. The latter means that the selectivity of the respective sensor to different gas components can be enhanced by monitoring the spectral position of sensitivity edge.

The inset in Fig. 25.10 exhibits the maximum sensitivity for each material which, however, appears at different frequencies.

25.5.2 Capacitive Gas Sensitive Devices

The dependence of the capacitance of the functional structure Pt – $As_2Te_{13}Ge_8S_3$ – Pt on the frequency of the applied voltage in dry air and its mixture with 1,5 ppm

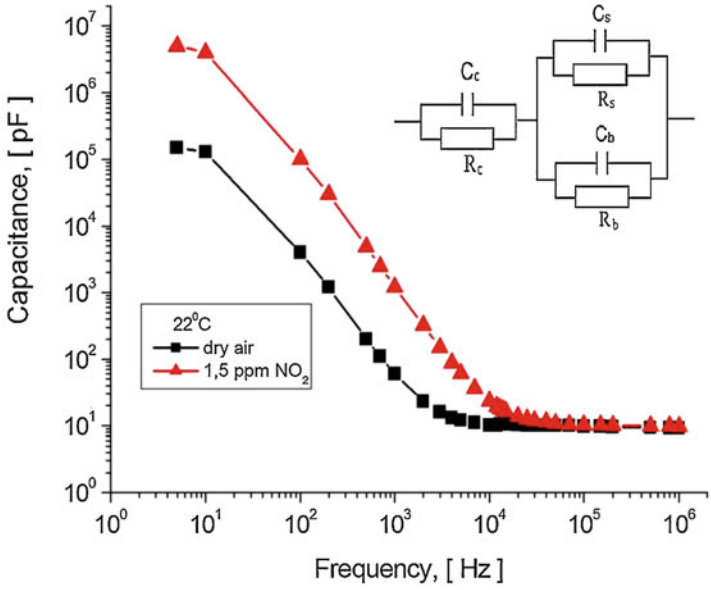

Fig. 25.11 The capacitance spectra of Pt – $As_2Te_{13}Ge_8S_3$ – Pt functional structure by different ambient environments at room temperature. Inset shows the equivalent circuit used for analysis

NO_2 at 22 °C is shown in Fig. 25.11. It is seen that in normal ambient the capacitance is independent on the frequency above $\omega \approx 10^4$ Hz, but at lower frequencies it sharply increases by several orders of magnitude.

Obviously, the constant value of the capacitance at frequencies higher than 10^4 corresponds to a geometric capacitor $C_h = \varepsilon\varepsilon_0 S/d$, where d and ε represent the interdigital distance and permittivity of the GCh film respectively, and S is the GCh/Pt contacting area. The rapid and huge increase of the capacitance with the frequency decrease below 10^4 Hz indicates the existence of a narrow high resistive regions near the contacts and the equalization of the dielectric relaxation time $\tau_r = \varepsilon\varepsilon_0\rho$ (ρ is the resistivity of the film) with the period of the applied voltage variation [19]. The application of a mixture of dry air with 1,5 ppm of NO_2 does not modify the shape of C vs. ω spectra but leads to an increase of the sample capacitance in a definite frequency range by approximately 100 times. This effect looks like a strong, gas induced shift of the rising edge of the capacitance spectrum toward higher frequencies. Besides, note that the gas (e.g. NO_2) adsorption affects the capacitance of the structure namely at low frequencies, that is frequency range, where the sample capacitance is assumed to be controlled by high resistive barriers at the contacts. This behavior can be analyzed assuming the equivalent circuit inserted in Fig. 25.11. The equivalent circuit of Pt -$As_2Te_{13}Ge_8S_3$ – Pt structure (Fig. 25.9a) can be represented by a parallel combination of bulk resistance (R_b) and capacitance (C_b) connected in parallel with a further parallel combination of surface resistance (R_s) and capacitance (C_s). As the device structure has a planar design there is also a

parallel combination of resistance (R_c) and capacitance (C_c) corresponding to thin insulating layers usually formed at the contacts, put in series with the above-mentioned network. Due to the small thickness of the contact insulating layer it can be assumed that $C_c >> C_b$ and at high frequencies, the whole capacitance can be approximated as $C_h = C_c C_b / C_c + C_b \approx C_b$. The asymptotic values for low frequency capacitance derived using the H. Wey approach [20] is:

$$C_l = C_c R_c^2 / \left(R_c + \frac{R_s R_b}{R_s + R_b} \right)^2 \tag{25.6}$$

Assuming that $R_c << R_s << R_b$:

$$C_l \approx \frac{C_c R_c^2}{R_s^2} \tag{25.7}$$

This expression shows that the low frequency capacitance should strongly raise with the surface conductance increase, which meets the above presented experimental results. The fact itself of increasing of the $As_2Te_{13}Ge_8S_3$ conductivity by gas (e.g. NO_2) adsorption has been clearly demonstrated above. Thus, the functional structures in question can be used as active elements of capacitive gas sensors. To assess this possibility, we have calculated via expression (25.5) the frequency dependent sensitivity to NO_2 for functional structures based on glassy $As_2Te_{13}Ge_8S_3$ films and the results are shown in Fig. 25.12. It can be seen that the capacitive sensitivity of the functional structures in question depends very strongly on the frequency of the applied electric field, showing a threshold at about 50 kHz. At frequencies higher than this threshold, the sensitivity to NO_2 is only 3÷5%/ppm. When crossing this threshold towards lower frequencies, the sensitivity of the Pt-$As_2Te_{13}Ge_8S_3$- Pt structure increases sharply by over three orders of magnitude.

As far as the functional structure based on pure Te film is concerned, no evident frequency dependence of the capacitance is observed in the applied frequency range, since the effect of nitrogen dioxide results in a small increase of the capacity. That is why, the capacitive sensitivity of these functional structures to NO_2 is only ~ 1÷3%/ppm (Fig. 25.12). Perhaps this is caused by the relative small resistivity of the Te films, which results in a short dielectric relaxation time. In such conditions the bulk capacitance controls the entire capacitance of the functional structure and the gaseous species adsorbed from the environment cannot affect it.

25.6 Conclusions

The gas adsorption on chalcogenide glassy semiconductors can result in modification of the dominant mechanism of electric charge transport at the surface. Adsorption of nitrogen dioxide molecules on the surface of $As_2Te_{13}Ge_8S_3$ films leads to

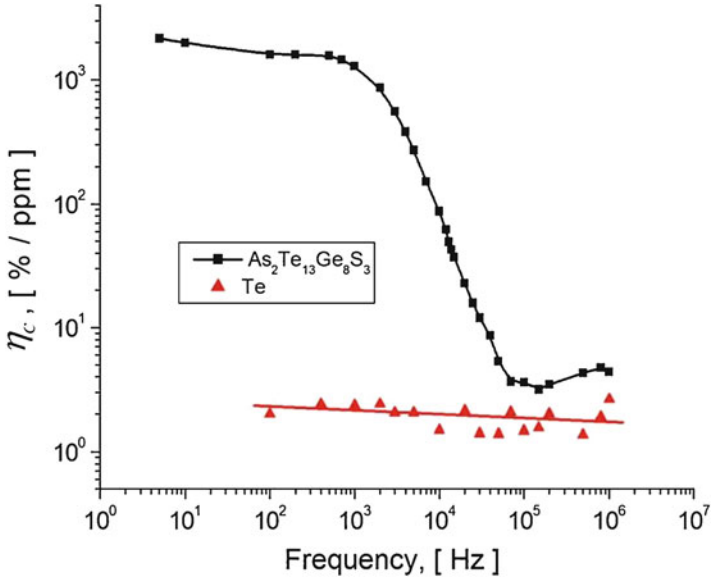

Fig. 25.12 The capacitive sensitivity of functional structures based on glassy $As_2Te_{13}Ge_8S_3$ and pure Te films to nitrogen dioxide in dry air

modification of the mechanism of current flow from hopping of the charge carriers between the tail localized states in the forbidden gap, towards a mechanism connected with carrier drift via extended states of the valence band. This phenomenon strongly influences the spectrum of dynamic conductivity in the $10^4 < \omega < 10^5$ Hz frequency range; however, this influence can be diminished by heating, which provokes the desorption processes.

The variation of the charge state of the surface, as well as the modification of the mechanism of surface charge transport of glassy and nanocrystalline chalcogenides caused by gas adsorption can be used for development of impedance or capacitive gas sensitive devices, operating at room temperature with a high sensitivity and selectivity in the ppm and sub-ppm concentration range.

Acknowledgments This work was financially supported by Technical University of Moldova through Institutional Grant 15.817.02.29A and National Agency for Research and Development of Moldova, project PS 20.80009.5007.21. The authors express gratitude to Dr. M. Enache from NCMST of TUM for SEM analyses and Dr. G. F. Volodina from IAP ASM for XRD analyses.

References

1. Kolomiets BT, Mamontova TN, Pivovarova LV (1973) On the influence of surface conditions upon photoconductivity in vitrious As_2Se_3. Phys Status Solidi A 19:609
2. Kolomiets BT, Mamontova TN, Pivovarova LV (1973) Kinetics of photoconductivity and surface conditions for vitreous arsenic selenide. Phys Status Solidi A 20:367

3. Mamontova TN, Kochemirovskii AS, Pivovarova LV (1988) Electronic processes on the surface of As – Se chalcogenide glassy semiconductors. Phys Status Solidi A 107:11
4. Marian SI, Potje-Kamloth K, Tsiulyanu D, Liess H-D (2000) Dimorphite based gas sensitive thin films. Thin Solid Films 359:108
5. Tsiulyanu DI, Marian SI, Miron VS, Liess H-D (2001) High sensitive tellurium based NO_2 gas sensor. Sensors Actuators B Chem 73:35
6. Kumar V, Sen S, Sharma M, Muthe KP, Jagannath, Gaur NK, Gupta SK (2009) Tellurium nano-tructure based NO gas sensor. J Nanosci Nanotechnol 9:5278
7. Popescu M, Velea A, Sava F, Lorinczi A, Tomescu A, Simion C, Matei E, Soco G, Mihailescu IN, Andonie A, Stamatin I (2010) Structure and properties of silver doped $SnSe_2$ and $Ge_2Sb_2Te_5$ thin films prepared by pulsed laser deposition. Phys Status Solidi A 207:516
8. Koleva K, Popov C, Petkova T, Petkov P, Mihailescu IN, Reithmaier J-P (2009) Complex $(As_2S_3)(100-x)(AgI)x$ chalcogenide glasses for gas sensors. Sensors Actuators B Chem 143:395
9. Wüsten J, Potje-Kamloth K (2010) Chalcogenides for thin film NO sensors. Sensors Actuators B Chem 145:216
10. Tsiulyanu D, Ciobanu M (2016) Room temperature a.c. operating gas sensors based on quaternary chalcogenides. Sensors Actuators B Chem 223:95
11. Tsiulyanu D (2006) Chalcogenide semiconductor based gas sensors. In: Grimes CA, Dickey EC, Pishko V (eds) Encyclopedia of sensors, vol 10. American Scientific Publishers, Stevenson Ranch, pp 1–11
12. Petkov P, Tsiulyanu D, Kulish W, Popov C (2015) Nanoscience advances in CBRN agents detection, information and energy security. Springer, Dordrecht, p 535
13. Tsiulyanu D, Ciobanu M, Mocreac O (2018) Impedance characterization of gas sensitive chalcogenide films. In: Petkov P et al (eds) Advanced nanotechnologies for detection and defence against CBRN agents. Springer, Dordrecht, pp 317–332
14. Nagels P (1982) Electronic transport in amorphous semiconductors. In: Brodsky MH (ed) Amorphous semiconductors. Mir, Moscow, pp 146–200. (in Russian)
15. Davis EA, Mott NF (1970) Conduction in non-crystalline systems. Philos Mag 22:903
16. Mott NF, Davis EA (1979) Electron processes in non – crystalline materials. Clarendon press, Oxford
17. Wolkenstein T (1991) Electronic processes on semiconductor surfaces during chemisorption. Consultants Bureau, New York
18. Ciobanu M (2017) Features of contact and surface processes in glassy $As_2Te_{13}Ge_8S_3$ based structures with Pt electrodes upon interaction with nitrogen dioxide. Moldavian J Phys Sci 16:234
19. Simashkievici AA, Shutov SD (1984) Evidence of Schottky barrier formation at contact of metal with chalcogenide glassy semiconductor. Phys Status Solidi A 84:343
20. Wey HY (1976) Surface of amorphous semiconductors and their contacts with metals. Phys Rev B 13:3495

Chapter 26
Phase Composition and Spectroscopic Characterization of Barium Titanate Containing Glass Ceramics

Ruzha Harizanova, Ivailo Gugov, Ivalina Avramova, Irena Mihailova, Georgi Avdeev, and Christian Rüssel

Abstract Glasses are synthesized in the system $Na_2O/BaO/TiO_2/SiO_2/B_2O_3/Al_2O_3$ for different Na_2O/Al_2O_3 ratios. X-ray photoelectron spectroscopy is utilized for the estimation of the valence states of titanium and the occurrence of solely Ti^{4+} is observed. The presence of bonds from the type Si-O-Al, Si-O-Si and Na-O-Si is detected in the glasses and it is concluded that the increasing alumina concentration leads to decreasing binding energy of the Al^{3+} ions in the glass. The glasses are subjected to thermal treatment in order to crystallize barium titanate with controllable size and in a high-volume fraction. The phase composition of the prepared glass ceramics is studied by X-ray diffraction. The precipitation of cubic barium titanate but also of other crystalline phases is observed while increasing alumina concentration and temperature. The structure of selected glass ceramics is investigated by infrared spectroscopy. The effect of crystallization on the main structural units and their change during the course of the crystallization is traced and the presence of the $BaTiO_3$ phase is confirmed by the peak at about 570 cm^{-1}. The peaks in the range of 1200–1500 cm^{-1} are with varying intensities and witness the occurrence of changing as number during the course of crystallization BO_3 triangles containing non-bridging oxygen ions. The presence of BO_4 and SiO_4 tetrahedra in the glass ceramics is suggested from the peaks in the range of 800–1200 cm^{-1}.

R. Harizanova (✉) · I. Gugov · I. Mihailova
University of Chemical Technology and Metallurgy, Sofia, Bulgaria
e-mail: rharizanova@uctm.edu

I. Avramova
Institute of General and Inorganic Chemistry, Bulgarian Academy of Sciences, Sofia, Bulgaria

G. Avdeev
Institute of Physical Chemistry, Bulgarian Academy of Sciences, Sofia, Bulgaria

C. Rüssel
Otto Schott Institute, University of Jena, Jena, Germany

P. Petkov et al. (eds.), *Nanoscience and Nanotechnology in Security and Protection against CBRN Threats*, NATO Science for Peace and Security Series B: Physics and Biophysics, https://doi.org/10.1007/978-94-024-2018-0_26

Keywords Barium titanate · Glass ceramics · Crystallization · XPS · IR spectroscopy

26.1 Introduction

Barium titanate, $BaTiO_3$ was discovered in the 1950s and ever since it has found various applications as part of resistive sensors, multilayered capacitors and optoelectronic devices [1–7]. $BaTiO_3$ has a very high melting temperature of about 1600 °C [8] and possesses four allotropic modifications – orthorhombic (stable up to −90 °C), rhombohedral (existing between −90 and 0 °C), tetragonal (stable from 0 to 120 °C) and cubic with stability region above 120 °C. The stable modification of $BaTiO_3$ at room temperature depends on the preparation method and the size of the precipitated $BaTiO_3$ crystals [3]. In order to avoid the heating to extremely high temperatures, barium titanate has been produced by using different synthesis methods as for example sol gel [4], hydrothermal method [7], sintering [6, 7] and controlled crystallization from oxide glasses [5, 9–11]. Using the classical technology of melting, a glass with high concentration of oxides of the alkaline earth and 3d-transition metals and less than 30% of glass forming oxides, can be prepared at the significantly lower temperature of 1250 °C [5, 9–11]. The crystallization of dielectric phases from oxide glasses with different compositions enables the controlled precipitation of the desired crystalline phase with tailorable size, a narrow-size-distribution and a large volume fraction as already observed in [11]. In order to prepare glass ceramics from the glasses, an appropriate time-temperature regime should be applied to them and thus, the preparation of $BaTiO_3$ will be possible. The applicability of the prepared glass ceramic materials requires the thorough investigation of their properties – physicochemical and electrical, as well as gathering of information about the structure of the parent glasses and its evolution during the course of crystallization. Important is also the influence of the obtained microstructures on the physical properties. Actually, the system proposed here is supposed to be prone to phase separation and prior precipitation of Ba and Ti ions in one of the phases [12]. Some information on the microstructure and its evolution with the changing composition and the different crystallization conditions has already been obtained and reported in [10]. However, no information concerning the valence states of the ions participating in the glass and on the structure and its evolution with changing the composition and the advancing time in case of isothermal crystallization is available. Such knowledge could be very useful regarding the potential applications of the obtained glass ceramics.

The synthesis of glasses and glass ceramics derived hereof is studied for the following series of compositions $(23.1\text{-}x)Na_2O/xAl_2O_3/23.1BaO/23TiO_2/9.8B_2O_3/21SiO_2$ with $x = 3$, 7, 11 and 15 mol %. The resulting phase compositions and microstructures are investigated. Information about the valence states and binding energies is supplied by X-ray photoelectron spectroscopy. The structure of selected glass ceramics is studied by means of infrared spectroscopy.

26.2 Experimental

26.2.1 Preparation of the Glasses

Reagent grade raw materials: Na_2CO_3, SiO_2, $BaCO_3$, $B(OH)_3$, $Al(OH)_3$ and TiO_2 were used for the preparation of the glasses. The batches (60 g) were homogenized and melted in Pt-crucibles using a molybdenum disilicide furnace and a melting temperature of 1400 °C for 1 h in air. Some of the melts were quenched on a Cu-block and after quenching transferred into a pre-heated graphite mould. The glasses cast into the graphite mould were transferred to a muffle furnace and kept at 450 °C for 10 min. Then, the furnace was switched off and the samples were allowed to cool to room temperature with a velocity of approximately 2 K/min. All glassy samples were heat treated at temperatures above T_g for different times.

26.2.2 Characterization Methods

The phase compositions were analyzed by X-ray diffraction (XRD) on powdered samples, using $Cu_{K\alpha}$-radiation with the 2θ-values in the range from 10 to 60° (Philips PW1050). The X-ray photoelectron spectroscopy (XPS) analyses were performed on a *ESALAB MkII* system (England) with $Al_{K\alpha}$ radiation (1486.6 eV) using a total instrumental resolution of ~1 eV and a pressure of 10^{-8} Pa. The binding energies (BE) were referred to the C1s line (of the adventitious carbon) at 285.0 eV. The concentrations of the elements on the surface were evaluated from the integrated peak areas after Shirley-type background subtraction using theoretical Scofield's photoionization cross-section. The accuracy of the measured binding energy was around 0.2 eV. The Infrared spectroscopy (IR) investigations were carried out with a FTIR spectrophotometer VARIAN 600 on powdered samples pressed in KBr in the wave-number range 400–4000 cm^{-1}.

26.3 Results and Discussion

Previous work in the system $(23.1\text{-}x)Na_2O/xAl_2O_3/23.1BaO/23TiO_2/9.8B_2O_3/21SiO_2$ for x = 3, 7, 11 and 15 mol% [10], where the ratio of Na_2O to Al_2O_3 was varied in order to trace its influence on the glass formation ability, showed that glasses were successfully synthesized by utilizing conventional glass melting technique. It was established that the higher the alumina concentration, the better the glass-forming ability. After an appropriate thermal treatment, barium titanate in a large volume fraction could be crystallized in these glasses.

The investigation of the phase composition of the obtained glass ceramics with 3 mol% alumina showed that for each crystallization temperature cubic $BaTiO_3$ is the first phase to be formed and only for higher temperatures and longer times also another phase – barium fresnoite, $Ba_2TiSi_2O_8$ will occur, as seen in Fig. 26.1. For the

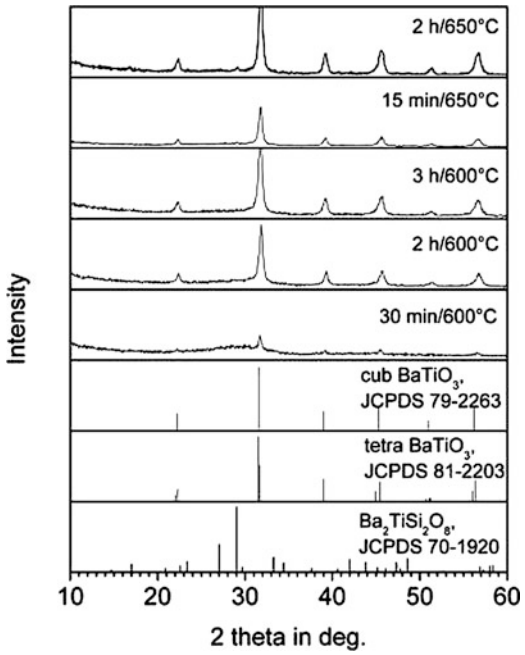

Fig. 26.1 XRD patterns of glass ceramics with 3 mol % Al_2O_3 and different thermal history

higher alumina concentrations more complicated crystallization behavior is observed as witnessed by Figs. 26.2 and 26.3 where also traces of nepheline, $NaAlSiO_4$ and minor quantity of $BaTi_2O_5$ are detected. These observations of the X-ray analysis are supported by the microstructural investigations on the same glass ceramics and reported in [10]. Previous micro-computed tomography investigation of the glass ceramic samples revealed that the barium titanate phase is crystallized in a large volume fraction of 58 ± 1% [10] which is important for potential practical applications. Additionally, according to the preliminary information gathered by SEM imaging about the studied system [10, 12], the currently investigated system is prone to phase separation which results in the formation of droplet-like structures enriched in Ba and Ti where later $BaTiO_3$ is precipitated [9, 10, 12].

Important for the precipitation of the desired $BaTiO_3$ phase is the valence state of the titanium ions which can occur as both Ti^{3+} and Ti^{4+} in the glass. In order to answer this question, XPS investigation is performed on the glasses from the system of interest and the results show that Ti ions are present in all glasses as Ti^{4+}, as seen in Fig. 26.4a for the Ti2p spectra and supported by the binding energy of Ti ions which is determined to be 458.3 eV. The binding energy of the divalent Ba ions is determined from the Ba3d XPS spectrum and is about 779.5 eV. These binding energies of Ba^{2+} and Ti^{4+} ions are typical for the compound $BaTiO_3$ [13] and are estimated for the glasses with 3 and 15 mol % Al_2O_3 while for the samples with 7 and 11 mol % Al_2O_3 the binding energy of barium is shifted to higher values. The peak in these cases is centered at about 780.5 eV which is typical for the compound $BaCO_3$ and could be explained by the occurrence of this phase as a relaxation phase formed on the $BaTiO_3$ surface which reduces the deformations/distortions existing in the barium titanate lattice [14]. Figure 26.5a shows the O1s XPS spectra from which,

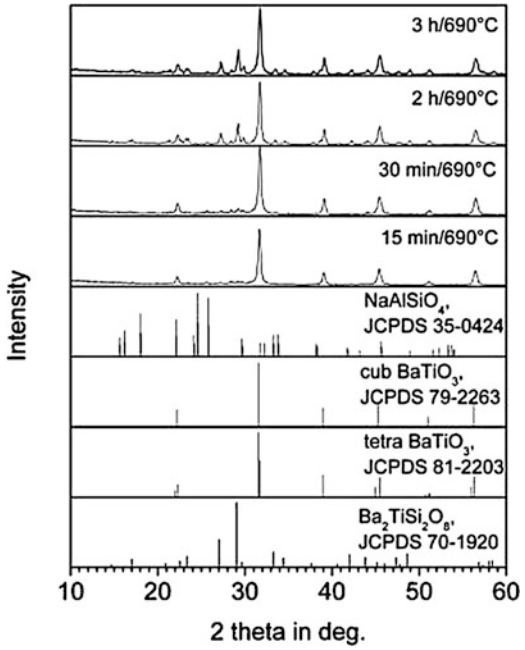

Fig. 26.2 XRD patterns of glass ceramics with 7 mol % Al_2O_3 and different thermal history

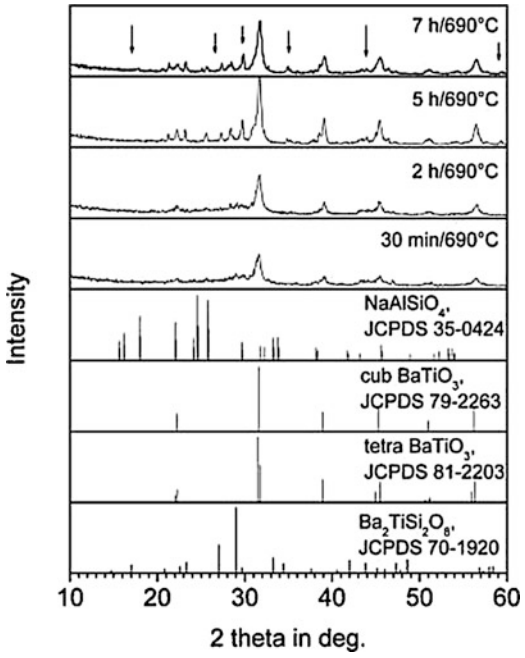

Fig. 26.3 XRD patterns of glass ceramics with 11 mol % Al_2O_3 and different thermal history

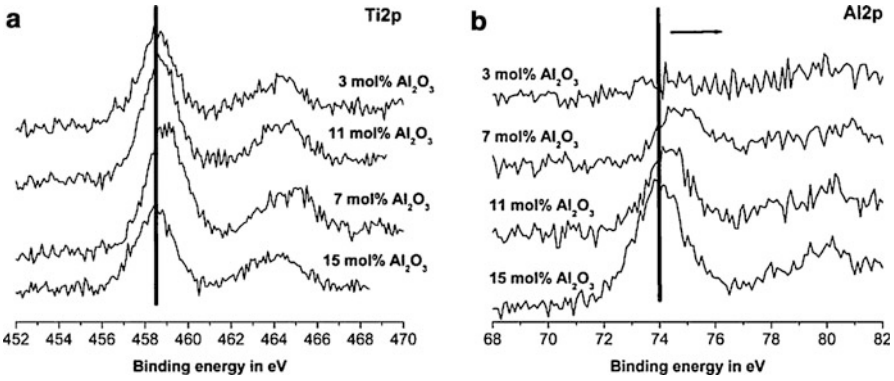

Fig. 26.4 (**a**) XPS spectra of the Ti2p peak for the glasses with different alumina concentrations. (**b**) XPS spectra of the Al2p peak for the glasses with different alumina concentrations

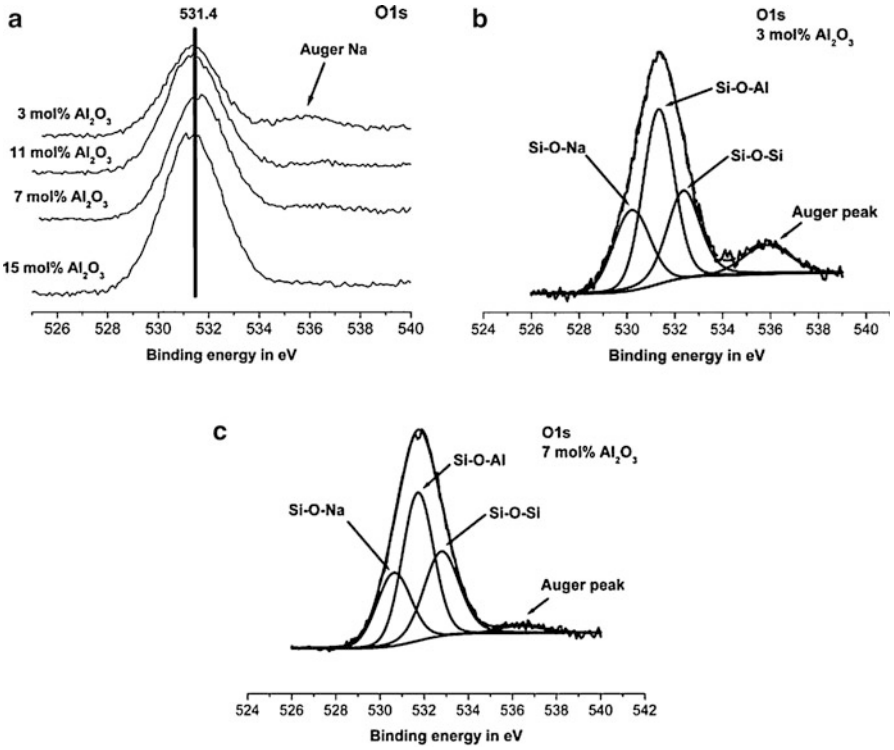

Fig. 26.5 (**a**) XPS spectra of the O1s peak for the glasses with different alumina concentrations. (**b**) Deconvoluted XPS O1s peak for the glass with 3 mol % alumina. (**c**) Deconvoluted XPS O1s peak for the glass with 7 mol % alumina. (**d**) Deconvoluted XPS O1s peak for the glass with 11 mol % alumina. (**e**) Deconvoluted XPS O1s peak for the glass with 15 mol % alumina

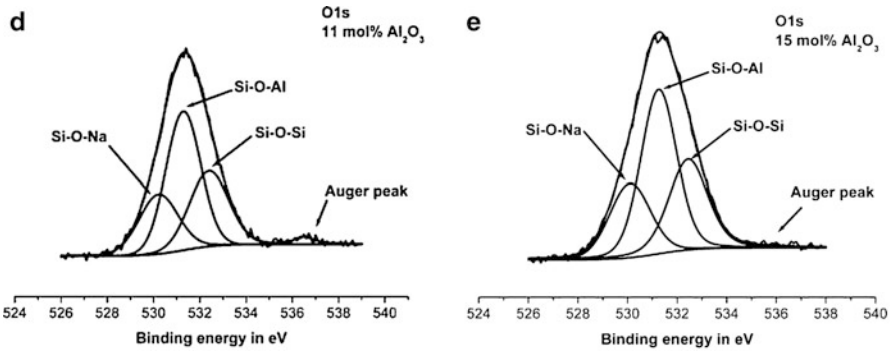

Fig. 26.5 (continued)

after deconvolution, information about the bonds existing in the glass as well as the respective binding energies could be extracted. The obtained O1s photoelectron spectra and the attributed binding energy of 531.5 eV are evidence that the process of synthesis leads to the oxidation of the elements constituting the glass. The recorded peaks are broad and can be deconvoluted into three components centered at 532, 531 and 530 eV, corresponding to the formation of Si-O-Si, Si-O-Al or Si-O-Na bonds, respectively. In the same region also a small Auger peak of Na is detected at about 536 eV. From the obtained photoelectron spectra for Si2p (not shown here) it becomes clear that the Si^{4+} ions have the same electronic surrounding as in the compound Al_2SiO_5. The silicon ions are tetrahedral coordinated with the O^{2-} ions and form Al-O-Si bonds. In the region of the photoelectron lines for Al2p, given in Fig. 26.4b, shift of the binding energies to the higher values with the decreasing alumina concentration is observed which could be attributed to the possibility of Al^{3+} participating initially in tetrahedral coordination with oxygen ions but with their increasing concentration also in octahedral one. The comparison of the peak areas of the three components in Figs. 26.5b, c, d and e shows that the higher alumina concentration results in an increasing number of both Si-O-Al and Si-O-Si bonds up to 7 mol %, then for 11 mol % a decrease is observed and afterwards again an increase for 15 mol % alumina. The latter could be attributed to the different types of structural units formed in the respective glasses.

IR spectroscopy analyses are performed on selected glass ceramics from the composition with 7 mol % Al_2O_3. The typical appearance of the IR spectra is shown for three glass ceramic samples with different thermal history in Figs. 26.6, 26.7 and 26.8. Here are also seen the fits performed by the program Fityk using Gaussian shaped peaks for the deconvolution of the recorded spectra. From the fit we suggest that initially boron takes part in the glass structure in the form of BO_4 tetrahedra which during the crystallization course are transformed into BO_3 triangles with non-bridging oxygen ions as indicated by the peak at about 1460 cm^{-1}. The concentration of the BO_3 units reaches a maximum for the glass ceramics heat-treated for 1–2 h at 690 °C and for times $\geq$3 h decreases again. This could be

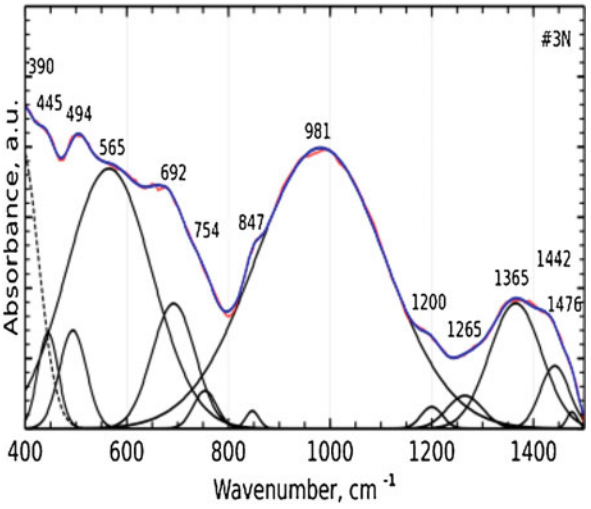

Fig. 26.6 Deconvolution of the IR spectrum of a sample with 7 mol % Al_2O_3 – 15 min at 690 °C

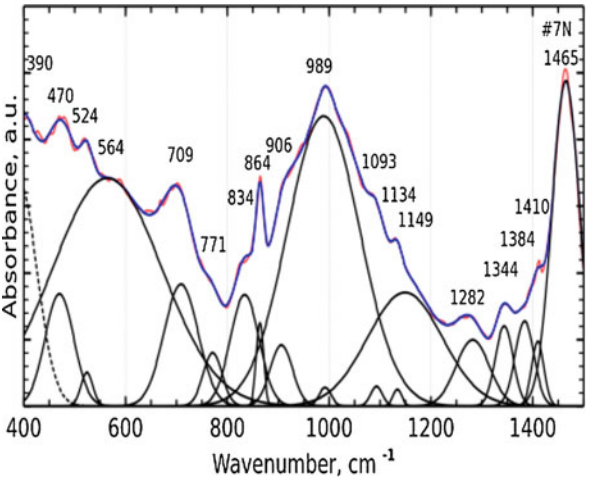

Fig. 26.7 Deconvoluted IR spectrum of the glass ceramic with 7 mol% Al_2O_3–3 h at 690 °C

explained by the building of a shell with varying composition around the growing barium titanate crystals. When the crystal growth stops, the variation in the shell composition is compensated by diffusion processes which results in the homogenization and stabilization of the rest glass structure. According to [15, 16], $BaTiO_3$ has a single peak in the wave number range above 400 cm^{-1} – at about 540–580 cm^{-1} for both cubic and tetragonal modifications. As revealed by XRD the phase precipitating in large concentrations is $BaTiO_3$, thus the peak at about 570 cm^{-1} should be attributed to this phase. The peaks in the region 1200–1500 cm^{-1} could be assigned to different types of borate groups based on the BO_3 triangles containing non-bridging oxygen ions. The intensity of these peaks increases for times up to

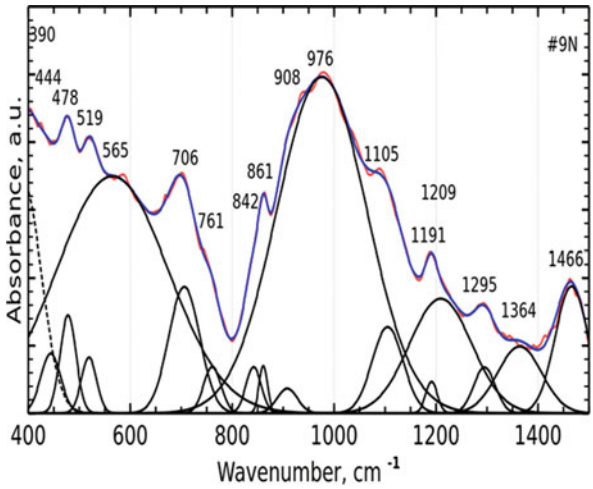

Fig. 26.8 Deconvoluted IR-spectrum of the glass ceramic with 7 mol% Al_2O_3–7 h at 690 °C

3 h and then starts to decrease again which is attributed to the building of shells with varying composition around the growing crystals.

During the crystallization course local change of the rest glass structure occurs which is supported by the change of the intensities of the peaks at 480, 520, 705, 840 and 864 cm^{-1} and which could be attributed to the oscillations of the BO_3-containing structures. It could be suggested that the structure of the glass ceramic with 7 mol % alumina crystallized for 7 h at 690 °C consists of $BaTiO_3$ crystals (peak at 569 cm^{-1}) and a borate phase with composition which is difficult to be determined. From the IR spectrum deconvolution, as seen in Fig. 26.8, it could be supposed that this borate phase contains BO_3 triangles with non-bridging oxygen ions (peak at 1463 cm^{-1}), sodium-borate silicate phase with three dimensional structure and consisting of SiO_4 and BO_4 tetrahedra whose charge is compensated by the Na^+ ions (peaks between 800 and 1200 cm^{-1}).

26.4 Conclusions

Glasses were synthesized in the system $Na_2O/BaO//TiO_2/B_2O_3/SiO_2/Al_2O_3$ with up to 15 mol % Al_2O_3. The glass composition and the valence of the prepared glasses are studied by XPS and the increase of the binding energy of aluminium ions with the decreasing alumina concentration is concluded. XPS also confirms the building of bonds from the type Si-O-Al, Si-O-Si and Si-O-Na with prevailing number of the Si-O-Al bonds for all alumina concentrations. Heat treatment of the glasses always results in the crystallization of cubic $BaTiO_3$ as the first phase and for higher alumina concentrations and longer crystallization times also $NaAlSiO_4$ and $Ba_2TiSi_2O_8$ are precipitated. The IR spectroscopy performed on the glass ceramics with 7 mol % alumina confirms the crystallization of barium titanate and reveals the presence of

BO_3, BO_4 and SiO_4 structural units whose number varies with the advancing crystallization time in case of constant alumina concentration and crystallization temperature.

Acknowledgments This work is financially supported by the Bulgarian National Scientific Fund under the contract KP-06-N28/1.

References

1. Mohammadi M R, Rad A E, Fray D J, Water-based sol–gel nanocrystalline barium titanate: controlling the crystal structure and phase transformation by Ba:Ti atomic ratio, (2009) J Mater Sci 44:4959–4968
2. Libor Z, Wilson SA, Zhang Q, Rheological properties of magnetic and electro-active nanoparticles in non-polar liquids, (2011) J Mater Sci 46:5385–5393
3. Capsal JF, Dantras E, Laffont L, Dandurand J, Lacabanne C, Nanotexture influence of $BaTiO_3$ particles on piezoelectric behaviour of PA 11/$BaTiO_3$ nanocomposites, (2010) J Non-Cryst Solids 356:629–634
4. Joshi U, Yoon S, Baik S, Lee JS, Surfactant-free hydrothermal synthesis of highly tetragonal barium titanate nanowires: a structural investigation, (2006) J Phys Chem B 110:12249
5. Maiti RP, Basu S, Bhattacharya S, Multiferroic behavior in silicate glass nanocomposite having a core–shell microstructure, (2009) J Non-Cryst Solids 355:2254–2259
6. Du GP, Hu ZJ, Han QF, Qin XM, Shi WZ, Effects of niobium donor doping on the phase structures and magnetic properties of Fe doped $BaTiO_3$ ceramics, (2010) J Alloys Compd 492: L79–L81
7. Vijatović MM, Bobić JD, Stojanović BD, History and challenges of barium titanate: Part II, (2008) Sci Sinter 40:235–244
8. Smith MB, Page K, Siegrist T, Redmond PL, Walter EC, Seshadri R, Brus LE, Steigerwald ML, Crystal structure and the paraelectric-to-ferroelectric phase transition of nanoscale $BaTiO_3$, (2008) J Am Chem Soc 130:6955–6963
9. Harizanova R, Mazhdrakova A, Vladislavova L, Avdeev G, Bocker C, Gugov I, Rüssel C, Crystallization Behaviour of the Systems $Na_2O/BaO/TiO_2/SiO_2/B_2O_3/Al_2O_3$ and $Na_2O/BaO/TiO_2/SiO_2/B_2O_3/Fe_2O_3/Al_2O_3$, (2015) J Chem Technol Metall 50:375–380
10. Harizanova R, Tatchev D, Avdeev G, Bocker C, Karashanova D, Mihailova I, Gugov I, Rüssel C, Investigation on the crystallization behaviour of sodium-aluminoborosilicate glasses with high concentrations of Ba and Ti, (2017) Bulg Chem Commun 49:119–125
11. Buscaglia V, Buscaglia MT, Viviani M, Mitoseriu L, Nanni P, Trefiletti V, Piaggio P, Gregora I, Ostapchuk T, Pokorny J, Petzelt J, Grain size and grain boundary-related effects on the properties of nanocrystalline barium titanate ceramics, (2006) J Eur Ceram Soc 26:2889–2898
12. Vogel W (1985) Glass chemistry, 2nd edn. Springer, Berlin
13. Ayouchi R, Martın F, Ramos-Barrado JR, Leinen D, Compositional, structural and electrical characterization of barium titanate thin films prepared on fused silica and Si(111) by spray pyrolysis, (2000) Surf Interface Anal 30:565–569
14. Mukhopadhyay SM, Chen TCS, Surface chemical states of barium titanate: Influence of sample processing, (1995) J Mater Res 10:1502–1507
15. Wada S, Suzuki T, Noma T, Role of lattice defects on size effect of barium titanate particles, (1996) J Ceram Soc Jpn 104:383–392
16. Wada S, Chikamori H, Noma T, Suzuki T, Tsurimi T, Synthesis and characterization of nanometer-order barium titanate single crystal particles using an improved low temperature direct synthesis method, (2000) J Ceram Soc Jpn 108:728–735

Chapter 27
Near Infrared Photoluminescence of Nd-Doped ZBP Glasses

Irena Kostova, Farley Chicilo, Tinko Eftimov, Georgi Patronov, Dan Tonchev, and Safa Kasap

Abstract In this work we report on a study of a series of zinc-borophosphate (ZBP) glasses doped with neodymium oxide (Nd_2O_3). The synthesis of the samples was performed by a high temperature melt quenching procedure in an air atmosphere. We present a complex photoluminescence study on a series of (72.31-*x*) ZnO-18B_2O_3-9.69P_2O_5-*x*Nd_2O_3 glasses doped with trivalent neodymium oxide (with concentration *x*) in a range 0.15–1.00 mol%) to explore possible applications. The excitation and luminescence properties were measured, and the photoluminescence was studied within the spectral range from 200 nm to 950 nm under different excitation wavelengths. Emission spectra in the 850–1500 nm range were obtained under an excitation wavelength of 808 nm. We have also measured the thermal properties by differential scanning calorimetry (DSC). A strong emission peak is observed at 1060 nm with a width of 30 nm and an exponential decay with a characteristic

I. Kostova (✉)
Department of Chemical Technology, Plovdiv University "Paisii Hilendarski", Plovdiv, Bulgaria

Photonics Research Center at the Université du Québec en Outaouais in Gatineau, Gatineau, Québec, Canada

F. Chicilo · S. Kasap
Department of Electrical and Computer Engineering, University of Saskatchewan, Saskatoon, SK, Canada

T. Eftimov
Photonics Research Center at the Université du Québec en Outaouais in Gatineau, Gatineau, Québec, Canada

G. Patronov
Department of Chemical Technology, Plovdiv University "Paisii Hilendarski", Plovdiv, Bulgaria

D. Tonchev
Department of Chemical Technology, Plovdiv University "Paisii Hilendarski", Plovdiv, Bulgaria

Department of Electrical and Computer Engineering, University of Saskatchewan, Saskatoon, SK, Canada

P. Petkov et al. (eds.), *Nanoscience and Nanotechnology in Security and Protection against CBRN Threats*, NATO Science for Peace and Security Series B: Physics and Biophysics, https://doi.org/10.1007/978-94-024-2018-0_27

time of 95 μs. The results of a series of Nd-doped zinc-borophosphate glasses show potential as a medium for solid state infrared laser applications.

Keywords Zinc-borophosphates · Near infrared · Photoluminescence · Nd-doped glasses

27.1 Introduction

There is an ongoing interest in glass materials doped with rare earth (RE) ions for laser applications. Many glass materials are a good host matrix for rare earth ions and are easily fabricated, when compared to single crystals. For example, in some applications Nd:YAG laser crystals have been successfully replaced by Nd-doped glasses [1]. The Nd:YAG crystal produces laser output primarily at 1064 nm; whereas the Nd:glass medium lases at wavelengths ranging from 1054 to 1056 nm, depending on the type of glass used. Nd ions in YAG crystals are limited to a maximum concentration of 1.0–1.5% [2]. Higher concentration leads to increased collision decay, resulting in a reduced laser upper level lifetime. At room temperature, the 1064 nm radiative transition is homogeneously broadened with a narrow emission line width of 0.45 nm and the upper level lifetime is 230 μs. Nd:YAG rods have good heat conduction properties, which make them desirable for high-repetition rate ion laser operation. These have a disadvantage, however, since they are limited by crystal growth capabilities to small laser rods with sizes up to 1 cm in diameter and lengths of the order of 10 cm. Doping YAG with neodymium results in a blue to violet crystals. Comparatively, Nd can be doped to very high concentrations in glass and many types of phosphate and silicate glasses have been used for lasers. The outstanding practical advantage compared to crystalline materials is the tremendous size capability for high-energy applications. For Nd:glass laser gain media, very large-size materials have been produced. These can be fabricated into special laser configurations such as slabs and fibers as well as with standard rod designs. Rods of up to 2 m length and 0.75 m in diameter and disks of up to 0.05 m in thickness have been successfully demonstrated [1, 2]. The optical quality can be excellent, and beam angles approaching the diffraction limit can be achieved. The glass is easily fabricated and can be produced to a good optical finish. The photoluminescence lifetime is approximately 300 μs, and the emission line width 18–28 nm, wider than that of Nd:YAG. This increased emission line width (inhomogeneous broadening) in effect reduces the laser gain. The drawback of Nd:glass laser materials is their relatively poor thermal conductivity, which restricts these lasers to relatively low pulse repetition rates for pulsed lasers and a lower operating power for CW lasers [2–4].

Phosphate glasses doped with rare earths have been studied and fabricated in the past. Long photoluminescence lifetimes associated with these Nd:glass materials make it easy to accumulate high-energy-level Nd^{3+} ions, and the glasses can be easily made into a variety of sizes with excellent optical uniformity. Rare earth

doped glass materials have been used in laser nuclear fusion, high-power laser amplifiers, waveguide lasers, medium and small energy devices, and optical fiber communications. The Nd:glasses of interest include silicate, borate [5] silico-phosphate, aluminates, fluorophosphate [6], zinc-phosphatate [7] and chalcogenide glasses [14].

Zinc borophosphate glasses (ZBP) with high concentrations of zinc oxide (up to 70 mol%) are perspective materials for laser media due to proven thermo-physical characteristics and desirable host matrix properties. This material is non-hygroscopic and water durable, superior to the phosphate glasses. They have glass transition temperature (T_g) in the range of 520–530 °C depending on the concentration of rare earth (RE) dopants [8–10]. In this work, we report on the synthesis and optical properties of materials from the glass system (72.31-x)ZnO-18B_2O_3-9.69P_2O_5-$x$$Nd_2O_3$.

27.2 Materials and Methods

27.2.1 Synthesis of Nd-Doped Glasses

The synthesis of Nd-doped ZBP glasses was performed by a conventional melt-quenching procedure at a temperature of 1100 °C for 2 h in a zirconium furnace (Zircar 1100). The starting reagents ZnO, B_2O_3, P_2O_5 and Nd_2O_3 (all purchased from Alfa Aesar) were mixed and placed in alumina crucibles in a furnace at a room temperature. Afterwards, heating rate of approximately 18 °C/min was applied until a temperature of 1100 °C was reached. The melts were quenched at room temperature and then tempered at 250 °C for 2 h. The compositions of the glasses in mol% used in this work are given in Table 27.1.

27.2.2 Methods of Analysis

For the DSC Thermal Analysis, TA Instrument DSC Q100 with attached Fast Air Cooling System (FACS) was used at heating rates of 5 °C/min. Absorption/transmission measurements were preformed using a USB2000 Ocean Optics

Table 27.1 List of Neodymium doped ZBP samples

Sample	Composition (mol%)			
	ZnO	B_2O_3	P_2O_5	Nd_2O_3
1	72.16	18	9.69	0.15
2	72.06	18	9.69	0.25
3	71.81	18	9.69	0.50
4	71.56	18	9.69	0.75
5	71.31	18	9.69	1.00

spectrometer (350 nm–1100 nm) in combination with a Micropack Halogen lamp source HL-2000. Small pieces of glass samples were polished to a thickness of 3.2 mm with 15 μm and 9 μm particle sized sandpaper for the measurement of absorption spectra.

The excitation-emission measurements and the corresponding three-dimensional photoluminescence plots were taken using Energetiq LDLS laser driven white light source in combination with an Ocean Optics scanning monochromator MonoScan 2000 and an Ocean Optics 9500 spectrometer.

Photoluminescence (PL) emission spectra were obtained using a laser diode with a wavelength of 808 nm and the photoluminescence was collected using a Cornerstone 1/8 m monochromator with a holographic grating of 1200 lines/mm and an InGaAs cooled detector.

Lifetime measurements were collected using the same 808 nm excitation source and a mechanical chopper to modulate the excitation source with a frequency of 325 Hz. The decay of the signal was registered using a InGaAs detector and the PL decay was measured using an oscilloscope (PicoScope).

27.3 Results and Discussion

The prepared glass samples were fully transparent with a typical violet-blue color due to neodymium ions (Nd^{3+}) and homogenous without gas bubbles. The structural properties and the general physical and chemical characteristics of ZBP glass matrix have been studied in detail previously [8–10]. Here we present the results from the study of the thermal and optical properties of these ZBP glasses doped with Nd_2O_3 as listed in Table 27.1.

27.3.1 Thermal Analysis

Thermal analysis measurements were performed in the temperature range of 40–600 °C. The results show a glass transition temperature (T_g) around 530 °C for all samples as shown in Fig. 27.1, which indicates the thermal stability of the glass matrix. There is no observed dependence of the glass transition temperature of the concentration of Nd_2O_3.

27.3.2 Absorption Spectra

The room temperature absorption spectra of the samples were recorded within the range of 350–1100 nm. As can be seen in Fig. 27.2, the highest absorption intensity was registered for the sample with the highest Nd_2O_3 content (1 mol%).

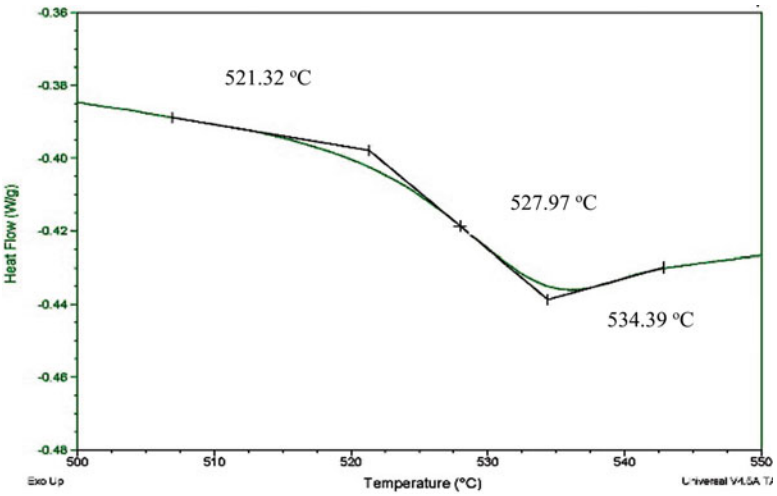

Fig. 27.1 A typical thermogram (heat flow vs sample temperature) for Sample 1 (Nd_2O_3 0.15 mol % conc)

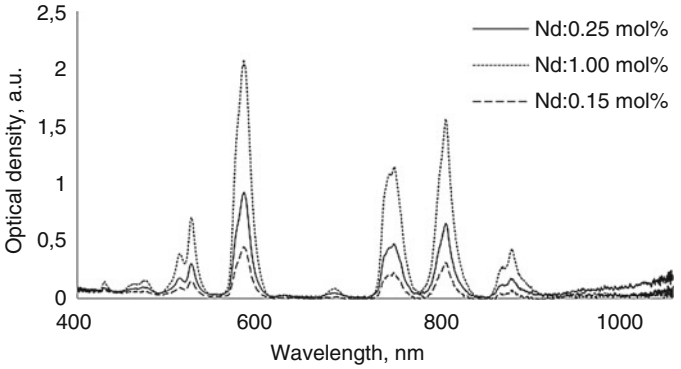

Fig. 27.2 Absorption spectra of Nd:ZBP samples (3.2 mm in thickness)

Three high intensity peaks at 582 nm, 748 nm and 804 nm, as well as several low intensity peaks were observed in the spectra. From this set of data and the published spectral work on Nd^{3+} ions, one can assign the transitions shown in Table 27.2 to the various peak wavelengths. The high intensity absorption peak around 808 nm corresponds to the $^4F_{5/2}$ level. From level $^4F_{5/2}$, the ions drop to level $^4F_{3/2}$ without radiation. Therefore, the pumping transition ($^4I_{9/2}$ to $^4F_{5/2}$) occurs over two levels different from those of the laser transition ($^4F_{3/2}$ to $^4I_{11/2}$).

Table 27.2 Absorption channels and the respective transitions in Nd^{3+}-doped materials [11, 12]

Absorption channels	Transitions
λ, nm	absorption levels
430	$^4I_{9/2} \rightarrow {}^2P_{1/2}$
476	$^4I_{9/2} \rightarrow {}^4G_{11/2} + {}^2G_{9/2} + {}^2D_{3/2} + {}^2K_{15/2}$
513–526	$^4I_{9/2} \rightarrow {}^4G_{7/2} + {}^4G_{9/2} + {}^2K_{13/2}$
582	$^4I_{9/2} \rightarrow {}^4G_{5/2} + {}^2G_{7/2}$
628	$^4I_{9/2} \rightarrow {}^2H_{11/2}$
684	$^4I_{9/2} \rightarrow {}^4F_{9/2}$
748	$^4I_{9/2} \rightarrow {}^4F_{7/2} + {}^4S_{3/2}$
804	$^4I_{9/2} \rightarrow {}^4F_{5/2} + {}^2H_{9/2}$
877	$^4I_{9/2} \rightarrow {}^4F_{3/2}$

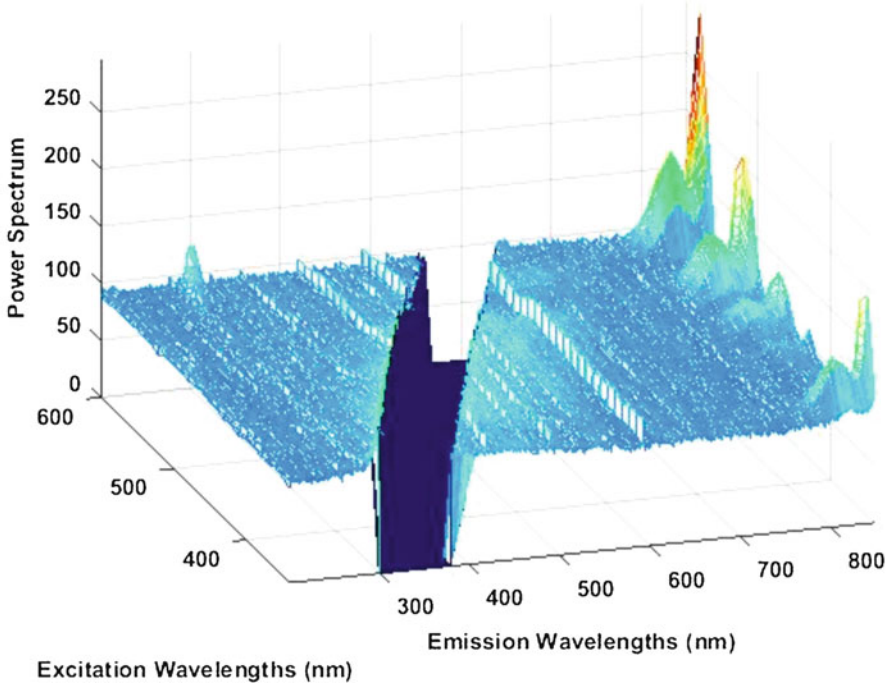

Fig. 27.3 3D PL graph in the spectral range of 350–600 nm

27.3.3 Photoluminescence Spectra

The photoluminescence spectra were recorded in the reange of 350–1100 nm. The 3D view graphs in the spectral ranges of 350–600 nm and 600–820 nm are given in Figs. 27.3 and 27.4, where the spectral power of the emission is plotted at different excitation wavelengths. The figures show high efficiency excitation wavelengths at

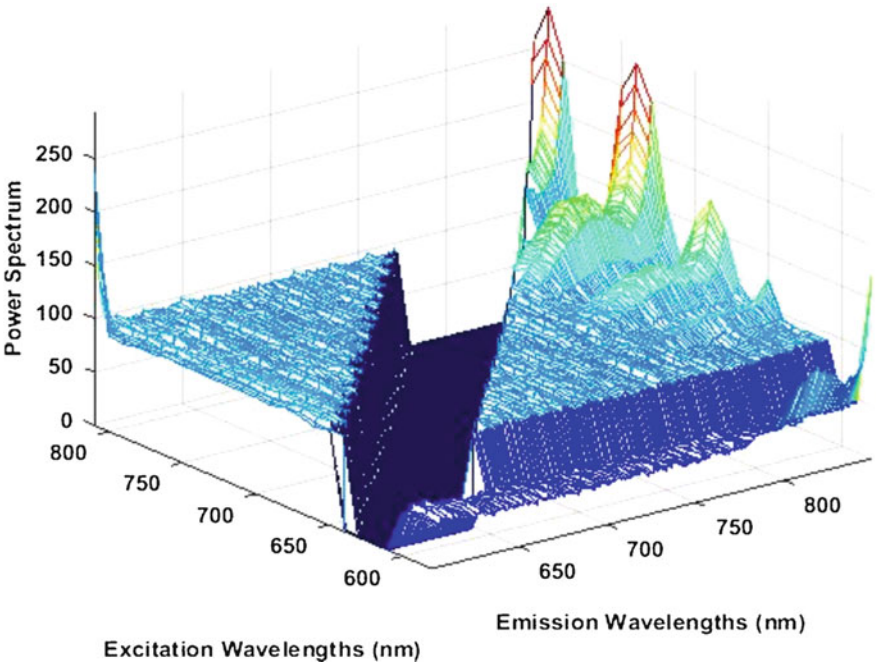

Fig. 27.4 3D PL graph in the spectral range of 600–820 nm

580, 750 and 804 nm. The maximum emission in this region is at 900 nm corresponding to the transition $^4F_{3/2} \rightarrow {}^4I_{9/2}$.

The electron transition at 900 nm in these Nd-doped glasses is one of the four emission signals with a pumping source in the 800 nm region; the others are at 1061 nm, around 1100 nm and around 1300 nm. When the transition around 900 nm is used, Nd-doped material (for example Nd:YAG with a peak at 946 nm) is a quasi-three-level gain medium, requiring significantly higher pump intensities. All other transitions are four-level transitions [13].

The photoluminescence spectrum measured in the 850–1500 nm range from one of the Nd:ZBP glasses excited at 808 nm is shown in Fig. 27.5. The emission peaks at 900, 1060 and 1330 nm can be seen, which correspond to the following laser transitions, $^4F_{3/2} \rightarrow {}^4I_{9/2}$, $^4F_{3/2} \rightarrow {}^4I_{11/2}$, and $^4F_{3/2} \rightarrow {}^4I_{13/2,}$ respectively. The emission which corresponds to the $^4F_{3/2} \rightarrow {}^4I_{11/2}$ transition has a relatively sharp emission peak, with an approximate full width at half maximum (FWHM) of 30 nm, as seen in Fig. 27.5. The photoluminescence decay was measured for each emission peak and in all cases an exponential decay characteristic with a decay time of 95 μs was observed, which agrees with the results previously reported for Nd^{3+}-doped glasses [14], shown in the inset of Fig. 27.5.

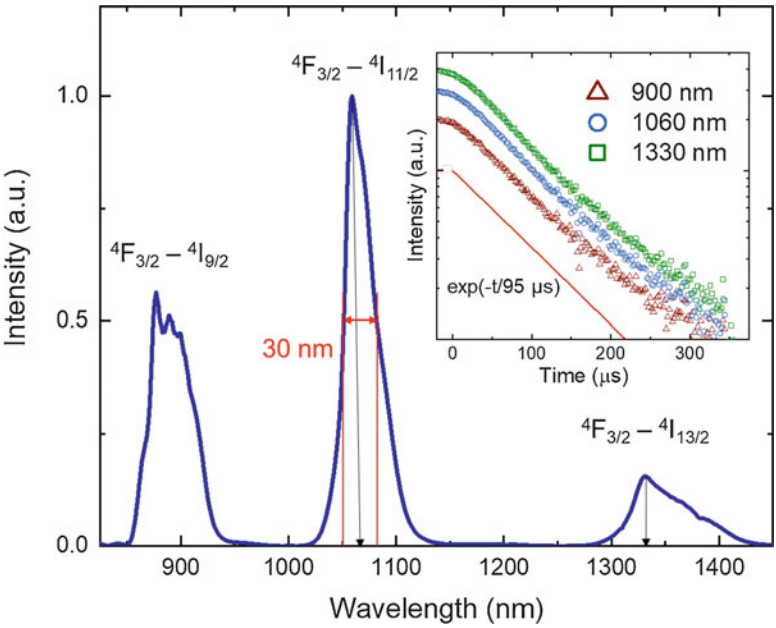

Fig. 27.5 Photoluminescence spectrum of Sample 5 (1 mol% Nd_2O_3) in the range of 850–1500 nm using an excitation source of 808 nm. Inset in the graph shows the measured lifetimes of the $^4F_{3/2} \rightarrow {}^4I_{9/2}$, $^4F_{3/2} \rightarrow {}^4I_{11/2}$, and $^4F_{3/2} \rightarrow {}^4I_{13/2}$ transitions (900, 1060 and 1330 nm, respectively). The solid line is a guide corresponding to the exponential decay with a lifetime of 95 µs

27.4 Conclusions

In this work we present the synthesis of a series of Nd-doped samples from the system (72.31-*x*) ZnO-18B_2O_3-9.69P_2O_5-*x*Nd_2O_3. These glasses are fully transparent and homogenous with a blue-violet color, typical for the glasses with neodymium ions. The glass samples have high thermal stability (glass transition temperature $T_g = 530$ °C) and water durability. The recorded absorption spectra of the Nd:ZBP glass samples show the possible energy transitions of the Nd^{3+} ion including the laser transition $^4F_{3/2} \rightarrow {}^4I_{11/2}$. In the spectral range of 200–1100 nm infrared peaks are observed at 900 nm ($^4F_{3/2} \rightarrow {}^4I_{9/2}$). From the photoluminescence and absorption analyses and 3D excitation and emission plots, the most effective excitation wavelengths were found to be at 580, 750 and 804 nm, corresponding to the most intensive peaks in the absorption spectra. The photoluminescent spectra in 850–1500 nm region shows three emission peaks at 900, 1060 and 1330 nm, which correspond to the laser transitions $^4F_{3/2} \rightarrow {}^4I_{9/2}$, $^4F_{3/2} \rightarrow {}^4I_{11/2}$, and $^4F_{3/2} \rightarrow {}^4I_{13/2}$, respectively. The most intense peak at 1060 nm has a FWHM of 30 nm and an exponential decay with a characteristic time of 95 µs. The results for the studied Nd^{3+}-doped zinc-borophosphate glasses show their potential as a medium for solid state infrared laser applications.

Acknowledgments We are grateful to the National Program of the Ministry of Education and Science "Young Scientists and Postdoctoral Students", Bulgaria.

References

1. Campbell JH (1996) Recent advances in phosphate laser glasses for high-power applications, Proceedings of the SPIE 10286, Inorganic Optical Materials: A Critical Review, 1028602 (August 1996). https://doi.org/10.1117/12.245185
2. Semwal K, Bhatt SC (2013) Study of Nd3+ ion as a dopant in YAG and glass laser. Int J Theor Phys 1(1):15–21. https://doi.org/10.12691/ijp-1-1-3
3. Marshall LR, Hays AD, Kasinski HJ, Burnham R (1991) Highly efficient optical paramet-ric oscillators. SPIE 1419:141–152. https://doi.org/10.1117/12.43855
4. Stultz RD et al (1991) In: Johnson AM (ed) Eyesafe lasers: components, systems, and applications, vol 1419. Bellingham, SPIE, p 64. https://doi.org/10.1117/12.43847Optics, electro-optics, and laser applications in science and engineering, Los Angeles, CA, United States, January 1991. Eyesafe high-pulse-rate laser progress at Hughes, Proc. SPIE
5. Parandamaiah M, Venkatramana Reddy MS, Chandrasekhar AV (2016) Int J Adv Res Sci Eng Technol 3:9
6. He D, Kang S, Zhang L, Chen L, Ding Y, Yin Q, Hu L (2017) Research and development of new neodymium laser glasses. High Power Laser Sci Eng 5(e1):1–6. https://doi.org/10.1017/hpl.2016.46
7. Mahraz ZAS, Sazali ES, Sahar MR, Amran NU, Yaacob SNS, Aziz SM, Mawlud SQ, Noor FM, Harun AN (2019) Spectroscopic investigations of near-infrared emission from Nd3 +−doped zinc-phosphate glasses: Judd-Ofelt evaluation. J Non-Cryst Solids 509:106–114. https://doi.org/10.1016/j.jnoncrysol.2018.05.013
8. Patronov G, Kostova I, Tonchev D (2017) Bul Chem Comm A 49:40–45
9. Kostova I, Patronov G, Tonchev D (2018) J Chem Technol Metall 53(6):1087–1094
10. Patronov G, Kostova I, Tonchev D (2019) Abstracts of the 28th International Conference On metallurgy and materials – metal 2019, Brno, 22–24 May 2019
11. Ramos-Lara F, Ramírez MO, Flores M, Arroyo R, Caldiño U (2006) Optical spectroscopy of Nd3+ ions in poly(acrylic acid). J Phys Condens Matter 18(34):7951–7959. https://doi.org/10.1088/0953-8984/18/34/008
12. Da Gama AAS, de Sá GF, Porcher P, Caro P (1981) Energy levels of Nd3+ in LiYF4. J Chem Phys 75(6):2583–2587. https://doi.org/10.1063/1.442410
13. Chaoyang L, Yong B, Feng Y, Zhichao W, Yiting X, Yuanbin W, Hongwei G, Qinjun P, Dafu C, Zuyan X (2010) 106.5 W high beam quality diode-side-pumped Nd:YAG laser at 1123 nm. Opt Express 18:7923–7928. https://doi.org/10.1364/OE.18.007923
14. Koughia C, Soundararaja G, Kasap S, Allen T, Haugen C, Decorby R, Aoki NO, Fujihashi C (2009) Characterization of 4I9/2 ↔ 4F3/2 optical transitions in trivalent Nd3+ ions in Ga-LaS glass. J Mater Sci Mater Electron 20(Suppl 1):19–22. https://doi.org/10.1007/s10854-007-9423-1

Chapter 28
Determination of the Surface Properties of Combined Metal-Oxide Layers, Obtained by AC-Incorporation of Ni and Cu in Preliminary Formed AAO Matrices

Christian Girginov, Stephan Kozhukharov, and Boriana Tzaneva

Abstract Since anodization of aluminum is the most conventional method for obtaining highly ordered surface matrices, this method has been an object of great scientific interest over the last decades. In addition, these highly ordered anodized aluminium oxide (AAO) layers can efficiently protect the metallic substrates against corrosion in aggressive media and can be successfully used as primers for advanced multilayered corrosion protective coatings. An additional important advantage of these films is the possibility to incorporate various metals, in order to modify the AAO composition and surface properties. Furthermore, the resulting Al-O-Metal systems enable the subsequent chemical deposition of a variety of metallic and semiconductor layers, resulting in formation of layered conjunctions with valuable properties. In this sense, the present research presents results of an evaluation of the surface properties of Ni and Cu containing AAO layers, obtained by AC-electrochemical incorporation. The respective modified AAO layers are obtained from aqueous solutions. The surface topology of the obtained films, as well as some of their most important properties, such as color and spectral characteristics, barrier ability and hydrophobicity, were examined in order to define the mechanism and kinetics of metal incorporation.

Keywords AAO layers · Ni and Cu incorporation · Spectral characteristics · Barrier properties · Hydrophobicity

C. Girginov (✉)
Laboratory for Advanced Materials Research, University of Chemical Technology and Metallurgy, Sofia, Bulgaria
e-mail: girginov@uctm.edu

S. Kozhukharov
Department of Physical Chemistry, University of Chemical Technology and Metallurgy, Sofia, Bulgaria

B. Tzaneva
Department of Chemistry, Technical University, Sofia, Bulgaria

P. Petkov et al. (eds.), *Nanoscience and Nanotechnology in Security and Protection against CBRN Threats*, NATO Science for Peace and Security Series B: Physics and Biophysics, https://doi.org/10.1007/978-94-024-2018-0_28

28.1 Introduction

Anodization of aluminum is the most conventional method for obtaining highly ordered oxide matrices [1–3]. In comparison to other technological approaches, it does not require specific equipment, such as vacuum chambers, laser sources, etc. In addition, these highly ordered anodized aluminium oxide (AAO) layers can efficiently protect the aluminum surface against corrosion [4, 5] and can be used as primers for advanced multilayered corrosion protective coatings.

Another important advantage of these films is the possibility to incorporate various metals, in order to modify the AAO composition and surface properties [6]. Furthermore, the resulting Al-O-Metal systems enable the subsequent chemical deposition of a variety of metallic and semiconductor layers, resulting in formation of layered conjunctions with valuable properties. In this sense, special attention is paid to the incorporation of transition elements in the AAO pores. This approach enables the creation of active layers which can change their chemical composition and physical properties in contact with reducing or oxidizing environments. Undoubtedly, such layers can be successfully used as catalysts and sensing elements. Indeed, several authors have published successful synthesis of doped Ni/Al_2O_3 [7–16] and $NiAl_2O_4$ spinel [17] catalysts. Further synthesized systems include Cu/Al_2O_3 [18–21] and copper alumina systems doped with Ce [22], Pt [23], Cs-Fe [24], Cs-Zn [25], Cu-Zn [26, 27], Zn-graphene [28], B_2O_3 [29], Co-Ni [30], Co-Ag-Pd [31], Mn [32, 33], etc. The great interest towards both Ni and Cu incorporated Al_2O_3 has led to intensive investigation of the catalytic activity of the combined (Cu-Ni-Al_2O_3)-systems [34–45]. On the other hand, the electrochemical deposition enables large scale production with relatively simple control of the (Ni/Cu)-O deposition conditions [7, 46], enabling formation on aluminum [47–51] and copper [52–56] substrates. In this sense, the current paper represents results of an evaluation of the surface properties of Ni and Cu containing AAO layers, obtained by AC-electrochemical incorporation. The respective modified AAO layers are obtained from aqueous solutions. Some of their most important properties, such as barrier ability, hydrophobicity, color and spectral characteristics, were examined in order to define the mechanism and kinetics of metal incorporation.

28.2 Experimental

28.2.1 Sample Preparation

Eight samples of aluminum alloy AA1050 were anodized in 15% H_2SO_4 by applying galvanostatic polarization (15 mA cm^{-2}) for 50 min at 20 °C. Before anodization, preliminary surface treatment was performed, which included etching in NaOH solution (50 g dm^{-3}) for 2 min at 60 °C and subsequent activation in

Table 28.1 Incorporation conditions of the prepared samples

Sample type	Electrolyte composition
Referent (2 samples)	Porous Al_2O_3 matrixes
Cu-incorporated (2 samples)	0.4 Mol dm^{-3} $CuSO_4$ 30 g dm^{-3} $(NH_4)_2SO_4$ 50 g dm^{-3} H_3BO_3
Ni-incorporated (2 samples)	0.4 Mol dm^{-3} $NiSO_4$ 30 g dm^{-3} $(NH_4)_2SO_4$ 50 g dm^{-3} H_3BO_3
(cu + Ni)-incorporated (2 samples)	0.2 Mol dm^{-3} $CuSO_4$ + 0.2 Mol dm^{-3} $NiSO_4$ 30 g dm^{-3} $(NH_4)_2SO_4$ 50 g dm^{-3} H_3BO_3

diluted nitric acid (HNO_3:H_2O – 1:1) for 2 min at room temperature with final vigorous washing with both tap and double distilled water.

Afterwards, these samples underwent subsequent metal incorporation in different solutions, in order to obtain four sets of two samples each. The compositions and the conditions of incorporation are given in Table 28.1.

Regardless of electrolyte composition, the incorporation was performed for 15 min at 20 °C in conditions of AC polarization at 60 Hz with defined voltage of 20 V.

28.2.2 Surface Characterization

The above-described specimens were subjected to systematic analyses, in order to distinguish their surface properties in respect to the incorporated metal. These characterizations comprised determination of the color characteristics, the hydrophobicity and their electrochemical properties.

Color characteristic determination: The color characteristics were determined using a Lovibond RT-100 reflectance tintometer, product of "Paragon Scientific Ltd. (UK)", according to the CIE (L^*,a^*,b^*) color space. This color space is based on 3D plots, composed of brightness (L^*), green-red tonality (a^*) and yellow-blue hue vectors (b^*).

Sessile drop tests: The surface hydrophobicity was determined by Theta Lite Optical Contact Angle Meter, product of "Dynatesting Co. (UK)". The contact angle was determined immediately after falling of a drop of distilled water with 0.10 ml of volume from Gastight-1001 type syringe, product of "Hamilton (Nevada, USA)", mounted 1.0 cm above the surface of the sample.

Electrochemical characterizations: All samples were subjected to comparative electrochemical measurements after 24 h of exposure to a 0.01 M NaCl solution, using an Autolab PGStat 30 potentiostat/galvanostat of "Metrohm (Netherlands)" equipped with FRA-2 frequency response analyzer. These measurements were

performed in a standard, three electrode "flat" cell (ISO 16773-2), equipped with a platinum mesh as a counter electrode and a Ag/AgCl/3 M KCl reference electrode. Test areas (2 cm^2) from the specimens served as working electrodes. The measurements included electrochemical impedance spectroscopy (EIS) and potentiodynamic scanning (PDS). The EIS spectra were acquired in the frequency range from 10 kHz to 0.01 Hz, distributed in 50 measurement points. The excitation signal amplitude was 35 mV regarding the open circuit potential (OCP), in order to acquire readable spectra. The PDS measurements were based on curves acquisition (from −60 to +600 mV vs. OCP) at a sweep rate of 10 mV s^{-1}.

All measurements were performed twice, in order to determine both repeatability and reproducibility of the obtained results, thus avoiding execution of a large number of measurements. The results in all tables below are represented in the following form:

$$\mathrm{AV} = \left(\frac{\mathrm{MV}_1 + \mathrm{MV}_2}{2}\right) \pm \left(\frac{\mathrm{MV}_1 - \mathrm{MV}_2}{2}\right) \tag{28.1}$$

where AV is the average value, MV_1 (the higher value) and MV_2 (the lower value) the measured values during the first and the second measurements, respectively.

The electrochemical measurements were performed just once for each sample, since the obtained EIS spectra were completely identical and there was no need for further measurements. Besides, the potentiodynamic scans could not be repeated, due to simultaneous polarization of the electrodes, caused by the gradual potential input signal.

28.3 Results and Discussion

28.3.1 Color Characteristics

Systematic measurements were performed in order to determine the impact of the Cu, Ni and Cu + Ni incorporation on the outlook of the resulting samples. These measurements were performed according to the CIE ($L^*a^*b^*$) color space (Fig. 28.1). The respective results are presented in Table 28.2.

The data in Table 28.2 reveal that the Cu-incorporation results in an obvious darkening of the almost white anodized oxide layer to a definitive grey. This effect is even more pronounced during Ni incorporation, which converts the light anodized layer to almost black. This color change was observed for the combined samples (Cu + Ni), as well. The deviation of the rest color parameters is almost indistinguishable, tending to zero in all cases. A unique exception appears during copper incorporation. In this case, the parameter a^* was shifted towards the yellow tonality. Indeed, these samples revealed clear brownish hue, due to their coincident darkening and yellowing. These simultaneous color changes of the Cu-incorporated samples reveal that copper is more probably in both oxidized forms: CuO (black) and Cu_2O

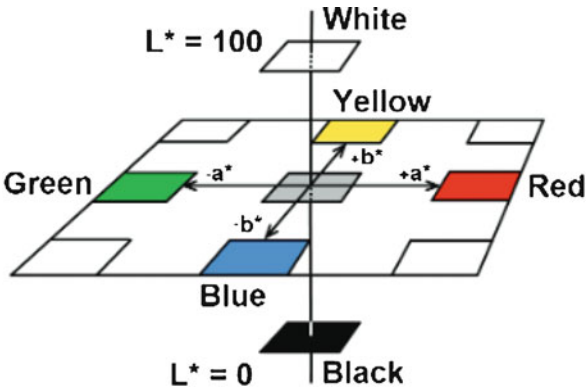

Fig. 28.1 Illustration of the CIE ($L^*a^*b^*$) color determination system. Reprinted with permission from [57]

Table 28.2 Results of the color determinations

	Sample 1	Sample 2
References	$L^* = 89.21 \pm 0.34$ $a^* = -0.40 \pm 0.02$ $b^* = 2.34 \pm 0.02$	$L^* = 88.20 \pm 0.25$ $a^* = -0.38 \pm 0.04$ $b^* = 2.35 \pm 0.05$
(Cu)-incorporation	$L^* = 56.91 \pm 0.19$ $a^* = 1.21 \pm 0.15$ $b^* = 16.80 \pm 0.36$	$L^* = 54.62 \pm 0.51$ $a^* = 0.77 \pm$ n.a.# $b^* = 16.35 \pm 1.31$
(Ni)-incorporation	$L^* = 19.53 \pm 0.01$ $a^* = 1.24 \pm 0.04$ $b^* = 0.18 \pm 0.16$	$L^* = 19.03 \pm 0.04$ $a^* = 0.19 \pm 0.10$ $b^* = -0.25 \pm 0.12$
(Cu/Ni)-incorporation	$L^* = 17.87 \pm 0.08$ $a^* = -0.14 \pm 0.08$ $b^* = -0.51 \pm 0.24$	$L^* = 18.30 \pm 0.10$ $a^* = -1.45 \pm 0.20$ $b^* = -1.77 \pm 0.21$

the marked deviation value is not determinable, because the MV2 in this case is equal to zero

(reddish). The applied anodic polarization (i.e. the negative semi-periods during the AC polarizations) promotes oxidation reactions, resulting in the formation of various metallic oxides, whereas the cathodic one (i.e. the positive semi-periods) results in reverse reduction of the already oxidized CuO.

Indeed, the converting into black color for the Ni-incorporated specimens evinces that this element is probably in the form of black Ni_2O_3, and the absence of any change in the color parameter b^* shows only insignificant traces or even complete absence of NiO.

The color related characteristics are a consequence of the reflectance spectra in the visible wavelength range, which confirms the obvious difference among the respective groups of samples (Fig. 28.2).

The reference samples show a high reflectance in the entire visible spectrum, resembling a white color. The opposite aptitude of maximal light absorbance was demonstrated by the Ni and mixed (Cu + Ni) samples. The samples incorporated with Cu exhibit intermediate reflectance. Their spectra reveal about 20% reflectance in the yellow-orange range, which gradually increases up to 40% in the red color

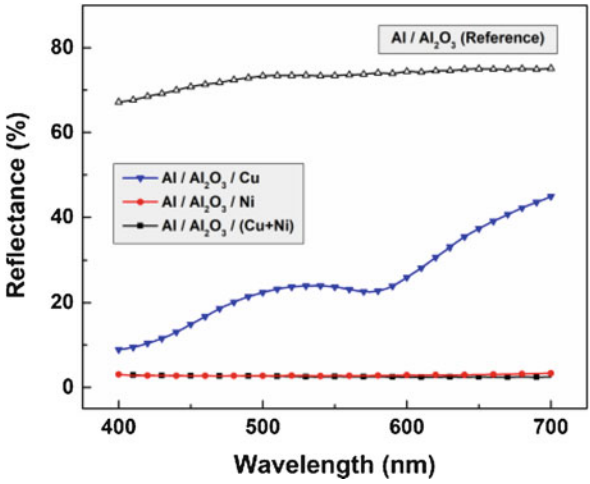

Fig. 28.2 Reflectance spectra acquired from the samples

range. Both lower reflectance values reveal that these samples are rather darker than the references due to the occurrence of black CuO. Further, the appearance of two maxima shows that this oxide is accompanied by two reduced forms: yellowish metallic copper and red Cu_2O.

28.3.2 Sessile Drop Tests

Since both types of treatment (anodization of AA1050 and Cu + Ni incorporation) are methods for surface modification, they result in changes of the surface properties. These changes originate from alteration of both morphology and composition of the treated surfaces. For this reason, sessile drop tests were performed in order to obtain supplemental information regarding the resulting surface hydrophobicity. Examples for the obtained drop test results are presented in Fig. 28.3.

The figure shows that the incorporation has no remarkable influence on the surface tension and all investigated samples remain definitely hydrophilic. Only Ni-incorporation results in a slightly more hydrophobic surface. That is the reason for the larger dissipation of the results for the combined Cu + Ni coating, which suggests the occurrence of domains with uneven Cu and Ni contents. These inferences are confirmed by the data in Table 28.3.

The data do not reveal any remarkable impact of metal incorporation on the surface hydrophobicity. All Cu, Ni and mixed (Cu + Ni) incorporated samples possess the same hydrophilic properties, like the reference ones. This fact is evidence for the preferential incorporation of metals inside the pores, as it was established in several works on silver incorporation [57–60]. Consequently, the surface of the anodized aluminum oxide (AAO) layer remains unchanged, being composed of hydrated Al_2O_3 and boehmite [61].

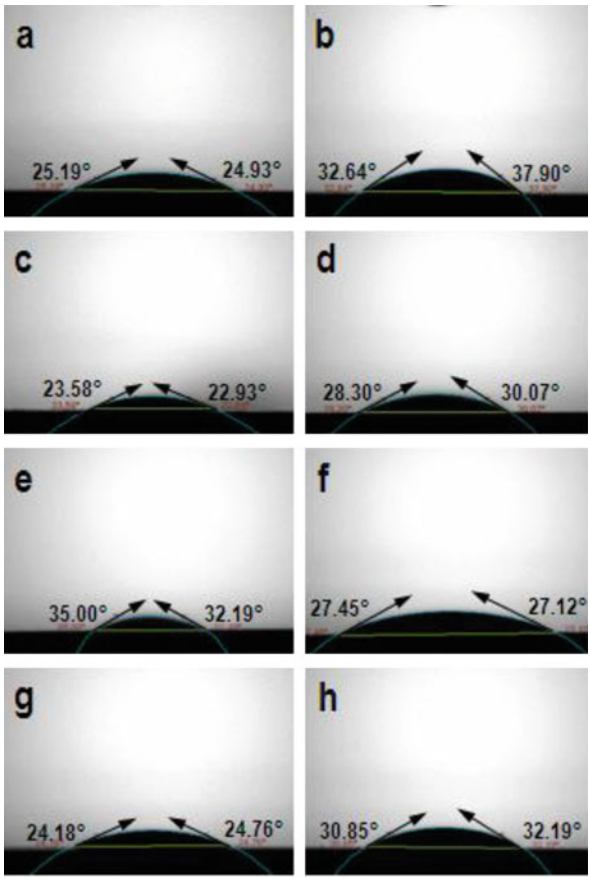

Fig. 28.3 Contact angles obtained for the anodized specimens: (**a**, **b**) reference; (**c**, **d**) after Cu incorporation; (**e**, **f**) after Ni incorporation; (**g**, **h**) after Cu + Ni incorporation

Table 28.3 Average values of the contact angles obtained from the samples

	Sample 1	Sample 2
References	25.65 ± 0.96	33.76 ± 0.56
Cu incorporation	23.11 ± 0.05	29.53 ± 2.97
Ni incorporation	33.07 ± 5.50	27.22 ± 2.97
Cu + Ni incorporation	24.40 ± 3.20	31.99 ± 3.53

28.3.3 Electrochemical Characterizations

The EIS data acquired after 24 h of exposure to a model corrosive medium (0.01 M NaCl solution) exhibit a definite capacitive behavior of the specimens due to the clearly formed anodic oxide films on their metallic surfaces. The incorporation of metals does not reveal any remarkable impact on the electrochemical characteristics of the (Cu + Ni)-O-Al films, as it can be seen from Fig. 28.4.

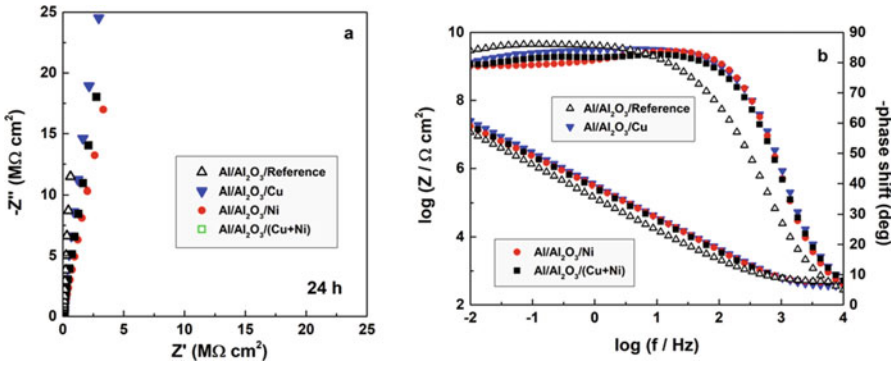

Fig. 28.4 Bode (**a**) and Nyquist (**b**) plots of the EIS spectra acquired from the respective samples

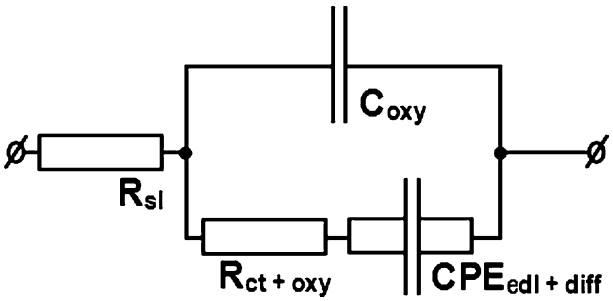

Fig. 28.5 Model equivalent circuit used for EIS data quantification

The obtained results were subjected to further analyses using a suitable model equivalent circuit (MEC). Since the spectra possess identical shapes, the results were interpreted with only one MEC, shown in Fig. 28.5.

Following the rule of thumb regarding the simplification of the MEC mentioned elsewhere [62, 63], it was composed by only one modified time constant (RC unit), associated with the solution resistance (R_{sl}). The MEC configuration used for the present research is a simplified version of that applied in previous works [4–6, 57, 59]. This time constant was composed of the pure capacitance of the dense barrier layer of the oxide (C_{oxy}), connected to the charge transfer resistance ($R_{(ct\ +\ oxy)}$), which includes the resistance of the solution, enclosed in the pores of the oxide layer as well. A constant phase element ($CPE_{(edl\ +\ diff)}$) was assigned to the detected additional incomplete capacitance. This element combines the electric double layer (edl) and the hindered diffusion (diff) of the electrolyte inside the pores of the oxide layer. Thus, the used MEC was composed suggesting an incomplete filling of the pores with Ni and Cu oxides. The solution penetration and diffusion are namely hindered by the capillary forces, resulting from the narrow cross-section of the pores. This suggestion is confirmed by the lack of any remarkable changes in the contact

angle before (reference samples) and after the metal incorporation. The obtained results are summarized in Table 28.4.

Although the impedance spectra look identical (Fig. 28.4), their analysis has revealed that the incorporation of metals results in a drastic change of the capacitance of the oxide layer from ~500 $pFcm^{-2}$ to about 266–348 $nFcm^{-2}$ after the incorporation. Another interesting phenomenon is the decrement of $R_{(oxy\ +\ ct)}$ for the combined Cu + Ni incorporated specimens with an entire order of magnitude, probably due to additional redox reactions between the respective Cu and Ni oxides inside the pores.

The potentiodynamic curves have shown that the oxide layer does not passivate the substrates completely, since the anodic branches possess a slope for all samples (Fig. 28.6).

Nevertheless, all potentiodynamic curves are situated at very low current densities, again showing that the anodization has a much more remarkable impact than the incorporation of metals. According to the reference samples, it looks that copper activates the AAO layer, whereas the Ni causes supplemental sealing of the layer. These results are confirmed by the *Tafel* slope analysis, whose data are summarized in Table 28.5.

Since the PDS method is not able to detect capacitance, unlike the EIS, it has revealed rather high values of the polarization resistance (R_p) reaching $10^7\ \Omega\ cm^2$, compared to the more than three orders of magnitude lower $R_{(ct\ +\ oxy)}$ values. Again, the R_p values for all samples look rather similar to each other.

Nevertheless, the corrosion potential (E_{corr}) values vary significantly in accordance to the incorporated metal. The registered E_{corr} values for all samples are shifted towards the reference electrode due to an Ohmic drop resulting from the high solution resistance. Thus, the Ni incorporation alters E_{corr} in negative direction, whereas the Cu incorporation shifts it in the opposite (positive) direction regarding the E_{corr} of the reference electrode.

This fact can be explained taking into account that copper is nobler than nickel [64]:

$$Cu^{2+} + 2e^- \rightarrow Cu^{\circ}, \qquad +337\ \text{mV vs. SHE} \tag{28.2}$$

$$Cu^{+} + e^- \rightarrow Cu^{\circ}, \qquad +521\ \text{mV vs. SHE} \tag{28.3}$$

$$Ni^{+2} + 2e^- \rightarrow Ni^{\circ}, \qquad -250\ \text{mV vs. SHE} \tag{28.4}$$

Finally, the E_{corr} values of the mixed (Cu + Ni)-O-Al films tend to these of Cu, revealing that this metal has a stronger impact on the resulting E_{corr} value.

Table 28.4 Values obtained from the analysis of the obtained EIS spectra

Anodized reference samples				
Element	Unit	Sample 1	Sample 2	Average
R_{sl}	$\Omega\ cm^2$	489.00 ± 4.34	503.00 ± 5.99	496 ± 5.17
C_{oxy}	$pF\ cm^{-2}$	551.00 ± 11.10	519.00 ± 16.95	535 ± 14.02
$R_{(oxy + ct)}$	$k\Omega\ cm^2$	2.61 ± 0.23	1.69 ± 0.22	2.15 ± 0.23
$Q_{(edl + diff)}$	$s^n\ (\Omega\ cm^2)^{-1}$	(66.13 ± 1.26) × 10^{-8}	(70.25 ± 1.85) × 10^{-8}	(68.19 ± 1.56) × 10^{-8}
n	–	0.90 ± 0.01	0.89 ± 0.01	0.90 ± 0.01
Anodized samples with copper incorporation				
Element	Unit	Sample 1	Sample 2	Average
R_{sl}	$\Omega\ cm^2$	441.00 ± 2.17	353.00 ± 2.32	397.00 ± 2.24
C_{oxy}	$pF\ cm^{-2}$	(282.20 ± 5.08) × 10^3	(312.60 ± 2.60) × 10^3	(297.0 ± 3.84) × 10^3
$R_{(oxy + ct)}$	$k\Omega\ cm^2$	1.72 ± 0.33	10.46 ± 1.17	6.09 ± 0.75
$Q_{(edl + diff)}$	$s^n\ (\Omega\ cm^2)^{-1}$	(26.22 ± 0.54) × 10^{-8}	(22.28 ± 0.31) × 10^{-8}	(24.25 ± 0.43) × 10^{-8}
n	–	0.84 ± 0.01	0.84 ± 0.01	0.84 ± 0.01
Anodized samples with nickel incorporation				
Element	Unit	Sample 1	Sample 2	Average
R_{sl}	$\Omega\ cm^2$	404.00 ± 4.76	449.00 ± 3.59	426.50 ± 4.18
C_{oxy}	$pF\ cm^{-2}$	(277.80 ± 7.63) × 10^3	(348.00 ± 3.00) × 10^3	(312.90 ± 5.32) × 10^3
$R_{(oxy + ct)}$	$k\Omega\ cm^2$	3.17 ± 0.04	6.02 ± 0.07	4.60 ± 0.05
$Q_{(edl + diff)}$	$s^n\ (\Omega.cm^2)^{-1}$	(43.04 ± 0.92) × 10^{-8}	(30.72 ± 0.43) × 10^{-8}	(36.88 ± 0.68) × 10^{-8}
n	–	0.77 ± 0.01	0.75 ± 0.01	0.76 ± 0.01
Anodized samples with combined (cu/Ni)- incorporation				
Element	Unit	Sample 1	Sample 2	Average
R_{sl}	$\Omega\ cm^2$	425.00 ± 0.81	461.00 ± 1.80	443.00 ± 1.30
C_{oxy}	$pF\ cm^{-2}$	(266.00 ± 3.78) × 10^3	(240.10 ± 6.00) × 10^3	(253.05 ± 4.89) × 10^3
$R_{(oxy + ct)}$	$k\Omega\ cm^2$	(229.00 ± 21.76) × 10^{-3}	(452.00 ± 67.35) × 10^{-3}	(340.50 ± 44.56) × 10^{-3}
$Q_{(edl + diff)}$	$s^n\ (\Omega\ cm^2)^{-1}$	41.34 ± 0.40	41.45 ± 0.63	41.40 ± 0.52
n	–	0.86 ± 0.01	0.84 ± 0.01	0.85 ± 0.01

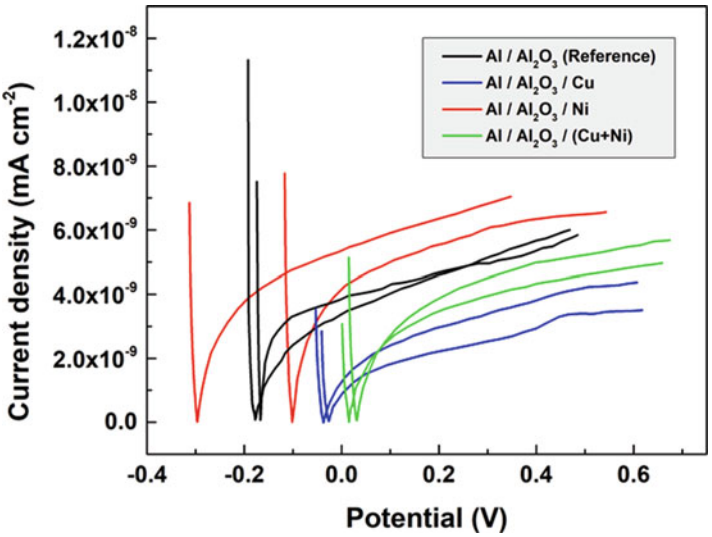

Fig. 28.6 Potentiodynamic curves obtained after 24 h of exposure to 0.01 M NaCl solution

Table 28.5 Results of the analysis of the polarization curves

Sample 1		Sample 2		Average	
Anodized reference samples					
E_{corr} (Vvs.Ag/AgCl)	R_p (MΩ cm^2)	E_{corr} (Vvs. Ag/AgCl)	R_p (MΩ cm^2)	E_{corr} (V vs. Ag/AgCl)	R_p (MΩ cm^2)
−0.168	14.80	−0.166	3.01	−0.167 ± 0.01	8.91 ± 5.90
Anodized samples with copper incorporation					
−0.036	14.99	−0.027	14.90	−0.030 ± 0.05	14.95 ± 7.48
Anodized samples with nickel incorporation					
−0.106	8.14	−0.297	7.02	−0.202 ± 0.096	7.58 ± 0.56
Anodized samples with combined incorporation					
−0.015	12.20	−0.030	9.26	−0.023 ± 0.08	10.73 ± 1.47

28.4 Conclusions

The present work summarizes results of systematic elucidation of the surface properties of Cu, Ni and Cu + Ni containing AAO layers, obtained by AC-electrochemical incorporation. The barrier ability, hydrophobicity, color and spectral characteristics were examined, in order to define the metal incorporation mechanism and kinetics. The color characterizations reveal that the incorporation results in obvious darkening of the almost white AAO layer to definite grey after Cu-incorporation, whereas the incorporation of Ni converts the color of the oxide layer to almost black. This color change remains for the combined (Cu + Ni) samples, as well. The changes in the rest color parameters remain almost

indistinguishable, tending to zero in all cases. Only the addition of copper leads to a clear brownish hue, due to the coincident darkening and yellowing, probably due to the occurrence of metallic Cu (orange), Cu_2O (reddish) and CuO (black). The black color of the Ni-incorporated specimens shows the presence of black Ni_2O_3, with complete absence or insignificant traces of NiO.

The sessile drop tests did not reveal any remarkable impact of the metal incorporation on the surface hydrophobicity. All modified samples possess the same hydrophilic properties as the reference ones, probably due to the preferential involvement of the metals inside the pores of the AAO layer composed of hydrated Al_2O_3 and boehmite.

The EIS data revealed definite capacitive behavior of the specimens, due to the clearly formed AAO films. The incorporation did not induce any remarkable impact on the electrochemical characteristics of the Cu/Ni-O-Al films. The obtained results were subjected to further analyses employing a suitable model equivalent circuit. It included all the basic impedance elements: (i) solution resistance; (ii) AAO capacitance; (iii) charge transfer resistance; (iv) electrolyte resistance, enclosed in the AAO pores, and (v) incomplete capacitances of the electric double layer and the hindered diffusion inside the AAO pores. The EIS data analysis revealed that the metal incorporation results in a drastic change of the capacitance of the oxide layer and decrement of the resistance of the combined (Cu + Ni) incorporated specimens with an order of magnitude, probably due to additional redox reactions between the respective Cu and Ni oxides inside the pores.

The PDS measurements showed that the oxide layer does not passivate the substrates completely, since for all samples the anodic branches possess a slope. All curves were situated at very low current densities, exhibiting that the anodization has a much more remarkable impact than Cu/Ni incorporation. The copper inclusion activated the AAO layer, whereas nickel caused supplemental layer sealing.

The corrosion potential values varied significantly in accordance to the incorporated metal. The registered values for all samples are shifted towards the reference electrode due to an Ohmic drop, resulting from the high resistance of the electrolyte. Thus, Ni incorporation shifts the potential in negative direction, whereas Cu incorporation alters its values in the opposite (positive) direction regarding E_{corr} of the reference electrodes. This fact can be explained considering that copper is a nobler metal than nickel.

Acknowledgments The financial support of the Bulgarian National Research Fund, contract "Functional nanocomposite layers based on anodic aluminium oxide and its metallization" (КП-06-Н29/1 (2018)) is gratefully acknowledged.

References

1. Stępniowski WJ, Moneta M, Norek M, Michalska-Domańska M, Scarpellini A, Salerno M (2016) The influence of electrolyte composition on the growth of nanoporous anodic alumina. Electrochim Acta 211:453–460
2. Giffard K, Arurault L, Blanc C, Di Caprio D (2018) Accurate evaluations of both porosity and tortuosity of anodic films grown on rolled AA 1050 and on rolled or machined AA 2024 T3. Surf Interface Anal 51:1184–1193
3. Stepniowski WJ, Moneta M, Karczewski K, Michalska-Domanska M, Czujko T, Mol JMC, Buijnsters JG (2018) Fabrication of copper nanowires via electrodeposition in anodic aluminum oxide templates formed by combined hard anodizing and electrochemical barrier layer thinning. J Electroanal Chem 809:59–66
4. Girginov CA, Kozhukharov SV, Milanes MJ (2018) Durability of Anodic Aluminum Oxide. films formed on technically pure AA1050 alloy against corrosion. Bulg Chem Commun 50-A:6–12
5. Kozhukharov SV, Girginov CA (2018) Comparative electrochemical and topographical elucidation of Anodic Aluminum Oxide (AAO) layers formed on technically pure aluminum (TPA) and AA2024-T3 aircraft alloy. Bulg Chem Commun 50-A:13–21
6. Kozhukharov S, Girginov C, Tsanev A, Petrova M (2019) Elucidation of the Anodization and Silver Incorporation Impact on the Surface Properties of AA1050 Aluminum Alloy. J Electrochem Soc 166(10):C231–C242
7. Bahramian A, Eyraud M, Vacandio F, Knauth P (2019) Cu/Ni/Au multilayers by electrochemistry: A crucial system in electronics - A critical review. Microelectron Eng 206:25–44
8. Becerra A, Dimitrijewits M, Arciprete C, Luna A (2001) Stable Ni/Al_2O_3 catalysts for methane dry reforming. Granul Matter 3:79–81
9. Wysocka I, Hupka J, Rogala A (2019) Catalytic Activity of Nickel and Ruthenium–Nickel Catalysts Supported on SiO_2, ZrO_2, Al_2O_3, and $MgAl_2O_4$ in a Dry Reforming Process. Catalysis 9:540. 1–19
10. Feng X, Liu J, Zhang P, Zhang Q, Xu L, Zhao L, Song X, Gao L (2019) Highly coke resistant Mg–Ni/Al_2O_3 catalyst prepared via a novel magnesiothermic reduction for methane reforming catalysis with CO_2: the unique role of Al–Ni intermetallics. Nanoscale 11:1262–1272
11. Arandia A, Remiro A, García V, Castaño P, Bilbao J, Gayubo AG (2018) Oxidative Steam Reforming of Raw Bio-Oil over Supported and Bulk Ni Catalysts for Hydrogen Production. Catalysts 8:322. 1–25
12. Arandia A, Coronado I, Remiro A, Gayubo AG, Reinikainen M (2019) Aqueous-phase reforming of bio-oil aqueous fraction over nickel-based catalysts. Int J Hydrog Energy 44 (26):13157–13168
13. Torres D, Luis Pinilla J, Suelves I (2018) Co-, Cu- and Fe-Doped Ni/Al_2O_3 Catalysts for the Catalytic Decomposition of Methane into Hydrogen and Carbon Nanofibers. Catalysts 8:300. 1–15
14. Yang L, Pastor-Pérez L, Gu S, Sepúlveda-Escribano A, Reina TR (2018) Highly efficient Ni/CeO_2-Al_2O_3 catalysts for CO_2 upgrading via reverse water-gas shift: Effect of selected transition metal promoters. Appl. Catal. B 232:464-471
15. Aghamohammadi S, Haghighi M, Maleki M, Rahemi N (2017) Sequential impregnation vs. sol-gel synthesized Ni/Al_2O_3-CeO_2 nanocatalyst for dry reforming of methane: Effect of synthesis method and support promotion. Mol Catal 431:39–48
16. Ahmed W, Awadallah AE, Aboul-Enein AA (2016) Ni/CeO_2–Al_2O_3 catalysts for methane thermo-catalytic decomposition to CO_x-free H_2 production. Int J Hydrog Energy 41:18484–18493
17. Valle B, García-Gómez N, Arandia A, Remiro A, Bilbao J, Gayubo AG (2019) Effect of phenols extraction on the behavior of Ni-spinel derived catalyst for raw bio-oil steam reforming. Int J Hydrog Energy 44(25):12593–12603

18. Lyu L, Zhang L, Wang Q, Nie Y, Hu C (2015) Enhanced Fenton Catalytic Efficiency of γ-Cu–Al_2O_3 by σ-Cu^{2+}–Ligand Complexes from Aromatic Pollutant Degradation. Environ Sci Technol 49(14):8639–8647
19. López-Suárez FE, Bueno-López A, Illán-Gómez MJ (2008) Cu/Al_2O_3 catalysts for soot oxidation: Copper loading effect. Appl Catal B 84(3–4):651–658
20. Chen L, Horiuchi T, Osaki T, Mori T (1999) Photocatalytic degradation of thiocarbamate herbicide active ingredients in water. Appl Catal B 23(4):259–269
21. Shimizu K, Kawabata H, Maeshima H, Satsuma A, Hattori T (2000) Intermediates in the Selective Reduction of NO by Propene over Cu−Al_2O_3 Catalysts: Transient in−Situ FTIR Study. J Phys Chem B 104(13):2885–2893
22. Zhang X, Shi P (2003) Production of hydrogen by steam reforming of methanol on CeO_2 promoted Cu/Al_2O_3 catalysts. J Mol Catal A 194(1–2):99–105
23. Le Saché E, Santos JL, Smith TJ, Centeno MA, Arellano-Garcia H, Odriozola JA, Reina TR (2018) Multicomponent Ni-CeO_2 nanocatalysts for syngas production from CO_2/CH_4 mixtures. J CO2 Util 25:68–78
24. Pastor-Pérez L, Baibars F, Le Sache E, Arellano-Garcia H, Gu S, Ramirez Reina T (2017) CO_2 valorisation via Reverse Water-Gas Shift reaction using advanced Cs doped Fe-Cu/Al_2O_3 catalysts. J CO2 Util 21:423–428
25. Walter KM, Serrer M-A, Kleist W, Grunwaldt J-D (2019) Continuous production of higher alcohols from synthesis gas and ethanol using Cs-modified CuO/ZnO/Al_2O_3 catalysts. Appl Catal A 585:117150
26. Anton J, Nebel J, Song H, Froese C, Weide P, Ruland H, Muhler M, Kaluza S (2016) The effect of sodium on the structure–activity relationships of cobalt-modified Cu/ZnO/Al_2O_3 catalysts applied in the hydrogenation of carbon monoxide to higher alcohols. J Catal 335:175–186
27. Pastor-Pérez L, Le Saché E, Jones C, Gu S, Arellano-Garcia H, Reina TR (2018) Synthetic natural gas production from CO_2 over Ni-x/CeO_2-ZrO_2(x = Fe, Co) catalysts: Influence of promoters and space velocity. Catal. Today 317:108-113
28. Ma Q, Geng M, Zhang J, Zhang X, Zhao TS (2019) Enhanced Catalytic Performance for CO_2 Hydrogenation to Methanol over N-doped Graphene Incorporated Cu-ZnO-Al_2O_3 Catalysts. CemistrySelect 4(1):78–83
29. Nanda MR, Yuan Z, Shui H, Xu C-C (2017) Selective Hydrogenolysis of Glycerol and Crude Glycerol (a By-Product or Waste Stream from the Biodiesel Industry) to 1,2-Propanediol over B_2O_3 Promoted Cu/Al_2O_3 Catalysts. Catalysts 7:196. 1–16
30. Awad A, Masiran N, Salam MA, Vo D-V, Abdullah B (2019) Non-oxidative decomposition of methane/methanol mixture over mesoporous Ni-Cu/Al_2O_3 Co-doped catalysts. Int J Hydrog Energy 44(37):20889–20899
31. Yuan E, Wu C, Hou X, Dou M, Liu G, Li G, Wang L (2017) Synergistic effects of second metals on performance of (Co, Ag, Cu)-doped Pd/Al_2O_3 catalysts for 2-ethyl-anthraquinone hydrogenation. J Catal 347:79–88
32. Yadav D, Kavaiya A, Mohan D, Prasad R (2017) Low Temperature Selective Catalytic Reduction (SCR) of NOx Emissions by Mn-doped Cu/Al_2O_3 Catalysts. Bull Chem React Eng Catal 12(3):415–429
33. Tabakova T, Ivanov I, Karakirova Y, Karashanova D, Venezia A-M, Petrova P, Avdeev G, Kolentsova E, Ivanov K (2018) Promotional Effect of Gold on the WGS Activity of Alumina-Supported Copper-Manganese Mixed Oxides. Catalysts 8(11):563. 1–18
34. Furukawa S, Ieda M, Shimizu K (2019) Heterogeneous Additive-Free Hydroboration of Alkenes Using Cu–Ni/Al_2O_3: Concerted Catalysis Assisted by Acid–Base Properties and Alloying Effects. ACS Catal 96:5096–5103
35. Dasireddy VDBC, Valand J, Likozar B (2018) PROX reaction of CO in H_2/H_2O/CO_2 Water–Gas Shift (WGS) feedstocks over Cu–Mn/Al_2O_3 and Cu–Ni/Al_2O_3 catalysts for fuel cell applications. Renew Energy 116-A:75–87
36. Ivanov DP, Kharitonov AS, Pirutko LV, Noskov AS, Abrashenkov PA, Golovachev VA, Kondrashev DO, Kleimenov AV (2017) Hydrodeoxygenation of methyl-substituted ketones

using the composite loading of hydrogenation and dehydration catalysts. Catal Ind 9 (4):299–307
37. Mondal S, Malviya H, Biswas P (2019) Kinetic modelling for the hydrogenolysis of bio-glycerol in the presence of a highly selective Cu–Ni–Al_2O_3 catalyst in a slurry reactor. React Chem Eng 4:595–609
38. Pandey DK, Biswas P (2019) Production of propylene glycol (1,2-propanediol) by the hydrogenolysis of glycerol in a fixed-bed downflow tubular reactor over a highly effective Cu–Zn bifunctional catalyst: effect of an acidic/basic support. New J Chem 43:10073
39. Zavrazhnov S, Esipovich A, Zlobin S, Belousov A, Vorotyntsev A (2019) Mechanism Analysis and Kinetic Modelling of Cu NPs Catalysed Glycerol Conversion into Lactic Acid. Catalysts 9:231
40. Tuan LA, Luong NT, Ishihara KN (2016) Low-Temperature Catalytic Performance of Ni-Cu/Al_2O_3 Catalysts for Gasoline Reforming to Produce Hydrogen Applied in Spark Ignition Engines. Catalysts 6(3):45. 1–17
41. Han SJ, Song JH, Bang Y, Yoo J, Park S, Kang KH, Song IK (2016) Hydrogen production by steam reforming of ethanol over mesoporous Cu–Ni–Al_2O_3–ZrO_2 xerogel catalysts. Int J Hydrog Energy 41(4):2554–2563
42. Yan L, Tian S, Zhou J, Yuan X (2016) Catalytic hydrolysis of gaseous HCN over Cu–Ni/γ-Al_2O_3 catalyst: parameters and conditions. Front Environ Sci Eng 10(5)
43. Xie Z, Chen B, Wu H, Liu M, Liu H, Zhang J, Yang G, Han B (2019) Highly efficient hydrogenation of levulinic acid into 2-methyltetrahydrofuran over Ni–Cu/Al_2O_3–ZrO_2 bifunctional catalysts. Green Chem 21:606–613
44. Gandarias I, Requies J, Arias PL, Armbruster U, Martin A (2012) Liquid-phase glycerol hydrogenolysis by formic acid over Ni–Cu/Al_2O_3 catalysts. J Catal 290:79–89
45. Zaikovskii VI, Chesnokov VV, Buyanov RA (2006) State of disperse alloy particles catalyzing hydrocarbon decomposition by the carbide cycle mechanism: TEM and EDX studies of the Cu-Ni/Al_2O_3 and Cu-Co/Al_2O_3 catalysts. Kinet Catal 47(4):603–609
46. Vazquez-Arenas J, Treeratanaphitak T, Pritzker M (2012) Formation of Co–Ni alloy coatings under direct current, pulse current and pulse-reverse plating conditions. Electrochim Acta 62:63–72
47. Girginov C, Kanazirski I, Dimitrov T (2012) Electrolytic coloring of anodic alumina in $CoSO_4$ solution. Part one: Influence of pretreatment and the AC polarization frequency. Ann Proceeds Univ Rousse (Bulgaria) 51:57–63. Access via: http://conf.uni-ruse.bg/bg/docs/cp12/9.1/9.1-10.pdf
48. Girginov C, Kanazirski I, Zahariev A, Stefchev P (2012) Electrolytic colouring of anodic alumina films in metal ions containing solution, Part one: Electrolytic colouring in $NiSO_4$ containing solution. J Univ Chem Technol Metall 47:187–192
49. Shang Y, Liu C, Fernandez C, Rajendran L, Kirthiga M, Wang Y, Niu D, Liu D, Wang L (2017) The analysis and fabrication of a novel tin-nickel mixed salt electrolytic coloured processing and the performance of coloured films for Al-12.7Si-0.7Mg alloy in acidic and alkali corrosive environments. Int J Precis Eng Manuf 18:93–98
50. Kanazirski I, Girginov C, Girginov A (2012) Electrolytic colouring of anodic alumina films in $NiSO_4$, $CuSO_4$ and ($NiSO_4$ + $CuSO_4$) containing electrolytes. Adv Nat Sci 1:45–51
51. Casademont C, Roche J, Arurault L (2019) Alternative black coatings prepared on aluminium alloy 1050. Surf Eng 35:899–905
52. Ignatova K, Piroeva I, Vladimitova-Atanasova S (2016) Effect Of The Electrodeposition Conditions On The Morphology And Corrosion Behavior Of Ni-Co Alloys Part 1: Chemical Composition, Cathodic Current Efficiency, And Morphology Of Ni-Co Alloys Electrodeposited From Citrate Electrolyte. J Chem Technol Metall 51:99–105
53. Ignatova K, Avdeev G (2016) Effect Of The Electrode Position Conditions On The Morphology And Corrosion Behavior Of Ni-Co Alloys Part 2: Phase Composition And Corrosion Behavior Of Ni-Co Alloys, Electrodeposited From Citrate Electrolyte. J Chem Technol Metall 51:106–111

54. Ignatova K, Kozhukharov S, Vladimirov L, Milanes M (2015) Impact of the electroplating regime on the chemical composition of Ni-Co-P based coatings in non-complexing acidic electrolyte. Ann Proceed Univ Rousse (Bulgaria) 54:81–85. Access via: http://conf.uni-ruse.bg/bg/docs/cp15/10.1/10.1-16.pdf
55. Ignatova K, Kozhukharov S, Alakushev M (2018) Barrier ability and durability of Ni-Co-P coatings in accordance to the content of H_3PO_3 and NaH_2PO_2 as phosphorus sources. Mater Chem Phys 219:175–181
56. Ignatova K, Alakushev M, Kozhukharov S, Marcheva Y, Vladimirova S, Avdeev G (2019) Effect of H_3PO_3 and NaH_2PO_2 in the electrolyte on the composition and microstructure of Ni-Co-P alloys. J Chem Technol Metall 54(6):1271–1280
57. Kiradzhiyska D, Mantcheva R, Girginov C, Kozhukharov S (2018) Optical and color characteristics of porous alumina with electrochemically incorporated silver. J Chem Technol Metall 53:745–748
58. Pornnumpa N, Jariyaboon M (2019) Antibacterial and Corrosion Resistance Properties of Anodized AA6061 Aluminum Alloy. Engl J 23(4):171–181
59. Girginov C, Kozhukharov S, Kiradzhiyska D, Mancheva R (2018) Characterization of porous anodic alumina with AC-incorporated silver. Electrochim Acta 292:614–627
60. Dimitrov A, Paunović P, Popovski O, Slavkov D, Kamberović Z, Hadžijordanov S (2009) Effect of non-stationary current regimes on the morphology of silver electrodeposits. J Serb Chem Soc 74(3):279–289. UDC 546.57+544.654.2:548.19 JSCS–3830
61. Kozhukharov S, Girginov C, Avramova I, Machkova M (2016) Anodic galvanostatic polarization of AA2024-T3 aircraft alloy in conventional mineral acids. Mater Chem Phys 180:301–313
62. Salve AA, Kozhukharov S, Pernas JE, Matter E, Machkova M (2012) A Comparative Research On Hybrid And Hybrid Nano- Composite Protective Primary Coatings For AA2024 Aircraft Alloy. J Univ Chem Technol Metall 47(3):319–326
63. Kozhukharov SV, Girginov CA (2019) Chapter 1: Classical and modern methods for corrosion impact rate determination for Aluminium and strengthened aircraft alloys. Fundamentals and practical applications. In: Gergely A (ed) Phenomena and theories in corrosion science. Methods of prevention. NOVA Science Publishers, Hauppauge, pp 3–150. ISBN 978-153-615253-1
64. Mortimer CE, Mueller U (2014) In: Georg Thieme (ed) Chemie. Das Basiswissen der Chemie, 11th edn. Thieme, Stuttgart, pp 353–355

Part X
Applications: Sensors and Detectors

Chapter 29
Testing of pH Nanosensors Based on Polyaniline/Carbon Nanostructures Coated Screen Printed Electrode

Aleksandar Petrovski, Perica Paunović, Anita Grozdanov, and Aleksandar T. Dimitrov

Abstract The aim of this study is to analyze the sensor activity of polyaniline (PANI) based nanocomposites reinforced with carbon nanostructures (CNSs) such as graphene (G) and multi walled carbon nanotubes (MWCNT), in order to use them as pH sensors. For their realization the nanocomposites are applied on screen printed electrode (SPE) by means of steady state electrochemical polarization. The optimal conditions for electropolymerization of the PANI/CNSs on gold SPE were defined by steady state polarization measurements. It was found that the optimal potential for electropolymerization of the PANI based nanocomposites on gold SPE is 1.15 V vs. saturated calomel electrode (SCE). The prepared nanosensors are characterized by scanning electron microscopy (SEM) and Fourier transform infrared spectroscopy (FTIR). The stability of the nanosensors was tested in synthetic sea water with pH = 8.4 and the most stabile was 3% MWCNT reinforced PANI nanocomposite at average of 12 min time, with minimal deviations for a period of more than 30 days. The results show also that decreasing the temperature leads to lower resistivity, which is attributed to reduced diffusion in the process of doping and dedoping. On the other side this reflects in the increased stabilization time of the nanosensor. Tests were conducted by *two probe* method to study the sensor activity of the nanocomposites against pH changes. The pH changes varied from 8.49 to 7.96 and represent simulation of the changes happening in real sea water. It was found that with changing the pH of the water, time of 1 min was needed for stabilization of the sensor resistivity. The resistivity changes versus pH changes show linear dependence by increasing the resistivity of the nanosensor with decreasing the pH of the water.

Keywords PANI/CNSs nanocomposites · pH nanosensors · Steady state · Electropolymerization · Sensory activity · Sensor stabilization · Resistivity

A. Petrovski (✉) · P. Paunović · A. Grozdanov · A. T. Dimitrov
Faculty of Technology and Metallurgy, University "SS Cyril and Methodius", Skopje, Republic of North Macedonia
e-mail: aleksandar@tmf.ukim.edu.mk

P. Petkov et al. (eds.), *Nanoscience and Nanotechnology in Security and Protection against CBRN Threats*, NATO Science for Peace and Security Series B: Physics and Biophysics, https://doi.org/10.1007/978-94-024-2018-0_29

29.1 Introduction

Human activities such as industry, transportation etc. affect the surface waters leading to pollution, which disrupts the ecological balance of the ecosystem. Monitoring the pH changes of the surface waters is one of the appropriate methods for detecting the presence of undesirable chemicals and corresponding chemical reactions in these waters. The application of polymer/CNSs nanocomposites as pH-sensors is one of the new promising approaches for monitoring of the pH changes, compared to the traditional methods [1].

Due to its excellent properties (electrical, electrochemical, redox behavior, electroluminescence, environmental stability, etc.), the simple preparation and the low cost of the precursor (aniline), PANI has been considered as one of the most promising material among the family of the conductive polymers [2–4]. Emeraldine base is the only one conductive form of polyaniline, when converted into emeraldine salt. As a result, PANI has been recognized as a suitable material for use in electronics, optical and energy storage devices, sensors etc. [5–7]. However, there are also some limitations for PANI applications, which are attributed to its poor mechanical properties and low processability.

After the discovery of the carbon nanostructures (CNSs) such as carbon nanotubes (CNTs) [8] and graphene [9], and revealing their extraordinary properties, one of the first effective applications was for reinforcement of polymers. Reinforcing of PANI with CNSs is very appropriate method to overcome the limitations of PANI applications. Due to the synergetic effect that occurs between the polymer matrix and the reinforcement, the newly formed structure exhibits improved properties and behavior compared to the pure polymer, and in some cases even better than the pure nanostructures [10, 11]. PANI/CNSs nanocomposites can be prepared by chemical or electrochemical polymerization [3, 12].

The aim of this work is to test the sensing activity of our previously prepared PANI/CNS nanocomposites [13–15], which are deposited on gold screen printed electrode (SPE) in order to use them for detecting the pH changes in the marine waters.

29.2 Experimental

PANI/CNSs nanocomposites were deposited on SPE in order to produce nanosensors for monitoring the pH of the marine water. The procedure is actually steady state electropolymerization of aniline to PANI in presence of CNS such as graphene and MWCNT. The electrochemical polymerization was performed in a standard electrochemical cell with capacity of 50 ml, equipped with three electrode system (Fig. 29.1). Gold SPE was used as working electrode and platinum mesh net as a counter electrode, while a saturated calomel electrode (SCE) was used as a reference electrode. The electrolyte contained 0.1 M aniline and 0.5 M H_2SO_4. CNSs

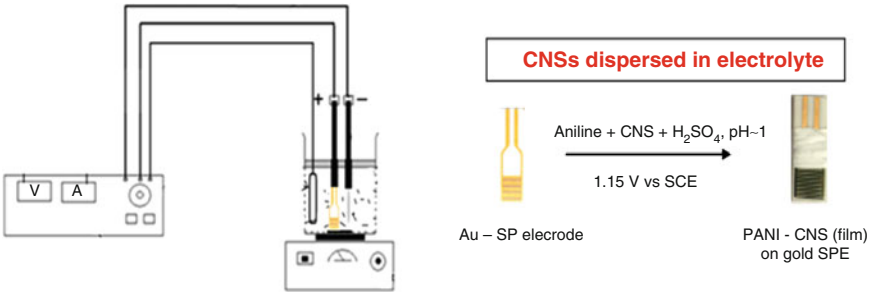

Fig. 29.1 Electrochemical polymerization of PANI/CNSs nanocomposites on SPE

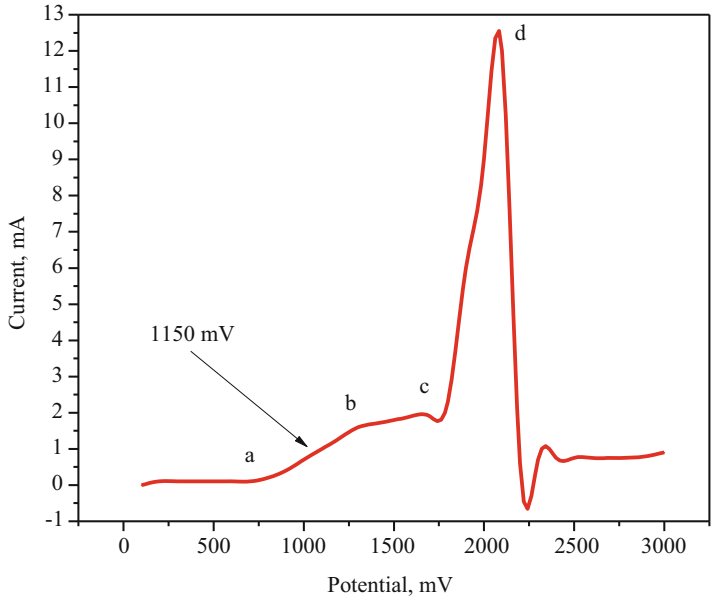

Fig. 29.2 Polarization curve of electropolymerization of PANI (electrolyte: 0.1 M aniline +0.5 M H_2SO_4 + CNSs)

(produced by molten salt electrolysis in the laboratory of the Faculty of Technology and Metallurgy in Skopje) were firstly modified in concentrated solution of H_2SO_4 and HNO_3 with ratio 3:1 respectively, then purified with boiled deionized water and dried at 70 °C in air atmosphere.

Before the electropolymerization process, CNSs were dispersed in the electrolyte by sonification for 30 min in an ultrasonic bath. Electropolymerization was carried out at a constant potential of +1.15 V vs. SCE until the current reached 1.1 mA. These data were obtained from the steady-state polarization measurements presented in Fig. 29.2. The prepared nanocomposites have CNSs content of 3 wt. % vs. wt. of the aniline.

The morphology of the nanocomposites was analyzed with a scanning electron microscope FEI Quanta 2000 using a secondary electron detector and acceleration voltage of 30 kV. FTIR spectroscopy was conducted in a region of 400–4000 cm^{-1} using Perkin Elmer spectrum 100 system. For analyzing the sensor activity of the nanocomposites vs. pH changes, *two probe method* was applied with YH187 Digital Meter Electrical Auto Multimeter High Accuracy DMM True RMS AC/DC OHM Tester.

29.3 Results and Discussion

Figure 29.2 shows a steady state polymerization measurement for electropolymerization of aniline in presence of CNSs. The measurements were performed in the region from 0 to 2 V. All steps of transformation from aniline to polyaniline were observed. The most important is the part from *a* to *b,* where the emeraldine form of PANI is formed. Therefore, from this investigation it can be found that the optimal potential is 1.15 V in order to obtain emeraldine salt with 50% oxidized and reduced amino groups. This form of PANI actually possesses the highest electrical conductivity [16, 17]. After production, the nanosensors were characterized by SEM and FTIR.

From the SEM microphotographs (Fig. 29.3) it can be seen that the PANI has granular and porous morphology [18] and the diameters of the grains vary from 10 to

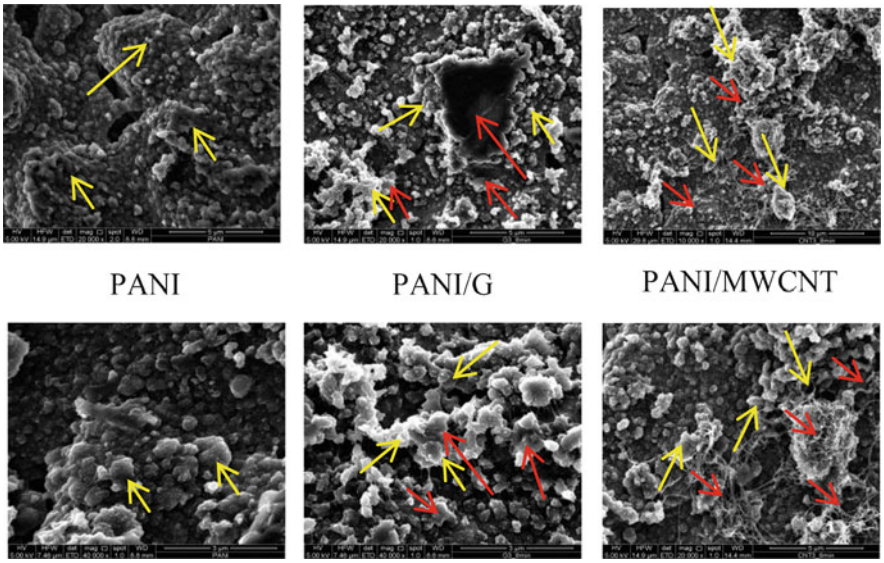

Fig. 29.3 SEM images of the PANI/CNSs nanocomposites on SPE (yellow arrows show PANI, red – CNSs)

300 nm. CNSs are embedded into the polymer matrix forming conductive nets, which play a role of catalysts in the electropolymerization process. From both types of nanocomposites, PANI/MWCNTs have shown better morphology than the PANI/G nanocomposites.

All the characteristic chemical bonds in the obtained nanocomposites were detected by FTIR spectroscopy. The peaks around 1050 cm^{-1} are characteristic for the activated CNSs, the peaks around 1480 and 1580 cm^{-1} for the emeraldine salt form of PANI, and those around 1150, 1250, and 2920 cm^{-1} for the formed nanocomposites [19] (Fig. 29.4).

After the characterization of the nanosensor morphology and structure, the next step was to test its stability (Fig. 29.5a). The obtained results revealed that the nanosensor is stable for 30 days with several changes that are classified in four main periods. In the first period the nanosensor is stable for 9 days in synthetic sea water and after that its resistance decreases. This resistivity remains only for 1 day and after that the sensor tries to recover in its previous stable form, due to the processes of doping and dedoping in the polymer matrix. After this period, the sensor is stable for 9–10 days and the same processes start all over again. From the results it is confirmed that the processes of doping and dedoping occur without any obstacles when the sensor is rinsed in water, and this should be taken into account within the pH sensor assembling.

The dependency of the nanosensor resistance versus the temperature changes and the time of stabilization were also investigated within this period (Fig. 29.5b). The stabilization time was measured from the moment when the sensor was plugged until the moment when the resistance reached a stabile value without oscillations. This can be seen from the yellow curve in the Fig. 29.5b. The initial stabilization time varied around 12 min (green curve in Fig. 29.5b) with some deviations which can be attributed to the temperature changes (black curve in Fig. 29.5b). It was found that the nanosensor resistivity decreases with decreasing the temperature, but the time of stabilization increases. This is due to the diffusion impacts in the processes of doping and dedoping.

The sensor activity was investigated in synthetic sea water by varying the pH from 8.49 to 7.96, which was a simulation of the real pH changes of the marine waters (Fig. 29.6). It was confirmed that the nanosensor shows linear dependency and the time for stabilization of the resistivity between every pH change is only 1 min. By decreasing the pH of the water, the resistivity of the nanosensor increases following a linear function.

29.4 Conclusion

From the presented results it can be concluded that the optimal potential for electropolymerization of PANI/CNS based nanocomposites on gold SPE is 1.15 V vs. saturated calomel electrode. The best stability was exhibited by 3% MWCNT reinforced PANI nanocomposite nanosensor at average of 12 min with

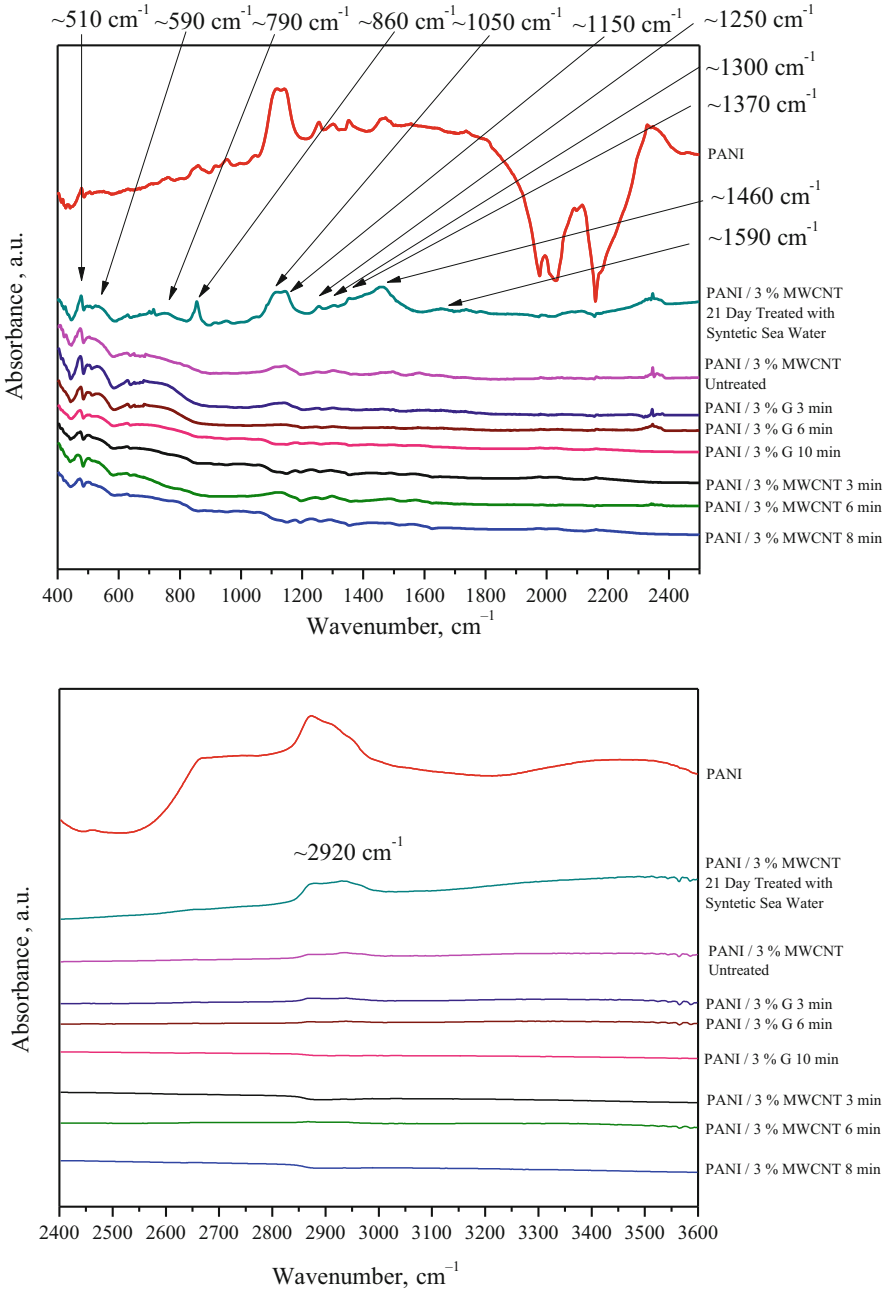

Fig. 29.4 FTIR spectra of PANI/CNSs on SPE

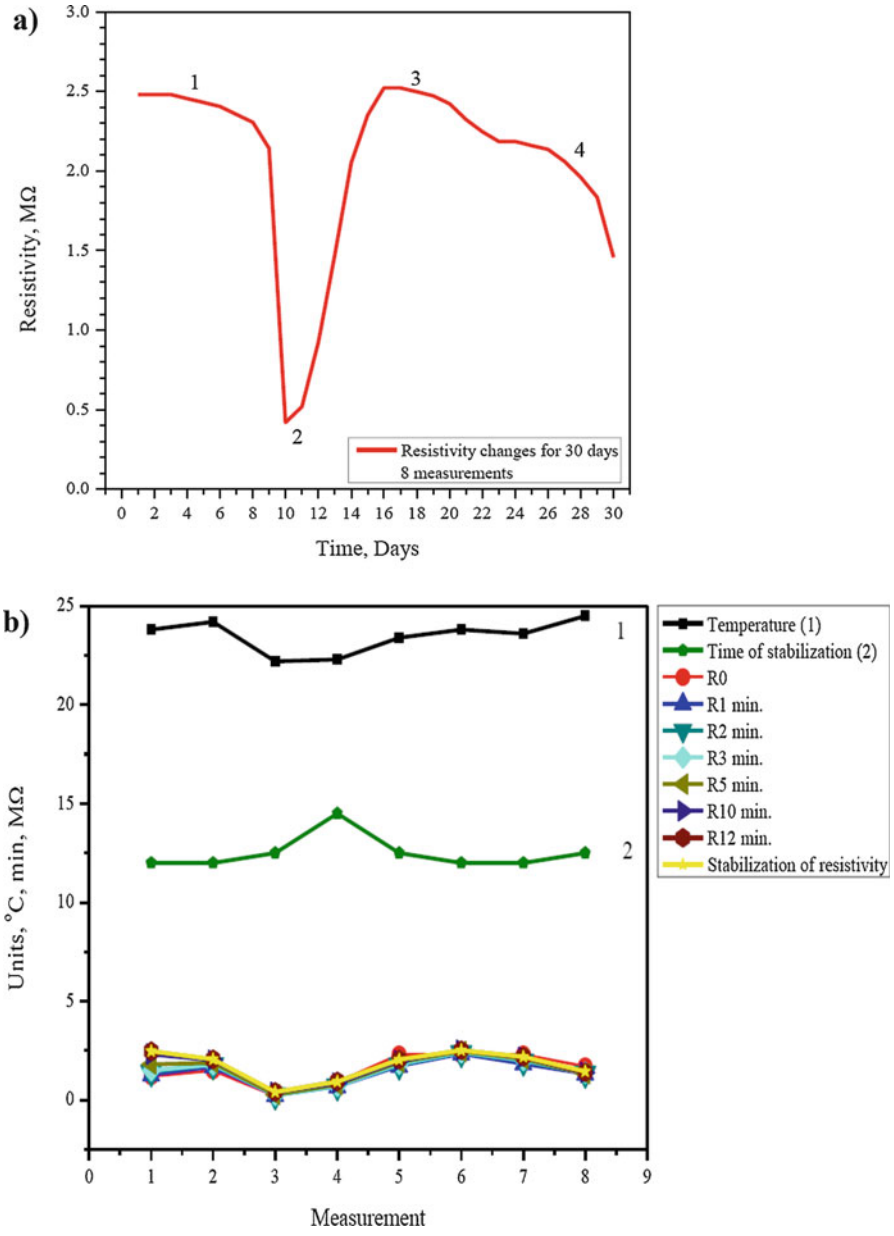

Fig. 29.5 Resistivity changes of the nanocomposites vs. time (**a**) and vs. temperature and time of stabilization (**b**) in a period of 30 days

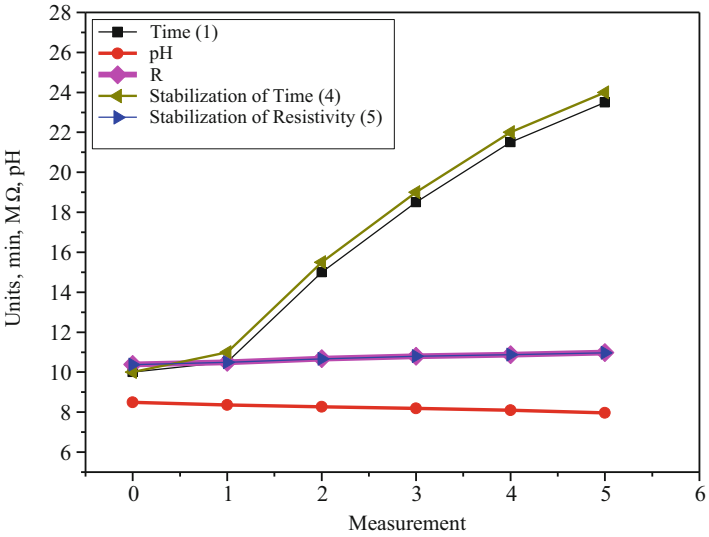

Fig. 29.6 Resistivity changes of PANI/MWCNTs SPE nanosensor vs. pH changes in synthetic sea water

minimal deviations. The sensor is stabile for more than 30 days. Temperature decrease leads to decreased resistivity, which is attributed to the reduced diffusion in the processes of doping and dedoping. On the other side this reflects in the increased stabilization time of the nanosensor. With changing the pH of the water, response of 1 min is needed for stabilization of the sensor resistivity. The resistivity changes versus pH show a linear dependence of increasing the resistivity of the nanosensor with decreasing the pH of the water. Based on the obtained results, processes of doping and dedoping in the polymer matrix can be considered as the main sensory mechanisms for these types of nanocomposites.

Acknowledgments This research was performed within FP7 Project "Cost-effective sensors, interoperable with international existing ocean observing systems, to meet EU policies requirements" (Project reference 614155)**.**

References

1. Salavagione HJ, Díez-Pascual AM, Lázaro E, Vera S, Gómez-Fatou MA (2014) Chemical sensors based on polymer composites with carbon nanotubes and graphene: the role of the polymer. J Mater Chem A 2:14289–14328
2. Boeva ZA, Sergeyev VG (2014) Polyaniline: Synthesis, properties, and application. Polym Sci Ser C Sel Top 56:144–153
3. Gajendran P, Saraswathi R (2012) Polyaniline-carbon nanotube composites. Pure Appl Chem 80:2377–2395

4. Jung Kim WJ, Huh DS (2012) Preparation of Honeycomb-patterned Polyaniline-MWCNT/Polystyrene Composite Film and Studies on DC Conductivity. Bull Kor Chem Soc 33:2345–2351
5. MacDiarmid AG, Yang LS, Huang WS, Humphrey BD (1987) Polyaniline: Electrochemistry and application to rechargeable batteries. Synth Met 18:393–398
6. Roth S, Graupner W (1993) Conductive polymers: Evaluation of industrial applications. Synth Met 57:3623–3631
7. Talaie A, Lee JY, Lee YK, Jang J, Romagnoli JA, Taguchi T, Maeder E (2000) Dynamic sensing using intelligent composite: an investigation to development of new pH sensors and electrochromic devices. Thin Solid Films 363:163–166
8. Iijima S (1991) Helical microtubules of graphitic carbon. Nature 354:56–58
9. Geim A, Novoselov K (2007) The rise of graphene. Nat Mater 6:183–191
10. Baibarac M, Romero PG (2006) Nanocomposites based on conducting polymers and carbon nanotubes: from fancy materials to functional applications. J Nanosci Nanotechnol 6:289–302
11. Dai L (2007) Electrochemical Sensors Based on Architectural Diversity of the π-Conjugated Structure: Recent Advancements from Conducting Polymers and Carbon Nanotubes. Aust J Chem 60:472–483
12. Gvozdenović MM, Branimir ZJ, Stevanović JS, Trišović LT, Branimir GN (2011) Electrochemical Polymerization of Aniline. In: Schab-Balcerzak E (ed) Electropolymerization. InTech, Rijeka, pp 77–96. ISBN: 978-953-307-693-50
13. Petrovski A, Paunovic P, Avolio R, Errico ME, Cocca MC, Gentile G, Grozdanov A, Avella M, Barton J, Dimitrov AT (2017) Synthesis and characterization of nanocomposites based on PANI and carbon nanostructures prepared by electropolymerization. Mater Chem Phys 185:83–90
14. Petrovski A, Paunović P, Grozdanov A, Dimitrov AT, Gentile G, Avella M (2018) Electrochemical Synthesis of PANI/Graphene Nanocomposites Aimed for Sensors. In: Petkov P, Tsiulyanu D, Popov C, Kilisch W (eds) Advanced nanotechnologies for detection and defence against CBRN agents. Springer Science+Business Media B.V, Dordrecht, pp 221–227
15. Grozdanov A, Petrovski A, Avella M, Paunovic P, Errico ME, Avolio R, Gentile G, De Falco F, Dimitrov AT (2019) Spectroscopically Study of Nanocomposites Based on PANI and Carbon Nanostructures for pH Sensors. Bulg Chem Commun 51(Special Issue D):36–41
16. Mickova I, Prusi A, Grcev T, Arsov Lj (2006) Electrochemical poly -merization of aniline in presence of TiO2 nano particle. Bull Chem Technol Maced 25:45–50
17. Taranu BO, Fagadar-Cosma E, Popa I, Plesu N, Taranu I (2014) Adsorbed functionalized porphyrins on polyaniline modified platinum electrodes. comparative electrochemical properties. Dig J Nanomater Biostruct 9(2):667–679
18. Wang H-Z, Zhang P, Zhang W-G, Yao S-W (2012) Electrodeposition and characterization of polyaniline film. Chem Res Chin Univ 28:133–136
19. Gao Z, Wang F, Chang J, Wu D, Wang X, Wang X, Xu F, Gao S, Jiang K (2014) Chemically grafted graphene-polyaniline composite for application in supercapacitor. Electrochim Acta 133:325–334

Chapter 30
WO_3-Based Glass-Crystalline Sensor for Selective Detection of Ammonia Gas

Mohamed Ataalla, Amr Mohamed, Mohamed A. Ali, Mohamed Hassan, Nagat Hamad, and Ahmed Sabry Afify

Abstract In this study, WO_3-based glass-crystalline material from the WO_3-ZnO-La_2O_3-Al_2O_3 system, containing high amount of tungsten oxide was synthesized by melt-quenching technique. The sol-gel technique was used to prepare the glass powder which was then dispersed in an organic solvent to make a printable ink. The latter afterwards was screen-printed as a thick film on an alumina substrate having interdigitated platinum electrodes in order to be used as a gas sensor. The fabricated material was characterized by X-ray diffraction (XRD), field emission scanning electron microscopy (FE-SEM) and thermo-gravimetric analysis (TGA).

M. Ataalla (✉)
Faculty of Engineering and Technology, Badr University in Cairo (BUC), Badr, Egypt
e-mail: mohamed.sobhi@buc.edu.eg

A. Mohamed (✉)
Chemistry Department, College of Science, Taibah University, Al-Madinah Al-Munawarah, Saudi Arabia

The Higher Institute of Optics Technology (HIOT), Heliopolis, Cairo, Egypt
e-mail: addeck@taibahu.edu.sa

M. A. Ali
Department of Chemistry, Faculty of Pharmacy, Badr University in Cairo (BUC), Badr, Egypt

M. Hassan
High Institute for Engineering & Technology, Al-Obour, Egypt

N. Hamad
Department of Physics, College of Science and Humanitarian Studies, Prince Sattam Bin Abdul Aziz University, Alkharj, Saudi Arabia

Department of physics and Mathematical Engineering, Faculty of Electronic Engineering, Monifia University, Shibin el Kom, Egypt

A. S. Afify
Department of Physics, College of Science and Humanitarian Studies, Prince Sattam Bin Abdul Aziz University, Alkharj, Saudi Arabia

Department of Basic Sciences, Higher institute of Engineering and Automotive and Energy Technology, New Heliopolis, Cairo, Egypt

P. Petkov et al. (eds.), *Nanoscience and Nanotechnology in Security and Protection against CBRN Threats*, NATO Science for Peace and Security Series B: Physics and Biophysics, https://doi.org/10.1007/978-94-024-2018-0_30

The sensitivity of the prepared sensor was noticeably high at low concentrations of NH_3 at different temperatures. Moreover, the sensing film was selective as there was no response toward both CO_2 and CH_4 at the same conditions.

Keywords WO_3-based glass · Melt-quenching · Screen printing · Ammonia sensing

30.1 Introduction

The fabrication of selective gas sensors useful in different fields such as agriculture, food, medicine, and industries has been of a high interest during the last decade. Among various gases, NH_3 is one of the major toxic atmospheric pollutants which causes adverse effects on human beings as well as on the whole ecosystem. Therefore, it is crucial to continuously monitor the levels of NH_3 gas [1]. Tungsten is the most widely used transition element in the sensor technology utilized to measure the levels of H_2S or NO_2 in addition to some other gases [1–4]. Moreover, different WO_3-based systems including other non-transition metal oxides, such as ZnO and SnO_2, have been prepared to enhance the gas-sensing properties [5–11]. As the chemical, physical and sensing characteristics of the metal oxide sensors are greatly affected by the method of synthesis, many preparative routes have been used for the preparation of WO_3 and WO_3-based gas sensing materials. They include electrospinning [12], solvothermal [13], modified thermal evaporation [14], precipitation [15], flame spray pyrolysis [16] and sol-gel technique [17]. Thus, the development of new preparation routes as well as the compositional variations are the two main promising perspectives to achieve significantly improved sensitive and selective gas-sensing materials.

ZnO is n-type semiconductor oxide with a large excitation binding energy (60 meV) and a wide band gap energy (3.37 eV). Due to its excellent structural, optical and catalytic properties, it is often used in many applications [18, 19]. Great attention is paid to study the ZnO sensing properties towards relative humidity and different gases such as methanol, ethanol, propyl alcohol and methane [19–23].

Keeping in mind the abovementioned information in addition to our previous results [24, 25] utilizing melt-quenching and crystallization for the preparation of materials in the WO_3-ZnO-Nd_2O_3-Al_2O_3 system for ammonia and humidity sensing applications, in the current study we have investigated the WO_3-ZnO-La_2O_3-Al_2O_3 system [25]. The aim of this research was to synthesize glass-crystalline materials from the WO_3-ZnO-La_2O_3-Al_2O_3 system containing high content of WO_3 by applying controlled glass crystallization methods and to validate its sensitivity towards ammonia under different conditions.

30.2 Materials and Methods

30.2.1 Powder Preparation and Characterization

The raw materials (reagent grade WO_3, ZnO, La_2O_3 and Al_2O_3) purchased from Alfa Aesar, USA, were with purity of 99.95%. Two batches with nominal compositions $76WO_3{\cdot}9.5ZnO{\cdot}9.5La_2O_3{\cdot}5Al_2O_3$ and $60WO_3{\cdot}7.5ZnO{\cdot}7.5La_2O_3{\cdot}25Al_2O_3$ were mixed and homogenized using porcelain pestle and mortar, and afterwards molten in platinum crucible at 1240 °C for 20 min in an aerobic atmosphere. Those thermal conditions were selected based on the phase diagrams for the desired system. The melt was then quenched (fast cooled) by pouring and pressing between two copper plates (cooling rates $10–10^2$ K/s). The obtained powders were characterized by X-ray phase analysis in the range $0 < 2\theta < 60$ with a Bruker D8 Advance Diffractometer, using Cu-Kα radiation in order to study the phase formation in the prepared samples.

The glass transition (T_g), crystallization (T_p) and melting temperatures (T_m), as well as the thermal stability were determined using differential thermal analysis (DTA) (instrument STA PT1600 TG-DTA/DSC). The obtained glasses were subjected to a heat treatment for 6 h at 530 °C then for 3 h at 550 °C and finally for 12 h at 560 °C in air in platinum crucibles, where the glass-crystalline specimens were obtained. The phase formation of the glass-crystalline samples was investigated by XRD analysis.

The glass-crystalline samples were studied by scanning electron microscopy (SEM) and energy dispersive X-ray spectroscopy (EDS). SEM analyses were performed on a JSM 6390 electron microscope (Japan) in conjunction with energy dispersive X-ray spectroscopy (EDS, Oxford INCA Energy 350) equipped with ultrahigh resolution scanning system (ASID-3D) in regimes of secondary electron imaging (SEI) and back scattered electrons (BEC) imaging. The samples were carbon-coated (time of coating was about 20 s), at that thickness carbon should have little or no effect on the elemental analysis. The accelerating voltage was 20 kV and the current 65 mA. The pressure was on the order of 10^{-4} Pa.

30.2.2 Ammonia sensor Preparation and Sensing Mechanism

The sensors were prepared and tested as follows:

30.2.2.1 Preparation of the Interdigitated Platinum Electrodes

Platinum conductor paste (ESL 5545, from Electro-Science, King of Prussia, PA, USA) was deposited manually by screen-printing technique onto 0.85 cm × 5 cm planar α-alumina substrates (ADS-96 R, 96% alumina, Coors Tek, USA) by using a

rubber squeegee through a 270 mesh steel screen. After drying overnight, these devices were heated at 500 °C for 20 min with a 2 °C/min heating/cooling ramp to optimize the electrical conductivity of the electrodes (based on the ink manufacturer's recommendations).

30.2.2.2 Preparation of the Screen-Printable Ink

The ink was prepared by dispersing the prepared powders in a suitable amount of the organic solvent ethylene glycol monobutyl ether (Emflow 227, Emca-Remex products, England) to reach the appropriate rheological behavior, adherence to the substrate, and to achieve the correct thermal shrinkage properties during the process of screen-printing to obtain a consolidated film.

30.2.2.3 Preparation of the Sensing Film

The screen-printable ink was then manually deposited onto the interdigitated platinum electrodes by the conventional screen-printing technique using a rubber squeegee through a 270-mesh steel screen. Once these films were dried, the sensors were heated at 500 °C for 1 h with a 2 °C/min heating/cooling ramp. The formed thick films had thicknesses of about 30–40 μm and surface areas of about 1 cm^2. Scotch tape tests on the films revealed a good adhesion onto the substrates.

30.2.2.4 Testing of the Ammonia Sensors

The sensors were electrically characterized using a laboratory apparatus including a thermostated chamber working at 25 °C in which the relative humidity (RH) could be controllably varied between 0 and 96% where the experimental details have been previously reported [26]. RH values were measured by a commercial humidity and temperature probe (Delta Ohm DO9406, Italy) with accuracy of ±2.5% in the 5–90% RH range. The NH_3 concentration (in ppm) was estimated by chemical computation from the vapor pressure of ammonia at 27 °C diluted into water in the ratio 1:20 [27]. These values were then transformed in mole fractions in order to determine the amount of ammonia in 1 L air and to obtain the ppm corresponding value from the volume of 1 mol ammonia at 27 °C. All sensors were first tested in humid atmosphere, then in NH_3 atmosphere and their electrical characterizations were evaluated by comparing the gas response to the RH and the ammonia concentration. In particular, the sensor response expressed in % (SR %) was defined as the relative variation of the initial resistance compared to the resistance measured in the atmosphere of the intended gas, as in Eq. (30.1):

$$SR(\%) = 100\frac{|R_0 - Rg|}{R_0} \tag{30.1}$$

where R_0 is the original resistance in the presence of air flow and R_g the resistance after exposure to NH_3 gas at equilibrium, i.e. when the active surfaces of the sensor are saturated by the gas in the atmosphere (specifically NH_3).

30.3 Results and Discussions

30.3.1 Materials Characterization

The two studied compositions of the obtained glass phase before the heat treatment of $76WO_3{\cdot}9.5ZnO{\cdot}9.5La_2O_3{\cdot}5Al_2O_3$ and $60WO_3{\cdot}7.5ZnO{\cdot}7.5La_2O_3{\cdot}25Al_2O_3$ will be referred to as "A" and "B", respectively. The samples will then be annotated as "C" and "D" for the obtained glass-crystalline samples which contain WO_3 and glass. Both A and B were amorphous according to the XRD analysis, which was also confirmed by the DTA curves of the synthesized glasses (Fig. 30.1). The glasses are characterized by a hump in the DTA curves, corresponding to the glass transition temperature (T_g) followed by an exothermic effect connected with the crystallization temperatures of the glasses (T_x). The calculated $\Delta T = T_x - T_g$ was 80 °C for the sample A and 100 °C for the sample B, which corresponds to a good thermal stability of the obtained amorphous specimens.

Heat treatment was applied for different durations at a temperature around the crystallization temperatures T_x for the samples A and B. The obtained phases in the treated samples were investigated using XRD, showing that glass-crystalline specimens were obtained for samples C and D, since they contain WO_3 as a crystalline phase. The XRD results for the samples C and D were in a good agreement with the

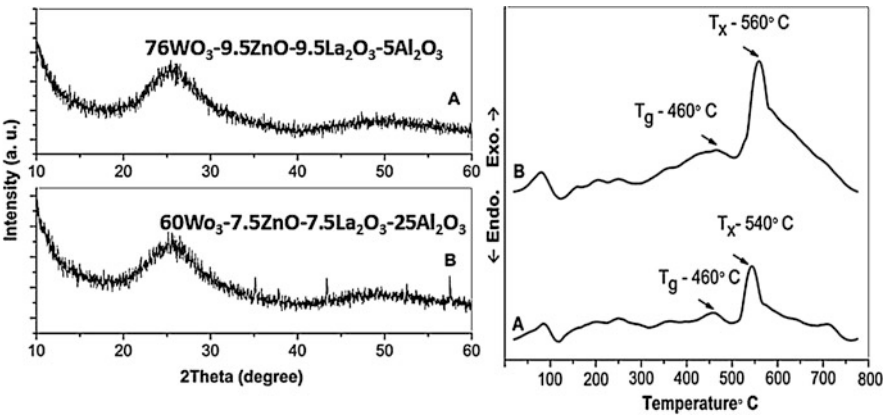

Fig. 30.1 XRD patterns (left) and DTA curves (right) of the samples A and B

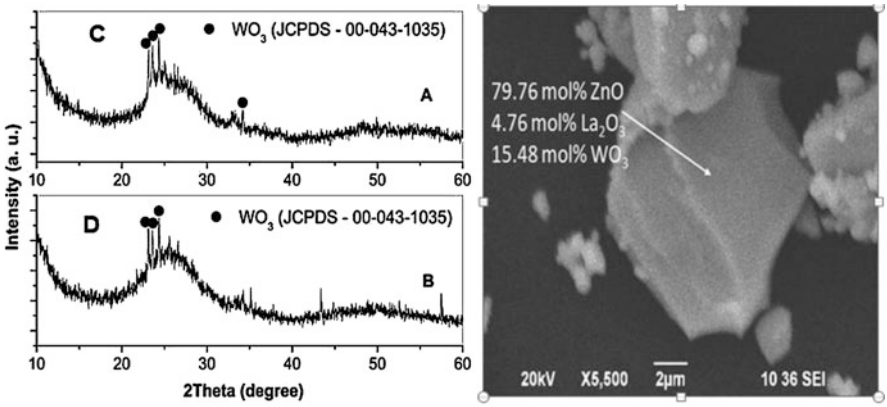

Fig. 30.2 XRD patterns of the samples C and D (left) and SEM and EDX of the sample C (right)

SEM analysis. The glass-crystalline samples are amorphous with some peaks indicating the presence of WO_3 crystals (JPCD card 43-1035), which was also confirmed by the EDX elemental analysis that calculated the WO_3 content at about 16 mol% as can be seen in Fig. 30.2.

30.3.2 Measurement of Sensitivity Towards NH_3

It is well known that the oxygen from the atmosphere is adsorbed on the exposed layer of the sensor and then captures electrons from it, increasing the concentration of the holes. For that reason, when the sensor is exposed to an NH_3 atmosphere, the electrons are trapped which causes a strong decrease of the electrical resistance, resulting in a strong increase of the sensor response.

The electrical responses of both investigated samples C and D varied starting from 10 ppm NH_3, then the increase of NH_3 concentration induced capillary condensation although sample C showed better response and sharp increase starting from 45 ppm NH_3 which can be seen in Fig. 30.3. This may be attributed to the higher content of WO_3 in its composition, which enhanced the electron transfer in the sensing layer if compared to sample D.

The response and recovery times of both samples are reported in Table 30.1, where the response time is the time taken by a sensor to achieve 50 or 90 ppm of NH_3 in the case of gas adsorption, and the recovery time is the time necessary to describe the total resistance changes in the case of gas desorption. These response and recovery times are quite fast for both samples, although the sample C is quite faster than the sample D.

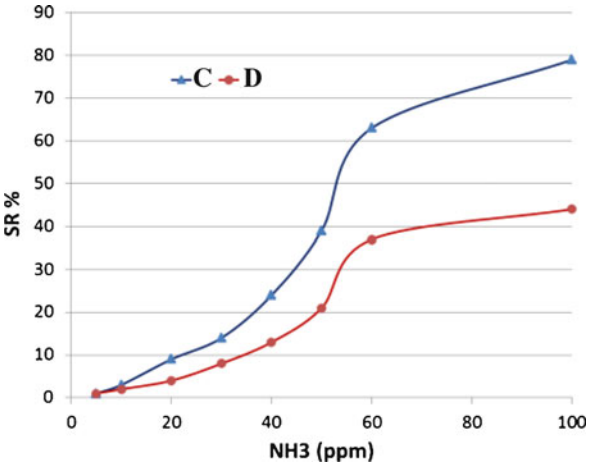

Fig. 30.3 Sensor responses (SR) of the samples C and D toward NH_3 changes

Table 30.1 Response and recovery times of the samples C and D

Response time (min)	C	D
From 0 to 50 ppm NH_3	2.8	5.1
From 0 to 90 ppm NH_3	4.5	5.7
Recovery time (min)	C	D
From 50 to 0 ppm NH_3	0.8	1.6
From 90 to 0 ppm NH_3	1.1	2.3

30.3.3 Cross-Sensitivity Measurements

Cross-sensitivity measurements were finally performed with respect to CH_4 (100 ppm) and CO_2 (200 ppm), where the concentrations of both gases were determined by a specified probe. It was found that there was no variation in the electrical resistance of both samples when exposed to these gases, which means that the sensor was selectively sensitive towards NH_3 and insensitive towards CH_4 and CO_2.

30.4 Conclusions

Glass-crystalline materials of the system $WO_3{\cdot}ZnO{\cdot}La_2O_3{\cdot}Al_2O_3$ with different compositions were prepared using screen-printed technique to be employed as ammonia gas sensors. In NH_3 atmosphere, the samples showed good responses starting from 10 ppm NH_3. The best response was found for the sensor with the higher content of WO_3. The response and recovery times were quite fast for both tested samples. Additionally, the fabricated gas sensors showed selective sensitivity towards NH_3, and insensitivity towards CH_4 and CO_2 gases.

References

1. Kulkarni S, Navale Y, Navale S, Stadler F, Ramgir N, Patil V. Hybrid polyaniline-WO_3 flexible sensor: A room temperature competence towards NH_3 gas. Sensors and Actuators B: Chemical. (2019); 288:279–288.
2. He M, Xie L, Zhao X, Hu X, Li S, Zhu Z-G. Highly sensitive and selective H_2S gas sensors based on flower-like WO_3/CuO composites operating at low/room temperature. Journal of Alloys and Compounds. (2019); 788:36–43.
3. Kamble C, Panse M, Nimbalkar A. Ag decorated WO_3 sensor for the detection of sub-ppm level NO_2 concentration in air. Materials Science in Semiconductor Processing. (2019); 103:104613.
4. Staerz A, Liu Y, Geyik U, Brinkmann H, Weimar U, Zhang T, et al. The effect of platinum loading on WO_3 based sensors. Sensors and Actuators B: Chemical. (2019); 291:378–384.
5. Lee I, Choi S-J, Park K-M, Lee SS, Choi S, Kim I-D, et al. The stability, sensitivity and response transients of ZnO, SnO_2 and WO_3 sensors under acetone, toluene and H2S environments. Sensors and Actuators B: Chemical. (2014); 197:300–307.
6. Sun J, Sun L, Han N, Pan J, Liu W, Bai S, et al. Ordered mesoporous WO_3/ZnO nanocomposites with isotype heterojunctions for sensitive detection of NO_2. Sensors and Actuators B: Chemical. (2019); 285:68–75.
7. Shakya V, Pandey NK. Structural and moisture sensing properties of WO_3-ZnO nanocomposites synthesized by a soft chemical route. Materials Today: Proceedings. (2018); 5(3):9082–9088.
8. Park S. Enhancement of hydrogen sensing response of ZnO nanowires for the decoration of WO_3 nanoparticles. Materials Letters. (2019); 234:315–318.
9. Zheng H, Ou JZ, Strano MS, Kaner RB, Mitchell A, Kalantar-zadeh K. Nanostructured tungsten oxide - properties, synthesis, and applications. Advanced Functional Materials. (2011); 21 (12):2175–2196.
10. Potje-Kamloth K. Semiconductor junction gas sensors. Chemical Reviews. (2008); 108 (2):367–399.
11. Kamali Heidari E, Marzbanrad E, Zamani C, Raissi B. Nanocasting Synthesis of Ultrafine WO_3 Nanoparticles for Gas Sensing Applications. Nanoscale Research Letters. (2009); 5(2):370–373.
12. Leng J-y, Xu X-j, Lv N, Fan H-t, Zhang T. Synthesis and gas-sensing characteristics of WO_3 nanofibers via electrospinning. Journal of Colloid and Interface Science. (2011); 356(1):54–57.
13. Liu B, Cai D, Liu Y, Wang D, Wang L, Wang Y, et al. Improved room-temperature hydrogen sensing performance of directly formed Pd/WO_3 nanocomposite. Sensors and Actuators B: Chemical. (2014); 193:28–34.
14. Ponzoni A, Comini E, Ferroni M, Sberveglieri G. Nanostructured WO_3 deposited by modified thermal evaporation for gas-sensing applications. Thin Solid Films. (2005); 490(1):81–85.
15. Sriyudthsak M, Supothina S. Humidity-insensitive and low oxygen dependence tungsten oxide gas sensors. Sensors and Actuators B: Chemical. (2006); 113(1):265–271.
16. Siriwong C, Wetchakun K, Wisitsoraat A, Phanichphant S, editors. Gas sensing properties of WO_3-doped ZnO nanoparticles synthesized by flame spray pyrolysis. SENSORS, IEEE; 25–28 Oct. (2009).
17. Kim S-J, Cho P-S, Lee J-H, Kang C-Y, Kim J-S, Yoon S-J. Preparation of multi-compositional gas sensing films by combinatorial solution deposition. Ceramics International. (2008); 34 (4):827–831.
18. Ong H, Lei D, Li J, Xu J. ZnO platforms for enhanced directional fluorescence applications. Metal-Enhanced Fluorescence: John Wiley and Sons; (2010); p. 393–418.
19. Hahm Ji. Enhanced fluorescence detection enabled by zinc oxide nanomaterials. Metal-Enhanced Fluorescence: John Wiley and Sons; (2010); p. 363–391.
20. Kanan SM, El-Kadri OM, Abu-Yousef IA, Kanan MC. Semiconducting metal oxide based sensors for selective gas pollutant detection. Sensors. (2009); 9(10):8158–8196.

21. Cheng X, Zhao H, Huo L, Gao S, Zhao J. ZnO nanoparticulate thin film: preparation, characterization and gas-sensing property. Sensors and Actuators B: Chemical. (2004); 102 (2):248–2452.
22. Nunes P, Fortunato E, Lopes A, Martins R. Influence of the deposition conditions on the gas sensitivity of zinc oxide thin films deposited by spray pyrolysis. International Journal of Inorganic Materials. (2001); 3(8):1129–1131.
23. Pál E, Hornok V, Kun R, Oszkó A, Seemann T, Dékány I, et al. Hydrothermal synthesis and humidity sensing property of ZnO nanostructures and $ZnOIn(OH)_3$ nanocomposites. Journal of Colloid and Interface Science. (2012); 378(1):100–109.
24. Ataalla M, Milanova M, Hassan M, Afify AS, Tulliani J, Dimitriev Y. Nano-and microsized phases in the WO_3-ZnO-Nd_2O_3-Al_2O_3 system for applications in environmental monitoring. Nanoscience Advances in CBRN Agents Detection, Information and Energy Security: Springer; (2015); p. 451–459.
25. Ataalla M, Afify AS, Hassan M, Adam A, Milanova M, Piroeva I. Humidity Sensing Properties of Tungsten Based Glass Crystalline Materials in the WO_3-ZnO-La_2O_3-Al_2O_3 System. Advanced Nanotechnologies for Detection and Defence against CBRN Agents: Springer; (2018); p. 417–425.
26. Tulliani J-M, Bonville P. Influence of the dopants on the electrical resistance of hematite-based humidity sensors. Ceramics International. (2005); 31(4):507–514.
27. Don WG, Marylee ZS. Perry's Chemical Engineers' Handbook, 9th Edition. McGraw-Hill Education; (2019).

Part XI
Applications: Water Treatment, Environment and Energy

Chapter 31
Optimizing Bacterial Cellulose Production Towards Materials for Water Remediation

Víctor Calvo, Javier Torrubia, Domingo Blanco, Enrique García-Bordeje, Wolfgang K. Maser, Ana M. Benito, and Jose M. González-Domínguez

Abstract Cellulose is a renewable alternative to mass consumption plastics, but its manufacture by the classical methods is not sustainable due to the use of large amounts of strong acids, bases and/or organic species (e.g. ionic liquids) in its production, generating many residues. Bacterial cellulose (BC) has a simpler processing because it is much more cleanly generated. In this work, BC aerogels and xerogels are compared in order to ascertain how the bacterial culture conditions (pH, carbon and nitrogen sources) and the raw hydrogels processing determine their thermal stability, crystallinity index, swelling ratio and flammability. The most notable results are the influence of the drying method on the swelling ratio and the carbon source on the thermal stability. Finally, a feasible application of BC aerogels is presented by treating contaminated water and by capturing water within a non-polar solvent, taking advantage of the dry BC sorption capacity.

Keywords Bacterial cellulose · Sustainability · Nanotechnology · Environment · Water remediation

31.1 Introduction

Polymers are fundamental materials in our society, being present in a myriad of products such as computers, food packaging or textiles. The main reasons of their importance are versatility, low costs of production and a wide variety of properties;

Authors Víctor Calvo and Javier Torrubia have equally contributed to this chapter.

V. Calvo · E. García-Bordeje · W. K. Maser · A. M. Benito · J. M. González-Domínguez (✉)
Instituto de Carboquímica, ICB-CSIC, Zaragoza, Spain
e-mail: jmgonzalez@icb.csic.es

J. Torrubia · D. Blanco
Department of Animal Production and Food Science, Veterinary Faculty Instituto Agroalimentario de Aragón (IA2), Zaragoza, Spain

P. Petkov et al. (eds.), *Nanoscience and Nanotechnology in Security and Protection against CBRN Threats*, NATO Science for Peace and Security Series B: Physics and Biophysics, https://doi.org/10.1007/978-94-024-2018-0_31

however, there are different problems related to the environmental burden associated to polymer production from non-renewable materials (e.g. petrol) [1] and the deficient management that has been traditionally followed for plastics re-use and recycling.

Bioplastics are an alternative to the ordinary plastics as they are produced from renewable sources, entailing a lesser extent of contaminants upon degradation. Nevertheless, the bioplastics possess a higher cost of production and not so many areas of application, reasons why it is imperative to continue exploring and investigating a way to reach a sustainable development of these materials [2].

An additional risk associated with an excessive consumption is the contamination of drinking water, a renewable resource but not endless, with about four billion people facing scarcity of drinking water at least 1 month per year [3]. This is a problem not only derived from a consumer society but also due to different industrial processes and to the degradation of plastics and other materials in rivers and underground wells.

Cellulose is the most abundant biopolymer on Earth, and the main structural component of plants, widely used to produce paper and cardboard, or more specific applications like coatings, membranes or pharmaceuticals. Its structure is fibrillar and is formed by polymerized D-glucose rings linked by β-1,4 bonds. Its most important characteristics are a hydrophilic character, chirality, biodegradability and the possibility of chemical modification to create products like cellulose acetate or nitrocellulose [4].

There are multiple renewable sources containing cellulose, namely cotton, wood pulp or agricultural/food waste, but in these vegetable materials the concomitant presence of other biopolymers such as lignin or hemicelluloses (that are not as useful as cellulose) makes it necessary to perform a thorough separation procedure to isolate the cellulose. Traditional methods to process cellulosic materials need strong acids and bases, or even organic liquids, in order to obtain cellulose with a certain degree of purity. This approach does not match at all with the principles of green and sustainable chemistry because of the excessive energy and reagents input, significantly rising the price of the final products [4, 5].

To improve the sustainability and affordability of cellulose production, besides improving its native properties, it is of paramount importance to develop a straightforward process leading to a high purity product with the minimum generation of residues. These principles can be fulfilled by bacterial cellulose (BC). Aerobic bacteria belonging to the acetobacter genus are able to produce hydrogels of BC by oxidative fermentation of simple sugars (mono and disaccharides) like glucose, fructose or saccharose. Such cellulose hydrogels are produced at the interface between the culture medium and the air, generating a three-dimensional network of nanosized fibres, randomly oriented with high surface area and porosity [6].

Bacteria produce BC without the need of any other inputs, easing the processing and generating purer and more crystalline cellulose. The composition of the culture medium can be optimized to increase the production rate and the characteristics of the materials [5]. The as-made hydrogels can be dried, ending up in xerogels or aerogels, having a critical influence on the swelling degree and the porosity of the

final material [6]. Actually, there is a huge investigation effort to make use of residues, derived from large-scale production surpluses, to generate BC; for instance, corn steep liquor [7] or industrial waste [8], thus reasserting the feasibility and affordability of the BC production. However, every bacterial strain needs particular conditions not only to optimally produce BC, but also to provide useful materials with the best features, being the reason why it is of special relevance to study the influence of the bacterial culture conditions on the eventual characteristics of processed BC materials.

In the present work, we report on the synthesis and characterization of BC materials, in which the composition of the bacterial culture medium (namely pH and carbon source) has been explored to be related to the final properties of derived xerogels and aerogels, with particular focus on their thermal stability and crystallinity. The aim is to achieve nanocellulose materials with optimal properties to be used for water remediation by tuning the production step.

31.2 Experimental

31.2.1 Materials and Production Methodology

BC hydrogels were produced by *Komagateibacter xylinus* bacteria, bought from the *Colección Española de Cultivos Tipo* (CECT), Valencia (Spain), in a fresh form (CECT/473). All reagents were purchased from Sigma Aldrich (reagent grade) and applied without further treatment. The initial culture medium was the Hestrin-Schramm (HSM) broth [9]. To modify the pH, sodium hydroxide or citric acid were used. Additionally, different carbon sources were tested, e.g. glucose, fructose or saccharose. The bacterial culture was carried out in 250 ml Erlenmeyer flasks at a stable temperature in the range of 28–30 °C. At the interface between the air and the culture medium BC hydrogels are formed, and when their size is large enough, they tend to fall to the bottom of the flask, so then they can be removed and processed. Once a hydrogel pellicle falls from the culture medium interface, another hydrogel is formed subsequently, being some sort of a discontinuous multilayer production.

31.2.2 Cleaning and Drying of Bacterial Cellulose Hydrogels

Hydrogels need to be cleaned in order to eliminate the residues from the bacteria and the culture medium. The cleaning procedure, for every hydrogel pellicle, starts by immersion in 250 ml of boiling deionized water for 40 min. Afterwards, it is soaked four times in 150 ml of fresh 0.1 M NaOH solution at 90 °C for 20 min. A subsequent neutralization is then performed with an excess of deionized water for at least 24 h until pH becomes neutral. Once the hydrogels are clean, they can be dried by two different means: on the one hand, the drying under an extraction hood

followed by desiccator renders BC xerogels; on the other hand, the freezing of BC hydrogels with liquid nitrogen and incorporation into a freeze-dryer (Telstar Cryodos, −49 °C, 0.3 mbar) provides BC aerogels.

31.2.3 Characterization

The production rate in the different culture media has been carefully analysed and compared. To evaluate the properties of the BC xerogels and aerogels generated by drying BC hydrogels, four techniques have been applied:

31.2.3.1 X-Ray Diffraction

A Bruker D8 Advance diffractometer was used, and the data were processed with Topas 5.0 software. The source of the X-rays was a copper tube with 40 kV acceleration voltage and 40 mA current. Diffractograms were registered in intervals of 0.05° and 3 s of accumulation time, in a Bragg-Brentano methodology in a range of 2θ = [10–40°] [10]. They were processed with the Origin 9.1 software to compare the diffractometers, the crystallinity index (CI) was calculated from the relationship between the (200) peak intensity, $I_{(200)}$, and the valley of the amorphous cellulose $I_{(am)}$ [6]:

$$CI(\%) = \frac{\left(I_{(200)} - I_{(am)}\right)}{I_{(200)}} \cdot 100$$

31.2.3.2 Thermogravimetric Analysis

Samples were registered with a Netzsch TG 209F1 device in a nitrogen atmosphere. The heating ramp was 10 °C/min from 30 °C to 800 °C [10]. The thermal degradation profiles were evaluated according to three parameters: the temperature of the degradation onset, the temperature of maximum degradation rate (T_{max}) and the final residue ratio (in %). This latter value can be related to the oxygen index (OI) and the flammability of the sample through the empirical Van Krevelen equation [11]:

$$OI\ (\%) = 17,5 + 0,4 * (\%Residue)$$

A material can be considered flammable when OI $\leq$ 26%.

31.2.3.3 Swelling Degree

With this procedure, the capability of water uptake exhibited by BC xerogels and aerogels was assessed. The samples were weighed in dry form and then immersed in water. The weighing was performed again (preceded by gentle removal of the excess water) at intervals of 1 min until reaching 15 min. From this point on, the weighing was made at 30 min, 1 h and day by day until a stable and unchanged mass is recorded (meaning that the material has reached its maximum water uptake capacity). This maximum swelling degree was calculated with the following equation, in which m is the maximum mass and m_0 the initial mass:

$$Swelling\ degree = \frac{m - m_0}{m_0} * 100$$

31.2.3.4 Scanning Electron Microscopy

Images of the surface microstructure and morphology were acquired with a JEOL-200FXII scanning electron microscope and collected in the secondary electron mode. Given the electrically insulating nature of BC, it was necessary to cover its surface with a thin layer of gold (15 nm) before visualizing.

31.3 Results and Discussion

31.3.1 Influence of the Drying Methods

As stated above, from the produced BC hydrogels, one can obtain useful nanocellulose-based materials upon drying. The characteristics of such materials can be very dependent on the drying method, what we illustrate here. From the various possible drying methods which could be applied, we have focused on two specific ones: drying in ambient conditions (by aid of a fuming hood and a desiccator), and lyophilization (by aid of a freeze-drying device).

The as-obtained aerogels and xerogels from the same culture conditions were compared, in order to isolate the influence of the drying method. The biggest difference found was in the swelling degree (Fig. 31.1), the aerogels have about six times more water absorption capacity than the xerogels and are able to take a mass of water nearly 100 times its weight. This aspect is determined by the lack of pore-filling fluid in the xerogels, whereas in the aerogels the original porous structure of hydrogels is maintained, but these are filled with air. The porosity is also appreciable by SEM (Fig. 31.2), in which the space between the fibres within the aerogel is clearly seen, but in contrast, the xerogel fibres are visibly compact. In the real images of the samples (insets in Fig. 31.2), this aspect is also observed, the

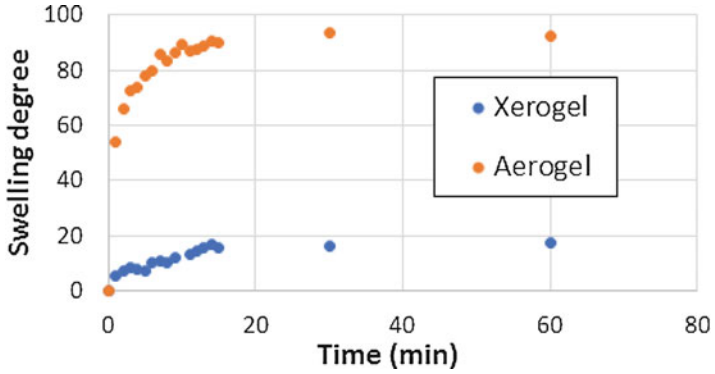

Fig. 31.1 Swelling degree of a BC xerogel and a BC aerogel coming from the same hydrogel, cultured in optimal conditions, but dried differently

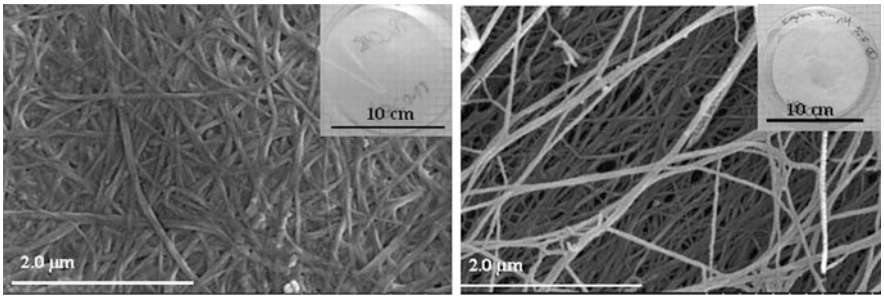

Fig. 31.2 SEM images of a BC xerogel (left) and a BC aerogel (right). Insets show real photographs of these materials

aerogels are thicker and more opaque than the xerogels. The obtained morphologic profiles present a similar aspect like those reported in the literature with the same bacterial strain or with *K. sucrofermentans* but differ from others like the ones produced with *Gluconacetobacter hansenii* or *G. europaeus* [6–8]. This reveals the influence of the bacterial strain on the microstructure of the BC aerogels and xerogels.

Differences in thermal stability were noticed as well (Fig. 31.3). According to their respective thermograms, the BC aerogels generated less amount of solid residue upon heating than the xerogels, but their degradation profile is very similar. The influence of the drying method on the percentage of residue can be critical as for the material's flammability. In Fig. 31.3, the xerogels are non-flammable (residue above 20 wt%, hence OI $\geq$ 26%) and their lyophilized counterparts are mostly flammable (residue below 20 wt%, hence OI $\leq$ 26%).

The comparison between the X-ray diffractograms of the xerogels and the aerogels displays also differences between both types of BC materials (Fig. 31.4). The (110) crystalline plane is more intense in the aerogels, as compared to xerogels,

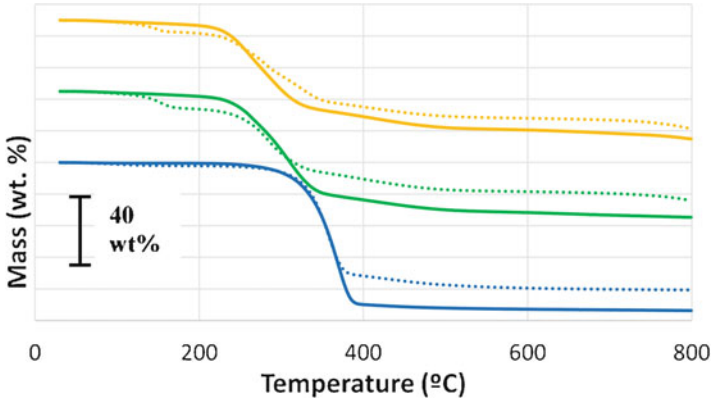

Fig. 31.3 Thermograms, in a relative scale, of dried BC hydrogel samples (3 equivalent replicas of a given hydrogel). Solid lines correspond to aerogels, while dotted lines correspond to xerogels

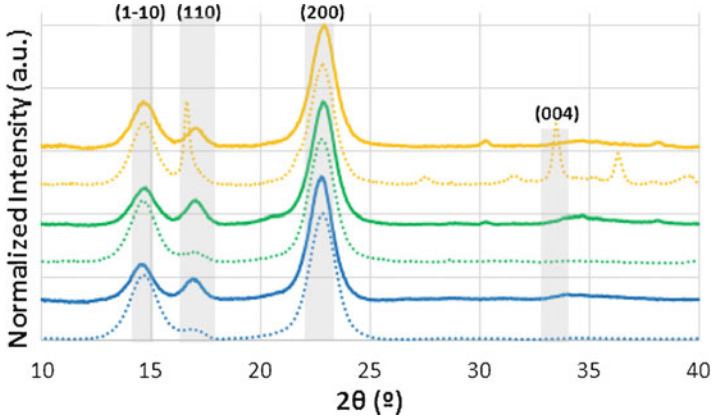

Fig. 31.4 X-ray diffractograms of dried BC hydrogel samples (3 equivalent replicas of a given hydrogel). Solid lines correspond to aerogels, while dotted lines correspond to xerogels. Miller planes are indicated by grey fringes

and the inverse trend is observed for the (1–10) plane. The CI is also different, slightly higher in the xerogels (89.31%) than in aerogels (86.08%), evidencing the influence of the drying method on the ordering of the cellulose fibres. By comparing our XRD profiles with other ones from BC produced with different bacteria, such as *G. hansenii* [7] or *Asaia bogorensis* [12], the relative intensity between the two main peaks is somewhat different, but the difference in XRD profiles between the aerogels and the xerogels is not observed, as it was reported elsewhere for the same bacteria [6]. So the drying method is particularly influent in the case of *K. xylinus*. In essence, the selected drying method of BC hydrogels stemming from *K. xylinus* is of paramount importance to tailor the BC physical properties, being able to provide a specific water uptake capacity or thermal degradation and flammability profiles.

31.3.2 Bacterial Culture Conditions

In general terms, the production of BC hydrogels from *K. xylinus* was optimized by varying certain parameters, namely the medium pH, the incubation temperature, the carbon and the nitrogen sources. By simple visual inspection, the amount and quality of the hydrogels were taken as representative features to decide the most suitable parameter choices. The temperature influence perfectly matched with that reported in the literature: 30 °C provides an optimal production rate (less than 7 days per hydrogel pellicle) [9], whereas temperatures above (up to 37 °C) and below (down to 5 °C) are detrimental for the production (hydrogels produced in a time span of 14–21 days). The pH values were varied systematically from 4.4 to 7 (at a fixed temperature of 28–30 °C) and the production rate of each hydrogel pellicle was more favorable at lower pH values: 5 days at pH = 4.4; 6 days at pH = 5–5.5; 6–7 days at pH = 6; and finally no appreciable BC production at pH =7; this tendency is also observed elsewhere [13]. As regards to the carbon source, no hydrogels were formed with lactose or sorbitol, while mannitol gave a low production rate (~10 days) and with a very low quality. Fructose provided much better results, but the best carbon sources were glucose and saccharose, the former being even better than the latter. The best nitrogen source was a mixture of yeast extract and peptone (0.5% m/m each), whereas a mixture of yeast extract and ammonium sulfate was not as good as the former. For all these reasons, the best culture conditions, directed towards the best quality and the highest yield of BC hydrogels were chosen to be glucose (4–5%), pH = 4.4, and yeast extract + peptone (0.5–1% each). Besides, the culture needs to be as static as possible, because the stirring of the culture medium prevents the formation of a consistent hydrogel. Indeed, the medium stirring leads to a shapeless coil, devoid of all physical consistency, which was extremely difficult to extract. The bacterial culture in a medium with a small amount of ethanol was also tried and no appreciable change in the production rate was noticed, but conversely, a total loss of the production occurred when NaCl was introduced in the culture medium.

All the aforementioned statements are given for the optimal hydrogels production, but these do not take into account the characteristics of BC upon drying. The possible influence of the bacterial culture conditions on the physical properties of the final materials (i.e. the BC aerogels and xerogels) has hardly ever been explored [6, 7, 13]. In the following sections, we attempt to compare the particular effects that the bacterial culture conditions may exert over the physical properties (thermal stability and crystallinity) of the resulting aerogels and xerogels.

31.3.2.1 Influence of the pH of the Culture Medium

The comparison of samples cultured at different pHs has been carried out using glucose as a carbon source. The selected pH values were 4.0, 5.5, 6.0 and 7.0, but as

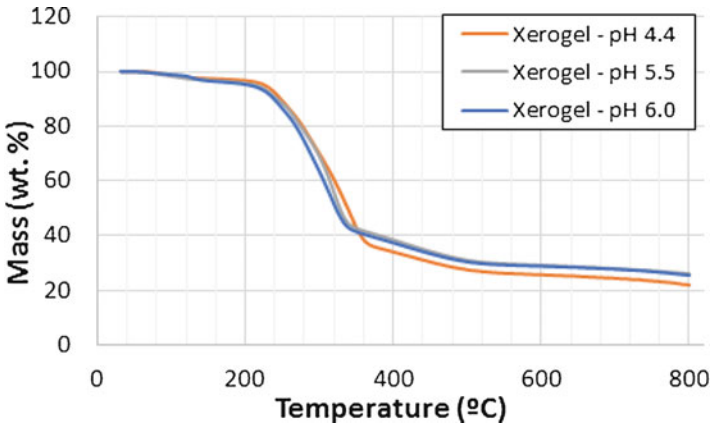

Fig. 31.5 Thermograms of BC xerogel samples stemming from hydrogels cultured at different pHs

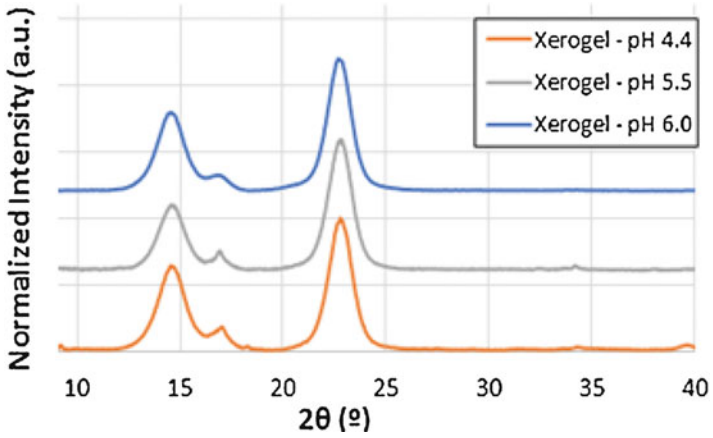

Fig. 31.6 X-ray diffractograms of BC xerogel samples stemming from hydrogels cultured at different pHs

commented earlier, no hydrogel was produced at pH = 7.0. The highest production rate was observed at pH 4.4 in 5 days. Once these hydrogels were obtained, both aerogels and xerogels were produced from them respectively, and subsequently characterized. In Fig. 31.5, an example is given for BC xerogels, and it is visible that there are not significant differences in their thermal degradation profile, concluding that pH does not have a clear influence on the thermal stability of the dried BC. A similar observation was inferred from the BC aerogels (data not shown).

The same observation can be made when comparing the X-ray diffractograms (Fig. 31.6). There are no shifts in the position of the peaks and the normalized

intensities are similar for all samples. However, the CI values are higher when the pH of the culture medium is increased, the average is 91.47% for pH = 6.0, 88.45% for pH = 5.5 and 88.00% for pH = 4.0. Thus, it can be concluded that a higher pH results in a BC with a higher CI but entailing a slower production rate.

31.3.2.2 Influence of the Carbon Source in the Culture Medium

This section is focused on the three carbon sources that provided a satisfactory production of BC hydrogels, namely glucose, fructose and saccharose. With these three sources, the hydrogels quality is similar, but the production is faster with glucose (5 days per hydrogel pellicle), in contrast to the 6–7 days needed with fructose and saccharose.

The BC materials produced with fructose show higher thermal stability with a large upshift of about 50 °C in the T_{max} value in comparison to the other carbon sources. The saccharose-derived ones are a bit more stable than those from glucose, but this difference is small. This trend is observed in both BC xerogels and BC aerogels, but as a matter of example only the aerogels are shown (Fig. 31.7). The residue amount reveals that the fructose-derived dried samples have a smaller OI (22.9% with glucose and 27.3% with saccharose) making it flammable in contrast to the others, which are not. In other words, fructose-derived dried BC materials show excellent thermal stability but a flammable behaviour, whereas the glucose- or saccharose-derived ones show lower thermal stability but a strong non-flammability. However, no clear trends or visible effects of the carbon source were noticed neither in the XRD profiles, nor in the CI values.

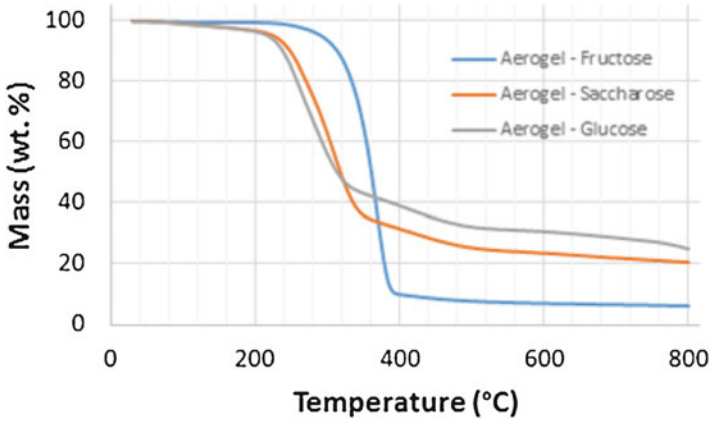

Fig. 31.7 Thermograms of BC aerogel samples coming from hydrogels cultured with different carbon sources

31.3.3 Application of Optimized BC Materials in Water Remediation

After revealing the effects that the bacterial culture conditions have, not only on the rate and quality of BC hydrogels production, but also on the eventual aerogels/xerogels derived from them after drying, we have attempted to apply them in a simulated application regarding the safety, such as remediation of contaminated water. For this specific purpose, we have selected the optimized BC aerogels for their higher capacity to absorb water. Two cases have been studied: (i) a small quantity of water in toluene (previously dyed with Sudan III) (Fig. 31.8, top panel); (ii) an emulsion of dyed toluene into water (Fig. 31.8, bottom panel).

We observed a more pronounced and faster sorption effect in the case of the water in toluene, because the cellulose is a very hydrophilic material. A more modest, yet appreciable, effect is also observed in the case of the toluene-in-water emulsion, probably because the sorption of toluene is irreversible. This test reasserts the fact that BC aerogels are extremely useful for water-related applications, such as the drying of apolar solvents, water decontamination or control of an organic spill. These applications can be studied from a nanotechnological and sustainable

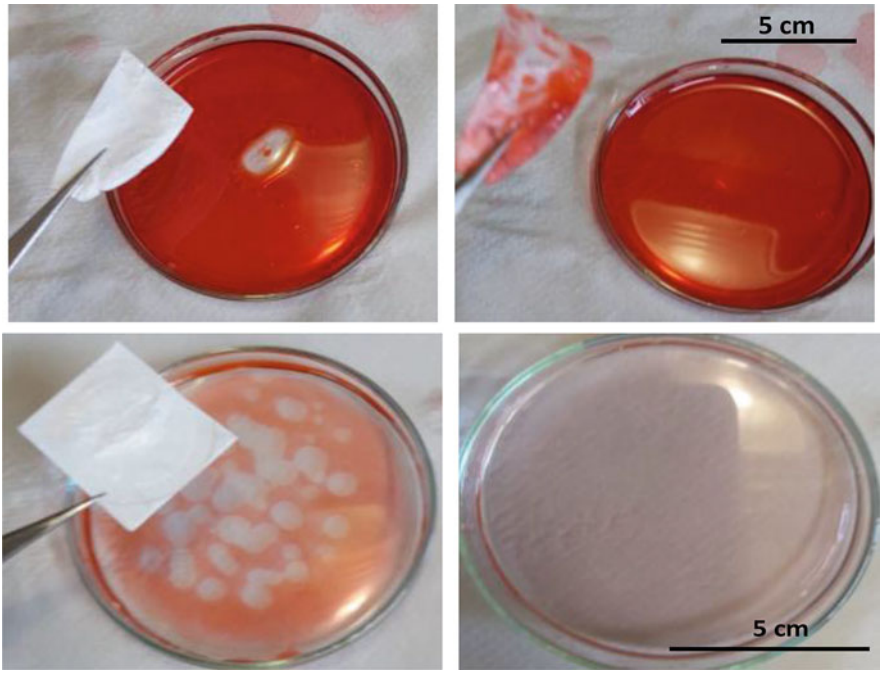

Fig. 31.8 Sorption tests with a BC aerogel. Top panel, an impurified toluene with water; bottom panel, an emulsion of toluene in water. Left side images represent the starting point while right side images show the eventual result after soaking the hydrogel (few seconds in each case)

perspective, and have important repercussions in human safety, as regards to the management of drinking water and control over possible threats in this matter. To improve the efficiency, it is possible to modify the BC to remove contaminants [14].

31.4 Conclusion

BC hydrogels production, stemming from *K. xylinus*, has been optimized in terms of bacterial culture and subsequently tailored in their physical properties after drying. It is possible to control the BC hydrogel properties by rationally selecting the appropriate drying method. In this regard, the aerogels (obtained by lyophilisation) have a much larger sorption capacity and a higher porosity, whereas xerogels (obtained by drying in open air) are more compact, as observed by SEM. Contrary to the aerogels, the BC xerogels are non-flammable. The pH of the culture medium does not have a great influence on the thermal stability of the xerogels and aerogels, but it is important for the hydrogel production rate and slightly influences the CI. The carbon source has a greater influence in the thermal stability of the final materials. Fructose provides a higher thermal stability; however, its dry materials are flammable; glucose and saccharose show an inverse trend as compared to fructose. The advantage of glucose over the fructose and saccharose is its somewhat faster production rate.

The accomplishment of a sorption test demonstrates that BC aerogels, once optimized in production and physical properties, can be applied as an efficient sorbent, taking advantage of their porosity and hydrophilic character. There are other possible implementations, such as filters to purify water, with critical implications in human safety and defence against chemical threats.

Acknowledgments Financial support was obtained from the Spanish Ministry of Economy, Industry and Competitiveness (MINEICO), through project IJCI-2016-27789, the Spanish Research Agency (AEI) through GRAPEROS project (ref ENE2016-79282-C5-1-R1 and associated EU Regional Development Funds), and from Gobierno de Aragón (Grupo Reconocido DGA T03_17R, A02_17R and associated EU Regional Development Funds). Dr. J.M.G.-D. greatfully acknowledges MIENICO for his 'Juan de la Cierva – Incorporación' research contract.

References

1. Shchipunov Y (2012) Bionanocomposites: green sustainable materials for the near future. Pure Appl Chem 84(12):2579–2607
2. Mohanty AK, Misra M, Drzal LT (2002) 14- Sustainable bio-composites from renewable resources in green materials world. J Polym Environ 10(April):19–26
3. Mekonnen MM, Hoekstra AY (2016) Sustainability: four billion people facing severe water scarcity. Sci Adv 2(2):1–7
4. Klemm D, Heublein B, Fink H-P, Bohn A (2005) Cellulose: fascinating biopolymer and sustainable raw material. Angew Chemie Int Ed 44(22):3358–3393

5. Esa F, Tasirin SM, Rahman NA (2014) Overview of bacterial cellulose production and application. Agric Agric Sci Procedia 2:113–119
6. Zeng M, Laromaine A, Roig A (2014) Bacterial cellulose films: influence of bacterial strain and drying route on film properties. Cellulose 21(6):4455–4469
7. Costa AFS, Almeida FCG, Vinhas GM, Sarubbo LA (2017) Production of bacterial cellulose by *Gluconacetobacter hansenii* using corn steep liquor as nutrient sources. Front Microbiol 8 (OCT):1–12
8. Tsouko E, Kourmentza C, Ladakis D, Kopsahelis N, Mandala I, Papanikolaou S, Paloukis F, Alves V, Koutinas A (2015) Bacterial cellulose production from industrial waste and by-product streams. Int J Mol Sci 16(7):14832–14849
9. Pourramezan GZ, Roayaei AM, Qezelbash QR (2009) Optimization of culture conditions for bacterial cellulose production by Acetobacter Sp. 4B-2. Biotechnology 8(1):150–154
10. Gonzalez-Dominguez JM, Ansón-Casaos A, Grasa López L, Abenia L, Salvador A, Colom E, Mesonero JE, Garcia-Bordeje JE, Benito AM, Maser WK (2019) Unique properties and behavior of non-mercerized type-II cellulose nanocrystals as carbon nanotube biocompatible dispersants. Biomacromolecules 20(8):3147–3160
11. González-Domínguez JM, Ansón-Casaos A, Castell P, Díez-Pascual AM, Naffakh M, Ellis G, Gómez MA, Martínez MT (2010) Integration of block copolymer-wrapped Single-Wall carbon nanotubes into a trifunctional epoxy resin. Influence on thermal performance. Polym Degrad Stab 95(10):2065–2075
12. Penttilä PA, Imai T, Capron M, Mizuno M, Amano Y, Schweins R, Sugiyama J (2018) Multimethod approach to understand the assembly of cellulose fibrils in the biosynthesis of bacterial cellulose. Cellulose 25(5):2771–2783
13. Soemphol W, Hongsachart P, Tanamool V (2018) Production and characterization of bacterial cellulose produced from agricultural by-product by Gluconacetobacter strains. Mater Today Proc 5(5):11159–11168
14. Fontana JD, Koop HS, Tiboni M, Grzybowski A, Pereira A, Kruger CD, da Silva MGR, Wielewski LP (2017) New insights on bacterial cellulose. Elsevier Inc.

Chapter 32
Sodium Ferrites: New Materials to Be Applied in Energy Storage Devices in a Wide Frequency Range

Sílvia Soreto Teixeira, Manuel P. F. Graça, and Luís C. Costa

Abstract Materials for energy storage have been a subject of high interest in recent times. The development of new materials with high dielectric constant and low losses is one of the main goals in scientific research for electronic applications. These properties allow reduction of the size and weight of the electronic devices. In this work, powders of sodium ferrite were prepared by sol-gel, using iron nitrate and sodium acetate as raw materials, according to the Pechini route. In order to optimize the synthesis parameters, the materials were heat-treated, and structural, morphological and dielectric characterization was performed to find the most suitable ones for storing energy. The sample structure was characterized by X-ray diffraction (XRD), Raman spectroscopy and the morphology surface by scanning electron microscopy (SEM). The dielectric properties were studied in a frequency range between 100 Hz and 1 MHz at temperatures from 200 up to 370 K by impedance spectroscopy measurements. The complex permittivity at 2.7 GHz and 5 GHz ($T = 300$ K) was determined using the small perturbation method through resonant cavities. The sample of sodium ferrite heat-treated at 1100 °C is the most promising for energy storage with a dielectric constant of ≈818 ($f = 1$ kHz; $T = 300$ K) and ≈6 ($f = 5$ GHz; $T = 300$ K), with low losses. The dielectric constant increases with the presence of $Na_3Fe_5O_9$ phase and with the grain size and consequently porosity decreases. At low frequencies, this sample presents two relaxation processes described by Cole-Cole model and the relaxation time versus temperature has an Arrhenius behaviour.

Keywords Sodium ferrites · Impedance spectroscopy · Dielectric relaxation · Microwaves

S. S. Teixeira (✉) · M. P. F. Graça · L. C. Costa
I3N and Physics Department, University of Aveiro, Aveiro, Portugal
e-mail: silvia.soreto@ua.pt

P. Petkov et al. (eds.), *Nanoscience and Nanotechnology in Security and Protection against CBRN Threats*, NATO Science for Peace and Security Series B: Physics and Biophysics, https://doi.org/10.1007/978-94-024-2018-0_32

32.1 Introduction

Ferrites belong to the ceramic soft materials which show interesting properties with potential to be applied in industry, for instance, as gas sensors [1], ion batteries [2], gas absorbers [3] among others. Oxides of the type ($AFeO_2$) (A = Li, Na, Ag) can have characteristics of multiferroics [4, 5] and are a type of ferrites in which, depending on the conditions of preparation, polymorphous compounds can be formed. The sodium ferrite $NaFeO_2$ can occur through three structures: γ-$NaFeO_2$, α-$NaFeO_2$ and β-$NaFeO_2$ [6], which possess different properties. According to the literature, α-$NaFeO_2$ crystal phase, which is paramagnetic and with a cubic system of oxygen atoms where the octahedral interstices are occupied by sodium and oxygen ions, is obtained at the lowest temperature [7]. Around 800 °C, this structure changes to an orthorhombic crystal system, known as β-$NaFeO_2$ [8] and around 1010 °C the γ-$NaFeO_2$ crystal phase with tetragonal structure can be formed. The β-$NaFeO_2$ crystal phase (Fig. 32.1a) presents a weak ferromagnetic behavior, at room temperature [9] with Néel temperature (T_N= 723 K) [4]. In the system Na_2O-Fe_2O_3, a phase different from the others can be found, $Na_3Fe_5O_9$, showing a monoclinic crystalline system. It presents an antiferromagnetic behaviour and can be formed just at higher temperatures (≈ 1100 °C). Actually, under specific conditions of pressure and temperature (p > 20 kbar; $T \approx$ 500 °C), this structure can also decompose into $NaFeO_2$ and Fe_2O_3 [7].

The sol-gel process is widely used to develop nanoparticles. In this method, first the metallic ions are complexed with a chelate agent and then the mixture is polymerized with a polymer, which aims the formation of a three-dimensional network. The sol-gel routine used is the Pechini's method [10, 11].

The impedance spectroscopy technique allows us to investigate the fundamental aspects of the dielectric properties and the results can be correlated with other properties, such as the structural, studied by X-ray diffraction (XRD) and Raman spectroscopy, and morphologic by scanning electron microscopy (SEM).

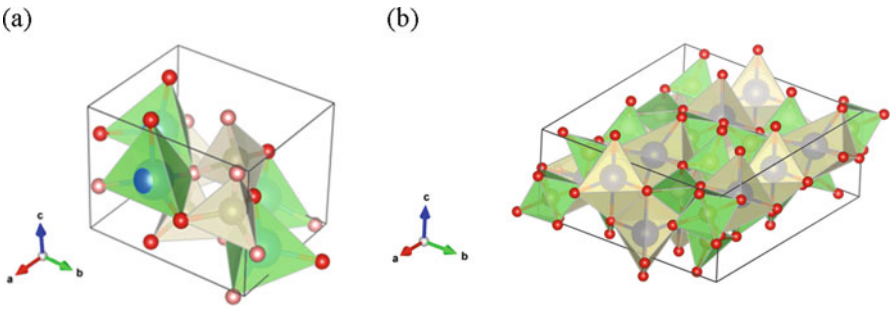

Fig. 32.1 Crystalline systems: (**a**) β-$NaFeO_2$ (cubic) and (**b**) $Na_3Fe_5O_9$ (monoclinic)

32.2 Experimental

The sodium ferrite powders were obtained by the sol-gel method, through the Pechini route. In this case, the citric acid (CA) was used in excess (1:3 molar ratio between metallic ion and CA) as a chelate agent to obtain the esterification reaction [12]. Ethylene glycol (EG) was applied for polymerization with a molar ratio between CA-EG of 2:3 [12, 13]. Metal solutions of sodium acetate [$NaCH_3COO.3H_2O$, purity >99%, VWR] and iron nitrate [$Fe(NO_3)_3.9H_2O$, purity >99%, Mateck], were used as initial materials. The suspension contained stoichiometric amounts of each metal. To promote the solubility, the suspension was stirred for 30 min, at room temperature. The final suspension, after the addition of EG, was mixed and stirred together for 24 h in order to obtain a gel. To evaporate the solvent, the mixture was dried at 250 °C for 60 h. After that, the powders were pressed into pellets and heat-treated at 600, 800, 1000 and 1100 °C for 4 h with a heating rate of 5 °C/min.

X-ray diffraction (XRD) patterns were obtained with a *PANalytical Empyrean powder X-ray Diffractometer* (CuKα radiation, $\lambda = 1.54056$ Å) at 40 kV and 30 mA, with a curved graphite monochromator, an automatic divergence slit (irradiated length 20.00 mm), a progressive receiving slit (height 0.05 mm) and a flat plane sample holder in a Bragg-Brentano parafocusing optics configuration. Intensity data were collected by the step counting method (step 0.02° in 1 s) in the 2θ angle range of 10–60°.

The micro-Raman spectroscopy measurements were performed in backscattering geometry at room temperature with a 532 nm laser line using a *HR-800-UV Jobin Yvon Horiba* spectrometer. A microscope objective with amplification lens 100 x focused the exciting light onto the sample.

The surface morphology was analysed by scanning electron microscopy (SEM) using a *TESCAN - Vega III*. Before the microscopic observation, the samples were covered with carbon to improve the surface conductivity.

The impedance spectroscopy (IS) was used to analyse the samples in the pellet form with a thickness less than 1 mm and a diameter ≈10 mm. The surfaces of the opposite sides were painted with silver paste. These measurements were performed in the frequency range from 10^2 to 10^6 Hz using an *Agilent 4294A* at temperature between 200 and 370 K in the C_p–R_p configuration. During the measurements, in order to improve the heat transfer and to homogenize the temperature, the sample holder was kept in a helium atmosphere. At microwave (MW) frequencies, the measurement of the complex permittivity $\varepsilon^* = \varepsilon' - i\varepsilon''$ was performed using the small perturbation theory with a resonant cavity operating in $TE_{1,0,5}$ mode at a resonant frequency of 2.7 GHz and a second cavity operating in the $TE_{1,0,11}$ mode at 5 GHz. To apply this method, the diameter of the samples must be, at least, half of the thickness. In this work, the samples had a diameter of 5 mm maximum. These measurements were carried out using a *HP 8753D* network analyser, coupled to the cavity resonator.

32.3 Results and Discussion

The diffractograms of the samples heat-treated at 600, 800, 1000 and 1100 °C are shown in Fig. 32.2.

The diffraction peaks at 29, 34 and 55° correspond to the crystalline phase of $NaFeO_2$ [1, 4] which is present only in the sample treated at 600 °C. This phase is orthorhombic, with space group *Pna21(33)* being also known as β-$NaFeO_2$. According to the literature [8], this phase is obtained at approximately 800 °C. Also in this sample, diffraction peaks characteristic of the α-Fe_2O_3 phase at 24, 33, 35, 41, 49 and 54° are detected [14, 15]. At higher temperatures, structural transformations occur, where β-$NaFeO_2$ reacts with α-Fe_2O_3 giving rise to the monoclinic crystalline phase $Na_3Fe_5O_9$, represented by Eq. (32.1):

$$3NaFeO_2 + Fe_2O_3 \rightarrow Na_3Fe_5O_9 \tag{32.1}$$

The crystalline phase of $Na_3Fe_5O_9$ is detected in the sample treated at 800 °C with diffraction peaks at 22.2, 26.9, 30.4, 33.7, 34.6, 35, 49.4 and 53°, together with the crystalline hematite phase. The $Na_3Fe_5O_9$ is obtained by this sol-gel method and these raw materials at a lower temperature than the reported in the literature (≈1100 °C) [7].

Above 800 °C heat treatment temperature, a decrease of the crystalline phase containing sodium is visible, which leads to increase of the hematite phase, suggesting the sodium volatilization through the release of sodium oxide according to Eq. (32.2).

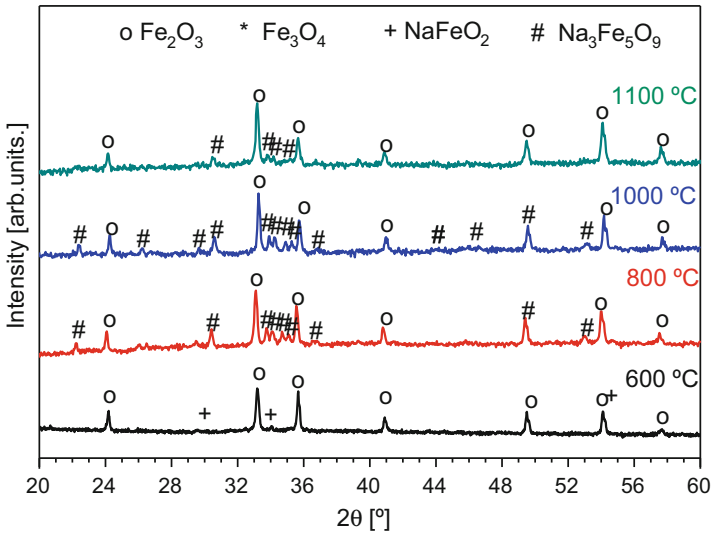

Fig. 32.2 XRD patterns of the powders treated at 600, 800, 1000 and 1100 °C

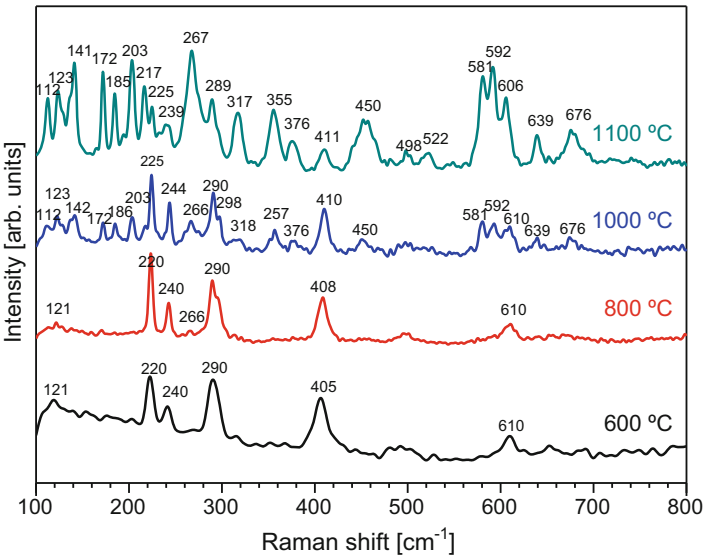

Fig. 32.3 Raman spectra of all samples studied in the current work

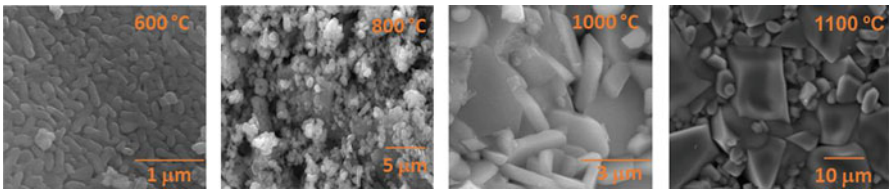

Fig. 32.4 SEM micrographs of samples treated at 600, 800, 1000 and 1100 °C

$$2Na_3Fe_5O_9 \rightarrow 3Na_2O + 5Fe_2O_3 \tag{32.2}$$

By Raman spectroscopy (Fig. 32.3), the main vibration modes of the α-Fe_2O_3 phase were identified at 225, 245, 292, 411 and 611 cm^{-1} approximately in all the samples [16]. In the sample treated at 600 °C according to the XRD results, the phases of α-Fe_2O_3 and β-$NaFeO_2$ are present, whereas the 405 cm^{-1} centred band may be characteristic of the β-$NaFeO_2$ phase, since it is the only sample that contains this crystal phase. The β-$NaFeO_2$ and $Na_3Fe_5O_9$ structural properties are not well described in the literature, so according to the spectra of the samples treated at 800, 1000 and 1100 °C, it can be inferred that the vibration modes centred at 266–267, 317, 376, 450, 581, 592, 639 and 676 cm^{-1} are assigned to the $Na_3Fe_5O_9$ phase.

Figure 32.4 presents the micrographs of the surfaces of the samples, from which it is visible that the average grain size increases with the heat treatment temperature.

The grain habits of the sample treated at 600 °C are different from the others, showing a needle-like habit which, according to XRD and Raman spectroscopy results, can be attributed to the β-$NaFeO_2$ crystal phase [1] and another prismatic type habit attributed to the α-Fe_2O_3 phase [15], wherein the sample treated at 1100 °C is present in clusters. The samples treated at 800, 1000 and 1100 °C show grains with prismatic habit but with different sizes, i.e., growing tendency with the heat treatment temperature. According to the previous results, these grains can be attributed to the crystalline phases $Na_3Fe_5O_9$ and α-Fe_2O_3.

The impedance spectroscopy allows the determination of the real and imaginary parts of the permittivity by the measured C_p and R_p, values [17]:

$$\varepsilon' = C_p \frac{d}{A\varepsilon_0} \tag{32.3}$$

$$\varepsilon'' = \frac{d}{\omega R_p A \varepsilon_0} \tag{32.4}$$

where d represents the sample thickness, A the area of the electrodes, ε_0 the empty space permittivity and ω the angular frequency. Figure 32.5 shows the dependence of the real part of the permittivity and the dielectric losses on the frequency for all samples at 300 K.

The most suitable sample to store electric energy is the one treated at 1100 °C, since it has a high dielectric constant with low losses. Due to that, just this sample was characterized for the dependence of the relaxation time with the temperature, allowing the construction of the relaxation map and giving the dynamic fingerprint of the material. As shown in the representation of the imaginary part of the permittivity (ε'') as a function of the frequency, the relaxation processes are not visible, probably because they are masked by the high conductivity and/or electrode polarization (Fig. 32.6a). Furthermore, in the modulus formalism ($M^* = 1/\varepsilon^*$) (Fig. 32.6b), the experimental data are not enough to ensure this characterization.

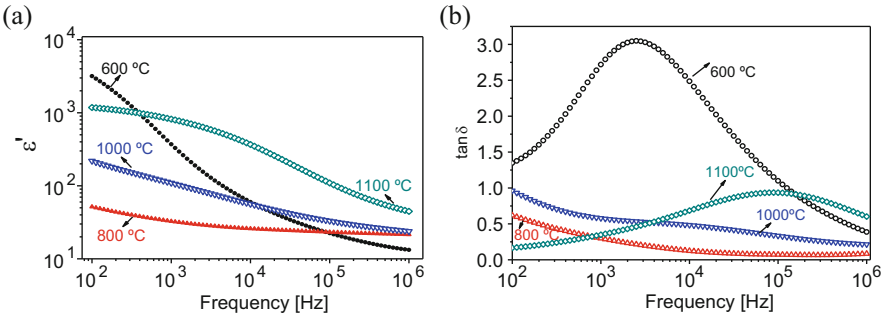

Fig. 32.5 (**a**) Dielectric constant and (**b**) dielectric losses (tan δ) versus frequency for all samples at 300 K

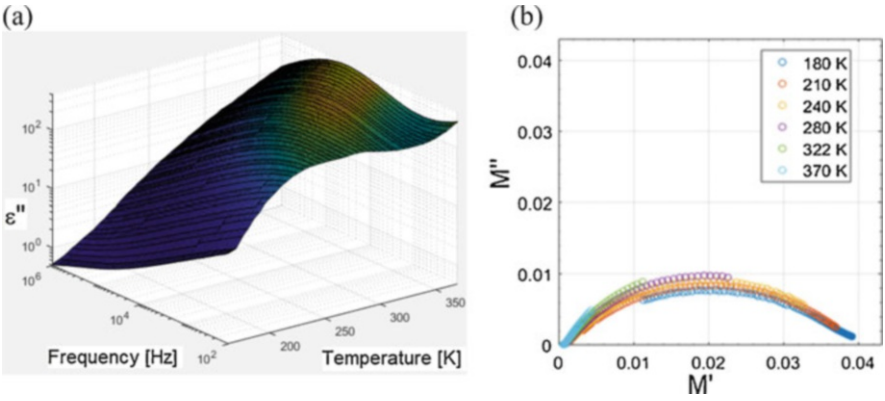

Fig. 32.6 (**a**) 3D plot of ε'' versus frequency/temperature and (**b**) Nyquist plot at different temperatures for the sample heat-treated at 1100 °C

Therefore, a completely different method was used, known as Wubbenhorst or derivative method [18]. This has the added benefit of not considering the effect of conductivity and the polarization due to the electrodes allowing the detection of the relaxation processes. The imaginary part of the complex permittivity can be obtained from Eq. (32.5):

$$\varepsilon''(\omega) \approx -\frac{\pi}{2} \times \frac{d\varepsilon'(\omega)}{dln(\omega)} \tag{32.5}$$

According to the 3D permittivity plot (Fig. 32.6a), the dependence of ε'' on the temperature at low frequencies seems to show two relaxation processes in the studied sample (1100 °C) but this analysis is not conclusive and needs further study. Also, the curve in Fig. 32.6b is broad and centred below the x-axis (*M'*) suggesting that only one Debye relaxation mechanism cannot describe this system. Figure 32.7 shows the analysis of the dependence of $\varepsilon''(\omega)$ obtained by the derivative method which is helpful to interpret this kind of relaxation mechanisms.

Using the software *WinFit* from *Novocontrol*, the experimental data $(\varepsilon'(\omega)$ and the $\varepsilon''(\omega)$ obtained by derivative method) (Fig. 32.7) were fitted using the Havriliak-Negami (HN) function [19], expressed by Eq. (32.6):

$$\varepsilon^*(\omega) = \varepsilon_\infty + \frac{\Delta\varepsilon}{\left(1 + (i\omega\tau)^\alpha\right)^\beta} \tag{32.6}$$

where α and β are the form parameters, ε_∞ the dielectric constant for high frequency, $\Delta\varepsilon$ the dielectric strength and τ the relaxation time. In the HN empiric model, if $\alpha \neq 1$ and $\beta = 1$ it can be interpreted as the Cole-Cole model [20]. Also, by Cole-Cole representation (ε'' vs. ε'), each semi-circle corresponds to a relaxation process,

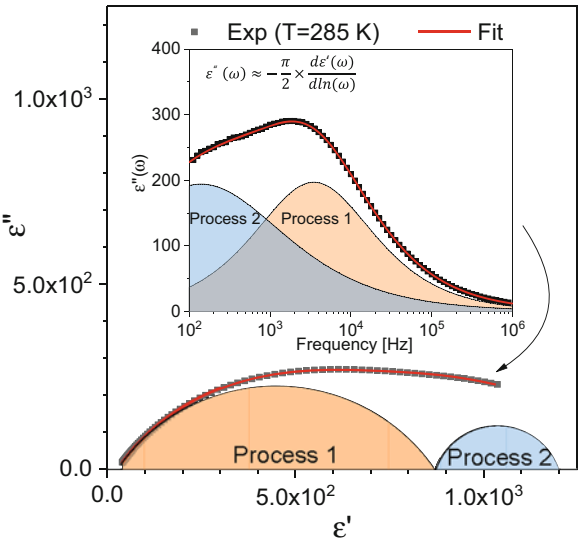

Fig. 32.7 Fittings of the Cole-Cole plot and imaginary part of the permittivity by the derivative method as a function of the frequency (inset) for the sample heat-treated at 1100 °C

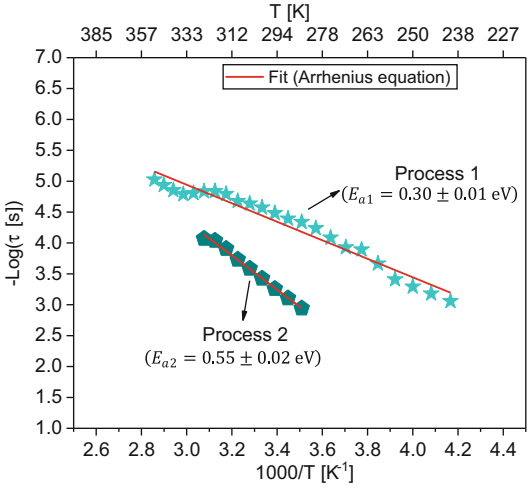

Fig. 32.8 Relaxation map of the sample heat-treated at 1100 °C, showing two relaxation processes with Arrhenius behaviour

differing from the Debye model because of the translation of the centre of the circle, corroborating with the previous suggestions by the analysis of Fig. 32.6a, b.

The dependence of the relaxation time (τ) with the inverse of the temperature, shows that the two relaxation processes have a behaviour (Fig. 32.8), described by the Arrhenius equation. This analysis allows the calculation of the thermal activation energy (E_a) of each relaxation process:

$$\tau \propto \exp\left[-\frac{E_a}{k.T}\right] \tag{32.7}$$

where k is the Boltzmann constant and T the temperature.

By the small perturbation theory, using a resonant cavity, it is possible to determine the complex permittivity (ε^*) at microwave frequencies [21]. Figure 32.9a shows the perturbation in the transmission of the 2.7 GHz resonance frequency by the insertion of a PTFE (standard sample with known permittivity $\varepsilon' = 2.1$ and $\varepsilon'' = 0.00042$) and a sample treated at 800 °C. The sodium ferrite sample perturbs much more the cavity than the PTFE, indicating a higher dielectric constant. Figure 32.9b shows the real part of the complex permittivity and the dielectric losses measured at 2.7 and at 5 GHz frequency as functions of the heat treatment temperatures.

The results in MW frequency region maintain the same tendency, i.e., higher dielectric constant is obtained in the samples which contain the $Na_3Fe_5O_9$ crystal phase. The sample treated at 1100 °C again presents the lowest dielectric losses. It must be noticed that considering the experimental error (<10%), the values of the dielectric constant at 2.7 GHz are as expected lower than at 5 GHz. Table 32.1 summarizes the results for all studied samples.

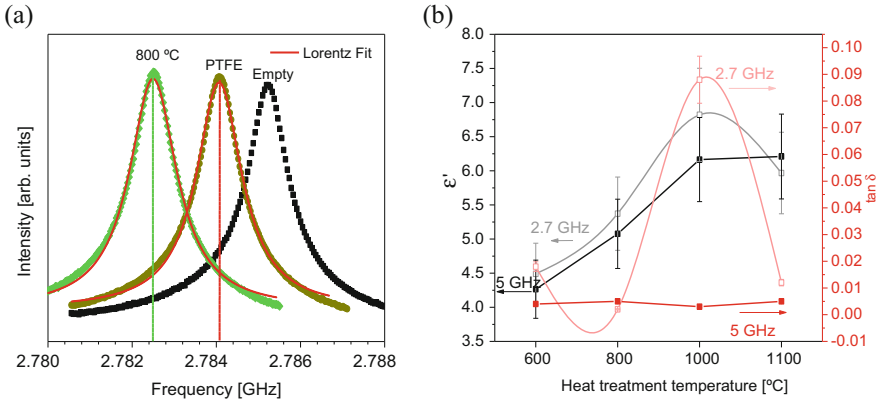

Fig. 32.9 (**a**) Transmission of the 2.7 GHz resonant cavity for unperturbed (empty) and perturbed by PTFE and sample treated at 800 °C, leading the calculation of the dielectric constant and (**b**) the dependence of ε' and tan δ with the temperature of the heat treatment at 2.7 and 5 GHz

Table 32.1 Dielectric constant and dielectric losses at 1 kHz, 2.7 GHz and 5 GHz at 300 K

Heat treatment temperature [°C]	ε'	ε''	tan δ	ε'	ε'' (10^{-2})	tan δ (10^{-2})	ε'	ε'' (10^{-2})	tan δ (10^{-2})
600	370.9	1008.5	2.72	4.49	8.09	1.80	4.26	1.94	4.55
800	119.4	196.8	1.65	5.37	1.07	0.20	5.08	2.49	4.91
1000	109.4	63.38	0.58	6.87	60.6	8.82	6.16	1.93	3.12
1100	817.8	285.1	0.35	5.97	7.31	1.22	6.21	3.14	5.06
	f = 1 kHz			f = 2.7 GHz			f = 5 GHz		

32.4 Conclusions

Sodium ferrites can be obtained by a sol-gel method using iron nitrate and sodium acetate as raw materials. Different crystal phases of sodium ferrite were obtained: β-$NaFeO_2$ at lower heat treatment temperature (600 °C) and $Na_3Fe_5O_9$ for heat treatments at higher temperatures. The structural changes and the increase of the grain sizes with the temperature of the heat treatment promote the increase of the dielectric constant keeping the dielectric losses low. The most promising sample for energy storage in the studied range of frequencies is the one treated at 1100 °C. The dependence of the dielectric processes on the temperature was characterized showing the presence of two relaxation processes described by the Cole-Cole model. This analysis was performed using the derivative or Wubbenhorst method.

References

1. Bakaimi I, Papadopoulou EL, Kenanakis G et al (2018) Thin film growth of delafossite β-NaFeO2 on a ZnO layer by pulsed laser deposition. Thin Solid Films 645:424–430. https://doi.org/10.1016/j.tsf.2017.11.022
2. Armstrong AR, Tee DW, La Mantia F et al (2008) Synthesis of tetrahedral LiFeO2 and its behavior as a cathode in rechargeable lithium batteries. J Am Chem Soc 130:3554–3559. https://doi.org/10.1021/ja077651g
3. Yanase I, Kameyama A, Kobayashi H (2010) CO2 absorption and structural phase transition of α-LiFeO2. J Ceram Soc Jpn 118:48–51. https://doi.org/10.2109/jcersj2.118.48
4. Viret M, Rubi D, Colson D et al (2012) β-NaFeO2, a new room-temperature multiferroic material. Mater Res Bull 47:2294–2298. https://doi.org/10.1016/j.materresbull.2012.05.040
5. Terada N, Khalyavin DD, Perez-Mato JM et al (2014) Magnetic and ferroelectric orderings in multiferroic α-NaFeO2. Phys Rev B Condens Matter 89:1–11. https://doi.org/10.1103/PhysRevB.89.184421
6. Hewston TA, Chamberland BL (1987) A survey of first-row ternary oxides LiMO2, (M= SC-Cu). J Phys Chem Solids 48:97–108. https://doi.org/10.1016/0022-3697(87)90076-X
7. Romers C, Rooymans CJM, Graaf RAG (1967) The preparation, crystal structure and magnetic properties of Na3Fe5O9. Acta Crystallogr Sect B: Struct Sci 22:766–771. https://doi.org/10.1107/S0365110X67001537
8. Théry J, Lejus AM, Briançom MD, Collongues R (1961) No title. Bull Soc Chim Fr 973
9. Watanable H, Fukase M (1961) Weak ferromagnetism in β-NaFeO2. J Phys Soc Jpn 16:1181–1184. https://doi.org/10.1143/JPSJ.16.1181
10. Pechini MP (1967) Method of preparing lead and alkaline earth titanates and niobates and coating method using the same to form a capacitor. US Pat. 3330697
11. Popa M, Crespo D, Calderon-moreno JM (2007) Powders from a polymeric precursor. J Am Ceram Soc 90:2723–2727. https://doi.org/10.1111/j.1551-2916.2007.01779.x
12. Razak JA, Sufian S, Shaari KZK et al (2012) Synthesis, characterization and application of Y3Fe5O12 nanocatalyst for green production of NH3 using magnetic induction method (MIM). AIP Conf Proc 1482:633–638. https://doi.org/10.1063/1.4757548
13. Kuzmenko AP, Abakumov PV (2011) Raman imaging of domains and fine structure of domain walls in YFeO3 crystals. Tech Phys Lett 37:1058–1061. https://doi.org/10.1134/S1063785011110265

14. Bolarín-Miró AM, Sánchez-De Jesús F, Cortés-Escobedo CA et al (2014) Structure and magnetic properties of GdxY1- xFeO3 obtained by mechanosynthesis. J Alloy Compd 586: S90–S94. https://doi.org/10.1016/j.jallcom.2013.04.029
15. Jezini VS (2015) Síntese e caracterização de óxido de ferro e do compósito óxido de ferro/óxido de grafeno reduzido para aplicação em supercapacitores. Universidade Federal do Amazonas - Instituto de Ciências Exatas
16. Nasibulin AG, Simas R, Jiang H et al (2009) Simple and rapid synthesis of ambient conditions α-Fe2O3 nanowires under amnient conditions. Nano Res 2:373–379. https://doi.org/10.1007/s12274-009-9036-5
17. Jonscher AK (1999) Dielectric relaxation in solids. J Phys D Appl Phys 32:R57–R70. http://iopscience.iop.org/0022-3727/32/14/201
18. Wubbenhorst M, Van Turnhout J (2002) Analysis of complex dielectric spectra. I. One-dimensional derivative techniques and three-dimensional modelling. J Non-Cryst Solids 305:40–49. https://doi.org/10.1016/S0022-3093(02)01086-4
19. Havriliak S, Negami S (1966) A complex plane analysis of α-dispersions in some polymer systems. J Polym Sci, Part C Polym Symp Symp 14:99–117. https://doi.org/10.1002/polc.5070140111
20. Cole KS, Cole RH (1941) Dispersion and absorption in dielectrics I. Alternating current characteristics. J Chem Phys 9:341–351. https://doi.org/10.1063/1.1750906
21. Teixeira SS, Graça MPF, Costa LC (2017) Microwave dielectric properties of sodium ferrite. Int J Mater Res Eng Innov 8:87–95

Chapter 33
Fluorescent Thin Film Probe for Nitro Compounds: Si Containing Poly [Diphenylacetylene] Case Study

Diana Harea, Jiři Zednik, Evghenii Harea, and Vladimir Sedlařík

Abstract This article examines poly[1-phenyl-2-(p-trimethylsilyl) phenylacetylene] (PTMSDPA) films as fluorescent probes for detection of water dissolved p-nitrophenol (NP) and 2.4-dinitrophenol (DNP). Thin film probes exhibited a tenacious quenching effect, manifested through a persistent decrease of luminescence, evolved with an increase of pollutant concentrations ($1.0*10^{-2}$ M, $5.5*10^{-3}$ M, and $1.0*10^{-3}$ M) and resulting in their detection. Quenched samples presented time dependent florescent emission recovery reaching up to 88% from the initial intensity for DNP and more modest 70% for NP solutions after 24 h conditioning in ambient atmosphere. The quenching mechanism employing the internal charge transfer complexes formation between the solid probe and the liquid pollutants is discussed and accounted for.

Keywords Chemosensors · Fluorescence · Quenching · Water pollutants

33.1 Introduction

Nitro compounds are broadly used in the synthesis of many products, including dyes, polymers, pesticides, and explosives. Their extensive application in diverse human activities led to heavy soil and groundwater contamination. During the last two decades, numerous methods for nitro compounds detection were developed including gas chromatography-mass spectroscopy [1], Raman spectroscopy [2], electrochemical methods [3], capillary X-ray imaging [4], and chemiluminescent methods [5]. Each method has its own advantages and disadvantages. Development

D. Harea (✉) · E. Harea · V. Sedlařík
Centre of Polymer Systems, University Institute, Tomas Bata University in Zlin, Zlin, Czech Republic

J. Zednik
Department of Physical and Macromolecular Chemistry, Faculty of Science, Charles University, Prague 2, Czech Republic

P. Petkov et al. (eds.), *Nanoscience and Nanotechnology in Security and Protection against CBRN Threats*, NATO Science for Peace and Security Series B: Physics and Biophysics, https://doi.org/10.1007/978-94-024-2018-0_33

of new methods for environmental pollutants detection, including water pollutants recognition, is still in high demand.

Nowadays various types of fluorescent chemical (FLC) sensors are under intensive research, and they are highly appreciated because of their sensitivity and selectivity in various fields of applications. FLC sensors have already demonstrated their ability to detect explosive compounds [5], heavy metals ions [6], and to measure dissolved oxygen concentrations [7]. Furthermore, luminescent molecular sensors are frequently used for selective detection in biochemistry [8]. FLC sensors are mainly based on the fluorescence quenching effect, consisting in a decrease of fluorescence intensity caused by excited state reactions, energy transfer, complex formation, and molecular collision [9]. An important role in the FLC sensors progress played the advances in the synthesis of π-conjugated polymers (CPs) which often demonstrate good fluorescent behavior. CPs exhibit significant fluorescence quenching even in the solid state owing to a strong intermolecular $\pi - \pi$ interaction. CPs fluorescent sensing mechanisms depend on modifications of the CP backbone or side chains to include specific recognition elements, while others rely on nonspecific Coulombic attraction between charged CP components with oppositely charged dipoles or ionic moieties of the target analytes [10]. Being in contact, thin polymer films readily absorb organic molecules. This process may be completely reversible [11].

PTMSDPA (Fig. 33.1) is a substituted acetylene polymer that can be dissolved in numerous organic solvents and easily shaped into freeze-dried nanofibers, spin-coated films and solvent-cast thin films [12]. The incorporation of Si containing groups into the conjugated polymer backbone leads to some advantages for solid-

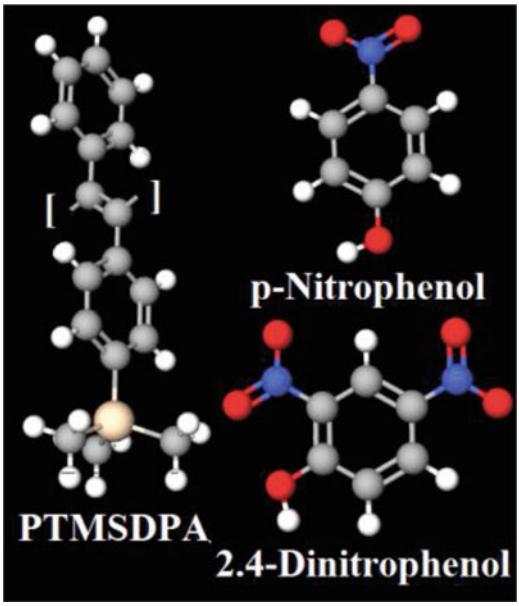

Fig. 33.1 3D view of PTMSDPA, NP and DNP, used in the current work

state FLC probes such as maintaining high fluorescence quantum yields and spectroscopic stability through prevention of π-stacking of the polymer backbones, and modifying the solubility characteristics of the polymers because of reduced interpolymer interactions (similar to ref. [13]). PTMSDPA thin films are highly fluorescent and possess an extremely large fractional free volume of about 0.26 [14]. Various gases and liquids easily diffuse into the film due to high porosity at a molecular level [14, 15]. A strong fluorescence (FL) in PTMSDPA occurs in the visible region due to the effective exciton confinement within the main chain by the steric hindrance or intramolecular electron interactions of the aromatic substituents [16]. Such a FL emission is highly sensitive because PTMSDPA exhibits collective properties that are susceptible to slight electronic perturbations generated by the external stimuli such as light or heat [17].

Among nitro compounds, nitro-aromatic ones make up a class of materials subjected to extensive research because of their toxicity, carcinogenicity, and mutagenicity [18]. In this paper, water-dissolved p-nitrophenol (NP) and 2.4-dinitrophenol (DNP) (Fig. 33.1) were used as detectable pollutants. The spin-coated films of PTMSDPA on quartz substrates were applied to investigate the influence of water dissolved nitro-aromatic compounds on their FL emission properties. Besides the study of possible FL reversibility in the FLC probes, the FL sensing mechanism was in the focus of the present research that includes the formation of a complex between the electron-rich π-system of the FLC sensor and the electron deficient π-system of the nitro-aromatic analyte [19]. The appeared decrease of the FL emission can be measured to evaluate the presence and concentration of water pollutants.

33.2 Experimental

33.2.1 Materials

PTMSDPA was used as synthetized at Charles University, Prague, following the method described in [20]. An analytical grade solvents and nitro-aromatic compounds were used as purchased from Sigma-Aldrich Co. Ltd. with purity over 99%.

33.2.2 Sample Preparation and Treatment

PTMSDPA conjugated polymer was dissolved in chlorophorm to a concentration of 0.67 wt%. Films with thickness of 300 nm were prepared on quartz substrates (Fig. 33.2) by spin coating for 30 s at 3000 rpm using WS-650-23B Spin Coater (Laurell Technologies Corporation, USA).

The solutions of nitro-aromatic compounds were prepared by direct dissolution in ambient atmosphere of the following components: DNP/water and NP/water. Direct

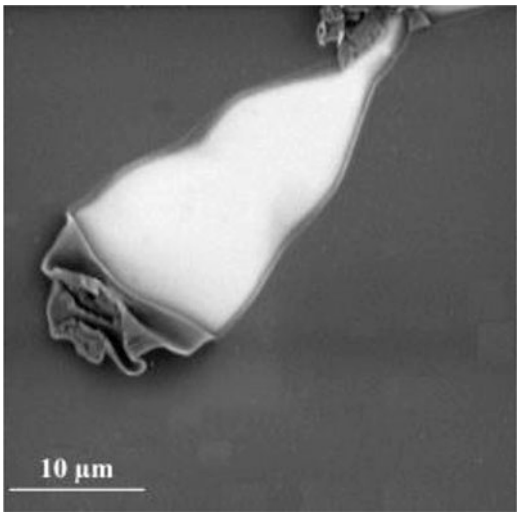

Fig. 33.2 SEM image of PTMSDPA film pilled area

dissolution was preferred to simulate a natural water contamination process including atmospheric moisture, pressure, temperature, etc. Three stock solutions with concentrations of $1.0*10^{-2}$ M, $5.5*10^{-3}$ M, and $1.0*10^{-3}$ M were prepared for each nitro-aromatic 'pollutant'.

PTMSDPA thin films on quartz substrates were fully immersed in the stock solutions for 5 min followed by 3 min drying in ambient atmosphere just before FL emission testing.

33.2.3 Measurements

Phenom Pro Desktop scanning electron microscope (SEM, Thermo Fisher Scientific, USA) was used for imaging the PTMSDPA film surface.

Steady-state photoluminescence spectra were obtained with FLS1000 spectrofluorometer. The excitation source was a 900 W Xenon Light Source ($\lambda_{max} = 425$ nm) focused on the sample. The spectra were recorded with a CCD-detector in the wavelength range of 400 to 750 nm. UV/vis absorption spectra were measured with a Cary Varian 300 spectrophotometer (Agilent Technologies, USA).

33.3 Results and Discussion

33.3.1 PTMSDPA Thin Films for Sensing of Nitro-aromatic Compounds

As was already mentioned in the Introduction, FLC sensors are usually used in liquid states and it is a big challenge to find an adequate solvent compatible simultaneously with the FL polymer solute or dye and the contaminated water. There, besides the often-observed immiscibility of the organic solvents and the water, many different phenomena should be also carefully taken into consideration, such as the modification of the partial molar volumes of the water and the alcohols which are miscible in water and good solvents for a range of luminophores. Solid state FLC sensors (films, fibers, powder, etc.) were considered more convenient in this sense, but in the case of nitro-aromatic compounds mainly vapors detection was performed. Just a few reports on the detection of water-dissolved analytes can be found, for example Ref. [21].

PTMSDPA thin films exhibited a well visible yellowish FL emission under UV illumination (Fig. 33.3a). A contact between the films and the water, or the stock solutions of the nitro-aromatic compounds, did not present any observable differences upon white light (Fig. 33.3b). However, UV illumination identified the naked-eye detectable quenching of FL emission caused by the investigated pollutants, while the interaction with pure water did not affect the FL at all (Fig. 33.3c). An unexpected result was the difference in the diffusion of the analytes in the PTMSDPA film in vertical direction, easily detected by the aforementioned quenching process. Explicitly, the NP solution quenched not only the contact region but the whole surface of the probe. More modest was the diffusion process of the DNP solution, where the emission was quenched below the solution-air interface and only partially above it. This finding may be very useful for fast comprehension of the pollutant nature.

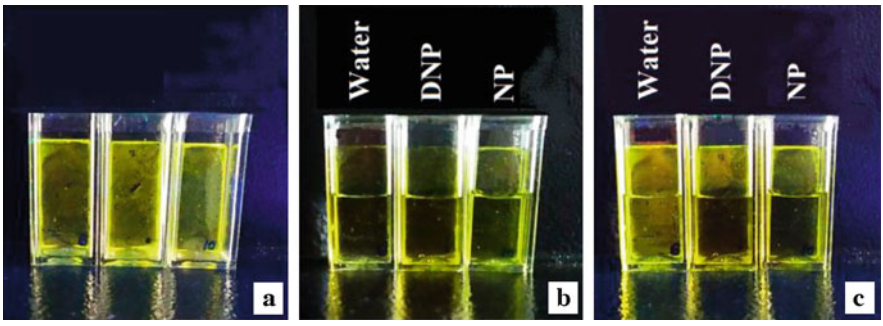

Fig. 33.3 (**a**) FL emission of PTMSDPA thin film on quartz substrate inside dry quartz cuvettes upon exposure to UV light; (**b**) Image of the same cuvettes filled with water, DNP, and NP stock solutions (10^{-3} M) upon white light; (**c**) Image of the cuvettes with water, DNP, and NP stock solutions upon UV light

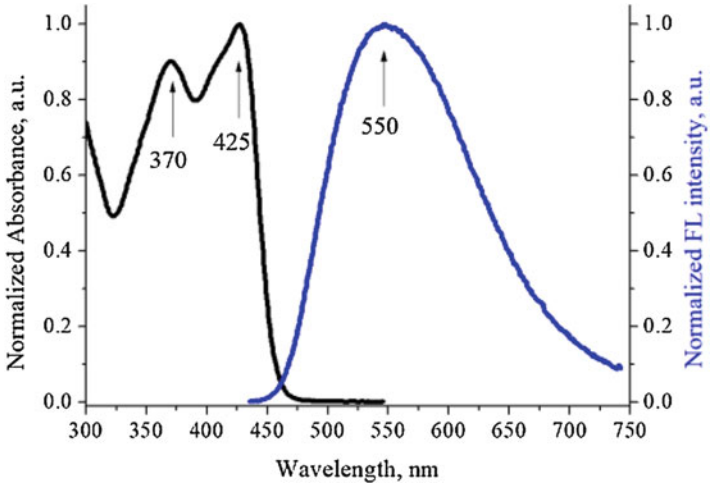

Fig. 33.4 Absorption and FL spectra of PTMSDPA film

More detailed information on the quenching processes was obtained by FL intensity measurements preceded by absorbance spectra detection. A typical absorbance spectrum of the PTMSDPA film is shown in Fig. 33.4. The polymer film has a strong absorbance maximum around 425 nm and a weaker absorbance peaks at 370 nm. Both of these transitions are assigned to π–π^* transitions in the conjugated polymer backbone.

The maximum of emission is exhibited n at wavelength of 550 nm (Fig. 33.4), which originated from intramolecular excimer emission because of a confocal phenyl-phenyl stack in the side chains [22].

Further investigations were performed on samples fully immersed into the corresponding stock solutions according to the procedures described in the Experimental section of the present paper.

Quenching of the fluorescent emission intensity of the PTMSDPA films was observed for both used nitro-aromatic compounds at all concentrations. An excited wavelength was set at 425 nm. Figure 33.5 shows the FL spectra of probes recorded immediately after 5 min immersing, then 3 min conditioning, and drying in ambient atmosphere, regardless the time for occurring of FL quenching steady state regime. This regime of measurements was selected to keep the same conditions and time of reaction between the probes and the pollutants.

Regarding the sensing performance of the PTMSDPA films, the results revealed an important difference not only between the different pollutants but also with respect to their concentrations. The FL intensity of the PTMSDPA films is reduced upon exposure to DNP and NP solutions and can reach steady-state values within tens of minutes [19]. Several factors contribute to the observed fluorescence quenching including the mechanism of electron transfer from the excited polymer to the analyte and PTMSDPA film oxidization upon exposure to nitro-aromatic

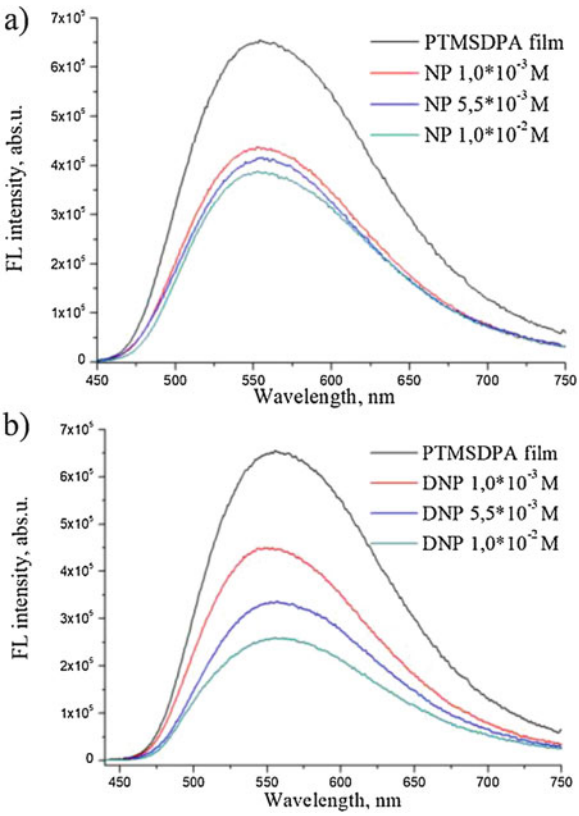

Fig. 33.5 FL spectra of PTMSDPA films reacted with (**a**) NP; and (**b**) DNP, with various concentrations in comparison with the initial FL

compounds. More detailed discussion on the quenching mechanisms will be presented below in the text.

The enhanced sensitivity towards DNP (Fig. 33.5a) is ascribed to a higher electron transfer quenching rate and a larger adsorbate binding constant compared to those of NP. It can be assumed that the nonbonding electrostatic interactions between the electron-rich polymer and the electron deficient nitro-aromatic molecules are critical in the case of a rapid FL response processing (before reaching the steady-state quenching), corresponding to the implemented measurement regime. In such a way, the maximal quenching was obtained for the maximum pollutant concentrations exhibiting a 58% and 41% decrease of FL intensity of DNP and NP, respectively, for 10-2 M concentrations of both of them. As a general trend, also a quenching decrease via decreasing the pollutant concentration can be mentioned (see Table 33.1).

Table 33.1 Quenching ratio for various pollutant concentrations

Concentration, M	Quenching by DNP, %	Quenching by NP, %
$1.0*10^{-2}$	58	41
$5.5*10^{-3}$	46	37
$1.0*10^{-3}$	30	33

33.3.2 Reversible Quenching

An important parameter for any probe sensing is the reversibility of changes induced by the analyte, which opens a wide opportunity for repeated usage of the sensors. The reversible quenching in polymers was largely discussed [19, 23], including reversible quenching of PTMSDPA emission [12]. Repeated measurements of FL emission of quenched samples exhibited a FL enhancement with the time (Fig. 33.6). As can be observed, FL quenching by the used nitro-aromatic compounds has been only partially reversible, and this process was faster in the first 10 h followed by a slowly reached equilibrium in the next 14 h.

A reversible quenching was more evident in the samples treated with DNP solutions, and FL reached approximately 88% on the average of its initial value in 24 h (Fig. 33.6a). For the NP solutions, the recovery was lower - 70% on the average (Fig. 33.6b).

According to Ref. [19], the FL quenching mechanism can be divided into two parts: reversible quenching of luminescence and irreversible one. The reversible quenching may be realized by an interfacial charge transfer, an interfacial energy transfer, introduction of nonradiative surface traps, and dielectric medium effects. In the PTMSDPA films, the mechanism of FL attenuation can be attributed to the electron transfer [17] from the excited polymer to the electron acceptors (NP or DNP). The irreversible quenching mechanism of FL is explained by the film oxidization upon exposure to nitro-aromatic compounds, both in presence or absence of oxygen [19].

When analyzing water contaminations, which actually motivated the present research, it is necessary to work with water solutions and this fact adds some additional complications. Water itself can be detected by FL sensors based on PTMSDPA films. For example, in ref. [24] the authors reported on-line real-time monitoring of water concentration in organic solvents. In our case, pure water did not react with the studied probes and did not affect their FL emission. On the contrary, the nitro-aromatic compounds dissolved in water drastically changed the properties of obtained solutions. Even different concentrations of the identical solute lead to differences in pH, electrical conductivity, etc., and finally affect the complex formation at the polymer/pollutant interface and the internal charge transfer. All these phenomena disturb the quenching process, but the exact relationship between pH of stock solutions and the quenching of the PTMSDPA film FL emission is not the case of this report. Since the topic of the present work is the detection of nitro-aromatic compounds, the FL quenching/recovery based on the complex formation/

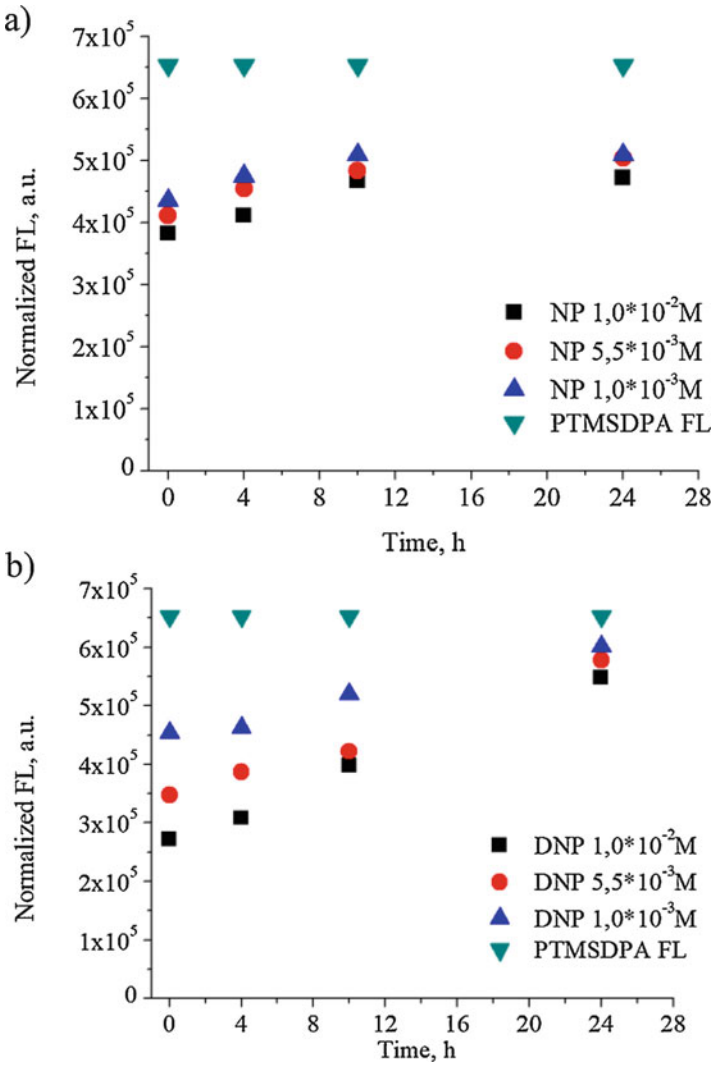

Fig. 33.6 Time evolution of normalized florescent spectra for PTMSDPA films reacted with (**a**) NP; and (**b**) DNP solutions with various concentrations. PTMSDPA FL shows normalized initial emission intensity of the untreated samples, considered to be constant in time

dissociation is discussed below taking into consideration the π-stacking interactions between the aromatic rings of PTMSDPA films and the analyte.

The term "complex" is defined here as a group of atoms with a binding energy that is higher than their thermal energy kT but lower than that yielded by new chemical species [28].

It is well known that in NP and DNP molecules there are different electron displacement effects (mesomeric, resonance, inductive) and an intramolecular

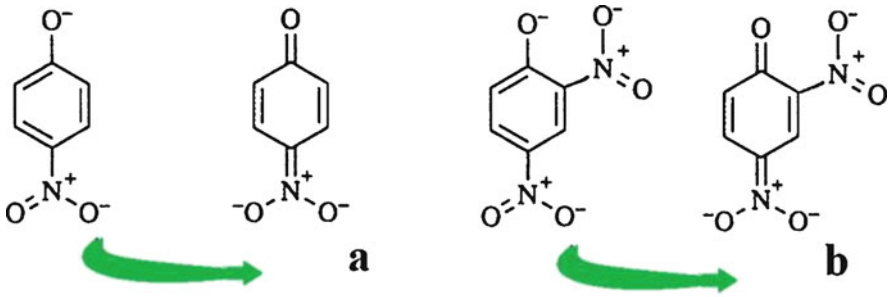

Fig. 33.7 Scheme of (**a**) NP anion and its stable conjugated base; and (**b**) DNP anion and the corresponding conjugated base

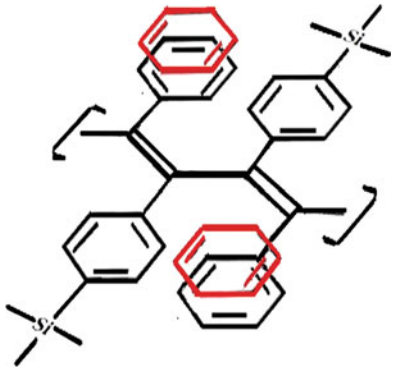

Fig. 33.8 Scheme of π-stacking interaction between the PTMSPDA sensors and the electron deficient aromatic ring

hydrogen bonding. When dissolved in water, these molecules form a stable conjugated base (Fig. 33.7) involving the nitro groups that can easily delocalize the negative charge of the phenoxide anion and finally create the electron deficiency of the aromatic ring.

The electron between the rich polymer film and the analyte anion are dominated by electrostatic and ion-induced polarization [26], leading to formation of a quite stable complex when immersed in solution. The nature of the electrostatic interaction can be explained by the presence of permanent quadrupole moment of the arene. The π–π interaction in the benzene dimer is governed by dispersion effects [26].

Due to steric hindrance and positive inductive effect of the p-trimethylsilyl group in PTMSDPA, the most convenient place for complex formation is the pendant benzene ring situated in a trans position with respect to the benzene ring containing p-trimethylsilyl group in each repeat unit of the π-conjugated polymer backbone (Fig. 33.8).

The complexes formed by internal charge transfer events led to considerable quenching of PTMSDPA FL emission. Sensor immersing in an analyte solution starts two processes: complex formation and solution diffusion into the polymer film. The second process is highly facilitated by the porous structure of a PTMSDPA

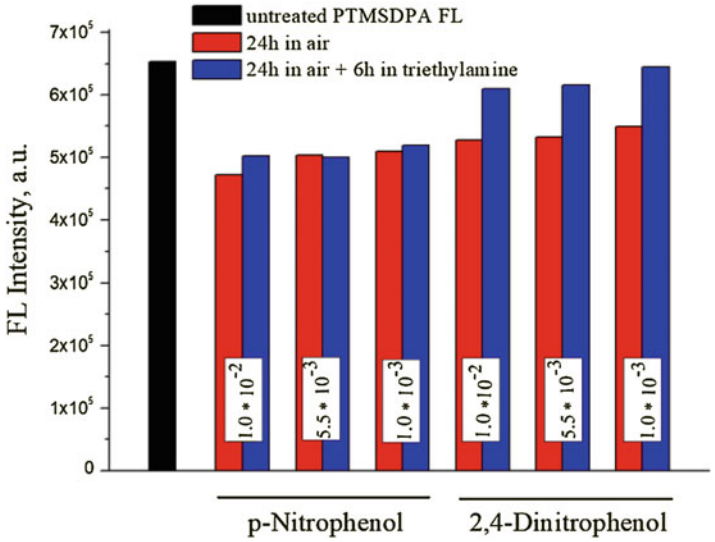

Fig. 33.9 FL recovering for PTMSDPA films treated with different concentrations of NP and DNP in water solutions in comparison with untreated one

film. Unreacted solution, which is localized in pores, continues to create complexes even after withdrawing and drying the film.

In a liquid, the component species are typically in equilibrium with the complex (es) and for a wide range of interactions the forward and back reactions are fast [25]. After withdrawing of the film from a liquid, the process of formation of the charge transferring complexes inside the filled pores and the dissociation of the formed complexes exposed to ambient atmosphere take place simultaneously until the FL emission quenching reaches steady-state values [19]. A longer exposure to ambient atmosphere led to evaporation of the analyte and a gradual recovery of FL.

After 24 h of atmosphere exposure, the FL intensity quenched by the studied nitro-aromatic compounds was restored gradually for all tested samples and finely achieved a quasi-stable value. Therefore, the quenching of FL was almost reversible for DNP, but only partially reversible for NP (Fig. 33.6).

To enhance the dissociation of the complexes, all samples were immersed in a triethylamine solution as suggested in ref. [27] for 6 h. According to the authors, the contact with a triethylamine liquid or its vapors almost completely recovered the original emission of the solvent quenched PTMSDPA film due to an electric bias effect induced by the reducing agent (triethylamine).

The results depicted in Fig. 33.9 showed up to 93% FL intensity recovery, compared with the initial one, for the samples treated with 10^{-2} M, and 98% for those treated with 10^{-3} M of DNP solutions (Fig. 33.9). The recovering process of the polymer thin films treated with NP solutions was much more modest and did not show an essential improvement of FL – 70% for the samples treated with 10^{-2} M

and 75% for those treated with 10^{-3} M of NP, indicating probably some locked π-stacking complexes inside the film.

33.4 Conclusions

In summary, PTMSDPA conjugated polymer films have been produced and tested as sensing probes for water-soluble nitro-aromatic compounds. They exhibited appreciable FL quenching behavior in contact with the investigated stock solutions and can be conditionally used for detection of nitro-aromatic pollutants. The results of the quenching and its recovery should be carefully taken into consideration for correct appreciation of pollutant concentration. Although the recovery effect was largely present in PTMSDPA films, the repeated usage of the probes can be considered undesirable because the recovery of the FL even after long term treatment with trimethylamine was dependent on the pollutant origin and concentration. A mechanism for the complex formation with internal charge transfers was proposed based on a π-stacking theory of conjugated polymers.

Acknowledgments This work was financially supported by the Czech Science Foundation (Grant no. 17-05318S) and the Ministry of Education, Youth and Sports of the Czech Republic (Grant no. LO1504).

References

1. Håkansson K, Coorey RV, Zubarev RA, Talrose VL, Håkansson P (2000) Low-mass ions observed in plasma desorption mass spectrometry of high explosives. J Mass Spectrom 35:337–346
2. Jamil AKM, Sivanesan A, Izake EL, Ayoko GA, Fredericks PM (2015) Molecular recognition of 2,4,6-trinitrotoluene by 6-aminohexanethiol and surface-enhanced Raman scattering sensor Sens. Actuators B 221:273–280
3. Mbah J, Moorer K, Pacheco-Londoño L, Hernandez-Rivera S, Cruz G (2013) Zero valent silver- based electrode for detection of 2,4,-dinitrotoluene in aqueous media. Electrochim Acta 88:832–838
4. Luggar RD, Farquharson MJ, Horrocks JA, Lacey RJ (1998) Multivariate analysis of statistically poor EDXRD spectra for the detection of concealed explosives. X-Ray Spectrom 27:87–94
5. Rembelski D, Bordet J, Brouard Q, Minot B, Barthet C, Frénois C (2015) Fluorescent sensing for nitrated compounds: study of the sensor microstructure for improvement on explosives detection. Proc Eng 120:1011–1014
6. de Acha N, Elosúa C, Corres JM, Arregui FJ (2019) Fluorescent sensors for the detection of heavy metal ions in aqueous media. Sensors 19:599–633
7. Choi MMF, Xiao D (1999) Linear calibration function of luminescence quenching-based optical sensor for trace oxygen analyses. Analyst 124:695–698
8. Suzuki Y, Yokoyama K (2015) Development of functional fluorescent molecular probes for the detection of biological substances. Biosensors 5(2):337–363
9. Lakowicz JR (2006) Principles of fluorescence spectroscopy. Springer Science+Business Media, LLC, New York, p 960

10. Duniho TL, Laughlin BJ, Buelt AA, Baker WF, Conrad CA, Smith RC (2014) Conjugated polymers for the fluorescent detection of nitroaromatics: influence of side-chain steric and π-system electronics. J Polymer Sci Part A: Polymer Chem 52(10):1487–1492
11. Yan HM, Kraus G, Gauglitz G (1995) Detection of mixtures of organic pollutants in water by pol- ymer film receptors in fibre-optical sensors based on reflectometric interference spectrometry. Anal Chim Acta 312(1):1–8
12. Han DH, Lee WE, Kim SJ, Park SD, Kwak G (2012) Solvent-driven reorganization of poly (diphenylacetylene) in film and nanofiber by means of swelling method: solvent anneal- ing effects on fluorescence emission properties and microstructures. Polym Bull 69:49–61
13. Yang JS, Swager TM (1998) Fluorescent porous polymer films as TNT Chemosensors: electronic and structural effects. J Am Chem Soc 120(46):11864–11873
14. Toy LG, Nagai K, Freeman BD, Pinnau I, He Z, Masuda T, Teraguchi M, Yam-polskii YP (2000) Pure-Gas and Vapor Permeation and Sorption Properties of Poly[1-phenyl-2-[p-(trimethylsilyl)phenyl]acetylene] (PTMSDPA). Macromolecules 33(7):2516–2524
15. Jeong H, Lee WE, Kwak G (2010) Enhancements in emission and chemical resistance of substituted acetylene polymer via in situ sol-gel reaction in film. Macromolecules 43:1152–1155
16. Shukla A (2004) Theory of two-photon absorption in poly(diphenyl) polyacetylenes. Chem Phys 300(1–3):177–188
17. Kwak G, Fujiki M, Sakaguchi T, Masuda T (2006) Mono- and multicolor FL image patterning based on highly luminous diphenylacetylene polymer derivative by facile photobleaching. Macromolecules 39(1):319–323
18. Kovacic P, Somanathan R (2014) Nitroaromatic compounds: environmental toxicity, carcinogen- icity, mutagenicity, therapy and mechanism. J Appl Toxicol 34(8):810–824
19. Content S, Trogler WC, Sailor MJ (2000) Detection of nitrobenzene, DNT, and TNT Vapors by quenching of porous silicon photoluminescence. Chem A Eur J 6(12):2205–2213
20. Tsuchihara K, Masuda T, Higashimura T (1992) Polymerization of silicon-containing diphenyla- cetylenes and high gas permeability of the product polymers. Macromolecules 25 (21):5816–5820
21. Xu S, Ni Y (2019) NH2-MIL-53(Al) nanocrystals: a fluorescent probe for the fast detection of aromatic nitro-compounds and ions in aqueous systems. Analyst 144:1687–1695
22. Lee WE, Oh CJ, Park GT, Kim JW, Choi HJ, Sakaguchi T, Fujiki M, Nakao A, Shinoharae K, Kwak G (2010) Substitution position effect on photoluminescence emission and chain conformation of poly(diphenylacetylene) derivatives. Chem Commun 46:6491–6493
23. Park SJ, Gesquiere AJ, Yu J, Barbara PF (2004) Charge injection and photooxidation of single conjugated polymer molecules. J Am Chem Soc 126(13):4116–4117
24. Han DC, Jin YJ, Lee JH, Kim SI, Kim HJ, Song KH, Kwak G (2014) Environment- specific fluorescence response of microporous, conformation-variable conjugated poly- mer film to water in organic solvents: on-line real-time monitoring in fluidic channels. Macromol Chem Phys 215:1068–1076
25. Foster (1980) Electron donor-acceptor complexes. J Phys Chem 84:2135–2141
26. Frontera A, Quiñonero D, Costa A, Ballester P, Deyà PM (2007) MP2 study of cooperative effects between cation–π, anion–π and π–π interactions. New J Chem 31:556–560
27. Lee WE, Park H, Kwak G (2011) Solvent-assisted, accelerated photobleaching and fluorescence recovery of conjugated polymer film. Chem Commun 47:659–661

Chapter 34
Determination of Surface Groups of Activated Carbons from Different Sources and Their Application for Heavy Metals Treatment

Halyna Yankovych, Viktoriia Novoseltseva, Olena Kovalenko, Inna V. Melnyk, and Miroslava Václavíková

Abstract Investigation of the carbon content and the concentration of surface groups is important for making activated carbons selective to pollutant adsorption. Potentiometric Boehm titration was applied to study the quantitative composition of the surface groups for three activated carbons – granulated activated carbon and biochars prepared from pea peels and grape woody vine. It was found that all examined activated carbons have carboxylic groups, which make a major contribution to their acidity. The most basic character due to total basicity/total acidity ratio had the biochar prepared from pea peels. The ability of the activated carbons to remove Ni(II), Fe(III), Cd(II), Cu(II), Pb(II), Mn(II) ions from aqueous solutions by adsorption was tested.

Keywords Biochar · Activated carbon · Boehm titration · Heavy metals

H. Yankovych (✉) · M. Václavíková
Institute of Geotechnics SAS, Košice, Slovak Republic
e-mail: yankovych@saske.sk

V. Novoseltseva
Institute of Geotechnics SAS, Košice, Slovak Republic

Odesa National Academy of Food Technologies, Odesa, Ukraine

O. Kovalenko
Odesa National Academy of Food Technologies, Odesa, Ukraine

I. V. Melnyk
Institute of Geotechnics, SAS, Kosice, Slovakia

Chuiko Institute of Surface Chemistry, NAS of Ukraine, Kyiv, Ukraine

P. Petkov et al. (eds.), *Nanoscience and Nanotechnology in Security and Protection against CBRN Threats*, NATO Science for Peace and Security Series B: Physics and Biophysics, https://doi.org/10.1007/978-94-024-2018-0_34

34.1 Introduction

The surface of activated carbons does not consist of only carbon atoms, but contains other heteroatoms like hydrogen, oxygen, nitrogen, sulfur, phosphorus, halogens, etc. The clean carbon surface is hydrophobic. Surface oxides provide sites for adsorption of water and other polar compounds. The more surface oxides, the more distinct is the hydrophilic behavior of the carbon [1]. The chemical composition influences the charge of the surface, its character and affinity towards different species. The existence of surface functional groups such as carboxyl, lactone, phenol, etc., determines surface acidity. The basicity of the activated carbon is predetermined by two types of structures: the presence of oxygen containing groups with basic character such as pyrone, chromene and carbonyl structures, and oxygen free Lewis basic site on the graphene layers. The Lewis basicity of delocalized π electrons is influenced by the aromatic system on the carbon surface [2].

Hanns-Peter Boehm developed in 1966 a titration method for simple determination of surface oxides on activated carbon, graphite, diamond, silica, titanium oxide and alumina [3]. This technique was named after him and is commonly used until now. The main idea is to determine the acidic oxygen surface functional groups on the carbon samples whereby bases of various strengths ($NaHCO_3$, Na_2CO_3 and NaOH) neutralize different acidic oxygen surface functionalities. The weakest base, $NaHCO_3$, neutralizes only the carboxylic groups, while Na_2CO_3 neutralizes carboxylic and lactonic groups. The strongest base typically used, NaOH, neutralizes carboxylic, lactonic and phenolic groups. The number of each type of acidic groups can be determined by the difference between the uptake of each reaction base [4]. The total basicity can be calculated from titration curves of the activated carbon previously neutralized by HCl. It must be pointed out that the identified acidic and basic groups on oxidized carbon usually do not account for all of the oxygen present on the surface.

In our investigation we examined three activated carbons – commercial granulated activated carbon (GAC) and two self-made biochars obtained from pea peels (PP) and grapes woody vine (GWV). The total basicity and total acidity, as well as the amount of carboxylic, lactonic and phenolic surface groups were determined by Boehm titration and screening adsorption tests for a mixture of several heavy metals were performed.

34.2 Experimental

Granulated activated carbon from ITES Vranov, s.r.o. (Slovakia) [5] and two previously obtained biochars from pea peels [6] and grape woody vines were used. Solutions of 0.05 M $NaHCO_3$, Na_2CO_3 and NaOH were prepared by dissolving of accurate weight of these compounds in 500 mL distillated water. HCl solution was obtained by dilution of concentrated hydrochloric acid (36%). NaOH and HCl solutions were standardized by potentiometric titration before use. Nitrate salts of copper (II), cadmium (II), iron (III), manganese (II), nickel (II) and lead (II) were used for screening adsorption experiments. Adsorbent dosage was 2 g/L and agitation time 24 h. All reagents were purchased from ITES Vranov, s.r.o. (Slovakia). The pH of the solutions was measured by MeterLab PHM210 pH meter.

For Boehm titration, 0.5 g of different activated carbons were placed in different flasks with 50 mL of 0.05 M Na_2CO_3, 0.05 M $NaHCO_3$, 0.05 M NaOH and 0.05 M HCl, respectively. The suspensions were carefully mixed by magnetic stirrer for 24 h with rotation speed of 800 rpm. Then, an aliquot of 10 mL of each filtrate was titrated by standardized HCl for basic solutions and by standardized NaOH for acidic solutions. The total acidity was calculated from the equivalent volume of HCl used for neutralization of the residual volume of NaOH under the assumption that NaOH neutralizes carboxylic, lactonic and phenolic groups. In the same way, Na_2CO_3 neutralizes carboxylic and lactonic groups and $NaHCO_3$ only carboxylic ones. The amount of phenolic groups was calculated as a difference between the total acidity and the sum of carboxylic and lactonic groups obtained from Na_2CO_3 titration. The amount of lactonic groups was calculated from the difference between the results from sodium carbonate and sodium bicarbonate titrations. The total basicity was obtained from titration of HCl solution as the amount of acid that reacted with carbon basic surface groups [7].

34.3 Results and Discussion

The surface oxides on activated carbon can have acidic as well as basic properties. The potentiometric titration curves of the three examined samples are presented in Fig. 34.1.

Based on the obtained data, the amount of carboxylic, lactonic and phenolic surface groups, the total acidity and total basicity were calculated (Table 34.1).

These results reveal that GAC possesses three types of surface groups which cause its acidity. The acidity of CWV sample is predetermined by the carboxylic and lactonic groups, and of PP – only by the carboxylic ones. The presence of these groups on the surfaces of biochars could be explained by incomplete carbonization of the raw materials that had high content of organic matter such as lignin, cellulose, hemicellulose, natural pigments, etc. [6]. The most basic properties possesses the biochar from pea peels, as revealed by the TB/TA ratio.

The adsorption ability of activated carbons towards metals ions was investigated by a screening test. For this purpose, an aqueous mixture of Ni(II), Fe(III), Cd(II), Cu (II), Pb(II), Mn(II) nitrates with concentration of 20 mg/L of each metal was prepared. The values of hydration energy $-\Delta G_h$ for these cations decrease in the following order: $Cu^{2+} = Ni^{2+} > Mn^{2+} > Cd^{2+} > Pb^{2+} > Fe^{3+}$. The pH of the prepared mixture was ~3 and the calculated ionic strength was 0.02. The results of the adsorption test are shown in Fig. 34.2.

The adsorption order for GAC determined by the uptake values was as follows: $Pb^{2+} > Mn^{2+} > Cu^{2+} > Fe^{3+} = Ni^{2+} > Cd^{2+}$. For PP and GWV samples the order was identical: $Fe^{3+} > Pb^{2+} > Cu^{2+} > Mn^{2+} > Cd^{2+} > Ni^{2+}$. It is known that for adsorption of Fe^{3+}, Pb^{2+} and Cu^{2+} ions the carboxylic and N-containing basic groups play predominant role through ion exchange mechanism and complexation, respectively [8]. Since PP and GWV acidity is mainly caused by the carboxylic groups and the

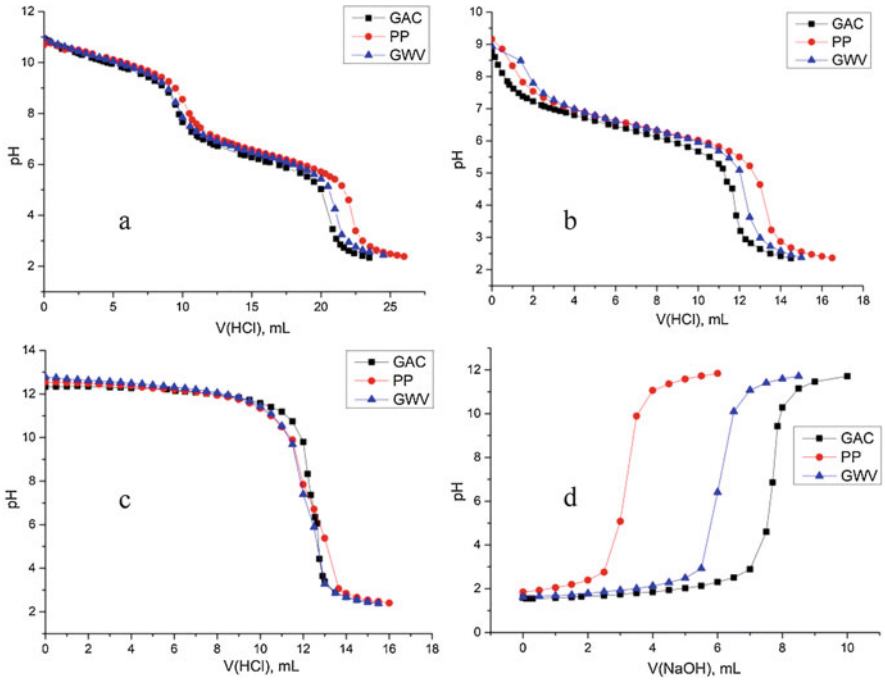

Fig. 34.1 Potentiometric titration curves of granulated activated carbon (GAC), biochar from pea peels (PP) and biochar from grape woody vine (GWV): (**a**) 0.05 M Na_2CO_3, (**b**) 0.05 M $NaHCO_3$, (**c**) 0.048 M NaOH, titrant 0.038 M HCl in all cases; (**d**) 0.044 M HCl, titrant – 0.048 M NaOH

Table 34.1 Amounts of surface oxides of the examined samples calculated from Boehm titrations

	Samples		
Functional group	GAC	GWV	PP
Carboxylic, mmol/g	0.10	0.22	0.21
Lactonic, mmol/g	0.15	0.06	0
Phenolic, mmol/g	0.05	0	0
Total acidity (TA), mmol/g	0.30	0.28	0.21
Total basicity (TB), mmol/g	0.61	0.33	0.61
TB/TA ratio	2	1	3

amount of basic adsorption centers is sufficient, they showed high uptake capacity for these ions. The iron ions have higher removal due to the lower hydration energy in comparison to lead and copper ions.

GAC sample showed low uptake capacity towards all inorganic cations. The highest uptake for lead ions reached only 10%. It can be assumed that the groups on the GAC surface are at considerable distance from each other and ion exchange between the oxygen-containing groups and the metal ions cannot be realized. As the removal efficiency for Mn^{2+}, Cd^{2+} and Ni^{2+} is less than 10%, further studies seem to

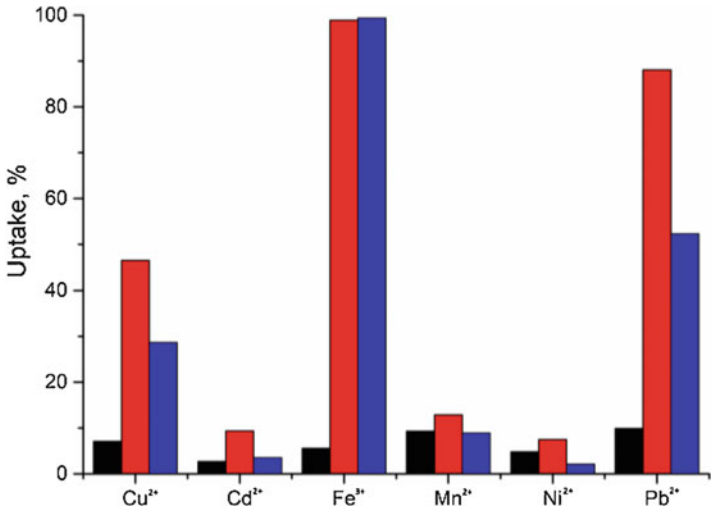

Fig. 34.2 Adsorption efficiency towards heavy metals by their simultaneous presence in the mixture ($pH_{mixture}$~3, concentration of each metal 20 mg/L). Black columns are related to granulated activated carbon, red columns to biochar from pea peels and blue columns to biochar from grape woody vine

be unprofitable. However, since the adsorption mechanisms are still not clear, further investigations are needed.

34.4 Conclusions

Three activated carbons were examined by Boehm titration and the content of the main surface groups was calculated. It was found that the commercial granulated activated carbon has three types of acidic groups on its surface and high content of basic surface groups. The biochars prepared from natural raw materials (pea peels and grape woody vine) possess mainly carboxylic acidic groups. This fact can be explained by incomplete carbonization of the source materials with high lignin, cellulose and hemicellulose content. In order to study their removal ability towards heavy metals a model mixture of Ni(II), Fe(III), Cd(II), Cu(II), Pb(II), Mn(II) was prepared and subjected to screening adsorption test. The results showed that both biochars can be used as effective adsorbents for iron, lead and copper ions removal. The granulated activated carbon exhibited low affinity towards all inorganic cations. The adsorption mechanisms are still not clear and further studies are needed.

Acknowledgments The research has been supported by the project VEGA 2/0156/19 of the Scientific Grant Agency of the MŠVVaŠ SR, Marie Curie Program H2020-MSCA-RISE-2016-NANOMED project No 734641 as well as by the National Scholarship Program of the Slovak Republic.

References

1. Salame I, Bandosz TJ (2001) Surface chemistry of activated carbons: combining the results of temperature-programmed desorption, Boehm, and potentiometric titrations. J Colloid Interface Sci 240:252–258
2. Prahas D, Kartika Y, Indraswati N, Ismadji S (2008) Activated carbon from jackfruit peel waste by H_3PO_4 chemical activation: pore structure and surface chemistry characterization. Chem Eng J 140:32–42
3. Boehm HP (1966) Chemical identification of surface groups. In: Eley DD, Pines H, Weisz PB (eds) Advances in catalysis. Academic, New York, pp 179–274
4. Oickle AM, Goertzen SL, Hopper KR, Abdalla YO, Andreas HA (2010) Standardization of the Boehm titration: part II. Method of agitation, effect of filtering and dilute titrant. Carbon 48:3313–3322
5. Yankovych H, Vaclavikova M Elimination of p-halogenophenols from wastewater by granulated activated carbon. In: Book of abstracts, NATO advanced study institute on nanoscience and nanotechnology in security and protection against CBRN threats, Sozopol, Bulgaria, 12–20.09.2019, p 79
6. Novoseltseva V, Kovalenko O, Yankovych H, Vaclavikova M, Melnyk I Investigation of structure and composition of biosorbents, obtained from pea and grape waste processing. In: Food and feed technology: book of abstracts, international practical and scientific conference, Odessa, Ukraine, National Academy of Food Technologies 24–27.09.2019, p 42
7. Wibowo N, Setyadhi L, Wibowo D, Setiawan J, Ismadji S (2007) Adsorption of benzene and toluene from aqueous solutions onto activated carbon and its acid and heat-treated forms: influence of surface chemistry on adsorption. J Hazard Mater 146:237–242
8. Yang X, Wan Y, Zheng Y, He F, Yu Z, Huang J, Gao B (2019) Surface functional groups of carbon-based adsorbents and their roles in the removal of heavy metals from aqueous solutions: a critical review. Chem Eng J:608–621

Chapter 35
Recent Trends of the Use of Rare Earth Elements for Efficient Environmentally Compliant Corrosion Protection of Aluminum and Its Alloys

Stephan Kozhukharov and Christian Girginov

Abstract Aluminum and its alloys find various applications in both mass production and hi-tech industrial sectors. This metal is widely used in the form of both low and high-doped alloys. The low-doped Al-alloys are generally used for household and hi-tech applications since they do not possess satisfactory mechanical strength related properties. The extended mechanical properties of the high-doped alloys enable their use as construction materials for the aircraft and automotive industries, for marine transport, as well as for exterior and interior architectonic constructions. However, reliable long-term exploitation of the Al-based facilities and equipment is strongly restricted due to their aptitude to undergo corrosion, especially in neutral or alkaline media with dissolved O_2^{2-} and Cl^- ions. Recently, cerium compounds were found to be efficient environmentally friendly corrosion inhibitors and protective primer layers. In this sense, the present brief review aims to comprise the recent trends in the field of cerium compounds use for the elaboration of advanced corrosion protective coatings.

Keywords Aluminum alloys · Cerium based inhibitors · Cerium conversion coatings · Inhibitor encapsulation

S. Kozhukharov (✉)
Laboratory for Advanced Materials Research, University of Chemical Technology and Metallurgy, Sofia, Bulgaria

C. Girginov
Department of Physical Chemistry, University of Chemical Technology and Metallurgy, Sofia, Bulgaria

P. Petkov et al. (eds.), *Nanoscience and Nanotechnology in Security and Protection against CBRN Threats*, NATO Science for Peace and Security Series B: Physics and Biophysics, https://doi.org/10.1007/978-94-024-2018-0_35

35.1 Introduction

The exceptional aptitude of lanthanides to form insoluble hydroxides in alkaline media [1] predetermines their high cathodic corrosion inhibitive efficiency. Recently, it was evinced that cerium compounds possess the highest corrosion inhibition activity among the lanthanides [2], being the most promising candidates for advanced coating systems elaboration. Besides, the cerium oxide/hydroxide precipitates possess excellent adhesion to the substrate and cover the entire metallic surface by forming Ce-O-Al covalent bonds [3]. Alternatively, an approach for cerium inhibitor encapsulation in the exterior coating layers is also proposed [4, 5].

Since the corrosion protective coating systems nowadays are multilayered and each layer has its own function [6–8], the present brief review summarizes the options for Ce-compound introduction for elaboration of advanced multilayered corrosion protective systems, following the recent concepts regarding environmental compatibility and active corrosion protection.

35.2 Corrosion Inhibition

In simple terms, the Ce^{3+} or Ce^{4+} ions of any dissolved Ce-salt in the corrosive medium form insoluble Ce(III) or Ce(IV) hydroxides near the metallic surface with the OH^- ions, produced by the oxygen reduction reaction (ORR) on the cathodic zones. Nevertheless, the mechanism is more complicated and includes intermediate stages of aqua-complex formation [9, 10]. This mechanism was practically confirmed, since the Ce(IV) compounds appear rather activators, instead of inhibitors of the aluminum corrosion [11]. The interaction of the Ce-ions with hydroxyl anions results in island-like deposition, followed by sealing of the cathodic areas of the respective alloy [12] (Fig. 35.1).

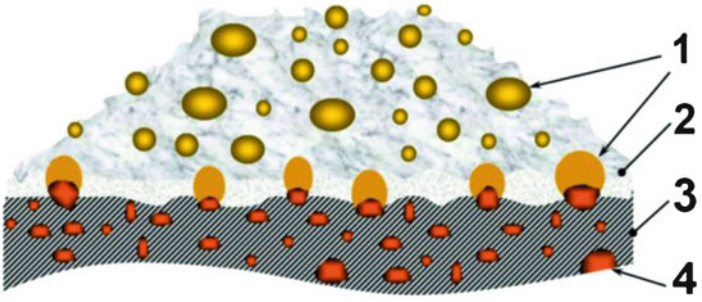

Fig. 35.1 Visual model of Al-Cu alloy with Ce-inhibitor deposits on its surface: (*1*) inhibitor deposits, (*2*) surface oxide layer, (*3*) aluminum matrix, (*4*) intermetallic inclusions. Reprinted with permission from [12]

The activation of the corrosion process in the case of Ce(IV) compounds can be explained with the activation of the ORR by the reduction of Ce^{4+} to Ce^{3+} near the cathodic areas.

Although the Ce-based water soluble compounds are considered as definite cathodic inhibitors, the anionic parts of the respective Ce-compounds have an impact on the entire inhibitive efficiency (IE), as well [13]. Thus, when the IEs of basic Ce (III) compounds were compared, it was established that at the optimal concentration (i.e. 0.03–0.05 M), the higher efficiency belongs to $CeCl_3$ and $Ce(NO_3)_3$, whereas $(NH_4)_2Ce(NO_3)_5$ and $Ce_2(SO_4)_3$ possess lower IEs. The superior behavior of the former salts was explained by the more intensive OH^- ions generation by the ORR, which leads to more intensive Ce-hydroxide precipitation and sealing of the respective cathodic zones. It is promoted either by enhancement of the anodic zones, due to the oxide layer perforation by Cl^- ions or by removal of the Cu_2O/CuO thin layer on the copper enriched cathodic zones by the NO_3^- ions, whereas the SO_4^{2-} ions did not have any distinguishable effect on the inhibition efficiency.

The recent trends in the use of cerium salts for corrosion mitigation include their combination with organic inhibiting compounds [14–18], which are known as mixed or anodic inhibitors [19–21]. Similar combinations are examined by mixtures of other compounds, such as $LaCl_3$ and Na-dodecyl benzene sulphonate as surfactant [22]. In this sense, Zheng et al. [23] have proposed the use of combination between $Ce(NO_3)_3$ and levofloxacin for corrosion protection of AA2024-T4. This approach enables to reach a synergism between the cathodic inhibition by the Ce-compound and prevention of Microbially Induced Corrosion (MIC) by the antibiotic. Another approach for achievement of such synergistic corrosion inhibition effect is by direct use of cerium based organometallic compounds, such as $(CH_3COO)_3Ce$ [24], cerium cinnamate [25], cerium tartarate [26] and others [27].

Nevertheless, the direct addition of inhibitors to the corrosive medium has only limited application in liquid recycling systems, such as heat exchange and cooling installations, or in offshore drilling, even though the liquid flow could disturb the corrosion inhibition by mechanical removal of the Ce deposits at more intensive hydrodynamic regimes. Consequently, it is more reasonable to apply the Ce-compounds in form of thin layers and films, instead of adding them as dissolved corrosion inhibitors.

35.3 Cerium Oxide Primer Layers (CeOPL)

Recently, the concepts of Sholes et al. [9] and Aldykiewicz et al. [10] were extended by Conde et al. [28], who propose supplemental chemisorption processes on the superficial oxide layer of the aluminum, enabling the entire covering by uniform Ce-O-Al layer. Consequently, the CeOPL formation begins from the nobler intermetallic inclusions until their complete sealing and subsequently spreads over the rest of

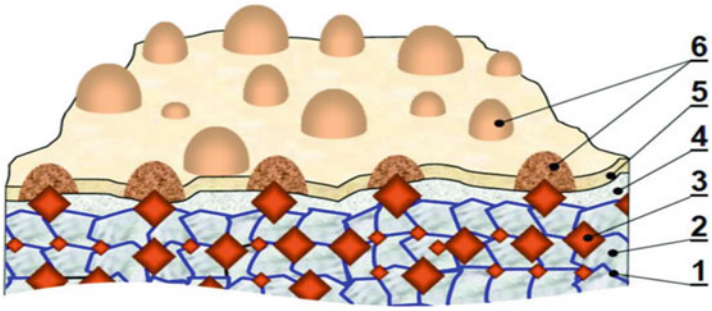

Fig. 35.2 Illustration of CeOPL layer on Cu-doped Al alloy: (*1*) grain boundaries, (*2*) grains of the basic aluminum matrix, (*3*) cathodic copper intermetallic inclusions, (*4*) native oxide layer, (*5*) CeOPL layer, (*6*) initial Ce-oxide/hydroxide deposits

the surface. Hence, the CeOPL growth passes through alteration of the formation mechanism from island-like nucleation [9, 10] to subsequent layer formation [28], as shown in Fig. 35.2. This assumption was evinced in previous research works, where globular morphology was observed by scanning electron microscopy.

Nevertheless, the practical deposition of CeOPL has some related difficulties, originating from undesirable precipitation, instead of formation of uniform, dense and adhesive layers. In this sense, it was recently evinced that the optimal concentration of the Ce-precursor should be between 0.03 and 0.05 mol dm^{-3} [29–33], and the maximal possible amount of added 30% H_2O_2 as deposition activator is up to about 10 ml for 1000 ml of precursor solution. The experience so far has shown that the deposition of these coating layers can be performed by dip-coating [29, 30] or by electrodeposition in galvanostatic [31, 33] or potentiostatic [32] regimes. In all cases, the CeOPL formation requires activation energy in form of elevated temperatures (up to 60 °C, in order to avoid considerable thermal H_2O_2 decomposition), applied potential (i.e. up to −1 V) versus Ag/AgCl reference electrode or defined current density (from −2 to −5 mA cm^{-2}). In all cases, the superior values of these parameters result in $Ce(OH)_3/Ce(OH)_4$ precipitation, instead of formation of thin, uniform CeOPL. Regardless of the method of CeOPL deposition, the sequence of the related operations includes: (i) preliminary treatment; (ii) layer deposition procedure and (iii) final CeOPL sealing [34, 35]. These additional stages impose the study of other important factors related to the CeOPL deposition, such as the concentrations of the alkaline and acidic pretreatment solutions, the temperature and continuation of the pretreatment process and the final sealing [36, 37], etc. In this sense, it was recently demonstrated that the anodization procedure predetermines the formation of thick Ce-O-Al layers with uniform element distribution. Furthermore, the remarkable durability of these films (up to 2520 h in 3.5% NaCl, prior to pitting initiation) has revealed dense structure of the Ce-O-Al layers, obtained by filling of the alumina layer pores by Ce(III)/Ce(IV) species [38].

35.4 Encapsulation of Cerium-Based Inhibitors in Self-Healing Protective Coatings

Among the basic concepts, related to the active and passive corrosion protection, described in a recent review paper [39], the encapsulation of free corrosion inhibitors was described as a main approach for elaboration of advanced self-healing corrosion protective coatings. Both approaches of encapsulation and preliminary incorporation of the corrosion inhibitors result in their gradual release near the area of coating disruption, as illustrated on Fig. 35.3 [40].

These approaches promote deposition of corrosion inhibitors near the naked corroding zone under the coating damage (Fig. 35.3b), instead of corrosion inhibitor leaching and loss (Fig. 35.3a). In this sense, various corrosion protective composite coatings are tested in recent years [41–47].

Finally, it should be mentioned that due to their remarkable mechanical properties, the CeO_2 [48] and Ce-Al-O [49] nanoparticles can be used for increasing the wear resistance of various types of protective coatings or to be added directly to high strength Al-based composites [50], as well.

35.5 Other Main Fields of Application of the Ce-Compounds

Since the oxidation state of cerium can vary reversibly, its oxides can often be in mixed CeO_2/Ce_2O_3 states. For this reason, highly defected crystalline lattices with elevated ionic conductivity [51] are formed. This advantage was recently applied in CeO_2-TiO_2-SiO_2 [52], CeO_2-TiO_2-SiO_2-ZrO_2 [53] humidity sensors, as well as in efficient ZrO_2-Ce_2O_3-Y_2O_3 electrocatalysts for chlorine generation [54] and Ce-CeO_2-Al_2O_3 catalyst for the transesterification reaction of canola oil [55].

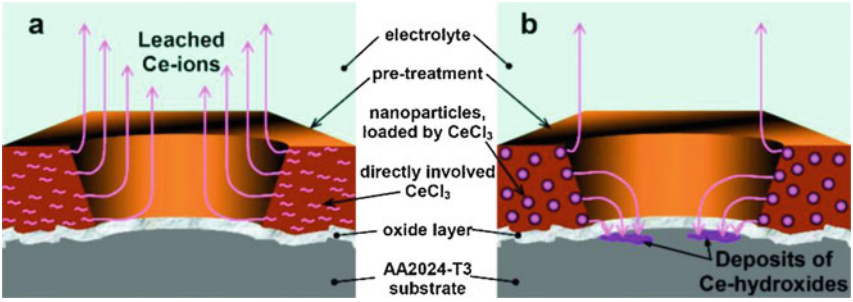

Fig. 35.3 Schematic view of the role of nano-containers for decrease of undesirable leaching of the inhibitor: (**a**) inhibitor included directly in the hybrid matrix and (**b**) inhibitor loaded nanoparticles

35.6 Conclusions

The water-soluble cerium compounds can be successfully used as cathodic corrosion inhibitors, since these compounds have an aptitude to form insoluble hydroxide precipitates on the cathodic areas. However, recent studies have shown that the mechanism of their precipitation is more complicated and in the cases of high concentration additions, especially of Ce(IV) compounds, corrosion activation could be observed. Despite the cathodic character of the corrosion inhibition by Ce-compounds, their anionic moieties also affect the inhibition mechanism and kinetics. The recent trends in the field of Ce-assisted corrosion inhibition are related to the enhancement of the resulting inhibition effect by use of Ce-based organometallic compounds or by addition of mixed organic or anodic inhibitors. In this sense, the use of detergents or antibiotics looks like a rather perspective approach.

The mechanisms of Ce-hydroxides precipitation can also be used for spontaneous and electrochemical cerium oxide primer layers (CeOPL) deposition. However, the CeOPL formation process requires moderate conditions, in order to obtain a uniform, dense and adherent layer, instead of precipitates. Furthermore, the properties of the resulting Ce-based protective layers depend on the preliminary treatment and the final sealing stages, as well. In this sense, the preliminary anodization results in formation of thick combined Ce-O-Al layers with remarkable protective properties.

The encapsulation and incorporation of Ce-based inhibitors in nanoparticles prior to their addition in the final paint compositions improves the self-healing effect. In these cases, the inhibitor precipitates on the bare metallic surface under the coating damage, instead of inhibitor loss due to leakage. Furthermore, CeO_2 and Ce-Al-O nanoparticles can be used to increase the wear resistance of various types of protective coatings or to be added directly to high strength Al-based composites. These compounds can be also used for hosting Ce-based corrosion inhibitors. In addition, the ionic conductivity of the cerium oxide lattices enables to elaborate advanced sensing elements and catalysts.

Finally, it can be concluded that the Ce-based compounds can be successfully used in various forms, as (i) free corrosion inhibitors; (ii) primers for multilayered coatings; (iii) encapsulated or incorporated inhibitors, and (iv) reinforcing phase, able to host any corrosive inhibitor (including Ce-based one). The exceptional properties of the Ce-based compounds enable versatile applications of these substances for corrosion protection, environment monitoring sensors and catalysts for novel synthesis and contaminant decomposition.

Acknowledgments The present work is developed under the financial support of the Bulgarian National Research Fund under contract КП-06-М38/1 (2019) “Characterization of the physical properties of functional oxide layers, formed on aluminum and its alloys”.

References

1. Rodič P, Milošev I (2016) Corrosion inhibition of pure Aluminium and alloys AA2024-T3 and AA7075-T6 by cerium(III) and cerium(IV) salts. J Electrochem Soc 163:C85–C93
2. Bethencourt M, Botana FJ, Calvino JJ, Marcos M, Rodriguez-Chacon MA (1998) Lanthanide compounds as environmentally-friendly corrosion inhibitors of aluminium alloys: a review. Corros Sci 40:1803–1819
3. Zivkovic LS, Popic JS, Jegdic BV, Dohcevic-Mitrovuic Z, Bajat JB, Stankovic VBM (2014) Corrosion study of ceria coatings on AA6060 aluminum alloy obtained by cathodic electrodeposition: effect of deposition potential. Surf Coat Technol 240:327–335
4. Cotting F, Aoki I (2016) Smart protection provided by epoxy clear coating doped with polystyrene microcapsules containing silanol and Ce (III) ions as corrosion inhibitors. Surf Coat Technol 303:310–317
5. Figueira RB, Fontinha IR, Silva CJR, Pereira EV (2016) Hybrid sol-gel coatings: smart and green materials for corrosion mitigation. Coatings 6(12):1–19
6. Kozhukharov SV (2017) Chapter 10: advanced multifunctional corrosion protective coating systems for light-weight aircraft alloys – actual trends and challenges. In: Thirumalai J (ed) Thin film processes – artifacts on surface phenomena and technological facets. Intech Open, London, pp 179–210
7. Presuel-Moreno F, Jakab MA, Tailleart N, Goldman M, Scully JR (2008) Corrosion-resistant metallic coatings, mater. Today 11:11–23
8. Kozhukharov SV, Girginov CA Chapter 1: classical and modern methods for corrosion impact rate determination for aluminium and strengthened aircraft alloys. Fundamentals and practical applications. In: Gergely A (ed) Phenomena and theories in corrosion science, Methods of prevention. NOVA Sci. Publ, Hauppauge, pp 3–150
9. Scholes FH, Soste C, Huges AE, Hardin SG, Curtis PR (2006) The role of hydrogen peroxide in the deposition of cerium-based conversion coatings. Appl Surf Sci 253:1770–1780
10. Aldykiewicz AJ, Davenport AJ, Isaacs HS (1996) Studies of the formation of cerium-rich protective films using X-ray absorption near-edge spectroscopy and rotating disk electrode methods. J Electrochem Soc 143:147–154
11. Matter EA, Kozhukharov S, Machkova M, Kozhukharov V (2012) Comparison between the inhibition efficiencies of Ce(III) and Ce(IV) ammonium nitrates against corrosion of AA2024 aluminum alloy in solutions of low chloride concentration. Corros Sci 62:22–33
12. Pernas JE, Kozhukharov S, Salve AA, Matter E, Machkova M (2012) A Comparative research on hybrid nano-composite protective primary coatings for AA2024 aircraft alloy. J Univ Chem Technol Metall 47(3):311–318
13. Machkova M, Matter EA, Kozhukharov S, Kozhukharov V (2013) Effect of the anionic part of various Ce(III) salts on the corrosion inhibition efficiency of AA2024 aluminium alloy. Corros Sci 69:396–405
14. Coelho LB, Taryba M, Alves M, Noirfalise X, Montemor MF, Olivier M-G (2019) The corrosion inhibition mechanisms of Ce(III) ions and triethanolamine on graphite—AA2024-T3 galvanic couples revealed by localised electrochemical techniques. Corros Sci 150:207–217
15. Coelho LB, Mouanga M, Druart M-E, Recloux I, Cossement D, Olivier M-G (2016) A SVET study of the inhibitive effects of benzotriazole and cerium chloride solely and combined on an aluminium/copper galvanic coupling model. Corros Sci 110:143–156
16. Liu J, Wang D, Gao L, Zhang D (2016) Synergism between cerium nitrate and sodium dodecylbenzenesulfonate on corrosion of AA5052 aluminium alloy in 3 wt.% NaCl solution. Appl Surf Sci 389:369–377
17. Zhu C, Yang HX, Wang YZ, Zhang DQ, Chen Y, Gao LX (2019) Synergistic effect between glutamic acid and rare earth cerium (III) as corrosion inhibitors on AA5052 aluminum alloy in neutral chloride medium. Ionics 25:1395–1406

18. Udoh II, Shi H, Liu F, Han E-H (2020) Microcontainer-based waterborne epoxy coatings for AA2024-T3: effect of nature and number of polyelectrolyte multilayers on active protection performance. Mater Chem Phys 241:. 122404:1–15
19. Nnaji N, Nwaji N, Fomo G, Mack J, Nyokong T (2019) Corrosion resistance of aluminum against AcidActivation: impact of Benzothiazole-substituted gallium Phthalocyanine. Electrocatalysis 24:. pp. 207:1–22
20. Shehu NU, Gaya UI, Muhammad AA (2019) Influence of side chain on the inhibition of aluminium corrosion in HCl by α-amino acids. Appl Sci Eng Prog 12(3):186–197
21. Coelho LB, Cossement D, Olivier M-G (2018) Benzotriazole and cerium chloride as corrosion inhibitors for AA2024-T3: an EIS investigation supported by SVET and ToF-SIMS analysis. Corros Sci 130:177–189
22. Hu T, Shi H, Wei T, Liu F, Fan S, Han E-H (2015) Cerium tartrate as a corrosion inhibitor for AA 2024-T3. Corros Sci 95:152–161
23. Zheng T, Wang L, Liu J (2020) Corrosion inhibition of levofloxacin and $Ce(NO_3)_3$ for AA2024-T4 in 3.5% NaCl, Corros. Eng. Sci. Technol 55(1):75–82
24. Rodič P, Milošev I (2019) The influence of additional salts on corrosion inhibition by cerium (III) acetate in the protection of AA7075-T6 in chloride solution. Corros Sci 149:108–122
25. Rodič P, Milošev I, Lekka M, Andreatta F, Fedrizzi L (2019) Study of the synergistic effect of cerium acetate and sodium sulphate on the corrosion inhibition of AA2024-T3, Electrochim. Acta 308:337–349
26. Riazaty P, Naderi R, Ramezanzadeh B (2019) Synergistic corrosion inhibition effects of benzimidazole-samarium (III) molecules on the steel corrosion prevention in simulated seawater. J Molec Liq 296: pp. 111801:1–14
27. Umoren SA, Solomon MM (2017) Synergistic corrosion inhibition effect of metal cations and mixtures of organic compounds: a review. J Environ Chem Eng 5:246–273
28. Conde A, Arenas MA, de Frutos A, de Damborenea J (2008) Effective corrosion protection of 8090 alloy by cerium conversion coatings. Electrochim Acta 53:7760–7768
29. Rodríguez DS, Kozhukharov S, Machkova M, Kozhukharov V (2013) Influence of the deposition conditions on the properties of D16 AM clad alloy, dip-coated in Ce-containing baths. Bulg Chem Commun 45-A:24–32
30. Kozhukharov S, Ayuso JAP, Rodríguez DS, Acuña OF, Machkova M, Kozhukharov V (2013) Optimization of the basic parameters of cathodic deposition of Ce-conversion coatings on D16 AM clad alloy. J Chem Technol Metall 48(3):296–307
31. Ayuso JAP, Kozhukharov S, Machkova M, Kozhukharov V (2013) Electrodeposition of cerium conversion coatings for corrosion protection of D16 AM clad alloy. Bulg Chem Commun 45-A:33–40
32. Gil TP, Kozhukharov S, Girginov C (2014) Deposition of cerium conversion coatings on AA2024-T3 aircraft alloy at fixed potentials. Ann Proc Univ Ruse (Bulgaria) 53(10.1):9–13
33. Kozhukharov S, Milanes M, Girginov C, Machkova M (2016) Comparative evaluation of cerium oxide primers electrodeposited on AA2024-T3 and D16 AM aircraft alloys. Mater Corros 67(7):710–720
34. O'Keefe MJ, Geng S, Joshi S (2007) Cerium-based conversion coatings as alternatives to hex chrome. Meta:25–28
35. Castano CE, Fahrenholtz WG, O'Keefe MJ (2020) Ceria-based coatings and pigments. Metal Oxides 6:211–257
36. Alba-Galvín JJ, González-Rovira L, Bethencourt M, Botana FJ, Sánchez-Amaya JM (2019) Influence of aerospace standard surface pretreatment on the intermetallic phases and CeCC of 2024-T3 Al-cu alloy. Metals 9:. pp. 320:1–21. https://doi.org/10.3390/met9030320
37. Andreeva R, Stoyanova E, Tsanev A, Datcheva M, Stoychev D (2018) On the role of pretreatment of aluminum substrate on deposition of cerium based conversion layers and their corrosion-protective ability. Int J Electrochem Sci 13:5333–5351. https://doi.org/10.20964/2018.06.71

38. Kozhukharov S, Girginov C (2018) Enhancement of the cerium oxide primer layers deposited on AA2024-T3 aircraft alloy by preliminary anodization. J Electrochem Sci Eng 8(2):113–127. https://doi.org/10.5599/jese.478
39. Kozhukharov SV, Samichkov VI, Girginov CA, Machkova MS (2017) Actual trends in the elaboration of advanced multifunctional coating systems for the efficient protection of light-weight aircraft alloys. Corros Rev 35(6):383–396. ISSN (Online) 2191–0316
40. Matter E, Kozhukharov S, Machkova M, Kozhukharov V (2009) Influence of the interactions between the corrosion inhibitor and nano-containers over the corrosion protective capability of hybrid nano-composite pre-treatments. Ann Proc Univ Ruse 48:19–23. Accessible via: http://conf.uni-ruse.bg/bg/docs/cp09/9/9-3.pdf
41. Abdeen DH, El Hachach M, Koc M, Atieh MA (2019) A review on the corrosion behaviour of Nanocoatings on metallic substrates. Materials 12(210):1–42. https://doi.org/10.3390/ma12020210
42. Zheludkevich ML, Shchukin DG, Yasakau KA, Möhwald H, Ferreira MGS (2007) Anticorrosion coatings with self-healing effect based on Nanocontainers impregnated with corrosion inhibitor. Chem Mater 19(3):402–411. https://doi.org/10.1021/cm062066k
43. Suleiman R, Khalil A, Khaled M, El Ali B (2019) Chapter 4, hybrid organosilicone materials as efficient anticorrosive coatings in marine environment. In: Marine coatings and membranes. Central West Publishing, Australia, pp 81–114
44. Noiville R, Jaubert O, Gressier M, Bonino J-P, Taberna P-L, Fori B, Menua M-J (2018) Ce(III) corrosion inhibitor release from silica and boehmite nanocontainers. Mater Sci Eng 229:144–154
45. Liu MM, Hu HX, Zheng YG, Wang JQ, Gan ZH, Qiu S (2019) Effect of sol-gel sealing treatment loaded with different cerium salts on the corrosion resistance of Fe-based amorphous coating. Surf Coat Technol 367:31–326
46. Matsuda T, Kashi KB, Fushimi K, Gelling VJ (2019) Corrosion protection of epoxy coating with pH sensitive microcapsules encapsulating cerium nitrate. Corros Sci 148:188–197
47. Owczarek E (2019) Methods of modifying anticorrosive protective properties of Silane films. Acta Phys Polon 135:147–152. https://doi.org/10.12693/APhysPolA.135.147
48. Suzuki K, Kato M, Sunaoshi T, Uno H, Carvajal-Nunez U, Nelson AT, McClellan KJ (2019) Thermal and mechanical properties of CeO_2. J Amer Ceram Soc 102:1994–2008
49. Mohammed H, Reddy MP, Ubaid F, Shakoor A, Mohamed AMA (2018) Structural and mechanical properties of CeO_2 reinforced Al matrix Nanocomposites. Adv Mater Lett 9:602–605
50. Sharma VK, Kumar V, Joshi RS (2019) Effect of RE addition on wear behavior of an Al-6061 based hybrid composite. Wear 426(427):961–974
51. Finny SA, Othman FA, Andreescu S (2020) Chapter 7. Cerium oxide nanoparticles for chemical and biological sensors: properties, sensing designs, and applications. Metal Oxides:259–277
52. Nenova Z, Kozhukharov S, Nenov T, Nedev N, Machkova M (2016) Combined influence of titania and silica precursors on the properties of thin film humidity sensing elements prepared via a sol–gel method. Sensors Actuators B-224:143–152
53. Kozhukharov S, Nenova Z, Nenov T, Machkova M, Kozhukharov V (2013) Influence of Ce (III)/Ce(IV) - supplements on the characteristics of humidity sensors with TiO_2 films prepared via a sol-gel method. Bol Soc Esp Cerám Vidrio 52:71–78
54. Petkov LN, Yosifov KS, Tsanev AS, Stoychev D (2013) Glassy carbon (GC) electrode modified with electrodeposited ZrO_2 and ZrO_2 + Ce_2O_3 + Y_2O_3 nanostructures as a cathode in the obtaining of active chlorine. Bulg Chem Commun 45-A:122–128
55. Salinas D, Pecchi G, Fierro JLG (2016) K_2O supported on sol-gel CeO_2-Al_2O_3 and La_2O_3-Al_2O_3 catalysts for the transesterification reaction of canola oil. J Molec Catal A-423:503–510

Part XII
Applications: Health and Biological Threats

Chapter 36
Synthesis of PLGA-PEG-PLGA Polymer Nano-Micelles – Carriers of Combretastatin-Like Antitumor Agent 16Z

Gjorgji Atanasov, Iliyan N. Kolev, Ognyan Petrov, and Margarita D. Apostolova

Abstract One of the most important tendencies for the development of modern chemistry is related to the new trends in biomedicine and pharmacy. Today, significant advances have been made in the development of biodegradable and biocompatible polymer materials and the synthesis of corresponding polymer nano-micelles. In this work we aimed to synthesize new biodegradable and biocompatible block copolymers based on poly(lactide-co-glycolide) (PLGA) and poly (ethylene glycol) (PEG) with linear (ABA-type) architecture, to investigate their ability to form nanosized micelles and its aptitude to acts as carriers of combretastatin-like antitumor agents. The synthesis of linear $PLGA_{1000}$-PEG_{1000}-$PLGA_{1000}$ block copolymer was carried out in line with standard procedures. The size and morphology of the obtained micelles were determined by transmission electron microscopy (TEM) and dynamic light scattering (DLS). The capability of obtained micelles to adsorb and deliver combretastatin-like antitumor agents into living cells was also demonstrated. We showed that the obtained copolymers formed nanosized micelles with the combretastatin-like antitumor agent 16Z. *In vitro* biocompatibility results denote that all tested blank-nano-micelles are devoid of cytotoxic effects and may be used as non-toxic drug carriers to target cells. Cellular uptake of 16Z-loaded $PLGA_{1000}$-PEG_{1000}-$PLGA_{1000}$ micelles by HepG2 cells showed continuous uptake up to 72 h and a delay in the cytotoxic effect of 16Z. In an attempt to design new biomimetic analogs of natural combretastatin A-4 (CA-4) and its synthetic amino-

G. Atanasov · M. D. Apostolova (✉)
Medical and Biological Research Laboratory, Roumen Tsanev Institute of Molecular Biology, Bulgarian Academy of Sciences, Sofia, Bulgaria
e-mail: margo@obzor.bio21.bas.bg

I. N. Kolev
Department of Pharmaceutical Sciences, Medical University Varna, Varna, Bulgaria

O. Petrov
Faculty of Chemistry and Pharmacy, Sofia University "St. Kliment Ohridski", Sofia, Bulgaria

P. Petkov et al. (eds.), *Nanoscience and Nanotechnology in Security and Protection against CBRN Threats*, NATO Science for Peace and Security Series B: Physics and Biophysics, https://doi.org/10.1007/978-94-024-2018-0_36

derivatives, we selected benzothiazolone heterocycles as a scaffold for a bioisosteric replacement. *In silico,* drug-likeness and toxicity predictions showed better properties of benzothioazolone CA-4 analogs. The obtained results are very promising and need future detailed investigations.

Keywords Nano-micelles · Combretastatin · Drug-likeness · Toxicity

36.1 Introduction

Cancer is one of the most life-threatening diseases and the second major cause of death worldwide. A series of changes brought by cancer cells via DNA modifications gives them an advantage over normal cells. Despite the advancement, combating cancer remains to be a challenge and thus, a prime focus nowadays.

The cellular microtubule system is essential for many important cellular processes such as cell division, formation and maintenance of cell shape, regulation of motility, cell signaling, secretion and intracellular transport [1]. Microtubules are generally recognized as an attractive target for the development of potential new anticancer agents [2]. Among the tubulin targeting agents, combretastatin A-4, derived from the bark of the South African tree Combretum caffrum [3, 4], is one of the well-known natural tubulin-binding molecules. CA-4 is a very attractive leading compound because of its simple structure, as well as its high cytotoxicity against a variety of human cancer cell lines, including the multi-drug resistance phenotype [5]. CA-4 strongly inhibits the polymerization of tubulin by binding to the colchicine site and displays selective toxicity toward tumor vasculature by inhibiting their blood supply [6]. However, the application of CA-4 as an anticancer agent is limited by its poor solubility. This failing led to the development of a water-soluble phosphate derivative as a prodrug, which is currently in human clinical trials. The obtained hopeful results encouraged the synthesis of a large number of CA-4 analogs [7].

Recently, we designed, synthesized and studied a series of styrylbenzoxazolones as new analogs of combretastatin A-4 with potential anticancer properties [8]. These styrylbenzoxazolones also have pure water solubility, similar to more than 40% of the new chemical entities developed in the pharmaceutical industry [9]. To overcome the pure water solubility, different nanocarrier-based drug delivery systems continue to gain considerable attention due to their potential to improve the bioavailability and efficacy of the drugs [10]. Several nanocarriers such as biologically erodible microspheres [11], micelles [12], different nanoparticles and quantum dots [13–15] have been investigated as potential drug delivery systems.

The FDA has approved copolymers containing polyethylene glycol and polylactic-glycolic acid blocks for human use. They are attracting great interest both in academia and industry for biomedical applications due to their biodegradable nature and biocompatible properties [16, 17]. In our study, we have used PEG and PLGA as block copolymer compounds for the synthesis of polymeric nano-micelles to make

an *in-vitro* evaluation of the biological responses obtained when micelles are loaded with 16Z, the newly synthesized structural analogs of the CA-4.

36.2 Experimental

36.2.1 Preparation of PLGA-PEG-PLGA Micelles and Determination of Critical Micelle Concentration

The synthesis of 16Z and the preparation of $PLGA_{1000}$-PEG_{1000}-$PLGA_{1000}$ triblock copolymers are described in detail in Gerova et al. [8] and Ivanova et al. [18], respectively. The obtained $PLGA_{1000}$-PEG_{1000}-$PLGA_{1000}$ triblock copolymer was lyophilized (Cryodos, Telstar) to dryness and then dissolved in an appropriate amount of water to obtain a stock solution with a concentration of 500 μM. To achieve the full dissolution of the polymer, the mixture was stirred for 24 h at 4 °C.

The critical micelle concentration (CMC) of $PLGA_{1000}$-PEG_{1000}-$PLGA_{1000}$ block copolymers was determined using 1,6-diphenyl-1,3,5-hexatriene (DPH, 98%) as a hydrophobic probe. The obtained series of copolymer solutions (0.250–500 μM) were spiked with a standard solution of DPH in methanol. The final concentration of DPH was 4.0 μM. All samples were kept in the dark at room temperature for 24 h to reach the solubilization equilibrium of DPH in the aqueous phase before analysis with UV-VIS spectroscopy ($\lambda = 285$ nm; Beckman L-80 UV–Vis spectrometer, Beckman-Coulter, USA).

36.2.2 Formation of 16Z-Loaded PLGA-PEG-PLGA Triblock Copolymer Micelles

The loading of 16Z into the polymeric micelles was realized by diluting a stock solution of 16Z with a predetermined volume of aqueous $PLGA_{1000}$-PEG_{1000}-$PLGA_{1000}$ triblock copolymer solution. The final concentration of polymer in the micellar solution was kept constant (300 μM) and that of 16Z varied from 0.5 μM to 1.5 μM. The resulting solutions were shaken and kept in the dark at 4 °C for 24 h. Then they were allowed to equilibrate at room temperature for 2 h. The obtained solutions were filtered through 0.22 μm Teflon membrane filters to separate the insoluble matter.

The particle diameter of the formed micelles was measured with Brookhaven instruments 90plus at 37 °C (angle = 90.00, wavelength = 657.0 nm). The morphology of the polymeric micelles was studied by transmission electron microscopy. A sample from the micellar solution was dropped on copper Formvar coated grid and naturally air-dried for several hours at room temperature. The experiments were performed on a JEOL (JEM-100B) microscope with an accelerating voltage of

80 kV. TEM size and morphology of 16Z loaded micelles were analyzed with ImageJ [19].

36.2.3 Determination of Drug Encapsulation Efficiency and Loading Capacity

16Z-loaded micelles were dissolved in ethanol to measure 16Z concentration through UV spectrophotometry. This method was used to determine the content of 16Z in the micelle solution. The encapsulation efficiency (EE) and drug loading (DL) were calculated according to Chen et al. [20]. Since 16Z is not soluble in water, its content in water was ignored when compared with the loading content of 16Z into the micelles. Thus, the content of free 16Z in water was not included when calculating the loading content and entrapment efficiency.

36.2.4 In Vitro 16Z Release Study

16Z-loaded micelles and 16Z were dispersed in 2 ml PBS solution in a dialysis membrane and placed at 37 °C incubator. Aliquots of the solution were removed and placed in Eppendorf tubes after 2, 6, 8, 24, 48, 72, and 96 h. Before determination of the drug concentration by HPLC (Proteome Lab PF2D, Beckman-Coulter, USA; C18 column, a linear gradient of acetonitrile in water from 0% to 100%, 30 min), the solution was centrifuged at 10000 rpm at 20 °C for 5 min and the supernatants were tested. The released drug concentrations against time were plotted into a curve.

36.2.5 Cytotoxicity Assay

Human liver hepatocellular carcinoma cell line (HepG2) was obtained from American Type Culture Collection (HB-8065) and maintained in DMEM (Dulbecco's Modified Eagle Medium, Applichem, Germany) supplemented with 10% (v/v) FBS (BioWhittaker, USA), penicillin (100 μg/ml), streptomycin (100 μg/ml), and 4.0 mM L-glutamine at 37 °C in a humidified atmosphere of 5.0% CO_2 and 95% air.

The cell proliferation inhibitory effect of 16Z-loaded micelles was assayed by 3-(4,5-dimethylthiazol-2-yl)-2,5-diphenyltetrazolium bromide (MTT) method. The MTT proliferation assay is based on the ability of live cells to reduce the yellow MTT dye to purple formazan crystals. Logarithmic growing HepG2 cells were plated at a density of 1.0×10^4 cells/well in 100 μl DMEM. Twenty-four hours later, the growth medium was changed with a growth medium containing

16Z-loaded micelle (16Z concentrations of 250, 500, 750 nM, and 150 μM micelles) and the cells were further incubated up to 72 h. Following the incubation period and a change with 100 μl/well of fresh media, 10 μl of MTT solution (5.0 mg/ml) was added to the wells and incubated for further 3 h. 16Z was prepared by dissolving in dimethyl sulfoxide (DMSO) and subsequent dilution with medium to different concentrations in the range of 25 μM to 10 nM. DMSO in the medium never exceeded 0.1%. Cells were also treated with a mixture of 100 μl DMEM with DMSO or 16Z as controls. The formed MTT-formazan product was dissolved in isopropanol and the absorption at 550/630 nm was measured on a vertical spectrophotometer (Bio-Tek Instruments Inc., USA). For each concentration tested, a set of 3 independent experiments of eightplicates was performed.

36.2.6 In Silico Drug-Likeness and Toxicity Predictions

In an attempt to design new biomimetic analogs of natural CA-4, we selected benzothiazolone heterocycle as a scaffold for a bioisosteric replacement of the CA-4 ring B (Fig. 36.2b). Following the main strategy of bioisosterism, we proffer the synthesis of novel CA-4 benzothiazolone hybrids S19, S21, S23, and RS10 with potential antitumor effects. The *in silico* drug-likeness and toxicity predictions of the designed CA-4 analogs were carried out using OSIRIS Property Explorer 2017 and the estimated partition coefficients were calculated with the SwissADME program (http://www.swissadme.ch/).

36.2.7 Statistical Analysis

The data were evaluated by analysis of variance (ANOVA) followed by Tukey's post-hock test. Differences in the results at the level of $p < 0.05$ were considered statistically significant. The statistical analysis was carried out using the PASW 18.0 statistical software package (IBM) for Windows**.**

36.3 Results and Discussion

36.3.1 Preparation and Characterization of 16Z-Loaded Micelles

The CMC research was carried out to prove the formation of the $PLGA_{1000}$-PEG_{1000}-$PLGA_{1000}$ nano-micelles in aqueous media. DPH was used as a probe in the measurement of CMC. The plot of DPH's absorption maximum at 285 nm as a

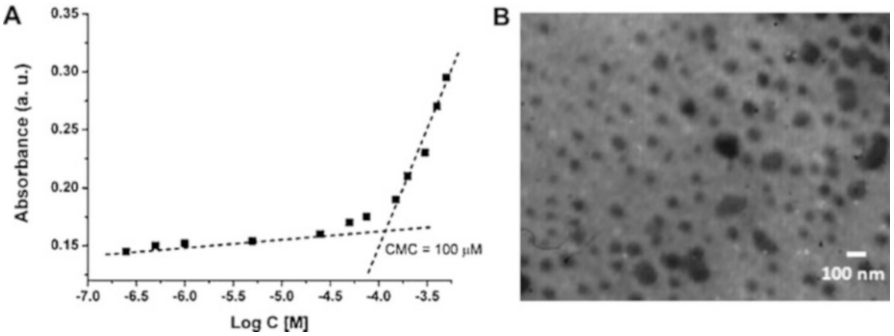

Fig. 36.1 Characterization of PLGA-PEG-PLGA-based micelles and its 16Z-loaded forms. (**a**) DPH absorbance at 285 nm vs. lgC for $PLGA_{1000}$-PEG_{1000}-$PLGA_{1000}$ in water; (**b**) TEM micrograph of 16Z-loaded micelles (scale bar 100 nm)

function of the polymer content is shown in Fig. 36.1a. The CMC was obtained from the intersection of the tangent to the curve at the inflection with the horizontal tangent through the points at low concentrations. It revealed that the CMC of $PLGA_{1000}$-PEG_{1000}-$PLGA_{1000}$ was 100 μM in aqueous solutions, suggesting that when the concentration of $PLGA_{1000}$-PEG_{1000}-$PLGA_{1000}$ conjugates was above 100 μM, nanomicelles would spontaneously form in aqueous solutions. This low CMC value indicated that there is a strong capacity to form micelles at a lower concentration.

The size distributions are known to affect pharmacokinetics and endocytosis in a polymeric drug delivery system. In our research, particle sizes and size distributions of 16Z loaded $PLGA_{1000}$-PEG_{1000}-$PLGA_{1000}$ micelles were measured by particle size analyzer in an aqueous solution at room temperature. Table 36.1 shows the size distributions of the micelles for the observed in batch dispersions. The blank $PLGA_{1000}$-PEG_{1000}-$PLGA_{1000}$ micelles showed a narrow size distribution (polydispersity index Pdi: 0.106) with main effective diameter of micelles of ca. 70 nm. An increasing amount of 16Z does not influence the micelles' size. The dispersions of 16Z-loaded micelles are dominated by a single mode with a peak-size close to 110 nm. In some batch dispersions, there was a second mode (by number) in size-range around 50–70 nm, probably revealing a presence of non-loaded micelles. The size results suggested a possible efficient passive targeting potential to tumor tissue.

TEM image was used to observe further the morphology and size of the micelles. As shown in Fig. 36.1b, the shapes of 16Z loaded $PLGA_{1000}$-PEG_{1000}-$PLGA_{1000}$ micelles were almost spherical with diameters ranging from 80 nm to 130 nm, which confirmed the shell–core structure of the polymeric micelles. The smaller sizes of 80 nm observed by TEM as compared to those measured by the particle size analyzer might attribute to evaporation shrinkage of the PEG shell during the drying process of the TEM sample preparation.

Table 36.1 Characterization of 16Z loaded micelles

Micelles (μM)	16Z (μM)	Effective diameter (nm)	Polydispersity index (Pdi, nm)	Encapsulation efficiency (%)	Loading efficiency (%)
300	0	71.0 ± 2.2	0.106 ± 0.002	–	–
300	0.5	115.2 ± 5.4	0.205 ± 0.003	56 ± 1	24 ± 1
300	1.0	111.7 ± 7.5	0.214 ± 0.005	69 ± 2	26 ± 1
300	1.5	109.4 ± 4.7	0.218 ± 0.003	70 ± 2	25 ± 2

Furthermore, we also found that increasing the concentration of 16Z from 0.5 μM to 1.5 μM has a small impact on the encapsulation and loading efficiencies. The encapsulation efficacy increased from 56% to 70%, however, the 16Z's drug loading efficiencies stayed constant at approximately 25%. These results indicated that the capacity of the triblock polymer influenced drug loading and encapsulation efficiency with only slight increases when drug concentrations increased.

36.3.2 In Vitro Drug Release Profiles and Effect on HepG2 Viability

To exploit the utility of 16Z-loaded micelles for an effective drug delivery system, we employed the *in vitro* drug release of 16Z from $PLGA_{1000}$-PEG_{1000}-$PLGA_{1000}$ micelles at different time intervals and compared the results to that of 16Z. The release profiles of 16Z micelles were investigated in PBS solution at 37 °C. The cumulative *in vitro* release of 16Z was significantly different from that of the micelles. Compared to the fast release of 16Z in dissolution medium, 16Z-loaded micelles exhibited a slow release in the initial 8 h (40%). 60% of 16Z was released from the micelles at 24 h, which was followed by the gradual and sustained release of 16Z up to 72 h (80%). The observed slow-release stage might result from a slow degradation of micelles, whereas the sustained release was attributed to the release of the encapsulated 16Z from the micelles. Recently, the two-step release pattern was observed in other drug-loaded micelle formulations [21]. Thus, our results proved that the release of 16Z from the $PLGA_{1000}$-PEG_{1000}-$PLGA_{1000}$ micelles in a controlled manner is beneficial for prolonging the drug release behavior.

We determined the anti-proliferative properties of 16Z-loaded micelles in HepG2 cells. As shown in Fig. 36.2a, blank micelles do not show cytotoxicity at 150 μM concentrations (48 and 72 h), which confirms that the $PLGA_{1000}$-PEG_{1000}-$PLGA_{1000}$ micelles have good biocompatibility. Moreover, Fig. 36.2a indicates that HepG2 cells exposed to 16Z after 48 h of treatment exhibited significant cytotoxicity in a dose-dependent manner. Although there was a similar cytotoxicity between 16Z and 16Z-loaded micelles at the concentration studied (250 nM, 500 nM, and 750 nM), a notably greater degree of cytotoxicity was observed at a lower dose (250 nM) of 16Z-loaded micelles when compared to 16Z alone. We might speculate that this

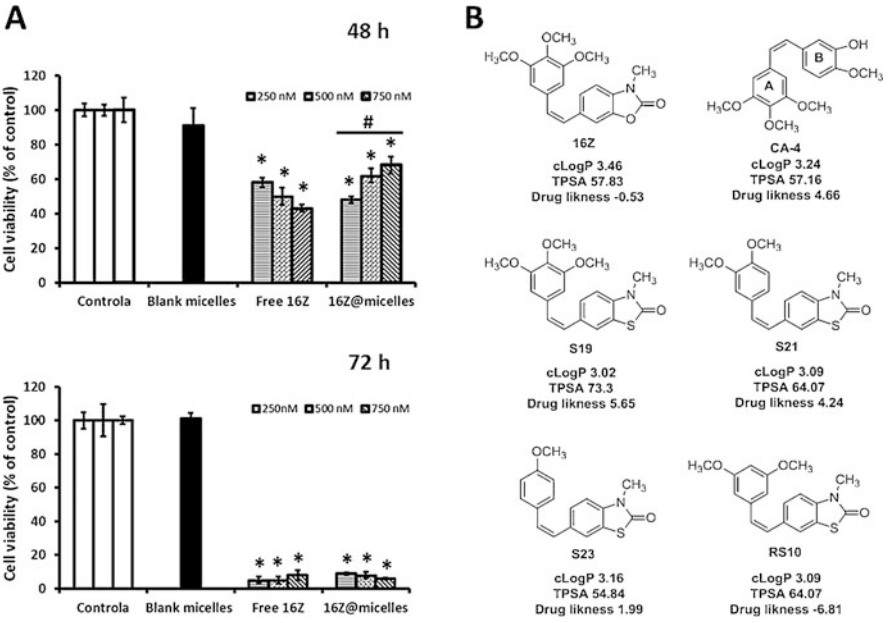

Fig. 36.2 *In vitro* cytotoxicity against HepG2 cells after incubation with 16Z-loaded $PLGA_{1000}$-PEG_{1000}-$PLGA_{1000}$ micelles at different concentrations for 48 and 72 h is shown in (**a**) and schematic representation of the compounds 16Z, CA-4, S19, RS10, S21 and S23 in (**b**). $*p < 0.01$ versus blank micelles and control group; $\#p < 0.05$ versus 16Z. CA-4: combretastatin A-4; 16Z@micelles: 16Z-loaded micelles

effect is possibly observed by increased 16Z-loaded micelle solubility and enhanced micelle-mediated cellular uptake at lower concentrations. Probably the dissolution of the polymer into water improves the capacity of the solution to dissolve drugs directly. Furthermore, when concentration increased to 500 or 750 nM, the cytotoxicity of 16Z on HepG-2 cells was higher than that of 16Z-loaded micelles, thus indicating a different mechanism of drug release from the micelles. No differences between the effect of the free 16Z and 16Z-loaded micelles were observed following 72 h of treatment.

One of the common difficulties with intravenous drug delivery is the low solubility of the drug. In our study, a better solubility of 16Z was accomplished because the drug has a high solubility in the micelle and the $PLGA_{1000}$-PEG_{1000}-$PLGA_{1000}$ micelles have a high solubility in the cell culture media. The phase segregation of polymer-blocks into micellar morphology creates an environment, where 16Z can dissolve in the hydrophobic core. PEGs are commonly employed as biocompatible hydrophilic polymers and PLA and PGA degrade over time into acids that can be safely eliminated from a living system, thus allowing us to perform future research for testing the possible anti-cancer effect of 16Z-loaded micelles *in vivo*.

36.3.3 *In Silico Results of Risks and Drug-Likeness of Ligands*

As a part of our ongoing research program to discover novel anticancer agents, we previously reported CA-4 analogs with benzoxazolone scaffold as potent anticancer agents [8]. In continuation of these efforts for development of selective tubulin polymerization inhibitors as potential chemotherapeutic agents, we have designed 4 (S19, RS10, S21, S23) new compounds structurally based on CA-4 and benzothiazolone moiety (Fig. 36.2b). The benzothiazolone was chosen based on its special significance in synthetic chemistry, pharmaceutical chemistry, as well as its anti-tumor properties, and cardiotonic activity.

ChemDraw was used to generate the simplified molecular-input line-entry system further used in OSIRIS Property Explorer [22] for calculation of the drug-likeness as a prediction that determines, whether a particular pharmacological agent has properties consistent with being an orally active drug [23–25]. It also provides information on the hydrophilicity of the compound (cLogP), solubility (LogS), molecular weight, drug-likeness and drug score. All four compounds (S19, RS10, S21 and S23) had molecular weights less than 500, which showed that they are likely to be absorbed and can reach the place of action when administered as oral drugs (Fig. 36.2b). All six compounds including 16Z and CA-4 had cLogP values less than 5, suggesting good absorption and permeation across cell membranes [26]. Among the six compounds, CA-4 had the highest value of drug score (0.48). All other compounds had a drug score of less than 0.2, which could be a result of introducing benzoxazolone and benzothiazolone scaffolds. The higher drug-likeness was calculated for S19 (73.3). The LogS prediction of −5.38 (S19), −5.34 (RS10), −5.22 (S21), −4.50 (16Z) and −2.25 (CA-4) indicated that all the compounds should be moderately soluble in water. Low hydrophilicity and therefore high logP values cause poor absorption or permeation. It has been shown that S19, RS10, S21 and S23 compounds have a reasonable probability of well absorbing, since their cLogP value is not greater than 5.0. In general, the drug-likeness value of compound S19 (6.65) is bigger than that of 16Z (−0.53) and CA-4 (4.66). S19 exhibited good *in silico* ADMET properties but possessed high mutagenic, irritant, and reproductive effective toxicity risks and therefore, it has to be studied in detail *in vitro* before considering S19 for *in vivo* drug testing.

Acknowledgments The authors are thankful to the National Science Fund of Bulgaria (Project DN 19/13 (2017)) for the financial support.

References

1. Downing HK (2000) Annu Rev Cell Dev Biol 16(1):89
2. Risinger AL, Giles FJ, Mooberry SL (2008) Cancer Treat Rev 35(3):255
3. Pettit GR, Cragg GM, Herald DL, Schmidt JM, Lohavanijaya P (1982) Can J Chem 60 (11):1374

4. Pettit GR, Singh SB, Hamel E, Lin CM, Alberts DS, Garcia-Kendall L (1989) Experientia 45 (2):209
5. McGown AT, Fox BW (1990) Cancer Chemother Pharmacol 26(1):79
6. Lin CM, Ho HH, Pettit GR, Hamel E (1989) Biochemist 28(17):6984
7. Chaudhary A, Pandeya SN, Kumar P, Sharma PP, Gupta S, Soni N, Verma KK, Bhardwaj G (2007) Mini-Rev Med Chem 7(12):1186
8. Gerova MS, Stateva SR, Radonova EM, Kalenderska RB, Rusew RI, Nikolova RP, Chanev CD, Shivachev BL, Apostolova MD, Petrov OI (2016) Eur J Med Chem 120:121
9. Savjani KT, Gajjar AK, Savjani JK (2012) ISRN Pharm 2012:Article ID 195727
10. Chan JM, Zhang L, Yuet KP, Liao G, Rhee JW, Langer R, Farokhzad OC (2009) Biomaterials 30(8):1627
11. Mathiowitz E, Jacob JS, Jong YS, Carino GP, Chickering DE, Chaturvedi P, Santos CA, Vijayaraghavan K, Montgomery S, Bassett M, Morrell C (1997) Nature 386(6623):410
12. Kraft JC, Freeling JP, Wang Z, Ho RJ (2014) J Pharm Sci 103(1):29
13. Chen H, Li B, Qiu J, Li J, Jin J, Dai S, Ma Y, Gu Y (2013) Nanoscale 5(24):12409
14. Chen H, Chi X, Li B, Zhang M, Ma Y, Achilefu S, Gu Y (2014) Biomater Sci 2(7):996
15. Chen H, Li B, Zhang M, Sun K, Wang Y, Peng K, Ao M, Guo Y, Gu Y (2014) Nanoscale 6 (21):12580
16. Zentner GM, Rathi R, Shih C, McRea JC, Seo MH, Oh H, Rhee BG, Mestecky J, Moldoveanu Z, Morgan M, Weitman S (2001) J Control Release 72(1–3):203
17. Chen S, Pieper R, Webster DC, Singh J (2005) Int J Pharm 288(2):207
18. Ivanova L, Popov C, Kolev I, Shivachev B, Karadjov J, Tarassov M, Kulisch W, Reithmaier JP, Apostolova MD (2011) Diam Relat Mater 20(2):165
19. Rasband WS (1997–2018) ImageJ. US. National Institutes of Health, Bethesda
20. Chen X, Chen J, Li B, Yang X, Zeng R, Liu Y, Li T, Ho RJY, Shao J (2017) J Colloid Interface Sci 490:542
21. Hans M, Lowman A (2002) Curr Opin Solid State Mater Sci 6(4):319
22. Organic Chemistry Portal (2012) http://www.organic-chemistry.org/prog/peo/
23. Egbert M, Whitty A, Keseru GM, Vajda S (2019) J Med Chem 62(22):10005
24. Behrouz S, Rad MN, Shahraki BT, Fathalipour M, Behrouz M, Mirkhani H (2019) Mol Divers 23(1):147
25. Lipinski CA, Lombardo F, Dominy BW, Feeney PJ (2012) Adv Drug Deliv Rev 64:4
26. Wu CY, Benet LZ (2005) Pharm Res 22:11

Chapter 37
Poly(ε-caprolactone)/Chitosan Nanostructures for Cell Cultivation

Hilal Turkoglu Sasmazel

Abstract Hybridization of synthetic poly (ε-caprolactone) (PCL) and natural chitosan polymers to develop PCL/chitosan core-shell nanostructures for cell cultivation was aimed in this study. Coaxial electrospinning method was used for the fabrication of the nanostructures. The characterizations of the samples were done by X-ray photoelectron spectroscopy (XPS) analyses and mechanical tests. XPS analysis of the PCL/chitosan core-shell structures exhibited the characteristic peaks of PCL and chitosan polymers. The cell culture studies, MTT assay and Confocal Laser Scanning Microscopy (CLSM), carried out with L929 ATCC CCL-1 mouse fibroblast cell line, proved the biocompatibility of all materials. The cell viability on the hybrid nanostructures was ~two times better then on tissue culture polystyrene (TCPS) because of its three dimensional (3D) extracellular matrix (ECM)-like structure compared to 2D flat surface of commercially cell compatible TCPS. The performance was ~two times and ~ten times better compared to single PCL and single chitosan, respectively, even though both fabricated similarly by electrospinning as non-woven fibrous structures, because were either too hydrophobic or too hydrophilic to maintain cell attachment points.

Keywords Chitosan · PCL · Core-shell · Fibroblast · Electrospinning

37.1 Introduction

Electrospinning is a simple but very effective process to obtain micro and nanofibers with high surface area to volume ratio from a large diversity of materials including polymers, composites, and ceramics for tissue engineering applications [1, 2]. It includes a rapid evaporation of the solvent during the electrospinning process and the jet of polymer solution is continuously stretched because of the electrostatic

H. Turkoglu Sasmazel (✉)
Department of Metallurgical and Materials Engineering, Atilim University, Ankara, Turkey
e-mail: hilal.sasmazel@atilim.edu.tr

P. Petkov et al. (eds.), *Nanoscience and Nanotechnology in Security and Protection against CBRN Threats*, NATO Science for Peace and Security Series B: Physics and Biophysics, https://doi.org/10.1007/978-94-024-2018-0_37

forces between the surface charges. As a result, ultrafine fibers are deposited on the collector. One or more different polymer solutions as a shell and non-polymeric Newtonian liquid or a powder as a core could be coaxially electrospun by coaxial electrospinning method. In this process a core-shell droplet occurs at the exit of the core-shell needle tip, and it forms a Taylor cone with the help of the applied high electric field. Finally, the core-shell fibers are collected on the counter electrode [3, 4]. It is found that coaxially electrospun structures for tissue engineering applications are superior to their blended or individual forms [5].

In this study, 3D electrospun PCL/chitosan core-shell scaffolds for tissue engineering applications are developed. The main idea is to produce composite scaffolds in which PCL is used as core layer and chitosan is used as shell layer by coaxial electrospinning method. The characterization of fabricated scaffolds is done by mechanical tests and XPS analysis. Finally, the cell material interactions of the prepared materials are examined in vitro with L929 cell line over the course of 7 days.

37.2 Experimental Section

37.2.1 Preparation of PCL/Chitosan Core-Shell Structures and Their Characterization

PCL (15 wt. %) was dissolved in chloroform/methanol (75/25, v/v) mixture at 30 °C. Chitosan (8 wt. %) was dissolved in TFA at 50 °C. In order to achieve a stable jet for the coaxial electrospinning, the two immiscible solutions were fed through coaxial needles with diameters of 0.9 mm for the shell, and 0.57 mm for the core polymer. The coaxial electrospinning was performed under ambient temperature (24 °C) for 6 h.

The mechanical properties of the electrospun core-shell structures, cut into dog-bone shape with dimensions of 40 mm × 5 mm, were determined using a universal tensile testing instrument (Zwick/Roell 250 kn, Germany) with 100 N load cell. Furthermore, the surface chemistry of the developed scaffolds was examined with X-ray photoelectron spectroscopy system (PHI 5000 Versa Probe, Physical Electronics, USA). The surface composition and the functional carbon and oxygen groups of the fabricated scaffolds are examined by survey and high-resolution scans.

37.2.2 Cell Culture Studies

In order to observe cell-material interactions of PCL/chitosan core-shell scaffolds, L929 ATCC CCL-1 mouse fibroblast cell line was used for cell culture studies. Prepared coaxially electrospun scaffolds were placed in 24-well plate petri dishes

with the concentration of 1×10^5 cells/mL in medium. Studies of cell viability were conducted 7 days in a culture medium that consisted of, DMEM/F12 + %10 (v/v) FBS + 1% (v/v) penicillin + streptomycin (100 units/ml penicillin, 100 μg/ml streptomycin) in incubator at 37 °C under 5% CO_2. Samples were sterilized with UV for 30 min and cut into circular shapes with 1 cm diameter. Then they were placed in parafilm coated TCPS (tissue culture Polystyrene) well. In order to determine cell growth MTT technique was used. In addition to that, cell growth, proliferation and adhesion were examined by confocal laser scanning microscope (CLSM).

37.3 Results and Discussion

In this study, coaxial electrospinning method is used for the first time to produce a composite tissue scaffold with PCL as a core layer and chitosan as shell layer. The performance of the fabricated scaffolds was investigated by the following characterization methods and cell culture studies:

37.3.1 Mechanical Properties

The mechanical performance is critical for electrospun materials due to the fact that they need to tolerate the forces created by regeneration and physiological activities to a certain level [4]. The determined mechanical properties of the prepared materials are given in Table 37.1. When compared to the PCL nanofibers, the chitosan nanofibers were found to possess lower elastic modulus and also lower tensile strength. Additionally, the core-shell structured PCL/chitosan nanofibers were found to have higher elastic modulus (3.284 MPa ± 0.016) and tensile strength (1.318 MPa ± 0.042) and lower strain at break value (11.000% ± 2.345), compared to the chitosan and PCL nanofibers.

When the same load was applied to PCL, chitosan and PCL/chitosan core-shell structures, the latter exhibited decreased elastic and plastic deformation values. Also, the strain at break value was the lowest for the PCL/chitosan core-shell scaffolds comparing to the PCL and chitosan scaffolds; therefore, the PCL/chitosan core-shell scaffolds were more brittle, resulting in less elongation before failure.

Table 37.1 Tensile properties of the electrospun PCL/chitosan core-shell scaffolds

Sample	Elastic modulus (MPa)	Tensile strength (MPa)	Strain at break (%)
PCL	1.330 ± 0.002	0.909 ± 0.040	77.020 ± 3.000
Chitosan	0.668 ± 0.023	0.451 ± 0.010	40.090 ± 2.500
PCL/chitosan core-shell	3.284 ± 0.016	1.318 ± 0.042	11.000 ± 2.345

37.3.2 Surface Chemistry Analysis

The X-ray photoelectron spectroscopy (XPS) analysis was applied to get information on the chemical composition and binding states on the surfaces of the PCL/chitosan core-shell structures.

Surface chemical composition of 66.9 at% C, 31.4 at% O and 1.7 at% N was found for the PCL/chitosan core-shell samples by the XPS survey scan. Additionally, high resolution scans of C1s (285.0 eV), O1s (531.0 eV) and N1s (399.8 eV) peaks were performed for the samples. The analysis showed the characteristic peaks of the PCL components and chitosan that can be expected for the PCL/chitosan core-shell scaffolds (Table 37.2).

37.3.3 Cell Culture Studies

37.3.3.1 MTT Assay

The viability of cells was measured by MTT assay. Figure 37.1 shows that coaxially electrospun PCL/chitosan scaffolds caused no toxicity to fibroblast cells and there is a notable increase in cell viability and density during the cell culture period of 7 days. The highest cell growth and proliferation were acquired by PCL/chitosan core-shell nanofibers at the end of the cell culture tests (seventh day). The 3D structure of the fabricated PCL/chitosan scaffolds gives a higher surface to volume ratio which yields higher cell density. The combination of the natural polymer chitosan and the synthetic polymer PCL as a core-shell electrospun structure consisting of micro and nanosized fibers with inter fiber pores, biomimics the original ECM structure, which results in the highest cell growth and poliferation at the end of the cell culture tests.

Table 37.2 Surface composition (atomic %) of the PCL/chitosan core-shell scaffolds, as determined by deconvolution of C1s and O1s XPS peaks

		PCL/chitosan core-shell	
eV	Group	Area	%
285.0	C–C	10,254	38.6
285.6	C*–COO	6511	24.5
286.2	C–N		
286.6	C–OH, C*–OCO	5423	20.4
288.8	COO, COOH	4372	16.5
eV	**Group**	**Area**	**Ratio**
532.1	C=O	11,456	1.22
531.0	C–O	9354	

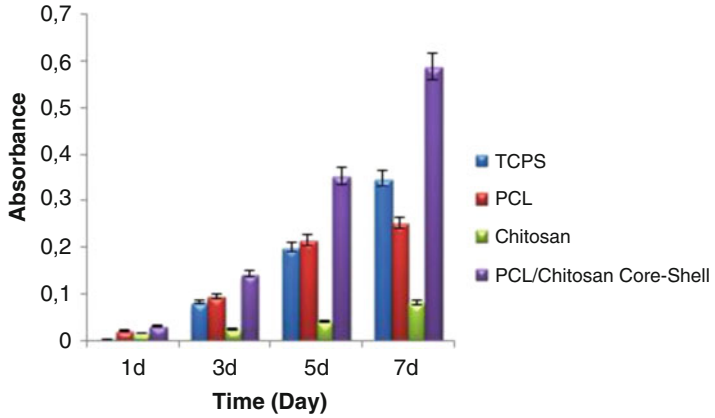

Fig. 37.1 Absorbance values of the control (TCPS Petri dishes), electrospun PCL, chitosan and PCL/chitosan core-shell scaffolds

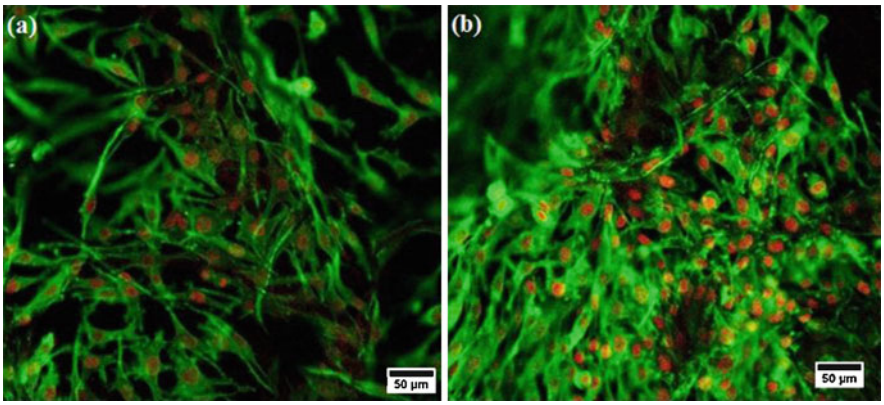

Fig. 37.2 Confocal microscopy images of the cells on/within PCL/chitosan core-shell scaffolds on the (**a**) third day; (**b**) seventh day. The magnification of the images is ×20

37.3.3.2 Confocal Laser Scanning Microscopy (CLSM) Analysis

On the third and seventh days of cell culture tests, cells on/within PCL/chitosan core-shell scaffolds were observed by CLSM. The cells were in a fusiform or possessed a spindle-like shape based on the cell response on/within the scaffolds, as shown in Fig. 37.2. On the third day of culture tests, the cells were able to attach to the matrix and proliferate and grow in the form of clusters. On the seventh day, the cells were alinged and their density was increased.

37.4 Conclusion

In this study coaxial electrospun PCL/chitosan composite scaffolds were developed for the first time. Based on the results of this work, it can be concluded that the electrospun PCL/chitosan core-shell scaffold was better candidate for cell adhesion, growth and proliferation than the commercial TCPS, PCL or chitosan scaffolds.

Acknowledgments I would like to thank the Scientific and Technological Research Council of Turkey (TUBITAK) for the scientific and financial support (Project Number: 114 M872).

References

1. H. Turkoglu Sasmazel, Novel hybrid scaffolds for the cultivation of osteoblast cells. Int. J. Biol. Macromol. 49, 838–846 (2011)
2. P. Taepaiboon, U. Rungsardthong, P. Supaphol, Drug-loaded electrospun matsof poly(vinyl alcohol) fibres and their release characteristics of four modeldrugs. Nanotechnology 17, 2317–2322 (2006)
3. H.L. Ga, S. Jun-Cheol, Y. Keun-Byoung, Controlled wall thickness and porosityof polymeric hollow nanofibers by coaxial electrospinning. Macromol. Res. 18, 571–576 (2010)
4. O. Ozkan, H. Turkoglu Sasmazel, Advances in electrospinning of nanofibers and theirbiomedical applications. Curr. Tissue Eng. 291–108 (2013)
5. D.H. Reneker, A.L. Yarin, Electrospinning jets and polymer nanofibers. Polymer 49, 2387–2425 (2008)

Chapter 38
Preparation and Characterization of Zinc and Magnesium Doped Bioglasses

Sílvia Rodrigues Gavinho, Mariana Castro Soares, João Paulo Borges, Jorge Carvalho Silva, Isabel Sá Nogueira, and Manuel Pedro Fernandes Graça

Abstract Peri-implantitis is an infectious disease that affects about one of five patients who receive a dental implant within 5 years after the surgery. To minimize this reaction the development of new biomaterials with antibacterial action is needed that can be used as a coating material in orthodontic implants. In addition, these biomaterials can be doped with several ions, which add specific properties that may act at the cellular level, such as increasing the angiogenesis efficiency. In this work, 45S5 Bioglass® has been used as the base material because it presents higher bioactivity compared to other biomaterials. To add antibacterial function and increase positive effects on bone metabolism, zinc and magnesium ions were introduced in the glass network. The main objective was the synthesis of the 45S5 glass by melt-quenching and study the biological performance as function of the zinc and magnesium concentrations. The structural and biological properties of the prepared samples are discussed.

Keywords Biomaterial · Bioactive glass · Implant coating · Cytotoxicity · Antibacterial properties

S. R. Gavinho · M. C. Soares · M. P. F. Graça (✉)
I3N and Physics Department, University of Aveiro, Aveiro, Portugal
e-mail: mpfg@ua.pt

J. P. Borges · J. C. Silva
I3N- CENIMAT, New University of Lisbon, Lisbon, Portugal

I. S. Nogueira
UCIBIO, REQUIMTE, Departamento Ciências da Vida, Faculdade de Ciências e Tecnologia, FCT-NOVA, Almada, Portugal

P. Petkov et al. (eds.), *Nanoscience and Nanotechnology in Security and Protection against CBRN Threats*, NATO Science for Peace and Security Series B: Physics and Biophysics, https://doi.org/10.1007/978-94-024-2018-0_38

38.1 Introduction

One of the main focuses in modern medicine has been the extension of human life with the highest quality of life that can be achieved. In the matter of quality, biomaterials have proved to be fundamental and their evolution has been remarkable with their greatest development in the twentieth century, although there are reports of materials being applied in the field of medicine by older civilizations [1]. A biomaterial is defined as "any natural or synthetic material that is intended to be introduced into living tissue as part of a medical device or implant" [2]. Initially, biomaterials had their main applications in artificial joints and cardiovascular devices, but recently the field of tissue engineering and organ regeneration began to be part of their applications [1].

Considering that a biomaterial is designed to interact positively with living tissues or organs, its main feature should be biocompatibility, which means that when placed in contact with the biological environment, the latter will not be damaged. There are three types of biomaterial-tissue interactions that can be observed: (i) bioinert, where the material is encapsulated by a fibrous tissue and no longer plays any role in the biological environment; (ii) bioresorbable, where the material is absorbed by the environment in vivo; or (iii) bioactive, where there is an active interaction between the implant and the tissues, i.e. superficial bonds are formed between the two parts [1].

In many cases, the materials that have the best implant characteristics, especially for bone implants, are metals due to their adequate mechanical properties. However, metals are not bioactive, and this increases their tendency towards failure. In order to improve this aspect and create a form of interaction between the metallic implants and the biological environment, chemical changes are applied to their surface or they are coated with another type of material. In the field of coatings, ceramics such as hydroxyapatite and bioglass are used due to their high bioactivity and good resistance to corrosion and compressive stresses [3]. One of the most popular bioactive ceramics is 45S5Bioglass®, discovered in the twentieth century by Larry Hench. This bioglass is composed of 45% SiO_2, 24.5% Na_2O, 24.5% CaO 6% and P_2O_5 (wt %) [4].

The 45S5Bioglass® is highlighted due to its bioactivity and ability to create strong bonds with tissues. In particular, when used in a bone environment, bioglass has the ability to form a hydroxyapatite layer, which will promote adhesion and proliferation of osteoblasts, the major cells responsible for the formation of new bone tissue [5–8].

In addition to all the advantages presented, 45S5Bioglass® has some limitations. For example, this biomaterial presents difficulties in the production of porous bioactive glass models for bone regeneration. However, this problem is overcome by adapting the composition of the bioglass, avoiding its crystallization. Sintering problems can also be avoided by changing the synthesis method and conditions, and in the sol-gel process the silica matrix is synthesized at room temperature [9]. Besides the importance of synthesis methods, the ionic modification of the vitreous network

also influences the functional properties, being possible to change the regeneration rate of the hard tissue or increase the antibacterial activity and angiogenesis [7].

There are several studies of ionic modification that have increased bioactivity, stimulated the effects of osteogenesis, angiogenesis and antibacterial properties of bioglass in a specific physiological environment [7, 10]. Ions such as Sr, Mg, Fe, B, Zn Li or Zr accelerate hard tissue regeneration and may be beneficial for patients who need help with tissue regeneration [7]. In addition, some of these ions lead to increased cell proliferative activity, apatite formation, and bone-related gene expression.

In this manuscript, we will focus on magnesium and zinc ions. In addition to all other functions referred above, magnesium has advantages in bone metabolism, fracture prevention and bone density, and helps to prevent osteoporosis [10, 11]. Zinc is a metallic substance that is associated with enzymatic reactions, cell development, immune function, and its deficiency is associated with various cardiovascular, neurological and bone diseases. Zinc is essential for DNA replication and also plays an important role in the growth, development and differentiation of specialized bone cells. In addition, zinc also has antibacterial properties [10]. This element acts as a cofactor of the alkaline phosphatase enzyme needed for mineralization and bone formation [11]. In relation to bone tissue in particular, zinc plays a role in its formation since it is responsible for stimulating the osteoblasts and inhibiting the absorption of osteoclasts by the bones. In addition, there are studies on zinc-containing ceramic composites showing that these materials exhibit good antibacterial properties, which may be helpful in decreasing surgical complications, for example after the introduction of an orthopedic implant [12–14]. Magnesium and zinc ions are present in the human biological system and both have very different roles in it. The main objective of this work is to understand what are the main structural, morphological and biological changes that the addition of these ions introduced in the bioglass.

38.2 Results and Discussion

Bioglass with magnesium, zinc or both elements were prepared with various concentrations (Table 38.1) (1, 2, and 4 wt%). The "base bioglass" was 45S5Bioglass® and the samples were prepared by the melt-quenching method. The morphological, structural and biological characteristics were studied.

Table 38.1 Sample compositions by weight percentage

	1 Mg	2 Mg	4 Mg	1Zn	2Zn	4Zn	2 Mg2Zn	2 Mg4Zn	4 Mg2Zn
Bioglass	99%	98%	96%	99%	98%	96%	96%	94%	94%
Magnesium	1%	2%	4%	–	–	–	2%	2%	4%
Zinc	–	–	–	1%	2%	4%	2%	4%	2%

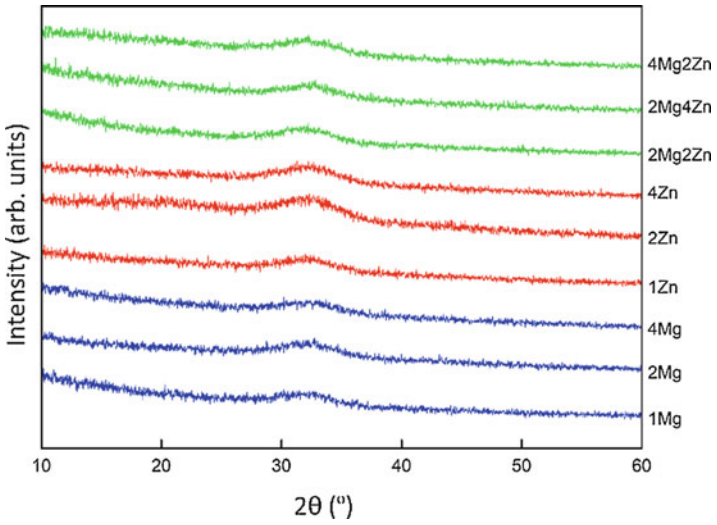

Fig. 38.1 X-ray diffraction patterns of all samples

It is possible to verify the similarity of all diffractograms presented in Fig. 38.1, both among them and in comparison to the bioglass without doping, presented in the literature [15]. All samples have a mostly amorphous structure, which is characteristic of any glass, which means that the addition of magnesium and/or zinc in the amounts used did not promote the crystallization of the glass. However, these crystalline phases may exist, but according to the diffractograms will be in very small quantity.

Raman spectra obtained for all samples are shown in Fig. 38.2. It is observed that both within the sample group and among the three groups, the spectra are quite similar and do not differ much from the results found in the literature for pure bioglass [16]. The amorphous structure of the samples is confirmed by this technique since there are broad bands in the spectra instead of well-defined peaks. Comparing the spectra of these doped samples with the spectra present in previous investigations of the bioglass without the presence of the dopant, it appears that the presence of magnesium and/or zinc in the amounts used does not produce a significant change in the glass structure.

The presence of broad bands in the FTIR spectra (Fig. 38.3) confirms the amorphous structure of the samples, which means that the addition of magnesium and/orzinc did not promote marked crystallization of the bioglass. Absorption bands are found in the spectra of all samples near 506, 600, 740, 873, 932, 1033 cm^{-1}, and all these values are in accordance with those described in the literature for the bioglass used. The stretching and flexing modes of Si-O-Si bonds are associated with the 1033 and 506 cm^{-1} bands. When there is a non-binder oxygen atom in SiO_2 molecules a different vibration mode is associated, which appears at 932 cm^{-1}. The remaining two bands (600 and 740 cm^{-1}) are related to P-O-P bonds and the

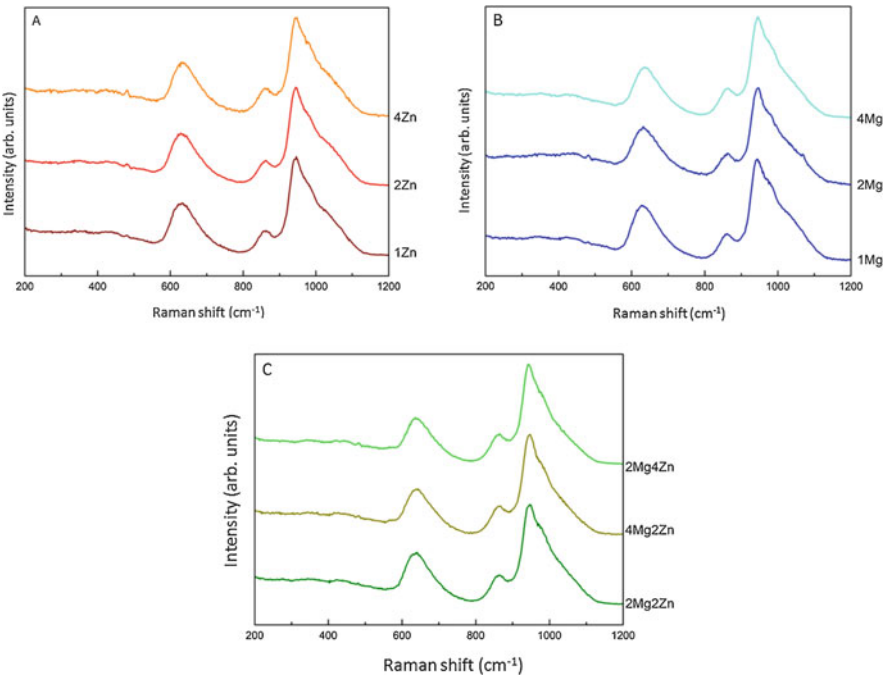

Fig. 38.2 Raman spectra obtained for all bioglass samples with: (**a**) magnesium; (**b**) zinc and (**c**) magnesium and zinc

presence of amorphous phosphates. The band centered at 873 cm^{-1} can certainly not be associated with any particular mode, since there are several different assignments made in the literature, such as the presence of calcium or sodium carbonates. This could be true having in mind that these compounds were introduced by initial mixing of the sample constituents, as stated in the literature, and may not completely disappeared, when calcination was performed. However, it may also be associated with SiO_4 units, although this band may be located at wave numbers slightly deviated from the value present in these samples.

Surface images of all samples were obtained by scanning electron microscopy and are shown in Fig. 38.4. For the magnesium group, all samples have a surface with a grainy texture. Using ImageJ software, it was possible to calculate the average grain size by a pixel-micrometer conversion. The average sizes calculated were 79, 187 and 225 nm for the 1Mg, 2Mg and 4Mg samples, respectively. As the amount of magnesium added to the glass increases, the average size of the grains that are present on the surface increases more than double for 2Mg compared to 1Mg.

In the group of samples containing zinc a very different surface is observed compared to the group mentioned above. In addition to the presence of some impurities, small spots are observed which decrease in quantity as the percentage of zinc increases. These spots suggest the existence of a kind of segregation which

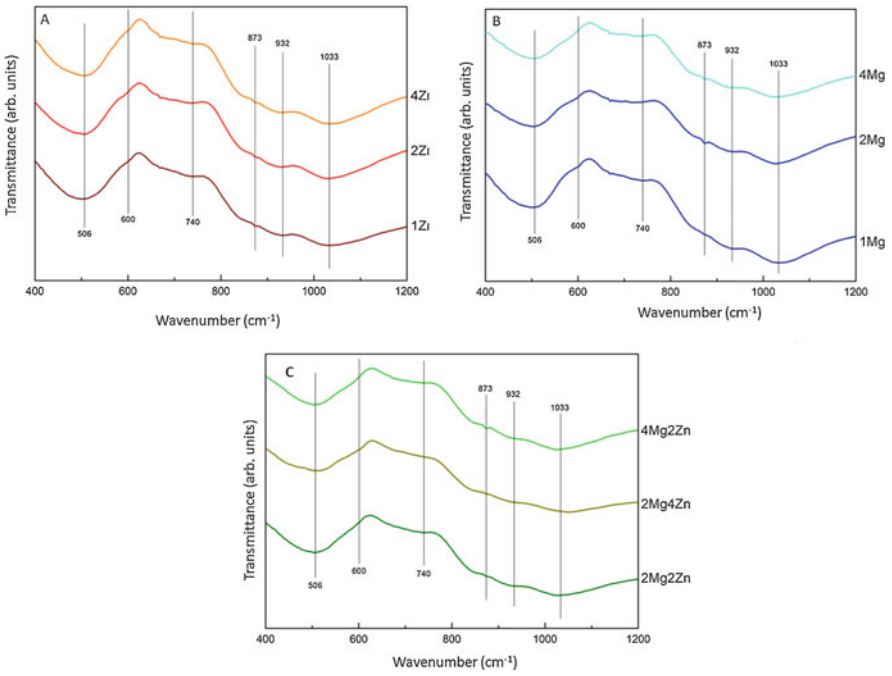

Fig. 38.3 FTIR spectra for all bioglass samples with: (**a**) magnesium; (**b**) zinc and (**c**) magnesium and zinc

only appears by certain amount of zinc incorporated in the bioglass since it is possible to verify that in the 4Zn sample image these spots are non-present.

In the images of the samples containing both magnesium and zinc, the phenomenon that gives rise to the aforementioned segregations is exponent. The segregations are observed in a larger extent for samples 2Mg2Zn and 4Mg2Zn, which are those that contain less zinc. For the 2Mg4Zn sample the segregations disappear and the granular appearance observed by the magnesium samples does not appear either, leading to the conclusion that this effect is nullified by zinc addition. Such segregations may be caused by the existence of a second phase within the amorphous structure of the glass.

38.3 Cytotoxicity Tests

Cytotoxicity tests were performed with three different concentrations by the extraction method applying SaOS-2 cells (human osteosarcomas). The viability of the cells was evaluated using resazurin as a colorimetric indicator (Fig. 38.5). The colorimetric indicator used is gray when the environment is cytotoxic and pink when it is not. None of the samples was cytotoxic except for the 2Mg sample by 25 mg/ml

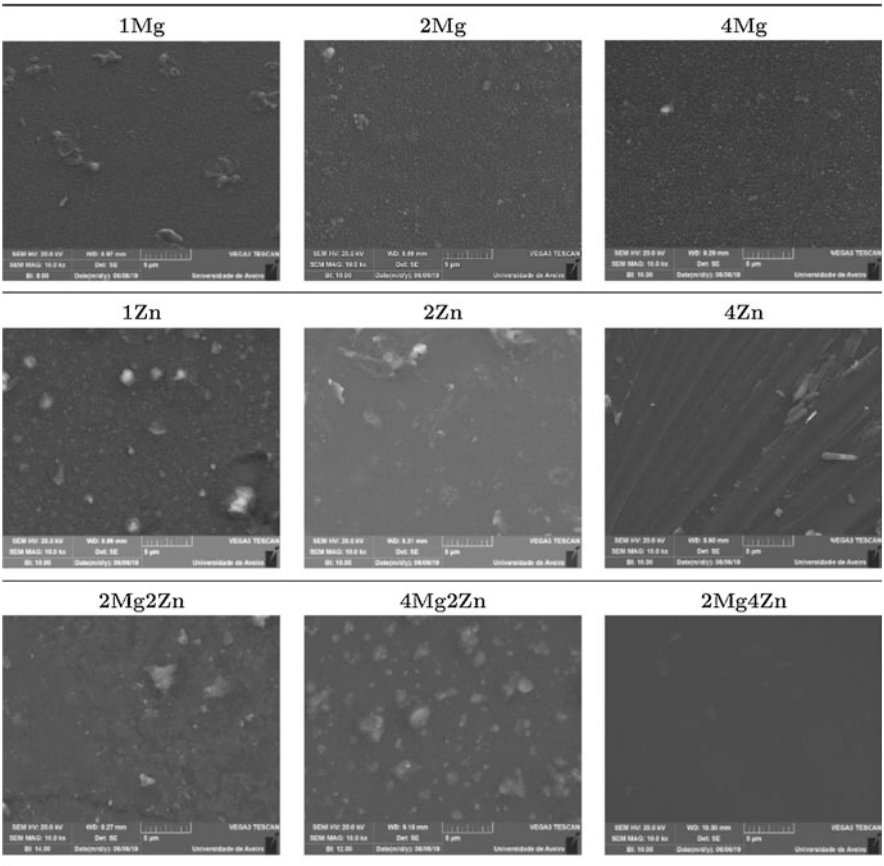

Fig. 38.4 Surface images of samples taken by scanning electron microscopy

concentration. It is thought that by this experiment an error in dilution occurred and the cells were exposed to a higher concentration of the sample. However, under normal conditions it would behave in the same manner as the other samples. At the concentration of 50 mg/ml, it is observed that the sample with the highest amount of zinc was the only one that was not cytotoxic, although the 2Zn sample also had a light pink color. By the samples containing both doping elements, the one with the highest amount of zinc was not cytotoxic. However, at the initial concentration, all samples were toxic to cells.

Cell culture population percentages for all samples and dilutions are shown in Fig. 38.6. Light and dark gray bars represent negative (non-cytotoxic environment) and positive (cytotoxic environment) control cultures, respectively.

From Fig. 38.6, it is possible to analyze more quantitatively the cytotoxicity of the samples. In general, the results shown in the graph confirm the analysis performed for concentrations of 100 mg/ml and 25 mg/ml through the images. Within the

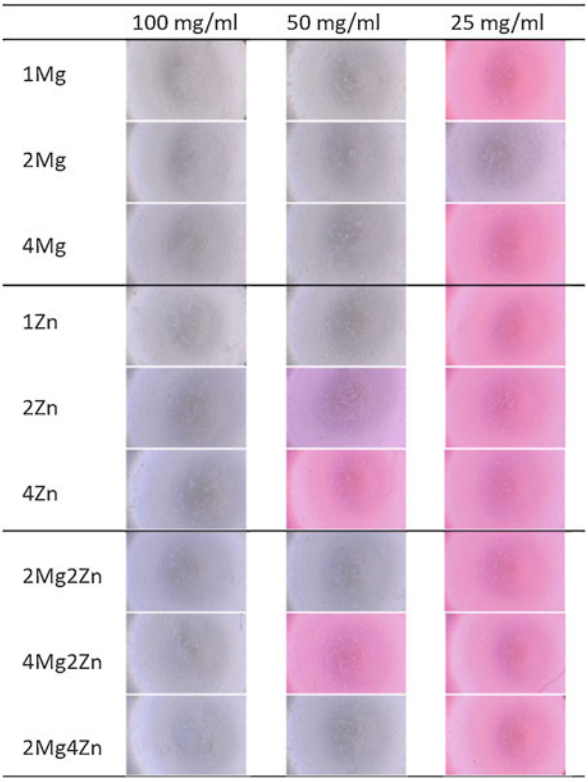

Fig. 38.5 Cell culture images of different samples at three concentrations applying colorimetric indicator

intermediate concentration, there are already some variations for the zinc group and the composites that become more obvious by looking at the graph. For the zinc samples, it should be noted that the increase in the percentage by weight of dopant is followed by a decrease of the cytotoxicity. For the samples with both dopants, it is observed that the sample with the highest percentage of zinc is the only one of the three that is not cytotoxic at the referred concentration.

38.4 Antibacterial Activity

Figure 38.7 shows the pellets of each sample after a procedure performed to verify the tested antibacterial activity for two bacteria. The gray ring observed around the tablets allows to evaluate the inhibitory effect of the samples in relation to the bacteria in question. The size of the ring is proportional to the inhibitory effect. In general, it is possible to verify from the images that all samples have a higher inhibitory effect for *S. aureus* bacteria than for *E. coli*. These results are confirmed by the measurements of the halo diameters, presented in Table 38.2.

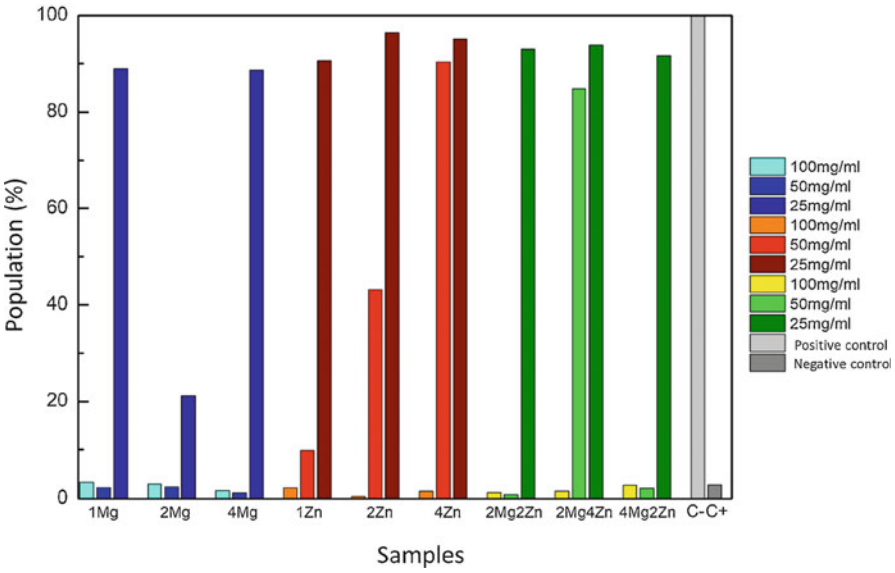

Fig. 38.6 Percentages relative to cell population

38.5 Conclusions

This work aimed to study what changes were caused to some of the characteristics of 45S5 bioglass when different dopants with different amounts are added. To understand the changes, various analyses were performed regarding the physical structure and biological activity of the samples. The results from the structural and physical characterization techniques allow to conclude that there is no significant change in the bioglass structure with the addition of magnesium and/or zinc, although the SEM images show surface changes in some samples compared to the pure bioglass. No significant differences were observed by Raman, FTIR and X-ray diffraction techniques regarding the analyzes of the base glass in the literature, confirming that the structure remains amorphous by any addition in the amounts used. The biological characterization of the samples was made considering their cytotoxicity and antibacterial activity. For the first property, it is concluded that almost all samples can only be used in the biological system if their concentration does not exceed 25 mg/ml. This suggests that all samples should then be combined with another biomaterial, so that the exposure of these doped bioglasses to the medium does not exceed the lowest concentration. However, the 4Zn and 2Mg4Zn samples show a favorable behavior at a higher concentration (50 mg/ml) and it is also observed that the addition of zinc contributed to the decrease of the cytotoxicity. Regarding the analysis of antibacterial activity, it was concluded that the combination of magnesium and zinc produces the best results for the inhibitory effect on *S. aureus* bacteria, assuming a joint action by the two substances. Furthermore, the inhibitory effect on all compositions was found to be most evident for *S. aureus* bacteria compared to *E. coli*.

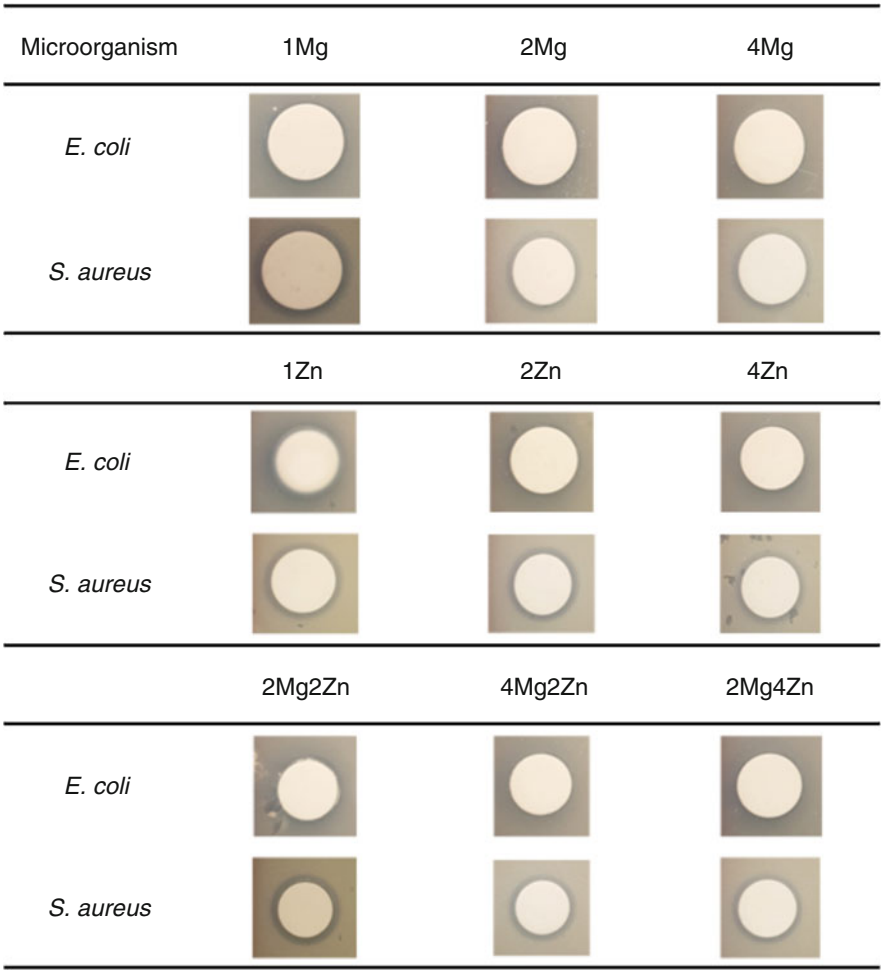

Fig. 38.7 Images of the pellets of each sample placed in bacterial medium and their inhibition halo (gray ring around the pellet)

Table 38.2 Average diameters of the inhibition halos

	E. coli	S. aureus
	Halo diameter (mm)	Halo diameter (mm)
1Mg	14,75 ± 0,64	15,63 ± 0,48
2Mg	14,63 ± 0,48	15,25 ± 0,29
4Mg	14,50 ± 0,71	15,13 ± 0,48
1Zn	16,00 ± 1,15	16,75 ± 1,26
2Zn	14,75 ± 0,29	16,00 ± 0,41
4Zn	14,00 ± 0,58	15,25 ± 0,29
2Mg2Zn	15,67 ± 0,76	17,13 ± 0,63
4Mg2Zn	14,00 ± 0	15,50 ± 0
2Mg4Zn	13,63 ± 0,25	16,00 ± 0,91

References

1. Bose S, Bandyopadhyay A (2013) Characterization of biomaterials: Chapter 1 – Introduction to biomatrials. Academic, New York, pp 1–9
2. Gilbert TR, Budinskaya O (2017) New frontiers in biomaterials. Oral Maxillofac Surg Clin North Am 29:105–115
3. Bose S, Banerjee D, Bandyopadhyay A (2017) Introduction to biomaterials and devices for bone disorders. Academic, New York
4. Hench L (2006) The story of bioglass®. J Mater Sci Mater Med 17:967–978
5. Jones JR (2013) Review of bioactive glass: from hench to hybrids. Acta Biomater 9:4457–4486
6. Lizzi F, Villat C, Attik N, Jackson P, Grosgogeat B, Goutaudier C (2017) Mechanical characteristic and biological behavior of implanted and restorative bioglasses used in medicine and dentistry: a systematic review. Dent Mater J 33:702–712
7. Vichery C, Nedelec JM (2016) Bioactive glass nanoparticles: from synthesis to materials design for biomedical applications. Materials 9:1–17
8. Lefebvre L, Chevalier J, Gremillard L, Zenati R, Thollet G, Ber-nache-Assolant D, Govin A (2007) Structural transformations of bioactive glass 45S5 with thermal treatments. Acta Mater 55:3305–3313
9. Hench L (1991) Bioceramics: from concept to clinic. J Am Ceram Soc 74:1487–1510
10. Bellucci D, Bolelli G, Cannillo V, Cattini A, Sola A (2011) In situ Raman spectroscopy investigation of bioactive glass reactivity: simulated body fluid solution vs TRIS-buffered solution. Mater Charact 62:1021–1028
11. Bellantone M, Coleman NJ, Hench L (2000) Bacteriostatic action of a novel four-component bioactive glass. J Biomed Mater Res 51:484–490
12. Rabiee S, Nazparvar AM, Vashace D, Tayebi L (2015) Effect of ion substitution on porperties of bioactive glasses: a review. Ceram Int 41:7241–7251
13. Su Y, Cockerill I, Wang Y, Quin Y, Chang L, Zheng Y (2019) Zinc-based biomaterials for regeneration and therapy. Trends Biotechnol 37:428–441
14. Blochberger M, Hupa L, Brauer D (2015) Influence of zinc and magnesium substitution on ion release from Bioglass 45S5 at physiological and acidic pH. Biomed Glass 1:93–107
15. Gavinho SR, Prezas PR, Ramos DJ, Sá-Nogueira I, Borges JP, Lança MC, Silva JC, Henriques CMR, Pires E, Kumar JS, Graça MPF (2019) Nontoxic glasses: preparation, structural, electrical and biological properties. Int J Appl Ceram Technol 16:1885–1894
16. Dziadek M, Zagrajczuk B, Jelen P, Olejniczak Z, Cholewa-Kowalska K (2016) Structural variations of bioactive glasses obtained by different synthesis routes. Ceram Int 42:14700–14709

Chapter 39
Polarized Light for Detection of Pathological Changes Within Biological Tissues

Ani Stoilova, Dimana Nazarova, Blaga Blagoeva, Velichka Strijkova, and Plamen Petkov

Abstract Here we present two techniques using polarized light for detection of abnormal morphological changes in tissue samples. A Zeta-20 polarized optical microscope has been used to visualize human lung histologic specimens with pathological changes caused by anthracosis, tuberculosis, influenzal pneumonia, pulmonary infarction and malignant tumour formation as well as tissue sample of normal lung. The images have been taken and reconstructed in accordance to the method reported by Jacques and Lee (Lasers in surgery: advanced characterization, therapeutics, and systems VIII: polarized video imaging of skin. In: SPIE. BiOS '98 international biomedical optics symposium, vol 3245, San Jose, CA, USA, 1998. https://doi.org/10.1117/12.312307). Tissue polarimetry has been also used to study the above-mentioned biological samples. The experimental set-up working in reflectance geometry consisted of a DPSS LASER with wavelength of 635 nm, which passes through linear polarizer, quarter wave-plate and focusing lens before reaching the biological sample at illumination angle of 45°. Basic polarimetric parameters such as azimuth, angle of ellipticity, degree of polarization and illuminating power were measured and used to evaluate the change in the polarisation state of the incident light after interaction with the biological samples.

Keywords Polarized optical microscopy · Tissue polarimetry

A. Stoilova (✉)
Department of Physics, University of Chemical Technology and Metallurgy, Sofia, Bulgaria

Institute of Optical Materials and Technologies, Bulgarian Academy of Science, Sofia, Bulgaria

D. Nazarova · B. Blagoeva · V. Strijkova
Institute of Optical Materials and Technologies, Bulgarian Academy of Science, Sofia, Bulgaria

P. Petkov
Department of Physics, University of Chemical Technology and Metallurgy, Sofia, Bulgaria

P. Petkov et al. (eds.), *Nanoscience and Nanotechnology in Security and Protection against CBRN Threats*, NATO Science for Peace and Security Series B: Physics and Biophysics, https://doi.org/10.1007/978-94-024-2018-0_39

39.1 Introduction

Polarized light is used for many purposes in the medicine. It is utilized in sensing devices for non-invasive blood glucose level measurement [2] or nerve fiber thickness measurement [3], in optical imaging systems as a tool for diagnostic pathology through visualization of birefringent structures in the human body, e.g. collagen [4] or metabolites in blood serum [5], or by clinical treatment of dermal burns, diabetic ulcers as well as by musculoskeletal injuries [6]. When the light is polarized, it can penetrate deeper into the human tissues and is safer to be used because of the reduced light emitted energy [7]. Nowadays, the challenges by using polarized light in the medicine are related to improving the sensitivity of the sensing elements, increasing the contrast of the images or explaining the mechanism of its healing effect. The latter is supposed to be due to conformational changes of the lipid bilayer in the cell membrane, which may influence the energy production of the cell, the immune processes and the enzyme reactions [7].

To visualize skin lesions at higher contrast Jacques and Lee reported in 1998 the follow described approach for processing of images obtained with polarized light [1]. They used an optical system including a light source, a polarizer for parallel linear polarization of the incident light to the source/sample/camera plane, an analyzer placed in front of a CCD camera, which was rotated to allow imaging of the light polarized in planes parallel (P_{par}) and perpendicular (P_{per}) to the polarization plane of the incident light. The specular reflectance from the glass/skin interface was reflected obliquely and missed the camera. From P_{par} and P_{per} images they obtained a final, reconstructed image P_{pol} using the following equation: $P_{pol} = (P_{par} - P_{per})/(P_{par} + P_{per})$ [1]. P_{pol} enables superficial imaging since the light single scattered elastically from the tissue superficies retains the polarization orientation of the incident light and vice versa the light returning from deeper tissue layers is multiple scattered and as a consequence the polarization is randomized. In this equation the numerator subtracts out the randomly polarized light due to multiple scattering processes, which the light beam undergoes penetrating deeply in the skin layers. The denominator takes the sum of the two acquired images, equivalent to a normal white light image. The resulting polarization picture has a higher contrast to the superficial skin layer than simple total reflectance images [8].

The approach proposed by Jacques and Lee is mostly developed for visualization of changes in the cell morphology due to malignant tumour formation aiming the detection of cancer at an early stage. Here we applied this method to human lung tissue samples with pathological changes caused by anthracosis, tuberculosis, influenza pneumonia, pulmonary infarction and cancer as well as to normal lung specimen. Our idea was to check if characteristic tissue structure changes caused by non-cancer diseases can be also imaged with improved contrast.

The paper presents also the results from polarimetric measurements of the tissues as another method for assessment of histological specimen. For evaluating the state of light polarization after interaction with the biological sample, the Stokes-Mueller matrix formalism has been applied [9–11]. The Mueller matrix polarimetry

represents a label-free technique, which can be easily combined with optical imaging equipment such as endoscope and microscope [12], therefore it is actively developed in the last years for surgical and diagnostic applications by malignant tumours [13–15].

39.2 Experiment

39.2.1 Polarized Light Imaging

In our experiments a Zeta-20 Optical Microscope (Zeta Instruments) operating in reflection mode was used. Objective lenses with 5× magnification and numerical aperture NA = 0.15 were chosen to obtain the images presented in Fig. 39.1.

39.2.2 Optical Set-Up for Measuring the Polarization Parameter

For measuring the azimuth (θ), the angle of ellipticity (χ), the degree of polarization (DOP) and the illuminating power we used a standard experimental set-up working in reflectance mode [14]. It consists of a light source, a DPSS LASER at wavelength of 635 nm, a linear polarizer, a quarter wave-plate for circular polarization, a focusing lens, a biological sample and a polarization analyzing system (Thorlabs polarimeter PAX5710VIS-T) [16]. The angle between the sample and the incident light was 45°. The azimuth and the angle of ellipticity were determined with an accuracy of ±0.25° and the degree of polarisation was measured with an accuracy of ±0.50%. Each sample was probed at three points for 15 s. The polarimeter was set to obtain 3.33 measurements per second, thus providing 50 values for each of the measured quantities.

39.2.3 Tissues Samples

Science kits containing hematoxylin and eosin stained human lung histological specimens were purchased from Konus Italia Group S.p.a. The tissue samples were formalin-fixed and paraffin-embedded, thinly sectioned, stained and placed between microscope slides.

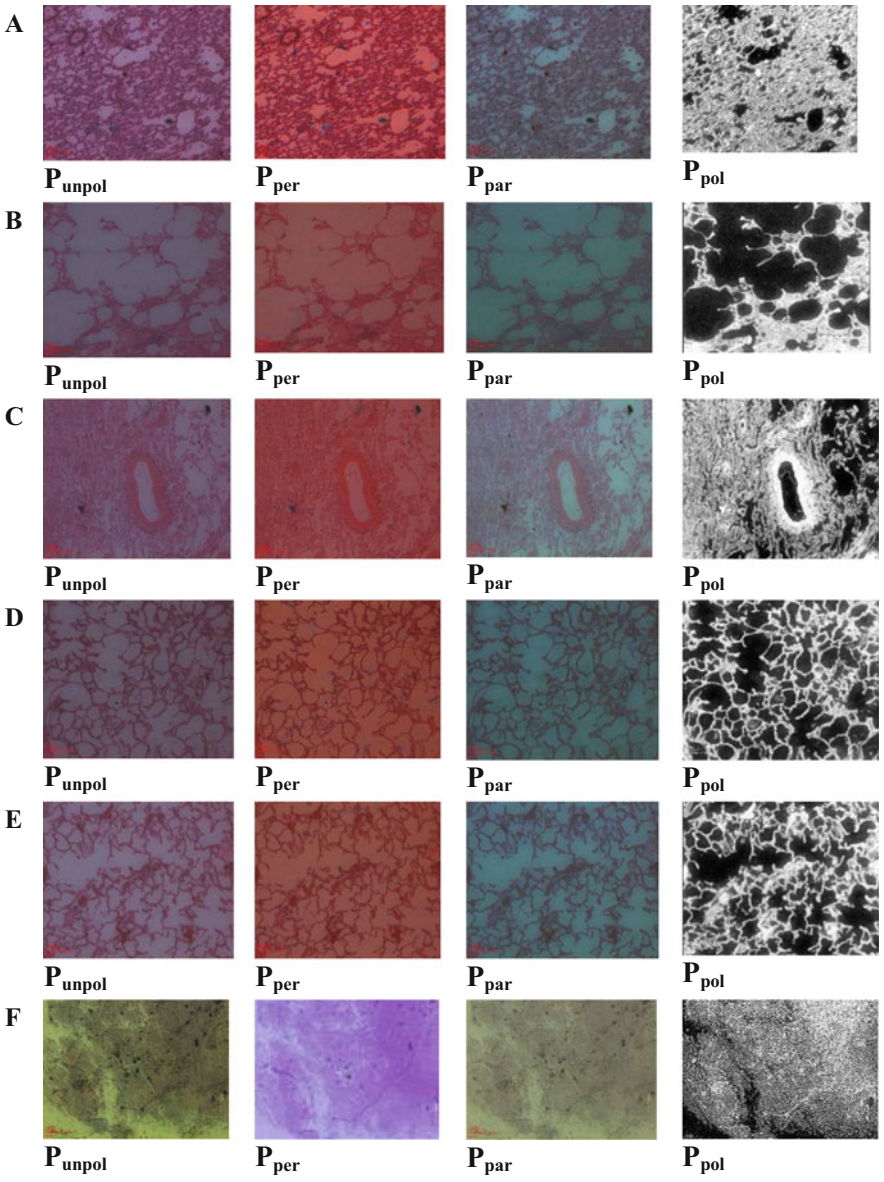

Fig. 39.1 Images of the samples: (**a**) normal lung tissue; Pathological changes in human lung tissue caused by (**b**) anthracosis, (**c**) tuberculosis, (**d**) influenzal pneumonia, (**e**) pulmonary infarction and (**f**) cancer taken with unpolarized light (P_{unpol}), with light polarized at 90° (P_{per}), with light polarized at 180° (P_{par}), and finally the reconstructed image (P_{pol})

39.3 Results

Figure 39.1 presents the images of the samples taken and reconstructed in accordance to the approach proposed by Jacques and Lee. For comparison images taken with unpolarized light are also presented. It can be seen that on the reconstructed images more details of the tissue are distinguishable. Diffuse alveolar damages, necrotic epithelial cells, hyperchromatic nuclei, presence of granulomas, anthracotic pigments and deposited collagen are more clearly identified in these images.

Figure 39.2 presents the results from the polarimetric measurements. Figure 39.2a shows a slightly change of the angle of ellipticity (χ) after interaction of the incident light with the tissue samples as this trend is more clearly expressed by the samples with pathological changes. Considering the azimuth (θ) in Fig. 39.2b, the values for all the samples are positive and assembled between 52° and 80°. The change in the θ values is higher for the lung tissue with pathological changes caused by pulmonary infarction.

From Fig. 39.2c it can be concluded that the samples with pathologies, except the sample with pathological changes caused by pulmonary infarction, scatter less the incident light, as the beam illuminating power decreases much more after interaction with the normal lung tissue, which means that the samples with histopathological

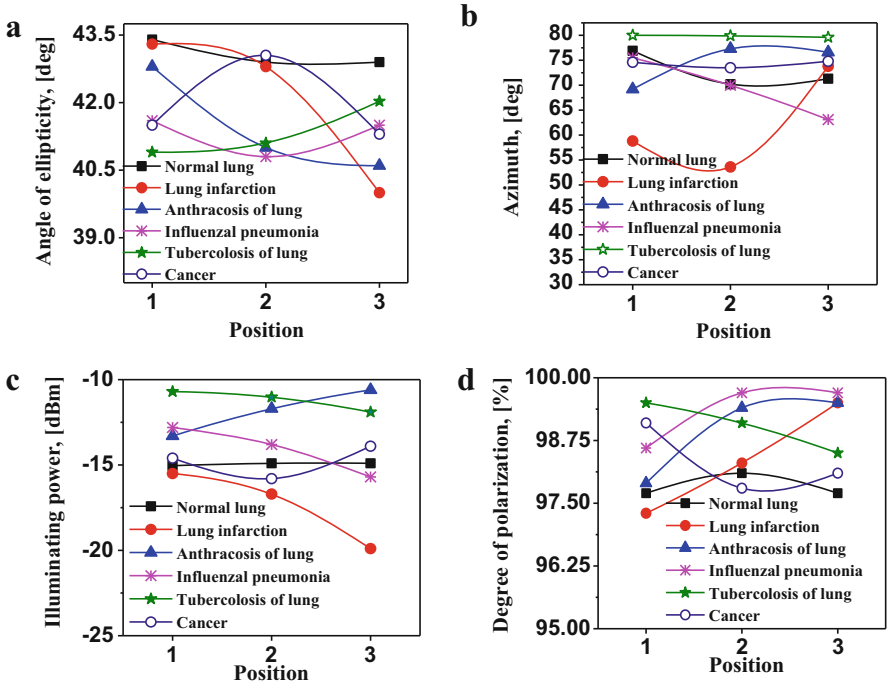

Fig. 39.2 Experimental results from tissue polarimetric study: (**a**) angle of ellipticity; (**b**) azimuth; (**c**) illuminating power; (**d**) degree of polarization

changes are optically more homogeneous than the healthy tissue. Figure 39.2d shows that the normal lung tissue depolarizes the incident light more strongly than the samples with pathologies. Similar behavior has been observed by other authors for cancerous epithelial structures and attributed to the lower optical anisotropy of the malignant tumor cells as a result of the reduced amount in collagen [14, 17]. The values of all polarimetric parameters obtained for the sample with pathological changes caused by pulmonary infarction show larger fluctuations in comparison to the other samples studied.

39.4 Conclusions

In this work the phenomenology of light interaction with different lung tissue pathologies caused by cancer and non-cancerous related diseases was presented. Polarized light has been used for visualization of the morphological changes in human lung specimens due to anthracosis, tuberculosis, influenzal pneumonia, pulmonary infarction and malignant tumor formation as well as in tissue sample of normal lung. The images, reconstructed in accordance to the method proposed by Jacques and Lee, have shown an enhanced contrast. For more detailed interpretation and understanding of the images, they have to be discussed by a medical specialist. Tissue polarimetry has been also applied to study the transformation of the light polarization state after interaction with the histological samples. The outcome of this measurement reveals that the angle of ellipticity, the azimuth, the illuminating power and the degree of polarization could be used to discriminate among different tissue pathologies, although this study is still in its early stage.

Acknowledgments This work is financially supported by UCTM, contract № 11923.

References

1. Jacques SL, Lee K (1998) Lasers in surgery: advanced characterization, therapeutics, and systems VIII: polarized video imaging of skin. In: SPIE. BiOS '98 international biomedical optics symposium, 1998. San Jose, CA, USA, vol 3245. https://doi.org/10.1117/12.312307
2. Purvinis G, Cameron B, Altrogge D (2011) Noninvasive polarimetric-based glucose monitoring: an in vivo study. J Diabetes Sci Technol 5(2):209–211. https://doi.org/10.1177/193229681100500227
3. Kasprzak J, Samsel D, Borkowska A, Kecik M (2011) Optical diagnostic in medicine – needs and possibilities. Acta Phys Pol A 120:678–685. https://doi.org/10.12693/aphyspola.120.678
4. Wolman M (1975) Polarized light microscopy as a tool of diagnostic pathology. J Histochem Cytochem 23:21–50. https://doi.org/10.1177/23.1.1090645
5. Savina L, Pavlishchuk S, Samsygin V, Bolotova E, Gotovtseva L, Chekmareva S, Nuzhnaia I (2003) Polarization microscopy in diagnosis of metabolic disorders. Klin Lab Diagn 3:11–14
6. Feehana J, Burrowsa S, Corneliusa L, Cooka A, Mikkelsenc K, Apostolopoulosc V, Husarica M, Kiatosa D (2018) Therapeutic applications of polarized light: tissue healing and

immunomodulatory effects. Maturitas 116:11–17. https://doi.org/10.1016/j.maturitas.2018.07.09
7. Fenyö M (1984) Theoretical and experimental basis of biostimulation by laser irradiation. Opt Laser Technol 16:209–215. https://doi.org/10.1016/0030-3992(84)90029-x
8. Jacques S, Roman J, Lee K (2000) Imaging superficial tissues with polarized light. Lasers Surg Med 119–129. https://doi.org/10.1364/bosd.2000.sug2
9. Azzam R, Bashara N (1977) Ellipsometry and polarized light. Elsevier, Amsterdam, p 148
10. Le Roy-Brehonnet F, Le Jeune B (1997) Utilization of Mueller matrix formalism to obtain optical targets depolarization and polarization properties. Prog Quantum Electron 21:109–151. https://doi.org/10.1016/S0079-6727(97)84687-3
11. Ghosha N, Banerjee A, Soni J (2011) Turbid medium polarimetry in biomedical imaging and diagnosis. Eur Phys J Appl Phys 54. https://doi.org/10.1051/epjap/2011110017
12. Liu T, Sun T, He H, Liu S, Dong Y, Wu J, Ma H (2018) Comparative study of the imaging contrasts of Mueller matrix derived parameters between transmission and backscattering polarimetry. Biomed Opt Express 9:4413–4428. https://doi.org/10.1364/boe.9.004413
13. Backman V, Wallace M, Perelman L, Arendt J, Gurjar R, Müller M, Zhang Q, Zonios G, Kline E, McGillican T, Shapshay S, Valdez T, Badizadegan K, Crawford J, Fitzmaurice M, Kabani S, Levin H, Seiler M, Dasari R, Itzkan I, Van Dam J, Feld M (2000) Detection of preinvasive cancer cells. Nature 406:35–36. https://doi.org/10.1038/35017638
14. Ivanov D, Genova-Hristova T, Borisova E, Nedelchev L, Nazarova D (2018) International conference and school on quantum electronics: laser physics and applications: multiwavelength polarimetry of gastrointestinal ex vivo tissues for tumor diagnostic improvement. In: Proceedings of Spie, vol 11047, pp 1–8. https://doi.org/10.1117/12.2516645
15. Qi JJ, Elson D (2017) Mueller polarimetric imaging for surgical and diagnostic applications: a review. J Biophotonics 10:950–982. https://doi.org/10.1002/jbio.201600152
16. Thorlabs, Operation Manual, Polarization Analyzing System: PAX5710/PAX5720 VIS/IR1/IR2/IR3
17. Giakos G, Marotta S, Narayan C, Petermann J, Shrestha S, Baluch J, Pingili D, Sheffer D, Zhang L, Zervakis M, Livanos G, Kounelakis M (2011) Polarimetric phenomenology of photons with lung cancer tissue. Meas Sci Technol 22:114018. https://doi.org/10.1088/0957-0233/22/11/114018

Chapter 40
Melanoma Cells Uptake and Hyperthermia Tests of Iron-Based Magnetic Nanoparticles

Luiza-Izabela Jinga, Gianina Popescu-Pelin, Cristian Mihailescu, Livia E. Sima, Victor David, and Gabriel Socol

Abstract The aim of this study was to synthesize iron oxide/silica core-shell nanoparticles (NPs) loaded with Doxorubicin (Dox) as hyperthermia-controlled drug delivery vehicles for cancer treatment. Simple and core-shell nanoparticles were evaluated with respect to their performances in the magnetic hyperthermia tests. The chemical composition and the morphological features of the magnetic nanoparticles were investigated by X-ray photoelectron spectroscopy (XPS) and high-resolution scanning electron microscopy (HRSEM). Preliminary flow cytometry and enhanced darkfield hyperspectral microscopy analyses revealed the ability of Dox-loaded core-shell magnetic nanoparticles to be uptaken by A375 human melanoma cells.

Keywords Hyperthermia · Iron oxide nanoparticles · Core-shell · Melanoma

40.1 Introduction

Nowadays, magnetic hyperthermia has attracted significant attention as an alternative method for cancer therapy. In the presence of radiofrequency (RF) magnetic field, the magnetic nanoparticles generate heat, which increase the temperature in

L.-I. Jinga
National Institute for Lasers, Plasma and Radiation Physics, Bucharest-Magurele, Romania

Faculty of Chemistry, University of Bucharest, Bucharest, Romania

G. Popescu-Pelin · C. Mihailescu · G. Socol (✉)
National Institute for Lasers, Plasma and Radiation Physics, Bucharest-Magurele, Romania
e-mail: gabriel.socol@inflpr.ro

L. E. Sima
Institute of Biochemistry of the Romanian Academy, Bucharest, Romania

V. David
Faculty of Chemistry, University of Bucharest, Bucharest, Romania

P. Petkov et al. (eds.), *Nanoscience and Nanotechnology in Security and Protection against CBRN Threats*, NATO Science for Peace and Security Series B: Physics and Biophysics, https://doi.org/10.1007/978-94-024-2018-0_40

tumors in a controlled manner, killing the tumor cells [1–3]. The surface modification of magnetic nanoparticles plays an important role in the interaction between the nanoparticles and the biological systems [3–5]. In this context, a silica coating not only enhances colloidal stability but also increases the biocompatibility of the nanoparticles. Moreover, surface functionalization of magnetic nanoparticles with anti-tumoral agents is expected to increase significantly the success rate of cancer treatment by hyperthermia [1–4].

40.2 Materials and Experimental

Iron (II) sulfate ($FeSO_4 \cdot 7H_2O$), iron (III) chloride ($FeCl_3$), ammonia solution (25%), Triton X, tetraethyl orthosilicate (TEOS) and ethanol were all purchased from Sigma-Aldrich. Doxorubicin·HCl was purchased from AvaChem Scientific.

Magnetic nanoparticles were obtained by mixing 2:1 molar ratio of $FeCl_3$ and $FeSO_4 \cdot 7H_2O$ solutions in a round bottom flask (Fig. 40.1). After 30 min of stirring, ammonia (NH_3) solution (25%) was added by introducing small droplets with a pipette, Triton-X was subsequently added, and the solution was left to stir one more hour [1]. The precipitate was collected and washed several times to remove the excess of ammonia solution [2]. Afterwards, 520 mg of the lyophilized powder was mixed with 20 mL ammonia solution 25%, 160 mL ethanol and 7 mL tetraethyl orthosilicate (TEOS). The suspension was allowed to react at room temperature for 18 h. After the reaction, the precipitate was collected with a magnet and washed several times with ethanol and water.

For loading of Doxorubicin (Dox) on the core-shell magnetic-silica nanoparticles, 10 mg of Doxorubicin was stirred for 24 h with 10 mL suspension from the above precipitate in 130 mL ethanol. The drug loading was calculated as a difference between the added and the remaining amount of Dox after the final step of synthesis. The quantity of unloaded drug was determined by UV-Vis spectroscopy, using a calibration curve obtained from the measurement of 12 samples with well-known concentration of Dox. By interpolation, the concentration of the unloaded drug was

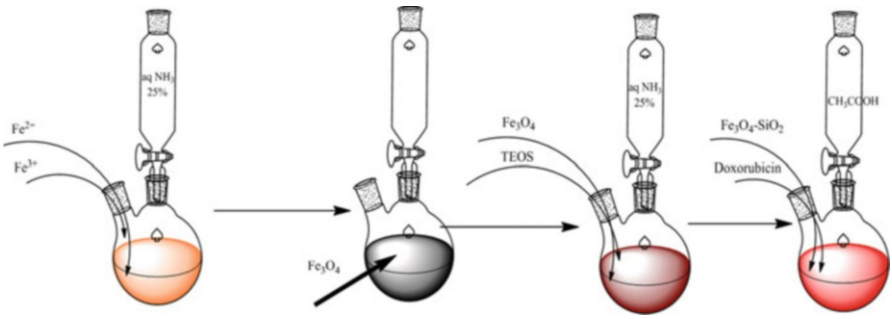

Fig. 40.1 The synthesis of Fe_3O_4, Fe_3O_4-SiO_2 and Fe_3O_4-SiO_2-Dox NPs nanoparticles

estimated to be 8 ppm. Due to the fact that the initial concentration of Dox was 100 ppm, we can conclude that 92 μg of drug was loaded on the nanoparticles.

40.3 Results and Discussion

40.3.1 Characterization of the Samples

HRSEM images of the synthesized Fe_3O_4, Fe_3O_4-SiO_2, Fe_3O_4-SiO_2-Dox NPs nanoparticles show that they are spherical with average size between 18 and 25 nm (Fig. 40.2).

The chemical composition was determined by XPS. The XPS measurements were performed with ESCALAB Xi+ (Thermo SCIENTIFIC Surface Analysis) equipped with a multichannel hemispherical electron analyzer (dual X-ray source) working with Al Kα radiation ($h\nu = 1486.2$ eV) and using C 1 s (284.4 eV) as energy reference. XPS data were recorded on slightly pressed power materials that had been outgassed in the pre-chamber of the setup at room temperature at a pressure of $<2 \times 10^{-8}$ Torr to remove the chemisorbed water from their surfaces. The surface chemical compositions and oxidation states were estimated from the XPS spectra by calculating the integral of each peak after subtraction of the "S-shaped" Shirley-type background using the appropriate experimental sensitivity factors by means of Avantage software (version 5.978).

The presence of carbon, oxygen, silicon and iron was determined by the survey spectra of the samples as shown in Fig. 40.3.

The elemental composition of the iron-based nanoparticles determined by XPS is given in Table 40.1. In the case of the core-shell nanoparticles, the iron composition cannot be detected due to the silica shell. High resolution spectra were taken and deconvoluted for detailed analysis (Fig. 40.4). The deconvolution of the oxygen spectra from Fe_3O_4 NPs shows three peaks, two of them at 529.44 eV and 530.86 eV typical for magnetite and the third peak at 532.47 eV specific for Fe_2O_3 which appears due to the oxidation of the magnetite (Fig. 40.4b). In the agreement with the peaks identified for oxygen, the deconvolution of the iron spectra shows three peaks at 710.01 eV, 712.26 eV and 718.41 eV, the first two are specific for the magnetite phase, whereas the third peak corresponds to Fe_2O_3 (Fig. 40.4a). The spectra of Si

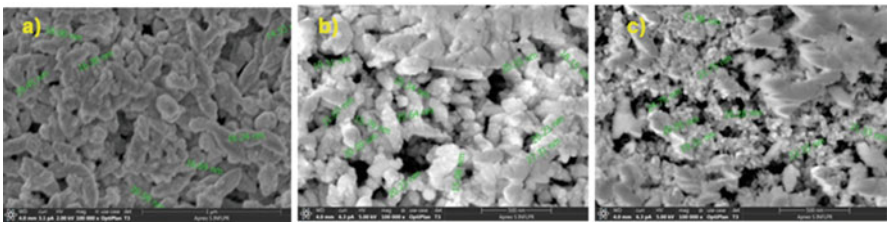

Fig. 40.2 HRSEM images of (**a**) Fe_3O_4, (**b**) Fe_3O_4-SiO_2, (**c**) Fe_3O_4-SiO_2-Dox NPs

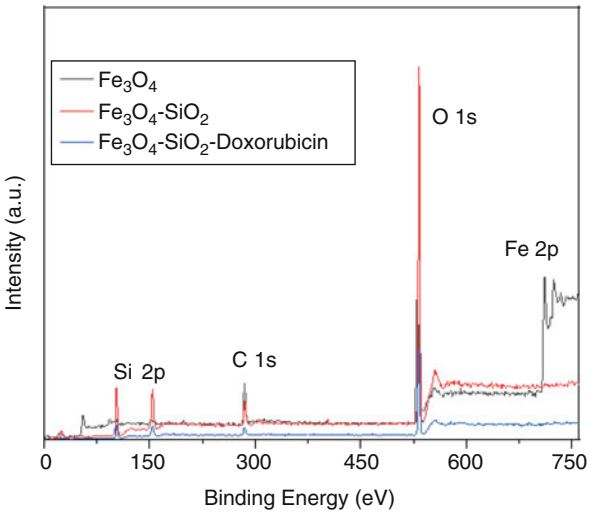

Fig. 40.3 XPS survey spectra of Fe_3O_4, Fe_3O_4-SiO_2 and Fe_3O_4-SiO_2-Dox NPs

Table 40.1 Chemical composition of Fe_3O_4, Fe_3O_4-SiO_2 and Fe_3O_4-SiO_2-Dox NPs as determined by XPS

	Atomic %			
Sample	C (carbon)	O (oxygen)	Iron (Fe)	Silicon (Si)
Fe_3O_4 NPs	36.52	48.82	14.66	–
Fe_3O_4-SiO_2 NPs	18.86	48.15	–	32.59
Fe_3O_4-SiO_2-Dox NPs	17.65	52.31	–	30.04

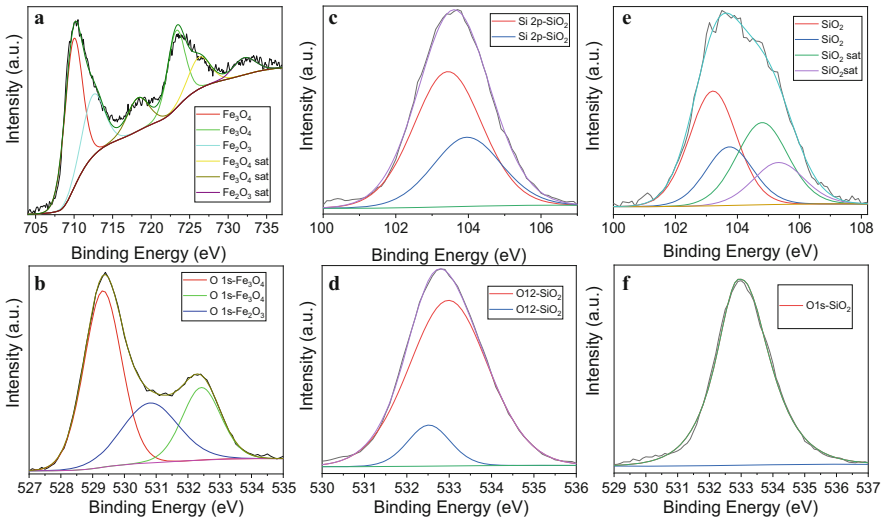

Fig. 40.4 High-resolution XPS spectra of (**a**) Fe 2p, (**b**) O 1 s for Fe_3O_4 NPs; (**c**) Si 2p (**d**), O 1 s for Fe_3O_4-SiO_2 NPs and (**e**) Si 2p, (**f**) O 1 s for Fe_3O_4-SiO_2-Dox NPs

show a peak at 103.43 eV for iron oxide/silica core-shell nanoparticles (Fig. 40.4c) and two peaks at 103.21 eV and 104.8 eV for their counterparts loaded with Dox (Fig. 40.4e). For these samples no peak of iron was found, which indicates that the magnetic nanoparticles are fully covered with a compact layer of silica.

40.3.2 Hyperthermia Tests

Hyperthermia tests were performed with Ultra Heat S Series (RF) with 2 kW maximum output power and a frequency of 322 kHz from UltraFlex Power Technologies apparatus. 3 mL of aqueous suspension based on magnetic nanoparticles are introduced into a Dewar vial, which is further placed inside the water-cooled copper solenoid [6]. The concentration of the nanoparticles was chosen in a way that at the end of the test temperature of 45 °C would be reached in maximum 30 min (Fig. 40.5).

The heating ability of the samples was evaluated by the hyperthermia tests. For the suspensions containing only Fe_3O_4 NPs, the specific absorption rate (SAR) was determined using the following equation:

$$SAR = C\frac{\Delta T}{\Delta t}\frac{m_{water}}{m_{Fe}}$$

where C is the specific heat of water, ΔT the variation of suspension temperature in the time interval Δt, m_{water} and m_{Fe} the mass of the water and Fe_3O_4 nanoparticles, respectively [1]. Consequently, a SAR value of 47 W/g was obtained for this sample. To reduce the cytotoxicity of the nanoparticles we optimized their concentration relative to the heating rate in the hyperthermia tests. Thus, the lowest concentration at which the samples optimally generate heat is 78 μg/mL for the Dox loaded

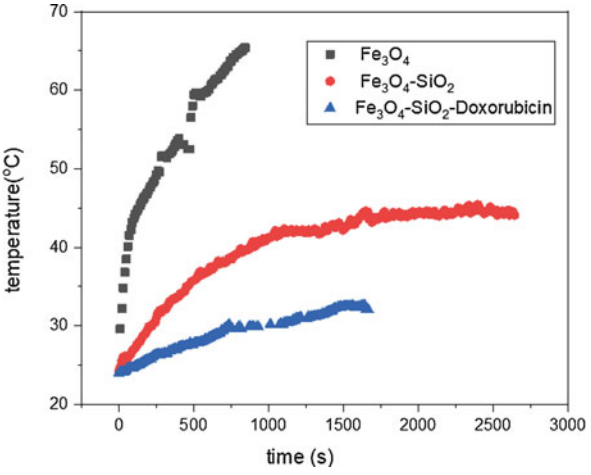

Fig. 40.5 Temperature versus time plots for Fe_3O_4, Fe_3O_4-SiO_2 and Fe_3O_4-SiO_2-Dox NPs

nanoparticles. In the case of core-shell samples, the heating effect is reduced because of the silica shell; the content of the magnetic component for the same concentration of nanoparticles is lower.

40.3.3 Iron NPs Uptake by A375 Human Melanoma Cells

In order to confirm the internalization of magnetic nanoparticles loaded with Dox, flow cytometry on A375 human melanoma cells was performed at 24 h and 48 h after treatment with different nanoparticle concentrations (Fig. 40.6). The study was made by comparing the results of cells treated with pure drug (Dox) with cells treated with magnetite core-silica shell and Dox loaded NPs. The results revealed a dose dependent decrease of the fluorescence signal for cells treated with Dox only, as shown by the decrease of the median fluorescence intensity (MFI) of the cell population. The cells treated with magnetite or silica shell coated magnetite had similar MFI signal

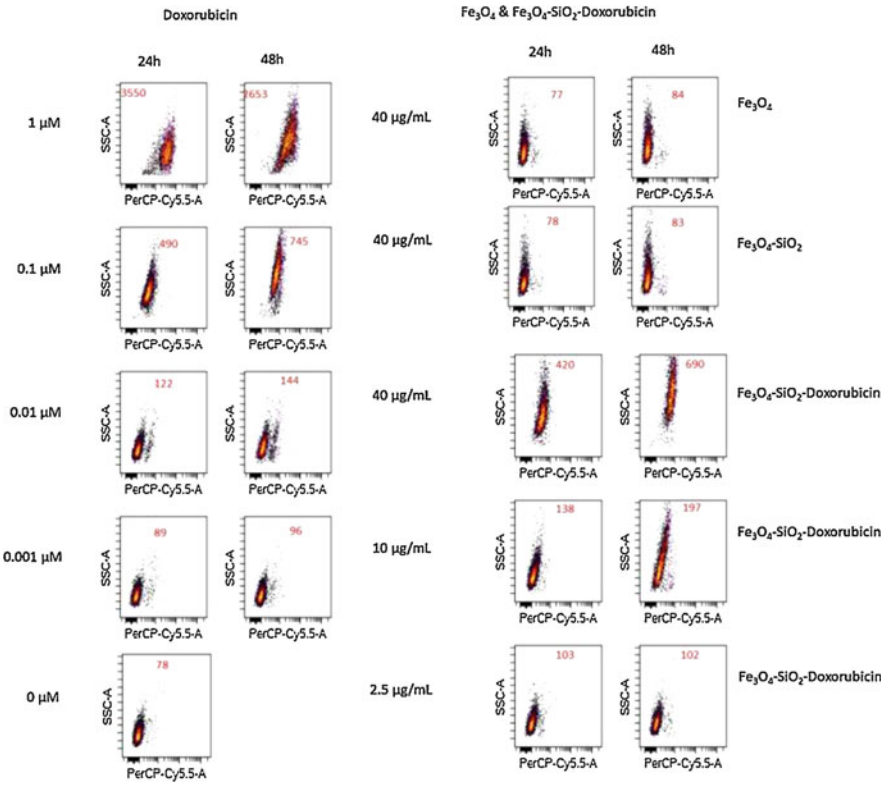

Fig. 40.6 Flow cytometry of Dox internalization (left) and magnetite NPs, magnetite core-silica shell NPs and Dox loaded NPs (right)

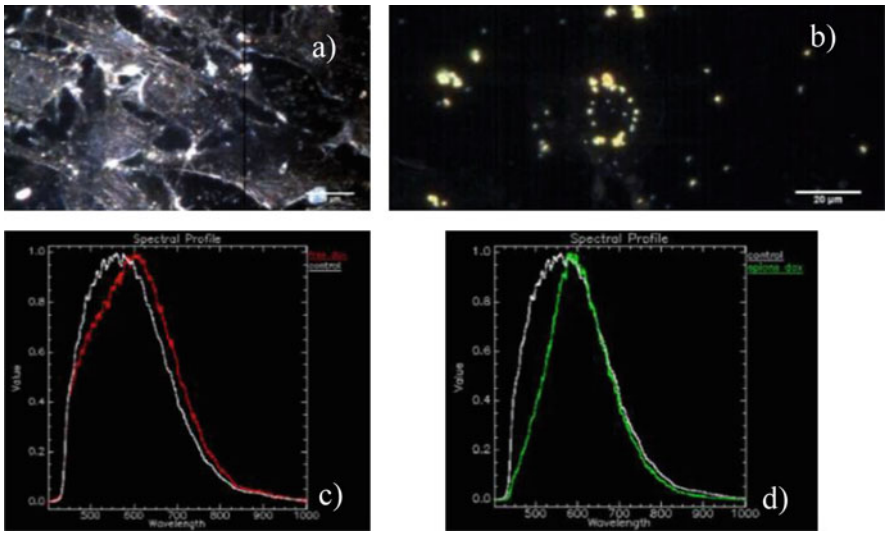

Fig. 40.7 Hyperspectral imaging of A375 melanoma cells: (**a**) treated with free Dox, (**b**) Fe_3O_4-SiO_2-Dox, (**c**) spectral profile of free Dox (**d**) spectral profile of Dox loaded NPs

with untreated cells (MFI between 77 and 84). Melanoma cells treated with 40 μg/mL Dox loaded NPs had a fluorescence signal comparable with that of cells treated with 0.1 μM Dox alone. The drug was still detectable in the cells even upon treatment with as low as 2.5 μg/mL Dox loaded NPs.

Enhanced Darkfield Hyperspectral Microscopy (CytoViva) revealed that the Dox loaded NPs have been uptaken by the melanoma cells (Fig. 40.7b, d) and concentrated around the nucleus, while free Dox was spread in the entire cell. The spectral profiles proved the loading of Dox on the magnetite core-silica shell NPs, as indicated by the 590 nm emission peak shift (Fig. 40.7c, d).

40.4 Conclusions

Magnetic hyperthermia studies revealed that the synthesized magnetite nanoparticles can generate optimal heat in a short period of time even at low concentration. Flow cytometry confirmed that the magnetite/silica core-shell nanoparticles loaded with Dox were internalized by human melanoma cells. Moreover, the flow cytometry results revealed that also by lowering the concentration of the loaded NPs the behavior was the same as for cells treated with a higher concentration of Dox. In addition, the dark field microscopy results showed that the nanoparticles successfully passed through the membrane of the melanoma cells and concentrated around the nucleus.

Acknowledgments This work was financially supported by *The Executive Agency for Higher Education, Research, Development and Innovation Funding* (UEFISCDI), Project No.63 PCCDI/2018 (PN-III-P1-1.2-PCCDI-2017-0728).

References

1. Gawali LS, Madan DP, Barick KC, Somani R, Hassan PA (2018) AIP Publishing, 1942. 040020-1-040020-4
2. Kaaki K, Herve-Aubert K, Chiper M, Shkilnyy A, Source M, Benoit R, Paillard A, Dubois P, Saboungi ML, Chourpa I (2012) Langmuir 28:1496–1505
3. Abenojar EC, Wichramasinghe S, Bas-Concepcion J, Samia AC (2016) Prog Nat Sci Mater Int 26:440–448
4. Akbarzadeh A, Mikaeili H, Mohammad R, Barkhordari A, Davaran S (2012) Int J Nanomedicine 7:511–526
5. Li Z, Kawashita M, Araki N, Mitsumori M, Hiraoka M, Doi M (2010) Mater Sci Eng C 30:990–996
6. Grumezescu V, Gherasim O, Negut I, Banita S, Holban AM, Florian P, Icriverzi M, Socol G (2019) Materials 12(16):E2521

Index

P. Petkov et al. (eds.), *Nanoscience and Nanotechnology in Security and Protection against CBRN Threats*, NATO Science for Peace and Security Series B: Physics and Biophysics, https://doi.org/10.1007/978-94-024-2018-0